Université Catholique de Louvain

De Duve Institute

Cell biology unit

Lipid domains in erythrocytes: mapping, biophysical properties and contribution to calcium exchanges

Louise CONRARD

Promoter: Donatienne TYTECA

Thesis for the PhD degree in Biomedical and Pharmaceutical Sciences

Jury members

Prof Jean-Baptiste DEMOULIN (president)

Université Catholique de Louvain

Prof Donatienne TYTECA (promotor)

Université Catholique de Louvain

Prof Maria VEIGA-DA-CUNHA

Université Catholique de Louvain

Prof Patrick GILON

Université Catholique de Louvain

Prof Giulio MUCCIOLI

Université Catholique de Louvain

Prof Magali DELEU

Université de Liège

Prof Lars KAESTNER

Saarland University

Remerciements

Voici que j'approche de la ligne finale de ce parcours doctoral… Et dans le rush des dernières heures, il est temps de prendre quelques minutes pour regarder en arrière et quelques lignes pour remercier toutes les personnes qui ont contribué de près ou de loin, de manière scientifique ou personnelle, à la réussite de cette thèse.

Tout d'abord, merci à ma promotrice, Donatienne, pour toutes ses qualités de chef de labo. Merci pour ta disponibilité, restée inchangée au fil des 6 dernières années malgré l'élargissement considérable de ton équipe. Merci pour ton enthousiasme très communicatif et ta capacité à continuer à t'émerveiller devant des images microscopiques de globules rouges. Merci pour ta confiance et merci d'avoir respecté et de t'être adaptée à mon rythme de travail parfois très phasique et aléatoire. Merci également d'avoir compris mon intérêt pour les échanges internationaux : merci de m'avoir donné l'opportunité de partir en congrès à plusieurs reprises et de collaborer avec différentes équipes. Ces échanges font la richesse du monde scientifique et du parcours doctoral et ils m'ont été extrêmement stimulants, tant professionnellement que personnellement. Je te souhaite tout le meilleur pour la suite de ta carrière académique, qui ne peut s'annoncer que brillante de par ton énorme l'investissement. Tu as réunis sous ton chef une équipe bourrée de qualités scientifiques, dont tu sais tirer le meilleur, mais aussi de qualités personnelles, que je ne peux que t'inviter à prendre le temps de découvrir de temps à autre.

Merci aux membres du jury qui m'ont accompagnée au fil de ces quatre années. Merci pour votre investissement et tout l'intérêt que vous avez porté à mon projet, pourtant parfois très éloigné de vos propres recherches. Merci d'avoir rendu chacune de nos rencontres pleines de challenges mais surtout très stimulantes et enrichissantes. Un merci particulier à Maria Veiga-da-Cunha, avec qui nous collaborons régulièrement, pour sa disponibilité, sa gentillesse et son expertise dans la purification de nos sondes lipidiques.

Merci aux deux membres externes qui se sont déplacés pour ma défense de thèse privée pour y apporter leur expertise. Merci au professeur Magali Deleu, pour son regard avisé sur les techniques développées dans cette thèse. Merci au professeur Lars Kaestner, une référence dans le milieu des globules rouges et dont le travail est d'ailleurs cité un nombre très important de fois dans ce manuscrit, pour son œil expert et les discussions constructives qu'il a amené lors de la défense.

Ensuite, merci à toutes les personnes avec lesquelles j'ai eu la chance de travailler ces dernières années. Merci à Andra et Mégane, du groupe de David Alsteens, grâce

auxquelles j'ai eu l'occasion de découvrir la microscopie à force atomique, avec ses infinies possibilités mais aussi ses challenges. Merci à Andra qui a répondu à mes panoplies de questions avec gentillesse et beaucoup de pédagogie. Merci à Patrick Van Der Smissen, que j'ai appelé à l'aide un nombre incalculable de fois lors d'expériences en microscopie, pour des bugs techniques ou pour combler mon incompétence, et qui a toujours répondu avec un humour déstabilisant. Merci à Jan, du Max Planck Institute, qui m'a initié à la spectroscopie à corrélation de fluorescence à Berlin. Merci à Emmanuel, du Victor Babes Institute, dont l'expertise en microscopie électronique nous a offert des possibilités infiniment excitantes à Bucarest et dont j'espère que le groupe saura tirer profit dans les années futures. Merci à Serena dont la collaboration m'a permis de garder un pied dans ces fameuses préparations DRMs tout en m'initiant à leur utilisation en neurosciences. Merci à tous les infirmier(/ère)s du service prise de sang de Saint-Luc qui voient débarquer la Lido-team chaque semaine depuis des années, à ceux/celles qui suivent les avancées du projet et à ceux dont l'humour laisse perplexe.

Merci aux chefs des autres groupes formant l'unité CELL. Un énorme merci à Patrick Henriet qui m'a été d'une aide précieuse au moment où je me suis lancée dans la biomol mais où la biomol n'a pas voulu de moi (et me l'a fait clairement comprendre). Merci d'avoir persévéré dans ce projet sans douter de mes capacités à réaliser une simple ligation au moment où moi-même j'étais prête à abandonner. Merci pour tout l'humour et la bonne humeur que tu distilles, merci pour ton accessibilité et la facilité d'échanger sur tous les domaines. Merci à Christophe Pierreux, dont l'esprit scientifique acéré et la rigueur en font un chef de labo dont le regard critique est très précieux. Le tout associé à un réel souci des membres de l'unité et à une volonté de maintenir l'harmonie et le bien-être au sein de la plateforme. Merci à Etienne Marbaix pour sa gentillesse bienveillante.

Merci à ma Lido team chérie, que j'ai vu s'agrandir et se renouveler au fil des années sans que l'esprit d'équipe et la bonne ambiance ne soit changée. Dans l'ordre des personnes rencontrées, merci à Mélanie tout d'abord, qui m'a encadré lors de mon mémoire et dont la rigueur dans le boulot comme dans la vie personnelle en fait un exemple impressionnant. Le tout allié à une bonne humeur extrêmement communicative et une envie de découverte de l'autre et du monde. Merci pour les milliards de discussions « voyage » échangées, les rêves d'évasion, et surtout les séjours randonnées partagés au Canada, en Belgique, en France ou tout récemment en Italie.

Merci à Hélène, qui aura été la collègue de choix avec laquelle j'aurai partagé la plus grande période au sein de la Lido-team. Merci pour ta disponibilité à tout moment pour régler un problème technique, rediscuter tout un chapitre de science

fondamentale, ou surtout échanger sur une panoplie de sujets non-scientifiques... Nos centres d'intérêts radicalement opposés et ta capacité à t'intéresser à tous les domaines ainsi qu'à transmettre tes passions ont rendu ces échanges extrêmement enrichissants pour moi, j'en ai même adopté la Kpop ☺. En plus de tout ça, merci d'avoir été une confidente avec une écoute attentive sans jamais aucun jugement pour toutes mes (més)aventures des 6 dernières années. J'ai hâte de suivre ta carrière d'illustratrice !

Merci à Anne-Sophie qui, d'une grande timidité à ses début dans l'équipe, a laissé éclore une personnalité tellement riche, avec un humour décapant et toujours bien placé, mais aussi beaucoup d'attention envers les personnes qui l'entourent et un grand sens de l'esprit d'équipe. Merci d'avoir veillé au bien-être de Myrtille pendant ces derniers mois au labo ! La poigne de fer que tu tiens sur tous les membres de la Lido-team (ou presque) ainsi que ta capacité à boucler une thèse en deux ans font de toi un très bon leader pour ce bureau, il ne te manque plus qu'à installer GraphPad pour finaliser ☺.

Merci à Amaury, le meilleur mémorant dont j'aurais pu rêver☺. Ça a été un grand honneur pour moi de passer de « marraine de baptême étudiant » à « marraine de labo » et j'espère avoir été meilleure dans ce dernier rôle. Un immense merci pour tout l'investissement que tu as mis dans notre projet, mais aussi et surtout merci pour la grande cohésion d'équipe que tu apportes au Lido. Cette capacité que tu as de réunir les gens autour d'un sentiment d'unité font de toi un énorme atout pour cette équipe. Je suis ravie de te « léguer » ma place de doctorante au sein de la Lido team, où je sais que tu feras une très belle thèse de par ta volonté et tout ton investissement. Tu peux croire en toi, tu recèles de qualités précieuses !!

Merci à Mauriane (ou Maurianne ? Qui sait vraiment comment l'épeler…), que nous avons recueilli dans notre équipe il y a un an et qui s'est extrêmement facilement intégrée ; et ce malgré son rejet de l'adoration fondamentale pour les globules rouges qui était normalement un prérequis dans la Lido team ☹. Merci pour ta motivation, ton sens de l'humour, tous les potins (parfois tellement fous qu'on pourrait croire qu'ils ont été revisités par certaines personnes !) que tu as apporté dans l'équipe, ainsi que ton talent de monteuse vidéo impressionnant !

Merci à Maxime, technicien qui s'était perdu au fond d'un couloir et qui finalement s'est fondu dans notre équipe grâce à des qualités indispensables : de l'esprit d'équipe, un sens de la papote aiguisé et une disponibilité en tout temps pour faire des pauses ☺. Blague à part, merci également pour les précieux coups de main comptage !

Merci à Marine, dernier padawan de l'équipe qui trace sa route vers tous les honneurs du mémoire, tout en trouvant le temps de nous produire du sujet pour les séances potins ! Merci pour ta naïveté adorable, ton auto-dérision, ton intérêt pour les personnes qui t'entourent et ton enthousiasme scientifique qui te pousse à vouloir comprendre même la moindre statistique normalisée !

En dehors de la Lido team, merci à chacun des membres de l'unité CELL avec qui j'ai pu partager quelques semaines/mois/années. Le renouvellement fréquent des équipes dans la recherche académique m'auront donné l'occasion de côtoyer pas mal de monde autour de la table de midi qui aura souvent été trop petite. Des échanges passionnants, des moments de partage et de rire, ainsi que des activités team-building avec toujours énormément de bonne humeur auront rythmé ces quelques années. Merci à tous ceux qui y ont participé !! Un merci particulier aux deux poumons de l'unité, Catherine et Charlotte, qui veillent chaque année à la bonne gestion des espaces communs du labo ainsi qu'à l'organisation de team-buildings diversifiés et excitants !

Au-delà de mes collègues et collègues-devenus-amis, il y a également quelques personnes très importantes que j'aimerais remercier pour tout le soutien affectif et moral qu'ils m'ont apporté pendant cette thèse.

Il est difficile de trouver suffisamment de mots pour remercier mes parents dont l'incroyable disponibilité, générosité et sens de la famille ont été précieux à chacune des étapes de cette thèse et de ma vie. À mon papa, dont la rigueur et la persévérance s'allient à une certitude rassurante que tout ne peut que bien se passer et à beaucoup de sagesse. À nos twists endiablés qui ont rythmé les premiers mois de cette année. À ma maman, qui m'a appris à quel point il était important d'équilibrer et d'harmoniser les différents pans de la vie. Pour ta douceur, ton écoute attentive et toute l'humanité avec laquelle tu appréhendes et rebondis à chaque épreuve. Aux nuits passées à la belle étoile des déserts jordaniens. Un merci infini à tous les deux pour votre soutien infaillible et tout votre investissement dans ma panoplie de projets.

Merci à mes sistahs licornettes, qui affrontent leurs tempêtes personnelles avec courage et détermination ; tout en étant énormément présentes pour célébrer les joies de cette année à mes côtés. À Marie, dont l'organisation et l'investissement impressionnant dans ses projets en font un leader exemplaire. À Alice, qui place sa famille et son rôle de future tatie au centre de ses priorités. Merci encore d'avoir été des témoins exceptionnelles pour l'aventure du mois d'avril et d'être présentes au quotidien.

Merci à Marie-Claude et Jo, qui m'ont accueilli dans leur petite famille avec énormément de chaleur et de douceur. Merci pour tout votre soutien dans cette thèse mais aussi et surtout dans tous les projets que nous menons sur le côté. Merci infiniment pour votre disponibilité et votre bienveillance exceptionnelle. Nous ne pourrions pas être mieux entourés dans tous nos défis actuels !

Merci à tous les amis et copains avec lesquels j'ai partagé des jeudredis mojitos, des voyages et des aventures, des folles soirées et des calmes après-midi jeux de société pendant ces 4 dernières années. Un merci particulier aux amis avec lesquels j'ai suivi le même parcours. Merci mon acolyte de toujours, Benoit. De nos siestes de lendemain de veille en auditoire jusqu'au bout de cette thèse, tu auras été un ami exceptionnel sur lequel j'ai toujours pu compter. Merci pour ton humour (parfois nul), ta capacité d'adaptation et ta disponibilité, que ce soit pour s'amuser ou donner un coup de main. Merci pour les dizaines (centaines ?) de temps de midi/pauses café/mojitos (avec ou sans alcool)/soirées hors labo partagés. Merci également à Sandrine, d'une amitié scellée à Montréal il y a quelques années, tu es restée une amie dont la franchise et la non-prise-de-tête sont précieuses. Merci pour les aventures partagées en congrès dans des villes plus ou moins excitantes☺. Merci à Mathilde, qui vient finaliser le trio Montréal, et qui est de loin la doctorante la plus méritante d'obtenir sa thèse ! Nos city-trips annuels auront rythmé cette thèse et il y a peu de personnes avec qui je peux voyager aussi facilement que vous deux.

Enfin, merci à mon meilleur co-équipier et partenaire de vie, mon mari, Lucas. T'avoir à mes côtés est une chance incroyable. Tu illumines mon quotidien et avec toi, les (très, parfois trop) nombreux défis de cette folle année deviennent relevables. Un immense merci pour tout le soutien que tu m'as apporté, des premiers jours de préparation FRIA à l'écriture de la dernière ligne de cette thèse, et qui m'aura été extrêmement précieux cet été. Merci pour ton énorme investissement dans notre couple et dans notre petite famille en construction. À nous deux ; aux sommets qui nous semblent encore inatteignables mais que nous allons franchir ensemble; à « Myrtille » ; et à toutes les superbes aventures qui nous attendent.

Table of contents

Abbreviation list

AA	Arachidonic acid
AFM	Atomic Force Microscopy
Ca^{2+}	Calcium ion
$[Ca^{2+}]_{ER}$	Calcium concentration in the endoplasmic reticulum
$[Ca^{2+}]_{ic}$	Calcium intracellular concentration
Ca_V channel	Calcium voltage-gated channel
Cer	Ceramide
CG	Coarse-grained
CO_2	Carbon dioxide
CRAC	Ca^{2+} release-activated Ca^{2+}
DAG	Diacylglycerol
DPG	Diphosphoglycerate
Epo	Erythropoietin
ER	Endoplasmic reticulum
FRET	Förster resonance energy transfer
GSL	Glycosphingolipid
Hb	Hemoglobin
HC	High curvature
HE	Hereditary elliptocytosis
HS	Hereditary spherocytosis
IP_3	Inositol-1,4,5-trisphosphate
LC	Low curvature
Ld	Liquid-disordered
Lo	Liquid-ordered
LPA	Lysophosphatidic acid
LPC	Lysophosphatidylcholine
LPS	Lysophosphatidylserine
LSCM	Laser scanning confocal microscopy
mβCD	Methyl-β-cyclodextrin
MD	Molecular dynamic
Mg^{2+}	Magnesium ion
MSC	Mechanosensitive channel
MSP	Membrane scaffold protein
Na^+	Sodium ion
NCX	Na^+/Ca^{2+} exchanger
NMR	Nuclear magnetic resonance
NO	Nitric oxide
O_2	Dioxygen molecule

PA	Phosphatidic acid
PC	Phosphatidylcholine
PE	Phosphatidylethanolamine
PG	Phosphatidylglycerol
PI	Phosphatidylinositol
PIP	Phosphatidylinositol-1-phosphate
PIP_2	Phosphatidylinositol-bisphosphate
PLA/C	Phospholipase A/C
PM	Plasma membrane
PMCA	Plasma membrane Ca^{2+} ATPase
PS	Phosphatidylserine
ROS	Reactive oxygen species
SERCA	Sarcoplasmic/endoplasmic reticulum Ca^{2+} ATPase
SM	Sphingomyelin
SMase	Sphingomyelinase
So	Solid-ordered
SOCE	Store-operated Ca^{2+} entry
SR	Sarcoplasmic reticulum
STIM	Stromal interaction molecule
TRP	Transient receptor potential
VGC	Voltage-gated channel

Abstract

Red blood cells (RBCs) are highly deformable cells that are able to go through the narrowest capillaries to deliver oxygen throughout the body. This deformability has been linked to RBC specific features like (i) its biconcave shape; (ii) the viscosity of its cytoplasm; (iii) the strong anchorage of its plasma membrane to a very stable spectrin cytoskeleton; and (iv) the tight regulation of the calcium exchanges. Indeed, intracellular calcium concentration is kept very low in RBCs at resting state thank to a low permeability and an efficient calcium extrusion pump named PMCA (for Plasma Membrane Calcium ATPase). During deformation, mechanically-activated ion channels like Piezo1 will rapidly lead to a significant increase of the intracellular calcium concentration. This will in turn favor the RBC deformation notably by uncoupling the anchorage between the membrane and the cytoskeleton as well as by inducing a local and transient dehydration.

However, the importance for RBC deformation of membrane biophysical properties and lateral heterogeneity of membrane lipids is still poorly understood. As a matter of fact, stable (> min) submicrometric (200-500 nm) lipid domains have been evidenced at the RBC plasma membrane external leaflet by the laboratory. Those domains, which are enriched in cholesterol (chol), sphingomyelin (SM), phosphatidylcholine (PC) or ganglioside GM1 respectively, have been evidenced first thank to the trace insertion of fluorescent lipid analogs at the membrane and then to the decoration of endogenous lipids by specific toxin fragments. As more and more evidences emerge for a role of lipid domains in various cell pathophysiological functions like vesicle release, antigen presentation and cell migration, our laboratory is wondering whether lipid domains could also play a role in RBC deformation.

I started my thesis by characterizing the lipid domains at the surface of resting state RBCs and by establishing a mapping of their coexistence. After that, we confirmed the existence of those lipid domains at the surface of unlabeled RBCs by using atomic force microscopy and studied their biophysical properties. We then simulated RBC deformation thank to stretchable silicon chambers and evaluated the possible involvement of some specific lipid domains in the calcium exchanges that take place during this deformation. Finally, we analyzed the RBCs from a patient suffering of hereditary elliptocytosis to further explore the potential pathophysiological roles of lipid domains and their possible link with calcium exchanges but also with the cytoskeleton-membrane anchorage.

In the first chapter of this thesis, I will first introduce the RBC physiology and the specific features necessary for its remarkable deformability. Among them, a great

interest is given to the plasma membrane calcium exchanges as they represent key contributors for cell deformation. The pathophysiological events associated with RBC deformation impairment, either upon cell senescence or in hereditary membrane fragility diseases, are also explored. After that, an overview of the plasma membrane composition, biophysical properties and organization in lipid domains is given. Finally, I introduce the technical approaches used to study the physiological importance of membrane lipid organization. The second chapter exposes the aims and strategies of the study. It is followed by a chapter resuming the results obtained during this thesis regarding the characterization and possible involvement in deformation of submicrometric lipid domains in healthy and elliptocytotic RBCs. The last chapter discusses the key findings of this study, its strengths and weaknesses, and proposes perspectives to the project. A large discussion section is also given to the hypothetical regulation means of membrane calcium transport proteins by lipids.

CHAPTER I - INTRODUCTION

1. RBC production, function and physiology

Red blood cells (RBCs) are small (~7 µm of diameter) anucleated cells which are the most abundant cell type in the blood (4-6 x10^6 RBCs/µL of blood) (section 1.1.). They ensure the primordial function of dioxygen transport (section 1.2.) thank to their ability to ensure energy supplies and to resist to oxidative aggressions (section 1.3.).

1.1. Erythropoiesis

1.1.1. Generalities

Erythropoiesis is the development of mature RBCs from erythroid stem cells. During foetal development, it successively takes place in the mesodermal cells of the yolk sac, the liver and the spleen, and finally the bone marrow where the production will continue after birth and throughout life (Palis and Segel, 1998). Extramedullary erythropoiesis can however occur when physiologic erythropoiesis cannot work properly in the bone marrow and the hematopoietic stem cells (HSC) have to migrate to other tissues. This is the case in thalassemias, where it represents a compensative mechanism to the ineffective erythropoiesis (Rivella, 2012), and in myelofibrosis, where marrow cells are replaced with collagenous connective tissue fibres (Chunduri et al., 2008), a.o..

Bone marrow is composed of hematopoietic cells, adipose tissue and supportive stromal cells (Travlos, 2006). The marrow is served by numerous blood arteries opening up into venous sinuses near the bone, which lead back to a central longitudinal vein. The hematopoietic microenvironment consists of a reticulin skeleton and adventitial reticular cells which furnish a proper environment for cell differentiation (Travlos, 2006). Erythroid progenitors are organized into a hematopoietic sub-compartment called “erythroid island”. Each island is made up of a central iron-containing macrophage surrounded by maturing erythroid precursors at various stages of development (figure 1.1) (Chasis and Mohandas, 2008). The central macrophage extends cytoplasmic protrusions and its function is to regulate erythroid proliferation, differentiation and enucleation and to clear the pyrenocytes (i.e. small, nucleated cells with a thin rim of cytoplasm) resulting from the enucleation process (Heideveld and van den Akker, 2017).

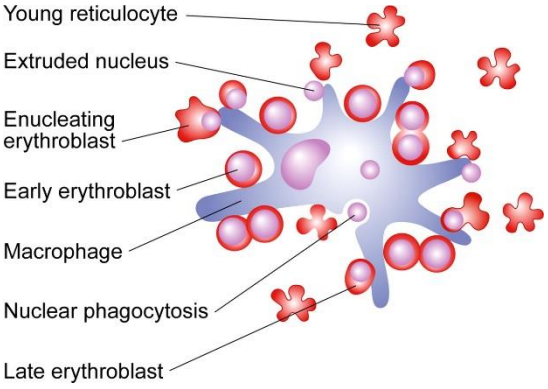

Figure 1.1. Proliferation and differentiation processes occurring within the "erythroid island". See text for information. Reproduced from (Chasis and Mohandas, 2008).

1.1.2. Differentiation steps

Erythroid cells are derived from hematopoietic stem cells (HSCs) (figure 1.2), which are self-renewal cells that are capable of giving rise to all blood cells. They differentiate into immature progenitors which are proposed to still have a great plasticity to potential fates (Dzierzak and Philipsen, 2013). Burst-forming unit erythroid (BFU-E), so-called because of their significant proliferative capacity which results into formation of multi-subunit colonies (i.e. burst), are the first immature lineage-committed erythroid progenitors. BFU-E cells have low numbers of erythropoietin (Epo) receptors (Sawada et al., 1990) but respond to Epo, as well as granulocyte–macrophage colony-stimulating factor (GM-CSF), stem cell factor (SCF) and interleukin-3 (IL-3) (Emerson et al., 1985).

In culture, they differentiate into colony-forming unit erythroid (CFU-E) in 7-9 days (Ramaiah et al., 2018). CFU-E are more differentiated but have a lower proliferative capacity. They expose a high number of Epo receptors and Epo thus becomes the primary growth factor involved in the proliferation and differentiation of CFU-E. After 3-5 days in culture, proerythroblasts (Pro-E) are formed. They are the earliest recognizable erythroid precursors, with a decreased number of Epo receptors but the highest number of transferrin receptors. As the maturation process advances to early and then late erythroblasts, the cell divides and accumulates iron and hemoglobin (Hb) while decreasing in size due to decreased RNA content and progressive nuclear condensation. The increase of Hb content is reflected by the cytoplasmic staining with Wright's stain (i.e. a mix of eosin and methylene blue dyes), which progressively switch from blue (basophilic, low Hb and

high nucleic acid) to gray (polychromatic) to gray-red (orthochromatic or acidophilic, high Hb and low nucleic acid) (Palis, 2014). At this stage, the cell has lost its ability of cell division and is only slightly larger than a mature erythrocyte as it does contain a small dense nucleus.

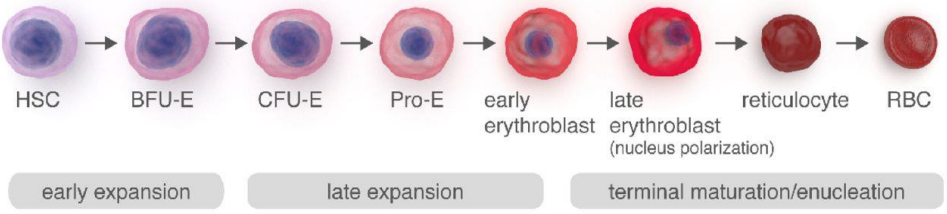

Figure 1.2. Schematic representation of erythroid differentiation. HSC, hematopoietic stem cell; BFU-E, burst-forming unit erythroid; CFU-E, colony-forming unit erythroid; Pro-E, proerythroblast. Reproduced from (Chiabrando et al., 2014).

Enucleation is the final step of maturation, resulting into the formation of a reticulocyte and the release of a pyrenocyte. The latter is eliminated by macrophages thank to the exposition of phosphatidylserine (PS) at its surface, a "eat me" signal (see section 4.1.) (Palis, 2014). Enucleation is a complex process involving multiple steps (Keerthivasan et al., 2011) including i) nuclear and chromatin condensation; ii) cell polarisation thank to microtubule action; iii) formation of contractile actomyosin ring, in a similar manner to cytokinesis but in an asymmetric way; iv) vesicle trafficking that creates an asymmetric protein distribution; and v) coalescence of lipid rafts in the furrow between reticulocyte and pyrenocyte, allowing completion of cytokinesis (Konstantinidis et al., 2012). During this process, erythroid proteins are selectively sorted between reticulocytes and pyrenocytes. For instance, Band3, ankyrin, 4.1R, glycophorin A, glycophorin C, RhAG and spectrins segregate to the nascent reticulocyte while β1 integrin, fibronectin receptor and transferrin receptor are selectively lost (Bell et al., 2013; Keerthivasan et al., 2011). Even though the mechanisms of protein sorting are not completely resolved, some of them might involve the spectrin/ankyrin/4.1R cytoskeleton (see section 2.3), as revealed by the aberrant protein sorting in mice lacking ankyrin or 4.1R proteins (Salomao et al., 2010).

Reticulocytes are then released from the bone marrow and undergo their terminal differentiation in the circulating blood. This step lasts 1-2 days and includes multiple cellular processes like Hb final production and cytosolic organelle elimination by autophagy (Moras et al., 2017; Palis, 2014). It also includes membrane remodelling through the loss of cytoskeletal actin and tubulin, the large

elimination of the Na^+/K^+ ATPase and the decrease of other proteins like glycophorin A and CD47 (Liu et al., 2010; Ovchynnikova et al., 2018). The loss of those proteins is thought to be achieved by vesicle release (Pan and Johnstone, 1983). Finally, RBCs loose 20-30% of their cell surface during this process, adopting a biconcave morphology with improved viscoelasticity (Ovchynnikova et al., 2018). Reticulocytes occur for about 1 % of circulating RBCs in physiological conditions, and their increase can be a sign of increased RBC production caused by a pathological condition.

1.1.3. Regulation

A major regulator of erythropoiesis is the cytokine Epo. It is secreted by the kidneys upon decreased dioxygen (O_2) concentration in the blood flow. O_2 decrease induces the binding of the hypoxia-inducible transcription factor (HIF2) to the HIF-responsive elements (HRE) sequence on the Epo promoter. As explained here above, whereas Epo is extremely important for late BFU-e and CFU-e state proliferation and differentiation, its action decreases afterward and is non-needed for the last stages of differentiation. The main mechanism by which Epo promotes precursor proliferation is by inhibiting apoptosis (Socolovsky, 2007). It also activates the iron regulatory proteins that up-regulate synthesis of transferrin receptors (Weiss et al., 1997). Other factors, like insulin and insulin-like growth factor, also positively regulate erythropoiesis, while inflammatory cytokines like γ-interferon (γ-IFN) and tumour necrosis factor α (TNFα) decrease it (Hattangadi et al., 2011; Nandakumar et al., 2016). The precise relevance of these pathways for *in vivo* erythropoiesis remains to be established. Finally, vitamins B12 and B9 are essential for erythropoiesis (Koury and Ponka, 2004) and physical activity has been shown to stimulate it, either by improving the hematopoietic environment or modulating several cytokines and hormones levels, a.o. (Hu and Lin, 2012).

1.2. RBC function

1.2.1. Primary function: O_2 transport and carbon dioxide (CO_2) elimination

Blood is an aqueous body fluid in which O_2 is poorly soluble at PO_2= 100mm Hg. Transport of O_2 throughout the body is therefore mostly (~98% of total O_2) ensured thank to a specialized protein inside the RBC, i.e. Hb. Hb has an O_2-binding capacity of 1.34 mL O_2 per gram, which increases the total blood O_2 capacity seventy-fold compared to dissolved O_2 in blood (Pittman, 2011).

Introduction

Hb is a tetrameric protein composed of two different pairs of globins, in which each monomer binds a heme group. The heme group is composed of a porphyrin ring which normally contains a ferrous iron (Fe(II)) atom in its center (figure 1.3 A). When the iron atom becomes oxidized, its valence state changes from (II) (ferrous) to (III) (ferric), the Hb loses its capacity to bind O_2 and is called metHb (see section 1.3.2.). As six different globin chains have been described in humans (α, β, γ, δ, ζ and ς), several combinations of globins leading to different Hb molecules are possible. However, in normal adult human, HbA (A for adult) makes up 92% of the total Hb content and is composed of two α chains and two β chains ($\alpha_2\beta_2$) (figure 1.3A). The concentration of Hb inside RBCs is highly regulated to 320-360 g/L (see section 2.2).

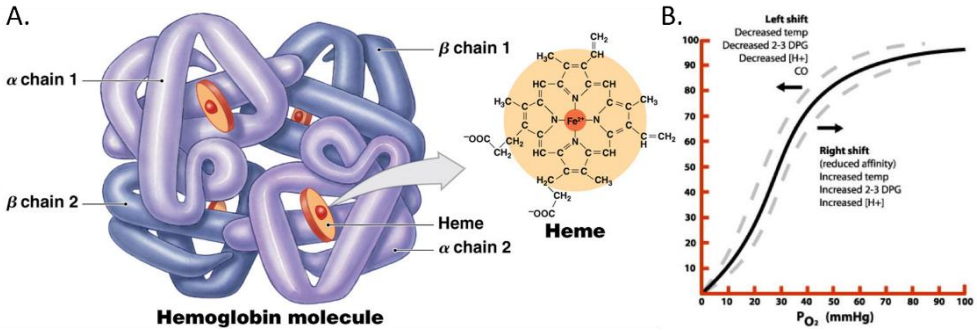

Figure 1.3. Hb and heme structures, and interaction with O_2. A. Hb and heme structure (Reece et al., 2011). **B.** Standard human O_2-Hb dissociation curve. pO_2: O_2 pressure. Left shift: increase of affinity of O_2 for Hb; right shift: reduction of the affinity. Reproduced from (Dunn et al., 2016).

There are several arrangements of the subunits possible within the tetramer, but two of them are much more stable than all the others. On one hand, the R (for relaxed) quaternary structure, with high O_2 affinity, is predominant when the iron atoms are saturated with O_2 (i.e. oxy structure). On the other hand, the T (for taut) configuration, with low O_2 affinity, predominates when these binding sites are vacant (i.e. deoxy structure). The binding of O_2 is a cooperative process. Indeed, as O_2 binds to one globin, the affinity of the other globins increases, and each additional O_2 binding will expand the affinity and the promotion of the T to R state transition (Pittman, 2011).

As a consequence to that cooperativity, the O_2 binding curve to Hb is sigmoidal (figure 1.3 B). P_{50} is defined as the PO_2 at which O_2 saturation is 50% in standard conditions (i.e. 37 °C, pH= 7.4, PCO_2 = 40 mm Hg). Several factors influence the binding of O_2 to Hb. For example, increasing temperature lowers the affinity, a

regulation that has physiological importance during exercise to favour O_2 release in muscles. Acidic pH, high [CO_2] and increased 2,3 diphosphoglycerate (2,3 DPG) also decrease the Hb affinity for O_2. 2,3 DPG is a glycolytic intermediate (see section 1.3.1) produced within the RBC whose generation is increased by basic pH. It plays a major role during acclimatization to high altitude, whereby hypoxic ventilation causes basified pH and decreased PCO_2, and therefore a left shift of the O_2 dissociation curve. However, the resulting increased 2,3 DPG production shifts the curve back to the right. Besides the O_2, Hb ligands also include competitive inhibitors (CO) and allosteric ligands (CO_2 or NO). Carbon monoxide (CO; from smoking or exhaust gas) competes with O_2 at the heme binding site with a high affinity (200-300 times that of O_2 in normal adults), forming a carboxyHb. CO_2 binds to amino groups of the globin proteins and competes with 2,3 DPG, forming carbaminoHb. Nitric oxide (NO) can also be transported by Hb by a specific thiol function into the globin protein, forming a S-nitrosoHb. S-nitrosoHb will dissociate when Hb releases O_2 (see section 1.2.2) (Layton, 2017).

CO_2 is transported in the blood from the tissues to the lungs in three ways (Arthurs and Sudhakar, 2005). First, as CO_2 is ~20 times more soluble than O_2, ~7 % diffuse effectively despite weak variation of the partial pressure. The second way, which accounts for ~23 % of total CO_2, occurs through binding to free Hb at exposed amino groups, forming carbaminoHb as exposed above. The last and major (~70 % of total CO_2) mean of transport is through combination with water under the carbonic acid form (H_2CO_3). H_2CO_3 is formed in a reaction catalyzed by the carbonic anhydrase, an enzyme present at the cytoplasmic surface of the RBC membrane. It then easily dissociates in bicarbonate ions (HCO_3^-) and hydrogen ion (H^+). While H^+ ions link the deoxyHb, HCO_3^- exit the cell in exchange for one chloride ion (Cl^-) thank to the anion exchanger protein Band3 (or AE1). Consequently, Cl^- concentration is lower in venous blood than in arterial blood. The opposite process occurs in the pulmonary capillaries of the lungs, as pO_2 rises and pCO_2 falls, releasing H^+ ions from Hb. The increased free H^+ concentration within RBCs shifts the equilibrium of the carbonic anhydrase towards CO_2 and water formation from HCO_3^- (Reece et al., 2011).

1.2.2. Secondary functions

The aerobic metabolism in a given tissue depends on matching O_2 delivery with O_2 demand. If tissue oxygenation is reduced, either by hypoxia or increased O_2 use (as in exercising muscle), this should be met by an increased O_2 delivery *via* the blood. This is achieved through vasodilation of precapillary resistance vessels (arterioles) and opening of precapillary sphincters, which

increase the local blood flow and recruit more capillaries. RBCs can act as sensors of reduced oxygenation and respond to regulate the blood flow.

Indeed, upon decreased O_2 saturation (hypoxia), shear stress in constricted vessels and osmotic pressure, RBCs are able to release ATP (Wan et al., 2011; Wan et al., 2008). This release may notably be induced by intracellular calcium (Ca^{2+}) accumulation upon shear stress (see section 3.2.1.) (Cinar et al., 2015). Extracellular ATP will act as a vasodilatory signaling molecule by binding and activating the purinergic P_{2Y} receptors on the vascular endothelial cells, which in turn induce the synthesis and release of NO (Bakhtiari et al., 2012).

NO is a well-known vasodilator, which causes relaxation of the vessel surrounding smooth muscle cells. RBC can directly synthetize NO enzymatically using L-arginine as substrate (Kleinbongard et al., 2006). The membrane and cytoplasmic NO synthases are activated upon exposure of RBCs to shear stress (Ulker et al., 2009). NO release from S-nitrosoHb, upon O_2 dissociation from Hb, also contributes to the NO increase (Jensen, 2009). The export of NO is believed to be processed via a cascade of transnitros(yl)ations from Hb to proteins at the endothelial or platelet membrane (Sonveaux et al., 2007).

Finally, RBCs can also produce hydrogen sulfide (H_2S) from cysteine or from the sulfur compounds of garlic, a signaling gas that acts to relax vessel walls (Wagner, 2009).

1.3. RBC physiology

1.3.1. Energy supplies

Glucose is the major energy source for the RBC. Mature erythrocytes, however, lack the oxidative enzymes present in mitochondria and cannot depend on aerobic glycolysis to extract energy from glucose. They therefore use the Embden-Meyerhof pathway to anaerobically process glucose into usable energy, i.e. ATP. As normal RBCs do not have glycogen, anaerobic glycolysis depends only on a continuous supply of glucose freely entering the cell through the glucose transporter GLUT1 (200.000/cell; ~10 % of the total protein mass (Montel-Hagen et al., 2009)). Approximately 90 % of glucose is catabolized anaerobically to pyruvate. The net gain is two ATP molecules and two NADH molecules for one glucose (Brown, 1996).

A metabolic complex, assembled next to the membrane, is responsible for the gathering of a pool of glucose, ATP, H^+ and of metabolic enzymes to ensure an effective production of energetic molecules. Glucose enters the RBCs via GLUT1

transporters and is metabolized via the neighbouring membrane-bound glycolytic complex. The anion exchanger protein Band3 has turned out to be a multipurpose protein around which cytoskeleton (see section 2.3.) and metabolic enzymes are gathered. It possesses three functional domains: i) the N-terminal cytoplasmic domain which is the key attachment site for the membrane skeleton, glycolytic enzymes and deoxyHb; ii) the transmembrane domain which forms the anion-exchange channel; and iii) the cytoplasmic C-terminal domain which presents a binding site for carbonic anhydrase II (Hassoun and Palek, 1996). The glycolytic enzymes associated with the N-terminal sequence of Band3 incorporate phosphofructokinase, aldolase, glyceraldehyde-3-phosphate dehydrogenase (GAPDH) and enolase. They stay inactive when bound to Band3 but are activated when the association is altered by phosphorylation of the binding sites or upon competition with deoxyHb for Band3 binding site (Puchulu-Campanella et al., 2013). Finally, the produced ATP is partly sequestered within the cytoskeletal-membrane complex, probably thanks to β-spectrin, ankyrin, Band3 and GAPDH (Chu et al., 2012).

The NADH molecules produced in anaerobic glycolysis can be used along with lactate dehydrogenase to catalyze the conversion of pyruvate to lactate, which is removed from the cell by the MCT-1 (monocarboxylate transporter) lactate transporter in an H^+-dependent manner. NADH/NADPH are also major cofactors in antioxidant systems and are necessary to maintain the glutathione in a reduced state, as well as to reduce metHb back to Hb (see section 1.3.2.). Their production can be increased by catabolizing ~10 % of entering glucose in the pentose phosphate pathway. This pathway results not only in two NADPH molecules production per glucose molecule, but also in one molecule of ribose-5-phosphate, which is used to generate ADP for use in the glycolysis. The rate-limiting step of the pentose phosphate pathway is catalyzed by the glucose-6-phosphate dehydrogenase, whose activity decreases with RBC aging, reducing energy production and ability to protect cell membrane integrity and Hb from oxidation (see section 4.1).

Finally and notably, RBCs possess a unique glycolytic bypass for the production of 2,3 DPG, i.e. the Rapoport-Luebering shunt (van Wijk and van Solinge, 2005). This shunt bypasses the phosphoglycerate kinase which catalyzes the formation of 3 PG from 1,3 DPG. Through the Rapoport-Luebering pathway, DPG mutase, an enzyme sensitive to pH, catalyzes the transfer of a phosphoryl group from C1 to C2 of 1,3-DPG, producing 2,3 DPG. 2,3 DPG, the most concentrated organophosphate in RBCs which regulates Hb's affinity for O_2 (see section 1.2.1.), forms 3-PG by the action of DPG phosphatase.

1.3.2. Antioxidant systems

Reactive oxygen species (ROS) production

Reactive oxygen species (ROS; figure 1.4, red) are oxygen-centered molecules that include non-radical species such as singlet oxygen (O_2) or hydrogen peroxide (H_2O_2) and radical species possessing an unpaired electron like superoxide anion ($O_2^{\bullet-}$), hydroxyl radical ($OH^{\bullet}$) and nitric oxide (NO). In healthy RBCs, ROS are continuously produced in small amounts, mostly by autoxidation of oxyHb (HbO_2) in metHb (figure 1.4A). This process results from the oxidation of the ferrous iron (Fe^{2+}) in ferric iron (Fe^{3+}) and includes the release of the superoxide anion $O_2^{\bullet-}$ (Cimen, 2008). Since the intracellular Hb concentration is around 5 mM, even if the autoxidation occurs with a small rate, it produces substantial levels of ROS into the RBCs. $O_2^{\bullet-}$ produced can be transformed by the superoxide dismutase (SOD) in H_2O_2, which is a substrate for the Haber-Weiss reaction (figure 1.4B). This reaction also requires $O_2^{\bullet-}$ and a Fenton reagent (ferric iron in hemichromes released by metHb, e.g.) and generates highly reactive hydroxyl radicals $OH^{\bullet}$ (Yoshida and Shevkoplyas, 2010).

ROS targets

The ROS will have several consequences on the RBC including peroxidation of lipids and alteration of proteins such as membrane channels, spectrin and Hb. First, the hydroxyl radicals $OH^{\bullet}$ will be able to induce lipid peroxidation cycles by reacting with (poly)-unsaturated lipids to create lipid radicals. Those radicals will in turn either induce the peroxidation of other lipids, crosslink with other radicals or release malondialdehyde (MDA). The latter will worsen the membrane function alteration by cross-linking RBC phospholipids and proteins (Cimen, 2008; Yoshida and Shevkoplyas, 2010) (figure 1.4C). Second, ROS as well as MDA will alter the activity of several membrane proteins, leading notably to the disruption of ion transports. Among those proteins, one can cite Band3 and PMCA. Once Band3 is oxidized, it also induces the self-aggregation of the protein. This then probably recruits the binding of the autologous IgG, which initiates the elimination of the senescent RBCs (see section 4.1.) (Lutz and Bogdanova, 2013). PMCA is also an important target of ROS as it presents sulfhydryl groups that are very susceptible to oxidation. Once oxidized, PMCA activity is highly altered, leading to Ca^{2+} accumulation (see section 4.1.) and consecutive ROS enhancement as both are highly interplayed (Gorlach et al., 2015). Third, whereas Hb is the major origin of ROS production, it is at the same time their principal target because of its sulfhydryl groups (Vitturi et al., 2013). Alteration of Hb will lead to its crosslinking with spectrin and Band3, participating to the disorganization of the former and the aggregation of the latter. Moreover, the accumulation of heme degradation

products has been linked to a decrease of the RBC deformability and an increased cellular stiffness (Mohanty et al., 2014).

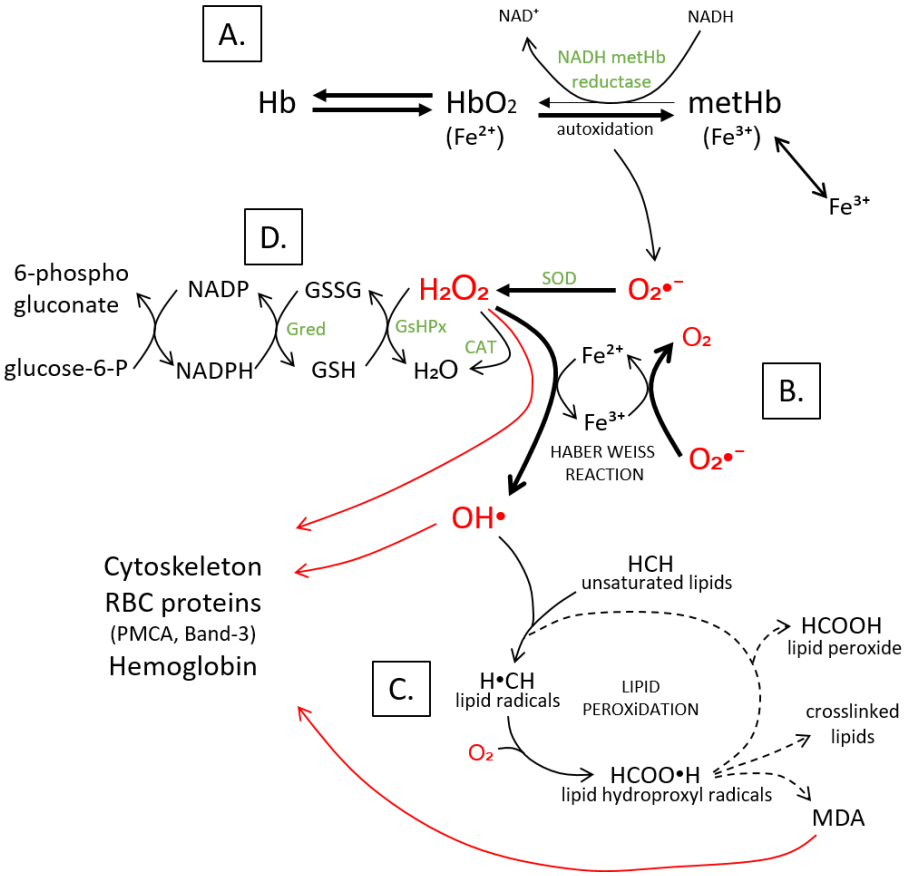

Figure 1.4. Main ROS pathways (red) and antioxidant defenses (green) in RBCs. (A) Initial ROS production. (B) ROS propagation. (C) Lipid peroxidation. (D) Antioxidant systems. Adapted from (Cimen, 2008; Yoshida and Shevkoplyas, 2010). SOD, superoxide dismutase; CAT, catalase; MDA, malondialdehyde; GSSG, reduced glutathione; GSH, oxidized glutathione.

Antioxidant defenses

Fortunately, RBCs present antioxidant systems, which allow to reduce the damages that might be caused by ROS. The antioxidant system includes enzymatic and non-enzymatic pathways. Major enzymes that prevent oxidative denaturation in RBCs (figure 1.4, green) include the NADH-metHb reductase, the superoxide dismutase (SOD), the catalase (CAT), the GSH/glutathione peroxidase (GSHPx) and the GSH reductase (Gred). Those enzymes rely on antioxidant cofactors like NADH or NAPDH, or the antioxidant tripeptide glutathione (GSH) (figure 1.4D). The reduced GSH scavenges H_2O_2 and reacts with another glutathione to form oxidized GSSG and releases the inoffensive H_2O. The GSH pool is then restored by the action of the GSH reductase and NADPH (Lutz and Bogdanova, 2013). Finally, NADPH is reformed thank to the pentose phosphate pathway, as explained above (see section 1.3.1.).

Along with those enzymatic defense systems, endogenous non-enzymatic systems also help to reduce free ROS. Those antioxidants are either lipophilic molecules (e.g. vitamin E and carotenoids) or water-soluble substances (e.g. vitamin C and uric acid). Vitamin C is a well-known synergistic agent for vitamin E and they work together to inhibit lipid peroxidation reactions in membranes (Cimen, 2008). Carotenoids present antioxidant effects and also a quenching effect of singlet oxygens O_2 (Miller et al., 1996).

ROS in diseases

A number of diseases have been linked to aberrant antioxidant systems or to an increase of ROS production. In general, the partial defect of an antioxidant system can harm RBCs and promote senescence, but without inducing chronic hemolytic problems. However, there are some rare inborn defects resulting from defects in the glycolysis or in the pentose phosphate pathways that lead to important ROS damages. The RBCs will release appreciable amounts of Hb, heme and iron into the circulation, which will enhance the formation of extracellular ROS and increase vascular and RBC damages, leading to a massive hemolysis (van Zwieten et al., 2014) .

On the other side, some common and often life-threatening hereditary RBC disorders, such as β-thalassemia or sickle cell disease, have been linked to an aberrant increase of ROS production (George et al., 2013). Indeed, the unstable Hb is more susceptible to auto-oxidation and Fenton reactions. In sickle cell disease, this leads to an increased hemolysis, increased adhesion of RBCs to endothelial cells, vasoconstriction and increased coagulant activity, a.o., that will promote the vaso-occlusion along with the cell sickling (van Zwieten et al., 2014). Therefore,

nutritional supplementation with antioxidants like vitamin E improves the clinical outcome (Tesoriere et al., 2001). Paradoxically, the beneficial effect of those diseases on survival of malaria infection might be due to the enhanced oxidative stress, which may inhibit the parasite growth and/or enhance uptake of infected RBCs by spleen macrophages (van Zwieten et al., 2014).

2. Specific features of RBC deformability

2.1. RBC deformation in the blood flow and in the spleen

From the high flow conditions in the aorta to the single micron-wide capillaries, RBCs experience a large range of flow conditions and changes in shear stress and hemodynamic forces. To deliver O_2 to the tissues, erythrocytes must be able to dynamically adapt to and to compensate for those changing flow conditions to deform significantly without rupturing. Assuming standard cardiovascular parameters for a human (cardiac output = 4.0–8.0 L/min, total blood volume = 5–6 L), one can calculate that a single erythrocyte traverses the circulatory system in ~1 min; therefore, during its average lifetime of 120 days, one RBC undergoes on the order of 10^5 cycles of high flow conditions in the aorta, followed by squeezing through the smallest capillaries (<5 µm of diameter) (Shemin and Rittenberg, 1946).

Under physiological conditions, normal RBCs at resting state exhibit a famous discoid shape, allowing them to minimize the bending energy. They however have a few possible modes of changing their shape in the blood flow (figure 1.5). In high shear rates, elongation of the principal ellipsoid axis is observed. This is the classical definition of cell deformability and is measured *via* ektacytometry (see section 6.1.2.). Other modes of motion in response to changes in flow are also end-over-end tumbling and periodic swinging, which are not changes in shape for an individual RBC, but can affect total flow conditions and viscosity of whole blood (Forsyth et al., 2011). Additionally, membrane tanktreading, where points on the RBC membrane traverse around the discoid without the cell changing shape, presents another observed mode of RBC motion. Tanktreading is a favorable deformation mode because it creates lift forces that push individual RBCs away from vessel walls and into the center of the blood stream, where the flow is the greatest. The combination of all of these motions links individual cell properties with the overall blood rheology (Kuhn et al., 2017).

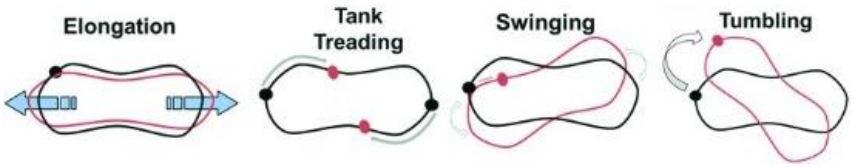

Figure 1.5. Modes of RBCs deformation. There are four distinct ways that RBCs deform while traveling in the blood stream. Reproduced from (Kuhn et al., 2017).

The high RBC plasticity will be tested numerous times during the RBC life when it flows through the spleen. The spleen is the largest filter of RBCs in the body where the shorter and narrower openings (0.5-1 µm in diameter) for RBC passage are located, forcing RBCs to adopt a dumbbell shape as they pass through (figure 1.6, right). Splenic parenchyma is made of white pulp nodules that contain mainly T and B lymphocytes, interspersed into the red pulp, a spongy tissue that accounts for 75% of the splenic volume. The red pulp comprises splenic sinusoids, which are blood vessels juxtaposed with the connective tissue of splenic cords. About 10% of blood entering the spleen is directed into so-called open circulation, where RBCs are forced to go from the cords into venous sinuses (figure 1.6) (Pivkin et al., 2016). The sinuses consist of a lining of endothelial cells that are positioned in parallel and connected by stress fibers to annular fibers, which are made up of extracellular matrix components. Abnormal or old RBCs have difficulty to manage this passage and stay blocked into the cords where they are phagocytosed (see section 4 for more explanations) (Mebius and Kraal, 2005).

The rheological properties of the RBC membrane that influence its deformability can be classified into mechanical coefficients, i.e. three elastic moduli and a viscous modulus (Kim, 2015). The elastic moduli are (i) the shear modulus, which represents the elastic energy storage associated with uniaxial elongation; (ii) the expansion modulus, which can be measured by aspiration of the RBC in a micropipette (see section 6.1.1); and (iii) the bending modulus which is characterized by the lipid bilayer properties of the RBC. Those properties are directly dependent on several RBC constitutive characteristics. Among them, one can cite (i) the RBC biconcave shape, characterized by a higher membrane surface:volume ratio as compared to a sphere of the same volume (membrane surface excess of ~40 %) that is maintained through the regulation of cytoplasmic volume and viscosity, which also directly regulate RBC deformability (see section 2.2) and (ii) the strong anchorage of its membrane to the underlying cytoskeleton through two anchorage complexes (see section 2.3). In addition to these specific characteristics, the membrane lipid bilayer composition, properties and organization (see section 5) could also participate to the RBC rheological properties

regulation and therefore to its deformation. This is precisely one of the goals of my thesis.

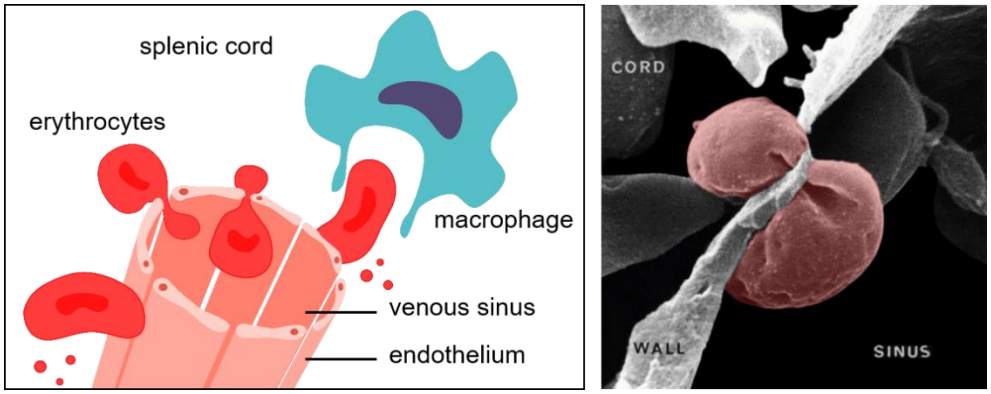

Figure 1.6. Venous sinuses in the red pulp of the spleen. Left, schematic representation of a venous sinus in the cords of the red pulp. Blood from the cords collects in the sinuses which consist of a lining of endothelial cells positioned in parallel. Ageing or abnormal RBCs that are no longer able to pass through the slits are phagocytosed. **Right,** scanning electron microscopy image of one RBC passing through an endothelial slit. Reproduced from (Mohandas and Gallagher, 2008).

2.2. RBC shape and volume control

The biconcave shape of the RBC is fundamental for its physiological function in gas exchanges, but also for the cell flexibility. This shape is defined by cytoskeletal structural proteins and ion channels (Mohandas and Gallagher, 2008). To maintain a discoidal shape, the internal volume of RBCs must not exceed a threshold that would overcome cytoskeleton organization forces. The average internal volume of a RBC is 94 μm^3 at 300 mOsmol/kg (Diez-Silva et al., 2010). Water moves through the RBC membrane sufficiently fast for its volume to be established as the result of the osmotic differences between its internal and external solutions.

The maintenance of the RBC volume thus requires to adapt to the changes in intracellular osmolarity; the extracellular one being kept nearly constant in the blood flow (i.e. ~285 mOsm). According to the important Hb concentration inside the cell and considering that the protein cannot cross the membrane, the cell would be expected to swell. However, the cytoplasmic content of potassium (K^+), sodium (Na^+) and Cl^- ions are tightly controlled thank to several ion transporters, as extensively described in (Gallagher, 2017). K^+ concentration in RBCs is high (~150

mM, compared to ~5 mM in the plasma) whereas Na^+ concentration is low (~15 mM, compared to ~150 mM in the plasma). This difference is maintained by the Na^+/K^+-ATPase which actively transports three Na^+ out and two K^+ in. Plasma membrane Ca^{2+}-ATPase (PMCA) plays the same role and drives the Ca^{2+} out of the cells to keep low intracellular concentrations (~50 nM, compared to ~1.8 mM in the plasma) (Bogdanova et al., 2013). This is especially important as Ca^{2+} is a universal and ubiquitous signaling molecule. The Ca^{2+} exchanges at the RBC membranes and their importance are described in section 3.2.

The RBC biconcave shape can be lost following several alterations. On one hand, alterations of ion transport will result either in (i) an overcome of the cytoplasmic volume over the cytoskeleton retaining forces and consecutive hypo-osmotic explosion; or (ii) shrinking of the RBC and increase of the cytoplasmic viscosity, which is determined by the $[Hb]_{ic}$ concentration. Increase of the viscosity has been shown to slow down considerably the cell response to shear stress and shape restoration (Evans et al., 1984). On the other hand, cytoskeleton impairment, as observed in membrane fragility hereditary diseases, will also induce a loss of the surface/volume ratio, as addressed in section 4.2.

Finally, a variety of agents can reversibly modify the RBC shape without changes in surface area or in cell volume (Lim et al., 2002). For instance, high salts, high pH, ATP depletion and proximity to a glass surface (negatively charged) induce a series of crenelated shapes, i.e. echinocytes that are characterized by convex rounded protrusions or spicules. If the action of these agents is extended, the spicules become smaller and more numerous before budding off irreversibly, forming extracellular vesicles. The resulting RBC is smaller and more spherical (spherocyte). On the other hand, low salts, low pH and increased ATP levels induce mono-concave shapes called stomatocytes, which might result from expansion of the inner leaflet area compared to the outer one (Gov and Safran, 2005; Lim et al., 2002; Sheetz and Singer, 1974).

2.3. RBC cytoskeleton composition and membrane anchorage

The intrinsic ability of RBCs to change their shape is mainly defined by the flexibility and the stability of the inner membrane-attached cytoskeleton. It is majorly composed of spectrin, i.e. the building blocks, and anchorage complexes named 4.1R- and ankyrin-based complexes. The flexibility of the RBC cytoskeleton depends on the strong, but dynamic, interactions between spectrin molecules themselves as well as between spectrin and anchorage complex proteins (Sheetz et al., 2006).

Introduction

Spectrin dimer is a long, flexible, worm-like protein composed of two parallel chains (α- and β-spectrin) oriented in opposite directions (Lux, 2016). Molecularly, each spectrin chain contains multiple spectrin-type repeats of ~106 amino acids along with specialized functional domains. Those domains regulate the spectrin dimers association in tetramers, but also the binding to protein 4.1R, actin and other proteins of the anchorage complexes. On average, six spectrin tetramers bind per actin filament at the 4.1R junctional complexes, leading to a pseudo-hexagonal spectrin meshwork in which every side consists of spectrin tetramers of 200 nm long (see figure 1.7 A) (Kapus and Janmey, 2013). This length was evaluated on electron micrographs of purified spectrin tetramers or on spectrin filaments in fully stretched cytoskeletons. However, filaments of native/unstretched skeletons are much more compact and simple calculations show that the average distance between actin filaments (i.e., the length of a spectrin tetramer) is only 60 to 70 nm *in vivo* (Boguslawska et al., 2014; Liu et al., 1987; Lux, 2016). Tetramers dissociate and reform under physiological conditions, and this process is greatly increased when the membrane is distorted by shear forces. This mechanism may be an evolutionary accommodation to support the enormous distortions that the RBC undergoes into the microvasculature (Lux, 2016).

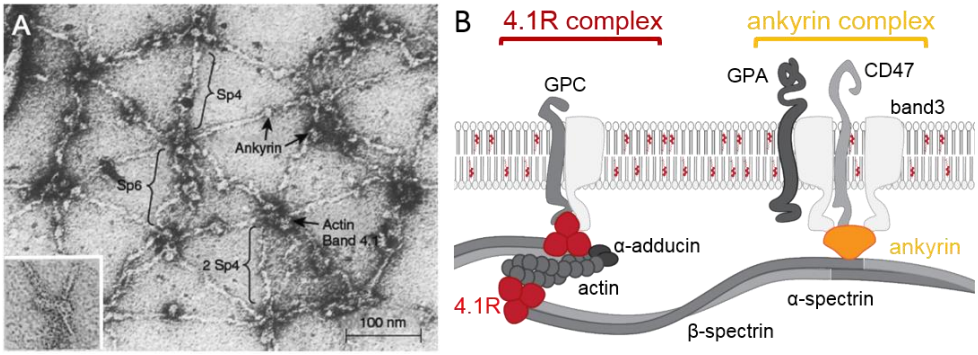

Figure 1.7. Anchorage of the membrane to the spectrin cytoskeleton by two complexes centred on Band 4.1R (4.1R) and ankyrin proteins. A. Transmission electron microscopy of the spectrin network at the inner face of the membrane. Inset: example of a 37-nm long F-actin protofilament. Sp4, spectrin tetramer; Sp6, spectrin hexamer; 2 Sp4, double spectrin tetramers. Reproduced from (Liu et al., 1987). **B.** Simplified representation of the complexes. GPC, glycophorin C; GPA, glycophorin A. Adapted from (Salomao et al., 2008).

The 4.1R anchorage complex is based, as indicated, on the protein 4.1R (figure 1.7 B, red). 4.1R protein contains several domains (figure 1.8) including a FERM (4.1R protein/ezrin/radixin/moesin) domain which presents binding sites for Band3, calmodulin, PS and phosphatidylinositol-4,5-bisphosphate (PIP_2) and whose activity is regulated through phosphorylation (Manno et al., 2005). Another domain is the FERM adjacent (FA) one, which is a substrate for phosphorylation by protein kinases A and C, while the spectrin-actin binding domain (SAB) is in the middle of the protein. Finally, the C-terminal domain (CTD) binds some membrane proteins (Baines et al., 2014). Concerning the 4.1R complex, aside from Band3, the other proteins involved are (i) glycophorin A; (ii) glycophorin C, which notably acts as a receptor for the malarial parasite; (iii) GLUT1; (iv) stomatin, whose function remains unclear but which may regulate ion channels and transporters; (v) blood group proteins like rhesus proteins; and (vi) F-actin and associated proteins (Lux, 2016). Interestingly, deficiency of 4.1R is accompanied by loss of other proteins like glycophorin C during enucleation, suggesting the importance of their association in the complex for the correct sorting (Salomao et al., 2010).

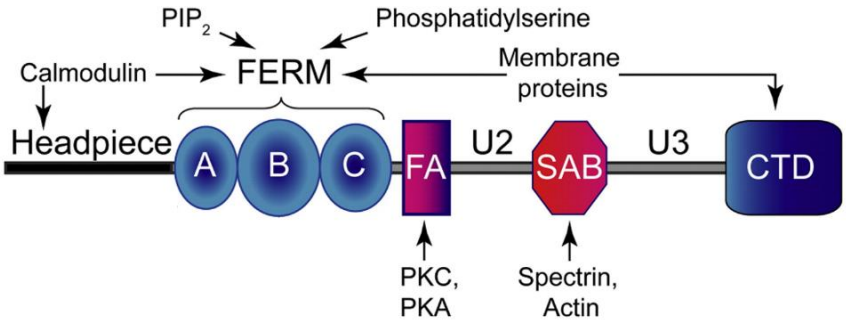

Figure 1.8. Overall domain structure of 4.1R protein, showing major regions of interaction and regulation. FA, FERM-adjacent domain; SAB, spectrin–actin binding domain; CTD, C-terminal domain. Reproduced from (Baines et al., 2014).

Actin filaments are key constituents of the 4.1R complexes. RBCs contain microfilaments of actin (F-actin) with a highly uniform length of ~37nm (Gokhin and Fowler, 2016). Mice that lack proteins regulating F-actin polymerization develop haemolytic anaemias with misshaped RBCs that present clumped or irregular cytoskeletons (Chan et al., 2013). RBC actin filaments are stabilized along their lengths by two tropomyosins and capped at their ends by two tropomodulin-1 molecules and a αβ-adducin heterodimer. The actin filaments, which bind to 4.1R, provide important sites for spectrin horizontal network formation, while both αβ-

adducin and 4.1R add additional vertical anchorage connections to the membrane *via* Band3 and glycophorin C. Thus RBC actin filaments simultaneously support "horizontal interaction" within the cytoskeleton and "vertical interactions" between the cytoskeleton and the membrane (Gokhin and Fowler, 2016).

The second anchorage complex is based on the ankyrin protein (figure 1.7 B, orange). The protein contains three domains: the N-terminal domain that binds Band3, the central domain that binds the spectrin, and the C-terminal domain that is thought to modulate the binding functions of the other two domains. Aside from Band3, the other proteins present in the ankyrin complexes are: i) glycophorin A; ii) CD47, a transmembrane protein "marker-of-self" with an extracellular IgG domain which prevents RBC clearance (see section 4.1); and iii) protein 4.2, a peripheral membrane protein that binds to the cytoplasmic domains of Band3, rhesus complexes and CD47 (Baines, 2010). The ankyrin complex seems to ensure a second function in addition to the vertical spectrin cytoskeleton anchorage to membrane. Indeed, the binding of Band3, CD47, protein 4.2 and rhesus complex to ankyrin is required for their efficient sorting to native RBC during the enucleation process (Salomao et al., 2010). For instance, upon ankyrin deficiency, those proteins are missorted and lost. On the other hand, RBCs lacking Band3 will also present a deficiency in protein 4.2 and glycophorin A (Peters et al., 1996) and RBCs devoid of protein 4.2 nearly lack CD47 (Bruce et al., 2002). Finally, this complex is involved in the metabolic complex presented in section 1.3.1.

3. Plasma membrane Ca^{2+} exchanges as key contributors of cell deformation

Ca^{2+} ions play key roles in cell physiology and biochemistry. Several Ca^{2+} transport proteins have been identified in mammalian cells (see section 3.1.) and have been shown to be regulated by several factors. In this thesis we focus on their regulation by membrane lipids. Some of those Ca^{2+} transport proteins are present on the RBC surface and contribute to increase the RBC deformability upon mechanical stress (for instance in small capillaries or during splenic filtration) through a transient but important Ca^{2+} increase through the plasma membrane (PM) (see section 3.2.1.). The consequences of the increased Ca^{2+} concentration are notably the cell dehydration, the local disruption of the cytoskeleton and the activation of the Ca^{2+} efflux pump (see section 3.2.2.).

Introduction

The following section (3.1.) is part of an invited review (Conrard, L.; Tyteca, D. Regulation of Membrane Calcium Transport Proteins by the Surrounding Lipid Environment. Biomolecules ***2019,*** *9, 513.)*

biomolecules

MDPI

Review

Regulation of Membrane Calcium Transport Proteins by the Surrounding Lipid Environment

Louise Conrard and Donatienne Tyteca *

CELL Unit, de Duve Institute and Université Catholique de Louvain, UCL B1.75.05, Avenue Hippocrate, 75, B-1200 Brussels, Belgium; louise.conrard@uclouvain.be

* Correspondence: donatienne.tyteca@uclouvain.be; Tel.: +32-2-764-75-91; Fax: +32-2-764-75-43

Received: 8 August 2019; Accepted: 10 September 2019; Published: 20 September 2019

check for updates

Abstract: Calcium ions (Ca^{2+}) are major messengers in cell signaling, impacting nearly every aspect of cellular life. Those signals are generated within a wide spatial and temporal range through a large variety of Ca^{2+} channels, pumps, and exchangers. More and more evidences suggest that Ca^{2+} exchanges are regulated by their surrounding lipid environment. In this review, we point out the technical challenges that are currently being overcome and those that still need to be defeated to analyze the Ca^{2+} transport protein–lipid interactions. We then provide evidences for the modulation of Ca^{2+} transport proteins by lipids, including cholesterol, acidic phospholipids, sphingolipids, and their metabolites. We also integrate documented mechanisms involved in the regulation of Ca^{2+} transport proteins by the lipid environment. Those include: (i) Direct interaction inside the protein with non-annular lipids; (ii) close interaction with the first shell of annular lipids; (iii) regulation of membrane biophysical properties (e.g., membrane lipid packing, thickness, and curvature) directly around the protein through annular lipids; and (iv) gathering and downstream signaling of several proteins inside lipid domains. We finally discuss recent reports supporting the related alteration of Ca^{2+} and lipids in different pathophysiological events and the possibility to target lipids in Ca^{2+}-related diseases.

Keywords: calcium exchanges; non-annular lipids; annular lipids; cholesterol; sphingolipids; acidic phospholipids; lipid domain; cell signaling; membrane curvature; membrane thickness; membrane lipid packing

3.1. Overview of Membrane Ca2+ Transport Proteins and Evidences for Their Modulation by Lipids

The majority of Ca^{2+} transport proteins has been proposed to be regulated by membrane lipids (Figure 1.9). As mentioned in the Introduction section, surface and intracellular membranes are quite complex in lipid composition as well as in lateral and transversal organization. Moreover, this complexity differs from mammalian cells as compared to yeast and bacteria. In mammalian cell membranes, one can distinguish three main lipid classes: the PLPs, SLs, and cholesterol. PLPs are divided in acidic and neutral ones, according to their polar head properties. Acidic PLPs include phosphatidic acid (PA), PS, and phosphatidylinositol (PI), alone or conjugated to one (PIP) or two (PIP_2) phosphates, a.o. Neutral PLPs consist of PC and PE. SLs are derived from ceramide (Cer), which is decorated with a phosphocholine headgroup in the case of sphingomyelin (SM) or with saccharides in the case of glycoSLs. The latter include cerebrosides, gangliosides and globosides, a.o. In the yeast *S. Cerevisiae*, ergosterol is the predominant sterol and three types of SLs that are different from the mammalian ones can be found. They are built on a Cer backbone linked to an inositol phosphate headgroup, forming inositol phosphate Cer (IPC). The latter might be linked to a complex oligosaccharide, forming mannosylated IPC derivatives (MIPC). In contrast, the membrane of most bacteria is devoid of sterols but enriched in PE, phosphatidylglycerol (PG), and cardiolipin (CL). For a comparison between the PM compositions of different cells, see (Carquin et al., 2016).

Besides differences in composition, membranes are susceptible to lipid enzymatic modifications, generating additional potential modulators for Ca^{2+} transport proteins. Phospholipases (PLs) hydrolyze PLPs. Four major classes are distinguished based on the type of reaction they catalyze. PLAs and PLB cleave acyl chains, either the first one (PLA_1), the second one (PLA_2), or both (PLB). PLA_2 can produce arachidonic acid (AA) as well as lysoPLPs. On its side, PLC hydrolyzes the ester bond between the glycerol and the phosphate group, releasing a diacylglycerol (DAG) and a phosphorylated headgroup, typically inositol-3-phosphate (IP_3). Both DAG and IP_3 released by PLC are important second messengers that control diverse cellular processes. While IP_3 diffuses through the cytosol to bind and open IP_3R channels at the ER membrane, DAG remains bound to the membrane and activates the protein kinase C (PKC). Finally, PLD cleaves after the phosphate, releasing PA and a headgroup (Haas and Stanley, 2007). Another enzymatic modification is achieved by sphingomyelinase (SMase), generating Cer, which can be subsequently hydrolyzed into sphingosine thanks to ceramidase, and both Cer and sphingosine can be phosphorylated by specific kinases.

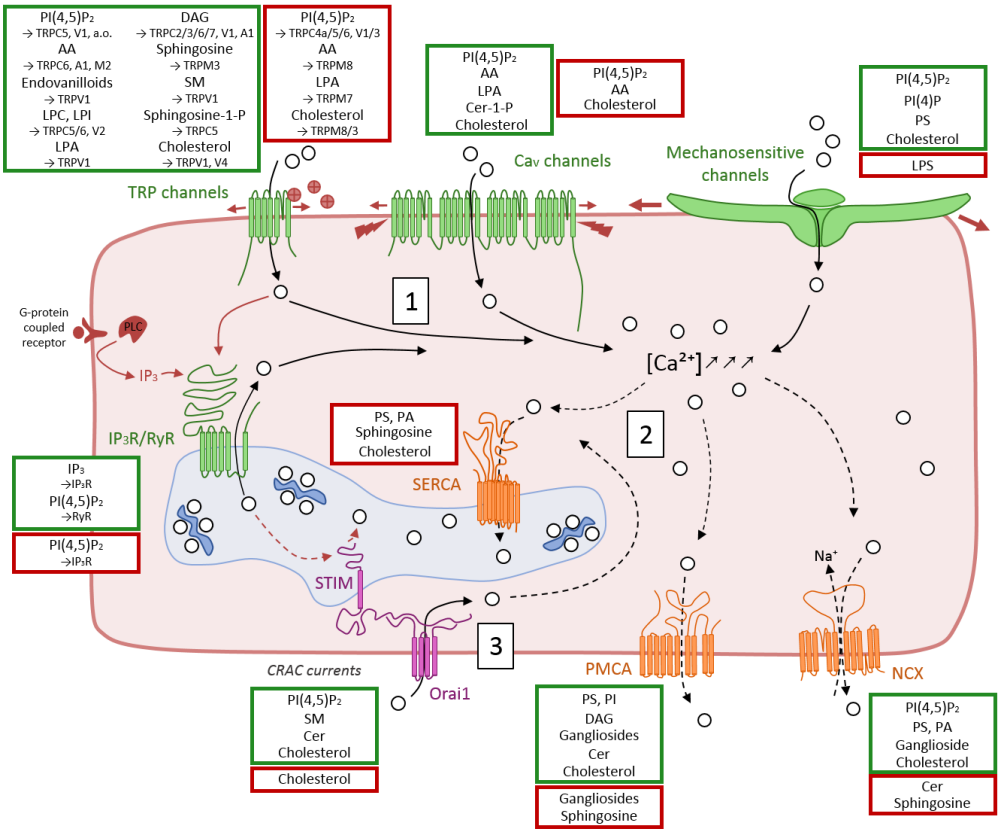

Figure 1.9. Main Ca^{2+} transport proteins and their known regulation by lipids. (**1**) Following a diversity of stimuli (in brick red), Ca^{2+} (white dots) influx into the cytosol will occur through channels at the plasma membrane (PM) or at the endo-/sarcoplasmic reticulum (ER/SR) membrane (in green). (**2**) Ca^{2+} increase will activate transport proteins (in orange) that export Ca^{2+} out of the cell or inside the ER/SR (in light blue), where it is sequestrated by calreticulin/calsequestrin (in blue). (**3**) Store-Operated Ca^{2+} Release-Activated Ca^{2+} (CRAC) currents (in pink) occur through the PM upon depletion of the ER/SR Ca^{2+} stores. Continuous and discontinuous arrows point to cytosolic Ca^{2+} increase and decrease, respectively. All Ca^{2+} transport proteins are represented based on their known structure (see description in the sections below), except for the Piezo mechanosensitive channel (MSC), for which a simplified view of the trimer is shown. For inositol-3-phosphate receptor (IP_3R) and ryanodine-receptor (RyR) tetramers and Orai1 hexamer, only one monomer is represented, while for Ca^{2+} voltage-gated (Ca_V) channels only the α-subunit is drawn. Regarding regulation of those Ca^{2+} transport proteins, only lipids are depicted: Those stimulating the transport proteins are boxed in green and those inhibiting them are in red.

3.1.1. Ca^{2+} Influx in the Cytosol Through Cation Channels

The increase of the cytosolic Ca^{2+} concentration can result from the activation of cation channels at the PM, like transient receptor potential channels, voltage-activated ion channels, or mechanosensitive channels, which respond to extracellular stimuli. The Ca^{2+} release into the cytosol can also originate from the ER/SR, through the ER/SR-associated inositol-3-phosphate receptor (IP_3R) and ryanodine-receptor (RyR) channels, and the PM-associated Orai1 channel.

Transient Receptor Potential Channels

Overview and Pathophysiological Implications

Transient receptor potential (TRP) channels are a group of non-selective cation channels activated by a large panel of stimuli and that are expressed mostly at the PM of numerous cell types. The TRP family comprises more than 30 channels, most of which are permeable for Ca^{2+}, but also for Mg^{2+} or Na^{+} (Pedersen et al., 2005). They share some structural similarities to each other, most of them being composed of six membrane-spanning helices with intracellular N- and C-termini (Islam, 2011). Based on sequence homology, the TRP family has been divided in seven main subfamilies: TRPC (C for “canonical”), TRPV (V for “vanilloid”), TRPM (M for “melastatin”), TRPA (A for “ankyrin”), TRPN (N for “no mechanoreceptor potential C”, not expressed in mammals), TRPP (P for “polycystin”), and TRPML (ML for “mucolipin”).

Although all TRP channels are molecular sensors, each sub-family is unique. Indeed, by acting as sensors of osmotic pressure, volume, stretch, and vibration, those channels mediate a wide range of sensory functions such as pain, temperature, different kinds of tastes, pressure, or vision. Moreover, even though they are not defined as voltage-gated (i.e., they do not require a change in membrane potential to open), they are often considered as voltage-sensitive (i.e., their activity is modulated by voltage). Additionally, they are emerging as polymodal ion channels, being sensitive to a multiplicity of mechanisms, activators, and inhibitors, suggesting that they may serve as integrative sensors of complex chemical signals (Abramowitz and Birnbaumer, 2009; Zeng et al., 2004). The most extensively-studied TRP channel is TRPV1, which responds to stimulation by temperature, acidic conditions, capsaicin, and the pungent component of wasabi. It induces a painful, burning sensation and is mainly found in nociceptive neurons as well as the central nervous system, where it mediates the transmission and modulation of pain (Cui et al., 2006). Mutations in TRP channels have been linked to several neurodegenerative disorders and skeletal dysplasia, but also kidney disorders, as extensively reviewed in (Nilius, 2007). Their altered expression also

often leads to tumorigenesis (Canales et al., 2019; Petho et al., 2019). On the other side, they represent therapeutic analgesic targets for reduction of chronic pain, as their antagonists reduce the sensitivity to stimuli of channels involved in nociception, like TRPV1 (Levine and Alessandri-Haber, 2007; Szallasi and Sheta, 2012).

Regulation by Lipids

TRP channels have been shown to be modulated by acidic PLPs (e.g., $PI(4,5)P_2$) and PLP derivatives (like AA, lysoPLPs, and DAG). For instance, $PI(4,5)P_2$ appears to activate most TRP channels (Rohacs, 2014). However, some of them (like TRPC4a, TRPV3) were shown to be inhibited (Doerner et al., 2011; Otsuguro et al., 2008) or to expose opposite behaviors depending on the experimental settings (like TRPC5), suggesting a complex regulation (Trebak et al., 2009). The effect of $PI(4,5)P_2$ on TRPV1 remains largely debated and is thought to be dual (Cao et al., 2013; Ufret-Vincenty et al., 2015). As a matter of fact, as least two sites of regulation have been evidenced, one on the C-terminal segment (Ufret-Vincenty et al., 2011), and the other in the capsaicin-binding pocket. The latter thussuggests a non-annular type of interaction, in which the PI acts as a competitive agonist and negative allosteric modulator, but may also function as positive, obligatory co-factor (Gao et al., 2016). Concerning TRPM3, it also binds $PI(4,5)P_2$ but no regulatory effect has been reported yet (Holendova et al., 2012). Altogether, those observations suggest that there are divergent and complex effects of $PI(4,5)P_2$ on TRP channels. As suggested for TRPV1, but also TRPC6 and TRPC4a, effects may occur through direct binding at a site in the C-terminus where it might compete with calmodulin (Kwon et al., 2007). Finally, the effect on some TRP channels (like TRPC4) might also depend on the actin cytoskeleton and PDZ-binding motifs (Otsuguro et al., 2008).

The PLP derivative AA and its many active metabolites are important stimulators of TRPC channels, most notably TRPC6 (Basora et al., 2003), but also of other TRP channels such as TRPA1 (Bandell et al., 2004) and TRPM2 (Hara et al., 2002). On the contrary, AA inhibits TRPM8 (Andersson et al., 2007) and has no effect on TRPC5 (Flemming et al., 2006). Endovanilloids are derived from AA and are endogenous agonists of the pro-nociceptive TRPV1 channels (De Petrocellis and Di Marzo, 2009).

On the other side, lysoPLPs, such as lysoPC (LPC), lysoPI (LPI), and lysoPA (LPA), also modulate TRP channels (Beech, 2012). LPC and LPI have been shown to activate TRPC5, but not TRPM2, in HEK293 and smooth vascular cells. The regulation has been shown to not involve G-protein receptors or other co-factors, and has been hypothesized to be linked either to a direct binding or to modifications of the

bilayer properties (Flemming et al., 2006). Another proposed way of activation of TRPC5 by LPC in endothelial cells involves TRPC6. Indeed, the latter's activation by LPC would lead to the TRPC5 trafficking at the PM and activation, inducing a prolonged increase in intracellular Ca^{2+} concentration and subsequent decreased cell migration and healing in atherosclerotic arteries (Chaudhuri et al., 2008). LPC and LPI also activate TRPV2, but this time through a G-protein signaling that induces translocation of TRPV2 at the PM. This activation has been linked to increased prostate cancer cell migration (Monet et al., 2009). Finally, LPA, which accumulates under tissue damage and ischemic conditions and is involved in the generation of chronic neuropathic pain, can activate TRPV1 through a binding site in its C-terminal domain, indicating its contribution to pain transduction (Nieto-Posadas et al., 2011). TRPM7 is, on the other side, inactivated by LPA (Runnels et al., 2002). All those results suggest that lysoPLPs may play important roles in a wide range of biological phenomena.

Finally, several TRPC channels, including TRPC2/3/6/7, are activated by DAG and its analogs (e.g., 1-oleoyl-2-acetyl-sn-glycerol (OAG) or 1,2-dioctanoyl-sn-glycerol (DOG)), either exogenously added (Lucas et al., 2003) or generated in response to PLC-coupled receptors (Startek et al., 2019). Studies on TRPC6 suggest a direct action of DAG on these channels, rather than an indirect effect through the activation of PKC (Hofmann et al., 1999). Nevertheless, a synergism with IP_3 appears to occur, potentially conferring greater sensitivity to DAG (Albert and Large, 2003). In contrast, TRPC1 does not appear to be directly activated by DAG but could be phosphorylated by PKC (Ahmmed et al., 2004), and TRPC4/5 are not activated by DAG (Hofmann et al., 1999; Venkatachalam et al., 2003). TRPV1 and TRPA1 are also activated by DAG with different potencies and probably through direct binding. Indeed, a TRPV1 mutant channel unable to bind capsaicin does not react with DAG (Woo et al., 2008). However, the concentrations required to produce these effects are quite high, suggesting the alternative possibility that DAG does not activate but, rather, "primes" both TRPV1 and TRPA1 for activation (Ciardo and Ferrer-Montiel, 2017).

Aside from PLPs and derivatives, some SLs and derivatives also modulate TRP channel activity. Indeed, sphingosine, but not Cer, has been shown to activate TRPM3 on HEK cells analyzed by whole-cell patch clamp (Grimm et al., 2005). Those TRPM3 channels have been identified on oligodendrocytes, where sphingosine-mediated Ca^{2+} increase contributes to cell differentiation (Hoffmann et al., 2010). On the other side, SMase treatment inhibits Ca^{2+} response through TRPV1, while neither Cer nor sphingosine influence the channel activation (Saghy et al., 2015). This suggests a modulation by reduction of SM content, rather than by the production of derivatives. Finally, sphingosine-1-phosphate has been shown to

stimulate TRPC5 in vascular smooth muscle cells via two mechanisms, one extracellular and one intracellular, consistent with its bipolar signaling functions (Xu et al., 2006).

Cholesterol also appears to regulate TRP channels. This is based on the observation that depletion of membrane cholesterol by treatment with methyl-β-cyclodextrin (mβCD) differentially affects TRP channels, stimulating TRPM8 and TRPM3, while reducing the activity of TRPV4 and TRPV1 (Saghy et al., 2015; Startek et al., 2019).

Voltage-Gated Channels

Overview and Pathophysiological Implications

Voltage-gated ion channels (VGCs) are particularly important in excitable cells such as muscular cells and neurons. They are activated by changes in the electrical PM potential near the channel proteins, which alter their conformation, resulting in their opening and closing. Those channels are usually ion-specific and channels specific to Na^+, K^+, Ca^{2+}, and Cl^- ions have been identified (Purves et al., 2001). The biochemically-characterized voltage-gated Ca^{2+} channels (VGCC or Ca_v channels) are complex proteins made of four or five distinct subunits, which are encoded by multiple genes. The α_1 subunit ($Ca_v\alpha_1$) of 190–250 kDa is the largest subunit, containing 24 TM domains. It incorporates the conduction pore, the voltage sensor and gating apparatus, and the known sites of channel regulation by second messengers, drugs, and toxins. Therefore, this subunit determines the physiological and pharmacological properties of the Ca^{2+} current and, as a consequence, the nomenclature.

Three major types of currents that correspond to three α_1 subunit gene families have so far been described. First, L-type Ca^{2+} currents, which occur through Ca_v1 channels, require a strong depolarization for activation and are long lasting. They are the main Ca^{2+} currents recorded in muscle and endocrine cells, where they initiate contraction and secretion. Second, N-, P/Q-, and R-type Ca^{2+} currents, which occur through Ca_v2 channels, also require strong depolarization for activation. They are expressed primarily in neurons, where they initiate neurotransmission at most fast synapses. Third, T-type Ca^{2+} currents, which take place through Ca_v3 channels, are activated by weak depolarizations and are transient (Ertel et al., 2000). As Ca_v2-type channels, they are critically important for regulating neuronal excitability, both in the central and peripheral nervous system, and are essential mediators of hormone secretion (Iftinca and Zamponi, 2009). Interestingly, some of those channels also appear to be mechanosensitive. For instance, Langton et al reported that whole-cell inflation (as a membrane stress) induces smooth muscle L-type Ca^{2+}

currents (Langton, 1993). Since then, the mechanosensitivity of the L-type Ca_v channels has been tested in myocytes in more native conditions using several mechanostimuli-like fluid pressure (Lee et al., 2008) or axial stretching (Iribe et al., 2009). Thus, Ca_v channels regulate a wide variety of processes in excitable cells, such as contraction, secretion, and neurotransmission. Consequently, Ca_v channel dysfunction has been associated with several diseases. Notably, channel hyperactivity has been shown in several neurological disorders like chronic pain conditions and epilepsy, but also muscular and vision syndromes (Bidaud et al., 2006). Therefore, several specific blockers are currently used as therapeutic agents (Zamponi et al., 2015). On the other side, as Ca_v channels also express a mechanosensitivity, their activation in hypertension, which exerts a mechanical pressure on the cardiomyocytes, could elicit a Ca^{2+} signaling that leads to cardiac hypertrophy (Takahashi et al., 2013).

Regulation by Lipids

$PI(4,5)P_2$ has been proposed to activate Ca_v channels in a voltage-independent pathway but the extent of this activation is not clear. In a patch clamp of excised patches containing P/Q- and N-type channels (i.e., Ca_v2 channels), the current is completely and rapidly abolished by $PI(4,5)P_2$ depletion (Wu et al., 2002). On the other hand, in a whole-cell patch clamp of HEK293 cells expressing L-type (i.e., Ca_v1) or P/Q-type channels, the current is only attenuated (~ 29 % to ~ 55 % of control current) upon $PI(4,5)P_2$ depletion (Suh et al., 2010). Ca_v current amplitude (mostly originating from L-type Ca_v channels) in pancreatic β-cells is also reduced upon $PI(4,5)P_2$ depletion. This depletion is achieved through muscarinic M1-receptor activation or activation of a voltage-sensitive phosphatase (de la Cruz et al., 2016; Xie et al., 2016). Therefore, $PI(4,5)P_2$ is expected to have a stimulatory effect on Ca_v channels, stabilizing their activity by reducing current rundown. Even if the molecular mechanism of regulation remains unclear, recent evidences reported that the subcellular localization of $Ca_v\beta$ subunit, and especially of its flexible "HOOK" region, is a key factor for the control of $PI(4,5)P_2$ sensitivity via dynamic electrostatic and hydrophobic interactions with the PM (Park et al., 2017). In contrast to this activation role, an antagonistic effect of $PI(4,5)P_2$, occurring at the same time, has also been suggested in some studies. For instance, $PI(4,5)P_2$ produces a voltage-dependent inhibition by shifting the activation curve to more positive voltages (Rodriguez-Menchaca et al., 2012). This inhibition is thought to be alleviated by phosphorylation by cAMP-dependent protein kinase A (PKA) (Wu et al., 2002).

The PLP derivative AA also modulates Ca_v channel currents, but at more than one site, resulting in biphasic effects. Indeed, AA inhibits currents in Ca_v1-3 on one

hand, and acts at a second distant site to enhance N-current at negative potentials on the other hand (Barrett et al., 2001; Liu et al., 2001). On the other side, LPA (but not PA) has also been shown to induce a Ca^{2+} influx in red blood cells (RBCs). The channel involved has not been identified, but the entry can be prevented by P-type channel blockers, suggesting a role of the erythrocyte $Ca_v2.1$ channels (Yang et al., 2000). This activation induces the erythrocyte aggregation and could be involved in the thrombus formation, around which LPA concentrations are increased (Kaestner et al., 2012).

Regarding SL-mediated regulation, SMase activity stimulates Ca_v channels expressed in oocytes (Combs et al., 2013), an effect that could be linked to the increased channel activity by Cer-1-phosphate in rat pituitary cells (Tornquist et al., 2004).

Finally and as exposed below (see Chapter IV, section 3.1.3), membrane fluidity and consequently cholesterol content also contribute to regulate Ca_v channel activity.

Mechanosensitive Ion Channels

Overview and Pathophysiological Implications

MSCs are located at the PM of many cells and are gated directly by physical stimuli. They transduce those stimuli into an electrical or chemical signal in hearing, touch, and other mechanical senses. MSCs vary in selectivity, from cation-selective to K^+-highly selective in eukaryotes. In comparison to other receptors, the identification of mechanically-activated ion channels has been delayed due to several difficulties: (i) Mechanosensory cells are not abundant and usually mixed with other cells; (ii) MSCs are usually expressed at low levels; and (iii) the channels may be associated in complexes with auxiliary proteins (Arnadottir and Chalfie, 2010).

The first well-studied MSCs were the prokaryotic MSCL (L for “large conductance”), MSCS (S for “smaller conductance”), MSCK (K for “K^+-dependent smaller conductance”), and MSCM (M for “mini-conductance”). They contribute to protection of bacteria from hypo-osmotic shock (Stokes et al., 2003), but also play roles during the cell wall re-modelling upon entry in, and exit from, stationary phase (Stokes et al., 2003). In eukaryotic cells, five different types of channels have been shown to transduce mechanical signals so far: (i) the degenerin/epithelial Na^+ channels (DEG/ENaC), (ii) two-pore domain K^+ (K_{2P}) channels like TREK and TRAAK,

(iii) MSCS-like channels, (iv) TRP channels, and (v) Piezo channels. The three last ones are non-selective for cations (Arnadottir and Chalfie, 2010; Coste et al., 2010).

Since their discovery (Coste et al., 2010), Piezo channels have encountered a great interest among scientists. This family of proteins comprises two members in human, Piezo1 and 2. The genes coding for those proteins share 47 % identity and have no similarity to any other protein. Piezo channels are trimers, each mouse protomer containing at least 26 TM helices, that are shaped like a propeller with three curved blades organized around a central pore. The flexible propeller blades can adopt distinct conformations, and consist of a series of four TM helical bundles (i.e., the Piezo repeats) (Saotome et al., 2017). Piezo1 is a sensor of mechanical forces in endothelial, urothelial, and renal epithelial cells. It is also involved in blood vessel development and integrity, as well as in RBC volume homeostasis. Piezo2, on the other hand, is majorly expressed in somatosensory neurons, where it regulates proprioception and lung inflation-induced apnea (Parpaite and Coste, 2017). As for other Ca^{2+} channels, stretch-activated channels have been associated with major pathologies including cardiovascular diseases, Duchenne muscular dystrophy, lymphatic dysplasia, distal arthrogryposis, and RBC diseases like stomatocytosis (Albuisson et al., 2013; Coste et al., 2013; Patel et al., 2010; Yin and Kuebler, 2010). Moreover, as their discovery is still recent, the extent to which they regulate development and physiology is yet to be completed.

Regulation by Lipids

MSCs are known to be modulated through $PI(4,5)P_2$ and PI(4)P. As a matter of fact, depletion of both species leads to the inactivation of Piezo1 and 2 (Borbiro et al., 2015). This depletion can be induced experimentally either by PI phosphatases or by the activation of TRPV1 channels through capsaicin. Such treatment indeed induces a Ca^{2+} increase, which in turn activates the PLC isoform δ, leading to the degradation of both PI(4)P and $PI(4,5)P_2$ (Rohacs, 2013). This capacity of TRPV1 activation to induce Piezo channel inhibition could partly explain the analgesic effects of capsaicin. On the other hand, activation of the PLC isoform β (through G-protein coupled receptors), an isoform which only targets $PI(4,5)P_2$ but not PI(4)P, only marginally inactivates Piezo currents (Borbiro et al., 2015). Acidic PLPs also appear important for the regulation of the prokaryotic MSCs (Powl et al., 2008) and of the mechano-gated K^+ channel TREK-1 (Chemin et al., 2007). Moreover, PS exposure at the surface of myoblasts suppresses piezo1 activation and in turn impairs myotube formation, suggesting that the appropriate localization of PS in the inner PM leaflet is crucial for the activity of piezo1 and that cell surface flip-flop of PS acts as a molecular switch for piezo1 activation that governs proper morphogenesis during myotube formation (Tsuchiya et al., 2018).

Regarding the PLP derivatives, lysoPS (LPS) suppresses Ca^{2+} influx via Piezo1 when it is incorporated into the outer PM leaflet of C2C12 myoblasts. On the other side, incorporation of LPC (a zwitterionic lysoPLP) shows no significant inhibitory effect on Ca^{2+} influx. All those data suggest that the PLPs with a phosphoserine headgroup present on the outer PM leaflet are responsible for the inhibition of piezo1 activation (Tsuchiya et al., 2018).

Finally, the activity of MSCs also appears to be regulated by lipid rafts and thus by cholesterol (see Chapter IV, section 3.1.4).

Endo/Sarcoplasmic IP_3R and RyR Channels

Overview and Pathophysiological Implications

The release of Ca^{2+} ions from the ER/SR is the most versatile cellular signaling mechanism and is responsible for several cellular effects including secretion (Petersen and Tepikin, 2008), smooth muscle contraction (Sanderson et al., 2008), gene transcription (Feske et al., 2001), and fertilization (Malcuit et al., 2006). Ca^{2+} release from those stores is mediated by two Ca^{2+}-release channels (i.e., the inositol-1,4,5-triphosphate receptors (IP_3Rs) and the ryanodine receptors (RyRs)), the latter being so named because they possess a high-affinity binding site for the plant alkaloid ryanodine (Sutko et al., 1997). The IP_3R family is ubiquitously expressed and is comprised of three homologous isoforms (types 1–3) encoded by separate genes. The IP_3R is formed of four 313 kDa-subunits that comprise three major regions: The N-terminal region to which IP_3 binds, the C-terminal region with its six TM domains, and a large intervening sequence (Galvan et al., 1999). RyR channels have similarities with IP_3Rs. First, the RyR family is also comprised of three isoforms, type 1 being expressed in skeletal muscle, type 2 in both cardiac muscle and brain, and type 3 at low levels in a wide range of tissues (Fleischer, 2008). Second, the RyR complex is also a tetramer, although a little bigger than the IP_3R complex. Third, the pore of both channels is formed by the final pair of TM domains (domains 5–6) and the luminal loop that links them from each of the four subunits (Ramos-Franco et al., 1999; Williams et al., 2001).

IP_3R and RyR channels are extremely efficient Ca^{2+}-cytosolic release channels with a large conductance, but only modest selectivity for Ca^{2+} over monovalent cations (Foskett et al., 2007; Williams et al., 2001). In the ER/SR, where most channels are located, this lack of selectivity is probably not problematic since Ca^{2+} exhibits an appreciable electrochemical gradient across the ER membrane. As their activation follows an increase of the Ca^{2+} concentration in the cytosol, IP_3R and RyR most probably do not contribute to the general enhancement of the Ca^{2+} concentration, but are rather responsible for complex patterns relative to both

space and time, such as Ca^{2+} waves, oscillations or sparks (Yoshida and Imai, 1997). For instance, "nuclear Ca^{2+} waves" that engulf the entire nucleus without spreading into bulk cytosol have been evidenced upon IP_3R/RyR activation in cardiomyocytes (Luo et al., 2008), and could activate Ca^{2+}-dependent transcription factors (Ljubojevic and Bers, 2015). Ca^{2+} sparks could also contribute to membrane hyperpolarization through the activation of plasmalemmal BK_{Ca} (large conductance Ca^{2+}-activated K^+ channels) (Jaggar et al., 1998). Dysfunction of these ion channels has been linked to a wide range of neurodegenerative and neuromuscular diseases like ataxia, but also heart disease, exocrine secretion deficit, and taste-perception deficit (Bezprozvanny, 2007; Durham et al., 2007).

Regulation by Lipids

Besides Ca^{2+} (Foskett et al., 2007), phosphorylation (Vanderheyden et al., 2009), ATP (Yule et al., 2010), and numerous interacting proteins (Choe and Ehrlich, 2006), IP_3R channel activity is regulated by IP_3, which is produced upon PLC activation by a variety of G protein-coupled receptors (GPCRs), including muscarinic, adrenergic, and angiotensin receptors (Wettschureck and Offermanns, 2005). $PI(4,5)P_2$ also regulates the ER/SR Ca^{2+} transport proteins by stimulating RyR while inhibiting IP_3R activity. This has been mostly tested by incorporation of the receptors into membrane bilayers containing, or not containing, $PI(4,5)P_2$ (Chu and Stefani, 1991; Lupu et al., 1998). However, the physiological relevance of this regulation can be asked, as $PI(4,5)P_2$ concentration at the ER/SR membrane is even lower than at the PM.

Store-Operated Ca^{2+} Release-Activated Ca^{2+} (CRAC) Currents

Overview and Pathophysiological Implications

At rest, the SERCA activity is sufficient to maintain high $[Ca^{2+}]_{ER}$, but after elevated Ca^{2+} signaling and release of ER-associated Ca^{2+} into the cytoplasm, the ER store may become depleted. The emptying of the ER stores is sensed by stromal interaction molecules (STIM) (Liou et al., 2005) that interact with Orai1 proteins (also called CRACM1) at the PM (Feske et al., 2006; Huang et al., 2006), allowing for *SOCE (for* store-operated Ca^{2+} entry) *currents* mediated by Orai1 channels (i.e., *CRAC* [for store-operated Ca^{2+} release-activated Ca^{2+}] *currents*).

The STIM protein family includes two members, STIM1 and STIM2, which share ~ 61 % sequence identity (Cahalan, 2009). Those single TM proteins contain (i) a N-terminal portion including the Ca^{2+}-sensing domain localized within the ER lumen,

and (ii) a long cytosolic strand, which couples to Orai channels in the PM. The Ca^{2+}-sensing domain is formed by an EF-hand (i.e., a low affinity Ca^{2+} binding domain which loses Ca^{2+} upon store depletion). The transmission of this loss is ensured through the sterile-α-motif (SAM) domain, which initiates the CRAC signaling cascade (Zheng et al., 2011). Thus, the Ca^{2+} depletion leads to a change of conformation of STIM protein in its active form (Ma et al., 2015). STIM1, normally homogenously distributed (Smyth et al., 2008), moves rapidly to multimerize while translocating along the ER membrane towards a location where the ER and the PM are in close proximity (i.e., a ~ 17 nm distance) (Wu et al., 2006). Subsequently, STIM1 couples to and stimulates Orai1, initiating pronounced CRAC currents (Zhou et al., 2010). However, STIM1 function is likely to be even more complex, since it has been shown to not only activate Orai1 but to also inhibit neighboring voltage-activated $Ca_v1.2$ channels (Wang et al., 2010) and to activate TRPC1 channels (Huang et al., 2006).

Orai proteins are highly selective Ca^{2+} channels present at the PM (Prakriya et al., 2006). The three homologs, Orai1–3, contain four TM domains that share ~ 81 % –87 % sequence identity, flanked by cytosolic N- and C-termini. Both cytosolic strands are required for functional coupling to STIM1 (Muik et al., 2008). Thanks to its crystal structure, unveiled in 2012, the channel has been shown to be composed of six Orai subunits, with the TM domains arranged in concentric rings around a central aqueous pore formed exclusively by the first TM helix of each subunit. Moreover, Orai monomers are arranged as three dimers, leading to a three-fold symmetry (Hou et al., 2012). Mutations in the STIM–Orai proteins have been linked with severe combined immune deficiency syndrome (Feske et al., 2006). Indeed, Orai channels play an important role in the activation of T-lymphocytes.

Regulation by Lipids

$PI(4,5)P_2$ appears critical for the SOCE mechanism and especially for the STIM1 interaction with the PM. Indeed, $PI(4,5)P_2$ depletion partially inhibits translocation of STIM1 into puncta, a process that can be recovered by overexpression of Orai1 (Walsh et al., 2009). Accordingly, upon activation, the exposed C-terminal polybasic segment of STIM1 interacts with $PI(4,5)P_2$ or $PI(3,4,5)P_3$ at the PM, trapping STIM1, which in turn binds to Orai1 (Ercan et al., 2009). Additionally, the Ca^{2+}-independent $iPLA_2\beta$ has been shown to be an essential component of signal transduction for the SOCE mechanism in several cells (Bolotina, 2008). As a matter of fact, lysoPLPs products of $iPLA_2\beta$ activate SOCE in excised membrane patches, suggesting a STIM-independent pathway (Smani et al., 2004).

SLs and derivatives also regulate the SOCE mechanism. Indeed, Orai1 activity is highly decreased by a SMase treatment, suggesting a positive effect of SM (Combs and Lu, 2015). On the other side, Cer induces activation of CRAC channels (Colina et al., 2005), an observation that apparently contrasts with the study showing that the addition of Cer-1-phosphate does not modulate the Orai1 activity (Combs and Lu, 2015).

Finally, Orai1 and its modulator STIM are also thought to be directly regulated by cholesterol (Derler et al., 2016; Pacheco et al., 2016). In fact, cholesterol has been shown by fluorescence binding studies to bind to the Orai1 amino-terminal fragment. The same group has revealed that cholesterol binds to the full-length Orai1 in mucosal-type mast cells, allowing them to conclude that Orai1 might sense the amount of cholesterol in the PM and their interaction might inhibit the channel activity, thereby limiting SOCE. As a consequence, cholesterol depletion enhances Orai1-mediated CRAC currents in HEK cells expressing Orai1 as well as in mast cells (Derler et al., 2016). Another study shows contradictory results on pulmonary endothelial cells, in which cholesterol reduction after chronic hypoxia decreases Orai1-mediated CRAC currents, suggesting that cholesterol is required for STIM–Orai1 interactions and SOCE. Moreover, using epicholesterol (the enantiomer of cholesterol), the authors concluded on cholesterol specificity and not on lipid raft integrity dependence (Zhang et al., 2018). Further studies are needed to understand the discrepancies between those studies. Finally, and in a similar mechanism to the one described above for $PI(4,5)_2$, STIM1 has a cholesterol-binding domain that is located in the "STIM–Orai activating region" (i.e., the region responsible for interaction with Orai1). However, the interaction between this domain and the inner PM leaflet cholesterol has an inhibitory effect on Orai1 activity, as it reduces the binding between the two proteins (Pacheco et al., 2016).

3.1.2. Ca^{2+} Efflux Through Exchangers and Selective Pumps

The PM presents two systems for Ca^{2+} extrusion: (i) A low-affinity, high-capacity NCX ; and (ii) a high-affinity, low-capacity PMCA . NCX and PMCA vary in relative proportion from one cell type to another, the NCX being particularly abundant in excitable tissues (e.g., heart and brain) where cells experience important Ca^{2+} peaks. Cytosolic Ca^{2+} is also restored to basal levels by sequestration in the ER/SR via the SERCA pump.

Introduction

Na^+/Ca^{2+} Exchanger (NCX)

Overview and Pathophysiological Implications

The NCX accomplishes Ca^{2+} extrusion by using the electrochemical gradient of Na^+: During each cycle, three Na^+ ions flow down their gradient across the membrane in exchange of the counter transport of one Ca^{2+} ion against its gradient. This antiporter is particularly abundant in the PM, the mitochondria, and the ER of excitable cells like in the heart, but is also expressed in other tissues such as the smooth and skeletal muscle, the kidney, and the brain. Structurally, NCX antiporter contains 10 TM domains with a pseudo-symmetry probably resulting from a gene duplication event (Cai and Lytton, 2004). Between the pseudo-symmetric halves, a large cytoplasmic loop is inserted containing regulatory domains that have C2 domain-like structures (Besserer et al., 2007). The binding of Ca^{2+} on those sites generally activates the exchanger, whereas binding of Na^+ ions has been shown to deactivate it (Brini et al., 2010).

The NCX does not bind very tightly to Ca^{2+} (i.e., low affinity), but it can transport the ions rapidly (i.e., high capacity), with up to 5000 Ca^{2+} ions per second (Carafoli et al., 2001). Therefore, it requires large concentrations of Ca^{2+} to be effective and is useful for ridding the cell of large amounts of Ca^{2+} in a short time. It plays a major role in neurons after an action potential, in cardiac muscle relaxation, or in excitation-contraction, a.o. However, the result of this channel activation is a brief influx of a net positive charge (Na^+), thereby causing cellular depolarization. Since the exchanger direction depends on the membrane polarization, it can change its transport direction if the cell is depolarized enough. The ability for the NCX to reverse direction of flow notably manifests itself during the cardiac action potential, as described in (Bers, 2002). As the transport can occur in both ways depending on the membrane potential, NCX activity has been linked to excitotoxicity, a pathological process in which nerve cells are damaged or killed by excessive stimulation and subsequent abnormal and harmful Ca^{2+} increase (Yu et al., 1997). NCX has been shown to play controversial roles, suggesting that it may operate in both forward (therefore, neuroprotective) and reverse (neurodamaging) directions simultaneously in different areas of the cell, depending on the combined effects of the Na^+ and Ca^{2+} gradients.

Regulation by Lipids

In 1996, Hilgemann et al showed that $PI(4,5)P_2$ activates the NCX1 in cardiac membranes (Hilgemann and Ball, 1996). Four years later, Philipson et al evidenced that $PI(4,5)P_2$ binds to the endogenous XIP region following putative TM helix 5, suggesting that this lipid directly interacts with the transporter as a non-annular

lipid (He et al., 2000). As a consequence, increase of $PI(4,5)P_2$ levels can eliminate the inactivation of the exchanger resulting from the decreased $[Ca^{2+}]_{ic}$ or increased $[Na^+]_{ic}$ (Reeves and Condrescu, 2008). On the other side, $PI(4,5)P_2$ depletion by PLC-coupled muscarinic M1-receptor agonists strongly inhibits NCX1 current (Yaradanakul et al., 2007). Additional indirect, and possibly opposing, mechanisms of NCX1 regulation by $PI(4,5)P_2$ have also been described. Those include the membrane trafficking of NCX1 and the contribution of the $PI(4,5)P_2$–cytoskeleton interactions in its activation (Yaradanakul et al., 2007).

Other acidic PLPs might regulate the activity of NCX1. Indeed, whereas barely any exchange activity is obtained upon reconstitution of NCX1 into pure PC vesicles, a higher activity (about 25 % of the value when reconstituted in vesicles from native sarcolemmal membranes) is observed in membranes containing PS, or PA. On the other side, PI and PG induce little activity enhancement in comparison to pure PC vesicles. Addition of cholesterol elevated transport activity to native-like levels for the former two anionic lipids, but not for PI or PG (Vemuri and Philipson, 1988). Those data suggest that PS and PA can interact with NCX1 unlike PG and PI, possibly because the negatively-charged moiety of the former lipids is less buried in the headgroup than the one of the latter (Denning and Beckstein, 2013).

Regarding SLs, Cer has been shown to inhibit NCX influx and efflux modes when expressed in Chinese hamster ovary (CHO) cells. Localized mutations of the exchanger have allowed to evidence that Cer impairs the Ca^{2+}-dependent activation of the exchanger while not affecting its Na^+-dependent activation (Condrescu and Reeves, 2001). Sphingosine seems to ensure a similar regulation as Cer (Condrescu and Reeves, 2001). On the other side, ganglioside GM1 (but not other gangliosides) appears to closely bind to the NCX at the nuclear membrane, activating thereby Ca^{2+} transfer from nucleoplasm to ER (Ledeen and Wu, 2008; Wu et al., 2009). The importance of such a regulatory role is demonstrated by the susceptibility to excitotoxicity and apoptosis of neurons in GM2/GD2-synthase KO mice, a phenotype that can be substantially reduced by injection of a semisynthetic analog of GM1 (Wu et al., 2005).

Plasma Membrane Ca^{2+} ATPase

Overview and Pathophysiological Implications

With a complementary activity to the NCX antiporter, PMCA ensures the maintenance of the very low $[Ca^{2+}]_{ic}$, thanks to its much higher affinity but much lower capacity. The PMCA pump is a minor component of the total PM proteins (<

0.1 %) and is quantitatively overshadowed by the NCX in excitable tissues. However, even in cells in which the NCX predominates, the PMCA pump is likely to be the fine tuner of cytosolic Ca^{2+}, as it can work in a concentration range in which the low affinity NCX is inefficient. The PMCA pump is a P-type ATPase, characterized by the temporary conservation of ATP energy in the form of a phosphorylated enzyme intermediate (P-type). There are four PMCA isoforms which exhibit tissue-specific expression (Brini and Carafoli, 2009). PMCA1 and 4 are expressed in most tissues while PMCA2 and 3 are mostly restricted to the brain, the striated muscle, and the mammary gland. The pump operates with a 1:1 Ca^{2+}:ATP stoichiometry. It is predicted to have 10 TM domains, two large intracellular loops, and N- and C-terminal cytoplasmic tails. The catalytic site is sealed by an auto-inhibitory domain, whose binding to calmodulin upon intracellular Ca^{2+} increase will free the site and allow the increase of the PMCA affinity for Ca^{2+} (Kd from ~ 10–20 to < 1 μM) (Brini and Carafoli, 2009). The pump also presents other modulation sites, like a binding site for 14-3-3 proteins (Rimessi et al., 2005), consensus sites for PKA and PKC, and a high-affinity allosteric Ca^{2+} binding site. The PMCA pump is also a substrate of intracellular proteases, as it contains target sequences for calpains (Guerini et al., 2003) and caspases (Paszty et al., 2007).

PMCA isoforms have been shown to be involved into several processes. Notably, PMCA2 is critical for hearing as it dissipates with peculiar kinetics the Ca^{2+} transiently increased by the opening of MSCs. PMCA4 prevents the Ca^{2+} overload and resulting mitochondrial damages in spermatozoids and is crucial to sperm motility and male fertility (Schuh et al., 2004). This pump isoform is also essential for the modulation of the activity of the neuronal nitric oxide synthase (nNOS) (Schuh et al., 2001) and thus for the control of NO production, itself contributing to the regulation of excitation–contraction coupling of the heart. Consequently, mutations in PMCA have been linked to several oxidative stress-related diseases, like atherosclerosis, diabetes, and neurodegenerative diseases. PMCA defects also have been reported in various cancer types (Monteith et al., 2007).

Regulation by Lipids

As for other Ca^{2+} transport proteins, PMCA is modulated by several lipids. First, the acidic lipids PS and PI (but not the neutral PE) increase the activity (V_{max}) of the PMCA pump by accelerating dephosphorylation (Filomatori and Rega, 2003) and increasing the Ca^{2+} affinity (i.e., decreased Kd) (Di Leva et al., 2008). The sensitivity of the PMCA to acidic PLPs is located in two domains of the enzyme, one close to the carboxyl terminus and partially shared with the calmodulin-binding site, and the other located between TM domains 2 and 3 (Filoteo et al., 1992). However, the importance of this regulation is debated. On one hand, Carafoli et al concluded that

the erythrocyte pump is probably permanently activated by acidic PLPs to ~ 50 % of its maximal activity (Niggli et al., 1981). On the other hand, Denning and Beckstein consider that, as acidic PLPs have to be at least 40 % of the total PLPs to have an effect (a concentration rarely encountered in mammalian membranes), it is quite unlikely that PMCA is regulated by acidic PLPs in vivo (Denning and Beckstein, 2013). This minimal concentration could, nevertheless, be reached thanks to compartmentation of the pump in acidic PLP-enriched domains, which remain nevertheless to be evidenced.

The PLP derivative DAG is also able to stimulate the PMCA pump, through the induction of an increment in the V_{max} of the enzyme and in the affinity of the protein for Ca^{2+}. The activation induced is additive to that produced by PKC, implying that DAG interacts with the PMCA through a different mechanism, which has been shown to be direct (Perez-Gordones et al., 2009).

SLs, and especially gangliosides, modulate PMCA activity in a complex pattern. Indeed, in cortical neurons and synaptosomes, polysialogangliosides (e.g., GD1b) stimulate, monosialogangliosides (e.g., GM1) slightly reduce the activity, and non-sialogangliosides (e.g., asialo-GM1) markedly inhibit PMCA2 and 3, predominant in those cells (Jiang et al., 2014; Zhao et al., 2004). Thus, the sialic acid residues of gangliosides are important for the modulation of PMCA. Besides, the ganglioside oligosaccharide length (e.g., one sialic acid combined with four sugars in GM1 vs three in GM2 vs two in GM3) also affects the PMCA activity (Zhao et al., 2004). Moreover, the effects of gangliosides on the PMCA appear to be isoform-specific. Indeed, in erythrocytes where PMCA1 and 4 are predominant, GD1b, GM1, GM2 at low concentration, and GM3 all stimulate the PMCA activity, while GM2 at high concentration inhibits it (Duan et al., 2006; Zhang et al., 2005). The mechanism by which gangliosides modulate the PMCA activity is still discussed. Indeed, while some studies show that the ganglioside effect is additive to that of calmodulin, affecting both the affinity for Ca^{2+} and the V_{max} of the enzyme (Zhao et al., 2004), others suggest that gangliosides interact with the calmodulin-binding domain, activating the phosphatase activity of the PMCA (Duan et al., 2006). Moreover, Cer increases both the affinity for Ca^{2+} and the V_{max} of the PMCA (Colina et al., 2002). On the other side, the Cer metabolite sphingosine exerts an antagonistic regulation by inhibiting the pump (Colina et al., 2002).

Finally, as exposed below (see Chapter IV, section 3.1.4), PMCA appears to be associated with cholesterol-enriched domains and the depletion of this lipid abrogates the pump activity in those domains.

Introduction

Sarco/Endoplasmic Ca^{2+} ATPase (SERCA)

Overview and Pathophysiological Implications

Sarco/endoplasmic Ca^{2+} ATPase (SERCA) is a P-type-ATPase that resides at the ER/SR membrane. It transports two Ca^{2+} ions in exchange of the hydrolysis of one ATP molecule and allows to restore luminal ER/SR Ca^{2+} levels (Guerrero-Hernandez et al., 2010). Distinct genes code for the three different pumps, SERCA1–3, generating 10 isoforms by alternative splicing. SERCA1 is mainly expressed in skeletal muscle, SERCA2a in cardiac and skeletal muscles, and SERCA2b and 3 in non-muscle cells (Brini and Carafoli, 2009; Periasamy and Kalyanasundaram, 2007). The pump contains 10 TM domains and three major domains on the cytoplasmic face: The phosphorylation and nucleotide-binding domains, which together form the catalytic site, and the actuator domain, which is involved in the transmission of major conformational changes. Small molecules, such as phospholamban (PLB; a SR Ca^{2+}-ATPase inhibitor, highly expressed in cardiac muscle) and sarcolipin (another small molecular weight protein), modulate SERCA activity according to cellular requirements and/or extracellular signals (Brini and Carafoli, 2009; Periasamy and Kalyanasundaram, 2007). For example, SERCA is not active when PLB is bound to it. Increased β-adrenergic stimulation induces the phosphorylation of PLB, reducing its association with the SERCA and favoring Ca^{2+} movements. Calreticulin, an ER protein, and calsequestrin, its SR homolog, play also a major role by sequestering Ca^{2+} within the ER/SR and thus reducing the concentration gradient against which the pump has to work. Indeed, the ER/SR exhibits a much higher Ca^{2+} concentration (10,000×) than the cytosol.

The pump process is carried out in two steps featuring two conformations: An E1 phase that allows for the binding of all substrates, and a post-ATP hydrolysis E2 phase that forces the movement of ions through the protein across the membrane. In smooth, skeletal, and cardiac muscles, SERCA exerts two main functions: It decreases Ca^{2+} levels in cytosol to initiate muscle relaxation and it reloads Ca^{2+} into SR, required for muscle contraction. Indeed, during contraction, the sarcoplasm is flooded with Ca^{2+} ions, which indirectly allows for the contraction of muscles through interactions between actin and myosin. It has also been evidenced that the SR regulates membrane excitability by a negative-feedback control step on Ca^{2+} entry. As a consequence of its function, mutations in the pump can result in a life-altering condition in cattle, as pseudomyotonia, a disease that restricts the relaxation of most muscles.

Regulation by Lipids

Unlike PMCA and NCX1, the SERCA pump is inhibited by PS and PA when the mole fraction of those acidic PLPs in a PC membrane exceeds 60 % (Dalton et al., 1998). Specifically, maximal levels of ATP binding are reduced below 40 % of the native membrane values, without a concomitant reduction in the pump affinity for ATP. Since acidic PLPs do not bind specifically to the protein, one possible explanation is that oligomerization of ATPases renders ATP binding sites inaccessible (Dalton et al., 1998). Sphingosine also inhibits the SERCA pump in a mechanism that is similar to the thapsigargin one (Benaim et al., 2016). Finally, the SERCA pump activity also depends on the surrounding membrane cholesterol. Indeed, using microsomes prepared from macrophages, Tabas et al evidenced that the enrichment in cholesterol of ER membranes (normally cholesterol-poor),i.e. in conditions somehow mimicking atherosclerotic lesions, inhibits SERCA2b (Li et al., 2004).

3.2. Ca^{2+} modulation during RBC deformation

3.2.1. Ca^{2+} increase

Among the Ca^{2+} channels present at the RBC membrane, one can cite TRPC6 (Foller et al., 2008) and $Ca_v2.1$ (Andrews et al., 2002) (figure 1.10, green). Those have been described in section 3.1.1 but their importance for, and role in, RBC pathophysiology is still poorly understood. Other surprising channels like NMDA receptors have also been identified. Those are especially present on RBC precursors and their abundance decreases through maturation (Makhro et al., 2013; Makhro et al., 2017). Finally, mechanosensitive Piezo1 channels have been described (Cahalan et al., 2015) (figure 1.10, green). They have been the object of a big focus as they are thought to be responsible for the major Ca^{2+} entry in RBCs upon mechanical stimulation (Danielczok et al., 2017; Lew and Tiffert, 2017). This is why we also concentrated on those channels during this thesis. As described above (section 3.1.1.), Piezo1 is a huge cation-permeable channel, which is activated in the microsecond timescale and closed in the millisecond range in the continued presence of the stimulus (Murthy et al., 2017). The mechanism of gating for this channel is under study by several groups (Cox et al., 2016; Moroni et al., 2018; Syeda et al., 2016) and could notably involve the local bending of the membrane that is supposedly induced by the channel's propeller shape (figure 1.11) (Saotome et al., 2018).

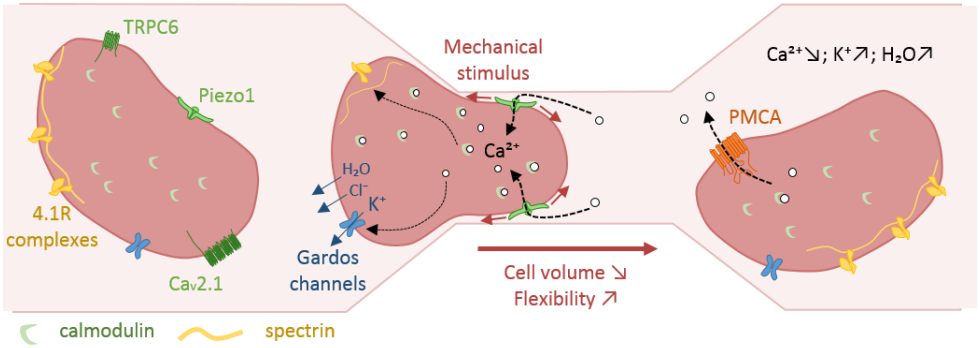

Figure 1.10. Ca^{2+} signaling in RBCs upon deformation. RBC Ca^{2+} influx channels comprise TRPC6, Cav2.1 and Piezo1 (green). Piezo channels are activated upon mechanical stimuli and induce an increase of $[Ca^{2+}]$ic during deformation. Ca^{2+} will (i) bind to calmodulin and induce the decoupling of the anchorage between the membrane and the spectrin cytoskeleton (yellow); (ii) activate the Gardos channels, leading to a loss of K^+ and H_2O (blue); and (iii) activate the PMCA which pumps the Ca^{2+} out of the cell after deformation (orange). Adapted from (Danielczok et al., 2017).

Piezo1 can be pharmacologically activated through the small molecule Yoda1, an irreversible activator that binds to a region located at the interface between the pore and the putative mechanosensory domains of each subunit (Lacroix et al., 2018). Piezo channels, and more generally all cationic MSCs, can be inhibited by the spider venom peptide GsMTx4. This peptide presents six lysine residues that are proposed to stabilize GsMTx4 placement at the membrane surface. The peptide would only occupy a small fraction of the surface area in unstressed membranes while, upon tension, the decreased lateral pressure imposed by membrane lipids would allow the peptide to penetrate deeper. GsMTx4 molecules could therefore act as “area reservoirs” leading to partial relaxation of the outer monolayer, reducing the effective magnitude of stimulus acting on the MSC gate (Gnanasambandam et al., 2017).

Mutations in Piezo1 have been associated with hereditary xerocytosis, also named dehydrated stomatocytosis. There is important heterogeneity in the clinical, laboratory and genetic bases of this disease, in which Piezo1 variants exhibit a partial gain-of-function phenotype. The mutations are thought to alter channel kinetics by slowing channel’s inactivation, but could also affect membrane protein trafficking and modify responses to osmotic stress (Glogowska et al., 2017). The

Ca^{2+} increased permeability induces permanent RBC dehydration (see 2.2.2.), which decreases its deformability and results in hemolytic anemia (Zarychanski et al., 2012).

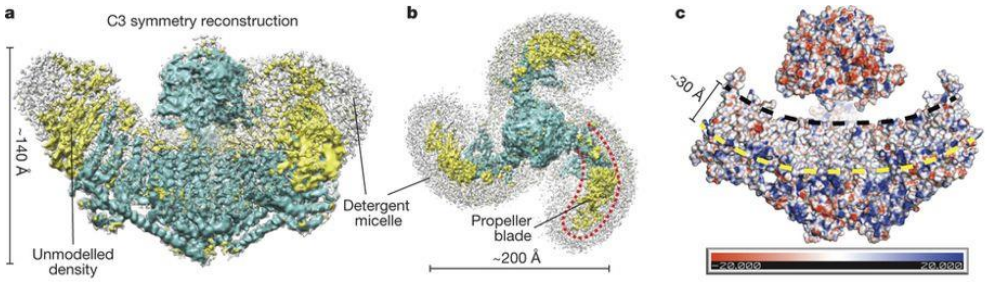

Figure 1.11. Piezo1 channel structure. Side **(a)** and top **(b)** views of Piezo1 obtained from cryo-electron microscopy maps. Density corresponding to modelled regions is colored green. Less resolved density that was not modelled is colored yellow. At lower thresholds (transparent grey map), scattered density probably originating from a detergent micelle can be observed. **(c)** Surface electrostatics of the Piezo1 core model. Note the bent hydrophobic stripe representing the transmembrane region. Dotted lines approximate the extracellular (black) and cytosolic (yellow) membrane boundaries. Reproduced from (Saotome et al., 2018).

3.2.2. Intracellular Ca^{2+} targets

The targets of intracellular Ca^{2+} include Gardos channels, calmodulin, PKCα but also μ-calpain and scramblase (see section 5.3.1.). Transient activation of Gardos channels and of calmodulin as well as PKCα-mediated activities will favour RBC deformation (figure 1.10). However, the extended Ca^{2+} increase and subsequent continuous activation of those proteins, in addition to μ-calpain protease and scramblase (see section 5.3.1), will promote the RBC loss of deformability and senescence, as described in next section (section 4.1.) (Bogdanova et al., 2013).

K^+ efflux through Gardos channels

Gardos channels (or KCNN4) are Ca^{2+}-activated K^+ channels with an EC50(Ca^{2+}) of ~4.7 μM (Leinders et al., 1992). Whole-cell patch-clamp recordings of normal human RBCs showed that brief suction pulses through the patch pipette elicit a Ca^{2+} influx sufficient to activate secondary currents through Gardos channels

(Dyrda et al., 2010). K^+ loss through channel opening leads to the hyperpolarization of the membrane, which in turn sets driving force for net anion (Cl^-) loss through electrodiffusional pathways (figure 1.10, blue). The consequent change in osmolarity induces RBC dehydration resulting in cell shrinkage (Dyrda et al., 2010). This surprising ability of RBCs to reduce their volume in response to mechanical forces could improve their ability to traverse through small-diameter capillaries and splenic sinusoids, as suggested by (Cahalan et al., 2015). Additionally, it is possible that this reduction in volume helps in O_2/CO_2 exchanges in the periphery by concentrating Hb within RBCs, which may promote release of O_2 from Hb. As a matter of fact, mechanical stimulation of RBCs by optical tweezers (see section 6.1.1) has been shown to cause such a release of O_2 (Rao et al., 2009). Finally, Gardos channels could have another physiological function related to coagulation. Indeed, platelet-released substances trigger the opening of RBC Ca^{2+} channels, therefore favoring RBC dehydration and aggregation in clot formation (Kaestner et al., 2004). Gardos channel hyperactivity has been linked to pathological conditions like hereditary xerocytosis (Rapetti-Mauss et al., 2015) or sickle cell disease. In the latter disease, abnormal Hb production (HbS) leads to its polymerization when it is deoxygenated. Interaction of HbS polymers with RBC membrane induces an increase in permeability to cations, including Ca^{2+} ("Psickle"). Resulting increase of $[Ca^{2+}]_{ic}$ initiates sickle cell dehydration, which greatly contributes to the disease pathophysiology (Lew et al., 2002).

Cytoskeleton remodelling

In addition to cell dehydration, an important cytoskeleton remodelling is also expected following $[Ca^{2+}]_{ic}$ increase (figure 1.10, yellow). First, calmodulin, i.e. a small protein comprising two globular EF-hands that bind Ca^{2+}, is recruited to the membrane upon Ca^{2+} binding. At the membrane, it notably interacts with 4.1R, reducing the latter's affinity for its partners (Nunomura and Takakuwa, 2006). It also binds with αβ-adducin, resulting in disruption of the actin protofilaments which are normally capped by this protein (see section 2.3) (Franco and Low, 2010). Second, Ca^{2+}-dependent activation of PKCα also causes its translocation at the PM, where it phosphorylates 4.1R and α-adducin, decreasing their interactions with the other components of the 4.1R complex, notably β-spectrin and F-actin (Manno et al., 2005). Ca^{2+} will thus promote a transient dissociation of the 4.1R complex-mediated anchorage between the membrane and the cytoskeleton, which **promotes RBC deformation.**

Ca^{2+} efflux through PMCA activation

Third, Ca^{2+} will activate the PMCA extrusion pump (see section 3.1.2.), allowing for the restoration of the initially low $[Ca^{2+}]_{ic}$ concentration and avoiding a too

important or too extended Ca^{2+} increase (figure 1.10, orange). RBCs express the PMCA isoforms 4 (~70 % of RBC total PMCA) and 1 (Strehler et al., 1990). The binding of Ca^{2+}-calmodulin to the C-terminal domain will lose its binding to the catalytic site, activating the pump (Lopreiato et al., 2014; Zaidi et al., 2018). Moreover, activated PKCα will phosphorylate a conserved aspartate residue to further activate the pump. The limiting factor to the transport capacity of PMCA is the ATP availability (Boguslawska et al., 2014). Even though PMCA mutations have not been described in RBC diseases, a strong association between multiple SNPs (single nucleotide polymorphisms) in the PMCA4 gene and severe malaria has been evidenced, suggesting that alteration of the pump expression/structure/function could contribute to the susceptibility to severe malaria (Timmann et al., 2012).

4. Pathophysiological events associated with RBC deformation impairment

4.1. Physiological senescence

Under normal circumstances, human RBCs live approximately 120 days in blood circulation, implying the existence of tightly regulated molecular mechanisms responsible for the programming of the lifespan and the nonrandom removal of senescent RBCs. After those 120 days, RBCs are trapped in the spleen and eliminated by the resident macrophages. The trapping results from both mechanical damages and biochemical alterations. The mechanical damages, i.e. loss of deformability, are tested by the endothelial slits through which the RBC has to deform to rejoin the venous sinuses, as explained in section 2.1. This loss of deformability is mostly due to loss of membrane through vesiculation, and it has been assessed that the average surface area loss would have to be of > 18 % (i.e. > 27 % reduced surface area-to-volume ratio) to induce a rapid and complete entrapment in the spleen (Safeukui et al., 2012).

The biochemical damages, on the other side, will contribute to the RBC recognition and elimination by macrophages. Among them, one can cite (i) the loss by vesiculation of CD47, a “marker-of-self”; (ii) the externalization of PS, a lipid normally restricted to the inner PM leaflet (see section 5.3.1); and (iii) the aggregation of Band3 (Bosman et al., 2005). Band3 clusters are proposed to be targets of natural occurring antibodies (Nabs) of the IgG isotype (Lutz, 2004) and are thought to be the major factor determining macrophage’s recognition. However, as Nabs are not efficient opsonins, it has been hypothesized that phagocytosis of RBC is enhanced by the activation of the classical pathway of the

complement system after NAb binding (Lutz and Bogdanova, 2013). Once the classical pathway is activated, a significantly lower amount of NAbs is needed for induction of phagocytosis. The other "eat me" signal at the RBC surface, i.e. PS externalization, is recognized through various receptors at the macrophage surface, and possibly through bridging proteins like glycoproteins (de Back et al., 2014). Finally, CD47 binds the signal regulatory protein alpha (SIRPα) expressed by macrophages, inhibiting the phagocytosis. Its loss in vesicles upon senescence thus removes the inhibition signal.

All those mechanical and biochemical damages are thought to result from three major perturbations, i.e. the accumulation of oxidative damages, which act in concert with Ca^{2+} accumulation and ATP decrease (Cimen, 2008). As a matter of fact, all those perturbations initially result from the inability for the RBC to renew its enzymes/transporters and to retrieve its damaged proteins/lipids. Indeed, upon RBC aging, the activity of several antioxidant proteins like superoxide dismutase 1 and catalase has been shown to decline (Bartkowiak et al., 1983; Bartosz, 1980). Moreover, the transport of glucose, as well as the activity of many glycolytic enzymes, also decrease with RBC aging (Bosman and Kay, 1990; Fornaini et al., 1985), contributing to a shortage of antioxidants cofactors (NADPH and GSH) production. As a consequence, gradual accumulation of irreversibly oxidized and denatured proteins occurs with ageing (Rifkind and Nagababu, 2013). In addition to this, the splenic environment in which poorly deformable RBCs are trapped is hostile: low pH, low glucose and low ATP concentrations as well as high concentrations of oxidants, a.o. (Perrotta et al., 2008). This "splenic conditioning" increases the level of damages inside the RBCs. An interesting fact is that cell age-related oxidation is largely a membrane-localized event, because free radical generators are compartmentalized. Most of them are localized within the membrane or are attached to membrane proteins from the cytosolic side, whereas antioxidant enzymes and their cofactors are randomly distributed within the cytosol (Lutz and Bogdanova, 2013). This compartmentalization can be explained by the fact that deoxyHb readily binds to the cytosolic domain of Band3 (see section 1.3.1) and that it dramatically facilitates oxyHb auto-oxidation, which is the major source of ROS in RBCs (see section 1.3.2) (Abugo and Rifkind, 1994; Walder et al., 1984).

As explained earlier in section 1.3.2, Hb is a major target for oxidative damages. If metHb is not reduced back to Hb, it will be slowly denatured into hemichromes in which Hb binds an amino acid (typically histidine) from a distal part of the globin chain for instance (Pauling and Coryell, 1936). Those hemichromes are still reversible until they undergo significant distortions in their tertiary structure, forming irreversible hemichromes (Kanias and Acker, 2010). Precipitations of

hemichromes (i.e. Heinz bodies) can be observed in RBCs undergoing high oxidant damages, as in α-thalassemia e.g.. Upon RBC aging, accumulation of hemichromes has also been observed. They bind to Band3 cytoplasmic domain with a higher affinity than native Hb (Waugh and Low, 1985) and are thought to be the major cause of its aggregation. The latter is also favoured by Band3 autoxidation and by lipid peroxidation (Arashiki et al., 2013; Pantaleo et al., 2009).

Ca^{2+} exchanges will also be highly impacted. As a matter of fact, PMCA pump activity has been shown to decrease following RBC aging (Lew et al., 2007), possibly due to oxidative damages (Zaidi, 2010) or poor ATP availability resulting from decreased glycolysis. Ca^{2+} influx could also be altered during RBC senescence through oxidative damages, as suggested by Lang et al (Lang et al., 2003). The resulting Ca^{2+} accumulation has several harmful repercussions. First, as explained above, increase Ca^{2+} will promote extended cytoskeleton uncoupling from the membrane, favouring membrane release in microvesicles (containing notably the marker of self CD47) and decrease of the cell deformability. Second, the extended activation of Gardos channels will promote the cell dehydration and density increase. Third, high Ca^{2+} concentration will activate μ-calpain, a protease that targets cytoskeleton proteins (worsening the vesiculation) and transporters like PMCA (Mortensen and Novak, 1992). Four, Ca^{2+} will inhibit the flippase and activate the scramblase, leading to the loss of asymmetry between both leaflets of membrane and subsequent externalization of PS (see section 5.3.1.).

4.2. Hereditary membrane fragility diseases

Hereditary diseases associated with altered RBC deformability and leading to chronic hemolytic anemia can be classified based on the initial alteration. On one hand, globin genes can be mutated, as in sickle cell disease and thalassemias. On the other hand, membrane or cytoskeleton proteins can be defective and cause alterations either in RBC mechanical properties (elliptocytosis, spherocytosis) or in the flux of ions through the membrane (xerocytosis, stomatocytosis). Here we mainly focus on elliptocytosis (section 4.2.1) as it has been extensively studied during this thesis, and briefly introduce spherocytosis (section 4.2.2).

4.2.1. Hereditary elliptocytosis

Clinical aspects

Hereditary elliptocytosis (HE) is an autosomal dominant RBC disorder. The worldwide incidence of HE is difficult to establish as its clinical severity is variable and many patients are asymptomatic, but it is estimated at 1 per 2000-4000

individuals (Gallagher, 2004). However, in regions where malaria in endemic, the prevalence highly increases up to 3 % (Bannerman and Renwick, 1962). This increase could be explained by the fact that the disease confers resistance to *Plasmodium falciparum* invasion (Hadley and Miller, 1988). HE results from a mechanical weakness or fragility of the RBC membrane cytoskeleton following defects in cytoskeleton and anchorage proteins (Gallagher, 2005). Those RBCs are extensively trapped and eliminated in the spleen with the pathological consequences of decreased RBC abundance and increased RBC degradation.

The disease is clinically very heterogeneous but generally characterized by the presence of numerous oval, elliptical or elongated RBCs in the peripheral blood (figure 1.12) (Faramarz, 2008). Heterozygotes individuals usually exhibit elliptocytes on the blood smear, but in most instances hemolysis is well compensated for by reticulocytosis (i.e. increase in reticulocytes in the blood following a high activation of the bone marrow). Those patients mostly do not present any clinical symptoms or mild to moderate anemia. However, asymptomatic carriers can potentially become symptomatic during pregnancy and vitamin B12 deficiency. Moreover, symptomatology may vary among family members sharing the same molecular defects as well as in the same individual over time (Gallagher, 2004). A variant to poorly symptomatic HE is ovalocytosis, which has been reported in up to 30% of the population of aborigines in Southeast Asia. It is characterized by spoon-shaped erythrocytes also with absence of mild clinical manifestations. On the other side, homozygotes or compound heterozygotes (i.e. two recessive heterogeneous alleles) individuals (~ 10 %) have sufficient weakening of the cytoskeleton to cause significant hemolysis accompanied by striking abnormalities in RBC morphology and thus clinical manifestations. Moreover, an uncommon autosomal recessive variant, named hereditary pyropoikilocytosis, is characterized by severe transfusion-dependent hemolytic anemia, jaundice, splenomegaly and marked spherocytosis and poikilocytosis (Da Costa et al., 2013).

HE diagnosis is based on clinical and familial history, physical examination and laboratory data (Bolton-Maggs et al., 2012). The latter comprise blood smear analysis, RBC morphology determination (mean corpuscular volume, MCV), full blood cell count, reticulocyte count, determination of mean corpuscular Hb concentration (MCHC) and bilirubin concentration. Blood smears are very characteristic, with few to 100% elliptocytes, from elongated “bacillus-like” shape to more oblong cells (Da Costa et al., 2013). Some silent carriers can show normal erythrocyte morphology (Gallagher, 2004) while patients with moderate to severe compensated haemolysis show elliptocytes, poikilocytes, spherocytes and cell fragments (figure 1.12 A), which can produce a marked decrease in measured MCV. In pyropoikilocytosis, severely altered RBCs can be observed like poikilocytes, RBC

fragments, (micro)spherocytes or triangulocytes (figure 1.12 B) (Andolfo et al., 2016; Da Costa et al., 2013). The reference technique for diagnosis of RBC membrane disorders is the osmotic gradient ektacytometry (see section 6.1.2.). However, in spite of its recognition as the reference technique, it is still rarely used as a routine diagnosis tool for RBC membrane disorders due to its limited availability (Da Costa et al., 2016).

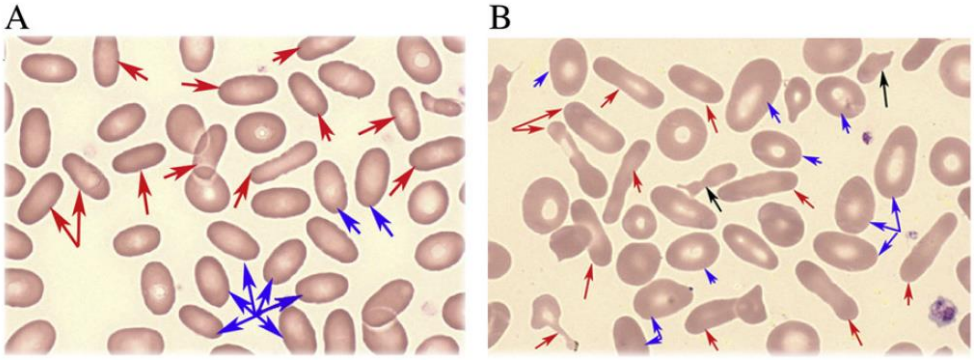

Figure 1.12. Smear of blood from patients suffering from HE and pyropoikilocytosis. A. HE: classical elliptic (red arrows) and oblong cells (blue arrows). **B.** Pyropoikilocytosis: elliptic (red arrows), ovalocytic (blue arrows) and fragmented cells (black arrows). Reproduced from (Da Costa et al., 2013).

Once the diagnostic is established, the patient follow-up as well as the routine treatment will depend on the disease severity. Upon severe anemia (6-8 g of Hb/dL in blood *vs* 12-17 g/dL in normal conditions), regular transfusions or Epo treatment might be needed. Folate supplementation is also highly recommended (Bolton-Maggs et al., 2012). Complications of HE include bilirubin gallstones and jaundice, as consequences of major RBC hemolysis, and of course splenomegaly. Patients are also warned against infection with parvovirus B19, whose infection induces transient aplastic crisis in hemolytic disorders (Kapavarapu et al., 2012), and against hepatitis B if they require regular transfusions (Da Costa et al., 2013). Splenectomy is only considered in severe cases of HE and in pyropoikilocytosis. It is followed by an increase in Hb concentration and a decrease in reticulocytes even if the cell volume might be extremely low and the osmotic fragility is increased. In any cases, total splenectomy should not be considered before 6 years-old since a functioning spleen is important in young children for protection against infections due to encapsulated bacteria (Glader, 2013).

Molecular and pathophysiologic aspects

Mutations leading to HE have been evidenced in genes coding for α-spectrin, β-spectrin and protein 4.1R. In α-spectrin gene, more than 25 mutations have been reported, most of them being missense mutations in the N-terminal domain (Gallagher, 2004). α-spectrin defects are the most prevalent defects in Caucasian populations. Moreover, the mutation consequences can be worsen by the expression on the other allele of a "low expression polymorphism", which does not cause any damages in a healthy individual as the α-spectrin chains are produced in excess in comparison to β-spectrin chains (Da Costa et al., 2013). Concerning the β-spectrin gene, a lower number of mutations has been described, most of which being associated with premature chain termination. Finally, mutations in 4.1R gene are less common and have been mostly described in the FERM domain-coding exon (Marchesi et al., 1990). Families with homozygous deficiency in 4.1R have also been described (Garbarz et al., 1995).

The mutations observed in HE affect the connections of cytoskeletal proteins at the 4.1R junctional complexes (Andolfo et al., 2016), leading to a mechanical weakness or fragility of the RBC cytoskeleton. Most mutations in α-spectrin are thought to result in alterations of their tetramerization with β-spectrin. Indeed, a good portion of identified mutations are found in the tetramer self-association contact site (i.e. in the N-terminal domain) (Zhang et al., 2013). Small regions in this region of α-spectrin undergo conformational changes upon binding to β-spectrin (Antoniou et al., 2008; Lam et al., 2009). The interface interactions are driven by clustering of the hydrophobic side chains and stabilized by electrostatic interactions (Antoniou et al., 2008). Missense mutations of α-spectrin are thought to alter the interactions between residues that allow α- to β-spectrin binding (Gaetani et al., 2008; Lam et al., 2009). As a matter of fact, some mutations have been shown to favour "closed" spectrin dimers, which are not able to tetramerize, over "open" spectrin dimers (Harper et al., 2013). On the other hand, consequences of mutations in 4.1R protein are less understood. Altered FERM domains could disrupt the association of 4.1R with membrane proteins (like Band3) or lipids (PS or PIP_2), and thereby lead to detachment of the 4.1R junctional complex from the membrane.

The pathophysiological pathways leading from altered spectrin tetramerization to elliptocyte transformation are not fully understood. It is believed that it is the prolonged or repetitive cellular deformation into the circulation that will lead to an abnormal rearrangement of skeletal proteins, preventing normal recovery of the biconcave shape (Gallagher, 2004). In a recent simulation study, the

endothelial slits crossing in the spleen has been shown to indeed induce sustained elongation of the HE RBCs, leading to fragmentation in severe cases (Li et al., 2018).

4.2.2. Hereditary spherocytosis

Hereditary spherocytosis (HS) also originates from altered cytoskeleton mechanical properties of RBCs, resulting in poorly deformable RBCs. It is one of the most common inherited anaemia (1:3000 in the Caucasian population) and is characterized, as HE, by a broad spectrum of clinical severity, i.e. from mild (~20 %, nearly asymptomatic) to moderate (~75 %, possible intermittent need for transfusions) to severe (~5 %, life-threatening anaemia and transfusion-dependent), as reviewed in (An and Mohandas, 2008; Andolfo et al., 2016; Perrotta et al., 2008).

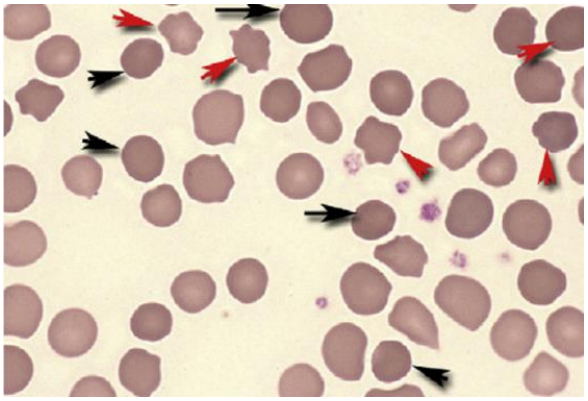

Figure 1.13. Smear blood of a patient suffering from HS. Spherocytic RBCs (black arrows) are associated with acanthocytes (red arrows). Reproduced from (Da Costa et al., 2013).

In ~75% of cases, HS results from an autosomal dominant inheritance of mutations in the genes encoding for ankyrin, Band3 or β-spectrin (Da Costa et al., 2013). Those mutations, which are very heterogeneous and mostly family-specific, cause the weakening of vertical linkages between the cytoskeleton and the lipid bilayer. The molecular genetic mechanisms of spherocytosis might however differ according to the mutated gene as well as the mutation itself, as reviewed in (He et al., 2018). As a consequence to the weakened linkages, the lipid bilayer is destabilised, which leads to the release of skeleton-free lipid vesicles, especially during deformation through the inter-endothelial slits of the spleen (Li et al., 2018; Reliene et al., 2002). The vesicle release process and consequences are reviewed in (Alaarg et al., 2013) and (Leal et al., 2018). The reduction of the membrane surface leads to the formation of a very wide range of RBC shapes, including spherocytes, stomatocytes or acanthocytes (figure 1.13). Those RBCs with reduced deformability that are eliminated by the spleen resident macrophages, leading to symptoms comparable to those of HE. The characterization of spherocytic RBCs has been

shown to correlate with the clinical severity. Indeed, RBCs from patients that suffer from moderate/severe spherocytosis have a low density, abnormally high intercellular heterogeneity and a prominent decrease in membrane stability and RBC deformability. On the other side, in RBCs from patient with mild spherocytosis, the less pronounced reduction in deformability results in prolonged red cell life-span and, hence, cells are subject to progressive loss of membrane and become denser before they are taken up by the spleen (Huisjes et al., 2019).

Unlike some other hemolytic anemias (like hereditary xerocytosis), splenectomy has been proven a very efficient therapy for HS and is almost always performed in late childhood. The removal of the spleen, either partial or total, slows down the vesicle loss by spherocytotic RBCs and removes the site of RBC destruction. Following splenectomy, the Hb concentration almost always increases, reticulocytes decrease, bilirubin levels return to normal, and RBCs exhibit a relatively normal life span. This very favorable response had led to the recommendation of splenectomy even for HS patients with moderate degrees of hemolysis (Glader, 2013). The diagnosis and management of HS are discussed in (Bolton-Maggs et al., 2012) while the income of partial splenectomy is addressed in (Buesing et al., 2011).

5. Membrane lipid composition, organization and properties

Membranes provide interfaces that not only separate two aqueous environments but also contribute to several functions in mammalian cells, including regulation of solute exchanges, signal transduction, lipid metabolism and membrane fusion and fission. To fulfill these roles, membranes must be tough and plastic at the same time. This could explain why they exhibit a so large variety of lipid species (see section 5.1) and specific biophysical properties (see section 5.2), but also why lipids are asymmetrically distributed accross the two membrane leaflets (see section 5.3.1) and why some of them cluster into membrane domains at the surface of a variety of cells (see section 5.3.2). RBC PM has a particular composition and presents lipid domains. Therefore, one could hypothesize that membrane composition, biophysical properties and/or organization could contribute to RBC deformation. Although this remains to be clearly demonstrated, I provide several lines of evidences in favor of this hypothesis in the result section.

5.1. Membrane lipid composition

Approximately 5% of the eukaryotic cell genes are used to generate thousands of different lipids (van Meer et al., 2008). Except for sterols, membrane lipids possess a hydrophobic portion (the tail), made of two fatty acyl chains, and a polar head-group (and are thus called "polar lipids"). Diversity of head-groups, fatty acyl chain length and saturation explain the enormous variety of lipids found in membranes. This large lipid diversity is nevertheless classified in three main groups: glycerophospholipids, sphingolipids and cholesterol. Additionally, lipids can be modified by oxidation (as exposed in section 1.3.2.) but also enzymes, leading to an additional diversity of lipids as well as signalling molecules.

Glycerophospholipids

Glycerophospholipids are the principal components of the membrane bilayer. Their basic structure is composed of two esterified fatty acyl chains attached to one glycerol (figure 1.14A). Predominant cell fatty acids chains contain 14-20 carbon atoms. Generally, fatty acids at the glycerol C1 are saturated or mono-unsaturated while fatty acids at the C2 are poly-unsaturated. Every double bond can drive a stable curvature to the acyl chain. The polar head (an ethanolamine, a choline, a serine or an inositol, a.o.) is attached to the glycerol C3 via a phosphoric acid and defines the name of the lipid. Polar heads present different electrical charges, bestowing distinct properties to the lipid. For instance, phosphatidylethanolamine (PE) and PC are neutral whereas PI can be modified by esterification of the hydroxyl functions of the inositol with one to five phosphates, creating heavily charged polyphosphoinositides (Pollard et al., 2017). Another factor to consider is the lipid global shape depending on the size of the head and the saturation and length of the tail. For instance, PC possesses a nearly cylindrical molecular geometry, leading to self-organisation as a planar bilayer, while PE assumes a conical molecular geometry because of the relatively small size of its polar head-group, imposing a curvature to the membrane (van Meer et al., 2008).

Glycerophospholipids can be hydrolyzed by phospholipases. Phospholipases A hydrolyze the carboxylic esters at the *sn*-1 (PLA_1) or *sn*-2 (PLA_2) positions of glycerol backbones. PLA_2 activity results in the production of lysophospholipids and free fatty acids, the former being active biomolecules. Phospholipase C (PLC) is a phosphodiesterase responsible for hydrolysis of the glycerophosphate bond between the polar head and the glycerol backbone, producing DAG and inositol-3-phosphate (IP_3) from PIP_2 (its main substrate). IP_3 diffuses in the cytosol while DAG stays in the membrane and both will activate PKC. They are therefore important second messengers of lipid signalling. Phospholipase D (PLD) catalyzes the

hydrolysis of the head group, producing phosphatidic acid. Finally, a phospholipase B (PLB) that is able to hydrolyze the carboxylic ester at the *sn*-1 or *sn*-2 position has been postulated. However, this is probably another enzyme with the preferred name lysophospholipase (Haas and Stanley, 2007).

Sphingolipids

Sphingolipids, the second major lipid class, are named based of the sphingosine, a nitrogenous base with an unsaturated fatty acid chain (figure 1.14B). A second fatty acid is attached by an amide bond to the sphingosine C2, forming a ceramide, while the polar head is attached to the hydroxyl function of C1. The polar head-group can be i) a phosphocholine, forming SM, the major sphingolipid; or ii) carbohydrates, forming the less abundant but highly diversified glycosphingolipids (GSLs). Among those GSLs, glucosylceramide represents the simplest, with one glucose as polar head. Gangliosides, which include GM1, are GSLs with terminal sialic acids. GM1 has been related to various cell functions and is the binding site of the cholera toxin. Sphingolipids generally have saturated (or trans-unsaturated) tails, thereby forming taller, narrower cylinders than PCs of the same chain length. As a consequence, they tend to pack tightly, adopting a solid gel phase if they are not fluidized by sterols and GSLs (van Meer et al., 2008).

SM can be hydrolyzed by SMase, generating Cer and phosphocholine. Five types of SMases have been identified according to their cation dependence and optimal pH of action: the lysosomal acid SMase, the secreted acid SMase, the Mg^{2+}-dependent and Mg^{2+}-independent neutral SMases, and the alkaline SMase. The cer produced is a bioactive lipid that plays important roles in coordinating cellular responses to extracellular stimuli and to stress, notably leading to apoptosis, cell differentiation and senescence (Hannun and Obeid, 2002). Moreover, cer can be subsequently hydrolyzed into sphingosine thank to ceramidase. Both cer and sphingosine can be phosphorylated by specific kinases, producing additional signaling lipid forms.

Cholesterol

Cholesterol is the less polar membrane component. It is composed of four carbon cycles forming a rigid hydrophobic core linked to a short hydrocarbon tail and to a polar hydroxyl group, responsible for the slightly amphipathic character of the molecule (figure 1.14C). It contributes to the regulation of membrane fluidity, lipid phase separation, cell mechanical resistance and membrane permeability (Simons and Vaz, 2004).

Introduction

Huge differences in membrane composition can be found between prokaryotes and eukaryotes, but also within eukaryotes. In RBC membrane for example, cholesterol is particularly enriched with up to 48 mol%, in comparison to other cells PM like platelets (32 mol%), fibroblasts (13 mol%) or macrophages (8 mol%) (Carquin et al., 2016). Since cholesterol plays a dominant role in the regulation of membrane organization, changes in cholesterol levels should differentially affect the physiology of those different cell types. In RBCs, it has been shown that an increase in the cholesterol-to-phospholipid ratio from 1.28 to 2.0 results in a decrease in their filterability (Cooper et al., 1975).

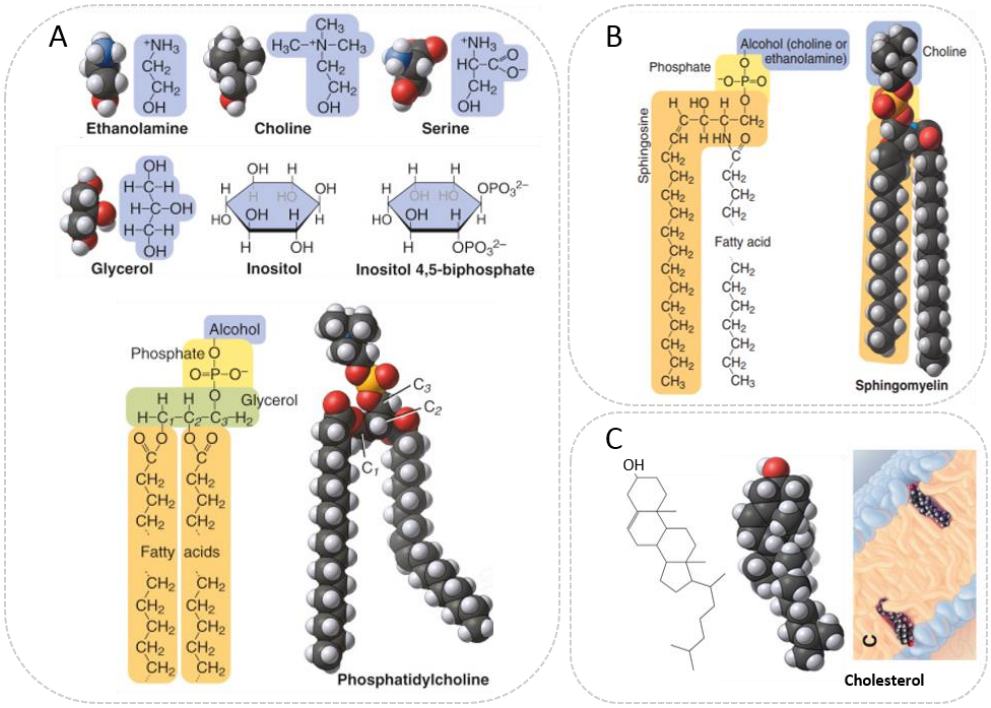

Figure 1.14. Structures of membrane lipids. A. Glycerophospholipids with their various polar heads. **B.** Sphingomyelin (SM), which is formed from sphingosine and a polar head of phosphocholine. **C.** Cholesterol. Adapted from (Pollard et al., 2017).

5.2. Membrane biophysical properties

Biophysical membrane properties, i.e. fluidity (see section 5.2.1), thickness (see section 5.2.2.) and curvature (see section 5.2.3), mostly depend on lipid

membrane composition as well as on the strength of membrane anchorage to the underlying cytoskeleton.

5.2.1. Membrane fluidity

Membrane fluidity refers to the viscosity of the lipid bilayer and affects the rotation and diffusion of proteins and lipids within the membrane, thereby modulating their functions. Lipid composition is the major regulator of fluidity and mostly results from the membrane composition (Feigenson, 2006; van Meer et al., 2008). Indeed, while long saturated acyl chains of phospholipids promote a tight lipid packing, unsaturated double bonds make harder for the lipids to pack together by putting kinks into the otherwise straightened hydrocarbon chain. Short chains will also favor fluidity as they are more susceptible to changes in kinetic energy due to their smaller molecular size and since they have less surface area to undergo stabilizing Vander Waals interactions with neighboring hydrophobic chains. Some lipids, like SM, tend to present long saturated chains and favor tight lipid packing, while others, like PC, mostly have unsaturated chains and therefore promote poor lipid packing. Cholesterol, on its side, acts as a bidirectional regulator of membrane fluidity. Indeed, in tightly packed, saturated lipids, cholesterol will intercalate and increase space between lipids; while in highly fluid polyunsaturated lipids, it will stabilize membranes and favor lipid packing (Heberle and Feigenson, 2011). In addition to lipid composition, temperature also regulates membrane fluidity. Indeed, by heating up the bilayer, lipids will acquire thermal energy, increasing their movement and their random arranging and rearranging. Each lipid has a defined phase transition temperature, above which the it changes from closely packed chains to fluid and randomly oriented chains.

Artificial membranes with different lipid composition have revealed the coexistence of multiple lipid phases with different fluidity and diffusion ability (figure 1.15). First, liquid-disordered (Ld) phases mostly contain unsaturated lipids like DOPC (dioleoylPC, a synthetic PC derivative). They have a low order and a fast translational diffusion coefficient. Second, liquid-ordered (Lo) phases, which mostly contain saturated lipids (like palmitoylsphingomyelin, PSM, the most common form of SM) and cholesterol, have a high order and a decreased translational diffusion. Finally, solid-ordered (So) phases nearly exclusively contain saturated lipids and are almost never observed *in vivo*. They are highly ordered and present a very slow translational diffusion. In biological membranes, a coexistence of Lo and Ld phases has been evidenced. This coexistence implies that an interface, or line tension, is formed between them. This line tension is believed to play a central role in the regulation of lipid domain size and shape as its length and the energy lost tend to be minimized (Heberle et al., 2013).

Introduction

A classical method to probe membrane fluidity is via the insertion of the fluorescent probe Laurdan at the membrane of living cells (Leonard et al., 2018). The dye spectroscopic properties are influenced by both the composition and the dynamics of its surrounding environment. Indeed, Laurdan emits at ~440 nm in an ordered membrane and at ~490 nm in a disordered membrane. From images generated at both wavelengths, a quantitative factor named "generalized polarization" (GP=$\frac{I440-I490}{I440+I490}$) can be calculated and will reflect the membrane fluidity. Accordingly, a high GP value corresponds to a high lipid ordered environment and therefore a low membrane fluidity.

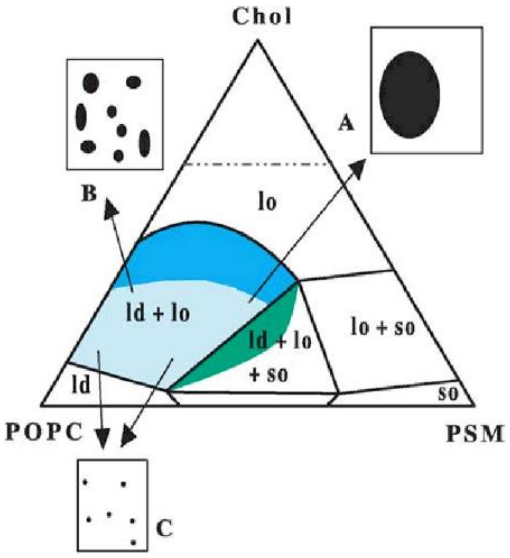

Figure 1.15. Ternary POPC:PSM:Chol phase diagram, showing the phase boundaries and schematic illustrations of the size of lipid domains. The colored regions represent coexisting phases that are encountered in living cells, i.e. Ld/Lo coexistence with dominance of Ld (light blue), Ld/Lo coexistence with dominance of Lo (dark blue) and coexistence of Ld/Lo/So in green. POPC, 1-palmitoyl-2-oleoyl-sn-glycero-3-PC; PSM, N-palmitoyl-SM; chol, cholesterol. Reproduced from (de Almeida et al., 2005).

5.2.2. Membrane thickness

The PM is expected to present a thickness of 7 to 9nm (Curtis, 1989). Differences are however expected in different membrane regions like Lo or Ld phases. Indeed, as the Lo phase is enriched in saturated long fatty acid chains, it is expected to have a slightly increased membrane thickness. To minimize energy loss, the hydrophobic thickness of the protein should be equal to that of the lipid bilayer (Andersen and Koeppe Ii, 2007; Killian, 1998). Proteins are thus expected to localize in part of the bilayer where the hydrophobic thickness is favorable. Surrounding lipids can also adjust to avoid any hydrophobic mismatch (i.e. when the hydrophobic section of a protein does not match the hydrophobic thickness of the

membrane). Proteins, on the other side, can change their conformation or tilt to fit the hydrophobic thickness (Cohen, 2018; Norimatsu et al., 2017). Membrane thickness has thus been proposed as a mean of regulation for membrane protein activity. However, if the mismatch is too important, the protein will aggregate to decrease the energy loss (Killian, 1998; Lee, 2004c).

5.2.3. Membrane curvature

Generation of transient or permanent highly curved membrane areas is necessary to fulfill several cell functions like trafficking, differentiation, cell motility and signal transduction (Alimohamadi and Rangamani, 2018). This explains the typical shapes of endocytic pits, microvilli, or organelles such as ER or the Golgi apparatus. High curvature membrane areas are also formed during the RBC deformation process (Leonard et al., 2017). Several passive and active mechanisms could be involved in generation, sensing and maintenance of high local curvature areas. Among them, one can cite (i) membrane lipid composition and asymmetric organization; (ii) clustering of shaped transmembrane proteins; (iii) reversible insertion of hydrophobic protein motifs; (iv) scaffolding by oligomerized hydrophilic protein domains; and (v) scaffolding by the cytoskeleton with forces generated by polymerization and by molecular motors (figure 1.16) (McMahon and Boucrot, 2015).

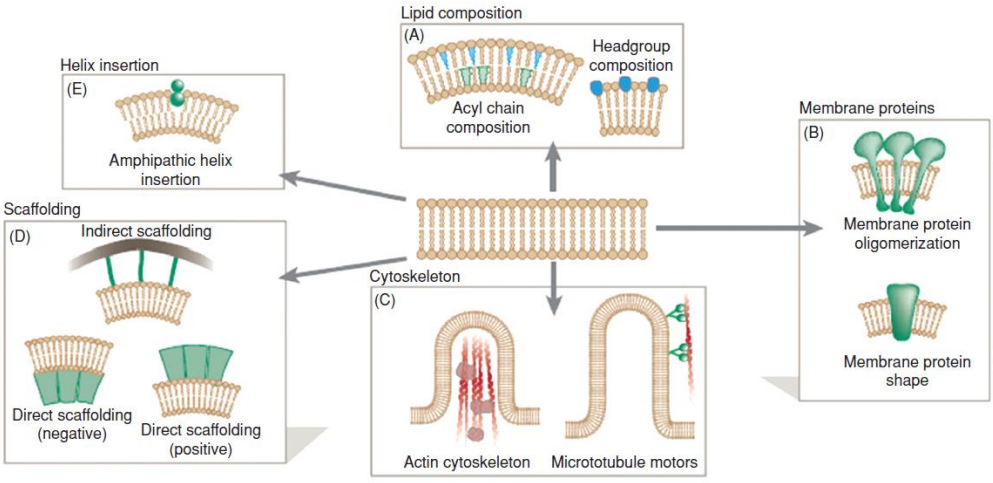

Figure 1.16. Mechanisms underlying membrane curvature formation. Curvature can be generated by **(a)** asymmetric lipid distribution; **(b)** intrinsic shape of transmembrane proteins or their complexes; **(c)** pushing or pulling the membrane by polymerisation of cytoskeletal filaments or by cytoskeletal motors; **(d)** scaffolding; and **(e)** insertion of amphipatic helices (Kapus and Janmey, 2013).

Introduction

In this section, I will only discuss the importance of intrinsic shapes of membrane phospholipids as well as their repartition between the two leaflets, as those are believed to be major regulators of curvature at the RBC membrane. As already shortly introduced in section 5.1., phospholipids can present different global shapes based on their head-group and the length and saturation of their acyl chains. As a matter of fact, PC and PS will have relatively cylindrical shapes, while PE and phosphatidic acid (PA) are conical (i.e. small polar head and extended acyl chains) and PI is an inverted-cone (i.e. big polar head with rather small and ordered acyl chains) (Harayama and Riezman, 2018; van Meer et al., 2008). The asymmetric repartition of those lipids between the two leaflets (see section 5.3.1.) will generate membrane curvature. Aside from phospholipids, cholesterol, which is cylindrical, could also modulate membrane curvature. Indeed, as explained beyond, cholesterol can rapidly switch from one leaflet to the other, therefore providing an excess of lipids at one leaflet, which results in membrane curvature.

5.3. Membrane lipid heterogeneity

5.3.1. Membrane transversal asymmetry

The PM displays an asymmetric lipid distribution between its two leaflets. While SM and GSLs are mainly present at the external leaflet, PS, PE, PI and PA are located at the cytosolic one (Zachowski and Devaux, 1990). The exact proportion of lipids in the two leaflets in RBCs is however still not clear as discrepancies exist according to the technique used to study this asymmetry (figure 1.17) (Murate and Kobayashi, 2016). Among those techniques, on can distinguish biochemical approaches, fluorescence approaches and immune-electron microscopy on freeze-fractured samples. First, in biochemical techniques, the outer leaflet lipids are irreversibly modified, either by conjugation of chemicals or by enzymatic degradation (like a phospholipase treatment, see left panel of figure 1.17). The ratio of modified/unmodified lipids of the samples are then analyzed. Second, the fluorescence techniques rely on the insertion in the PM of fluorescent analogs whose fluorescence is analyzed before and after quenching of the external leaflet fluorescence. Finally, in the last technique, the membrane is freeze-fractured to separate the two leaflets, which are then analyzed by electron microscopy thank to specific probes (right panel in figure 1.17).

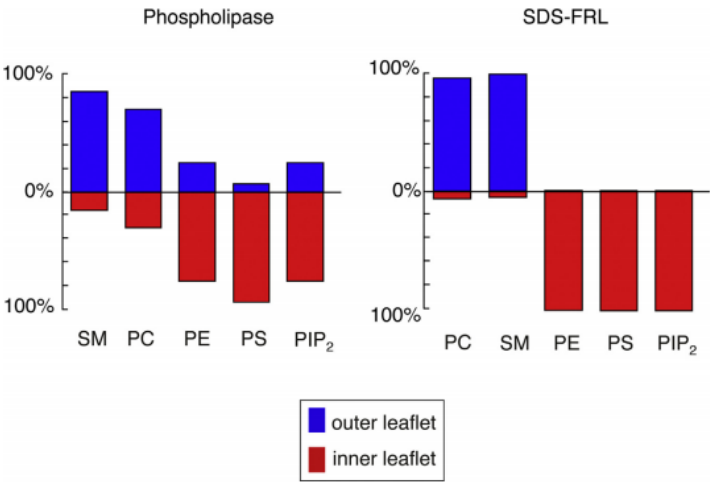

Figure 1.17. Asymmetric transbilayer distribution of SM and phospholipids in RBC membranes, obtained either by phospholipase treatment or via freeze-fractured immune-electron microscopy. Results are expressed as a percentage of each phospholipid. SDS-FRL, SDS-freeze fractured leaflets. Reproduced from (Murate and Kobayashi, 2016).

Even though the exact distribution between the two leaflets has still to be highlighted, the preferential localization of charged lipids at the inner leaflet *vs* neutral lipids at the outer leaflet results in a negatively charged inner leaflet. Moreover, lipids at the outer leaflet tend to present long saturated acyl chains (Steck and Lange, 2018), resulting in a difference of order between the two leaflets. This difference was revealed by electron spin resonance with spin-labelled lipids and lateral diffusion measurements by photobleaching with fluorescent lipids (Devaux and Morris, 2004; Morrot et al., 1986; Seigneuret et al., 1984).

The establishment and maintenance of the transversal asymmetry in ensured by several mechanisms. First, the difference in composition in sphingolipids between leaflets takes place during their biosynthesis. Sphingolipids are synthetized in the luminal leaflet of the Golgi apparatus and brought by vesicular traffic to the outer PM leaflet (Gault et al., 2010; van Meer et al., 2008). Phospholipids like PE, PC and PS, on the other side, are synthetized in the ER where they are homogenously distributed between the two leaflets. Their reorganization takes place at the PM via ATP-dependent transbilayer lipid translocators, namely flippases and floppases. Flippases transport PS and PE from the outer leaflet to the inner one while floppases do the opposite for PC. To note, the spontaneous

translocation ("flip-flop") across the leaflets is highly limited by the size and the polarity of the lipids. Indeed, the energy barrier imposed by the resistance to the passage of polar head-groups through the hydrophobic core of the bilayer is extremely high for lipids. For instance, the transbilayer movement of a GSL would take one day (10^{-15} s^{-1}) as compared to seconds for nearly apolar DAG, Cer and cholesterol (Contreras et al., 2010; van Meer et al., 2008). This asymmetry can however be altered upon activation of ATP-independent Ca^{2+}-dependent bidirectional lipid translocators named scramblases. Their activation upon RBC aging and stress induces the externalization of PS at the outer leaflet, which is a signal for RBC phagocytosis by spleen macrophages, as described in section 4.1. (Setty et al., 2002).

Concerning cholesterol distribution between both leaflets, a debate is still going on between scientists (Steck and Lange, 2018). Indeed, even though cholesterol spontaneous flip-flop is fast due to its low polarity and little size (Steck et al., 2002), it is difficult to conclude to a symmetrical distribution as its confinement with other lipids/proteins could promote its preferential segregation into one of the leaflets (Ikonen, 2008; Steck and Lange, 2018). As a consequence, while freeze-fractured autoradiography on RBCs labelled with radioiodinated concanavalin A shows ~60 % of cholesterol into the outer leaflet (Fisher, 1982; Steck and Lange, 2018), the quenching of dehydroergosterol fluorescence or NBD-cholesterol attests of the preferential accumulation of cholesterol (up to 75 %) in the inner leaflet (Schroeder et al., 1991). It has also been suggested that some cholesterol molecules may occupy the inter-leaflet midplane of the bilayer (Steck and Lange, 2018).

5.3.2. Membrane lateral heterogeneity

Even though it seems reasonable to hypothesise that, due to the intrinsic lipid complexity, cell membranes are arranged in far more intricate structures than simple homogenous fluid bilayers, lateral lipid heterogeneity has long been subjected to debates. Limited availability of reliable fluorescent probes, poor lipid fixation, imaging artefacts due to membrane protrusions/projections and use of highly disruptive methods of isolation have often been denounced. However, the existence of transient nanometric domains (or "rafts") and of larger submicrometric domains has now been evidenced in several cells by several complementary techniques.

Transient nanometric rafts

The first hypothesis that specific membrane lipids could gather together to form platforms or decks of lipids originated from the late 90's (Simons and Ikonen, 1997). This hypothesis was based on previous work showing asymmetric

composition of apical and basal membranes of epithelial cells thank to selective sorting of specific lipids (i.e. GSLs) and proteins (i.e. glycosylphosphatidylinositol-, or GPI-anchored proteins) (Lisanti et al., 1989; van Meer and Simons, 1988). Simons and Ikonen also took in account the work of Brown and Rose who observed that those membrane parts were resistant to solubilization by non-ionic detergents at 4°C (Brown and Rose, 1992). This technique of "detergent-resistant membranes", or DRMs, has become a reference technique for lipid raft isolation and study. However, DRM isolation has long been (and is still) extensively criticized due to its artificiality and aggressiveness which could promote artefacts like membrane reorganization (Munro, 2003). Moreover, visualization of lipid rafts by microscopy was lacking for long due to their nanometric size, instability and heterogeneity. However, recent biochemical techniques and super-resolution microscopy have provided support to DRM existence (Sezgin et al., 2017). Very recently, single molecule localization microscopy allowed Xu et al to observe the formation of raft-like nanodomains in the membrane of live mammalian cells at the remarkable spatial resolution of ~10 nm (Yan et al., 2018).

Lipid rafts are defined as small (20-100 nm), heterogeneous, highly dynamic (half-life of seconds), cholesterol and sphingolipid-enriched domains that compartmentalize cellular processes. Those rafts may coalesce into larger stabilized structures following lipid-lipid, lipid-protein and protein-protein interactions (Lingwood and Simons, 2010). As a consequence of their specific composition, lipid rafts create a transient thicker Lo phase inside a Ld phase membrane (Crepaldi Domingues et al., 2009). The membrane thickening on its side could help the recruitment of specific proteins with the same hydrophobic length (Andersen and Koeppe, 2007), as described in section 5.2.2.

Rafts isolated by DRMs from RBCs are enriched in SM, GSLs and specific proteins like stomatin and flotillins (Salzer and Prohaska, 2001) and are thought to be associated with the spectrin skeleton by electrostatic interactions (Ciana et al., 2011). Thank to electron paramagnetic resonance (EPR) spectroscopy, DRM membrane was found to display a higher order state compared with the RBC PM, which is compatible with the existence of Lo domains. The cholesterol ratio in DRMs is of ~55 mol% while it is of ~45 mol% in the RBC PM (Domingues et al., 2010).

Stable submicrometric domains

The first suggestion for the clustering of lipids into larger domains than rafts was brought by Edidin et al who, by fluorescence recovery after photobleaching of large membrane areas, pointed out a restriction to lateral diffusion of a fluorescent PC analog inserted in the fibroblast PM (Yechiel and Edidin, 1987). Later, Fujiwara et al have shown that phospholipids diffuse more slowly into the fibroblast

membrane than into artificial bilayer as they are temporarily confined into compartments of 30-700 nm before diffusing laterally by hop diffusion (Fujiwara et al., 2002). However, at that time, although domains were well documented in artificial membranes, generalization of this concept to the PM of living cells was less straightforward probably due to the lack of relevant lipid probes and imaging resolution. During the last decade, however, improvement of microscopy resolution as well as development of new observation techniques have allowed to evidence stable submicrometric lipid domains at the surface of a variety of living cells, from prokaryotes, to yeast and animal cells (figure 1.18). Those domains are bigger (~200-500 nm in diameter) and more stable (half-life of minutes) than lipids rafts.

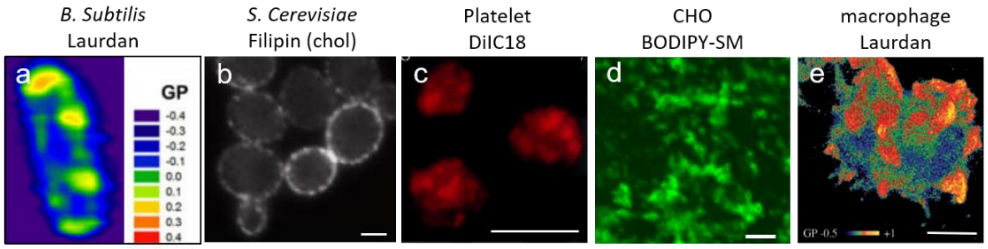

Figure 1.18. Visualization of PM submicrometric lipid domains by fluorescence/confocal imaging. (a) *Bacillus subtilis* labelled with Laurdan at 37°C (Bach and Bramkamp, 2013). **(b)** S. cerevisiae stained with filipin (ergosterol) (Grossmann et al., 2007). **(c)** Platelets labelled with DiIC18 and examined at 15°C (Gousset et al., 2002). **(d)** CHO cell labelled with BODIPY-SM, pretreated with latrunculin B and examined at 4°C (to prevent both endocytosis and membrane protrusions) (Tyteca et al., 2010d). **(e)** Macrophage labelled with Laurdan and examined at 37°C (Gaus et al., 2003). All scale bars, 2µm. Adapted from (Carquin et al., 2016).

However, those observations still remained questioned based on possible imaging artifacts due to non-resolved membrane projections, such as filopodia, microvilli or ruffles (instead of real domains). To circumvent this difficulty, the host laboratory turned to the use of RBCs. Those cells are indeed a model of choice to study lipid lateral organization as many artefacts can be ruled out. Among the RBC advantages, one can cite (i) their availability and easiness of isolation; (ii) their smooth membrane resulting from absence of membrane protrusions or vesicular trafficking; (iii) their minimal lipid metabolism; and (iv) their well-characterized membrane lipid and protein composition.

Another difficulty of the field is related to the probes that can be reliably used to image membrane lipids. The laboratory started with the use of lipid analogs substituted at one of their fatty acyl chain by a fluorophore and then inserted in the outer PM at trace level. The chosen fluorophore was the BODIPY ((4,4-difluoro-3a,4adiaza-s-indacene) (figure 1.19 A), which presents the advantages of having a high quantum yield and being photo-stable, therefore allowing the insertion at a low concentration and imaging at a low laser power (Johnson et al., 1991). Moreover, the lack of ionic charge on the BODIPY fluorophore is unusual for long-wavelength fluorescent dyes and results in exclusive localization of the fluorophore within the membrane. RBCs were immobilized on poly-L-lysine-coated coverslips and analyzed by vital fluorescence and/or confocal imaging. Lipid domains enriched in three of the most abundant and/or important polar lipids of the outer PM leaflet of RBCs, namely PC, GM1 and SM, were evidenced (figure 1.19 C, first three images) (D'Auria et al., 2013; D'Auria et al., 2011; Tyteca et al., 2010a).

BODIPY-lipids thus seemed the best validated probes for RBC lipid labelling. However, the substitution of the fatty acid chain by a fluorochrome remained a potential problem, and BODIPY-cholesterol was poorly validated (Carquin et al., 2016). The laboratory therefore decided to take advantage of fluorescent toxin fragments that recognize endogenous SM and cholesterol and that had been recently developed by Japanese teams with whom we collaborated. Their approach was the following. As cholera toxin which is specific to the ganglioside GM1, natural toxins that specifically recognize SM and cholesterol exist. SM-specific toxins notably include Lysenin, which is produced by the worm *Eisenia Foetida*. In its original form, the toxin binds to membrane SM and then oligomerizes to form pores at the membrane, leading to the target cell lysis. The N-terminal domain of the toxin was determined to be the one responsible for the lysis, while the C-terminal was in charge of the lipid recognition (De Colibus et al., 2012). Therefore, a minimal truncated form of the toxin, devoid of the lytic activity, has been produced and validated. It is named NT (for Non-Toxic)-Lysenin (Shogomori and Kobayashi, 2008). On the other hand, cholesterol-specific toxins include streptolysin O from *Streptococus pneumoniae*, listeriolysin O from *Listeria monocytogenes* and perfringolysin O from *Clostridium perfringens*. The latter, also named Theta toxin, displays four domains (D1-D4) and it has been shown that it is the C-terminal D4 domain that possesses a tryptophan-rich sequence responsible for cholesterol recognition. As for Lysenin, the D4 domain, i.e. the minimal segment necessary for cholesterol binding without cytolysis, was isolated and validated by the Japanese teams (Shimada et al., 2002). Those two toxin fragments (i.e. Lysenin and Theta) have been coupled to the fluorescent protein Dronpa, which is suited for super-resolution microscopy, allowing those teams to evidence SM- and cholesterol-enriched domains on fixed Hela cells (Mizuno et al., 2011).

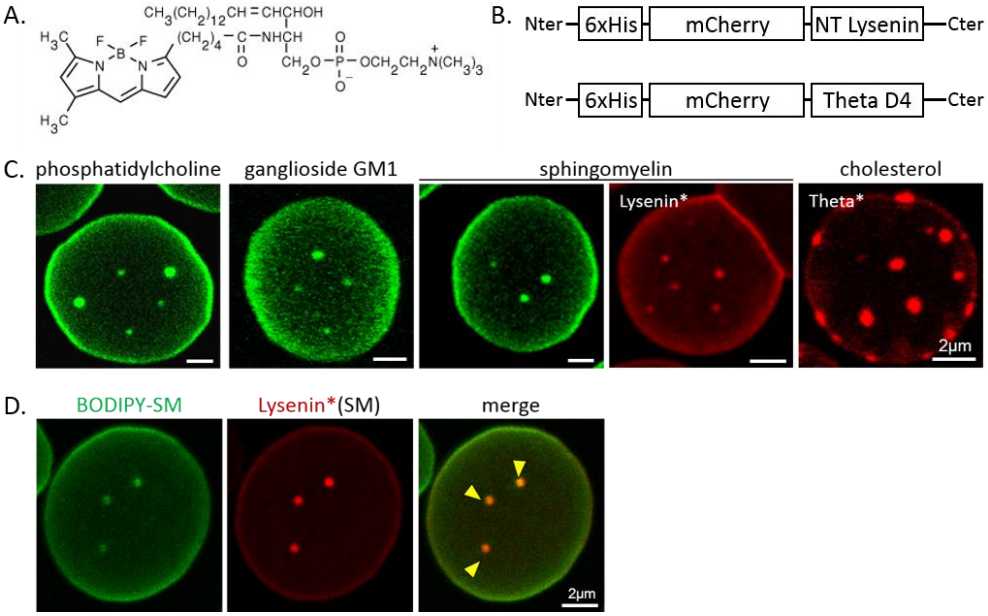

Figure 1.19. Fluorescence or confocal microscopy of polar lipid- and cholesterol-enriched domains at the PM of living spread RBC. **(A)** Structure of BODIPY-FL-C5-SM. **(B)** Coding plasmids for Lysenin (top) and Theta (bottom) toxin fragments. **(C)** Lipid domains revealed by insertion at the PM of BODIPY-PC, -GM1 or -SM; or by decoration of endogenous SM and cholesterol by mCherry-Lysenin and -Theta toxin fragments, respectively. **(D)** Co-labelling between BODIPY-SM and Lysenin reveals a perfect colocalization. Adapted from ((Tyteca et al., 2010a); (D'Auria et al., 2011); (D'Auria et al., 2013); (Carquin et al., 2014); (Carquin et al., 2015)).

By switching the Dronpa protein for the mCherry protein (suitable for fluorescence microscopy) and subsequent living RBC labeling with the mCherry-toxin fragments (figure 1.19 B), our group then revealed submicrometric domains for both SM and cholesterol on RBCs spread on poly-L-Lysine-coated coverslips (figure 1.19 C, two last images). Similar domains were then visualized on RBCs in suspension in a 3D-gel, suggesting relevance for RBCs *in vivo* (Carquin et al., 2015; Carquin et al., 2014). To validate *a posteriori* the use of BODIPY-lipid analogs, a double labeling between BODIPY-SM (inserted at trace levels at the membrane) and mCherry-Lysenin (which recognizes endogenous SM) was performed. A perfect co-labelling was evidenced, therefore validating the use of BODIPY-SM (figure 1.19 D) (Carquin et al., 2014).

6. Approaches to study the physiological importance of membrane lipid organization

6.1. Evaluation of RBC deformation

Several techniques have been developed to simulate and study RBC deformation. Some focus on individual cells precisely while others allow to analyze a large amount of cells with a loss of precision. The techniques thus all have their advantages and limits, and the choice of a technique has to be done carefully considering their differences and the study's objectives. Here under is a non-exclusive list of techniques currently used to study RBC deformability.

6.1.1. Measurement of individual cells

Micropipette aspiration

Developed in the 70s, the micropipette aspiration technique has been extensively used to measure the mechanical properties of RBC membranes, including membrane elastic modulus and membrane viscosity (Kim, 2015). Micropipettes are typically made of glass and have an inner diameter of 1-3µm. By applying a negative pressure, carefully controlled by a manometer system, the RBC is aspired into the micropipette and a hemispherical projection in visible in the capillary (figure 1.20A). By measuring the pressure required to aspire the RBC on a certain length (L), one can calculate the shear modulus of the membrane. For RBCs, it was determined to be around 9µN/m in normal conditions (Evans et al., 1984), but it increases as the RBCs are stored (La Celle, 1969). Other parameters like the relaxation time constant, surface viscosity and area compressibility moduli can be also calculated. However, the micropipette measurements are affected by the dependence on the size of the pipette used in the experiments (reliable comparisons can only be made between samples measured with the same pipette) and, in general, on the conditions of the experiments.

Optical tweezer

Optical tweezers use highly focused laser beams that transfer linear or angular momentum of light, in order to optically trap µm- and nm-sized dielectric spherical particles (Ashkin, 1970). Simply, a laser beam is focused onto a single spot, and this creates an "optical trap" that can hold a small particle at its center. Light refraction at a particle induces linear momentum change, resulting in trapping forces. Those forces usually stand in the pN range but can be highly increased by increasing laser power. To induce deformation of a RBC, two silica microbeads (~4µm of diameter)

are attached non-specifically to the opposite sides of the cell (figure 1.20B). One of the beads is anchored to the surface of a glass slide while the other is trapped using the optical tweezers. While the trapped bead remains stationary, moving the slide and attached left bead stretches the cell (Mills et al., 2004). This technique also allows to determine the shear modulus by analyzing the change in the projected diameter of the RBC in response to the optical force and is usually of 10 to 30 µN/m (Dao et al., 2003).

Atomic Force Microscopy

Micropipette aspiration and optical tweezers mostly subject the whole erythrocyte to stretching forces and have limited potential to study local alterations in mechanical properties. Atomic force microscopy (AFM) is a tip-scanning technique that images topographies of (biological) materials in atomic or molecular scale (Binnig et al., 1986). It uses a flexible cantilever with a sharp tip as a probe, whose vertical motion is monitored by photodiodes which precisely detect small changes in laser beam position reflected from the tip. Using a "dynamic mode", the cantilever oscillate close or at resonance frequency (figure 1.20C) and height changes of the surface alter the cantilever oscillation, which is used to adjust the tip–sample distance (Dufrene et al., 2017). As the tip can also be used to apply pN to nN forces to the sample surface, AFM has become a powerful technique for studying the mechanical properties of various biological materials, including RBCs. These properties can be quantitatively determined from force *vs* distance curves (FD curves) (figure 1.20D). In those analyses, the tip approaches the cell and remains undeflected until it comes in contact to the sample surface (distance= 0nm). The tip then applies a predetermined force to indent the sample. The more the cell is rigid, the less the tip will indent its surface. The resistance can come from the membrane, the cytoskeleton or the cytoplasmic viscosity. When the tip retracts, it will be briefly retained at the cell surface by adhesion forces (Vander Walls forces, capillary forces, a.o.) before the retraction force overcome those forces. Several parameters can be extracted from FD curves: distance (sample height) at maximum contact force, deformation, elasticity (reflected by Young's modulus), energy dissipation and adhesion (Dufrene et al., 2013). Young's modulus increases in pathologies like thalassemia, diabetes mellitus (Dulinska et al., 2006) and hereditary spherocytosis, as exposed in Chapter 2, section 2 (Dumitru et al., 2018).

Aside from cell deformability, AFM has also been proven useful for exploring the forces and the dynamics of the interaction between individual ligands and receptors, either on isolated molecules or on cellular surfaces. These studies require attaching specific biomolecules or cells on AFM tips, which can be achieved

by several means (Hinterdorfer and Dufrene, 2006) as: (i) streptavidin-coated tip and a biotinylated protein, (ii) a gold tip functionalized with a PEG (polyethylene glycol) spacer fused to trisnitrilotriacetate-Ni2+ (Tris-NTA) thats react with a HIS-tagged protein, or (iii) a tip with a PEG spacer fused with a hexaglycine peptide that links LPETGG-tagged protein (Antos et al., 2017).

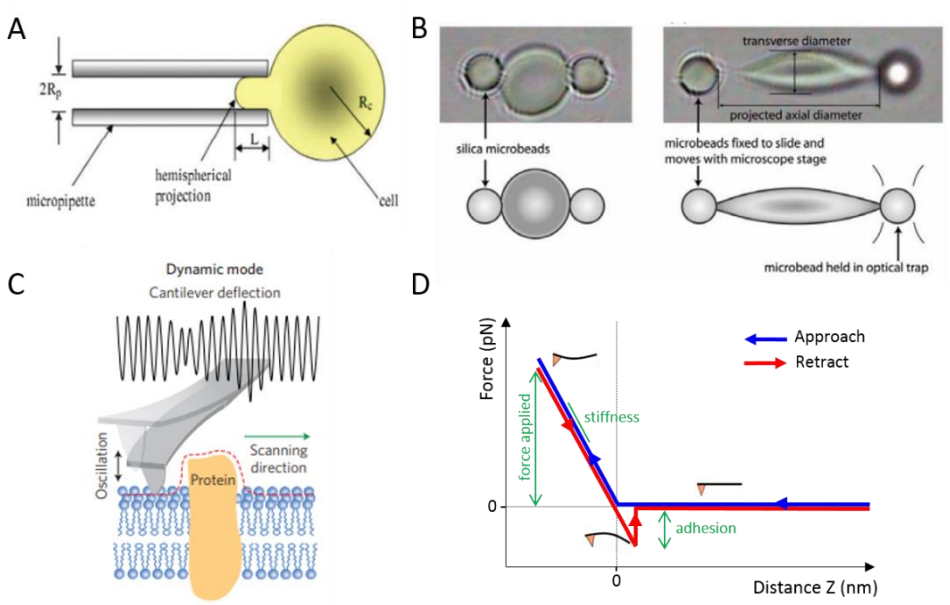

Figure 1.20. Individual cell deformation techniques. (**A) Micropipette aspiration.** Rp, the radius of the micropipette, Rc the radius of the cell, L the length of aspired RBC inside the micropipette upon the application of a negative pressure. Reproduced from (Wan et al., 2011). (**B) Optical tweezers**, reproduced from (Mills et al., 2004). (**C) AFM upon dynamic mode**, reproduced from (Dufrene et al., 2017). (**D) Force-distance curves** in AFM, adapted from (Dufrene et al., 2013).

6.1.2. Measurement of multiple cells

The techniques described here above present the advantage of measuring specific mechanical properties like shear or Young modulus. However, they do not allow to analyze, or to sort, populations of RBCs. Indeed, they suffer from poor time resolution, especially for AFM on living cells. Techniques presented here below allow to complement this limitation.

Filtration

The filtration method examines the ability of multiple cells to pass through membrane filters, whose diameter vary from 3 to 5µm for RBC studies (Kim, 2015). A negative pressure can be applied to force RBCs through the pores. Quantification of the process is achieved by measuring the time required to pass a certain volume of RBCs through the filter. Due to its simplicity, the filtration method has been widely used for the measurement of RBC deformability (Reid et al., 1976). This technique also allow to collect poorly deformable RBCs that would not be able to deform through the pores. However, blockage of the pore is a very typical practical problem and applied pressure could result into RBC hemolysis. An improvement to membrane filters was the development of microsphere-based filters. Using a mixture of 5- to 25-µm-diameter microbeads, Buffet et al designed a sorting device that mimics the geometry of narrow and short interendothelial splenic splits (figure 1.21A) (Deplaine et al., 2011). As heated RBCs, malaria-infected RBCs and spherocytotic RBCs are retained in the microbead layer without hemolysis, they can be isolated from deformable RBCs and characterized at the molecular level.

Microfluidic filtration

Microfluidic devices can be used to mimic human capillaries and study RBC deformability. In this technique, RBCs are flowed with a controlled velocity (i.e. the blood one) through capillaries with controlled diameter (2 to 8 µm) and observed under a microscope (figure 1.21B) (Li et al., 2007). Healthy RBCs will deform in "bullet-like" shape, in opposition to the "dumbbell" deformation observed through pores. Several parameters can be studied, like the deformability index (i.e. measure of the threshold pressure required for the sample to traverse the defined constriction), the recovery time after exit of the channel, or the cell circularity. Microfluidic presents several advantages like its cost efficiency and the fact that it can provide both individual RBC and population assessments of cellular deformability (Kim, 2015). For example, using high speed camera and an electrical measurement system, Sun et al were able to distinguish several RBC populations based on their deformability with a throughput of ~10 cells/second (Zheng et al., 2013). Malaria-infected RBCs at different stages have also been compared (Shelby et al., 2003) and microfluidic has been used to study the vaso-occlusions in sickle cell disease (Horton, 2017).

Ektacytometry

Osmotic gradient ektacytometry is the reference technique for the diagnosis of RBC membrane disorders like HE, HS or xerocytosis (Da Costa et al., 2016; Mohandas et al., 1980). This technique measures RBC deformability under a

defined shear stress as a function of suspending medium osmolarity. The basic configuration developed in the 70s (Bessis and Mohandas, 1975) comprises a viscometer with two cylinders constructed of an optically clear material. The cells were suspended in a viscous medium of defined osmolarity and introduced into the gap between the cylinders (typically 0.5 mm). Cell elongation under cylinder rotation is monitored by the diffraction of a laser beam directed normal to the cylinder axis (figure 1.21C).

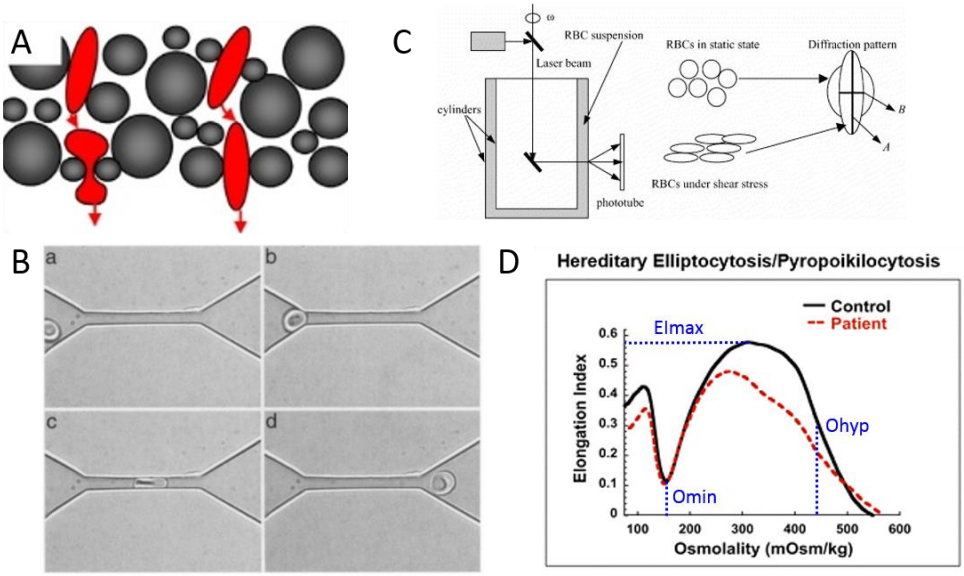

Figure 1.21. Multiple cell deformation techniques. (A) RBC deformation through microsphere-based filters, reproduced from (Deplaine et al., 2011). **(B) Imaging of RBCs going through microfluidic channel**, reproduced from (Li et al., 2007). **(C) Principle of ektacytometry diffraction pattern modification**, reproduced from (Yao et al., 2001). **(D) Typical control and patient (i.e. suffering from HE) curves of osmotic gradient ektacytometry**, adapted from (Da Costa et al., 2016). For additional informations, please refer to the text.

The obtained profile of an osmotic gradient ektacytometer (figure 1.21D) is different and characteristic for each membrane fragility disease. There are three distinct features that can be determined on the profiles (in blue at figure 1.21 D). First, Omin, which corresponds to the hypotonic osmolality at which 50% of the cells hemolyse, provides information on the initial surface-to-volume ratio of the cell sample. It is increased in spherocytosis (i.e. decreased surface-to-volume ratio), decreased in dehydrated xerocytosis (i.e. increased surface-to-volume ratio) and

nearly not altered in ellipocytosis. Second, the elongation index, EImax, which reaches a maximum near 300 mOsm/kg in normal RBCs. It suggests that the cell deforms optimally at the tonicity to which it is normally exposed and mostly depends on the cytoskeleton mechanics. It is decreased in both HE and HS. Third, Ohyp analyzes the declining portion of the curve in hyperosmolar medium and measures the osmolality value at which the cells are at half of the maximum elongation. It correlates with the initial intracellular viscosity of the cell sample and is also decreased in HE and HS.

Cell stretching

Finally, stretching devices that are compatible with imaging have been developed. They are based on thin membranes (100-200µm of thickness) of PolyDiMethylSiloxane (PDMS), a silicon-based organic polymer, on which cells are immobilized. As they are optically transparent, they are usable in optical and fluorescence microscopy. Moreover, the PDMS membranes can be micro-patterned in order to confine cells or tissues to a specific geometry (Carpi and Piel, 2014). The PDMS structure is then stretched in a mono- or multi-axial direction. Recently, an isotropic stretch system has also been developed. It uses a swivel mechanism that translates into a radial displacement of hooks attached to small circular membranes (Schurmann et al., 2016). The system shows good reproducibility concerning uniformity of direction and force. This approach has been validated on RBCs by our lab in previous studies, in which PDMS chambers were stretched mono-axially up to 15%, allowing a transient intracellular Ca^{2+} increase (figure 1.22A) but also a rearrangement of cholesterol-enriched domains in high curvature areas during stretching (figure 1.22B) (Leonard et al., 2017).

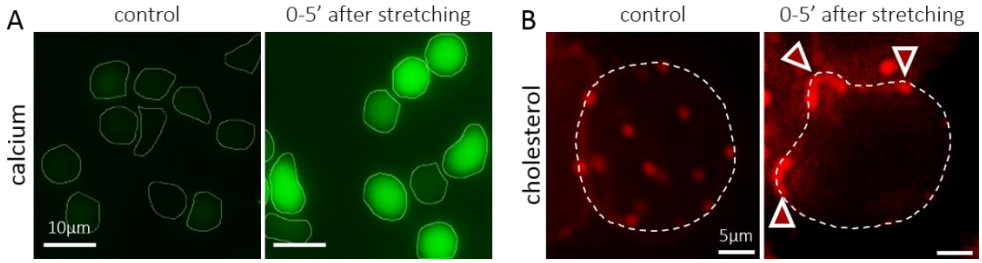

Figure 1.22. RBCs labelled for intracellular Ca^{2+} by Fluo 4 (A) or cholesterol by Theta toxin (B) and examined before stretching (left) or for 0-5 minutes after stretching (right). Arrowheads point to clusters of cholesterol-enriched domains in high curvature areas created during stretching. Adapted from (Leonard et al., 2017).

6.2. Evaluation of lipid-protein interactions

This section is part of an invited review (Conrard, L.; Tyteca, D. Regulation of Membrane Calcium Transport Proteins by the Surrounding Lipid Environment. Biomolecules ***2019****,* 9*, 513.).*

Even though the study of lipid–protein interactions has considerably progressed in the last decades, individual flaws of current techniques still need to be compensated by the overlay of several complementary approaches.

6.2.1. Cell Imaging

Cell Imaging Approaches and Lipid Tools

The development of powerful imaging approaches is essential to evaluate the potential interaction between proteins and the surrounding lipids. Those approaches have to present a high resolution and to be compatible with live cell imaging for two reasons: (i) Lipid imaging should avoid cell fixation and/or permeabilization, as those processes could redistribute membrane lipids; and (ii) the study of membrane protein–lipid interaction is not relevant on fixed cells.

Whereas laser scanning confocal microscopy (LSCM) does not provide sufficient resolution to explore protein–lipid interaction, the recent development of super-resolution microscopy techniques can help. Those include: (i) Photo-activation localization microscopy (PALM) and stochastic optical reconstruction microscopy (STORM), which use photoswitchable fluorescent probes to reveal spatial differences between molecules; and (ii) structured illumination microscopy (SIM), which relies on a grid pattern residing in one of the illumination apertures to generate a sinusoidal excitation wavefield that can be used to extract information from the image focal plane. However, these techniques are so far difficult to apply to living cells due to phototoxicity and photobleaching. Moreover, they are not able to simultaneously integrate high-resolution, sensitivity, and speed, precluding analysis of membrane protein–lipid interactions from a dynamical point of view**.** For advantages and limitations of super-resolution microscopy, see (Carquin et al., 2016).

The Fast Airyscan imaging opens up new avenues to explore this question and appears very promising (Gladwyn-Ng et al., 2018; Neu and Lawrence, 2015; Robison et al., 2016). Airyscanning is a new detection concept that uses an array detector to oversample each Airy disk in order to gain sensitivity, resolution, and speed. In this way, Airyscanning achieves resolutions comparable to an extremely small pinhole, as in confocal microscopy, but with a much better signal-to-noise ratio. Such equipment allows to integrate sample analysis at both the cellular and

molecular levels. It should also be more efficient than LSCM for a number of applications related to dynamic live cell imaging, such as ratio imaging, FRAP (Förster recovery after photobleaching) and FRET (Förster resonance energy transfer; see below).

Another difficulty, besides the imaging approaches, is the limitation of reliable fluorescent tools for membrane lipid imaging. For a long time, the lipid field was limited to the insertion in the PM of fluorescent lipid probes obtained by grafting a fluorophore (such as nitrobenzoxadiazole (NBD) or boron-dipyrromethene (BODIPY)) on the lipid headgroup or its fatty acyl chain (Carquin et al., 2016). Although useful and easy, this technique could present limitations since the probes can differentially partition as compared to endogenous lipids. Polyene lipids (i.e., fluorescent lipids containing several conjugated double bonds) could circumvent the above difficulty since they have a structure highly similar to their endogenous counterparts and distribute within the cell together with their physiological kin (Contreras et al., 2012; Kuerschner et al., 2005). Although suitable for in vitro and live cell analysis, those probes nevertheless also present some drawbacks, including a low quantum yield and high sensitivity to photobleaching (Kuerschner et al., 2005). During the last decades, innovative approaches dedicated to the analysis of endogenous lipid organization have been developed. They are based on fluorescent toxin fragments, proteins with phospholipid (PLP) binding domains, or nanobodies (for a review on these different classes of probes, see (Carquin et al., 2016)).

Förster Resonance Energy Transfer

FRET is highly suitable for the study of protein–lipid interaction. It is based on the energy transfer from an excited donor to an acceptor whose excitation spectra is covered by the emission spectra of the donor. The transfer is only possible when the two fluorescent molecules are extremely close, allowing to study molecular interactions. Again, lipid probes represent a limiting factor for this type of experiments. Polyene lipids presented above have been used by Brugger et al to analyze the interaction between the COPI (Coat Protein complex I) machinery TM protein p24 (in maltose-binding protein (MBP) fusion form) and SL species by FRET in a liposome-based assay. This study revealed a direct and highly specific interaction of exclusively one sphingomyelin (SM) species (i.e., SM with 18C) with the TMD of p24. Strikingly, the interaction depends on both the SL headgroup and the backbone and on a signature sequence within the TMD (Contreras et al., 2012). FRET using pyrene-labelled PLPs has also been used in micellar systems to determine the affinity between PLPs and the hydrophobic surface of the TM section of the PMCA, and to correlate those interactions with the thermal stability of the pump (Levi et al., 2000). Alternatively, single-pair FRET can be combined with

nanodiscs of specific composition (see Section 6.2.2), for example, to indirectly analyze the influence of specific lipid species on protein dimer formation. Thanks to this system, Sako et al have revealed the importance of lipid (especially acidic lipid)–protein interplay in dimerization of juxtamembrane domains of EGFR (Maeda et al., 2018).

A derivative from the FRET approach is the quenching of protein tryptophan fluorescence by halogenated (i.e., mainly bromylated) PLPs (Gonzalez-Manas et al., 1992). Those lipids behave much like conventional PLPs with unsaturated fatty acyl chains, but show significant absorption at the wavelength of tryptophan emission when localized directly around the residue. This technique has been used to show that SERCA1, which contains 13 tryptophan residues, has a higher binding constant for PC than for PE (East and Lee, 1982). However, it is not possible to determine whether PEs bind less well than PCs at all sites or only at some specific sites. On the other hand, the group of Lee has introduced tryptophan residues in specific regions of prokaryotic MSC, which normally do not contain any tryptophan residues. Thanks to this localized insertion, they have determined the exact binding sites for several lipids at the inner and the outer PM leaflets (Powl et al., 2005).

6.2.2. Reconstitution of Membrane Proteins in Artificial Environments

Reconstitution of Ca^{2+} transport proteins in a controlled membrane environment represents a model of choice to study the importance of lipids for their activity. Proteoliposomes (i.e., spherical vesicles composed of a lipid bilayer and the protein of interest) are widely used. Although the composition of such liposomes has evolved to mimic, as close as possible, the cell membrane composition, several drawbacks remain. First, the membrane protein solubilization often results in turbid and viscous samples, which may be especially troublesome in many biophysical methods. Second, as liposomes are spherical, they present a membrane curvature that may interfere with the normal Ca^{2+} channel activity and this problem is especially relevant for curvature-sensitive channels like MSCs (see Chapter IV, Section 3.1.3). This can be prevented by the use of planar bicelles rather than liposomes, which combine a flat bilayer-like plan and curved micelle-like ends. However, planar bicelles have a rather low structural integrity and stability.

Therefore, one should instead sometimes favor a stable planar bilayer model system of ~10 nm in diameter, which provides space for one or more membrane proteins and allows access to both sides of the bilayer for the association of substrates or signaling partners. As such, nanodiscs represent a robust tool for

revealing the structure and function of isolated membrane proteins, as well as their complexes with other proteins and lipids (Denisov and Sligar, 2016). Those self-assembled discoidal fragments of lipid bilayers can be controlled for their lipid composition and obtained in high yield. They are stabilized and rendered soluble in aqueous solutions by two amphipathic helical membrane scaffold proteins (MSP) (Figure 1.23) (Bayburt and Sligar, 2010; Schuler et al., 2013). Their diameter (8–16 nm) is determined by the MSP length and the stoichiometry of the lipids used in the self-assembly process. The MSP encircles the discoidal membrane fragment in a "double belt" configuration, as initially suggested by (Wlodawer et al., 1979). Moreover, scaffold proteins are available with a wide range of specific tags/anchors for isolation, in vivo targeting, imaging, and reversible or irreversible surface immobilization (Zoghbi and Altenberg, 2017).

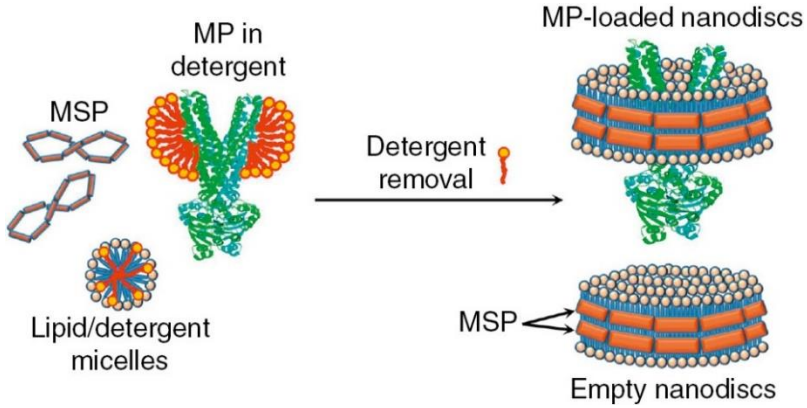

Figure 1.23. Traditional assembly of a nanodisc with a membrane protein (MP). Reproduced from (Zoghbi and Altenberg, 2017). MSP, membrane scaffold protein.

The most direct method for incorporating integral membrane proteins into the nanodisc bilayer is to self-assemble it from a detergent-solubilized mixture of MSP and lipids, maintaining the correct overall stoichiometry of the component parts (Figure 1.23). Moreover, the size and ratio of scaffold protein-to-membrane protein may be selected to favor incorporation of predominantly monomeric (in which there is a large excess of scaffold protein and lipids) or oligomeric target proteins into nanodiscs (Bayburt and Sligar, 2010). Problematically, this necessitates the isolation and purification of the target protein, a process often leading to its inactivation due to separation from its native environment. To circumvent this problem, one could detergent-solubilize a native membrane preparation in the presence of excess MSP and lipids and then remove the detergent, which would distribute the starting membrane protein population into individual nanodiscs, thus

forming a soluble library of all membrane proteins of the starting preparation (Civjan et al., 2003). This allows avoiding the purification step while accelerating the entire process of nanodisc self-assembly, which is sometimes critically important for preservation of the native and functional form of the target membrane protein. Proteins of many types, topologies, and sizes (from 1 to 24 TM domains) have been successfully self-assembled into nanodiscs (Bayburt and Sligar, 2010).

Nanodiscs have already been used in combination with several techniques. For example, using nuclear magnetic resonance (NMR) or (cryo-)electron microscopy, one can evaluate the impact of lipid composition and biophysical properties on the protein orientation in the membrane, as well as its conformation changes. Using the latter technique, the transient receptor potential channel TRPV1 atomic structures of three conformations have been assessed, revealing locations of some annular and regulatory lipids that form specific interactions with the channel (Gao et al., 2016). Besides conformation studies, nanodiscs are also very suitable to analyze, by spectroscopic methods, the activity of a single enzyme/channel embedded in a nanodisc of controlled composition (Laursen et al., 2014; Sadler et al., 2016). A third application relies on the solubilization of an entire cell membrane in nanodiscs, followed by the immunoprecipitation of nanodisc-containing specific embedded lipids (Borch et al., 2011; Borch et al., 2008). The embedded proteins that partition into those specific nanodiscs can then be identified (for example by mass spectrometry (Marty et al., 2012) or X-ray crystallography analysis). The reader could refer to Section 6.2.3 for a brief description of those methods.

6.2.3. Membrane Protein Structural Biology and Mass Spectrometry

Since the breakthrough in crystallizing membrane proteins (Knapp et al., 1985), the most powerful method to define lipid-binding sites on proteins has been X-ray and electron crystallography (Hunte and Richers, 2008). This method is based on the fact that crystals of membrane proteins usually contain lipid molecules (see Figure 1.24). They originate from the native membrane, from which they co-purify with the crystallized membrane protein. Most of the lipids resolved in high-resolution crystal structures of membrane proteins are likely to be non-annular lipids (i.e., specifically interacting with the protein, see Chapter IV, Section 3.1.1 and example in Figure 1.24a), their strong binding to the protein leading to immobilization of at least part of the lipids (Lee, 2003; Yeagle, 2014). Other lipids, considered as annular lipids (see Chapter IV, Section 3.1.2 and Figure 1.24b,c), might also co-crystallize because they are needed to maintain the stability of the membrane protein. Indeed, lipids have been shown to play a major role for TM protein folding and stabilization as they mediate between the protein and the bulk

lipids and seem to play a major role in the orientation of the membrane-spanning domain within the bilayer (Gonen et al., 2005). Upon analysis of crystallized proteins by X-ray or electron microscopy, these lipids appear in the density map as elongated structures mainly oriented perpendicular to the membrane plane. Specific binding sites on the protein can thus be identified and some lipid species can be characterized, even though they might not appear sufficiently definite to allow for their unambiguous characterization. Therefore, many lipid classes and molecular species can not be determined unequivocally. Progressively, more and more membrane protein X-ray structures show how lipids bind. For an extensive review describing the method development and applications, see (Yeagle, 2014). Focusing on Ca^{2+} transporters, electron density maps for crystals of the SERCA in different states were obtained by X-ray solvent contrast modulation. They allowed to evidence PLP binding to the protein, either by Arg/Lys-phosphate salt bridges or by hydrogen bonding, and this binding appears to affect conformational switching (Norimatsu et al., 2017).

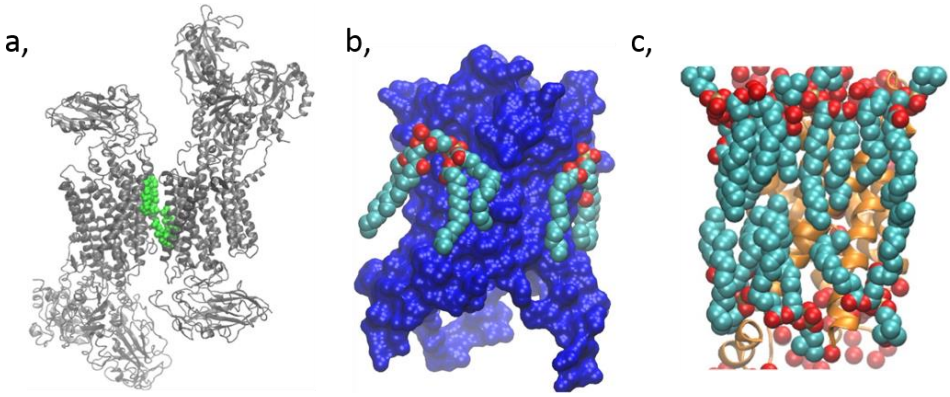

Figure 1.24. X-ray crystal structures of: (**a**) The porcine Na^+/K^+ ATPase (grey) with bound cholesterol molecules (green), most certainly as non-annular lipids; (**b**) the bovine ADP/ATP carrier (blue) with annular-bound diphosphatidylglycerol molecules (cyan); and (**c**) the lens aquaporin (orange) with several phosphatidylcholine (PC) molecules (in cyan) in a configuration approximating the bilayer. Those images were reproduced from (Yeagle, 2014).

Thus, X-ray or electron crystallography are increasingly used, not only to solve membrane protein structures with atomic resolution (till 0.5Å), but also to study their lipid environment (Contreras et al., 2011). However, those techniques still present huge limitations. The major one is that crystals of membrane proteins are mostly obtained from detergent solutions, which might alter the membrane

protein stability and/or conformation. Moreover, they could also induce a biased sample of tightly bound lipids around the protein. This limitation may be overcome as more membrane protein structures are determined using crystals obtained from lipid cubic phases (Caffrey, 2015), allowing the crystallization of membrane proteins that never leave the lipid bilayer environment. Nanodiscs represent an extremely precious tool for this type of crystal formation (Broecker et al., 2017; Nikolaev et al., 2017).

In contrast to X-ray or electron crystallography, NMR spectroscopy is an analytical technique that bypasses the need for crystallization. Two types of NMR exist, namely solution and solid-state NMR. Solution NMR allows to study membrane protein–lipid interactions with high resolution, but only for small proteins that are embedded in small bicelles or nanodiscs. On the other hand, solid-state NMR has no theoretical limitations on size and, thanks to recent technical improvements like magic-angle spinning and cross polarization approaches, its resolution is now close to the solution NMR one (Das et al., 2013; Tycko, 2001). Thus, solid-state NMR allows to prepare membrane proteins in lipid bilayers that more closely mimic their natural environment. However, practically, technical hurdles still limit the size of structures that can be solved by this method (Liang and Tamm, 2016). Several examples of protein–lipid interactions revealed by solid-state NMR are given in (Huster, 2014).

Cryo-electron microscopy relies on the instant freezing of a protein solution, leading to the formation of an amorphous solid without water molecule crystallization. The frozen sample is then screened and, thanks to the 2D images acquired, particle alignment and classification are carried out. The main advantages of this technique are that it requires only a small sample size and that proteins are maintained on a close-to-native state and are not required to be crystallized. However, it also presents defects like the quite low resolution of < 3.5 Å, that still renders it unusable for proteins with small molecular weight (Wang and Wang, 2017). However, this resolution is increased in recent studies to up to 2.9 Å for TRPV1 and 2.2 Å for the β-galactosidase (Bartesaghi et al., 2015). Cryo-electron microscopy may be the structural analysis technique where the advantages of nanodiscs are most effectively used, as the nanodisc can be analyzed as a soluble "single particle", removing the need of protein solubilization. Moreover, nanodisc use removes the usual difficulty of unknown orientations of the particle analyzed (Mio and Sato, 2018).

Mass spectrometry (MS) of solubilized protein–lipid complexes is also useful. The most widely-used approach relies on the capability to dissociate the lipids from a membrane protein complex in the gas phase (i.e., successive delipidation), which,

together with lipidomics analysis on purified membrane protein preparations, allows identification of key lipids (Marty et al., 2016). Briefly, membrane proteins, either extracted from or reconstituted in detergent micelles or in other membrane mimetics (like nanodiscs), are introduced into the mass spectrometer via nano-electrospray ionization. This soft ionization process can preserve non-covalent interactions under the appropriate conditions, making it ideally suited for the study of protein complexes. For native MS of membrane proteins, bound lipids appear as adduct peaks on individual protein peaks. The characteristic mass differences between the protein and adduct peaks can reveal the presence of lipids. However, mass alone does not provide a complete lipid identity. Multistage ion activation enables selection of lipid-bound protein ions and dissociation of lipid species in tandem MS experiments (Bolla et al., 2019). Derivations of this technique also allow to evidence lipids that are necessary for membrane protein oligomerization (Gupta et al., 2018).

6.2.4. Molecular Simulation

In silico approaches are more and more used to analyze the molecular mechanisms of protein–lipid interactions (Lindahl and Sansom, 2008; Muller et al., 2019). The atomistic simulations of molecular mechanics used to be limited by the calculation times on the available computer systems. This has been partially overcome by the use of parallelized super computers and a variety of optimized simulation softwares, which enable simulations in atomistic details for systems. The simulation of molecular dynamics (MD) allows the analysis of the interactions of atoms and macromolecules for a short time period by the established laws of physics and can be considered as an animation of Newtonian mechanics. Unlike NMR- and X-ray-based approaches, the motions and interactions of proteins and lipids can be monitored in atomistic detail with high temporal and spatial resolution (Contreras et al., 2011).

However, the computational cost of the simulations is such that length scales beyond a few microseconds are not currently readily accessible (Dror et al., 2012), especially for extended systems containing multiple membrane proteins. This is why we saw the emergence of more approximate coarse-grained (CG) representations of membrane lipids and proteins in MD simulations (Marrink and Tieleman, 2013), in which groups of atoms are represented as single particles (Figure 1.25A). CG simulations can enhance lipid exploration of the protein surface and candidate binding sites, while sacrificing the finer detail of lipid–protein interactions. These approximations may be reconciled to some degree by conversion of the endpoint of a CG system back to atomistic detail (Stansfeld and Sansom, 2011; Wassenaar et al., 2014) and subsequently running an atomistic

simulation to assess the validity of the CG system arrangement, a so called (serial) multiscale modelling approach (Ayton et al., 2007).

The structure of a membrane protein used as initial input for MD simulations may originate from X-ray or cryo-electron crystallography, or NMR. If the 3D structure of the protein is not known experimentally, a model may be built by modelling in some cases. The membrane protein is then embedded into a lipid bilayer (Stansfeld and Sansom, 2011). This may be achieved either by self-assembly simulations (Scott et al., 2008), in which short simulations are run to allow the spontaneous formation of a bilayer around an integral membrane protein, or by a number of methods which insert a membrane protein into a pre-assembled bilayer (Fosso-Tande et al., 2017; Wolf et al., 2010). Advances in lipid parameterization (Wassenaar et al., 2015), along with a growing appreciation of the in vivo compositional and spatiotemporal complexity of lipid membranes, enable simulations of proteins in complex lipid bilayers, providing approximations of in vivo PM composition (Ingolfsson et al., 2014; Koldso et al., 2014) and transversal and lateral asymmetry (Lyman et al., 2018). Such mixed lipid systems allow to address competition between different lipid species for interaction with a given protein, and provide a better approximation of lipid–lipid interactions which are linked to, and may influence protein–lipid interactions. Such mixed lipid systems can now be routinely assembled in CG.

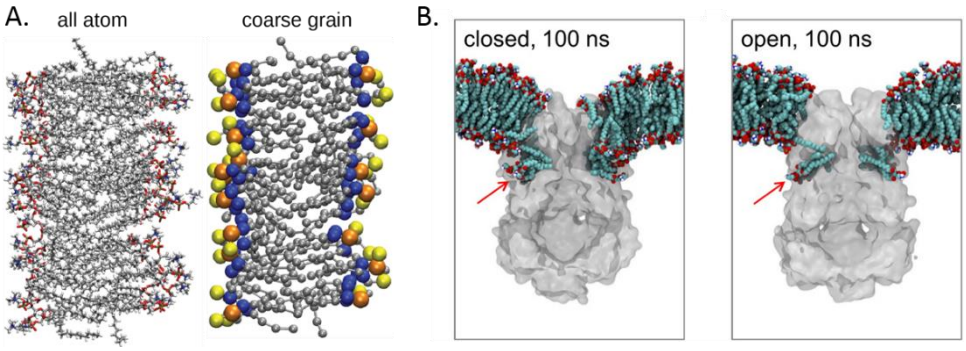

Figure 1.25. Molecular dynamic (MD) simulations. (**A**) A 1-palmitoyl-2-oleoyl-sn-glycero-3-PC (POPC) bilayer represented in an all-atom model (left) *vs* a Coarse-grained (CG) model (right). Reproduced from (Awoonor-Williams and Rowley, 2016). (**B**) Prokaryotic MSC of small conductance (MSCS)–lipid interactions upon closed (left) and open (right) conformations in CG MD simulations. The red arrow shows the lipid-binding cavity whose occupancy changes between the closed and the open conformation. Original MD simulation from (Pliotas et al., 2015).

Introduction

A number of recent simulation studies probing lipid interactions have identified annular solvation shells around proteins (Fosso-Tande et al., 2017) as well as specific lipid binding. These sites show good agreement with those identified from a range of structural studies. A number of other, presumably weaker, binding sites can also be resolved. While these weaker sites may not always be observed by X-ray crystallography, they can be probed through fluorescence, NMR, or MS. Overall, MD simulations have strong predictive power, are well-suited for identification of these sites, and could even characterize the identified sites through estimation of lipid-binding affinities while giving insight into mechanisms of lipid modulation. For example, MD simulations have allowed to show that TM pockets of the prokaryotic MSC of small conductance (MSCS) have a decreased volume upon channel opening, and that lysoPLPs (i.e., PLPs with one acyl chain per headgroup) displace normal PLPs from the pockets and trigger the channel opening (Figure 1.25B) (Pliotas et al., 2015; Schmidt et al., 2013).

CHAPTER II – AIMS AND STRATEGIES OF THE STUDY

During the last decade, the host laboratory has evidenced several submicrometric lipid domains at the RBC PM outer leaflet, thanks to the use and careful validation of complementary fluorescent probes that are compatible with confocal vital imaging. Those probes include exogenous fluorescent lipid analogs (Bodipy-lipids) inserted at trace level at the PM and fluorescent non-toxic fragments of natural toxins that recognize endogenous lipids (mCherry-Theta and -Lysenin). Specifically, domains enriched in cholesterol, sphingomyelin (SM), phosphatidylcholine (PC) and ganglioside GM1 were evidenced. The two former domains have been characterized, exhibiting a similar dependence to temperature and to cytoskeleton anchorage. However, they present differential order and curvature association, suggesting the existence at the RBC surface of several lipid domains. Those data are included in several papers, notably (Carquin et al., 2014; D'Auria et al., 2013; D'Auria et al., 2011; Leonard et al., 2018; Tyteca et al., 2010d) and (Carquin et al., 2015; Leonard et al., 2017), two papers to which I contributed (see Annex 1 and 2).

The characterization of the two other types of lipid domains as well as a mapping of the coexisting lipid domains at the PM of RBCs at resting state was still lacking. **The first aim of my thesis was thus to determine if lipid domains coexist at the RBC surface or are spatially related** (figure 2, #1)**.** To achieve this goal, I compared the four types of lipid domains (i.e. enriched in cholesterol, SM, PC and GM1) for their relative abundance, curvature association, fluidity and dependence to the membrane cholesterol content and temperature. I also performed co-labelling experiments. Based on those results, I suggested that, at resting state and at physiological temperature, three populations of lipid domains coexist at the RBC surface. The first ones, mostly enriched in cholesterol, are abundant (~8/hemi-RBC), associate with high curvature areas and exhibit higher lipid order than the other lipid domains. The second ones, enriched in GM1/PC/cholesterol (here after referred as GM1-enriched domains), are less abundant (~1.5/hemi-RBC), locate in low curvature areas and present lower ordering. The third ones, enriched in SM/PC/cholesterol (here after referred as SM-enriched domains), are rare (~0.6/hemi-RBC), also associate with low curvature areas and present a low

ordering ***((Conrard et al., 2018) PUBLICATION 1– PART 1; see Chapter III, section 1)***.

The above experiments were achieved in confocal/fluorescence microscopy, a technique that allow to visualize several lipids at a time, has a good temporal resolution and an acceptable spatial resolution. However, it relies on fluorescent probes that might result in artefactual gathering of lipids. **The second aim of this work was thus to test whether those lipid domains really exist or not through the analysis of RBCs in their native state (i.e. without any labeling) and to characterize their biophysical properties** (figure 2, #2). To this purpose, we used atomic force microscopy (AFM) in collaboration with the lab of David Alsteens (UCLouvain, LLN). This innovative technique allows the scanning in high resolution of RBC surface features as well as the analysis of their nanomechanical response to stress by force-distance curves. We evidenced lipid domains of differential size and elasticity at the surface of RBCs. Moreover, we showed that this technique is able to evidence differences between healthy and pathological RBCs. Indeed, by comparing healthy RBCs to poorly deformable RBCs from patients suffering from hereditary spherocytosis, we showed that pathologic RBCs were more rigid, which results from a decreased cytoskeleton anchorage but also from a decreased membrane elasticity ***((Dumitru*, Poncin*, Conrard et al, 2018) PUBLICATION 2; see Chapter III, section 2.1)***.

The AFM results thus strongly support the existence of several lipid domains at the RBC surface. **The next step is to evaluate the composition of this multitude of lipid domains evidenced and to directly correlate the variations of membrane elasticity to the lipid organization.** To do so, we continued to work with AFM but using functionalized tips with the toxin derivatives that specifically recognize cholesterol or SM at the membrane. My contribution to this study was to functionalize these tips. The probes were already tested and validated on artificial membranes of specific composition ***((Dumitru*, Conrard* et al, 2018) PUBLICATION 3; see Chapter III, section 2.2)***. Those validated functionalized tips should be soon tested on RBCs.

Reassured about the presence and coexistence of lipid domains at the resting RBC surface, **the third aim of my thesis was to explore whether and how those domains could be remodeled during the RBC deformation process** (figure 2, #3). To simulate deformation, RBCs were immobilized on silicon chambers that were then transiently stretched. First evidences for a rearrangement of cholesterol-enriched domains towards high-curvature membrane areas upon RBC stretching have been provided in the lab in 2017 (Leonard et al., 2017) (an article to which I contributed, see Annex 2). I extended this study to Ca^{2+} exchanges at the RBC

surface and to SM- and GM1-enriched domains. As the GM1-enriched domains increase in abundance during Ca^{2+} influx upon stretching, we explored the potential link between those domains and the activation state of the mechanosensitive channels Piezo1, the major channel responsible for Ca^{2+} entry during RBC deformation (Cahalan et al., 2015). We pharmacologically inhibited or activated the channel and showed a close relation between GM1-enriched domain abundance increase and Piezo channel activation. On the other side, our results in stretching chambers also showed an increase of SM-enriched domain abundance during the Ca^{2+} efflux upon shape restoration. We therefore tested this relation by indirectly activating or inhibiting Ca^{2+} efflux through the Ca^{2+} pump PMCA and demonstrated a close relation between SM-enriched domain abundance and the PMCA activation ***((Conrard et al., 2018) PUBLICATION 1 – PART 2; see Chapter III, section 3)***. The recent evidences in literature of Ca^{2+} transport protein regulation through lipids and the acknowledged or proposed means for this regulation are presented and discussed in a invited review to Biomolecules ***((Conrard and Tyteca, 2019); split between Chapter I, section 3.1 and 6.2.; and Chapter IV, section 3).***

In the last part of this work, I contributed to another project which consists in evaluating whether and how lipid domains could be altered in pathological conditions (figure 2, #4). We used RBCs from a patient suffering from hereditary elliptocytosis due to mutations in the α-spectrin gene. In this patient, RBC size and circularity are decreased and deformability is impaired. Membrane association and lateral distribution of cytoskeletal and membrane proteins are altered. SM- and GM1-enriched domains are modified in abundance, cholesterol content and response to Ca^{2+} exchange stimulation. This could result from several features that we have, and that are still currently, tested. First, the plasmatic acid sphingomyelinase is upregulated, which leads to increased ceramide-enriched domains. Second, the intracellular Ca^{2+} content is strongly increased with the following downstream consequences: (i) PKC-dependent cytoskeletal and membrane protein phosphorylation; (ii) NADPH oxidase-dependent ROS production and lipid peroxidation; and (iii) scramblase-dependent loss of membrane transversal asymmetry. Finally, the membrane content of long unsaturated PS and PC species is also decreased. All these features could lead to alteration of membrane lipids and lipid domains, and we suggest that this contributes to the pathophysiology of elliptocytosis ***((Pollet, Conrard et al, in preparation); see Chapter III, section 4)***.

Aims and strategies

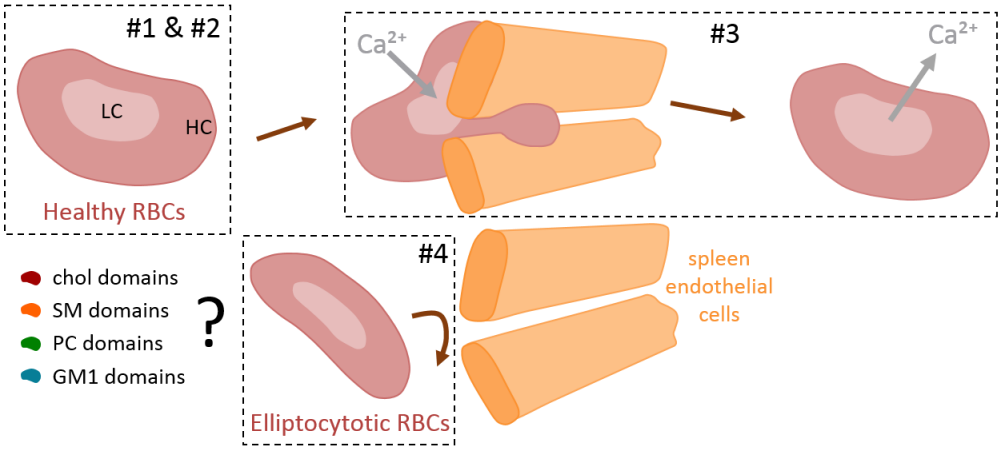

Figure 2. Major thesis objectives: #1 Lipid domain mapping at the surface of resting labelled RBCs by fluorescence microscopy? **#2** Relevance of lipid domains for unlabeled RBCs by AFM and characterization of their biophysical properties? **#3** Modulation of lipid domains upon RBC deformation (i.e. stretching) and shape restoration? **#4** Alterations of lipid domains in pathological poorly deformable RBCs from a patient suffering from hereditary elliptocytosis? LC, low curvature; HC, high curvature.

Aims and strategies

CHAPTER III – RESULTS

1. RBCs at resting state – Fluorescence microscopy-based study

PUBLICATION 1 – PART 1

For the sake of consistency, this publication has been split between this section (Introduction, Material and Methods, first part of the results) and the section 3 of this chapter (second part of the results and Discussion).

Cellular Physiology and Biochemistry

Cell Physiol Biochem 2018;51:1544-1565
DOI: 10.1159/000495645
Published online: 29 November 2018
Accepted: 21 November 2018

Original Paper

Spatial Relationship and Functional Relevance of Three Lipid Domain Populations At the Erythrocyte Surface

Louise Conrard[a] Amaury Stommen[a] Anne-Sophie Cloos[a] Jan Steinkühler[b] Rumiana Dimova[b] Hélène Pollet[a] Donatienne Tyteca[a]

[a]CELL Unit, de Duve Institute & Université catholique de Louvain, Brussels, Belgium, [b]Theory and Bio-Systems, Max Planck Institute of Colloids and Interfaces, Science Park Golm, Potsdam, Germany

Key Words
Fluorescence microscopy • Mechanical stimulation • Piezo1 • PMCA • PDMS stretching • Calcium exchanges

Results

Abstract

Background/Aims: Red blood cells (RBC) have been shown to exhibit stable submicrometric lipid domains enriched in cholesterol (chol), sphingomyelin (SM), phosphatidylcholine (PC) or ganglioside GM1, which represent the four main lipid classes of their outer plasma membrane leaflet. However, whether those lipid domains co-exist at the RBC surface or are spatially related and whether and how they are subjected to reorganization upon RBC deformation are not known. ***Methods:*** Using fluorescence and/or confocal microscopy and well-validated probes, we compared these four lipid-enriched domains for their abundance, curvature association, lipid order, temperature dependence, spatial dissociation and sensitivity to RBC mechanical stimulation. ***Results:*** Our data suggest that three populations of lipid domains with decreasing abundance coexist at the RBC surface: (i) chol-enriched ones, associated with RBC high curvature areas; (ii) GM1/PC/chol-enriched ones, present in low curvature areas; and (iii) SM/PC/chol-enriched ones, also found in low curvature areas. Whereas chol-enriched domains gather in increased curvature areas upon RBC deformation, low curvature-associated lipid domains increase in abundance either upon calcium influx during RBC deformation (GM1/PC/chol-enriched domains) or upon secondary calcium efflux during RBC shape restoration (SM/PC/chol-enriched domains). Hence, abrogation of these two domain populations is accompanied by a strong impairment of the intracellular calcium balance. ***Conclusion:*** Lipid domains could contribute to calcium influx and efflux by controlling the membrane distribution and/or the activity of the mechano-activated ion channel Piezo1 and the calcium pump PMCA. Whether this results from lipid domain biophysical properties, the strength of their anchorage to the underlying cytoskeleton and/or their correspondence with inner plasma membrane leaflet lipids remains to be demonstrated.

Donatienne Tyteca

CELL Unit, de Duve Institute & Université catholique de Louvain,
UCL B1.75.05, avenue Hippocrate, 75, B-1200 Brussels (Belgium)
Tel. +32-2-764.75.91, Fax +32-2-764.75.43, E-Mail donatienne.tyteca@uclouvain.be

KARGER

Introduction

Red blood cells (RBCs) are highly deformable cells that can go through capillaries 3-times narrower than their diameter to deliver oxygen throughout the body. The RBC deformation process is associated with a transient increase of the intracellular calcium [1] which plays a capital role, notably by activating Gardos channels and thus leading to cell dehydration, and by favoring a local uncoupling between the membrane and the underlying spectrin cytoskeleton [2]. RBC calcium entry is thought to be mostly operated by mechano-activated ion channels like Piezo1 [3], while calcium efflux is ensured by the RBC calcium pump, the Plasma Membrane Calcium ATPase (PMCA). This process is tightly regulated and an excessive increase of the intracellular calcium, as observed in physiological senescence or in pathological hereditary hemolytic anemias, has harmful consequences for the RBCs such as an increased vesiculation, the loss of the transverse lipid asymmetry and the consumption of the energy resources. This will lead to a decreased deformability resulting in the RBCs trapping in the spleen and their removal from the blood by the spleen resident macrophages [4].

Besides finely regulated calcium exchanges, RBC deformability has also been linked to other specific features, *i.e.* (i) the excess of plasma membrane (PM) surface in comparison with the cytoplasmic volume and the resultant biconcave shape; (ii) the tightly regulated intracellular hemoglobin concentration (32-36 g/dl); and (iii) the viscoelastic resistance of the membrane [5, 6]. The latter feature depends on the strong anchorage of the PM to a very stable cytoskeleton of spectrin thanks to two non-redundant anchorage complexes based on 4.1R and ankyrin proteins [7]. Membrane lipid composition is also suggested to regulate the membrane viscoelastic properties [8]. As a matter of fact, RBC PM exhibits a particularly high cholesterol level (~45 mol%) in comparison to other cell types (*e.g.* ~35 mol% in CHO cells or ~15 mol% in fibroblasts) [9]. Yet, this small lipid plays key roles in membrane by regulating fluidity, lipid phase separation, mechanic resistance and membrane permeability [10].

As the scientific community slowly realized the importance of membrane lipid composition for cell biological characteristics and processes, more and more evidences for lateral lipid asymmetric distribution have been provided. The first example was the well-known 'lipid rafts', defined as nanometric and transient lipid structures whose presence has been linked to several processes like lipid sorting in polarized cells and antigen presentation at the T-cell surface [11, 12]. In the last decades, advances in microscopy resolution and development of new observation techniques (*e.g.* super resolution microscopy or fluorescence lifetime spectroscopy) [13-16] and more relevant lipid probes [17, 18] have allowed to evidence bigger (submicrometric instead of nanometric) and more stable lipid domains. Those have been observed on prokaryotic cells [19], yeast [20, 21] and various eukaryotic cells like keratinocytes [22], fibroblasts [23] and RBCs [24-26]. Focus is generally made on sphingolipids and sterols as they are two major lipids of the PM external leaflet of many cells and because they are known to be enriched in rafts and associated with membrane fluidity regulation.

As a matter of fact, our group evidenced and extensively characterized cholesterol (chol)- and sphingomyelin (SM)-enriched submicrometric domains at the external PM leaflet of RBCs. These domains are stable in time and space and have been observed by fluorescence microscopy on RBCs immobilized on poly-L-lysine (PLL, *i.e.* spread), but also on RBCs in suspension in plastic chambers or in three-dimensional gels. To label the domains for fluorescence microscopy, we used fluorescent lipid analogs (*i.e.* BODIPY-SM) that get inserted at trace levels in the PM [27] and developed and carefully validated fluorescent toxin fragments specific to endogenous chol (theta*) and SM (lysenin*) [25, 26]. More recently, we also used atomic force microscopy, a high-resolution technique applicable to cells in their native state (*i.e.* without labeling), to study the biophysical properties of these domains [28]. The chol- and SM-enriched domains differ in abundance and biophysical properties (*i.e.* lipid order and association with membrane curvature areas) and differentially contribute to the

RBC deformation. For instance, chol-enriched domains gather in high-curvature membrane areas under RBC stretching and might thus increase deformability and membrane resistance under deformation; while SM-enriched domains, which increase in abundance after deformation, could be linked to RBC shape restoration after deformation [29].

Lipid domains enriched in phosphatidylcholine (PC) or glycosphingolipids like ganglioside GM1 have also been evidenced but not well-characterized [27]. Moreover, whether chol-, SM-, PC- or GM1-enriched domains coexist or are spatially related at the RBC surface and whether they are subjected to reorganization upon RBC deformation are not known. We explored the first issue on RBCs at resting state. Since multiple labeling could suffer from the use of several probes at the same time, possibly inducing toxicity and steric hindrance, we developed additional approaches aiming at comparing lipid domains for their abundance, biophysical properties (lipid order and curvature association, key properties involved in cell deformation) and ability to be modulated by temperature and controlled chol depletion. We next studied lipid domain organization through RBC deformation by mechanically stimulating RBCs (using stretchable silicon chambers) and modulating either the entry or the exit of calcium.

The present study shows the coexistence at the resting RBC PM outer leaflet of three lipid domain populations that differ in chol-, SM-, PC- and GM1-enrichment, abundance, curvature association, lipid order, temperature dependence and sensitivity to RBC spreading onto PLL. Regarding lipid domain contribution to RBC reshaping, we have previously shown that the first population of domains, *i.e.* those mostly enriched in chol, gather in increased curvature areas upon RBC deformation [29]. Here, we provide experimental evidence for the differential contribution of the two other populations of lipid domains in RBC calcium exchanges. This could occur either via the mechano-activated ion channel Piezo1 during deformation or via the calcium pump PMCA during shape restoration.

Materials and Methods

Red blood cell isolation

This study was approved by the Medical Ethics Committee of the Université Catholique de Louvain; each donor gave written informed consent. All methods were performed in accordance with the relevant guidelines and regulations. Blood was collected from 10 healthy volunteers by venopuncture into dry K^{+}/EDTA-coated tubes. For each experiment, blood was diluted 1:10 in Dulbecco's Modified Eagle Medium (DMEM containing 25 mM glucose, 25 mM HEPES and no phenol red, Invitrogen), then washed twice by centrifugation at 200 *g* for 2 min and resuspension. Washed RBCs were used at 5 * 10^7 cells/ml (washed RBCs:medium ratio of 1:10, *v:v*), then incubated or not with pharmacological agents or directly imaged by vital fluorescence/confocal microscopy or fluorescence correlation spectroscopy (FCS) (see below).

Pharmacological treatments

To modulate chol content, washed RBCs were preincubated in suspension at 37°C in DMEM supplemented with (i) the indicated concentrations of methyl-ß-cyclodextrin (mβCD; Sigma-Aldrich) for 30 min or (ii) 0.9 mM mβCD followed by repletion with 3.5 µg/ml mβCD:chol (Sigma-Aldrich) for 60 min. Chol content was determined as previously described [25]. SM content modulation was achieved with sphingomyelinase from *Bacillus Cereus* (Sigma-Aldrich) as described in [26]. To inhibit mechano-activated channels, labeled and immobilized RBCs were incubated with 7 µM GsMTx4 peptide (Abcam) for 15 min and observed upon treatment maintenance. To activate Piezo1 channels, labeled and immobilized RBCs were incubated with 0.5 µM Yoda1 (Biotechne) for 20 sec, washed and directly observed. To activate protein kinase C (PKC), RBCs were pre-incubated with 6 µM phorbol 12-myristate 13-acetate (PMA, Sigma-Aldrich) and 20 nM Calyculin A from Discodermia Calyx (CalA, Sigma-Aldrich) for 15 min at 37°C before labeling (upon maintenance of PMA/CalA treatment). To modulate calcium content, RBCs were pre-incubated in calcium-free homemade medium containing 1 mM calcium-chelating agent ethylene glycol-bis(β-aminoethyl ether)-N,N,N',N'-tetraacetic acid (EGTA, Sigma-Aldrich) for 10 min at RT before labeling (upon maintenance of EGTA). Residual calcium content was assessed as described below. RBCs were then possibly incubated

in 1.8 mM calcium-containing medium for 20 min to achieve calcium repletion. To modulate ATP content, RBCs were pre-incubated in glucose-free homemade medium for 2 h at 37°C before labeling. Residual ATP content was assessed by a luminescent ATP detection assay kit (Abcam). RBCs were then possibly incubated in 25 mM glucose-containing medium for 30 min to achieve glucose repletion. Treatment innocuity has been assessed by measuring the percentage of hemoglobin release (absorbance at 450 nm).

Vital fluorescence/confocal imaging

To immobilize RBCs for imaging, two complementary systems were used: RBCs spread onto poly-L-lysine (PLL, 70–150 kDa; Sigma-Aldrich)-coated coverslips and RBCs in suspension. For spread RBCs, coverslips were first coated with PLL:DMEM (1:1, *v:v*) at 37°C for 40 min, then washed with DMEM at 20°C for 5 min. Labeled RBCs were then dropped onto the coated coverslips at 20°C for exactly 4 min, the suspension was removed and replaced by fresh medium, and attached RBCs were allowed to spread for another 4 min. The coverslip was placed upside down on a Lab-Tek chamber and then observed. For the "in suspension" system, labeled RBCs were dropped to settle down in µ-Slide VI0.4 uncoated IBIDI chambers (IBIDI, Proxylab; 100 µl by channel). All preparations were examined at the labeling temperatures, either with a Zeiss LSM510 confocal/multiphoton microscope using a plan-Apochromat 63X NA 1.4 oil immersion objective or with a Zeiss wide-field fluorescence microscope (Observer.Z1) using a plan-Apochromat 100X/1.4 oil Ph3 objective.

Decoration of endogenous lipids by toxin fragments and fluorescent lipid insertion*

Washed RBCs were labeled with toxin* fragments, BODIPY-lipids (SM, PC, GM1) or TopFluor-TMR-PC. Lysenin* and theta* were produced as previously described [25, 26], dissolved in 1 mg/ml DMEM-BSA (Bovine Serum Albumin, Sigma) and cleared of aggregates before each experiment by centrifugation at 20, 000 *g* for 10 min. RBC labeling with toxins* was performed in suspension (*i.e.* before immobilization) with either 1.25 µM lysenin* or 0.55 µM theta* in DMEM/BSA at the indicated temperatures for 25 min under continuous agitation, then pelleted at 200 *g* for 2 min and resuspended in DMEM. RBC labeling with 0.6 µM BODIPY FL C5-SM, 1 µM BODIPY FL C5-GM1 or 1 µM BODIPY FL C5-HPC (Invitrogen) and 0.8 µM TopFluor-TMR-PC (Avanti polar lipids) was performed after RBC immobilization on coverslips at the indicated temperatures for 15 min. For co-labeling, RBCs were either labeled in suspension with toxin* fragments, immobilized and then labeled with fluorescent lipid analogs, or directly immobilized and co-labeled with fluorescent lipid analogs.

Lipid order

A stock solution of 2-dimethylamino-6-lauroylnaphthalene (Laurdan) was prepared in dimethyl sulfoxide (DMSO) and conserved as described in [30]. Washed RBCs were labeled at RT in suspension in DMEM/BSA containing 2.5 µM Laurdan for 60 min. 1.25 µM lysenin*, 0.55 µM theta* or 0.8 µM TopFluor-TMR-PC were added for the last 20 min. RBCs were then immobilized and examined using (i) confocal mode for lipids and (ii) multiphoton mode with acquisition at 440 nm and 490 nm and a Normaski prism for Laurdan. Lipid order determination was performed as described in [30] and in [31]. Briefly, domains and surrounding membrane ROIs and masks were obtained from the two fluorescent channels (440 nm and 490 nm) of Laurdan images. The determination of Laurdan domains co-localizing or not with the lipid domains and the following separation of the domain masks were done manually by comparing Laurdan and lipid images. A 2D GP map, where GP for each pixel were calculated from a ratio of the two fluorescence channels, was created from those masks using MATLAB (The MathWorks, Natick, MA). Briefly, each image was binned (2 × 2) and thresholded, then the GP image was calculated for each pixel using the GP equation as described in [30], and the G factor was measured as recommended in [30].

Fluorescence correlation spectroscopy

RBCs were immobilized on coverslips and labeled with 1 µM BODIPY-GM1 (as described above) and 25 nM FAST DiI (1, 1'-Dilinoleyl-3, 3,3',3'-Tetramethylindocarbocyanine, 4-Chlorobenzenesulfonate), then examined at RT on confocal microscope Leica TCS SP5 (Wetzlar, Germany) with a 63X 1.2 NA water immersion objective and 1 Airy unit. FAST DiI was excited using a 561 solid state laser and emission was collected between 607 nm and 683 nm using a filter cube. To check for bleed-through artifacts, RBCs were labeled with BODIPY-GM1 alone and in this case no significant signal was detected. The intersection

between confocal volume and RBC membrane was adjusted to the maximum photon count and positioned either on a membrane domain or a segment of the membrane exhibiting homogenous fluorescence. Photon counting was accomplished by avalanche photodiodes (Leica, Wetzlar, Germany) and time correlations were calculated at a sampling frequency of 200 kHz for a time interval of 30 sec. Each measurement point was repeated for three consecutive measurements. The obtained correlation curves were fitted using a 1-component 2D diffusion model: $G(\tau) = \frac{1}{<N>} \frac{1}{\left(1+\frac{\tau}{\tau_0}\right)}$

Here, τ_0 is the average residence time inside the intersection of the confocal volume and <*N*> is the average number of fluorophores in the detection volume. Only correlation traces with a satisfying fit to the model (R^2> 0.98) were considered in the analysis.

RBC (de)stretching on PDMS chambers

Deformation experiments were conducted by spreading BODIPY-SM-, GM1- or Fluo-4 (see below)-prelabeled RBCs on a 4 cm^3 polydimethylsiloxane (PDMS) stretchable chamber (Strex Inc). Briefly, PDMS chambers were coated with PLL:DMEM (1:1, *v:v*) at 37°C for 40 min, washed with DMEM at 20°C for 5 min and fixed to the stretching device (STREX, cell strain instrument, B-Bridge). Labeled RBCs were plated into the PDMS chamber for exactly 5 min, then the suspension was removed and replaced by fresh medium, and attached RBCs were allowed to spread for another 5 min. The PDMS chamber was then immediately observed at RT without stretching (unstretched) with a Zeiss wide-field fluorescence microscope (Observer. Z1) using a plan-Neofluar 63X/0.75 Ph2 objective. Stretching and destretching of the chamber were thereafter respectively performed by (i) quick (1 min) axial stretching of the right side of the PDMS chamber of 12 % of the chamber length (stretching); and (ii) return to the initial state (destretching).

Medium osmolarity modulation

CellASIC ONIX Microfluidic platform (Merck Millipore) has been used to achieve real-time imaging on living RBCs. The following media were disposed each in a well and allowed to flow successively to the central chamber: PLL (15 min, low flow), DMEM (5 min, medium flow), washed RBCs (4 min, high flow), DMEM (10 min, medium flow), toxin* or fluorescent lipid analog (15 min, low flow), DMEM (3 min, medium flow), hypo-osmolar medium (180 mOsm, 10 min, low flow). Images were acquired every 45 sec using a Zeiss LSM510 confocal microscope.

Calcium labeling and measurement

To label intracellular calcium, washed RBCs were incubated in suspension at 37°C with 3 μM Fluo-4 acetoxymethyl ester (Fluo-4 AM, Invitrogen) in 1.8 mM calcium-containing homemade medium for 60 min under continuous agitation, pelleted at 200 *g* for 2 min and resuspended in homemade medium, then let for 30 min at 37°C under agitation to allow the Fluo-4AM de-esterification. Fluo-4-labeled cells were then either immobilized, imaged with a Zeiss wide-field fluorescence microscope and analyzed as explained below; or measured in a 96-well plate with a spectrofluorimeter (SpectraCountTM, Packard BioScience Co.) at Exc/ Em 490/520 nm and analyzed using hemoglobin content for normalization. As the Fluo-4 fluorescence signal is not a linear function of the calcium concentration [32], only qualitative observations could be made.

Image analysis and data quantification

Lipid domain abundance, curvature association and colocalisation were assessed by manual counting on images from confocal or epifluorescence high-resolution microscope. Measurement of RBC projected area (referred as hemi-RBC area) and Fluo-4 quantification on images was performed using ImageJ software on images where the RBC projected contours have been manually drawn on the transmission images.

Statistical analyses

*V*lues are presented as means ± SEM. Statistical significance was tested either with two-sample t-test or one-way ANOVA followed by Tukey's post-hoc test (NS, not significant; * $p < 0.05$; ** $p < 0.01$ and *** $p < 0.001$).

Results

Polar lipid- and chol-enriched domains differ in abundance, curvature association and lipid order

We have previously shown that chol- and SM-enriched domains differ in abundance [25, 26] and preferentially associate with high and low curvature areas of the biconcave RBC membrane [29]. This analysis was limited to chol and SM while not considering PC, another abundant class of outer PM leaflet lipids, or glycosphingolipids, known to play key pathophysiological roles. Here, we questioned whether PC and GM1 could also participate to the formation of domains at the outer PM leaflet and whether they differ in abundance, curvature association and lipid order as compared to chol- and SM-enriched domains. To these aims, as fluorescent probes, we used (i) theta* toxin to decorate endogenous chol [25]; (ii) lysenin* toxin or PM trace insertion of BODIPY-SM to reveal SM [26]; (iii) PM trace insertion of BODIPY-PC [27] or TopFluor-TMR-PC, two PC analogs that evidence lipid domains of comparable size, shape, localization at the center of spread RBCs (Suppl. Fig. 1A - For all supplemental material see www.karger.com/10.1159/000495645/) and abundance (Suppl. Fig. 1B) and that perfectly co-localize (Suppl. Fig. 1C); and (iv) PM trace insertion of BODIPY-GM1, as in [33].

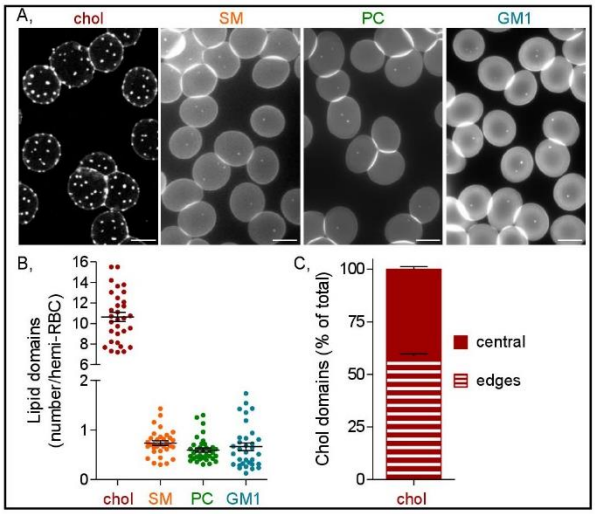

Fig. 1. Unlike polar lipid (SM, PC, GM1)-enriched domains, chol-enriched domains are abundant and equally associate with the center and the edges of spread RBCs. (A) Representative confocal/ fluorescence imaging of PLL-spread RBCs labeled with theta* (chol), BODIPY-SM, -PC or –GM1 and examined at 20°C. Scale bars 5 µm. (B) Quantification of lipid domains per hemi-RBC. Means ± SEM from 31-37 experiments, each dot representing one experiment in which >100 RBCs were counted. (C) Distribution of chol-enriched domains between the edges (stripped) and the center of the membrane (full) on spread RBCs. Means ± SEM of 4 independent experiments where >70 RBCs were analyzed.

As shown in Fig. 1A, insertion of BODIPY-PC or -GM1 also revealed well-defined round lipid domains on spread RBCs. These domains exhibited similar abundance as SM-enriched domains but were quite less abundant than those enriched in chol (green and blue dots, respectively, *vs* orange or red dots, Fig. 1B). Moreover, as SM-enriched domains and ~40 % of chol-enriched domains (pictures in Fig. 1A and quantification in Fig. 1C), those enriched in PC and GM1 seemed restricted to the central area of spread RBC membrane (defined as in [29]).

Since RBC spreading can impair RBC biconcavity, we also explored lipid domain topography using plastic chambers compatible with confocal microscopy (IBIDI chambers) as an alternative imaging system in which RBCs were laid down, resulting in suspended, non-spread RBCs (Fig. 2A). This technique allowed to observe alternating regions of high curvature (HC) at the edges of the RBCs and of low curvature (LC) at the center of the cell [29]. We showed that PC- and GM1-enriched domains were preferentially associated with the LC areas of the RBC, like SM-enriched domains (green, blue and orange arrowheads, Fig. 2A), while chol-enriched domains were preferentially located in HC areas (red arrows, Fig. 2A, [29]).

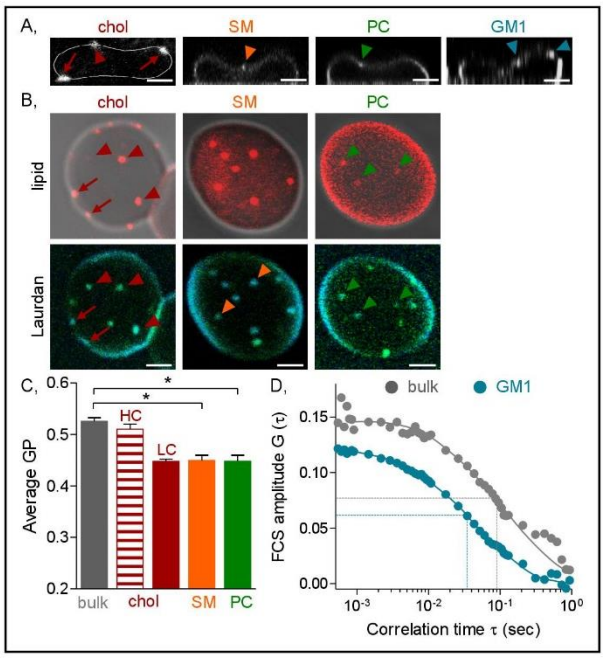

Fig. 2. Unlike polar lipid-enriched domains, chol-enriched domains associate with both low and high curvature areas of suspended RBCs and present differential lipid order. (A) Representative imaging of chol-, SM-, PC- and GM1-enriched domains on RBCs in suspension. RBCs were labeled at 20°C, put in IBIDI chambers and analyzed by confocal imaging. Images shown are reconstruction of Z-stacks and are representative of >2 experiments. (B, C) Membrane lipid order of chol-, SM- and PC-enriched domains determined by Laurdan. (B) RBCs double-labeled at 20°C with theta*, lysenin* or Top-Fluor-TMR-PC (top images) and the fluidity-sensitive probe Laurdan (bottom images) were spread and observed in confocal/ biphoton microscopy. Red arrows point to high-curvature chol/ Laurdan-enriched domains while red, orange and green arrowheads point to low-curvature lipid/Laurdan-enriched domains. (C) Generalized polarization (GP; proportional to membrane lipid order) of membrane without domains (bulk, grey bar) vs chol-enriched domains sorted according to their curvature localization (HC: high-curvature domains, stripped bar; LC: low-curvature domains, full bar) and polar lipid-enriched domains (orange and green bars). Means ± SEM of 2-3 independent experiments where >100 RBCs have been analyzed. Red and orange bars were reproduced from [31] to facilitate comparison with PC-enriched domains (green bar). (D) Diffusion in GM1-enriched domains determined by FCS. Example of a FCS curve of diffusion in GM1-enriched domains (blue dots) or in the surrounding membrane (grey dots) at 20°C. Time required to decrease the correlation amplitude by half in the studied spot is inversely proportional to the lipid diffusivity. Representative graph of 9 RBCs. All scale bars 2 μm.

Next, we examined whether these different lipid domains could exhibit a differential lipid order by using Laurdan (2-dimethylamino-6-lauroylnaphthalene), an artificial fluorescent probe known for its spectroscopic properties influenced by both the composition and dynamics of its local surrounding [34, 35]. Laurdan allowed us to reveal both the surrounding membrane and submicrometric domains. Hence, each class of lipid domains was recognized by co-labeling between a specific red fluorescent probe and Laurdan. We observed that the vast majority of chol-, SM- and PC-enriched domains in LC areas was marked by Laurdan (red, orange and green arrowheads, Fig. 2B) while only a part of chol-enriched domains in HC was labeled (red arrows, Fig. 2B), in agreement with our previous study [31]. Thanks to the Laurdan fluorescence emission at two wavelengths, we next calculated the Generalized Polarization (GP, see material and methods; proportional to the membrane lipid order) of the chol-, SM- and PC-enriched domains. As previously observed, chol-enriched domains located in HC exhibited a higher lipid order than those present in LC areas (compare stripped to full red columns, Fig. 2C) [31]. On the other hand, all the polar lipid-enriched domains in LC, including those enriched in PC, exhibited a lower lipid order than the surrounding membrane (compare colored columns to the grey column, Fig. 2C). These results indicate that, while lipid domains presented a differential lipid order based on their curvature area association,

those associated with LC cannot be discriminated by this criteria. As the only commercially-available, vital imaging-compatible, monomeric probe for GM1 has an emission wavelength similar to Laurdan, it was impossible to study GM1-enriched domain lipid order by this method. We therefore used Fluorescence Correlation Spectroscopy (FCS) to circumvent this difficulty and explored the diffusion properties of the dye FAST DiI in GM1-enriched domains or in the surrounding membrane (blue dots *vs* grey dots, Fig. 2D). Over 11 analyzed RBCs, 9 had a mean ratio between the diffusion time of GM1-enriched domains and the surrounding membrane of 0.53±0.12, indicating that the dye diffused twice faster in GM1-enriched domains than in the surrounding membrane. The other 2 RBCs had a mean ratio of 2.49±1.09 and exhibited thus domains in which the dye diffused more than twice slower than in the rest of the membrane. This opposite behavior might be explained by the co-existence of two distinct GM1-enriched domain populations or by the presence of lipid domains starting to vesiculate. Even if FCS does not measure the exact same membrane properties as Laurdan, these results seemed in agreement with the hypothesis that most submicrometric polar lipid domains exhibit a lower lipid order than the surrounding membrane. Such observation is in opposition with the general idea that lipid domains are more ordered than the membrane bulk. This could result from the high chol content and the strong membrane:cytoskeleton anchorage found in RBCs.

Altogether, these data suggest that at least two distinct lipid domain populations coexist at the outer PM leaflet of RBCs: those located in HC areas, exhibiting a similar lipid order than the surrounding membrane and mainly enriched in chol, *vs* those located in LC areas with a lower lipid order and enriched in polar lipids and/or chol.

Polar lipid-enriched domains depend on chol for their formation and maintenance

To next explore whether LC domains were co-enriched in polar lipids and chol, we performed double labeling with BODIPY-polar lipids and theta* on spread RBCs (Fig. 3). ~25 % of chol-enriched domains colocalized with polar lipids (yellow arrowheads in Fig. 3A and yellow portions of red columns, Fig. 3B). Considering that RBCs without any polar lipid-enriched domain were excluded from this quantification, this proportion and the lipid domain distribution in LC *vs* HC were in agreement with the simple labeling presented in Fig. 1, excluding artefactual redistribution upon double labeling. In addition, most polar lipid domains were also enriched in chol: ~65 % for SM- and ~85 % for PC- and GM1-enriched domains (yellow portions of

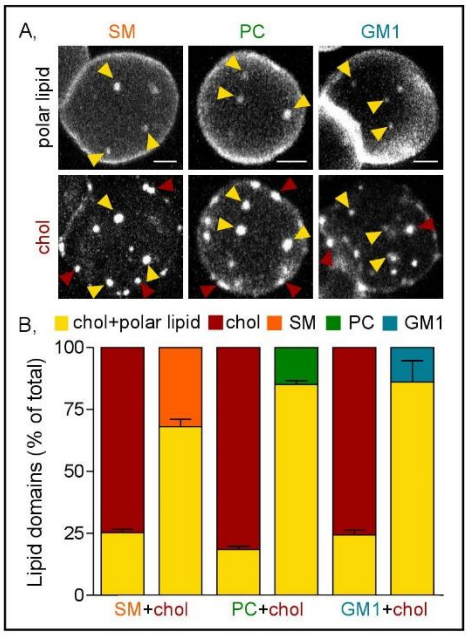

Fig. 3. The majority of lipid domains in low curvature areas are co-enriched in chol and polar lipids. (A) Representative images of PLL-spread RBCs double-labeled at 20°C for polar lipids (top images) and chol (bottom images). Yellow arrowheads point to lipid domains co-enriched in chol and polar lipid, while red arrowheads show domains mainly enriched in chol. Scale bars 2 µm. (B) Quantification. Percentages of chol-enriched domains that colocalize with polar lipid-enriched domains are shown as yellow portions of the red columns. Percentages of polar lipid-enriched domains that colocalize with chol-enriched domains are shown as yellow portions of orange, green or blue columns. Means ± SEM of 2 independent experiments where 24-38 RBCs were analyzed.

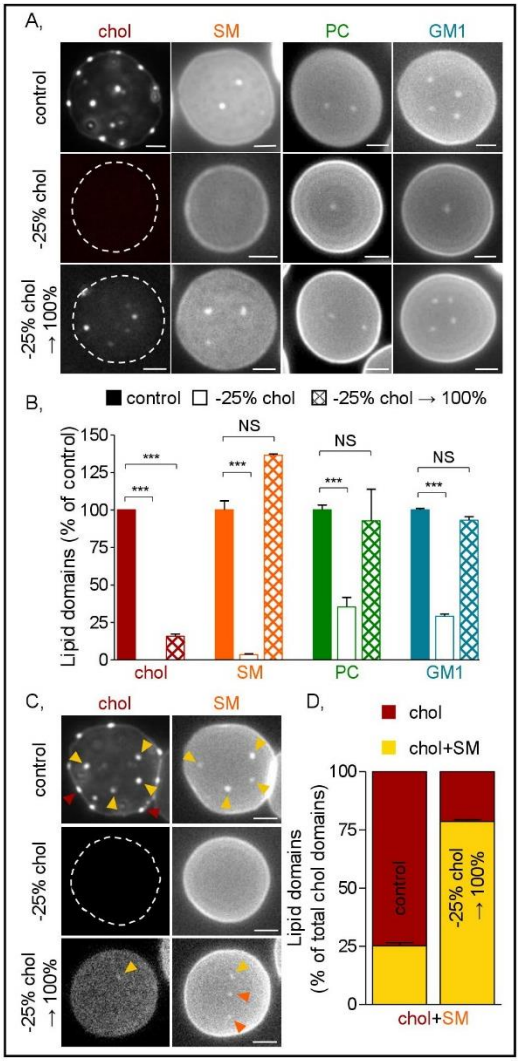

Fig. 4. All lipid domains vanish upon chol depletion and only those in low curvature areas can be restored after chol repletion. RBCs were either kept untreated (control) or chol-depleted by mβCD (0.9 mM; -25 % chol), followed or not by chol repletion (-25 % chol → 100 %) with encapsulated chol. RBCs were then either mono-labeled for chol, SM, PC or GM1 as in Fig. 1. (A, B) or double-labeled for chol and SM (C, D), spread on PLL and observed in fluorescence microscopy, all at 20°C. (A) Representative single-labeling images of different RBCs from 3 independent experiments. (B) Quantification of lipid domains in control (full bars), chol depletion (empty bars) and repletion (squared bars) conditions, expressed as percentage of the control values. Means ± SEM of 3 independent experiments where >300 RBCs were analyzed. (C) Representative double-labeling images of 2 independent experiments. Yellow arrows point to lipid domains co-enriched in chol and SM, while red and orange arrows show domains mainly enriched in chol or SM, respectively. (D) Quantification of chol- and SM-co-enriched domains (yellow portions of the bars), expressed as a percentage of the total chol-enriched domains. Means ± SEM of 2 independent experiments where >200 RBCs were analyzed. All scale bars 2 µm.

orange, green or blue columns, respectively, Fig. 3B). These results suggest that while chol-enriched domains in HC were not co-enriched in polar lipids, the majority of those located in LC was enriched in polar lipids.

To further evaluate the importance of chol for the formation and/or the maintenance of LC-associated lipid domains, we partially depleted membrane chol with methyl-β-cyclodextrin (mβCD), a cage-compound whose use on RBC membrane has been previously validated (-25 % of total membrane chol after a 0.9 mM treatment; open columns, Fig. 4B) [25]. As expected, chol-enriched domains completely disappeared under this treatment and theta* labeling was no more visible (red, Fig. 4A and B). Polar lipid domains were also affected, but to a differential extent: SM-enriched domains were almost completely abrogated while PC- and GM1-enriched domains decreased by ~65 % (orange, green and blue open columns, respectively, Fig. 4B). Hence, upon restoration of the chol content thanks to mβCD cages saturated with chol (squared columns, Fig. 4B), all polar lipid domains could be recovered.

Chol content is thus not only essential for maintenance, but also for the formation of LC-associated domains. In contrast, only a small percentage of chol-enriched domains (~15 %, red squared column, Fig. 4B) could reform upon chol repletion. As those domains were mainly located at the center of spread RBC membrane (*i.e.* in LC areas) and highly colocalized with SM-enriched domains (>75 % *vs* ~25 % in control conditions, yellow arrowheads in Fig. 4C and yellow portions of the columns in Fig. 4D), we suggest that chol-enriched domains associated with HC areas are biophysically less stable and thus require longer time or specific conditions to reform after this treatment.

We thus conclude that lipid domains associated with both HC and LC areas of the RBC outer leaflet are enriched in chol and depend on this lipid content.

GM1/PC-enriched domains are prevalent in resting RBCs at physiological temperature

To further investigate whether lipid domains associated with LC were co-enriched or not in all polar lipids, *i.e.* SM, PC and GM1, we analyzed polar lipid domain behavior upon temperature increase between 20 and 37°C. Indeed, temperature modulates membrane fluidity and thus phase separation and lipid domain organization [36]. Two opposite behaviors could be evidenced: (i) SM-enriched domains whose number decreased by ~30 % when temperature raised from 20°C to 37°C (orange circles, Fig. 5A) in agreement with [25], *vs* (ii) PC- and GM1-enriched domains whose number doubled in the same range of temperatures (green and blue circles, Fig. 5A). By performing double labeling of polar lipids at 20°C and 37°C (Fig. 5B), we evidenced a nearly perfect colocalisation between PC- and GM1-enriched domains whatever the temperature (columns 1 and 2, Fig. 5B), while the percentages of PC- or GM1-enriched domains also enriched in SM decreased between 20°C and 37°C (columns 3 and 5 *vs* 4 and 6, Fig. 5B). Those results suggest that domains co-enriched in PC and GM1 are dominant at physiological temperature while a drop in temperature induces their co-enrichment in SM. This observation also suggests that SM-, PC- and GM1-enriched domains can be either associated or dissociated based on RBC physiological needs.

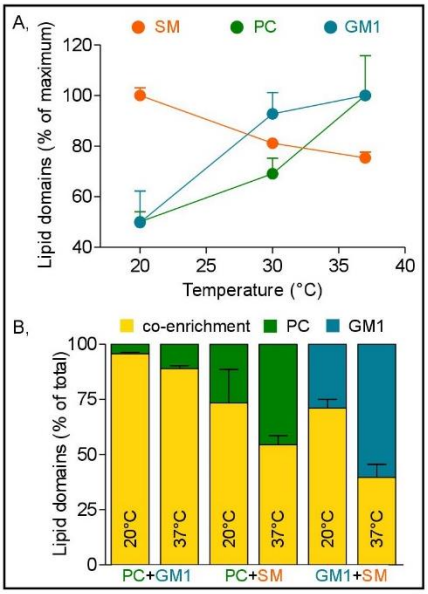

Fig. 5. In contrast to SM-enriched domains, PC- and GM1-enriched domains prevail in resting RBCs at physiological temperature. (A) Abundance of polar lipid-enriched domains at various temperatures, expressed as percentage of maximal abundance. RBCs were mono-labeled, spread and observed at the indicated temperatures. Means ± SEM of 2 independent experiments where >400 RBCs were analyzed. (B) Extent of polar lipid co-enrichment at 20°C and 37°C. Percentage of domains co-enriched in PC and GM1, PC and SM or GM1 and SM are shown as yellow portions of total PC (green)- or GM1 (blue)-enriched domains. Means ± SEM of 2 independent experiments where >200 RBCs were analyzed.

Supplementary Material

Spatial Relationship and Functional Relevance of Three Lipid Domain Populations at the Erythrocyte Surface

Louise Conrard[a] Amaury Stommen[a] Anne-Sophie Cloos[a] Jan Steinkühler[b] Rumiana Dimova[b] Hélène Pollet[a] Donatienne Tyteca[a]

[a]CELL Unit, de Duve Institute & Université catholique de Louvain, Brussels, Belgium, [b]Theory and Bio-Systems, Max Planck Institute of Colloids and Interfaces, Science Park Golm, Potsdam, Germany

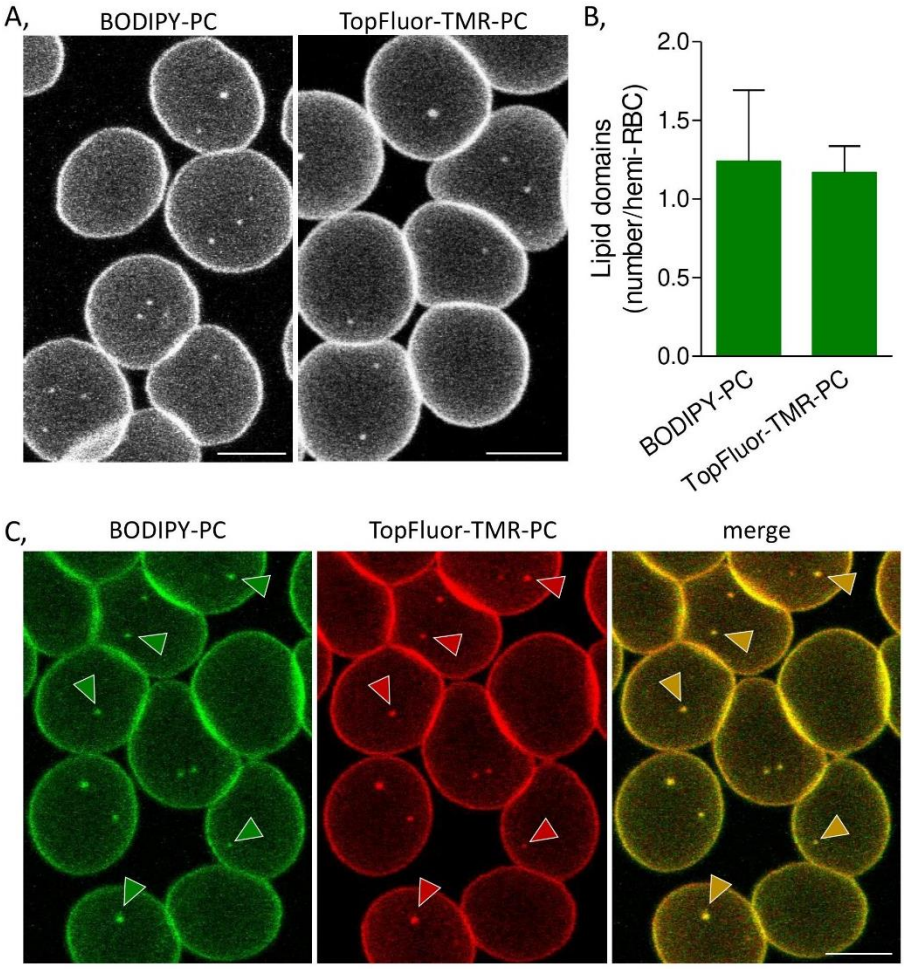

Suppl. Fig 1 Plasma membrane insertion of BODIPY-PC or TopFluor-TMR-PC at trace level reveals domains that are comparable and that perfectly co-localize. RBCs were spread and labeled with either BODIPY-PC or TopFluor-TMR-PC (A,B) or both probes (C) at 37°C. (A) Representative images of simple labeling. (B) Quantification of lipid domains per hemi-RBC. *Means ± SEM from 2-3 experiments where >480 RBCs were counted.* (C) Representative images of double-labeled RBCs. *All scale bars 5 µm.*

Results

2. RBCs at resting state – AFM-based study

2.1. PUBLICATION 2

Nanoscale Horizons

COMMUNICATION

View Article Online
View Journal | View Issue

Check for updates

Cite this: *Nanoscale Horiz.*, 2018, 3, 293

Received 15th November 2017,
Accepted 9th March 2018

DOI: 10.1039/c7nh00187h

rsc.li/nanoscale-horizons

Nanoscale membrane architecture of healthy and pathological red blood cells†

Andra C. Dumitru,‡[a] Mégane A. Poncin,‡[a] Louise Conrard,[b] Yves F. Dufrêne,[ac] Donatienne Tyteca[b] and David Alsteens *[a]

Conceptual insights

Red blood cells (RBCs) feature remarkable mechanical properties while navigating through microcirculation vessels and during spleen filtration. We investigated the architecture of RBC from at different scale, from the cellular level to the nanoscale and determined the biological properties by linking the nanoscale architecture with nanomechanical properties. Here, we report the use of force-distance curve-based atomic force microscopy to study the three-dimensional architecture and nanomechanical response of the red blood cells in physiological and pathological conditions. The study was carried out in parallel on RBCs from healthy volunteers and from patients with hereditary spherocytosis. Mechanical analysis of both patient types confirms previous studies showing that RBCs from patients with hereditary spherocytosis are stiffer. However our results demonstrate a novel correlation between the lipid composition and cell surface nanomechanics. We suggest that these domains contribute to the membrane homeostasis and to their mechanobiological function is directly involved in local cellular deformations. Our nanoscale observations provide direct links with RBC pathologies (spherocytosis, elliptocytosis,...) and open a new avenue towards a better understanding of these RBC diseases. In nanomedicine, this research demonstrates the power of AFM to decipher new pathological mechanisms, thus opening new avenues for therapies.

Cite this: *Nanoscale Horiz.*, 2018, 3, 293

Received 15th November 2017,
Accepted 9th March 2018

DOI: 10.1039/c7nh00187h

rsc.li/nanoscale-horizons

Nanoscale membrane architecture of healthy and pathological red blood cells†

Andra C. Dumitru,‡[a] Mégane A. Poncin,‡[a] Louise Conrard,[b] Yves F. Dufrêne,[ac] Donatienne Tyteca[b] and David Alsteens ★[a]

Red blood cells feature remarkable mechanical properties while navigating through microcirculation vessels and during spleen filtration. An unusual combination of plasma membrane and cytoskeleton physical properties allows red blood cells to undergo extensive deformation. Here we used atomic force microscopy multiparametric imaging to probe how cellular organization influences nanoscale and global mechanical properties of cells in both physiological and pathological conditions. Our data obtained in native conditions confirmed that, compared to healthy cells, cells from patients with hereditary spherocytosis are stiffer. Through vertical segmentation of the cell elasticity, we found that healthy and pathological cells display nanoscale architecture with an increasing stiffness along the direction of the applied force. By decoupling the mechanical response of the plasma membrane from its underlying cytoskeleton, we find that both components show altered properties in pathological conditions. Nanoscale multiparametric imaging also revealed lipid domains that exhibit differential mechanical properties than the bulk membrane in both healthy and pathological conditions. Thanks to correlated AFM-fluorescence imaging, we identified submicrometric sphingomyelin-enriched lipid domains of variable stiffness at the red blood cell surface. Our experiments provide novel insights into the interplay between nanoscale organization of red blood cell plasma membrane and their nanomechanical properties. Overall, this work contributes to a better understanding of the complex relationship between cellular nanoscale organization, cellular nanomechanics and how this 3D organization is altered in pathological conditions.

Conceptual insights

Red blood cells (RBCs) feature remarkable mechanical properties while navigating through microcirculation vessels and during spleen filtration. We investigated the architecture of RBCs at different scale, from the cellular level to the nanoscale and determined the biological properties by linking the nanoscale architecture with nanomechanical properties. Here, we report the use of force–distance curve-based atomic force microscopy (AFM) to study the three-dimensional architecture and nanomechanical response of the red blood cells in physiological and pathological conditions. The study was carried out in parallel on RBCs from healthy volunteers and from patients with hereditary spherocytosis. Mechanical analysis of both patient types confirms previous studies showing that RBCs from patients with hereditary spherocytosis are stiffer. Hence our results demonstrate a novel correlation between the lipid composition, organization in lipid domains and cell surface nanomechanics. We suggest that these domains contribute to the membrane homeostasis and that their mechanobiological function is directly involved in local cellular deformations. Our nanoscale observations provide direct links with RBC pathologies (spherocytosis, elliptocytosis,...) and contribute to a better understanding of these RBC diseases. In nanomedicine, this research demonstrates the power of AFM to decipher new pathological mechanisms, thus opening new avenues for therapies.

The unique structural organization of the human red blood cell (RBC) enables it to undergo large reversible deformations while maintaining constant volume and membrane surface area.[1–3] Lacking the actin–myosin–microtubule cytoskeleton that is responsible for shape changes in nucleated cells, RBCs maintain their structural integrity and can display dynamic local deformations thanks to a dynamic network of spectrin filaments tethered to the cytosolic side of the plasma membrane (PM) *via* multiprotein complexes centered on ankyrin and 4.1R protein.[4] The surface tension of the lipid bilayer and the constant remodeling of the flexible spectrin network are two key elements governing the elastic response of the RBC membrane skeleton. Currently, there is increasing evidence that submicrometric lipid domains exist at the RBC surface and could contribute to PM tension regulation, being involved in local deformations, such as local budding and vesicle formation.[5,6] Submicrometric domains may also serve as recruitment or exclusion platforms for membrane proteins, participating in the regulation of dynamic cellular processes such as signal transduction. For example, we have

[a] *Université catholique de Louvain, Institute of Life Sciences, Croix du Sud 4-5, bte L7.07.06, B-1348 Louvain-la-Neuve, Belgium. E-mail: david.alsteens@uclouvain.be*
[b] *Université catholique de Louvain, de Duve Institute, Avenue Hippocrate 75/B1.75.05, B-1200 Woluwe-Saint-Lambert, Belgium*
[c] *Walloon Excellence in Life sciences and Biotechnology (WELBIO), Belgium*

† Electronic supplementary information (ESI) available. See DOI: 10.1039/c7nh00187h

‡ A. C. D. and M. A. P. equally contributed to this work.

recently shown that sphingomyelin (SM)-enriched submicrometric domains increase in abundance along with secondary calcium (Ca^{2+}) efflux, a process involved in shape and volume restoration after deformation.[6] However, whether such submicrometric domains coexist with nanoscale structural or physical heterogeneities at the RBC surface and whether they contribute with the cytoskeleton to RBC deformation remain to be determined.

Disorders due to mutations in various membrane or skeletal proteins, such as in hereditary spherocytosis (HS), induce loss of membrane surface and reduced RBC deformability, in turn altering cell function and leading to splenic trapping and ultimately anemia. Dysregulation of lipid loss and the presence of altered membrane proteins have been alluded as key components altering RBC plasticity and biconcavity in pioneering biochemical studies of HS PMs several decades ago.[7–9] Though the aforementioned studies shed light on the link between cellular composition and pathology, direct evidence for a correlation between specific lipid distribution in submicrometric domains or PM-cytoskeleton anchorage and their role in PM deformability at the nanoscale is missing. While these domains have been suggested to contribute to the membrane homeostasis,[6] we believe that PM lateral organization also contributes to the cell mechano-function, being directly involved in local cellular deformations.

Numerous techniques have been used to study the changes accompanying RBCs during mechanical deformation, including micropipette aspiration, optical tweezers, atomic force microscopy (AFM), electric field deformation, membrane flickering analysis and vital confocal imaging.[2,6,10–12] Among these, AFM stands out as an ideal tool, which can integrate high-resolution, vital imaging and quantitative mechanical characterization of living cells. In the past, AFM has been applied to the investigation of whole RBCs or ghost cells in order to establish a link between RBCs in healthy or pathological conditions, focusing on their nanomechanical properties, morphology or roughness.[12–18] However, RBCs underwent different treatments in most of those AFM studies, including chemical crosslinking of lipids and proteins or air-drying, which alter their mechanical and morphological properties and makes it difficult to relate these observations with the behavior of cells in physiological conditions.[19–21] We use force distance (FD) curve-based AFM, which has been developed over the past 20 years and can now be applied to simultaneously image the topography of complex biological systems while mapping quantitative sample properties, such as physical, chemical and biological interactions.[22] This mode consists in recording the force while approaching and retracting the AFM tip from the surface (Fig. 1A). Recent advances pushed the limits of both spatial and temporal resolution, leading to so-called multiparametric imaging, thus opening the way to explore highly dynamic cellular processes occurring at the molecular scale.[23–25] In living cells, FD curve-based AFM was used to obtain topography and mechanical properties maps of cytoskeletal structures at unprecedented resolution in physiological conditions.[26–29] The operating principle of FD-based AFM is based on a cantilever being oscillated well below its resonance frequency, while using the tip–sample interaction force (peak force) as feedback (Fig. 1A–C). The tip is continuously approached and retracted from the sample and from each FD cycle the sample height is determined and tip–sample interactions are analyzed. Quantitative parameters, such as Young's modulus, stiffness, energy dissipation and adhesion, can then be extracted, mapped pixel-by-pixel and directly correlated to the sample topography.

Here, we report the use of FD-based AFM to study the nanoscale architecture and nanomechanical response of RBCs in physiological and pathological conditions. The study was carried out in parallel on RBCs from healthy volunteers (hRBCs) and from patients with HS (sRBCs). Vertical segmentation of the cell mechanics and use of cytoskeleton-disrupting drugs allowed us to estimate the relative contributions of PM and cytoskeleton in controlling cellular nanomechanics. Combined AFM and fluorescence microscopy imaging measurements enabled us to identify SM-enriched domains on the surface of RBC PM while extracting their heterogeneous nanomechanical properties. The current study sheds new light into the relation between membrane nanoscale organization, nanomechanical properties and RBC biological functions. Moreover, the present results unravel several key features of submicrometric lipid domains, *i.e.* their real existence, exact size, mechanical properties as well as interplay with the cytoskeleton in the control of RBC deformation. Indeed, we here reveal on RBCs in native conditions that submicrometric domains with differential nanomechanical properties as compared to the bulk membrane coexist with smaller domains and that both the cytoskeleton and the local membrane composition influence the local mechanical properties of the RBC.

Results and discussion

Probing the structure and mechanics of RBCs by AFM

RBCs are typically found in a biconcave shape when in suspension, but they partially lose their biconcavity during the first minutes of interaction with the poly-L-lysine (PLL)-coated substrate, probably due to the strong interaction forces between the PM and the positively charged surface.[6,12] Immobilization on PLL enables to avoid the most worrisome echinocyte conversion that could be generated by the repulsion between negative charges from the glycocalyx at the RBC surface and the silicates from the glass. We first evaluated the morphology, roughness and nanomechanical properties of healthy (hRBCs) and spherocytotic (sRBCs) RBCs. After immobilization on PLL-coated surfaces, RBCs in both physiological and pathological conditions feature a rounded shape (Fig. 1D and E). Due to the large curvature of the cells, fine structures are difficult to observe in raw height images. However, roughness analysis revealed a relatively smooth surface for both cell types, the root mean square (rms) roughness on height images being 3.34 ± 1.3 nm and 5.63 ± 2.6 nm for hRBCS and sRBCs respectively (from 20 cells for each condition, measured on 500×500 nm areas after a 2nd order polynomial fitting of the height image).

Results

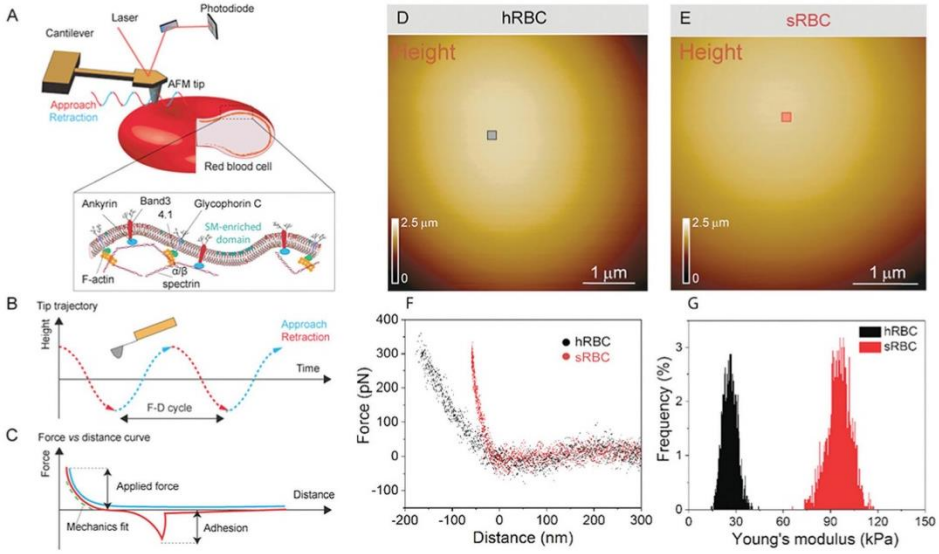

Fig. 1 Principle of using FD-based AFM to image and map mechanical properties of live RBCs. (A) The AFM cantilever bearing a long tip is oscillated well below its resonance frequency in a sinusoidal manner, while the RBC surface is contoured pixel-by-pixel. A schematic of the structural organization of a RBC shows the PM consisting of lipids and proteins, connected to the underlying actin–spectrin cytoskeleton through the peripheral membrane proteins ankyrin and 4.1R. The extracellular side of the PM is coated by a fuzzy-like glycocalyx. (B) A FD cycle is recorded for each approach and retraction of the oscillating cantilever. (C) FD curves recorded in each pixel of the image can be used to quantify mechanical properties of the sample, adhesion or deformation. (D and E) FD-based AFM height images of healthy and spherocytotic cells immobilized on a poly-L-lysine coated glass surface. (F) Superimposition of ~15 FD curves extracted from the maps shown in colored areas in (D) and (E). Black FD curves are extracted from hRBC and red curves from sRBC. The slope of the curves corresponding to sRBC is steeper than for hRBC. (G) Histograms showing the mechanical properties of hRBCs and sRBCs as measured by FD-based AFM. A 3-fold increase in Young's modulus is observed on sRBCs as compared to hRBCs. The data were acquired at an oscillation frequency of 0.25 kHz and are representative of 3 healthy donors and 3 patients with HS. A total of 27 cells for each condition were analyzed during 6 independent experiments.

The height of the cells varied between 1–3.5 µm, sRBCs being higher (2.5 ± 0.9 µm) than hRBCs (1.7 ± 0.5 µm, from 20 cells for each condition).

Recording single FD curves on the surface of the cells allowed us to evaluate the mechanical properties (Young's modulus) of RBCs from healthy donors and HS patients (Fig. S1A–C, ESI†). A 2 × 2 µm area in the central region of the cell, where the height reaches maximum values (>2–3 µm), was selected and the indentation range used for the analysis was chosen in such manner (<10% of the height) to avoid any substrate effect.[30] As can be directly observed from individual FD curves, hRBCs typically present a shallower slope than the one observed for sRBCs (Fig. S1C, ESI†). Young's moduli were extracted using a Hertz fit (Fig. S1C, ESI†) and the values for hRBCs and sRBCs are presented in Fig. S1D (ESI†). hRBCs have a mean Young's modulus value of 1.45 ± 0.66 kPa (N = 980 curves, from 10 different cells), while spherocytotic RBCs are stiffer at 2.04 ± 0.76 kPa (N = 561 curves, from 9 different cells), as can be directly observed from the FD curves. The increased stiffness of sRBCs lowers their ability to spread on the sample substrate and explains the differences in height observed.

We suggest that the structural and mechanical properties of sRBCs and hRBCs are of biological relevance. Mechanically stressed erythrocytes have been previously described as displaying surfaces with increased roughness,[31] while ageing was linked to decreased roughness values.[32] The correlation we observed between membrane roughness and stiffness for sRBCs as compared with hRBCs is in good agreement with these previous reports. These observations support previous observations in the literature that less deformable sRBCs are subjected to increased mechanical stresses during their passage through narrow capillaries in the microcirculation, which in turn decreases their life span.

Vertical segmentation of the RBC mechanical properties

To gain further insight into the complex mechanical architecture of living RBCs, we used multiparametric FD-based AFM imaging to simultaneously investigate at high-resolution the topography of individual RBCs and locally map their Young's modulus. hRBCs and sRBCs from patients were imaged in similar conditions, by acquiring simultaneous topography and Young's

modulus maps. We observed that FD curves recorded on sRBCs have a steeper slope as compared to the ones recorded on hRBCs (Fig. 1F), similarly to single FD curves (Fig. S1C, ESI†). We selected 2 × 2 μm areas in the central region of the hRBC and sRBC cells in Fig. 1D, E and calculated the corresponding Young's modulus values (~2500 points). Histograms showing a comparison of the mechanical properties of hRBCs and sRBCs as measured by FD-based AFM are shown in Fig. 1G. A 3-fold increase in Young's modulus is observed on sRBCs (91 ± 15 kPa) as compared to hRBCs (29 ± 9 kPa). In comparison with the indentation experiments performed in single FD curves mode (Fig. S1C and D, ESI†), the indentation velocities in FD-based AFM are about two orders of magnitude higher (~300 μm s^{-1} *vs.* 1 μm s^{-1} range). Given the fact that RBCs are viscoelastic bodies,[33,34] their mechanical response will depend on the frequency at which they are probed.[26,35–37] Our results are in good agreement with Young's moduli observed on other living mammalian cells, including different types of cancer cells, fibroblasts or cardiomyocytes.[26,38–40]

The architecture of the erythrocyte membrane includes lipids and proteins as well as an underlying actin–spectrin network.[4] To better understand how individual components contribute to cell mechanics, we fitted the different regions of the retract FD curve in the contact area using the Hertz model (see Methods and Fig. S2, ESI†). We selected three fitting ranges within our applied overall load (300 pN) (Fig. 2A), as follows: low load (5–20%), which could mainly comprise the contribution of the lipid PM; medium load (20–60%), which could correspond to a contribution of both the PM and the underlying actin–spectrin cytoskeleton and high load (30–90%), which could be attributed mostly to the cytoskeleton (as well as previous components). Topography images (Fig. 2B and C) were recorded simultaneously with the corresponding elasticity maps (Fig. 2D, F, H and Fig. 2E, G, I). Remarkably, we observed that Young's modulus progressively increased with the applied load for both hRBCs and sRBCs suggesting that the actin–spectrin cytoskeleton plays the major role in mechanical properties of erythrocytes.

At first sight, the spherocytotic cell shows a brighter contrast throughout the three indentation ranges meaning that sRBCs are less deformable than the hRBCs. We next quantified the mechanical properties of both physiological and pathological conditions at low, medium and high load (Fig. 2J). The in-depth characterization of the hRBCs membrane's mechanical behavior revealed that Young's modulus increases from 24 ± 23.9 kPa at low load to 32 ± 29.9 kPa at medium load and finally reaching 40 ± 34.9 kPa at high load. Contrastingly, sRBCs show a rapid increase of the Young's modulus with the applied load, *i.e.* from 87 ± 83.4 kPa at low load to 298 ± 362.7 kPa at medium load and 380 ± 482.9 kPa at high load. A vertical segmentation of the mechanical properties has been previously observed on nucleated cells with a 3D cytoskeleton.[41–43] However, RBCs have a less complex structure, lacking internal organelles, a nucleus and the actin–myosin–microtubule cytoskeleton found in nucleated cells. Their cytoskeleton is a 2D network with quasi-hexagonal symmetry. The main components are ~200 nm long flexible strands of $(\alpha_1\beta_1)_2$ spectrin tetramers interconnected to short actin filaments at junctional complexes centered on the protein 4.1R (horizontal linkages).[44] Hence, spectrin filaments are connected to the PM through 4.1R and ankyrin complexes (vertical linkages).[4] Hereditary spherocytosis is generally attributed to defects in proteins of the ankyrin complex, such as ankyrin, band-3 or β-spectrin, resulting in RBC morphology and deformability changes. In this study, we examined RBCs from three splenectomized patients with mutations in the gene coding for β-spectrin. Erythrocytes from these patients show a slightly reduced spectrin density compared to healthy donors. This could affect the distribution of anchorage points between the membrane and the underlying cytoskeleton, resulting in the impairment of its dynamic remodeling and contributing to a stiffer cytoskeleton. Although this remains to be determined, this hypothesis is actually in good agreement with theoretical studies showing that the loss of the spectrin:membrane anchorage stiffens the cytoskeleton[45,46] and with our observations of an almost 10-fold difference between Young's modulus of hRBCs and sRBCs at high loads. A recent study of the elastic properties of RBCs during morphological changes has shown that spectrin can be found in two independent conformations: a soft and easily deformable one in hRBCs, while a transition towards a stiff conformation and a bimodal distribution of spectrin conformations is observed in sRBCs.[47] Our AFM measurements suggest, for the first time directly in physiological conditions and on intact RBCs, the importance of the cytoskeleton in controlling the RBC mechanical properties. Surprisingly, our approach revealed that at low indentation load the difference between hRBCs and sRBCs is also present, indicating that besides the cytoskeleton, PM lipid content and its nanoscale organization should also influence the nanomechanics of erythrocytes.

Role of cytoskeleton in RBC mechanics

To further assess the influence of the cytoskeleton on the global cell mechanics, we used latrunculin A (LatA) and blebbistatin as inhibitors of actin polymerization and myosin respectively (Fig. 3). Although non-muscle myosin has been identified in mature erythrocytes, its importance in cytoskeleton remodeling was underestimated due to its low cellular abundance (actin : myosin ratio of 80 : 1).[48] While cells treated with either LatA (500 nM during 30 minutes) (Fig. 3C, D, I and J) or blebbistatin (50 μM during 30 minutes) (Fig. 3E, F, K and L) maintain their spherical shape, their height was slightly reduced in comparison with control cells, probably due to the collapse of their cytoskeleton (Fig. 3A, C and E). The effect of LatA and blebbistatin on the mechanical properties of hRBCs and sRBCs is shown in Fig. 3B, D, F and Fig. 3H, J, L respectively. The apparent Young's modulus was displayed as maps and extracted from the high load fits, since we previously observed a dominant effect of the cytoskeleton at this load. Both the depolymerization of actin filaments with LatA and the inhibition of myosin with blebbistatin led to a significant decrease of the Young's modulus for both hRBCs and sRBCs, as compared with the untreated cells. The Young's modulus drop is more pronounced in the case of sRBCs, with a ten-fold factor decrease. Nevertheless, Young's modulus of sRBCs remains

Results

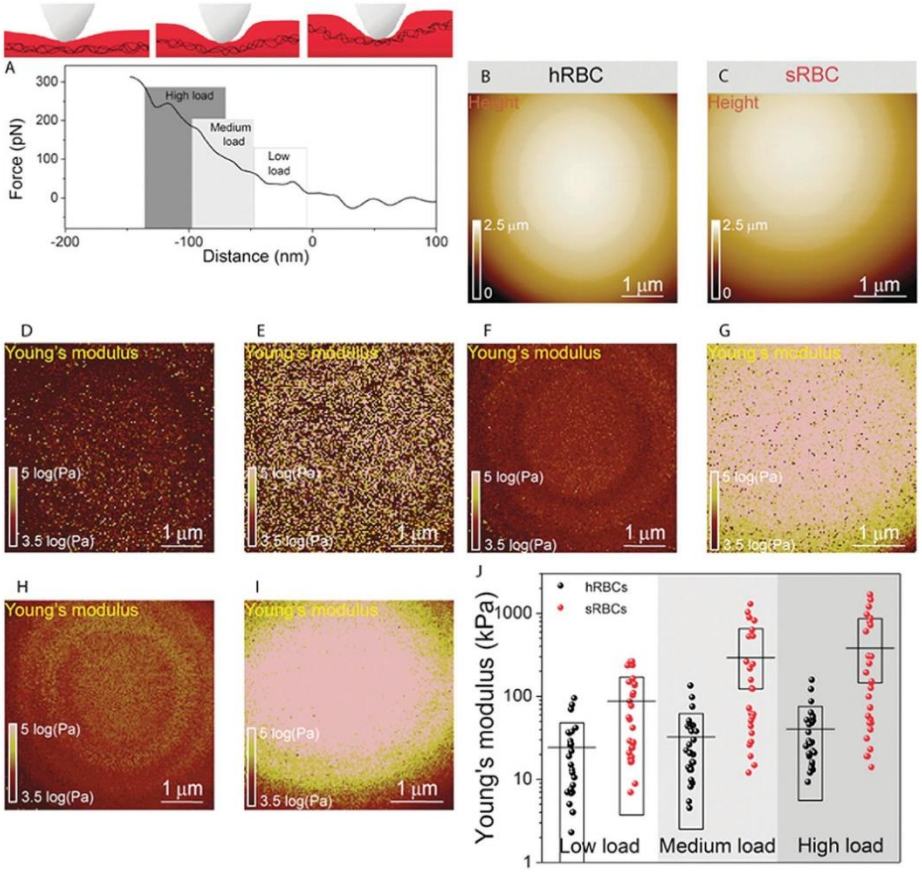

Fig. 2 Vertical segmentation of RBC mechanical properties. (A) Young's modulus is determined from the contact region of the FD curve using the Hertz model. Zoom on the contact area of a typical curve is shown. Three different fit ranges are defined to extract mechanical properties at different loads. Low load corresponds to a fit in the very first part of the curve, between 5–20% of the maximum applied force, medium load was considered between 20–60% and high load in the 30–90% range. At low load, the PM bends and as the tip indents deeper into the cell (medium and high loads) the contribution of the cytoskeleton becomes dominant. (B) FD-based AFM height image of a hRBC along with Young's modulus maps extracted at: (D) low load, (F) medium load and (H) high load. (C, E, G and I) Similar FD-based AFM images and corresponding Young's modulus maps recorded on sRBCs. (J) Graph showing the Young's modulus extracted for individual hRBCs (black spheres) and sRBCs (red spheres) at the different loads. sRBCs are stiffer than hRBCs for all indentation ranges and their Young's moduli show a sharper increase as compared to hRBCs. Horizontal lines represent mean values for each data set and boxes represent standard deviation. The data are representative of 3 healthy donors and 3 patients with HS. A total of 27 cells were analyzed during 6 independent experiments.

higher by a three-fold factor that the one of hRBCs for the three loads used (Fig. 3M, N and Table S1, ESI†), suggesting that mechanical differences could also originate from differences in the vertical cytoskeleton anchorage to integral membrane proteins or from non-cytoskeletal structures such as the glycocalix. Besides the decrease in Young's modulus, we also observed less heterogeneity in the mechanical properties dataset of LatA- and blebbistatin-treated RBCs, as compared to control cells. We hypothesize that these differences could originate from a heterogeneously aging population of RBCs. It has been already established that during their 120 days lifespan, RBCs release microvesicles, which alters their high surface area to volume ratio, thus increasing the cytoskeleton density and reducing deformability.[49] This is intrinsic to both hRBCs and sRBCs populations and it leads to a

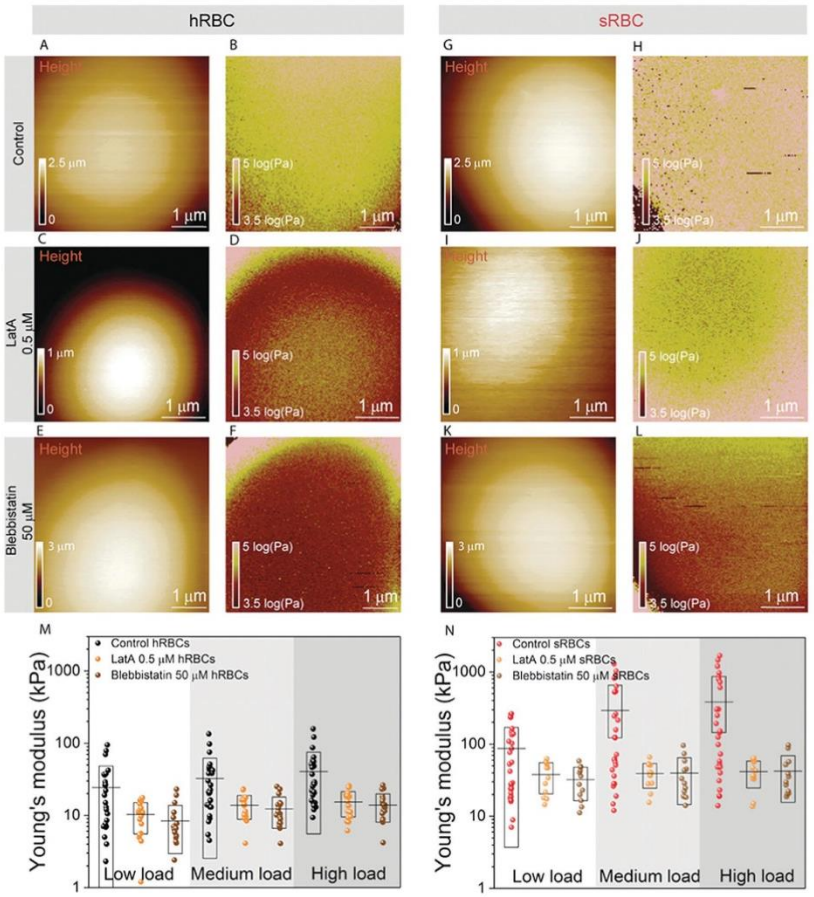

Fig. 3 Mechanical changes induced by cytoskeleton-disrupting drugs in healthy and pathological RBCs. Representative FD-based AFM height and Young's modulus images (at high load) of (A and B) non-treated hRBC, (C and D) hRBC treated with 0.5 µM latrunculin A (LatA) and (E and F) hRBC treated with 50 µM blebbistatin. Similar results are shown for non-treated sRBC (G and H), (I and J) sRBC treated with 0.5 µM LatA and (K and L) sRBC treated with 50 µM blebbistatin. The Young's modulus maps were extracted at high load to evaluate the effect of the drugs on the cytoskeleton. (M and N) Graphs of the Young's moduli of hRBCs (M) and sRBCs (N) before and after LatA and blebbistatin treatment for low, medium and high indentation loads. Treated cells become softer and differences in mechanical properties at the three indentation loads become less marked. sRBCs are still stiffer than hRBCs after treatment with LatA and blebbistatin. Each dot represents the average Young's modulus of an individual cell as extracted from the corresponding maps ($N \sim 4000$ points per cell). Horizontal lines represent mean values for each data set and boxes represent standard deviation. The data in (M) are from 3 healthy donors and are representative of 27 control hRBCs, 18 LatA and 18 blebbistatin treated hRBCs; data in (N) are from 3 patients with HS and are representative of 27 control sRBCs, 12 LatA and 12 blebbistatin treated sRBCs. All data was acquired during 3 independent experiments.

broad distribution of the measured Young's modulus values. Moreover, during our measurements, the AFM tip having a radius of 65 nm is probing the cell surface and recording a pixel every 20–40 nm, depending on the size of the image. Due to the meshwork architecture of the RBC cytoskeleton displaying 200 nm long spectrin filaments, the tip could probe either the freely spanning PM lying above a hole in the cytoskeleton mesh, or the actin–spectrin filaments. When measuring cells with a higher cytoskeleton density, such as upon aging, there is a higher probability of the AFM tip probing the less compliant actin–spectrin filaments, thus rendering higher Young's modulus values. On the other hand, on younger cells, the tip will probe

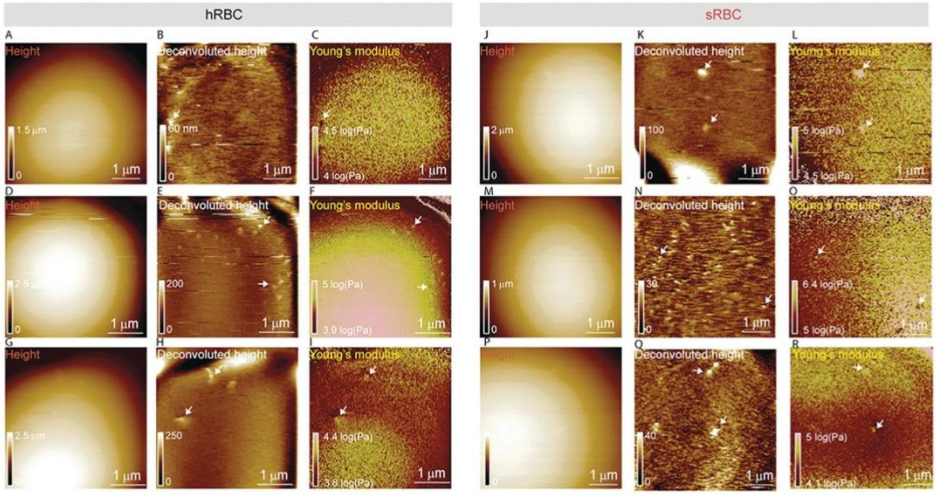

Fig. 4 Nanoscale and submicrometric heterogeneities observed on the surface of RBCs. Healthy RBCs are presented in the left panel and spherocytes in the right panel. For each condition, 3 cells are represented and the first column shows the FD-based AFM height images (A, D, G, J, M and P), with the corresponding deconvoluted image (B, E, H, K, N and Q) and the Young's modulus map at medium load (C, F, I, L, O and R). The data are representative of 3 healthy donors and 3 patients with HS. Arrows highlight lateral heterogeneities. A total of 15 cells per condition were analyzed during 6 independent experiments.

an average distribution of PM and the underlying cytoskeleton. When disrupting the cell cytoskeleton, we mostly probe the PM, which produces more homogenous results. Interestingly, while other groups have shown that LatA affects the cytoskeleton organization of RBCs, the effect of blebbistatin has been neglected so far.[11,50] We showed here for the first time that myosin contributes similarly to actin to the mature RBC mechanics. This could be important for future studies on cytoskeleton remodeling during enucleation of erythroblasts and to explore the role of the residual cytoskeletal and cytosolic myosin in the mature RBC deformation.

Following our vertical segmentation approach, we are able to discriminate cytoskeleton contribution to the overall cellular mechanics. The use of drugs supports our hypothesis that at low indentation loads we actually probe mainly the bending of the tensed PM. The three-fold difference observed between the Young's modulus values at low loads for healthy and spherocytosis cells (~10 kPa for hRBCs *vs.* ~30 kPa for sRBCs; see Fig. 3M and N) could originate from structural differences between the PMs of healthy and pathological cells.[47,51] The increased line tension of the lipid bilayer in spherocytes could lead to the formation of dimples of lipid domains to liberate tension.[52]

AFM multiparametric imaging reveals nanoscale structural and mechanical heterogeneities at the RBC surface

Multiparametric imaging was used with the goal to reveal nanoscale topographical and mechanical heterogeneities on the surface of hRBCs and sRBCs. As can be observed in Fig. 4 and 5, while raw height images showed featureless surfaces, deconvoluted height images revealed numerous submicrometric (~200 nm) and sub-100 nm protrusions with heights ranging between 5–100 nm for both hRBCS and sRBCs. These heterogeneities were correlated with local minima (Fig. 4B, C, N and O) or local maxima (Fig. 4E, F, H, I, K, L, Q and R) areas in Young's modulus maps. We found these protrusions to have similar morphological and nanomechanical properties on hRBCs and sRBCs. To gain further insights into the intrinsic mechanical properties of RBC membrane domains, we selected two representative images displaying sub-100 nm domains (Fig. 5A and D) and we quantitatively analyzed their domain sizes (Fig. 5B and E) and Young's moduli (Fig. 5C and F) (for further details see Fig. S3 (ESI†) and Methods). Our analysis revealed that these protrusions have heights between 5–20 nm (Fig. 5G) and appear as either local maxima or minima, independently from the region of the cell where they are found. Height and Young's modulus values for each of these domains were plotted and revealed a homogeneous distribution around cell average Young's modulus (Fig. 5H). We hypothesize that such heterogeneities are lipid-enriched domains, with or without recruited membrane proteins. Their mechanical properties will depend both on the specific composition of lipids, as well as on the global organization of the PM and the underlying cytoskeleton and could serve as reservoir for the generation of positive or negative curvature to navigate through human microcirculation vessels and through the pores during spleen filtration.

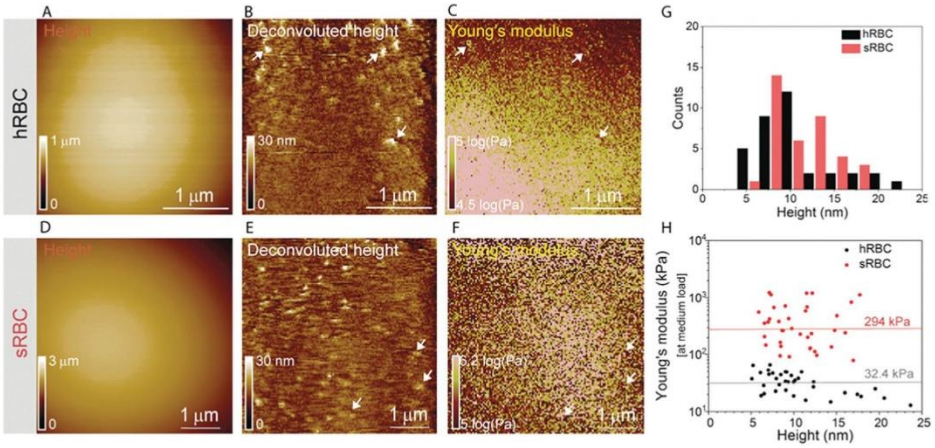

Fig. 5 High-resolution FD-based AFM multiparametric images reveal fine structures of the cell membrane. Comparison of hRBCs (first row) and sRBCs (second row). (A and D) FD-based AFM height images and (B and E) corresponding deconvoluted images. (C and F) Young's modulus images at medium load. Several sub-100 nm in diameter domains exhibiting mechanical heterogeneities as shown in the Young's modulus maps are indicated by arrows. (G) Height histograms of protrusions extracted from deconvoluted height images (B and C) show that they protrude between 5–20 nm away from the membrane surface on both healthy cells and spherocytes. (H) Dependency of Young's modulus on the height of the nanoscale domains showing that their Young's moduli distribution is centered around the average cell Young's modulus (32.4 kPa for hRBCs and 294 kPa for sRBCs). The data are representative of 3 healthy donors and 3 patients with HS. Arrows highlight lateral heterogeneities. A total of 15 cells were analyzed during 6 independent experiments.

Correlated AFM and fluorescence imaging reveals sphingomyelin submicrometric domains of variable stiffness

A pertinent question is whether these heterogeneities could arise from submicrometric aggregation of lipids in specific areas of the PM in order to liberate line tension. We therefore tested this hypothesis by combining FD-based AFM experiments with simultaneous fluorescence microscopy of SM-enriched submicrometric domains, revealed by PM insertion of the fluorescent lipid analog BODIPY-SM at low concentration (0.6 µM) to minimize modifications of the intrinsic PM properties, as tested previously.[51] Representative images correlating fluorescence microscopy and AFM on hRBCs and spherocytes are shown in Fig. 6A–D and Fig. 6F–I, respectively. The fluorescence was uniform in intensity on the RBC PM, except in the rim of the cells, in vesicles and in lipid domains, where the intensity is more strongly marked (Fig. 6A and F). Differential interference contrast (DIC) microscopy images were recorded simultaneously to exclude the presence of membrane vesicles (Fig. 6A and F, inset). Lipid domains enriched in SM are clearly observed on both hRBCs and sRBCs (Fig. 6A and F, encircled).

While height images of the hRBC showed only faint protrusions due to the cell curvature (Fig. 6B), the deconvoluted image allowed several topographical heterogeneities to be observed (Fig. 6C, highlighted by circles). The size of these heterogeneities varies from 50 to 500 nm in diameter and from 10 to 100 nm in height. Correlation with Young's modulus map analyzed at high load revealed that these three domains also present a mechanical behavior that differs from the surrounding environment. This clearly highlights that heterogeneities in the local PM composition are linked to local particular nanomechanical properties. On hRBCs, topographical protrusions coincide with a softer domain (Fig. 6E). To further put in evidence these observations, we performed simultaneous cross-sections of the fluorescence microscopy, height and Young's modulus images on the observed domains. The height measured by the AFM tip on soft surfaces will usually be lower than the true height of the sample, due to the deformation applied while scanning. We circumvented this issue through a pixel-by-pixel reconstruction of the real height of the sample, by adding the deformation and the measured height channels. The corrected real height cross-section along the SM domain shows that it is ~120 nm high and that its position is well correlated with a peak in the intensity of the fluorescence signal and a valley in the Young's modulus cross-section (Fig. 6E). We exclude the possibility of the identified SM domains being membrane vesicles, based on DIC images. We also performed control experiments on 4% PFA fixed hRBCs and observed the presence of SM-enriched domains with corresponding local nanomechanical heterogeneities similar to the ones found on living hRBCs (Fig. S5, ESI†).

Similarly, we investigated sRBCs (Fig. 6F–J) and observed that a fluorescent SM domain (Fig. 6F) coincides to a protrusion in the height image (Fig. 6G and H) as well as an heterogeneity in the Young's modulus map (Fig. 6I). Simultaneous cross-sections

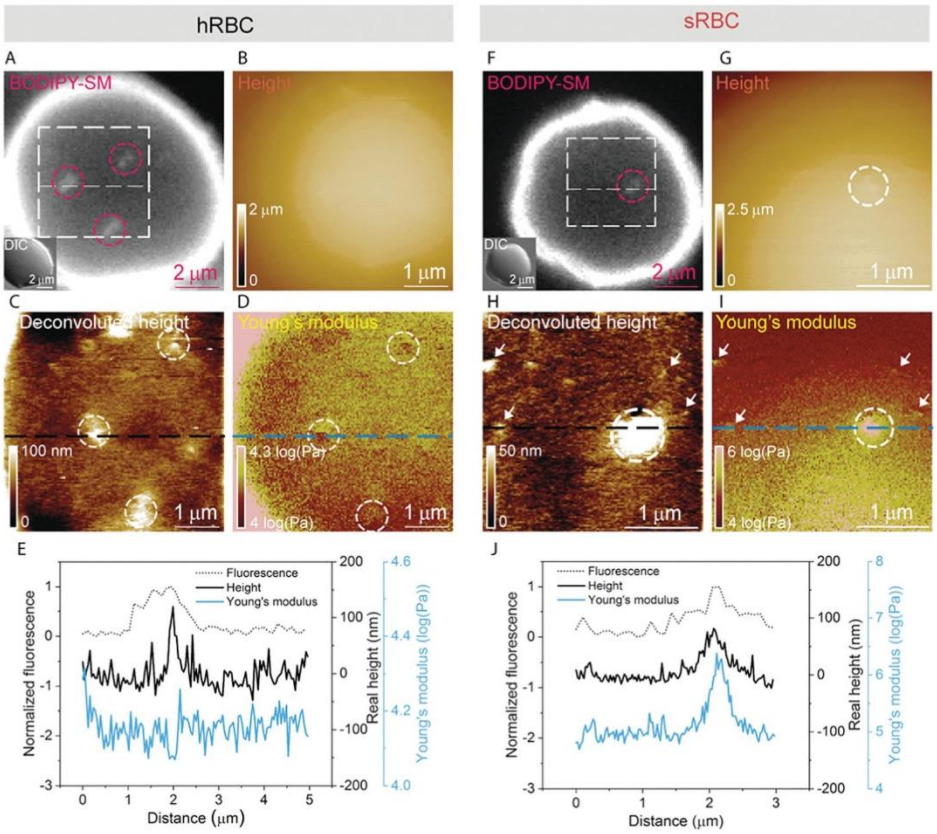

Fig. 6 Correlation of FD-based AFM and fluorescence microscopy images. Representative images of hRBCs are presented in the left panel and of sRBCs in the right panel. (A and F) Fluorescence images of RBCs labeled with BODIPY-SM with corresponding DIC images in insets (showing smooth RBC surface). (B and G) AFM height images and (C and H) corresponding deconvoluted images showing topographical heterogeneities at the RBC surface. Circles indicate submicrometric SM domains present in both fluorescence and AFM images. Arrows in deconvoluted height and Young's modulus maps at high load (D and I) point towards other heterogeneities absent in the fluorescent image of probably different lipid composition or under the optical diffraction limit. (E and J) Superimposed normalized fluorescence intensity, real height and Young's modulus cross-section profiles over SM domains show that they can appear either as local minima (E) or as maxima (J) in the mechanical properties maps. The real height of the protrusions was calculated by adding the deformation to each pixel of the height channel. The data is representative of 3 healthy donors and 3 patients with HS. A total of 28 cells were analyzed during 6 independent experiments.

along the SM domain show that the peak in the fluorescence image is again well correlated with the height protrusion and a maximum in the Young's modulus observed by AFM (Fig. 6J). However, in contrast to hRBCs, cross-sections of height and Young's modulus revealed that the protrusion is stiffer that the surrounding PM. Real height of the SM domain is ~86 nm. Other smaller protrusions are observed in the height images of both hRBCs and sRBCs (indicated by white arrows) and similarly to the SM domain, they appear as local maxima or minima in the Young's modulus maps. We believe that these heterogeneities could also represent lipid domains, however with smaller size below the diffraction limit and not resolved by our optical microscope, or other domains enriched with different lipids (see additional images in Fig. S4, ESI†). Accordingly, combined AFM and fluorescence microscopy imaging identified submicrometric SM-enriched domains on the surface of RBC that were either softer or stiffer than the surrounding areas. These domains could have a direct relevance for cell deformation while navigating through microcirculation vessels and during spleen filtration.

Conclusion

Here, we introduced an AFM-based approach to investigate the 3D architecture and mechanics of RBCs at the nanoscale and to determine how this architecture is altered in pathological states/conditions. We first confirmed that spherocytic RBCs are stiffer than healthy RBCs, a finding that can be directly related to the disease in which RBCs are less deformable, and therefore less compliant to the deformation during the splenic filtration across small pores ~ 3 μm of diameter.[53,54] Through a novel vertical segmentation approach on RBCs, we were able to isolate the contributions of the cytoskeleton and the PM from overall cell mechanics. We discovered that the cytoskeleton plays a major role in RBC mechanics. For patients with hereditary spherocytosis, the contribution of the cytoskeleton was strongly enhanced and can be related to their β-spectrin gene mutations leading to a reduced spectrin density and a stiffer cytoskeleton.[47,55,56] Correlated AFM and fluorescence imaging also revealed that the membrane lateral heterogeneity could influence the local mechanical properties of the RBCs. Therefore, our approach has demonstrated a novel correlation between the local lipid composition and RBC surface nanomechanics. We suggest that these lipid domains contribute to the membrane homeostasis and to their mechanobiological function by their direct implication in local cellular deformations. Our nanoscale observation provides direct links with membrane RBC pathologies (*e.g.* spherocytosis, elliptocytosis,...) and opens up new avenues for understanding of these RBC diseases.

Methods

RBC isolation and immobilization

This study was approved by the Medical Ethics Institutional Committee of the Université catholique de Louvain; each donor gave written informed consent. All methods were performed in accordance with the relevant guidelines and regulations. RBCs were freshly isolated from three healthy volunteers and three splenectomized patients with hereditary spherocytosis with β-spectrin gene mutations. Blood was collected by venipuncture into dry ethylenediaminetetraacetic acid (EDTA) (K^+ salt)-coated tubes, then diluted 1 : 4 (v/v) in Dulbecco's Modified Eagle Medium (DMEM containing 4.5 g L^{-1} of glucose, L-glutamine, and 25 mM HEPES, Gibco) and washed twice by centrifugation at 133*g* for 2 min. The working solution was obtained by resuspending washed RBCs in DMEM 1 : 10 ratio (v/v). For RBC immobilization, a 1 mg mL^{-1} poly-L-lysine (PLL, $M_w \sim 70$–150 kDa, Sigma-Aldrich) solution in cell culture grade phosphate buffered saline (PBS, Sigma Aldrich) was used. To this aim, glass-bottomed Petri dishes (WillCo) were covered with PLL : DMEM (1 : 1, v/v) and incubated at 37 °C for 30 min. After a washing step with DMEM at room temperature for 3 min, Petri dishes were dried at room temperature in a laminar flow hood for 2 hours. The RBC working solution was plated onto the PLL-coated Petri dishes at room temperature for 4 min. The solution was then replaced by fresh DMEM and attached RBCs were further allowed to spread for another 4 min. After 2 or 3 rapid washings with DMEM, the sample was used for AFM experiments performed in DMEM. For experiments on fixed cells, hRBCs were fixed with a 4% paraformaldehyde (PFA) in PBS solution for 10 min at room temperature. Fixed hRBCs were then immobilized on PLL-coated Petri dishes in the same manner as living cells.

RBC treatment with latrunculin A and blebbistatin

Stock solutions of 50 μM latrunculin A (Sigma-Aldrich L5163) and 100 mM blebbistatin (Sigma-Aldrich B0560) were obtained by dissolving the drugs in dimethylsulfoxide (DMSO). Washed RBCs were incubated with latrunculin A to a final concentration of 575 nM and with blebbistatin to a final concentration of 50 μM for 30 min. Previous studies have shown that these DMSO concentrations are not toxic for RBCs.[50,57] RBCs were then washed two times at 133*g* for 2 min and suspended in DMEM. RBCs were subsequently spread on PLL-coated Petri dishes as previously described.

FD-based AFM on living RBCs

AFM experiments were performed with a Bioscope Catalyst AFM (Bruker) operated in PeakForce QNM mode at ~25–30 °C in DMEM. PeakForce QNM Live Cell probes (Bruker) with spring constants ranging from 0.08 N m^{-1} to 0.1 N m^{-1}, a tip radius of curvature of 65 nm, and a tip half-angle of 15° were used. We chose these probes specifically due to their cantilever geometry and 17 μm long tip designed to reduce hydrodynamic forces. The long tip also enables imaging soft surfaces with large differences in height, by reducing the squeeze layer effect. The spring constant of the cantilevers was calibrated with a vibrometer (OFV-551, Polytec, Waldbronn) by the manufacturer. The pre-calibrated spring constant was used to determine the deflection sensitivity using the thermal noise method[58] before each experiment. FD-based multiparametric maps were acquired using a force setpoint of 300 pN. The AFM cantilever was oscillated vertically at 0.25 kHz with peak-to-peak oscillation amplitudes ranging from 600 to 1.2 μm. Images were recorded using a scan rate of 0.1 or 0.125 Hz and 128 pixels per line. For experiments at low indentation rates, individual FD curves were recorded in contact mode on the RBC surface. A force setpoint of 300 pN, approach and retraction velocities of 1 μm s^{-1} and 5 μm ramp size were used. Measurements were performed in the center of the cell, which is the highest part, to avoid substrate effects. Indentations were ranged between 300 nm and 1 μm depending on cell type. At least 60 FD curves were recorded per cell.

Combined FD-based AFM and fluorescence microscopy on living RBCs

RBCs spread on PLL-coated Petri dishes were labeled with 0.6 μM BODIPY FL C_5-SM (BODIPY, Thermo Fisher) in DMEM supplemented with 1 mg mL^{-1} bovine serum albumin (BSA fatty acid free, Sigma Aldrich) at room temperature for 15 min. The sample was then rinsed with DMEM and used for AFM experiments. Epifluorescence images of BODIPY-SM-labeled RBCs were acquired with an Axio Observer Z1 (Zeiss) inverted optical microscope coupled to a BioScope Catalyst (Bruker) AFM, using a 40×/100× oil immersion objective. This allowed

the localization of SM domains on RBCs prior to AFM imaging. The BODIPY fluorophore was excited at a wavelength of 498 nm and the emission was recorded at 516 nm.

Data analysis

Raw FD curves were processed offline using the NanoScope Analysis 1.80 Software (Bruker). We analyzed the retraction part of the FD curves to avoid plastic deformation contributions. For FD curves extracted from PeakForce QNM maps, the best quality of the fit was obtained by fitting the contact part of the curve with the Hertz model:[59,60]

$$F^{2/3} = \left(\frac{4}{3}\frac{E}{(1-\nu^2)}\sqrt{R}\right)^{2/3}\delta \quad (1)$$

where E is the Young's modulus, δ is the indentation depth, ν is the Poisson ratio, and R is the contact radius. We used a Poisson's ratio value of 0.3. Young's modulus was computed from the slope of eqn (1). The upper and lower boundaries of the fit region are defined as the percentage difference between the maximum and the minimum force. Therefore, these boundaries define the indentation depth taken into account in the analysis of the FD curves. We used fit ranges of 5–20%, 20–60% and 30–90%. Finally, the reduced Young's modulus, which takes into account the characteristics of the indenter, *i.e.* Young's modulus and Poisson's ratio was calculated:

$$\frac{1}{E_r} = \frac{(1-\nu_i^2)}{E_i} + \frac{(1-\nu^2)}{E} \quad (2)$$

In eqn (2), E_r is the reduced Young's modulus and the subscript i indicates the indenter material, which is silicon in our case. For consistency, we chose to use eqn (1) to analyze FD curves acquired in contact mode (low indentation loads) as well. In this case, we selected specific fit ranges for each experiment, so that only indentations of less than 10% of the cell height were taken into account. Images were processed using the Nanoscope Analysis 1.8 software. A second order plane fit was performed to obtain deconvoluted height images. Images did not undergo further processing. ImageJ software was used to analyze the images in Fig. 6 of the manuscript (see also Fig. S4, ESI†).

Conflicts of interest

There are no conflicts to declare.

Acknowledgements

The research of the authors is financially supported by the Fonds National de la Recherche Scientifique (F.R.S.-FNRS grant numbers: PDR T.0090.15 to D. A.), the Research Department of the Communauté française de Belgique (Concerted Research Action), the Université catholique de Louvain (Fonds Spéciaux de Recherche), the 'MOVE-IN Louvain' Incoming post-doc Fellowship programme and the Salus Sanguinis Foundation, the European Research Council (ERC) under the European Union's Horizon 2020 research and innovation programme (grant agreement no. [693630]), and the FNRS-WELBIO (Grant no. WELBIO-CR-2015A-05). Y. F. D. and D. A. are Research Director and Research Associate at the FNRS. We thank Professor Christiane Vermylen (Saint-Luc Hospital & Université catholique de Louvain) for providing blood from spherocytotic patients.

References

1 N. Mohandas and P. G. Gallagher, *Blood*, 2008, **112**, 3939–3948.
2 D. Discher, N. Mohandas and E. Evans, *Science*, 1994, **266**, 1032–1035.
3 N. Mohandas and E. Evans, *Annu. Rev. Biophys. Biomol. Struct.*, 1994, **23**, 787–818.
4 V. M. Fowler, in *Current Topics in Membranes*, ed. V. Bennett, Academic Press, 2013, vol. 72, pp. 39–88.
5 M. Carquin, L. D'Auria, H. Pollet, E. R. Bongarzone and D. Tyteca, *Prog. Lipid Res.*, 2016, **62**, 1–24.
6 C. Leonard, L. Conrard, M. Guthmann, H. Pollet, M. Carquin, C. Vermylen, P. Gailly, P. Van Der Smissen, M. P. Mingeot-Leclercq and D. Tyteca, *Sci. Rep.*, 2017, **7**, 4264.
7 H. S. Jacob, A. Ruby, E. S. Overland and D. Mazia, *J. Clin. Invest.*, 1971, **50**, 1800–1805.
8 C. F. Reed and S. N. Swisher, *J. Clin. Invest.*, 1966, **45**, 777–781.
9 H. S. Jacob, *Am. J. Med.*, 1966, **41**, 734–743.
10 G. Bao and S. Suresh, *Nat. Mater.*, 2003, **2**, 715–725.
11 R. B. Nowak, J. Papoin, D. S. Gokhin, C. Casu, S. Rivella, J. M. Lipton, L. Blanc and V. M. Fowler, *Blood*, 2017, **130**, 1144–1155.
12 L. Picas, F. Rico, M. Deforet and S. Scheuring, *ACS Nano*, 2013, **7**, 1054–1063.
13 M. Girasole, S. Dinarelli and G. Boumis, *Micron*, 2012, **43**, 1273–1286.
14 M. O'Reilly, L. McDonnell and J. O'Mullane, *Ultramicroscopy*, 2001, **86**, 107–112.
15 R. Nowakowski and P. Luckham, *Surf. Interface Anal.*, 2002, **33**, 118–121.
16 G. Ciasca, M. Papi, S. Di Claudio, M. Chiarpotto, V. Palmieri, G. Maulucci, G. Nocca, C. Rossi and M. De Spirito, *Nanoscale*, 2015, **7**, 17030–17037.
17 I. Dulińska, M. Targosz, W. Strojny, M. Lekka, P. Czuba, W. Balwierz and M. Szymoński, *J. Biochem. Biophys. Methods*, 2006, **66**, 1–11.
18 M. Lekka, M. Fornal, G. Pyka-Fosciak, K. Lebed, B. Wizner, T. Grodzicki and J. Styczen, *Biorheology*, 2005, **42**, 307–317.
19 Y. Li, L. Lu and J. Li, *Cell Biochem. Biophys.*, 2016, **74**, 365–371.
20 J. L. Maciaszek and G. Lykotrafitis, *J. Biomech.*, 2011, **44**, 657–661.
21 T. Betz, U. Bakowsky, M. R. Müller, C.-M. Lehr and I. Bernhardt, *Bioelectrochemistry*, 2007, **70**, 122–126.
22 Y. F. Dufrene, D. Martinez-Martin, I. Medalsy, D. Alsteens and D. J. Muller, *Nat. Methods*, 2013, **10**, 847–854.
23 Y. F. Dufrêne, T. Ando, R. Garcia, D. Alsteens, D. Martinez-Martin, A. Engel, C. Gerber and D. J. Müller, *Nat. Nanotechnol.*, 2017, **12**, 295.

24 D. Alsteens, M. Pfreundschuh, C. Zhang, P. M. Spoerri, S. R. Coughlin, B. K. Kobilka and D. J. Muller, *Nat. Methods*, 2015, **12**, 845–851.

25 D. Alsteens, R. Newton, R. Schubert, D. Martinez-Martin, M. Delguste, B. Roska and D. J. Müller, *Nat. Nanotechnol.*, 2016, **12**, 177.

26 A. Calzado-Martín, M. Encinar, J. Tamayo, M. Calleja and A. San Paulo, *ACS Nano*, 2016, **10**, 3365–3374.

27 D. Xia, S. Zhang, J. O. Hjortdal, Q. Li, K. Thomsen, J. Chevallier, F. Besenbacher and M. Dong, *ACS Nano*, 2014, **8**, 6873.

28 D. Alsteens, V. Dupres, S. Yunus, J. P. Latge, J. J. Heinisch and Y. F. Dufrene, *Langmuir*, 2012, **28**, 16738.

29 F. Eghiaian, A. Rigato and S. Scheuring, *Biophys. J.*, 2015, **108**, 1330.

30 N. Gavara and R. S. Chadwick, *Nat. Nanotechnol.*, 2012, **7**, 733.

31 Y. Ohta, H. Okamoto, M. Kanno and T. Okuda, *Artif. Organs*, 2002, **26**, 10–17.

32 M. Girasole, G. Pompeo, A. Cricenti, G. Longo, G. Boumis, A. Bellelli and S. Amiconi, *Nanomedicine*, 2010, **6**, 760–768.

33 M. Radmacher, *Methods in Cell Biology*, Academic Press, 2007, vol. 83, pp. 347–372.

34 L. M. Rebelo, J. S. de Sousa, J. Mendes Filho and M. Radmacher, *Nanotechnology*, 2013, **24**, 055102.

35 B. Fabry, G. N. Maksym, J. P. Butler, M. Glogauer, D. Navajas and J. J. Fredberg, *Phys. Rev. Lett.*, 2001, **87**, 148102.

36 A. Cartagena and A. Raman, *Biophys. J.*, 2014, **106**, 1033–1043.

37 A. Rigato, F. Rico, F. Eghiaian, M. Piel and S. Scheuring, *ACS Nano*, 2015, **9**, 5846–5856.

38 A. Rigato, A. Miyagi, S. Scheuring and F. Rico, *Nat. Phys.*, 2017, **13**, 771–775.

39 A. X. Cartagena-Rivera, W. H. Wang, R. L. Geahlen and A. Raman, *Sci. Rep.*, 2015, **5**, 11692.

40 A. Raman, S. Trigueros, A. Cartagena, A. P. Z. Stevenson, M. Susilo, E. Nauman and S. A. Contera, *Nat. Nanotechnol.*, 2011, **6**, 809.

41 C. Roduit, S. Sekatski, G. Dietler, S. Catsicas, F. Lafont and S. Kasas, *Biophys. J.*, 2009, **97**, 674–677.

42 J. R. Staunton, B. L. Doss, S. Lindsay and R. Ros, *Sci. Rep.*, 2016, **6**, 19686.

43 A. Wang, K. Vijayraghavan, O. Solgaard and M. J. Butte, *ACS Nano*, 2016, **10**, 257–264.

44 A. Nans, N. Mohandas and D. L. Stokes, *Biophys. J.*, 2011, **101**, 2341–2350.

45 N. S. Gov, *New J. Phys.*, 2007, **9**, 429.

46 L. Lai, X. Xu, C. T. Lim and J. Cao, *Biophys. J.*, 2015, **109**, 2287–2294.

47 Y. Park, C. A. Best, K. Badizadegan, R. R. Dasari, M. S. Feld, T. Kuriabova, M. L. Henle, A. J. Levine and G. Popescu, *Proc. Natl. Acad. Sci. U. S. A.*, 2010, **107**, 6731–6736.

48 V. M. Fowler, J. Q. Davis and V. Bennett, *J. Cell Biol.*, 1985, **100**, 47–55.

49 R. Waugh, N. Mohandas, C. Jackson, T. Mueller, T. Suzuki and G. Dale, *Blood*, 1992, **79**, 1351–1358.

50 D. S. Gokhin, R. B. Nowak, J. A. Khoory, A. d. l. Piedra, I. C. Ghiran and V. M. Fowler, *Mol. Biol. Cell*, 2015, **26**, 1699–1710.

51 L. D'Auria, M. Fenaux, P. Aleksandrowicz, P. Van Der Smissen, C. Chantrain, C. Vermylen, M. Vikkula, P. J. Courtoy and D. Tyteca, *J. Lipid Res.*, 2013, **54**, 1066–1076.

52 T. S. Ursell, W. S. Klug and R. Phillips, *Proc. Natl. Acad. Sci. U. S. A.*, 2009, **106**, 13301–13306.

53 R. E. Mebius and G. Kraal, *Nat. Rev. Immunol.*, 2005, **5**, 606–616.

54 I. V. Pivkin, Z. Peng, G. E. Karniadakis, P. A. Buffet, M. Dao and S. Suresh, *Proc. Natl. Acad. Sci. U. S. A.*, 2016, **113**, 7804–7809.

55 R. E. Waugh and P. Agre, *J. Clin. Invest.*, 1988, **81**, 133–141.

56 H. Li and G. Lykotrafitis, *Phys. Rev. E: Stat., Nonlinear, Soft Matter Phys.*, 2015, **92**, 012715.

57 K. Ubukawa, Y.-M. Guo, M. Takahashi, M. Hirokawa, Y. Michishita, M. Nara, H. Tagawa, N. Takahashi, A. Komatsuda, W. Nunomura, Y. Takakuwa and K. Sawada, *Blood*, 2012, **119**, 1036–1044.

58 J. L. Hutter and J. Bechhoefer, *Rev. Sci. Instrum.*, 1993, **64**, 1868–1873.

59 H. Schillers, C. Rianna, J. Schäpe, T. Luque, H. Doschke, M. Wälte, J. J. Uriarte, N. Campillo, G. P. A. Michanetzis, J. Bobrowska, A. Dumitru, E. T. Herruzo, S. Bovio, P. Parot, M. Galluzzi, A. Podestà, L. Puricelli, S. Scheuring, Y. Missirlis, R. Garcia, M. Odorico, J.-M. Teulon, F. Lafont, M. Lekka, F. Rico, A. Rigato, J.-L. Pellequer, H. Oberleithner, D. Navajas and M. Radmacher, *Sci. Rep.*, 2017, **7**, 5117.

60 H. Hertz, *J. Reine Angew. Math.*, 1882, **92**, 156–171.

Results

Supplementary files

Nanoscale membrane architecture of healthy and pathological red blood cells

Andra. C. Dumitru[1#], Mégane Poncin[1#], Louise Conrard[2], Yves F.Dufrêne[1,3], Donatienne Tyteca[2], David Alsteens[1*]

[1]Université catholique de Louvain, Institute of Life Sciences, Croix du Sud 4-5, bte L7.07.06, B-1348 Louvain-la-Neuve, Belgium ; [2]Université catholique de Louvain, de Duve Institute, Avenue Hippocrate 75/B1.75.05, B-1200 Woluwe-Saint-Lambert, Belgium ; [3] Walloon Excellence in Life sciences and Biotechnology (WELBIO), Belgium.

Results

Table S1. Young's modulus values of hRBCs and sRBCs before and after treatment with cytoskeleton disrupting drugs.

Cell type	Low load		Medium load		High load	
	Mean (kPa)	*SD (kPa)*	*Mean (kPa)*	*SD (kPa)*	*Mean (kPa)*	*SD (kPa)*
hRBCs (Control)	24.2	23.9	32.1	29.9	40	34.9
hRBCs LatrunculinA 0.5 µM	10.4	4.7	13.8	4.9	15	5.8
hRBCs Blebbistatin 50 µM	8.4	5.4	12.3	5.6	13.8	5.8
sRBCs (Control)	87	83.4	298	362.8	380	482.9
sRBCs LatrunculinA 0.5 µM	37.8	17.5	39.1	14.7	41	16.8
sRBCs Blebbistatin 50 µM	32	15.6	39.7	25.2	42	26.6

Results

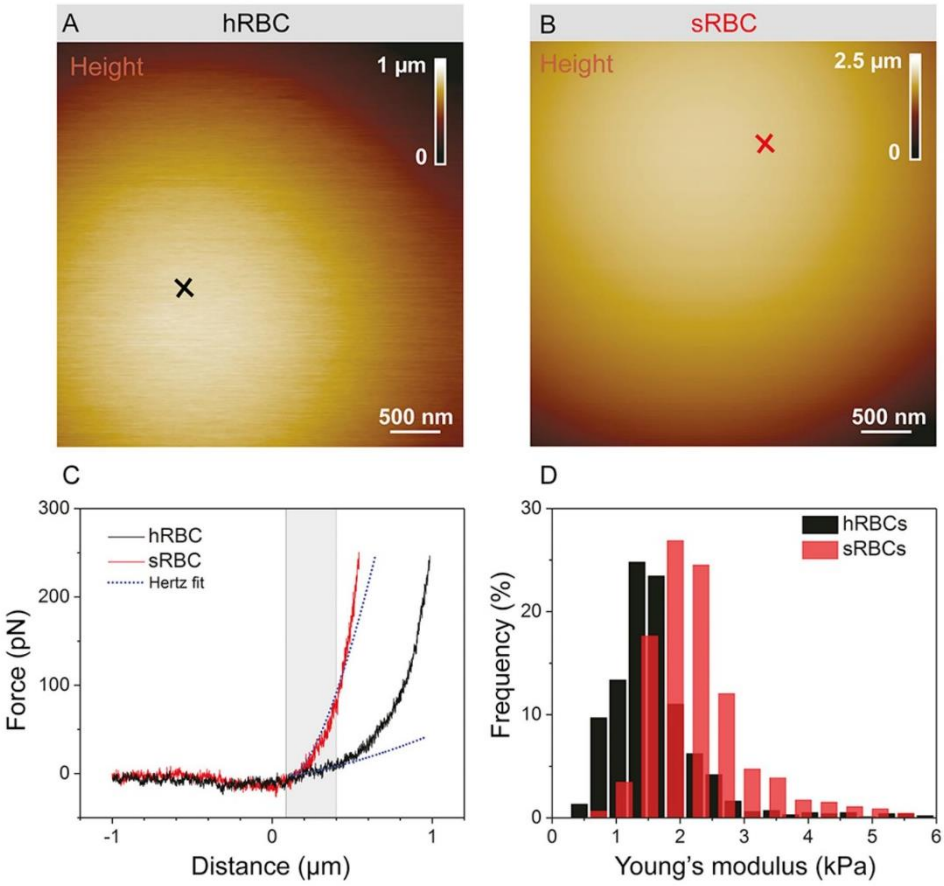

Figure S1. FD-based AFM of hRBCs and sRBCS. (A,B) Height images of a hRBC **(A)** and a sRBC **(B)** acquired in FD-based AFM. **(C)** Representative FD curves acquired in the central area of the cells, as indicated by crosses in (A-B) and corresponding Hertz fit of the 0-400 nm indentation part (blue dashed line). The slope of the FD curves is steeper on sRBCs. **(D)** Histograms showing the elastic Young's modulus of hRBCs and sRBCs at low indentation rates (~1 µm/s). The data are representative of 10 hRBCs from at least 3 patients and 9 sRBCs from a spherocytosis patient during at least 3 independent experiments per condition.

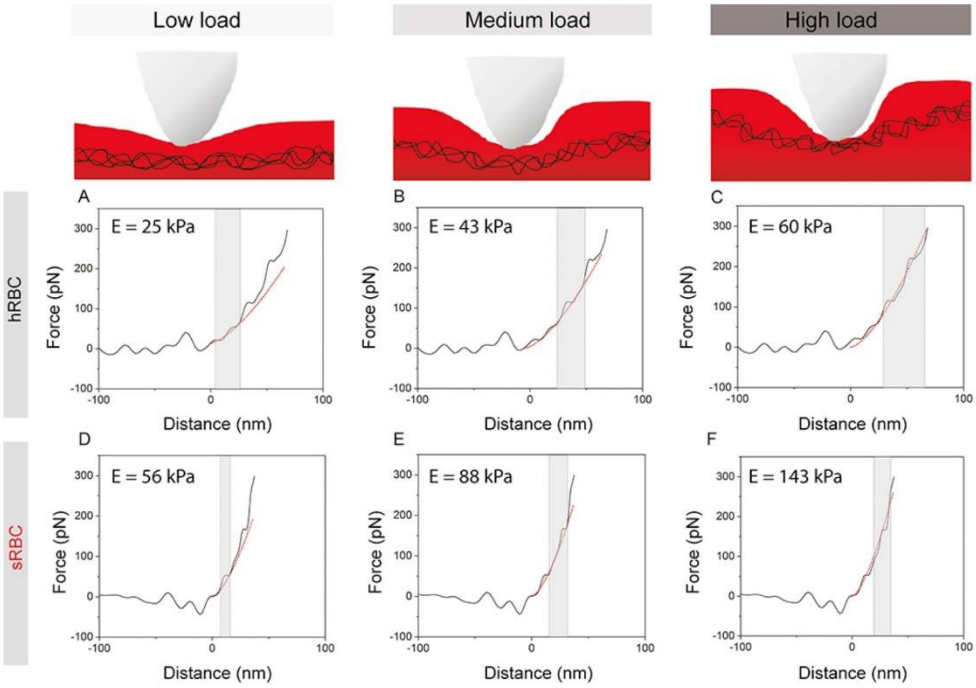

Figure S2. Representative FD-curves and fits for the different loads. (A-C) Representative FD curve obtained on a hRBC and corresponding best Hertz fit obtained for the low load (A), medium load (B) and high load (C). (D-F) Representative FD curve obtained on a sRBC and corresponding best Hertz fit obtained for the low load (D), medium load (E) and high load (F).

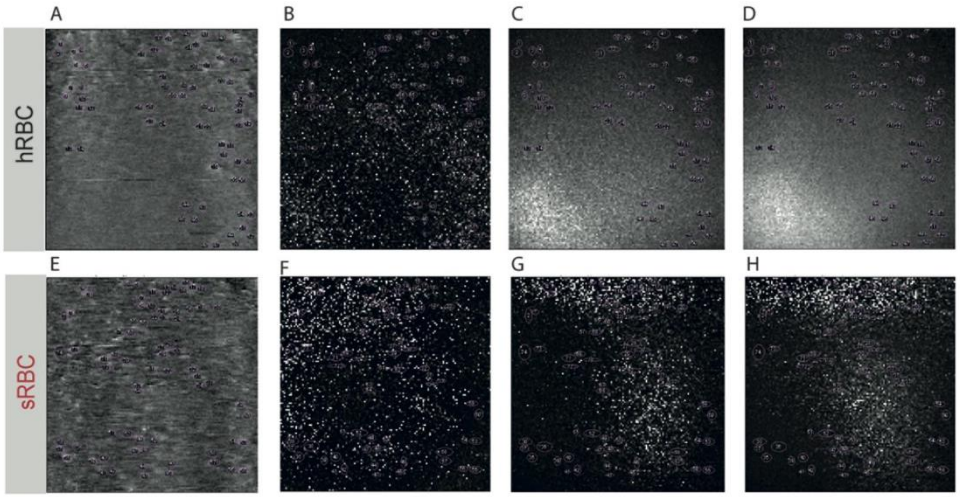

Figure S3. Analysis of correlation between height and Young's Modulus maps. Multiparametric height and Young's Modulus maps (at low, medium and high loads) were binarized into black and white images and loaded in the Image J software. First row shows results obtained on a healthy cell and the second row on a spherocyte. **(A)** and **(E)** Protrusions in the height image were selected manually and the corresponding areas in the Young's Modulus maps were marked automatically by the software for low load **(B,F)**, for medium load **(C, G)** and for high load **(D,H)**. The intensities of the peaks in both Height and Young's modulus images were saved in separate tables and further converted into real height and elastic moduli.

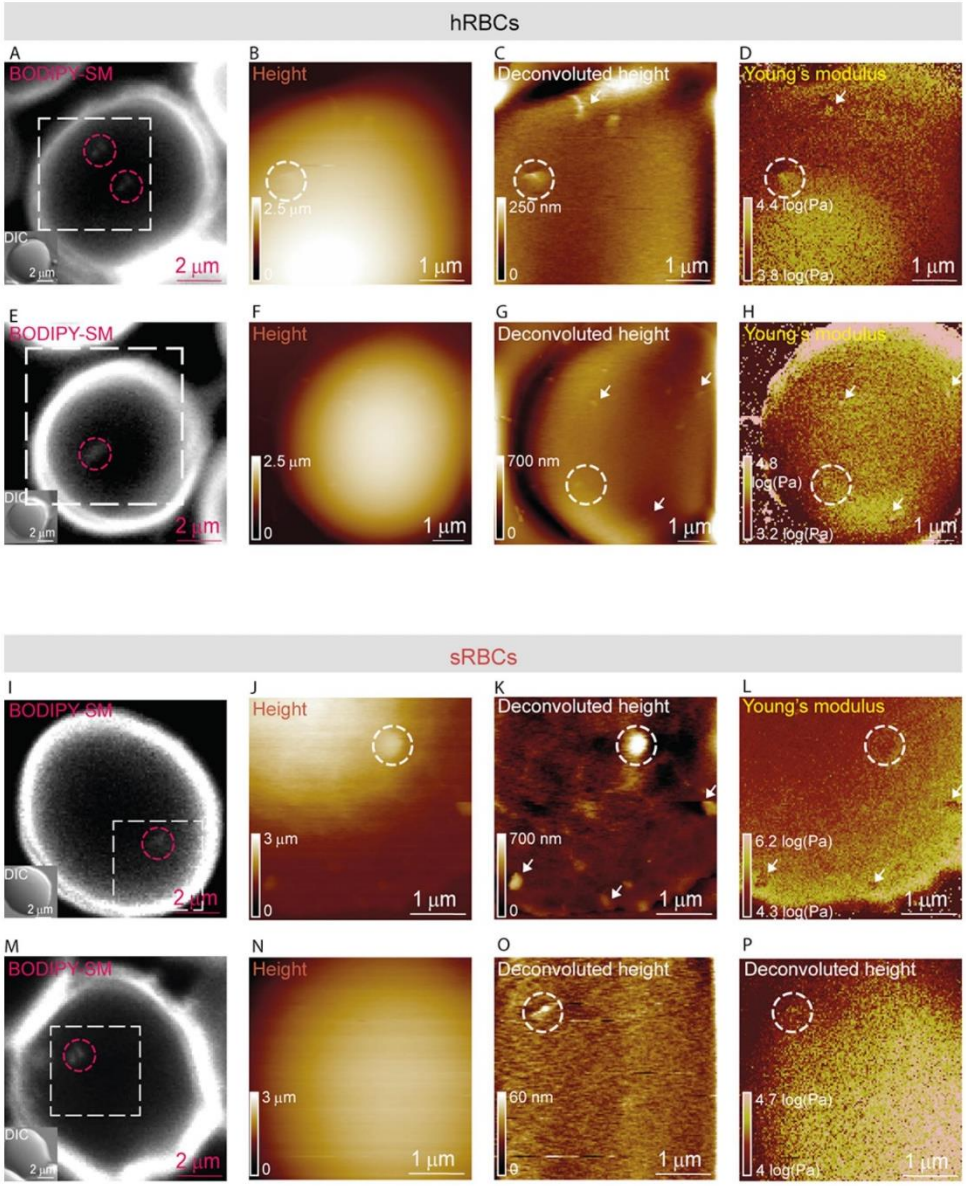

Figure S4. Correlation between FD-based AFM and fluorescence imaging on hRBCs (upper panel) and sRBCs (lower panel). Fluorescence images of hRBCs **(A),(E)** and **(I),(M)** sRBCs labeled with BODIPY-SM, along with corresponding DIC images in inset. The dashed square on the fluorescence image shows where the AFM image was recorded and circles indicate submicrometric SM domains. **(B),(F)** and **(J),(N)** FD-based AFM height images of hRBCs and sRBCs, respectively. **(C),(G)** and **(K),(O)** Deconvoluted height images of hRBCs and sRBCs. and corresponding Young's modulus maps in **(D),(H)** and **(L),(P)**. The images are representative of 28 cells from 3 healthy and 3 spherocytosis patients imaged in the same conditions during 3 independent experiments.

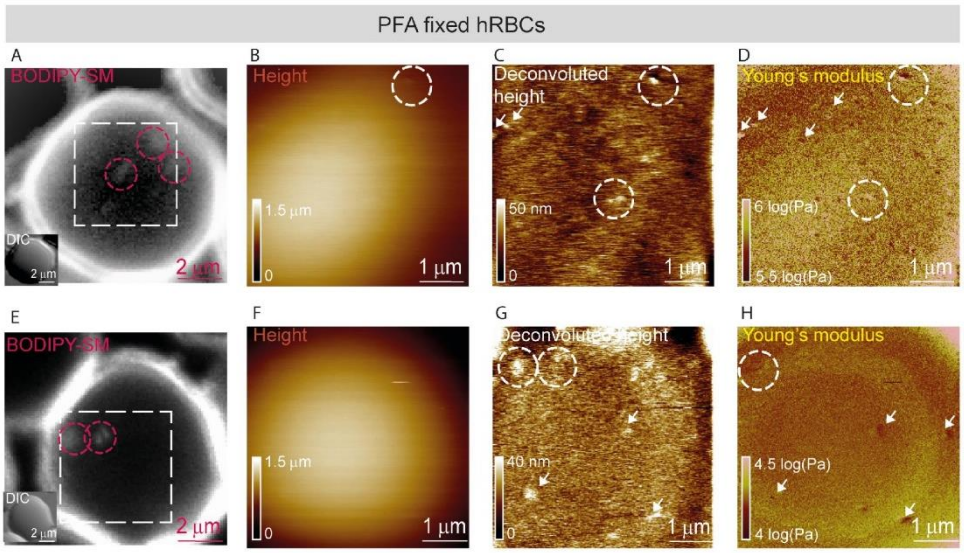

Figure S5. Correlation between FD-based AFM and fluorescence imaging on 4% PFA fixed hRBCs Fluorescence images of hRBCs **(A),(E)** labeled with BODIPY-SM, along with corresponding DIC images in inset. The dashed square on the fluorescence image shows where the AFM image was recorded and circles indicate submicrometric SM domains. **(B),(F)** FD-based AFM height images of fixed hRBCs , respectively. **(C),(G)** Deconvoluted height images of fixed hRBCs and corresponding Young's modulus maps in **(D),(H)**. The images are representative of 12 cells from 3 healthy individuals imaged in the same conditions during 3 independent experiments.

Results

2.2. PUBLICATION 3

ChemComm

COMMUNICATION

View Article Online
View Journal

High-resolution mapping and recognition of lipid domains using AFM with toxin-derivatized probes†

Andra C. Dumitru,[a] Louise Conrard,‡[b] Cristina Lo Giudice,[a] Patrick Henriet,[b] Maria Veiga-da-Cunha,[b] Sylvie Derclaye,[a] Donatienne Tyteca[b] and David Alsteens*[a]

Check for updates

Cite this: DOI: 10.1039/c8cc02201a

Received 20th March 2018,
Accepted 17th May 2018

DOI: 10.1039/c8cc02201a

rsc.li/chemcomm

Abstract

Cellular membrane lateral organization, in particular the assembly of lipids in domains, is difficult to evaluate at high resolution. Here, we used atomic force microscopy (AFM) to investigate at high-resolution lipid membranes containing variable amounts of sphingomyelin (SM) and cholesterol (Chol), two abundant membrane lipids. To this end, we developed new AFM tip functionalization strategies to specifically probe SM and Chol. Multiparametric AFM imaging allowed us to highlight the lateral submicrometric organization of these two lipids within lipid bilayers through the simultaneous topographic evidence of different phase regimes together with the extraction of their nanomechanical properties and the specific detection of lipid moieties by functionalized AFM probes. The combination of AFM topography and nanomechanical mapping with specific probes for molecular recognition of lipids represents a novel approach to identify lipid-enriched domains in supported bilayers and offers a unique perspective to directly observe lipid assemblies in living cells.

Cite this: DOI: 10.1039/c8cc02201a

Received 20th March 2018,
Accepted 17th May 2018

DOI: 10.1039/c8cc02201a

rsc.li/chemcomm

High-resolution mapping and recognition of lipid domains using AFM with toxin-derivatized probes†

Andra C. Dumitru, ‡[a] Louise Conrard,‡[b] Cristina Lo Giudice, [a] Patrick Henriet,[b] Maria Veiga-da-Cunha,[b] Sylvie Derclaye,[a] Donatienne Tyteca[b] and David Alsteens *[a]

Cellular membrane lateral organization, in particular the assembly of lipids in domains, is difficult to evaluate at high resolution. Here, we used atomic force microscopy (AFM) to investigate at high-resolution lipid membranes containing variable amounts of sphingomyelin (SM) and cholesterol (Chol), two abundant membrane lipids. To this end, we developed new AFM tip functionalization strategies to specifically probe SM and Chol. Multiparametric AFM imaging allowed us to highlight the lateral submicrometric organization of these two lipids within lipid bilayers through the simultaneous topographic evidence of different phase regimes together with the extraction of their nanomechanical properties and the specific detection of lipid moieties by functionalized AFM probes. The combination of AFM topography and nanomechanical mapping with specific probes for molecular recognition of lipids represents a novel approach to identify lipid-enriched domains in supported bilayers and offers a unique perspective to directly observe lipid assemblies in living cells.

In recent years, increasing evidence linked lipid submicrometric domains and rafts to several key biological functions, such as protein and lipid sorting, cell–cell signalling, immune response, viral pathogenesis and endo- and exocytosis.[1,2] Currently, most evidence of lipid domains relies on the use of fluorescence microscopy or spectroscopy techniques.[3] Nevertheless, direct observation of the architecture and structure–function relationship of these assemblies remains challenging due to their small size, dynamics and the lack of adequate imaging techniques with sufficient spatial and/or temporal resolution. Most of the methodologies currently used exploit fluorescent lipid analogs or stains, which have been the object of increasing concerns regarding their suitability to evidence lipid assemblies. Studies suggested that the covalent attachment of even a small fluorophore to a lipid molecule could abolish its ability to associate with rafts.[4] More recently, innovative approaches relied on the use of fluorescent proteins with phospholipid binding domain antibodies, Fab fragments or toxin fragments.[5–9] The prototype of these toxins is cholera toxin, a multimeric protein that binds to the GM1 ganglioside. One of the best-characterized cholesterol (Chol)-dependent cytolysins is theta toxin that consists of four domains, the D4 domain being the minimal toxin fragment able to bind Chol with high affinity without causing lysis.[10] Membrane Chol-enriched domains have been demonstrated in living red blood cells using a truncated theta limited to its C-terminal D4 domain (theta-D4) fused with mCherry.[11] Similarly, non-toxic lysenin (NT-lysenin), a fragment of lysenin, the pore-forming toxin able to bind to sphingomyelin (SM), has been developed to target SM lipids while preventing oligomerization and/or pore formation.[12,13] Upon fusion with mCherry, lysenin allowed revealing SM-enriched domains at the red blood cell surface.[14] Thus, among the toxin probes, theta toxin or lysenin derivatives appeared to be the most promising ones thanks to their monomeric state.[15,16] Nevertheless, their size could affect lipid properties such as lateral diffusion after membrane labelling, underlying the importance of investigating membrane organization in their native state, *i.e.* without labelling with lipid probes.

In this context, AFM appears to be a unique method that can simultaneously image at high-resolution biological samples under native conditions, while mapping mechanical and physico-chemical properties.[17] Thanks to its excellent signal-to-noise ratio, subnanometric resolution in height can be achieved allowing height differences to be observed between lipids existing in different phase regimes.[18] Recently, force–distance curve-based AFM (*FD* curve-based AFM) imaging was further developed, enabling higher data acquisition speeds while maintaining sufficient precision (0.5 nm) for high-resolution imaging.[19] Importantly, the force sensitivity achieved ($\approx$10 pN) allows the measurement of the physico-chemical properties of soft biological samples in their physiological state. Combined with

[a] *Louvain Institute of Biomolecular Science and Technology, Université catholique de Louvain, Croix du sud 4-5, 1348 Louvain-La-Neuve, Belgium. E-mail: david.alsteens@uclouvain.be*

[b] *de Duve Institute, Université catholique de Louvain, Avenue Hippocrate 75, 1200 Woluwe-Saint-Lambert, Belgium*

† Electronic supplementary information (ESI) available. See DOI: 10.1039/c8cc02201a

‡ A. C. D. and L. C. contributed equally.

Results

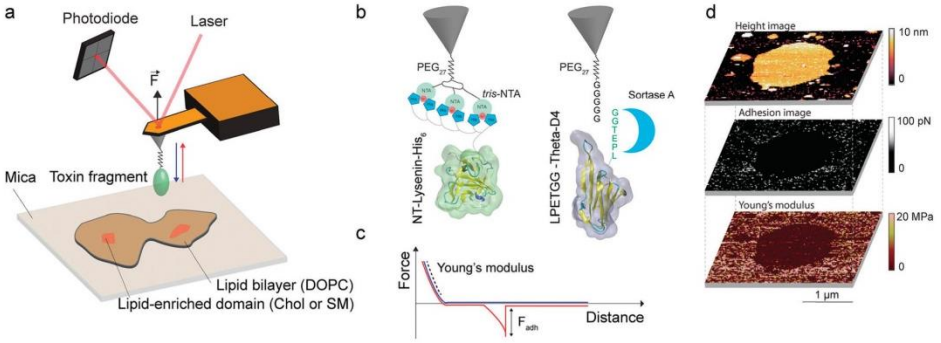

Fig. 1 High-resolution *FD* curve-based AFM imaging of a supported bilayer with toxin derivatized AFM tips. (a) Schematics of the force spectroscopy experiments performed between a toxin fragment grafted onto the AFM tip and a supported bilayer (DOPC/Chol or DOPC/SM). The AFM tip is approached towards (blue arrow) and retracted (red arrow) from the surface and the force is monitored using a laser focused on the AFM cantilever and deflected into a photodiode resulting in a force *vs.* distance curve. (b) The AFM tip is functionalized with a PEG spacer fused to either a tris-nitrilotriacetate-Ni^{2+} (Tris-NTA) or a hexaglycine peptide, which in turn reacts, respectively, with the His_6-tagged lysenin toxin or with the LPETGG-theta-D4 toxin *via* the sortase A enzyme. (c) The recorded tip–sample interactions are displayed as force–distance (*FD*) curves. Mechanical properties (including adhesion) can be extracted from individual force curves and directly correlated with the position on the sample allowing the reconstruction of maps (d).

functionalized probes, this tool can be extended to a powerful sensor allowing the localization of individual molecules or molecular assemblies on the nanoscale with high specificity.[4,20,21] To date, however, such high-resolution imaging of native membranes together with the identification of specific lipids has not been demonstrated.

Here, we report the use of *FD* curve-based AFM with tips functionalized with toxin fragments (theta-D4 (*θ*) and lysenin derivatives) to image and identify Chol- and SM-enriched lipid domains within 1,2-dioleoyl-*sn*-*glycero*-3-phosphocholine (DOPC) at high-resolution (Fig. 1a). Our findings demonstrate that AFM force spectroscopy with specific probes is a direct and simple approach for identifying the preferential localization of specific lipids without any fixation or labelling steps. In addition, high-resolution height images and Young's modulus variation provide additional evidence of lateral heterogeneities in lipid membranes.

To maximize the binding efficiency, we opted for tip chemistry that ensures the oriented grafting of the toxin fragments onto the AFM tip. To this end, both toxins were labelled with specific tags (Fig. 1b and Fig. S1, ESI†). Lysenin was labelled with a hexahistidine tag (His_6 tag) and tethered to a Tris-NTA functionalized tip (see the ESI† for details). θ Toxin was flanked by an LPETGG sequence and bound to a hexaglycine tip using a sortase-mediated reaction (see the ESI† for details, page S1).[22]

Using *FD* curve-based AFM we imaged model lipid bilayers adsorbed onto freshly cleaved mica in Tris-buffer solution. For every pixel of the AFM topography image, a *FD* curve was recorded (Fig. 1c). The maximum force applied was set up to 100 pN (see the ESI† for other details, page S2). From every *FD* curve recorded, the Young's modulus of elasticity and the adhesion were extracted from a fit with the Hertz model in the repulsive part of the approach curve[23] and from the retraction curve, respectively (Fig. 1c), and displayed as maps using coloured vertical scales (Fig. 1d).

We first imaged DOPC : SM (70 : 30) supported bilayers on mica with a lysenin-derivatized AFM tip (Fig. 2). The height image revealed nanometric and submicrometric lateral heterogeneities. Adhesion and Young's modulus channels clearly show that these areas correspond to stiffer and more adhesive regions, suggesting that these domains are rich in SM. In particular, the adhesion channel reveals clear differences between the lipid phase underlying that lysenin appears as an ideal tool to put in evidence SM-enriched lipid phases. In addition, the adhesion force remains stable over the whole image and individual *FD* curves present single rupture events with force in the 150 ± 50 pN range, in good agreement with single-molecule rupture forces. Finally, simultaneous cross-sections performed on the various AFM channels highlight the convergence of this multiparametric approach. At high resolution, as can be achieved on supported bilayers, topographical heterogeneities perfectly coincided with local variations in both the adhesion and Young's modulus channels. This also indicates that the lateral resolution obtained in the adhesion channel is not strongly affected by the linker length used to graft the toxin to the tip. Control experiments performed with a lysenin-tip on lipid bilayers lacking the SM component showed no specific adhesion events (Fig. S2a–c, ESI†). Also, when the DOPC:SM bilayer was probed with a bare AFM tip, the adhesion channel showed no contrast, while the Young's modulus maps did display local heterogeneities in nanomechanical properties (Fig. S3, ESI†). This result indicates that the toxin fragment present on the AFM tip does not induce SM domains.

Similarly, we also performed experiments on DOPC : Chol (70 : 30) supported bilayers on mica with the θ toxin fragment

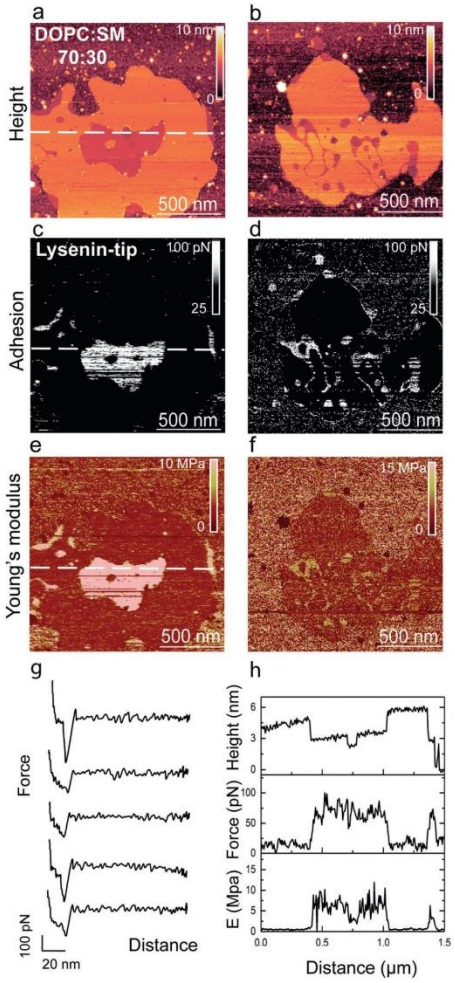

Fig. 2 Mapping SM-enriched domains with a lysenin AFM tip on DOPC : SM (70 : 30) lipid bilayers. (a and b) *FD*-Based AFM height images and the corresponding (c and d) adhesion and (e and f) Young's modulus maps. (g) Representative force–distance curves recording specific unbinding events between the lysenin tip and SM-enriched domains. Adhesion peaks appear 10–20 nm away from the surface and rupture forces are in the 100–200 pN range. (h) Simultaneous height, adhesion force and Young's modulus (*E*) cross-section profiles extracted from the corresponding maps in (a), (c) and (e). SM-enriched domains show specific topographical features that are correlated with local maxima in force and *E* values.

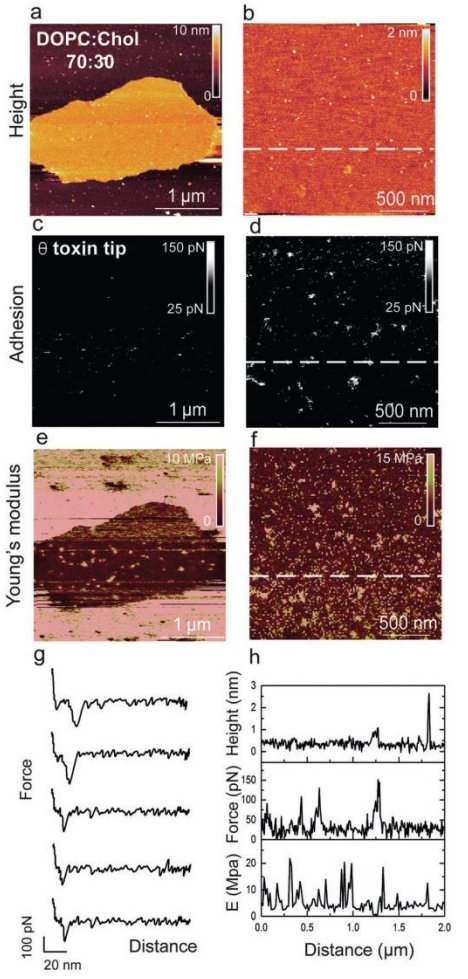

Fig. 3 Mapping Chol-enriched domains with a θ-functionalized AFM tip on DOPC : Chol (70 : 30) lipid bilayers. (a) Overview topography (height) images of lipid patches on mica and (b) high-resolution height image of the bilayer. The corresponding (c and d) adhesion and (e and f) Young's modulus maps. (g) Representative force–distance curves recording specific unbinding events between the θ tip and Chol-enriched domains. Adhesion peaks appear 10–20 nm away from the surface and rupture forces are in the 100–150 pN range. (h) Simultaneous height, adhesion force and Young's modulus (*E*) cross-section profiles extracted from the corresponding maps in (b), (d) and (f). Chol-enriched domains with or without topographical features are correlated with maxima in force and *E* values.

grafted onto the AFM tip. An overview image of the bilayers showed a mica surface covered with lipid patches (Fig. 3a). High-resolution images (Fig. 3b and Fig. S4a–c, S5, ESI†) only show very small lateral heterogeneities (~20–40 nm in diameter, Fig. S4d–g, ESI†).

The adhesion channel revealed that the θ toxin tip shows only sparsely distributed adhesion events along with some clusters. Molecular recognition events between the θ toxin tethered on the AFM tip and Chol-enriched domains were in the 100 ± 50 pN range. The adhesion events co-localize with stiffer areas, as shown in the cross-sections in Fig. S4d–g (ESI†), which is in good agreement with the coexistence of a lipid DOPC:Chol phase, surrounded by a lipid disordered phase.[24,25] The height, adhesion and Young's modulus channels in Fig. 3 reveal the existence of two types of Chol-enriched domains, both of nanometric size: (i) adhesive and stiffer domains with no topographical features and (ii) adhesive and stiffer domains that protrude 0.3–1 nm from the lipid bilayer. As predicted by Ursell *et al.*, in the context of lipid rafts, lipid domains can adopt a flat or dimpled morphology. In the latter case, this dimpled morphology facilitates a repulsive interaction that slows coalescence and helps regulate the domain size.[26] This transition between the dimpled and flat morphology depends on various factors such as the bilayer elastic properties and the domain size. Our data suggest that the dimpled domains are the larger ones, with an average diameter of 20 ± 10 nm for flat domains ($N = 40$) and 40 ± 20 nm for dimpled domains ($N = 25$), as determined from the adhesion and Young's modulus channels. To confirm the specificity of the observed interactions between the θ toxin AFM tip and the DOPC:Chol lipid bilayer, we performed two different control experiments. First, a bare AFM tip showed no specific adhesion events when DOPC:Chol bilayers were probed, while the Young's modulus channel did reveal local heterogeneities in the mechanical properties (Fig. S6, ESI†). This also indicates that the derivatized tip does not induce the Chol-enriched domains. In addition, probing the interaction between the θ toxin tip and DOPC:SM bilayers did not display any specific adhesion events (Fig. S2d–f, ESI†), confirming the specificity of the θ toxin tip for Chol domains.

While Young's modulus has already been used as a criterion to put in evidence lipid domains on cells,[18] we have shown here for the first time that specific mapping using AFM tips derivatized with toxin fragments targeting specific lipids appears to be a novel complementary and/or alternative approach to evidence lateral lipid heterogeneities at high resolution (~10 nm lateral resolution). We believe that this technique could open new avenues for the development of novel platforms to decipher lateral lipid organization from lipid model surfaces to living cells under native conditions.

This research was financially supported by the Fonds National de la Recherche Scientifique (F. R. S.-FNRS grant numbers: PDR T.0090.15 to D. A.), the Research Department of the Communauté française de Belgique (Concerted Research Action), the Université catholique de Louvain (Fonds Spéciaux de Recherche), the 'MOVE-IN Louvain' Incoming *post doc* Fellowship programme and the Salus Sanguinis Foundation. D. A. is a Research Associate of the FNRS. We thank Drs A. Miyawaki, M. Abe and T. Kobayashi (Riken Brain Science Institute, Saitama, Japan, & University of Strasbourg, France) as well as H. Mizuno (KU Leuven, Belgium) for supplying the Dronpa-NT-lysenin and Dronpa-theta-D4 plasmids.

Conflicts of interest

There are no conflicts to declare.

References

1 D. Lingwood and K. Simons, *Science*, 2010, **327**, 46–50.
2 K. Simons and M. J. Gerl, *Nat. Rev. Mol. Cell Biol.*, 2010, **11**, 688–699.
3 K. Bacia, D. Scherfeld, N. Kahya and P. Schwille, *Biophys. J.*, 2004, **87**, 1034–1043.
4 J. E. Shaw, R. F. Epand, R. M. Epand, Z. Li, R. Bittman and C. M. Yip, *Biophys. J.*, 2006, **90**, 2170–2178.
5 M. Carquin, L. D'Auria, H. Pollet, E. R. Bongarzone and D. Tyteca, *Prog. Lipid Res.*, 2016, **62**, 1–24.
6 A. Makino, M. Abe, M. Murate, T. Inaba, N. Yilmaz, F. Hullin-Matsuda, T. Kishimoto, N. L. Schieber, T. Taguchi, H. Arai, G. Anderluh, R. G. Parton and T. Kobayashi, *FASEB J.*, 2015, **29**, 477–493.
7 F. Spira, N. S. Mueller, G. Beck, P. von Olshausen, J. Beig and R. Wedlich-Soldner, *Nat. Cell Biol.*, 2012, **14**, 890.
8 H. Kuge, K. Akahori, K.-I. Yagyu and K. Honke, *J. Biol. Chem.*, 2014, **289**, 26783–26793.
9 D. Fitzner, A. Schneider, A. Kippert, W. Möbius, K. I. Willig, S. W. Hell, G. Bunt, K. Gaus and M. Simons, *EMBO J.*, 2006, **25**, 5037–5048.
10 Y. Shimada, M. Maruya, S. Iwashita and Y. Ohno-Iwashita, *Eur. J. Biochem.*, 2002, **269**, 6195–6203.
11 M. Carquin, L. Conrard, H. Pollet, P. Van Der Smissen, A. Cominelli, M. Veiga-da-Cunha, P. J. Courtoy and D. Tyteca, *Cell. Mol. Life Sci.*, 2015, **72**, 4633–4651.
12 H. Shogomori and T. Kobayashi, *Biochim. Biophys. Acta, Gen. Subj.*, 2008, **1780**, 612–618.
13 R. Ishitsuka and T. Kobayashi, *Anat. Sci. Int.*, 2004, **79**, 184.
14 M. Carquin, H. Pollet, M. Veiga-da-Cunha, A. Cominelli, P. Van Der Smissen, F. N'kuli, H. Emonard, P. Henriet, H. Mizuno, P. J. Courtoy and D. Tyteca, *J. Lipid Res.*, 2014, **55**, 1331–1342.
15 A. A. Waheed, Y. Shimada, H. F. G. Heijnen, M. Nakamura, M. Inomata, M. Hayashi, S. Iwashita, J. W. Slot and Y. Ohno-Iwashita, *Proc. Natl. Acad. Sci. U. S. A.*, 2001, **98**, 4926–4931.
16 R. Ishitsuka, A. Yamaji-Hasegawa, A. Makino, Y. Hirabayashi and T. Kobayashi, *Biophys. J.*, 2004, **86**, 296–307.
17 D. Alsteens, H. E. Gaub, R. Newton, M. Pfreundschuh, C. Gerber and D. J. Müller, *Nat. Rev. Mater.*, 2017, **2**, 17008.
18 A. Dumitru, M. Poncin, L. Conrard, Y. Dufrene, D. Tyteca and D. Alsteens, *Nanoscale Horiz.*, 2018, **3**, 293–304.
19 Y. F. Dufrêne, D. Martinez-Martin, I. Medalsy, D. Alsteens and D. J. Muller, *Nat. Methods*, 2013, **10**, 847–854.
20 D. Alsteens, M. Pfreundschuh, C. Zhang, P. M. Spoerri, S. R. Coughlin, B. K. Kobilka and D. J. Müller, *Nat. Methods*, 2015, **12**, 845–851.
21 T. Bhatia, F. Cornelius and J. H. Ipsen, *Nat. Protoc.*, 2017, **12**, 1563.
22 C. S. Theile, M. D. Witte, A. E. M. Blom, L. Kundrat, H. L. Ploegh and C. P. Guimaraes, *Nat. Protoc.*, 2013, **8**, 1800.
23 H. Hertz, *J. Reine Angew. Math.*, 1882, **92**, 156–171.
24 L. Redondo-Morata, M. I. Giannotti and F. Sanz, *Langmuir*, 2012, **28**, 12851–12860.
25 R. M. A. Sullan, J. K. Li, C. Hao, G. C. Walker and S. Zou, *Biophys. J.*, 2010, **99**, 507–516.
26 T. S. Ursell, W. S. Klug and R. Phillips, *Proc. Natl. Acad. Sci. U. S. A.*, 2009, **106**, 13301–13306.

Materials and methods

Materials. 1,2-dioleoyl-sn-glycero-3-phosphocholine (DOPC), brain and egg sphingomyelin (SM) and egg phosphatidylcholine (PC) were purchased from Avanti Polar Lipids. Cholesterol (Chol) was purchased from Sigma Aldrich. Two buffer solutions were freshly prepared and used as follows *i)* a fusion Buffer A containing 10 mM Tris, 150 mM, NaCl 3 mM and $CaCl_2$ and *ii)* an imaging Buffer B of 10 mM Tris, 150 mM NaCl at pH 7.4. Buffer solutions were filtered before use with a 0.2 µm pore size inorganic membrane filter.

Preparation of supported lipid bilayers. DOPC, SM and Chol were dissolved in chloroform to give a final lipid concentration of 10 mM. Aliquots of DOPC and SM or Chol solutions were mixed in different DOPC:SM and DOPC:Chol molar ratios (either 70:30 or 50:50), poured into a glass vial and evaporated to dryness under a nitrogen flow. Multilamellar vesicles were obtained by hydration with the Buffer A solution to give a final lipid concentration of 1 mM and then subjecting the vial to 3 x 2.5 min cycles of tip sonication to obtain unilamellar vesicles.

Circular mica surfaces were used as substrates for AFM experiments. Prior to use, mica surfaces were glued onto Teflon discs with epoxy-based mounting glue. Phospholipid supported bilayers were prepared by the deposition of the small unilamellar vesicles suspension on freshly cleaved mica followed by incubation at 59°C. The samples were then slowly cooled to room temperature and thoroughly rinsed with Buffer B solution.

Toxin production, purification and validation. The SM-specific toxin fragment, non-toxic (NT) lysenin, was expressed in E. coli BL21 (DE3) as a fusion protein with a 6xHis-tag followed by the fluorescent protein mCherry (total MW ~45 kDa) at N-terminal, as purified and validated previously[1]. The chol-specific toxin fragment, *i.e.* the fourth domain of perfringolysine (theta D4), was cloned in pET28 containing 6xHis- and LPETGG-tags in N- and C-terminal, respectively (Fig S1a). It was generated from pET28/His-mCherry-theta[2] by removing the mCherry sequence and adding the LPETGG-tag. The resulting plasmid was transformed in *E. coli* BL21 (DE3) and the protein expressed in LB medium for 72h at 16°C after addition of 0.4 mM isopropyl-β-D-thiogalactoside. Bacterial extracts and protein purification were prepared as previously described[2]. Analysis of the purified protein by western blot revealed recombinant theta at the expected size (~16 kDa; Fig. S1b). The most enriched fractions were pooled, concentrated using Vivaspin turbo 15 columns (Sartorius), and the imidazole was removed by desalting on NAP-5 columns (GE Healthcare). Purified protein was finally kept in aliquots in 10 mM HEPES (pH 7.2) 10 mM NaCl and stored at -80°C until use. Protein concentration in the purified fraction was estimated by measuring A_{280} and assuming a molar absorptivity of 44500 $M^{-1}.cm^{-1}$. From 1 l of culture, we obtained 10 g of protein. The toxin binding specificity was verified on MLVs containing increasing amounts of Chol (Fig. S1b) and prepared as previously described[1].

Results

AFM tip functionalization. Lysenin- and θ-functionalized AFM tips were obtained using NHS-PEG_{27}-acetal linkers[3]. To obtain NHS-PEG_{27}-acetal tips, AFM cantilevers were first cleaned with chloroform for 10 min, rinsed with ethanol, N_2 dried and then cleaned for 15 min in an ultraviolet radiation and ozone cleaner (UV-O, Jetlight, CA, USA). The cantilevers were immersed in an ethanolamine solution (3.3 g ethanolamine in 6.6 ml DMSO) overnight and then rinsed in DMSO (3 x 1 min) and ethanol (3 x 1 min), followed by N_2 drying. To attach the linker to the AFM tip, 1 mg of NHS-PEG_{27}-acetal was diluted in 0.5 ml chloroform with 30 µl triethylamine and cantilevers were immersed in this solution for 2 h. The cantilevers were then cleaned 3 x 10 min in chlorofom and dried with N_2. Next, the cantilevers were immersed in a 1% citric acid solution for 10 minutes and rinsed with pure water (3 x 5 min), followed by drying with N_2.

To obtain Lysenin-tips, 100 µl of a 100 µM tris-nitrilotriacetic amine trifluoroacetate (tris-NTA) solution was pipetted onto the cantilevers and 2 µl of a freshly prepared 1 M $NaCNBH_3$ solution was then added and gently mixed. The cantilevers were incubated for 1 h, then 5 µl of a 1 M ethanolamine solution pH 8.0 were added for 10 minutes to quench the reaction. Cantilevers were washed in Tris buffer (3 x 5 min) and then incubated for 1.5 h with 100 µl of a 10 µM Lysenin solution. Lysenin-tips were rinsed with Tris buffer and stored in individual wells of a multiwell dish until used in AFM experiments (typically within 48 h).

θ-functionalized AFM tips were obtained by incubating NHS-PEG_{27}-acetal cantilevers in 100 µl of a 1 mM GGGGGGGGGGK peptide (Gly_{10}Lys, Genscript, USA) solution to which 2 µl of a freshly prepared 1 M $NaCNBH_3$ solution was added. After 1 h, then 5 µl of a 1 M ethanolamine solution pH 8.0 were added for 10 minutes to quench the reaction. Cantilevers were then incubated with 20 µl of a 10 µM θ-toxin solution and 20 µl of a 10 µM Sortase A solution for 1 h at 37°C. θ-tips were rinsed with Tris buffer and stored in individual wells of a multiwell dish until used in AFM experiments the same day.

FD-based AFM on supported lipid bilayers. AFM experiments were performed with a Bioscope Resolve AFM (Bruker) operated in "PeakForce Tapping QNM mode" in imaging Buffer B at room temperature (≈24°C). Rectangular Si_3N_4 cantilevers (AC40, Bruker) with a sharpened tetrahedral silicon tip, nominal spring constants of 0.09 N/m and resonance frequency in liquid of ≈25 kHz were used. The spring constant of the cantilevers was calibrated using the thermal noise method at the end of each experiment[4] and was found to be of 0.08 ± 0.01 N/m.

In FD-based AFM measurements, the AFM cantilever is oscillated well below its resonance frequency in a sinusoidal manner, while the sample surface is contoured pixel-by-pixel. A force-distance curve is recorded for each approach and retraction of the oscillating cantilever. FD-based AFM height, Young's modulus and adhesion maps are then obtained by doing a pixel-by-pixel reconstruction of the acquired data. FD-based multiparametric maps were acquired using a force setpoint of 100-200

pN. The AFM cantilever was oscillated vertically at 0.25 kHz with peak-to-peak oscillation amplitudes of 100 nm. Images were recorded using a scan rate of 0.2 Hz and 256x256 pixels.

Data analysis. Raw FD curves were processed offline using the NanoScope Analysis 1.80 Software (Bruker). To reconstruct Young's modulus maps, we analyzed the approach part of the force-distance curves from PeakForce QNM maps. The best quality of the fit was obtained when by fitting the contact part of the curve with the Hertz model[5, 6]:

$$F^{2/3} = \left(\frac{4}{3}\frac{E}{(1-\nu^2)}\sqrt{R}\right)^{2/3}\delta \quad (1)$$

where E is the Young's modulus, δ is the indentation depth, v is the Poisson ratio, and R is the contact radius. We used a Poisson's ratio value of 0.3. Young's modulus was calculated from the slope of Equation 1.

Height images were processed using the Gwyddion free SPM software. A first or second order plane fit was performed. Images did not undergo further processing.

Results

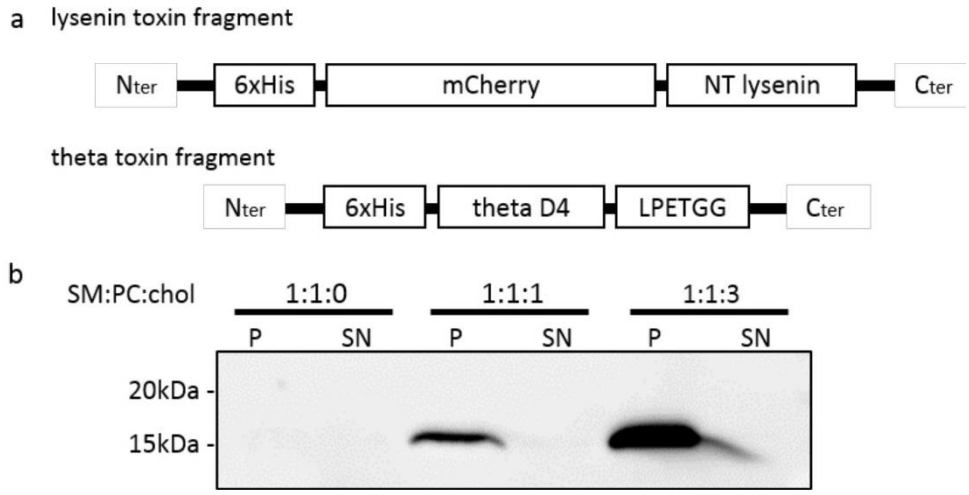

Fig. S1. Toxin fragment production (a) and validation of the theta toxin fragment (b). (a) Mapping of pET28-expressing lysenin or theta toxin. (b) Theta toxin fragment (16 kDa) binding specificity validation on multilamellar vesicles (MLVs) containing increasing Chol contents. Theta was incubated with MLVs made of SM and PC and containing (4 last wells) or not (2 first wells) Chol. After centrifugation, pellets (P) containing MLVs and supernatants (SN) were analysed by western blotting using anti-His antibodies. The 6xHis-tagged toxin only binds Chol-containing MLVs (P).

Results

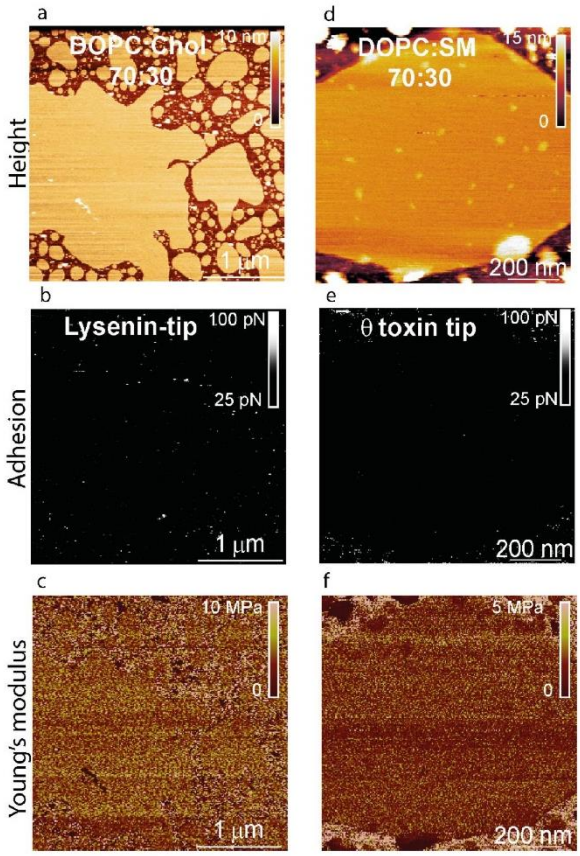

Fig. S2. Validating the specificity of the interactions detected by toxin-derivatized AFM tips. The lysenin-tip was used to probe a SM-free lipid bilayer of DOPC:Chol (70:30). (a,b,c) Height, adhesion and Young's modulus images of the DOPC:Chol (70:30). No specific unbinding event were observed between the Lysenin-tip and the DOPC:Chol sample. (d,e,f) A θ-functionalized AFM tip was used to map a Chol-free lipid bilayer made of DOPC:SM (70:30) (d) High-resolution height image of the DOPC:SM (70:30)bilayer and (e) corresponding adhesion showing no interaction between the tip and the sample and (f) Young's modulus map

Results

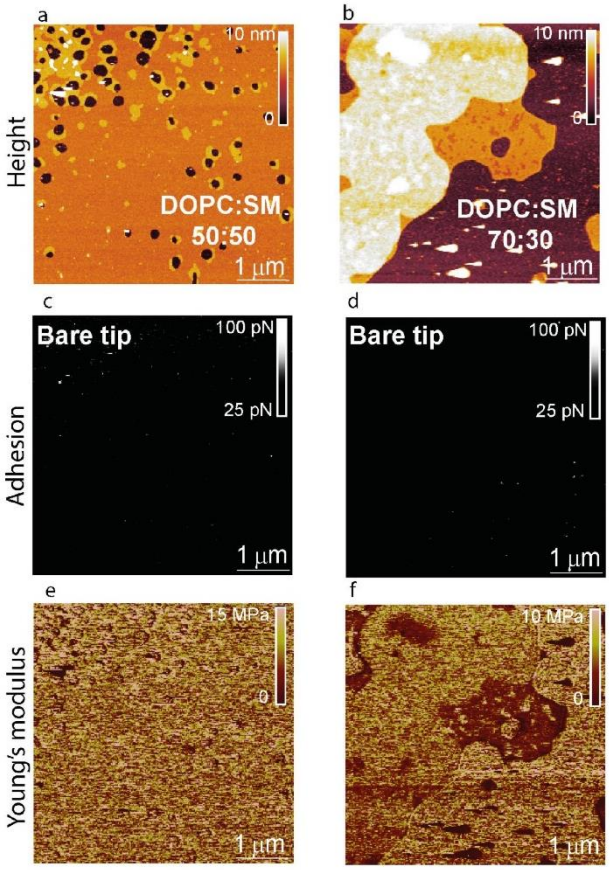

Fig. S3. Mapping SM-enriched domains with bare AFM tips on DOPC:SM 50:50 and 70:30 lipid bilayers. (a,b) Height images of the bilayers and corresponding (c,d) adhesion and (e,f) Young's modulus maps.

Results

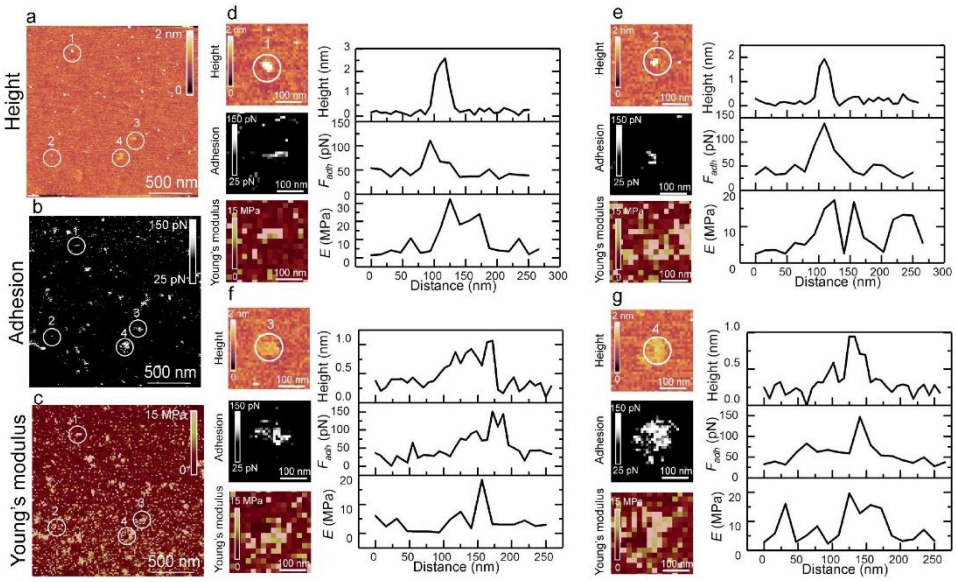

Figure S4. Mapping Chol-enriched domains with a θ-functionalized AFM tip on a DOPC:Chol (70:30) lipid bilayer. (a) High-resolution height image of the bilayer and (b,c) corresponding adhesion and Young's modulus maps. (d-f) Higher magnification maps of single Chol-enriched domains encircled in (a-c) along with the corresponding height, adhesion force and Young's modulus (E) cross-section profiles.

Results

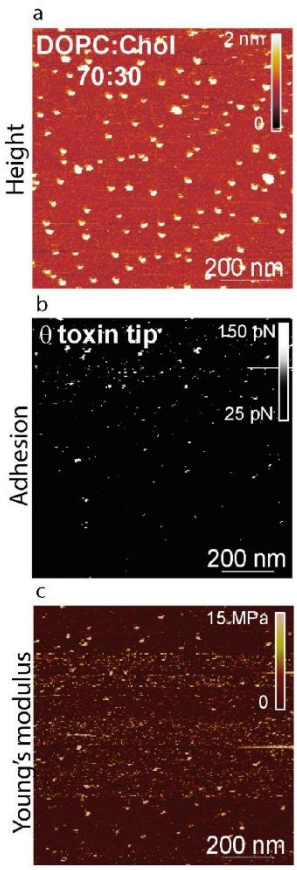

Fig S5. Mapping Chol-enriched domains with a θ-functionalized AFM tip on a DOPC:Chol (70:30) lipid bilayer. (a) High-resolution height image of the bilayer and (b,c) corresponding adhesion and Young's modulus maps.

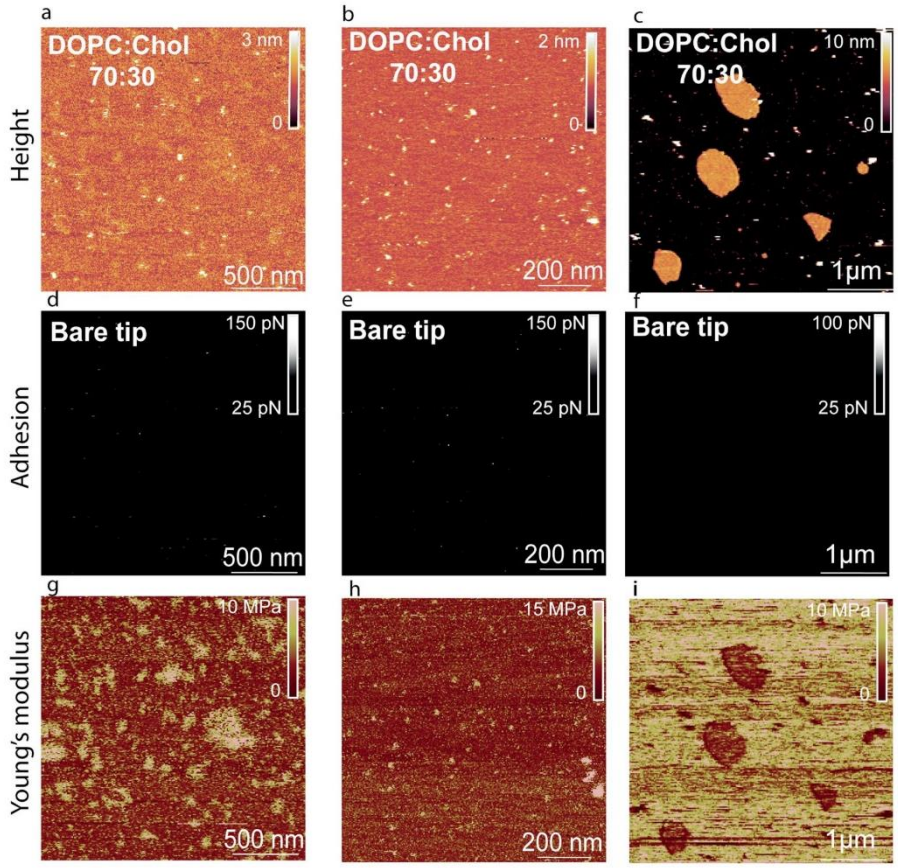

Fig. S6. Mapping Chol-enriched domains with a bare AFM tip on DOPC:Chol 50:50 and 70:30 lipid bilayers. (a,b,c) Height images of the bilayers and corresponding (d,e,f) adhesion and (g,h,i) Young's modulus maps.

References

1. M. Carquin, H. Pollet, M. Veiga-da-Cunha, A. Cominelli, P. Van Der Smissen, F. N'kuli, H. Emonard, P. Henriet, H. Mizuno, P. J. Courtoy and D. Tyteca, *Journal of Lipid Research*, 2014, **55**, 1331-1342.
2. M. Carquin, L. Conrard, H. Pollet, P. Van Der Smissen, A. Cominelli, M. Veiga-da-Cunha, P. J. Courtoy and D. Tyteca, *Cellular and Molecular Life Sciences*, 2015, **72**, 4633-4651.
3. L. Wildling, B. Unterauer, R. Zhu, A. Rupprecht, T. Haselgrübler, C. Rankl, A. Ebner, D. Vater, P. Pollheimer, E. E. Pohl, P. Hinterdorfer and H. J. Gruber, *Bioconjugate Chemistry*, 2011, **22**, 1239-1248.
4. J. L. Hutter and J. Bechhoefer, *Review of Scientific Instruments*, 1993, **64**, 1868-1873.
5. H. Schillers, C. Rianna, J. Schäpe, T. Luque, H. Doschke, M. Wälte, J. J. Uriarte, N. Campillo, G. P. A. Michanetzis, J. Bobrowska, A. Dumitru, E. T. Herruzo, S. Bovio, P. Parot, M. Galluzzi, A. Podestà, L. Puricelli, S. Scheuring, Y. Missirlis, R. Garcia, M. Odorico, J.-M. Teulon, F. Lafont, M. Lekka, F. Rico, A. Rigato, J.-L. Pellequer, H. Oberleithner, D. Navajas and M. Radmacher, *Scientific Reports*, 2017, **7**, 5117.
6. H. Hertz, *Journal für die reine und angewandte Mathematik*, 1882, **92**, 156-171.

Results

3. RBCs under deformation

PUBLICATION 1- PART 2

Cellular Physiology and Biochemistry

Cell Physiol Biochem 2018;51:1544-1565
DOI: 10.1159/000495645
Published online: 29 November 2018
Accepted: 21 November 2018

Original Paper

Spatial Relationship and Functional Relevance of Three Lipid Domain Populations At the Erythrocyte Surface

Louise Conrard[a] Amaury Stommen[a] Anne-Sophie Cloos[a] Jan Steinkühler[b] Rumiana Dimova[b] Hélène Pollet[a] Donatienne Tyteca[a]

[a]CELL Unit, de Duve Institute & Université catholique de Louvain, Brussels, Belgium, [b]Theory and Bio-Systems, Max Planck Institute of Colloids and Interfaces, Science Park Golm, Potsdam, Germany

Key Words
Fluorescence microscopy • Mechanical stimulation • Piezo1 • PMCA • PDMS stretching • Calcium exchanges

---

GM1-enriched domains increase in abundance upon RBC mechanical stimulation while SM-enriched domains increase thereafter upon RBC shape restoration

To further test this hypothesis, we analyzed domain abundance upon different approaches of mechanical stimulations: differential RBC spreading on PLL (Fig. 6A), hypo-osmotic swelling (Suppl. Fig. 2) and RBC (de)stretching on silicon (polydimethylsiloxane, PDMS) chambers (Fig. 6B).

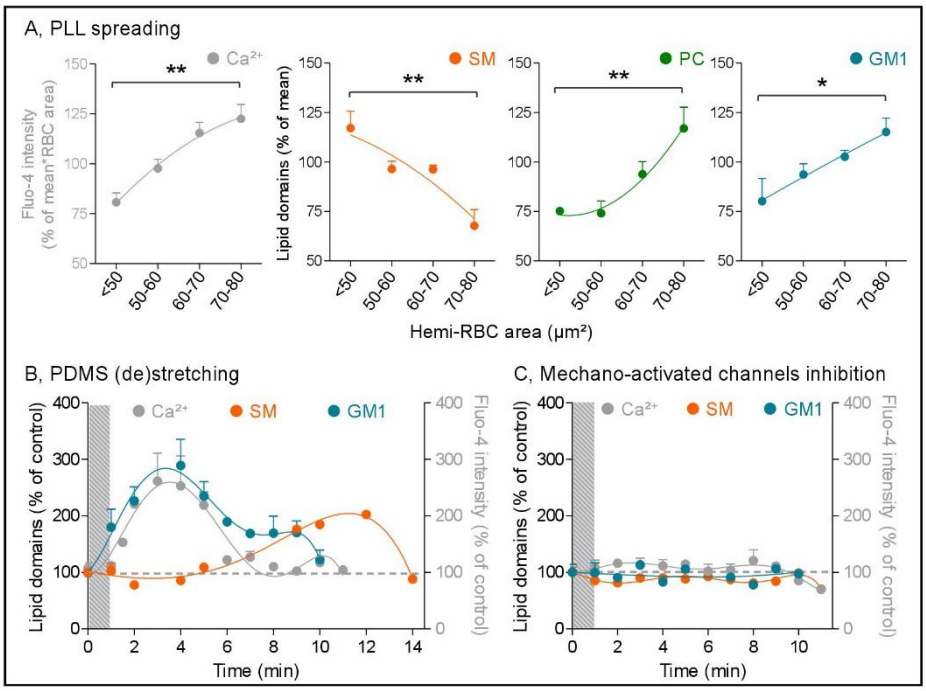

Fig. 6. PC- and GM1-enriched domains increase in abundance upon mechanical stimulation. (A) Differential spreading of RBCs on PLL. Morphometry of cell calcium content (grey dots) and domain abundance (SM, orange; PC, green; GM1, blue) under increasing projected areas of spread RBCs. RBCs were labeled at 37°C, immobilized on PLL for 4 min, washed and then let to spread for another 4 min, resulting in differential spreading (represented by different projected hemi-RBC areas). Means ± SEM of 3 independent experiments where >500 RBCs were counted. (B) (De)stretching of RBCs on silicon (PDMS) chambers. RBCs were labeled at 37°C for SM (orange dots), GM1 (blue dots) or calcium (grey dots). Lipid domains were counted and Fluo-4 intensity was measured before (t = 0 min) and after RBCs were stretched for 1 min (grey stripped zone) in PDMS chambers. Means ± SEM of 3 independent experiments where >200 RBCs were analyzed at each time. (C) (De)stretching of RBCs on PDMS chambers under inhibition of mechano-activated channels. RBCs were labeled as in (B), treated with 7 µM GsMTx4 for 15 min, stretched for 1 min (grey stripped zone) in PDMS chambers and analyzed during the indicated times upon destretching. Means ± SEM of 3 independent experiments where >100 RBCs were analyzed at each time.

We first took advantage of the differential spreading of RBCs on PLL that results from variations in the local PLL concentration, the RBC density and the adhesion duration. This heterogeneity, which was reflected in a 50 to 80 µm² range of immobilized RBC projected area (Fig. 6A) and a spreading-dependent accumulation of intracellular calcium (grey dots, Fig. 6A), differentially impacted lipid domains. Indeed, while PC- and GM1-enriched domains increased in abundance under RBC area increase (green and blue dots, Fig. 6A), SM-enriched domains tended to disappear (orange dots, Fig. 6A). In contrast, the abundance of chol-enriched was only slightly modified (red dots, Suppl. Fig. 3A). These observations point to the specific potential involvement of PC- and GM1-, but not SM-, enriched domains in RBC deformation upon mechanical stimulation.

We then checked whether basic mechanical stimulation by osmotic swelling could also lead to a differential modulation of lipid domains. Real-time imaging revealed the *de novo* formation of SM- and PC-enriched domains (orange and green arrowheads, Suppl. Fig. 2) shortly after the application of a hypo-osmolar medium, whereas GM1-enriched domains

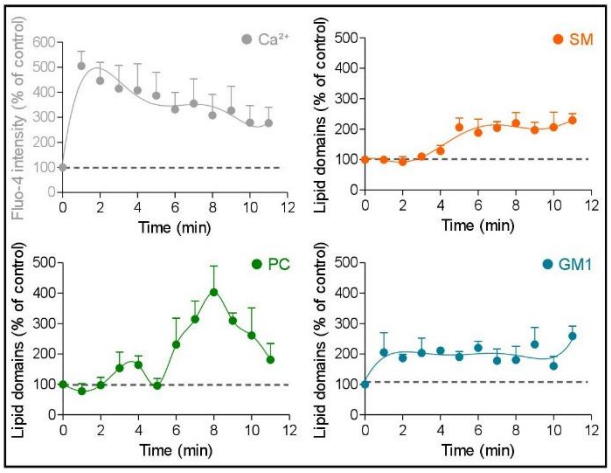

Fig. 7. PC- and GM1-enriched domains rapidly increase in abundance upon Piezo1 chemical activation while the increase in SM-enriched domains is delayed. RBCs were labeled for calcium (grey dots) or polar lipids (orange, green or blue dots) at 37°C, immobilized on PLL, treated with 0.5 µM Yoda1 for 20 sec to activate Piezo1 and immediately observed during the indicated times. Means ± SEM of 3 independent experiments for each panel where >300 RBCs were analyzed at each time.

disappeared (blue arrowhead, Suppl. Fig. 2) and chol-enriched domains remained unaffected.

Finally, we simulated RBC deformation using stretchable PDMS chambers that previously allowed us to evidence the gathering of chol-enriched domains in high-curvature membranes (Suppl. Fig. 3 B,C) and the increase of SM-enriched domains during shape restoration after deformation [29]. Immobilized RBCs were stretched for one min (grey stripped bar, Fig. 6B) and then let to recover for an additional 14 min time interval. As expected [1, 2, 29], RBC mechanical stress application occurred concomitantly with a transient intracellular calcium increase, which reached a maximal accumulation 3 min after stretching (grey dots, Fig. 6B). GM1-enriched domains showed a similar (~3fold) and transient increase (blue dots, Fig. 6B), thus perfectly coinciding with the transient calcium entry. After that, intracellular calcium decreased back to its initial concentration 6 min after stretching. From that time, the SM-enriched domain abundance started to increase (orange dots, Fig. 6B) [29].

Altogether, these results suggest that GM1-enriched domains could be linked to calcium influx during deformation whereas SM-enriched domains are linked to calcium efflux and shape restoration. This represents an additional line of evidence for the segregation between GM1- and SM-enriched domains at the RBC PM upon physiological conditions.

To further test the potential link between lipid domains and calcium exchange kinetics upon RBC deformation, we used the peptide GsMTx4, a validated inhibitor of the mechano-activated ion channels [37] which are mostly responsible for the calcium entry upon RBC deformation [1]. We showed that this treatment abolished calcium entry as well as GM1- and SM-enriched domain increase without inducing detectable toxicity (Suppl. Fig. 4). These results support our hypothesis of the correlation between GM1-enriched domain abundance and the calcium influx. Moreover, they suggest that the delayed SM-enriched domain increase is dependent on a primary calcium entry.

GM1-enriched domains are linked to Piezo1-mediated calcium influx

As GM1-enriched domains seemed to be involved into the deformation-dependent calcium influx, we explored the potential link between those domains and Piezo1. This non-selective mechano-activated cation channel plays a key role in the RBC deformation-dependent calcium influx and the following cellular volume regulation [3]. To test this hypothesis, RBCs were treated for 20 sec with Yoda1, a small agonist of this channel [38]. As expected, an immediate strong increase of the intracellular calcium concentration was observed (grey dots, Fig. 7) without detectable signs of toxicity (Suppl. Fig. 4). Intracellular calcium concentration then slowly decreased, suggesting the activation of the calcium efflux mechanisms and/or a possible slow desorption of Yoda1. The immediate increase

of intracellular calcium was concomitant with a 2-fold increase of GM1-enriched domains (blue dots, Fig. 7), while the SM-enriched domain increase was delayed and only appeared 5 min after the treatment (orange dots, Fig. 7). PC-enriched domains showed an intermediate behavior, with a first slight increase 3 min after the treatment followed by a second, more important, increase after 6 min (green dots, Fig. 7).

From all these data, we concluded that GM1-enriched domains, but not those enriched in SM, are closely linked to the Piezo1-mediated calcium entry into RBC upon deformation.

SM/PC-enriched domain abundance is closely related to the secondary calcium efflux and/ or the extent of the membrane:cytoskeleton anchorage

The delayed increase of SM-enriched domains and the intermediate behavior of PC-enriched domains under Yoda1 activation suggested that not only SM- but also PC-enriched domains might contribute to secondary calcium efflux. In RBCs, this efflux is exclusively operated by the energy-dependent PMCA. This pump is regulated by calmodulin binding (and thus intracellular calcium concentration) but also by calpain cleavage, intracellular domain modifications and even acidic lipids from the inner leaflet [39].

To test an eventual link between SM- and PC-enriched domains and PMCA activation, secondary calcium efflux was stimulated without activating the Piezo1-mediated influx. In 2002, Andrews and collaborators reported that the treatment of RBCs with a phorbol ester stimulates a protein kinase C (PKC) mediated $Ca_V2.1$-like calcium permeability pathway [40]. As this calcium entry is Piezo1-independent, we speculated that SM- and PC-, but not GM1-enriched domains, would be increased by this treatment. We thus used phorbol myristate acetate (PMA, a diacylglycerol analog) and calyculin A (CalA, a phosphatase inhibitor) to activate PKC. As expected, we observed a slight increase of intracellular calcium (data not shown) as well as a ~2-fold increase of SM- and PC-enriched domains that contrasted with the decrease of GM1-enriched domains (images in Fig. 8A and quantification in Fig. 8B).

We then stimulated calcium efflux in a more direct approach. To this aim, we used the calcium chelator EGTA to remove all traces of calcium in the extracellular medium (Fig. 8A, C) [29]. This treatment induced an important decrease of intracellular calcium (-95 % of control fluorescence, data not shown) and led to a ~2.5 fold increase of SM-enriched domains, as previously reported [29], but also a ~1.8 fold increase of PC-enriched domains (empty bars, Fig. 8C). The GM1-enriched domains were, on the other hand, decreased by this treatment, supporting the hypothesis of their involvement in calcium influx but not in its efflux. This treatment seemed not toxic since RBC re-incubation in 1.8 mM calcium-containing medium fully restored domain abundance (squared bars, Fig. 8C) and since hemoglobin release remained unchanged as compared to untreated RBCs (Suppl. Fig. 4).

We next aimed to target the PMCA pump by depleting the RBC energy content by incubation in a glucose-free medium for 2 h (Fig. 8D). This treatment, which led to a 75% decrease of the RBC ATP content (from ~2-3 mM in control cells to ~500-750 µM in depleted cells, data not shown), was not sufficient to directly inhibit the PMCA (K_M for ATP, ~3 µM). Nevertheless and in agreement with [41] and [42], it was able to indirectly impair the PMCA. Indeed, while calcium initial content was fully restored 6 min after stretching in control RBCs (see Fig. 6B and full grey points in Fig. 8E), it could not be restored even after 12 min in energy-deprived RBCs (empty grey points in Fig. 8E). Surprisingly, this PMCA inhibition also induced a high increase of SM- and PC-enriched domains, while GM1-enriched domains were not affected (empty bars, Fig. 8D). We can reasonably exclude toxicity to explain this observation, as revealed by the reversibility of the ATP depletion effect (squared bars, Fig. 8D) and the low hemoglobin release (Suppl. Fig. 4). Those results could be related to the increase of reactive oxygen species (ROS) upon energy privation through the inhibition of the anti-oxidant enzymes like the glutathione synthase (K_M for ATP, ~400 µM, [43]). Produced ROS might in turn disturb the PMCA, but also the membrane:cytoskeleton anchorage. This hypothesis is discussed in the last section of the Discussion but remains to be tested.

Our results suggest that while SM- and PC-enriched domains increase in abundance upon calcium efflux and/or cytoskeleton modulation, those enriched in GM1 are instead

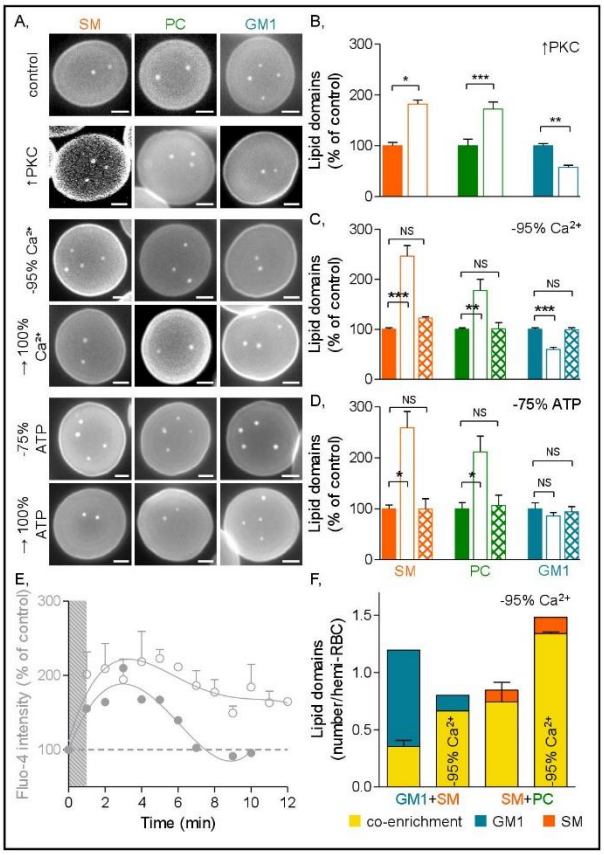

Fig. 8. Unlike GM1-enriched domains, SM- and PC-enriched domains increase upon secondary calcium efflux and/or membrane:cytoskeleton impairment. RBCs were either (i) kept untreated (control); (ii) treated with a phorbol ester (PMA, 6 µM) and a phosphatase inhibitor (CalA, 20 nM; ↑ PKC); (iii) incubated in a calcium-free medium containing 1 mM EGTA (-95 % Ca^{2+}), followed or not by reincubation in calcium-containing medium (→ 100 % Ca^{2+}); or (iv) incubated in a glucose-free medium for 2 h (-75 % ATP), followed or not by reincubation in a glucose-containing medium (→ 100 % ATP). All RBCs were then spread and labeled for polar lipids at 37°C. (A) Representative images. Scale bars 2 µm. (B-D) Quantification of lipid domains in control RBCs (plain bars), under treatment (empty bars) and in repletion conditions (squared bars). Means ± SEM of 3 independent experiments where >300 RBCs were analyzed. (E) Control (plain dots) and ATP-depleted (empty dots) RBCs were labeled for calcium at 37°C, stretched for 1 min (grey stripped zone) in PDMS chambers and analyzed during the indicated times upon destretching. (F) Double labeling between GM1 and SM or SM and PC on RBCs upon intracellular calcium depletion at 37°C. Percentage of domains double-enriched in GM1 and SM or in SM and PC are shown as yellow portions of total GM1 (blue)- or SM (orange)-enriched domains.

unaffected or even decreased. Hence, they suggest the association between SM- and PC-enriched domains upon calcium efflux, at the detriment of GM1-enriched domains. This was confirmed by double-labeling of RBCs upon EGTA treatment. Indeed, GM1-enriched domains that were not co-enriched in SM decreased (blue columns, Fig. 8F) as new lipid domains co-enriched in SM and PC, but not in GM1, were formed (orange columns, Fig. 8F).

Polar lipid domain integrity is needed for calcium exchanges at the RBC surface

Finally, we questioned whether polar lipid-enriched domains were only modulated through, or needed for, calcium exchanges at the RBC PM by abrogating lipid domains. We first used mβCD, which disrupted all lipid domains at moderate concentration (0.9- 1 mM, -25 % chol, see Fig. 4B). Under this concentration, calcium entry upon RBC stretching in silicon chambers was completely inhibited (from a 2.7-fold increase of fluorescence in untreated RBCs to no increase in mβCD-treated RBCs, grey dot at 1 mM, Fig. 9A). At a lower mβCD concentration (0.5 mM, -15 % chol, empty dot, Fig. 9A), chol- and SM-enriched domains were already disrupted (red and orange dots at 0.5 mM, Fig. 9A), while PC and GM1-enriched domains were not affected (green and blue dots at 0.5 mM). At this concentration, calcium

entry was non-significantly decreased (from a 2.7-fold increase of fluorescence in untreated RBCs to a 2.4-fold increase upon mβCD treatment, grey dot at 0.5 mM, Fig. 9A), indicating that RBCs were still able to respond to stretching by a calcium entry. The abolition of the stretching-induced calcium increase at 1 mM could result from the absence of resting-state GM1/PC-enriched domains for the primary Piezo1 activation or from the impossibility for these domains to get formed around Piezo1 under activation to sustain an efficient calcium entry. However, we cannot discard the possibility that this effect only resulted from the slight (~8 %) decrease of the chol content between 0.5 mM and 1 mM mβCD.

Finally, we used sphingomyelinase (SMase), a hydrolase catalyzing the breakdown of SM and allowing to decrease the PM SM content by up to 60 % (empty dots, Fig. 9B) without detectable cell toxicity [26]. We showed that a moderate SM depletion (-30 % at 3 mU/ml) led to the nearly complete disappearance of SM-enriched domains (-90 %, orange dots, Fig. 9B) and a ~2-fold increase of intracellular calcium (grey dots, Fig. 9B). As a matter of fact, the decrease of SM domains upon SMase treatment was proportional (R^2=0.9553) to the intracellular calcium increase. These data suggest that SM-enriched domains are not only a marker of active calcium extrusion, but are also required to maintain a low intracellular calcium concentration.

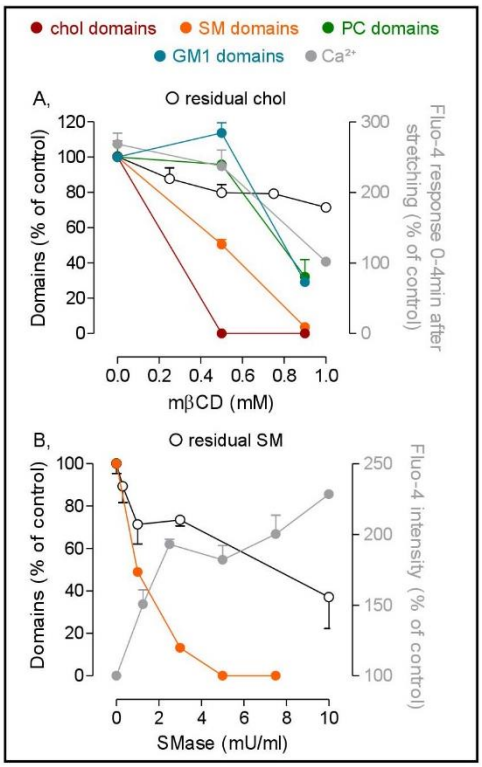

Fig. 9. Intracellular calcium content is altered upon lipid domain abrogation. (A) RBCs were treated in suspension with the indicated concentrations of mβCD and either (i) directly analyzed for chol residual content (empty dots); or (ii) spread onto PLL-coverslips for analysis of lipid domain abundance (red, orange, green or blue dots) at 37°C; or (iii) laid down on PDMS chambers and analyzed 2 min after stretching for intracellular calcium (expressed as the percentage of calcium content in unstretched RBCs; grey symbols). (B) RBCs were treated in suspension with the indicated concentrations of sphingomyelinase (SMase) and (i) directly analyzed for SM residual content (open dots) and intracellular calcium content (grey dots) at 37°C; or (ii) spread onto PLL-coated coverslips for SM-enriched domain abundance at 37°C counting (orange dots). Means ± SEM of 2-3 independent experiments where >200 RBCs were analyzed.

Discussion

In the last decades, evidence for lipid domains of various composition at the surface of several cells has emerged. First transient nanometric domains enriched in sphingolipids and chol [11] and then more stable and larger domains that could exhibit a differential lipid composition than rafts. In the last few years, we evidenced and characterized two types of submicrometric lipid domains at the RBC surface, mainly enriched in chol and/or SM [25, 26, 29]. We here extended this study to PC and GM1, two other main lipids of the outer PM leaflet, and mapped their relationship and functional relevance.

Results

Lipid domain diversity at resting state

Based on previous results on chol- and SM-enriched domains and on the new data we acquired on PC- and GM1-enriched domains, we suggest the coexistence of three populations of lipid domains in RBCs at resting state at physiological temperature: (i) mostly chol-enriched ones, abundant (~8/hemi-RBC), HC-associated and exhibiting high lipid order; (ii) GM1/PC/chol-enriched ones, less abundant (~1.5/hemi-RBC), LC-located and presenting lower ordering; and (iii) SM/PC/chol-enriched ones, rare (~0.6/hemi-RBC), also LC-located and with low ordering. Considering the wide range of domain features that lipid-lipid interactions can generate in molecular simulations of simple and complex bilayers, it is not so surprising to unveil such a diversity of lipid domains in living cell membranes. As a matter of fact, lipid clusters in simulated membranes show various (i) composition, as they are not only enriched in SM and chol, but also in gangliosides (GM1 and GM3) and in PC analogs [44, 45]; (ii) lipid order; and (iii) topography, as some GM3 nano-clusters have been shown to preferentially associate with concave (when viewed from the extracellular medium) membranes [46]. Such lipid domain diversity is also supported by several experimental data on simple lipid mixtures [47-49].

Direct lipid:lipid interactions could be able to induce lipid clusters in systems devoid of proteins and certainly help to understand some of the lipid domain behaviors that we evidenced on RBCs. For example, differential temperature dependence between GM1- and PC-enriched domains *vs* those enriched in SM is partly explainable by individual lipid intrinsic properties (*e.g.* head group, acyl chain length and saturation [50]). Moreover, lipid domain biogenesis and/or maintenance also depend on the chol content, as chol is a key regulator of membrane fluidity (and thus space between phospholipids for optimal head group interactions) and is able to directly interact with SM or GM1 [45, 51].

In a complex active system including lipids and proteins like living cell membranes, it is however unlikely that such lipid:lipid interactions are the only key regulators of lipid domains. We previously proposed several regulators for chol-enriched domains located in RBC HC areas [29]. We will here focus on the LC-associated lipid domains. The maintenance of GM1/PC/chol- and SM/PC/chol-enriched domains at a low level in LC areas of RBCs at resting state could involve membrane:cytoskeleton anchorage and/or charge-mediated interactions. Lipid domain stability in time and space at resting state supports the hypothesis of their restriction by anchorage of the membrane to the spectrin cytoskeleton, either via direct interactions with anchorage complex proteins or via an inner PM leaflet coupling. The strong dependence of SM/PC/chol-enriched domains to the intracellular calcium increase (either after stretching in PDMS chambers or under pharmacological treatments) suggests their restriction through the 4.1R anchorage complex. Indeed, anchorage through 4.1R complex is strongly decreased following calcium increase, as the binding of calmodulin/calcium to the proteins of this complex decreases their affinity for each other [2]. PKC activation and ATP depletion also led to the modulation of the anchorage through 4.1R, and SM/PC-enriched domains were also highly sensitive to those two treatments. GM1/PC/chol-enriched domains seemed on the other hand closely linked to the ankyrin-based anchorage complexes (our unpublished data).

Lipid domain modulation upon stretching and calcium exchanges

The three domain populations did not exhibit the same response to stimuli applied to the RBCs. Chol-enriched domains gather in increased curvature areas upon RBC deformation but do not increase in abundance. They could be involved in creating/maintaining HC areas needed for RBC deformation (red domains, Fig. 10) [29]. In contrast, both GM1/PC/chol- and SM/PC/chol-enriched domains were strongly increased during calcium exchanges accompanying RBC (re)shaping process, but in different kinetics. To the best of our knowledge, this is the first time that lipid domains of the external PM leaflet are proposed to contribute to calcium exchanges, crucial for the RBC to gain in flexibility when it is subjected to mechanical stress (*e.g.* in small capillaries or in the spleen). Indeed, a transient calcium influx will lead to the Gardos channel activation and a consequent cell dehydration, increasing the surface/volume

ratio and favoring cell deformation (Fig. 10) [1]. The importance of calcium for RBC mechanical stability and deformation is further illustrated by the demonstration that permanent calcium upregulation, linked to uncontrolled impairment of cytoskeletal density and/or anchorage (*e.g.* in RBCs of patients with haemolytic anemia), compromises mechanical stability of the RBC membrane [52].

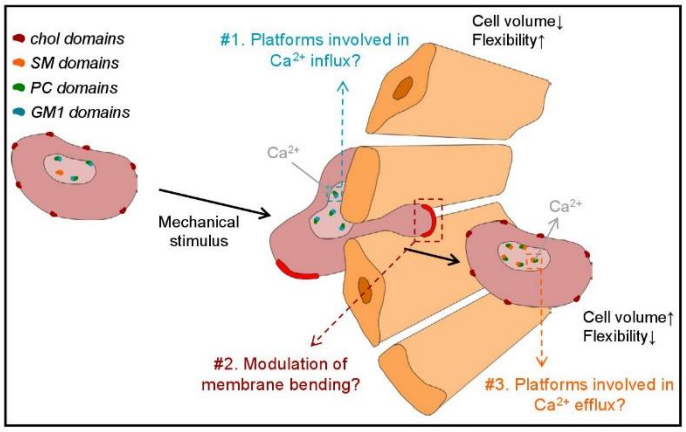

Fig. 10. Evidence-based hypothetical model of the contribution of lipid domains to RBC deformation. Under mechanical stress (e.g. in the spleen sinusoids), GM1/PC-enriched domains (blue/green) increase to favor calcium influx while chol-enriched domains (red) gather in the high-curvature membrane and modulate membrane bending. At the same time, cell volume decreases via activation of the Gardos channels and the RBC flexibility increases via uncoupling between membrane and the cytoskeleton at the 4.1R complexes. The cell volume is restored after the end of the stress application by calcium efflux thanks to the contribution of SM/PC-enriched domains (orange/green).

Calcium influx can occur through several channels like Piezo1, Cav2.1 and TRPC (*i.e.* transient receptor potential cation channel). Piezo1, a mechanically-activated cation channel, has been evidenced to play the major role in RBC deformation-induced calcium increase [3]. Moreover, mutations in Piezo1 causing an increased cation permeability have been linked to hereditary xerocytosis where RBCs are dehydrated [53]. Here, we show a close relation between the number of GM1/PC/chol-enriched domains at the RBC surface and the activation state of Piezo1 (blue/green, domains, Fig. 10), based on three lines of evidence: (i) the strong increase of lipid domain abundance under RBC stretching, which is inhibited by a mechano-activated channel inhibitor; (ii) the same increase under the chemical Piezo1 activation; and (iii) the concomitant inhibition of the stretching-mediated calcium entry and abrogation of domains under chol depletion.

SM/PC/chol-enriched domains seem also to be related to calcium exchanges, not during its influx but instead during its efflux (orange/green domains, Fig. 10). Calcium efflux is as important as influx since a prolonged calcium increase will lead to the RBC senescence and removal from the blood [2]. The involvement of SM/PC/chol-enriched domains in calcium efflux is based on the following evidences. First, they exhibit a delayed increase in abundance upon calcium entry (either by stretching or chemical activation). Second, they specifically increase in abundance when secondary calcium efflux is activated (either via PMA/CalA or EGTA treatment).

Lipid domains as modulators of Piezo1 and PMCA membrane localization and/or activity?

Sorting and activation of membrane proteins is the most studied function of lipid domains [54-57]. These effects can be attributed either to the modification of bilayer properties (thickness, curvature or surface tension) or to the binding of specific lipids to the protein surface. It is easily imaginable that mechanically-activated channels like Piezo could be affected by the surrounding membrane properties. Their activity have already been shown to be highly dependent on the membrane stiffening [58] and thus the membrane chol

content, but also on the level of fatty acid saturation [59]. Moreover, new insights in Piezo1 structure evidenced a bend in its transmembrane section [60], whose stabilization energy might be partly compensated by the surrounding lipids.

Based on the results presented in this article, we suggest that GM1/PC/chol-enriched domains could contribute to the regulation of Piezo1 by modulating its environment biophysical properties to allow an efficient and transient calcium influx. This is based on the three following facts. First, GM1 are inverted cone shaped lipids and the bend evidenced in the structure of Piezo1 at resting state supports the possibility that Piezo1 rests in a locally curved lipid bilayer environment, while upon rising membrane tension, the reduction of curvature could open the pore. Second, domains co-enriched in GM1 and chol should present a higher thickness than other domains, which could favor the recruitment/stabilization of Piezo1 transmembrane domains [61]. Indeed, a mechanically-activated protein has recently been shown to have a more expanded constriction pore in the presence of a positive mismatch (thicker lipids) than in negative mismatch (thinner lipids) [62]. Third, GM1-enriched domains appear dependent on the anchorage through ankyrin (our unpublished data) and the cytoskeleton is known to modulate Piezo1 activity [63].

While the sequence of events linking lipid domains to Piezo1 remains to be elucidated, several hypotheses can be suggested. First, GM1/PC/chol domains could be formed following the calcium ion influx and represent a secondary event. However, the fact that a Piezo1-independent calcium influx, as achieved through PKC activation [40], instead induced a decrease of GM1-enriched domains does not support this hypothesis. Second Piezo1 could modulate its surrounding environment upon activation by recruiting specific lipids such as GM1 and chol, forming domains which might modify Piezo1 dynamic properties and allow an efficient and transient calcium influx. Third, Piezo1 could be preferentially localized in GM1/PC/chol-enriched domains in RBCs at resting state, an association necessary for the primary activation of the channel. Simulation studies and localization experiments are needed to investigate these hypotheses.

While the results we present in this article suggest a correlation between calcium efflux and SM/PC/chol-enriched domain abundance, their specific role in PMCA regulation remains to be elucidated. We here propose two non-mutually exclusive hypotheses. On one hand, as for Piezo1, SM/PC/chol-enriched domains could represent a favorable environment for the protein activity. This could be linked to (i) the domain specific biophysical properties (*e.g.* lipid order); (ii) the strength of their cytoskeleton anchorage; and/or (iii) their correspondence with specific lipids in the inner leaflet, *a.o.*. The membrane lipid order hypothesis is supported by (i) our present observation that SM/PC/chol-enriched domains were more disordered than the rest of the membrane; (ii) our previous observation that lipid domain order increases to a bigger extent than the bulk membrane order upon stimulation of calcium efflux by treatment of RBCs with EGTA [31]; and (iii) several studies in model membranes, although with sometimes conflicting information. For instance, PMCA activity is decreased in highly-ordered areas of liposomes made of PC/SM/chol [64] but is favored in highly ordered lens fiber lipids in comparison with disordered DOPC liposomes [65]. Besides membrane fluidity, SM/PC/chol-enriched domains could contribute to the regulation of PMCA activity through the reversible and controlled modulation of membrane:cytoskeleton anchorage upon deformation-induced calcium entry. As a matter of fact, the protein 4.1R has been shown to directly interact with PMCA1 and to be essential for its activity in enterocytes [66]. The close relationship between the membrane:cytoskeleton anchorage, the PMCA activity and the SM/PC/chol-enriched domains could partly explain the *a priori* contradictory results we obtained by stimulating the PMCA through PKC activation *vs* impairing the pump through ATP depletion. Indeed, both treatments could induce the uncoupling of the membrane:cytoskeleton anchorage (by phosphorylation of the 4.1R complexes *vs* potential increase of ROS damages) and the increase of calcium (by stimulating a Piezo1-independent calcium influx *vs* indirectly impairing the PMCA) together with a secondary membrane:cytoskeleton uncoupling (by calmodulin binding). One hypothesis is that the reversibility of lipid domain abundance increase depends on the transient

membrane:cytoskeleton uncoupling, which became permanent under the two treatments, resulting into an incapacity to de-form the domains. Finally, SM/PC/chol-enriched domains at the external PM leaflet could contribute to the regulation of PMCA activity through their potential coupling with specific lipids in the inner PM leaflet, known to regulate PMCA activity [67, 68]. For example, electrostatic interactions and subsequent clustering of PIP_2 at the inner leaflet have been shown to be induced by a local calcium increase [69]. This could in turn induce a transbilayer clustering in superposition in the outer leaflet resulting into SM-enriched domain formation, as shown by super-resolution microscopy [70].

On the other hand, SM/PC/chol-enriched domains might modulate the PM distribution of PMCA to protect the pump from the reactions with ROS. Indeed, PMCA activity has been shown to be decreased by direct oxidation [71] or by binding of oxidized calmodulin [72]. This oxidation leads to conformational changes and the formation of aggregates that cannot recover their activity [73]. SM, on the other hand, is proposed to be a natural antioxidant that inhibits the peroxidation of unsaturated phospholipids and chol [74].

Altogether, our study opens new avenue to explore the importance of PM lipid domains in cell deformation associated to other physiological processes, such as the phagocytic cup, the immunological synapse, cell division or migration and invasion.

Abbreviations

BODIPY (*N*-(4,4-Difluoro-5,7-Dimethyl-4-Bora-3a,4a-Diaza-*s*-Indacene-3- Pentanoyl)); BSA (bovine serum albumin); CalA (calyculin A); Chol (cholesterol); FASTDil (1,1'-Dilinoleyl-3,3,3',3'-Tetramethylindocarbocyanine, 4-Chlorobenzenesulfonate); DMEM (Dulbecco's Modified Eagle Medium); EGTA (ethylene glycol-bis(β-aminoethyl ether)-N,N,N',N'-tetraacetic acid); FCS (fluorescence correlation spectroscopy); GM1 (monosialotetrahexosylganglioside); GP (generalized polarization); HC (high curvature); Laurdan (2-dimethylamino-6-lauroylnaphthalene); LC (low curvature); mβCD (methyl-β-cyclodextrin); PC (phosphatidylcholine); PDMS (polydimethylsiloxane); PKC (protein kinase C); PLL (poly-L-lysine); PM (plasma membrane); PMA (phorbol myristate acetate); PMCA (plasma membrane calcium ATPase); RBC (red blood cell); ROS (reactive oxygen species); SM (sphingomyelin); SMase (sphingomyelinase)

Acknowledgements

We thank Drs. A. Miyawaki, M. Abe and T. Kobayashi (Riken Brain Science Institute, Saitama, Japan & University of Strasbourg, France) as well as H. Mizuno (KU Leuven, Belgium) for generously supplying the Dronpa-NT-Lysenin and Dronpa-theta-D4 plasmids. We thank Pr. P. Gailly (Institute of Neuroscience, Université catholique de Louvain, Belgium) for providing us a mechanical cell strain instrument for PDMS chambers. J. Steinkühler was supported by the MaxSynBio consortium, which is jointly funded by the Federal Ministry of Education and Research (BMBF) of Germany (FKZ 031A359L) and the Max Planck Society (MPG). This work was supported by belgian grants from UCLouvain (FSR and Actions de Recherches concertées, ARC), F.R.S-FNRS and Salus Sanguinis foundation.

Disclosure Statement

The authors declare they have no conflict of interest.

References

1 Danielczok JG, Terriac E, Hertz L, Petkova-Kirova P, Lautenschlager F, Laschke MW, Kaestner L: Red Blood Cell Passage of Small Capillaries Is Associated with Transient Ca(2+)-mediated Adaptations. Front Physiol 2017;8:979-990.

2 Bogdanova A, Makhro A, Wang J, Lipp P, Kaestner L: Calcium in red blood cells-a perilous balance. Int J Mol Sci 2013;14:9848-9872.

3 Cahalan SM, Lukacs V, Ranade SS, Chien S, Bandell M, Patapoutian A: Piezo1 links mechanical forces to red blood cell volume. Elife 2015;4:e07370.

4 Klinken P: Red blood cells. Int J Biochem Cell Biol 2002;34:1513-1518.

5 Mohandas N, Gallagher PG: Red cell membrane: past, present, and future. Blood 2008;112:3939-3948.

6 Viallat A, Abkarian M: Red blood cell: from its mechanics to its motion in shear flow. Int J Lab Hematol 2014;36:237-243.

7 Byers TJ, Branton D: Visualization of the protein associations in the erythrocyte membrane skeleton. Proc Natl Acad Sci U S A 1985;82:6153-6157.

8 Uyuklu M, Meiselman HJ, Baskurt OK: Effect of decreased plasma cholesterol by atorvastatin treatment on erythrocyte mechanical properties. Clin Hemorheol Microcirc 2007;36:25-33.

9 Carquin M, D'Auria L, Pollet H, Bongarzone ER, Tyteca D: Recent progress on lipid lateral heterogeneity in plasma membranes: From rafts to submicrometric domains. Prog Lipid Res 2016;62:1-24.

10 Simons K, Vaz WL: Model systems, lipid rafts, and cell membranes. Annu Rev Biophys Biomol Struct 2004;33:269-295.

11 Lingwood D, Simons K: Lipid rafts as a membrane-organizing principle. Science 2010;327:46-50.

12 Janes PW, Ley SC, Magee AI, Kabouridis PS: The role of lipid rafts in T cell antigen receptor (TCR) signalling. Semin Immunol 2000;12:23-34.

13 Sydor AM, Czymmek KJ, Puchner EM, Mennella V: Super-Resolution Microscopy: From Single Molecules to Supramolecular Assemblies. Trends Cell Biol 2015;25:730-748.

14 Godin AG, Lounis B, Cognet L: Super-resolution microscopy approaches for live cell imaging. Biophys J 2014;107:1777-1784.

15 Hell SW, Sahl SJ, Bates M, Zhuang X, Heintzmann R, Booth MJ, Bewersdorf J, Shtengel G, Hess H, Tinnefeld P: The 2015 super-resolution microscopy roadmap. J Phys D Appl Phys 2015;48:443001-443002.

16 de Almeida RF, Loura LM, Prieto M: Membrane lipid domains and rafts: current applications of fluorescence lifetime spectroscopy and imaging. Chem Phys Lipids 2009;157:61-77.

17 Abe M, Kobayashi T: Imaging local sphingomyelin-rich domains in the plasma membrane using specific probes and advanced microscopy. Biochim Biophys Acta 2013;1841:720-726.

18 Mizuno H, Abe M, Dedecker P, Makino A, Rocha S, Ohno-Iwashita Y, Hofkens J, Kobayashi T, Miyawaki A: Fluorescent probes for superresolution imaging of lipid domains on the plasma membrane. Chem Sci 2011;2:1548-1553.

19 Barak I, Muchova K: The role of lipid domains in bacterial cell processes. Int J Mol Sci 2013;14:4050-4065.

20 Toulmay A, Prinz WA: Direct imaging reveals stable, micrometer-scale lipid domains that segregate proteins in live cells. J Cell Biol 2013;202:35-44.

21 Malinsky J, Opekarova M, Tanner W: The lateral compartmentation of the yeast plasma membrane. Yeast 2010;27:473-478.

22 Mound A, Lozanova V, Warnon C, Hermant M, Robic J, Guere C, Vie K, Lambert de Rouvroit C, Tyteca D, Debacq-Chainiaux F, Poumay Y: Non-senescent keratinocytes organize in plasma membrane submicrometric lipid domains enriched in sphingomyelin and involved in re-epithelialization. Biochim Biophys Acta 2017;1862:958-971.

23 Frisz JF, Lou K, Klitzing HA, Hanafin WP, Lizunov V, Wilson RL, Carpenter KJ, Kim R, Hutcheon ID, Zimmerberg J, Weber PK, Kraft ML: Direct chemical evidence for sphingolipid domains in the plasma membranes of fibroblasts. Proc Natl Acad Sci U S A 2013;110:613-622.

24 Tyteca D, D'Auria L, Van Der Smissen P, Medts T, Carpentier S, Monbaliu JC, de Diesbach P, Courtoy PJ: Three unrelated sphingomyelin analogs spontaneously cluster into plasma membrane micrometric domains. Biochim Biophys Acta 2010;1798:909-927.

25 Carquin M, Conrard L, Pollet H, Van Der Smissen P, Cominelli A, Veiga-da-Cunha M, Courtoy PJ, Tyteca D: Cholesterol segregates into submicrometric domains at the living erythrocyte membrane: evidence and regulation. Cell Mol Life Sci 2015;72:4633-4651.

26 Carquin M, Pollet H, Veiga-da-Cunha M, Cominelli A, Van Der Smissen P, N'Kuli F, Emonard H, Henriet P, Mizuno H, Courtoy PJ, Tyteca D: Endogenous sphingomyelin segregates into submicrometric domains in the living erythrocyte membrane. J Lipid Res 2014;55:1331-1342.

27 D'Auria L, Van Der Smissen P, Bruyneel F, Courtoy PJ, Tyteca D: Segregation of fluorescent membrane lipids into distinct micrometric domains: evidence for phase compartmentation of natural lipids? PLoS One 2011;6:e17021.

28 Dumitru A, Poncin M, Conrard L, Dufrêne Y, Tyteca D, Alsteens D: Nanoscale membrane architecture of healthy and pathological red blood cells. Nanoscale Horizons 2018;3:293-304.

29 Leonard C, Conrard L, Guthmann M, Pollet H, Carquin M, Vermylen C, Gailly P, Van Der Smissen P, Mingeot-Leclercq MP, Tyteca D: Contribution of plasma membrane lipid domains to red blood cell (re)shaping. Sci Rep 2017;7:4264-4281.

30 Owen DM, Rentero C, Magenau A, Abu-Siniyeh A, Gaus K: Quantitative imaging of membrane lipid order in cells and organisms. Nat Protoc 2011;7:24-35.

31 Leonard C, Pollet H, Vermylen C, Gov N, Tyteca D, Mingeot-Leclercq MP: Tuning of Differential Lipid Order Between Submicrometric Domains and Surrounding Membrane Upon Erythrocyte Reshaping. Cell Physiol Biochem 2018;48:2563-2582.

32 Kaestner L, Tabellion W, Weiss E, Bernhardt I, Lipp P: Calcium imaging of individual erythrocytes: problems and approaches. Cell Calcium 2006;39:13-19.

33 D'Auria L, Fenaux M, Aleksandrowicz P, Van Der Smissen P, Chantrain C, Vermylen C, Vikkula M, Courtoy PJ, Tyteca D: Micrometric segregation of fluorescent membrane lipids: relevance for endogenous lipids and biogenesis in erythrocytes. J Lipid Res 2013;54:1066-1076.

34 Parasassi T, Gratton E: Membrane lipid domains and dynamics as detected by Laurdan fluorescence. J Fluoresc 1995;5:59-69.

35 Sanchez SA, Tricerri MA, Gratton E: Laurdan generalized polarization fluctuations measures membrane packing micro-heterogeneity *in vivo*. Proc Natl Acad Sci U S A 2012;109:7314-7319.

36 van Meer G, Voelker DR, Feigenson GW: Membrane lipids: where they are and how they behave. Nat Rev Mol Cell Biol 2008;9:112-124.

37 Gnanasambandam R, Ghatak C, Yasmann A, Nishizawa K, Sachs F, Ladokhin AS, Sukharev SI, Suchyna TM: GsMTx4: Mechanism of Inhibiting Mechanosensitive Ion Channels. Biophys J 2017;112:31-45.

38 Syeda R, Xu J, Dubin AE, Coste B, Mathur J, Huynh T, Matzen J, Lao J, Tully DC, Engels IH, Petrassi HM, Schumacher AM, Montal M, Bandell M, Patapoutian A: Chemical activation of the mechanotransduction channel Piezo1. Elife 2015;4:e07369.

39 Lopreiato R, Giacomello M, Carafoli E: The plasma membrane calcium pump: new ways to look at an old enzyme. J Biol Chem 2014;289:10261-10268.

40 Andrews DA, Yang L, Low PS: Phorbol ester stimulates a protein kinase C-mediated agatoxin-TK-sensitive calcium permeability pathway in human red blood cells. Blood 2002;100:3392-3399.

41 Bruce J: Plasma membrane calcium pump regulation by metabolic stress. World J Biol Chem 2010;1:221-228.

42 Barrow SL, Voronina SG, da Silva Xavier G, Chvanov MA, Longbottom RE, Gerasimenko OV, Petersen OH, Rutter GA, Tepikin AV: ATP depletion inhibits Ca2+ release, influx and extrusion in pancreatic acinar cells but not pathological Ca2+ responses induced by bile. Pflugers Arch 2008;455:1025-1039.

43 Raftos JE, Whillier S, Kuchel PW: Glutathione synthesis and turnover in the human erythrocyte: alignment of a model based on detailed enzyme kinetics with experimental data. J Biol Chem 2010;285:23557-23567.

44 Ackerman DG, Feigenson GW: Multiscale modeling of four-component lipid mixtures: domain composition, size, alignment, and properties of the phase interface. J Phys Chem B 2015;119:4240-4250.

45 Gu RX, Ingolfsson HI, de Vries AH, Marrink SJ, Tieleman DP: Ganglioside-Lipid and Ganglioside-Protein Interactions Revealed by Coarse-Grained and Atomistic Molecular Dynamics Simulations. J Phys Chem B 2017;121:3262-3275.

46 Koldso H, Shorthouse D, Helie J, Sansom MS: Lipid clustering correlates with membrane curvature as revealed by molecular simulations of complex lipid bilayers. PLoS Comput Biol 2014;10:e1003911.

47 Veatch SL, Keller SL: Seeing spots: complex phase behavior in simple membranes. Biochim Biophys Acta 2005;1746:172-185.

48 Kahya N, Schwille P: Fluorescence correlation studies of lipid domains in model membranes. Mol Membr Biol 2006;23:29-39.

49 Sezgin E, Gutmann T, Buhl T, Dirkx R, Grzybek M, Coskun U, Solimena M, Simons K, Levental I, Schwille P: Adaptive lipid packing and bioactivity in membrane domains. PLoS One 2015;10:e0123930.

50 Chapman D: Phase transitions and fluidity characteristics of lipids and cell membranes. Q Rev Biophys 1975;8:185-235.
51 Garcia-Arribas AB, Alonso A, Goni FM: Cholesterol interactions with ceramide and sphingomyelin. Chem Phys Lipids 2016;199:26-34.
52 Manno S, Takakuwa Y, Mohandas N: Modulation of erythrocyte membrane mechanical function by protein 4.1 phosphorylation. J Biol Chem 2005;280:7581-7587.
53 Glogowska E, Schneider ER, Maksimova Y, Schulz VP, Lezon-Geyda K, Wu J, Radhakrishnan K, Keel SB, Mahoney D, Freidmann AM, Altura RA, Gracheva EO, Bagriantsev SN, Kalfa TA, Gallagher PG: Novel mechanisms of PIEZO1 dysfunction in hereditary xerocytosis. Blood 2017;130:1845-1856.
54 Koshy C, Ziegler C: Structural insights into functional lipid-protein interactions in secondary transporters. Biochim Biophys Acta 2015;1850:476-487.
55 Bhatia T, Cornelius F, Brewer J, Bagatolli LA, Simonsen AC, Ipsen JH, Mouritsen OG: Spatial distribution and activity of Na(+)/K(+)-ATPase in lipid bilayer membranes with phase boundaries. Biochim Biophys Acta 2016;1858:1390-1399.
56 Dawaliby R, Trubbia C, Delporte C, Masureel M, Van Antwerpen P, Kobilka BK, Govaerts C: Allosteric regulation of G protein-coupled receptor activity by phospholipids. Nat Chem Biol 2016;12:35-39.
57 Posada IM, Fantini J, Contreras FX, Barrantes F, Alonso A, Goni FM: A cholesterol recognition motif in human phospholipid scramblase 1. Biophys J 2014;107:1383-1392.
58 Qi Y, Andolfi L, Frattini F, Mayer F, Lazzarino M, Hu J: Membrane stiffening by STOML3 facilitates mechanosensation in sensory neurons. Nat Commun 2015;6:8512-8525.
59 Ridone P, Grage SL, Patkunarajah A, Battle AR, Ulrich AS, Martinac B: "Force-from-lipids" gating of mechanosensitive channels modulated by PUFAs. J Mech Behav Biomed Mater 2018;79:158-167.
60 Saotome K, Murthy SE, Kefauver JM, Whitwam T, Patapoutian A, Ward AB: Structure of the mechanically activated ion channel Piezo1. Nature 2017;554:481-486.
61 Wu J, Lewis AH, Grandl J: Touch, Tension, and Transduction - The Function and Regulation of Piezo Ion Channels. Trends Biochem Sci 2017;42:57-71.
62 Bavi O, Vossoughi M, Naghdabadi R, Jamali Y: The Combined Effect of Hydrophobic Mismatch and Bilayer Local Bending on the Regulation of Mechanosensitive Ion Channels. PLoS One 2016;11:e0150578.
63 Nourse JL, Pathak MM: How cells channel their stress: Interplay between Piezo1 and the cytoskeleton. Semin Cell Dev Biol 2017;71:3-12.
64 Pang Y, Zhu H, Wu P, Chen J: The characterization of plasma membrane Ca2+-ATPase in rich sphingomyelin-cholesterol domains. FEBS Lett 2005;579:2397-2403.
65 Tang D, Dean WL, Borchman D, Paterson CA: The influence of membrane lipid structure on plasma membrane Ca2+ -ATPase activity. Cell Calcium 2006;39:209-216.
66 Liu C, Weng H, Chen L, Yang S, Wang H, Debnath G, Guo X, Wu L, Mohandas N, An X: Impaired intestinal calcium absorption in protein 4.1R-deficient mice due to altered expression of plasma membrane calcium ATPase 1b (PMCA1b). J Biol Chem 2013;288:11407-11415.
67 Di Leva F, Domi T, Fedrizzi L, Lim D, Carafoli E: The plasma membrane Ca2+ ATPase of animal cells: structure, function and regulation. Arch Biochem Biophys 2008;476:65-74.
68 Pignataro MF, Dodes-Traian MM, Gonzalez-Flecha FL, Sica M, Mangialavori IC, Rossi JP: Modulation of plasma membrane Ca2+-ATPase by neutral phospholipids: effect of the micelle-vesicle transition and the bilayer thickness. J Biol Chem 2015;290:6179-6190.
69 Wang YH, Collins A, Guo L, Smith-Dupont KB, Gai F, Svitkina T, Janmey PA: Divalent cation-induced cluster formation by polyphosphoinositides in model membranes. J Am Chem Soc 2012;134:3387-3395.
70 Abe M, Makino A, Hullin-Matsuda F, Kamijo K, Ohno-Iwashita Y, Hanada K, Mizuno H, Miyawaki A, Kobayashi T: A role for sphingomyelin-rich lipid domains in the accumulation of phosphatidylinositol-4, 5-bisphosphate to the cleavage furrow during cytokinesis. Mol Cell Biol 2012;32:1396-1407.
71 Zaidi A, Barron L, Sharov VS, Schoneich C, Michaelis EK, Michaelis ML: Oxidative inactivation of purified plasma membrane Ca2+-ATPase by hydrogen peroxide and protection by calmodulin. Biochemistry 2003;42:12001-12010.
72 Sharp JS, Tomer KB: Analysis of the oxidative damage-induced conformational changes of apo- and holocalmodulin by dose-dependent protein oxidative surface mapping. Biophys J 2007;92:1682-1692.
73 Zaidi A: Plasma membrane Ca-ATPases: Targets of oxidative stress in brain aging and neurodegeneration. World J Biol Chem 2010;1:271-280.
74 Subbaiah PV, Sircar D, Lankalapalli RS, Bittman R: Effect of double bond geometry in sphingosine base on the antioxidant function of sphingomyelin. Arch Biochem Biophys 2009;481:72-79.

Supplementary Material

Spatial Relationship and Functional Relevance of Three Lipid Domain Populations at the Erythrocyte Surface

Louise Conrard[a] Amaury Stommen[a] Anne-Sophie Cloos[a] Jan Steinkühler[b] Rumiana Dimova[b] Hélène Pollet[a] Donatienne Tyteca[a]

[a]CELL Unit, de Duve Institute & Université catholique de Louvain, Brussels, Belgium, [b]Theory and Bio-Systems, Max Planck Institute of Colloids and Interfaces, Science Park Golm, Potsdam, Germany

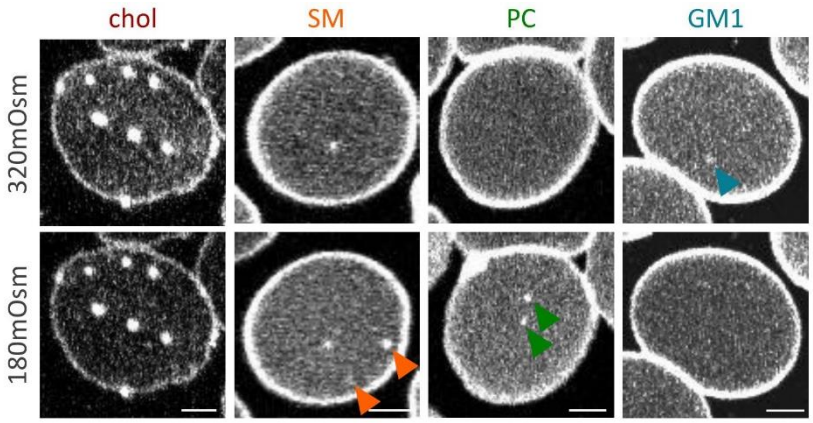

Suppl. Fig 2 Lipid domains differentially respond to osmolarity modulation. RBCs were spread in a microfluidic chamber (CellAsic ONIX), labeled with theta* or BODIPY-polar lipids in an iso-osmolar medium at 37°C and imaged (320 mOsm, top images). A hypo-osmolar flow (180 mOsm, bottom images) was then applied and the same RBCs were imaged after 3 min. Orange and green arrow heads show SM- and PC-enriched domains that appear under hypo-osmolar flow; blue arrow head shows a GM1-enriched domain that disappears under hypo-osmolar flow. *Representative images of >2 independent experiences. Scale bars 2 µm.*

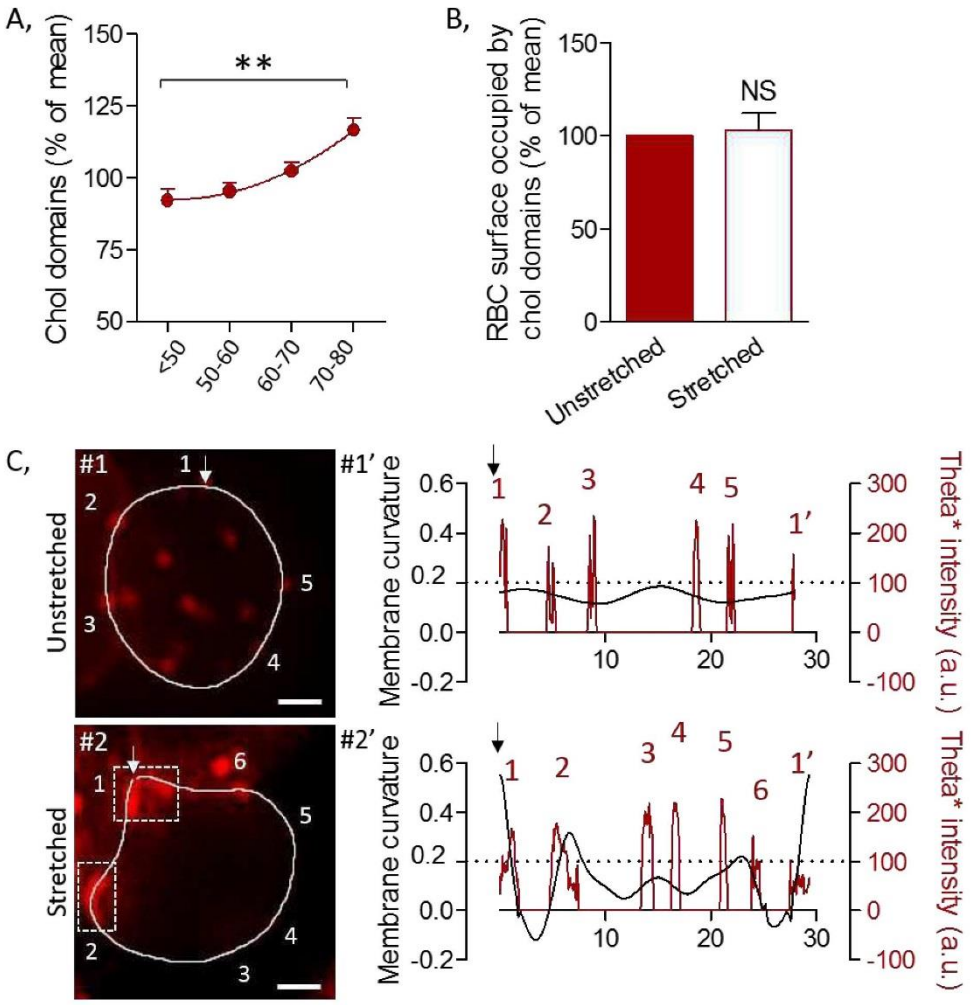

Suppl. Fig 3 Chol-enriched domains are modulated in size and distribution under RBC mechanical stimulation. (A) Chol-enriched domain abundance at 20°C upon increased spreading on PLL. (B, C) RBCs labeled for chol at 20°C and stretched in PDMS chambers. (B) Chol-enriched domain surface occupation of hemi-RBC in unstretched condition and under stretching in PDMS chambers. (C) Recruitment of chol-enriched domains in increased curvature areas of the RBC edges upon stretching (#2, #2' *vs* #1, #1'). *Panels B and C are adapted from [28]. Scales bars 2 µm.*

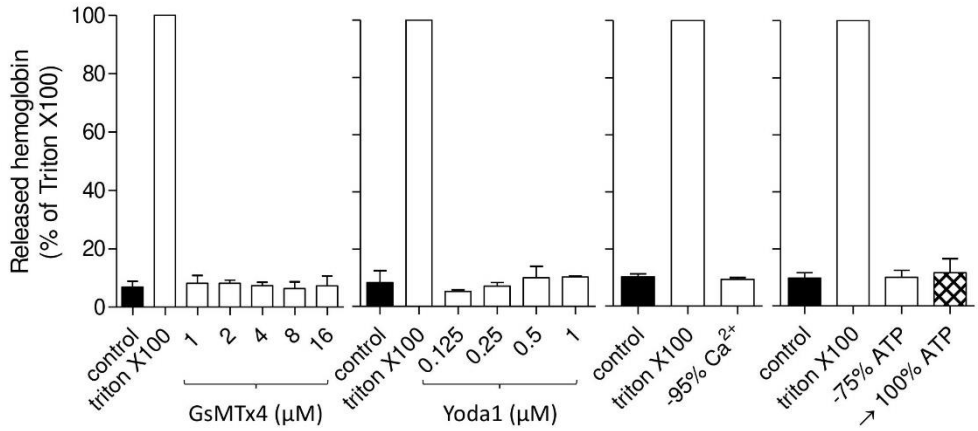

Suppl. Fig 4 Pharmacological agent innocuity. Released hemoglobin by RBCs either untreated (full bars) or incubated in (i) GsMTx4-containing medium, (ii) Yoda1-containing medium, (iii) Ca^{2}-free medium supplemented with EGTA followed or not by repletion in Ca^{2+}-containing medium, and (iv) glucose-depleted medium followed or not by repletion in glucose-containing medium. Results are expressed as percentage of full hemolysis obtained by 0.5 % Triton X100.

Results

4. Pathological RBCs (elliptocytosis)-
PUBLICATION 4

Alteration of membrane lipid composition and distribution impairs calcium exchange in elliptocytosis – A severe case study

H. Pollet[1], **L. Conrard[1]**, A.S. Cloos[1], A. Paquot[2], A. Stommen[1], M. Ghodsi[1], M. Carquin[1], C. Léonard[1], M. Guthmann[1], M. Lingurski[1], C. Vermylen[3], M. Rider[4], S. Pyr dit Ruys[4], D. Vertommen[4], M. Vikkula[5,6], P. Brouillard[5], P. Van Der Smissen[1], G.G. Muccioli[2] and D. Tyteca[1]

Université catholique de Louvain, 1200 Brussels, Belgium [1] CELL Unit & PICT imaging Platform, de Duve Institute [2] Bioanalysis and Pharmacology of Bioactive Lipids Research Group, Louvain Drug Research Institute [3] PEDI Unit, Institut de Recherche Expérimentale et Clinique & Saint-Luc Hospital [4] PHOS Unit, de Duve Institute [5] Human Molecular Genetics, de Duve Institute [6] Walloon Excellence in Life Sciences and Biotechnology (WELBIO), de Duve Institute

Corresponding author: Donatienne Tyteca, CELL Unit, de Duve Institute, Université catholique de Louvain, UCL B1.75.05, avenue Hippocrate, 75, B-1200 Brussels, Belgium. Phone: +32-2-764.75.91; Fax: +32-2-764.75.43; e-mail: donatienne.tyteca@uclouvain.be

Keywords : red blood cell fragility, spectrin cytoskeleton, calcium, PIEZO1, PMCA, lipid domains, membrane asymmetry, reactive oxygen species, oxidized lipids, polyunsaturated fatty acids, cell fragmentation, cholesterol, ascorbic acid, amitriptyline

Running title: RBC membrane impairment in elliptocytosis

Abstract

Hereditary elliptocytosis is a red blood cell (RBC) disease mainly caused by mutations in spectrin, leading to cytoskeletal destabilization. Although patients with heterozygous mutation in α-spectrin (SPTA1) are asymptomatic, morphological changes and hemolysis are observed upon reduced production of functional α-spectrin. The molecular mechanism is unknown. We analyzed the consequences of a α-spectrin mutation in a patient almost exclusively expressing the Pro260 variant of SPTA1 (pEl) and her asymptomatic mother. In pEl, RBC size and circularity are decreased, deformability is impaired and calcium exchanges through the mechanosensitive cation channel PIEZO1 and the efflux pump PMCA are altered. This results from four mechanisms. First, the abundance of those calcium transport proteins is decreased. Second, the intracellular calcium content is stronly increased, leading to increased calmodulin membrane association, calpain activity, PKC-dependent protein phosphorylation and reactive oxygen species production, and thereby inactivating PMCA. Third, the pEl membrane exhibited a decreased content in long unsaturated phosphatidylserine and phosphatidylcholine species and increased levels of lipid peroxidation and lysophosphatidylserine, which abrogates calcium entry. Fourth, the two populations of lipid domains associated with RBC low curvature areas are modified in abundance, cholesterol content and response to stimulation of calcium exchanges. Altogether, this study shows how cytoskeleton alteration, calcium accumulation/signaling as well as membrane lipid composition, biophysical properties and lateral distribution in lipid domains cooperate to impair calcium exchanges upon RBC deformation. It also provides the first evidence that α-spectrin defect leads to alteration of membrane lipid composition and distribution and could help develop novel therapies.

Results

Introduction

During its lifetime, the red blood cell (RBC) undergoes high deformations needed to pass through narrow capillaries to deliver oxygen to tissues. Such exceptional deformability relies on intrinsic features, including (i) a biconcave shape due to the excess of plasma membrane (PM) surface *vs* the cytoplasmic volume, (ii) a finely regulated cytoplasmic viscosity controlled by the hemoglobin concentration, and (iii) a cytoskeleton composed of a meshwork of spectrin tetramers linked to the membrane by two anchorage complexes based on 4.1R and ankyrin proteins [1]. RBC deformation is also associated with a transient intracellular calcium increase, which activates Gardos channels, leading to cell dehydration, and favors a local membrane:cytoskeleton uncoupling [2]. RBC calcium entry is mostly operated by mechano-activated ion channels like PIEZO1 [3], whereas calcium efflux is ensured by the PM calcium ATPase (PMCA), in a tightly regulated process. RBC deformation also depends on ATP content and antioxidant system which allows to neutralize the harmful reactive oxygen species (ROS) generated through the constant exposure to variable oxygen pressures [4].

The RBC membrane exhibits a very high cholesterol (chol)/phospholipid ratio and three types of lipid domains involved in its deformation [5-10]. The first ones, associated with high-curvature membrane areas, are mainly enriched in chol and gather upon RBC deformation. The second ones, associated with RBC low-curvature areas, are enriched in ganglioside GM1, phosphatidylcholine (PC) and chol. Their abundance increases upon PIEZO1 activation. The third ones, also associated with low-curvature areas, are enriched in sphingomyelin (SM), PC and chol. Their abundance rises upon calcium extrusion [5, 11].

RBC deformability and lifespan are altered in inherited RBC disorders, leading to chronic hemolytic anemia [12-14]. Contrary to other hemolytic anemias, elliptocytosis is asymptomatic in 90% of cases, leading to prevalence underestimation [15]. This group of heterogeneous diseases affecting α-spectrin-, β-spectrin- or 4.1R-coding genes is inherited in an autosomal dominant manner, with rare cases of *de novo* mutations. The only treatments are folate therapy, transfusions and splenectomy [16, 17].

A recent simulation study has revealed that elliptocytotic RBCs are unable to recover their original biconcave shape after passing through splenic interendothelial slits due to impaired elasticity, leading to fragmentation when the RBC cytoskeleton connectivity is lower than 20% [18]. However, the relevance of this model remains to be tested *in vitro*. Hence, the molecular mechanism is still unknown. In this study, we explored these questions by analyzing the morphology, deformability, cytoskeleton organization, calcium exchange and membrane composition and organization of RBCs from a female teenager diagnosed for elliptocytosis during infancy (pEl). She underwent cholecystectomy, required to

eliminate the cholelithiases accumulating in the gall bladder, but no splenectomy. Throughout the study period, pEl blood samples exhibited hemolysis markers, high reticulocyte count and low RBC mean corpuscular volume. The RBC mean corpuscular hemoglobin concentration and the RBC abundance were less affected (Figure S1A-F). None of her relatives consulted for similar symptoms nor were diagnosed but her mother nevertheless appeared midly affected (pElm).

Materials and methods

Blood collection and preparation. The study was approved by the Medical Ethics Committee of the University of Louvain, Brussels, Belgium. Blood was collected by venipuncture into K^+/EDTA-coated tubes from healthy volunteers (17 adults, 1 child), the patient (pEl) and her mother (pElm) who gave written informed consent. pEl blood samples were analyzed every 3-6 months from her 14 to 18 years, while pElm came only 3 times. Before experiments blood was diluted 10-fold in glucose- and HEPES (*N*-2-hydroxyethylpiperazine-*N*'-2-ethanesulfonic acid)-containing medium (Invitrogen) and washed twice by centrifugation at 200g for 2min and resuspended. Experiments were carried out on blood maintained for < 5 days at 4°C, except for storage studies.

Chemical treatments. All treatments, except amitriptyline, were performed on diluted washed RBCs. To activate PIEZO1, RBCs were incubated with 0.5µM Yoda1 (Biotechne) for 20sec at RT. To inhibit Cav channels, RBCs were incubated with 1µM ω-agatoxin (Alomone Labs) for 20min at RT. To inhibit NMDARs, RBCs were incubated with 50µM memantine for 90min at 37°C. To modulate the intracellular calcium content, RBCs were preincubated at RT either in a calcium-free medium containing 1mM of the calcium-chelating agent EGTA (Sigma-Aldrich) for 10min or with 20-40µM BAPTA-AM (Abcam) for 60-90min at 37°C. To activate protein kinase C (PKC), RBCs were preincubated with 6µM phorbol 12-myristate 13-acetate (PMA; Sigma-Aldrich) and 20nM calyculin A (CalA; Sigma-Aldrich) for 20min at 37°C. For chol depletion, RBCs were preincubated with 0.9mM methyl-β-cyclodextrin (mβCD; Sigma-Aldrich) for 30min at 37°C. To decrease oxidative stress, RBCs were preincubated with 1mM ascorbic acid for 1h at 37°C. For the plasmatic acid sphingomyelinase (aSMase) inhibition, whole blood was incubated with 5µM amitriptyline (Sigma-Aldrich) for 1h at 37°C, then diluted and washed as above. Only EGTA and PMA/CalA were maintained during the whole experiment. To insert lysoPS (Sigma) at the membrane, RBCs were treated with 3µM of the lysoPLP for 40min at RT.

Results

Membrane lipid vital imaging. Endogenous chol labeling (Theta* at 20°C) and BODIPY-lipid membrane insertion (BODIPY-SM, -PC and -ceramide at RT *vs* -GM1 at 37°C) were performed as in [5]. For co-labeling, RBCs were first incubated with Theta* then with BODIPY-lipids. RBCs were either spread onto poly-L-lysine (PLL)-coated coverslips and placed upside down in Lab-Tek chambers (ThermoFisher) or dropped to settle down in µ-Slide VI0.4 uncoated IBIDI chambers (Proxylab), both filled with medium. Samples were observed either with a Zeiss LSM510 confocal microscope (plan-Apochromat 63X 1.4 oil objective) or a Zeiss wide-field fluorescence microscope (Observer.Z1; plan-Apochromat 100X 1.4 oil Ph3 objective).

Calcium, ATP and reactive oxygen species measurements. Intracellular calcium was measured as previously [11]. Calcium exchanges upon RBC deformation were evaluated on RBCs spread onto a PLL-precoated polydimethylsiloxane stretchable chamber (PDMS; Strex Inc) as in [5]. Intracellular ATP content was measured using a chemiluminescence assay kit (Abcam). Intracellular reactive oxygen species (ROS) content was determined on RBCs incubated in suspension with 15µM 2',7'-dichlorodihydrofluorescein diacetate (H_2DCFDA; Invitrogen) in Krebs-Ringer medium for 60min at 37°C. RBCs were then pelleted, resuspended and measured by spectrofluorimetry (GloMax; Promega) at $\lambda_{exc}/\lambda_{em}$ of 490nm/520nm. Data were reported on the mean corpuscular value (MCV).

Lipid measurements. Total phospholipids were evaluated by phosphorus assay after lipid extraction [19]. Chol content, sphingosine kinase activity and lipid peroxidation were assessed using the following assay kits: Amplex Red chol (Invitrogen) [9, 20], luminescence (Echelon) [21] and malondialdehyde (Abcam) [22]. Phospholipids, chol and malondialdehyde levels were reported on the hemoglobin content. Plasmatic aSMase activity was evaluated on plasma freshly isolated after ficoll separation using the SMase kit (Abcam) [20].

Additional information. See supplemental Methods or contact donatienne.tyteca@uclouvain.be.

Results

The patient pEl expresses the Pro260 variant of SPTA1. NGS sequencing of pEl unravelled two heterozygous nucleotide substitutions in *SPTA1*, the gene encoding α-spectrin, resulting in a Leucine-to-Proline change (*c.779T>C*; p.Leu260Pro) and a premature stop codon (*c.5431C>T*; p.Arg1811*) (Figure 1A, Table). The *c.779T>C* (Leu260Pro) change was inherited from the mother (pElm), as confirmed by direct RNA sequencing (Figure 1A, bottom left). In pEl, the C-allele (corresponding to proline) was predominant at position c.779, with almost complete loss of the T-allele (corresponding to leucine). This is likely due to degradation by nonsense-mediated mRNA decay of the RNA of the paternal allele carrying the premature stop codon (Figure 1A, bottom right). Reduced quantity of the paternal mRNA allele was confirmed by sequencing a common polymorphism, which was heterozygous in pEl DNA (*c.525C*>A; p.Ala1764Ala; Figure 1A, Table) but squewed in its RNA (Figure 1A, bottom center). Based on these results, the phase of the alleles was deduced (Figure 1A, bottom), showing that pEl expressed mainly the proline-mutated allele inherited from her mother. In contrast, her second allele (presumably paternal, not available for testing), carrying the premature stop codon (p.Arg1811*), as well as the A-allele of the polymorphism at position *c.5292*, was degraded. Thus, at the protein level, pEl should almost exclusively express the Pro260 variant of SPTA1. This Pro260 variant has already been described in the literature [23-25] but consequences for the RBC morphology and deformability were not evaluated.

Results

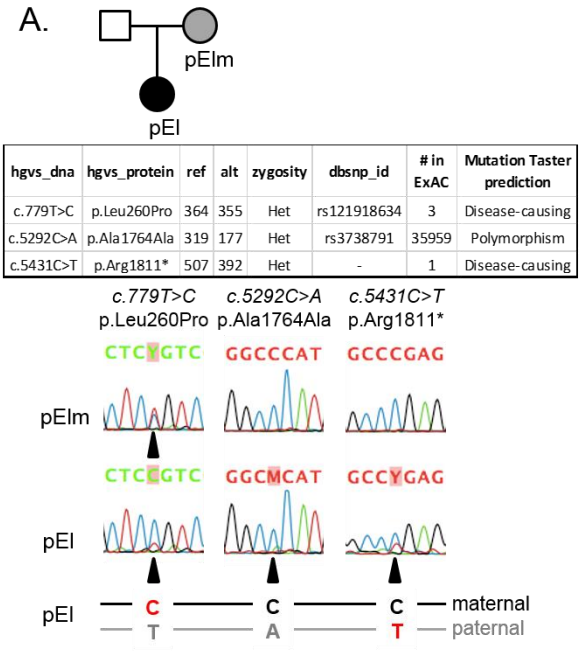

hgvs_dna	hgvs_protein	ref	alt	zygosity	dbsnp_id	# in ExAC	Mutation Taster prediction
c.779T>C	p.Leu260Pro	364	355	Het	rs121918634	3	Disease-causing
c.5292C>A	p.Ala1764Ala	319	177	Het	rs3738791	35959	Polymorphism
c.5431C>T	p.Arg1811*	507	392	Het	-	1	Disease-causing

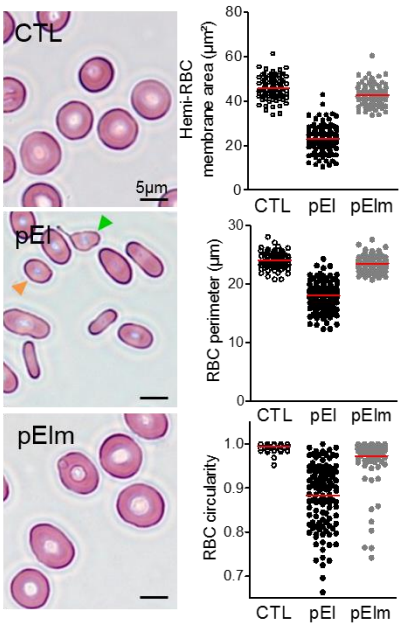

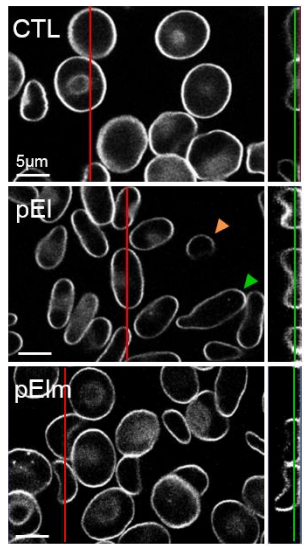

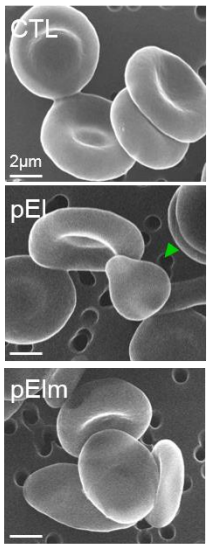

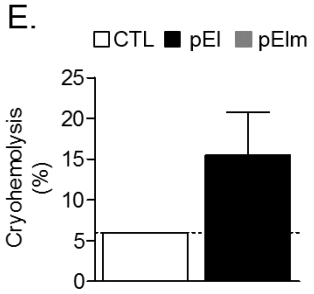

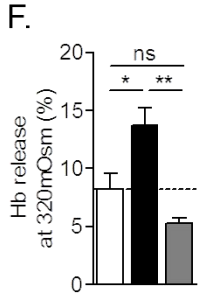

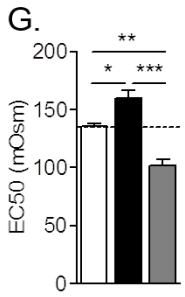

Figure 1. Pedigree, genetic defects and RBC morphology and fragility of the family enrolled in the study. (A) Pedigree and genetic defects. Affected patient (pEl) and her mother (pElm), partially affected but not diagnosed. Table, NGS results for pEl showing coverage (ref, reads with reference allele; alt; alternative allele), zygosity, code in dbSNP, number of occurrences in control population (The Exome Aggregation Consortium) and impact prediction from Mutation Taster, for two likely mutations and one heterozygous polymorphism. Sequences, RNA sequencing showing partial loss of the allele carrying the premature Stop codon (T-allele at position 5431) in pEl. pElm is heterozygous for Leu260Pro, whereas pEl is almost homozygous for the C at position 779 (Proline) and at position 5292, due to degradation. Y = T or C; M = C or A. **(B)** RBC membrane hemi-area, perimeter and circularity determined on May-Grünwald Giemsa-stained blood smears. Left, representative images; green arrowhead, poïkilocytotic RBC; orange arrowhead, small spherical RBC. Right, quantification for one representative blood smear (n=3; CTL *vs* pEl, ***; CTL *vs* pElm, ns; pEl *vs* pElm, ***). **(C,D)** RBC biconcavity evaluated on RBCs in suspension. (C) RBCs labeled with a BODIPY-lipid, laid down in IBIDI chambers and analyzed by vital confocal microscopy. The figure shows in left panels X-Y sections (positions indicated by the green lines in the right panels) and in right panels the corresponding X-Z sections (positions indicated by the red lines in the left panels). (D) RBCs fixed in suspension, laid down on filters and analyzed by scanning electron microscopy. Images are representative of 2 independent experiments at both C and D. Green arrowheads, poïkilocytotic RBCs; orange arrowhead, small spherical RBC. **(E-G)** RBC fragility evaluated in hyper- (E), iso- (F) and hypotonic media (G). (E) Cryohemolysis (mean ± SEM of 6 independent experiments). (F,G) Hemoglobin released in isosmotic medium and half-maximal effective osmolarity (EC50) determined upon RBC incubation in decreasing osmolarity media (means ± SEM of 3-4 independent experiments). For evolution of these parameters with time, see Figure S1G-J.

pEl RBCs exhibit decreased size and circularity and increased fragility but normal biconcavity and low microvesicle release. Blood smears of pEl revealed anisocytosis dominated by small elliptic RBCs (Figure 1B, orange arrowhead). The decreased projected membrane area, perimeter and circularity of pEl RBCs were shown by quantification on blood smears (Figure 1B, right) and poly-L-lysine (PLL)-coated coverslips (Figure S2), the system used below to analyze membrane organization. Poïkilocytosis was also observed, but to a lower extent (Figure 1B, green arrowhead). At first glance, blood smears of pElm appeared normal. However, quantification revealed a larger distribution of RBC circularity, suggesting the presence of elliptic RBCs as in pEl (Figure 1B, right). The decreased surface area and circularity of pEl RBCs were maintained throughout the 4-year study and did

not result from pEl young age since no difference can be seen between healthy donors whatever their age (Figure S1G,H & S3A-C).

Confocal microscopy on living suspended RBCs and scanning electron microscopy on fixed RBCs laid down on filters revealed that pEl and pElm elliptic cells preserved their biconcavity (Figure 1C,D). Moreover, the progressive appearance of echinocytes and spherocytes upon storage were delayed in pEl and pElm as compared to healthy donors. In addition, microvesicles isolated from pEl and pElm blood were less abundant than those from control blood (Figure S4A-D). These data indicated that, in contrast to RBCs upon storage at 4°C and from hemolytic anemias [14, 26], elliptocytotic RBCs appeared preserved from microvesiculation.

Cryohemolysis and hemoglobin release in iso- or hypotonic media were increased in pEl *vs* healthy donors but changed during the study period (Figure 1E-G; S1I,J & S5A). Surprisingly, pElm RBCs showed lower hemoglobin release and EC50 than healthy RBCs (Figure 1F,G). Altogether, those data indicated that pEl RBCs presented decreased size and circularity *vs* increased fragility, but preserved their biconcavity.

Cytoskeletal and membrane protein membrane association and lateral segregation are decreased whereas hemoglobin membrane retention is increased in pEl. Hemoglobin was more retained in the pEl than healthy or pElm ghost membrane (Figure S6). In contrast, cytoskeletal proteins, except the β-Tubulin, and membrane proteins exhibited a two-fold decreased association with the pEl ghost membrane than in healthy donors (Figure 2).

We then assessed whether abnormal protein association with membrane could result from alteration of the spectrin cytoskeleton organization. At the microscale level, spectrin occupancy was significantly decreased neither in pEl nor in pElm (Figure 3A,B). In contrast, the variation of the labeling intensity was greatly increased in pEl RBCs (Figure 3C), showing spectrin gathering at one cell edge in ~75% of pEl RBCs *vs* ~20% in pElm and ~5% in healthy RBCs (Figure 3A, arrowheads). Spectrin gathering was confirmed by eletron microscopy in pEl (Figure S7, arrowheads) and was exacerbated upon storage of pEl and pElm RBCs (Figure S4E), suggesting microvesiculation-independent changes upon RBC storage in elliptocytosis. Moreover, at the nanoscale level, less dense areas alternating with darker ones were revealed in pEl RBCs (Figure 3D, red areas), suggesting reorganization of the cytoskeleton:membrane anchorage complexes.

These observations were confirmed by RBC immunolabeling for glycophorin C (GPC) and CD47, respectively enriched in the 4.1R- and the ankyrin-based complexes. First, ~40% of pEl RBCs presented at one edge a stronger labeling for both CD47 and GPC *vs* only ~10% in control and pElm RBCs (Figure 3E, arrowhead; Figure S8). Second, the spatial dissociation between CD47- and GPC-enriched

clusters was significantly decreased in pEl but not in pElm RBCs (Figure 3F,G). Thus, pEl exhibited defects in spectrin organization, altering membrane protein distribution and raising hemoglobin membrane association.

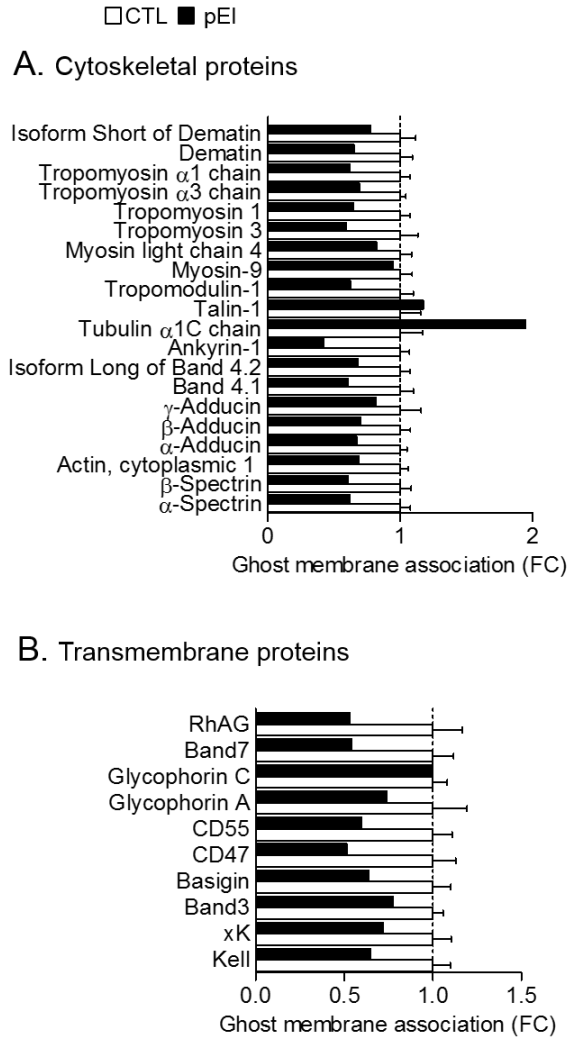

Figure 2. Except tubulin-1C, talin-1, myosin-9 and glycophorin C, all cytoskeletal and membrane proteins exhibit a decreased association with pEl ghost membrane. Association of cytoskeletal (A) and membrane (B) proteins evaluated by mass spectrometry on ghost membranes of pEl vs healthy donors. Data are expressed as fold changes (FC) of protein ghost membrane association in pEl (black colums) vs the mean of 6 healthy donors (open columns) and are representative of 2 independent experiments.

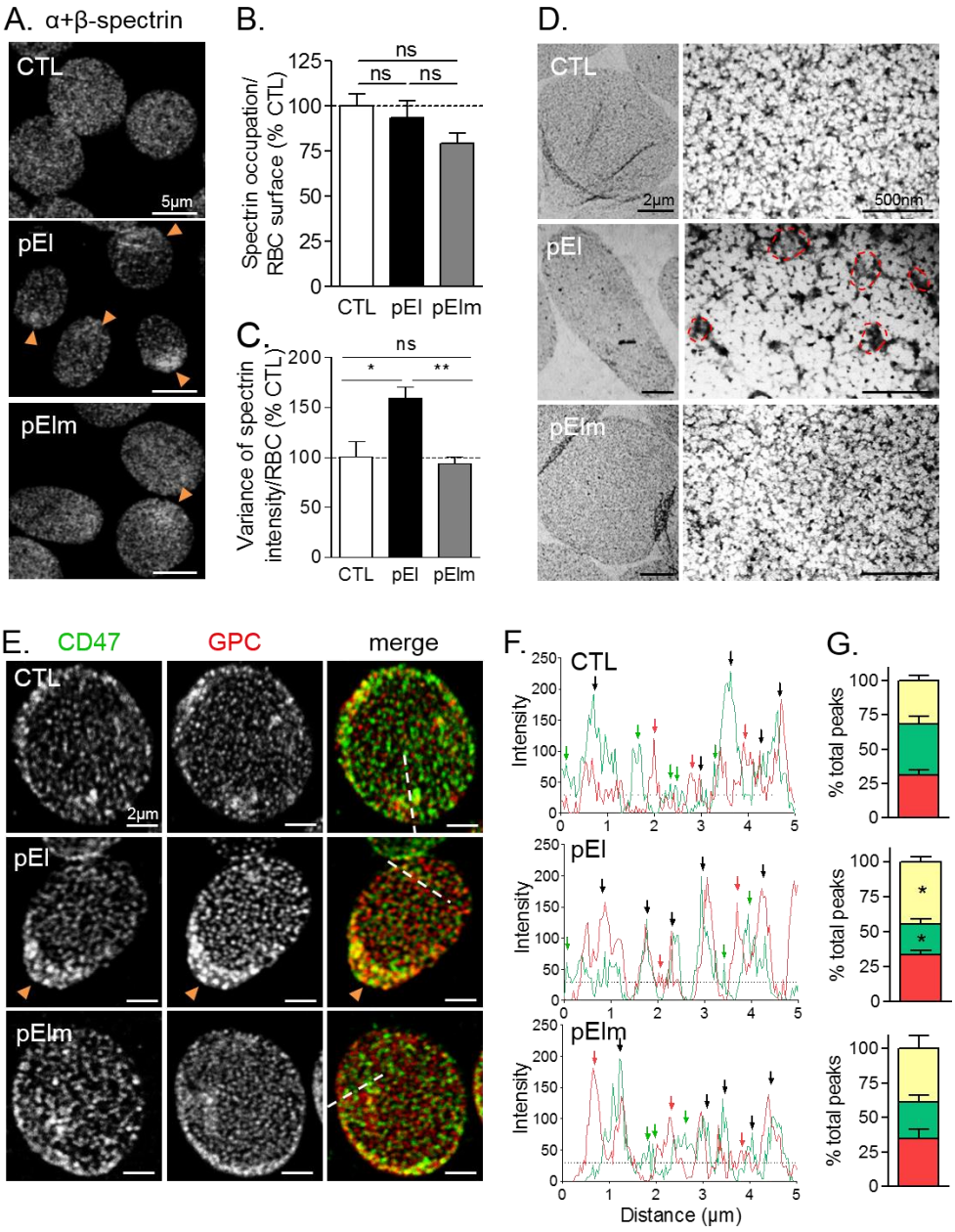
A. α+β-spectrin
CTL
5µm
pEl
pElm
B.
Spectrin occupation/ RBC surface (% CTL)
ns
ns
ns
125
100
75
50
25
0
CTL
pEl
pElm
C.
Variance of spectrin intensity/RBC (% CTL)
ns
*
**
200
150
100
50
0
CTL
pEl
pElm
D.
CTL
2µm
500nm
pEl
pElm
E.
CD47
GPC
merge
CTL
2µm
pEl
pElm
F.
CTL
pEl
pElm
Intensity
250
200
150
100
50
0
0
1
2
3
4
5
Distance (µm)
G.
% total peaks
100
75
50
25
0
*
*

Figure 3. **The spectrin network is hetereogeneous and membrane proteins from the two anchorage complexes show a decreased spatial segregation in pEl RBCs. (A-D)** Spectrin network analyzed by confocal (A-C) and transmission electron microscopy (D). RBCs were laid down on PLL-precoated coverslips (A-C) or formvar coated grids (D), permeabilized with 0.5% Triton X-100, fixed and stained with anti-pan spectrin antibodies (A-C) or not (D). (A,D) Representative images. Orange arrowheads at A and red areas at D, increased cytoskeleton density. (B,C) Quantification of spectrin occupation and dispersion on confocal images. Data are expressed by reference to the mean of control RBCs from the same experiment (means ± SEM from 5 independent experiments with 50-150 RBCs measured/condition). **(E-G)** Membrane protein distribution determined by confocal imaging. RBCs were laid down on PLL-precoated coverslips, fixed and stained with antibodies against CD47 (ankyrin complexes; green) and glycophorin C (GPC; 4.1R complexes; red). (E) Representative images. Orange arrowhead, high protein density. (F) Representative intensity profiles along the paths indicated at E by white dotted lines. Green arrows, CD47 only; red arrows, GPC only; black arrows, CD47/GPC overlapping. (G) Quantification of the abundance of CD47, GPC and CD47/GPC-overlapping peaks (yellow portion of the columns) determined on 30-40 profiles per condition generated from 3 independent experiments (expressed as percentage of total peaks from all the profiles; means ± SEM).

Lipid domains in pEl RBCs are altered in abundance and response to calcium exchange stimulation. We then asked whether alteration of cytoskeletal and membrane protein content and segregation could in turn affect membrane lipid lateral distribution into domains previously evidenced by our group both in low- and high-curvature RBC areas [5, 11]. The abundance of low curvature-associated SM- and PC-enriched domains was significantly increased in pEl RBCs as compared to healthy donors (Figure 4A, orange arrowheads; Figure 4B & S3D,E). In contrast, chol-enriched domains were not visible in the pEl RBC low-curvature areas but well associated with the high-curvature ones (Figure 4A, orange *vs* green arrowheads), resulting into a slight decrease of the total chol-enriched domain abundance (Figure 4B).

To assess lipid domain functionality, we used the PIEZO1 agonist Yoda1 to stimulate calcium influx and the extracellular calcium EGTA to deplete intracellular calcium [5, 11]. We observed that GM1-enriched domains did not increase upon Yoda1 in pEl contrasting with a 2-fold increase in controls. Moreover, SM-enriched domains increased by less than ~2-fold upon EGTA in pEl *vs* ~3-fold increase in controls (Figure 4C,D). Those data suggested that lipid domains were altered for their response to calcium exchange stimulations.

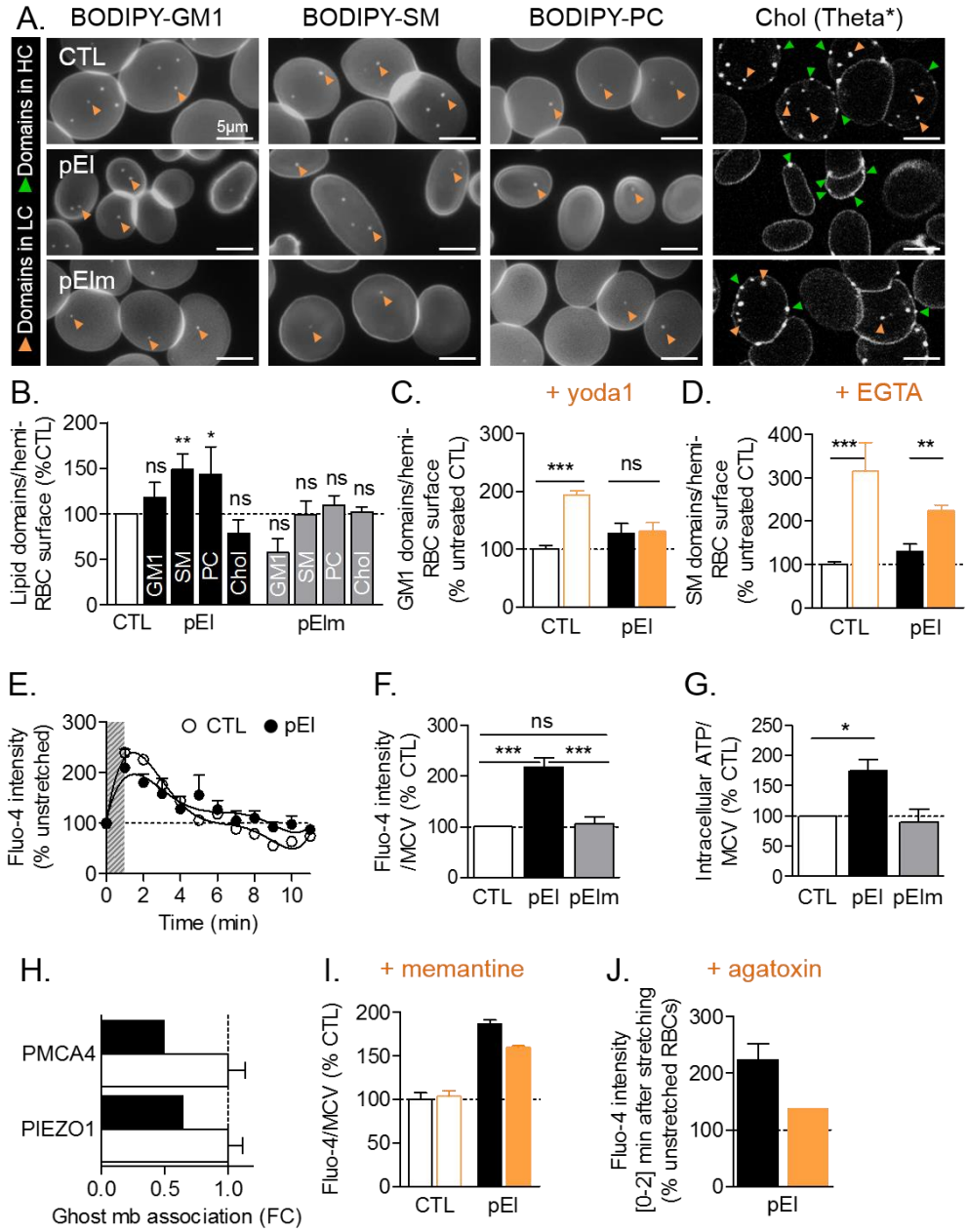
A.
BODIPY-GM1
BODIPY-SM
BODIPY-PC
Chol (Theta*)
Domains in HC
Domains in LC
CTL
pEI
pEIm
5µm
B.
Lipid domains/hemi-RBC surface (%CTL)
GM1
SM
PC
Chol
CTL
pEI
pEIm
C.
+ yoda1
GM1 domains/hemi-RBC surface (% untreated CTL)
D.
+ EGTA
SM domains/hemi-RBC surface (% untreated CTL)
E.
Fluo-4 intensity (% unstretched)
CTL
pEI
Time (min)
F.
Fluo-4 intensity /MCV (% CTL)
G.
Intracellular ATP/ MCV (% CTL)
H.
PMCA4
PIEZO1
Ghost mb association (FC)
I.
+ memantine
Fluo-4/MCV (% CTL)
J.
+ agatoxin
Fluo-4 intensity [0-2] min after stretching (% unstretched RBCs)

Figure 4. Lipid domains are impaired in abundance and response to calcium exchange stimulation in pEl RBCs and the intracellular calcium content is raised. (A,B) Lipid domains on RBCs at resting state. RBCs were either spread onto PLL-coated coverslips and labeled with BODIPY-GM1, -SM or -PC or labeled in suspension with Theta* and spread onto coverslips. All coverslips were directly visualized by vital fluorescence/confocal microscopy. (A) Representative images. Green arrowheads, domains in high curvature areas (HC); orange arrowheads, domains in low curvature areas (LC). (B) Quantification of lipid domain abundance per hemi-RBC area (means ± SEM from 3-19 independent experiments/lipid in which 300-600 RBCs were counted/experiment). **(C,D)** Abundance of lipid domains upon modulation of calcium influx stimulation (C, addition of Yoda1 just after labeling) or calcium depletion (D, incubation with EGTA). Data represent lipid domain abundance per hemi-RBC area (means ± SEM from 3-5 independent experiments/lipid in which 300-600 RBCs were counted per condition in each experiment). **(E)** Calcium exchange during RBC deformation on PDMS chambers. RBCs were labeled for calcium with Fluo-4 AM and measured for fluorescence intensity before (0min) and after stretching for 1min (grey stripped zone). Data are expressed as percentage of unstretched RBCs (means ± SEM of 5 experiments where 150-200 RBCs were analyzed at each time). **(F)** RBC intracellular calcium content evaluated by Fluo-4 AM and expressed by reference to the mean corpuscular volume (MCV; means ± SEM of 5-9 independent experiments). **(G)** Intracellular ATP content measured by luminescence after RBC incubation with luciferase and luciferin and expressed by reference to MCV (means ± SD/SEM of 2-4 independent experiments). **(H)** Association of PIEZO1 and PMCA4 with ghost membranes evaluated by mass spectrometry. Data are expressed as fold changes (FC) in pEl by reference to 6 healthy donors (representative of 2 independent experiments). **(I)** RBC intracellular calcium content upon NMDAR inhibition by memantine treatment and evaluated by Fluo-4 AM. Data are expressed by reference to the mean corpuscular volume (MCV; means ± SEM of 1 experiment). **(J)** Calcium entry shortly (0-2 min) after healthy RBC stretching in PDMS chambers performed as in (E) upon Cav channels inhibition by ω-agatoxin treatment (1 experiment).

To rule out aspecific effects of Yoda1 and EGTA, we then evaluated calcium exchanges upon RBC deformation in stretchable PDMS chambers [5, 27]. Control RBCs exhibited a rapid calcium raise followed by initial content restoration within 5min, whereas pEl RBCs showed a more flat calcium response with both a decrease of entry and a delay of exit (Figure 4E). We concluded that low curvature-associated lipid domains were less prone to respond to calcium exchange stimulation.

Results

The intracellular calcium content is increased in pEl. Based on calcium exchange impairment in pEl RBCs and since an increased calcium content is often described in patients with sickle cell disease, thalassemia or spherocytosis [26], the intracellular calcium content was measured at resting state. The calcium content was increased by ~2-fold in pEl but not in pElm as compared to the healthy donors (Figure 4F & S5B). The intracellular ATP content increase in pEl RBCs excluded the possibility that calcium accumulation resulted from ineffective extrusion due to disruption of the ATP pool fueling the PMCA (Figure 4G). In contrast, the decreased abundance of PIEZO1 and PMCA4 (one of the two PMCA isoforms found in RBCs [28]) associated with the ghost membrane in pEl RBCs (Figure 4H) could partially explain this accumulation. Indeed, upon memantine and ω-agatoxin treatments (to respectively inhibit NMDAR and Cav channels [29, 30]), the intracellular calcium content in pEl decreased by 25% and 90% respectively, indicating that Cav, and to a minor extent NMDAR, appeared to take over, leading to calcium accumulation (Figure 4I,J).Importantly, memantine allowed to reduce hemolysis (data not shown), suggesting that calcium accumulation contributed to the disease.

We concluded that elliptocytotic RBCs exhibited an increased intracellular calcium content at resting state and a decreased capacity to respond to calcium exchange upon RBC deformation. Since neither lipid domain nor calcium alterations were observed in pElm (Figure 4B,F), we focused on pEl for mechanistics. We suggested that the decreased abundance and functionality of PIEZO1 and PMCA4 at the RBC surface could result from impairment of lipid domain composition, distribution and/or dynamics.

Lipid domains are impaired for their chol content, thereby contributing to calcium accumulation in pEl. To test the above hypothesis, we first explored whether lipid domains could be altered in composition. Double-labeling indicated that GM1- and SM-enriched domains were less colocalized with those enriched in chol in pEl RBCs than in control RBCs (Figure 5A,B & S9). Hence, a ~30% chol depletion by mβCD [31], which induced the disappearance of chol-enriched domains and the decrease of GM1- and SM-enriched domain abundance in both pEl and control RBCs (Figure 5C), led to a ~3-fold increase of the calcium content in pEl RBCs *vs* a ~1.5-fold increase in healthy RBCs (Figure 5D), suggesting a synergistic effect between the lower chol enrichment of lipid domains in pEl and chol depletion by mβCD. Accordingly, mβCD decreased the resistance of pEl RBCs to hemolysis, without any modification on control RBCs (Figure 5E). Thus, alteration of calcium exchanges and decreased resistance to hemolysis of pEl RBCs could be linked to the alteration of the chol enrichment in GM1- and SM-enriched domains.

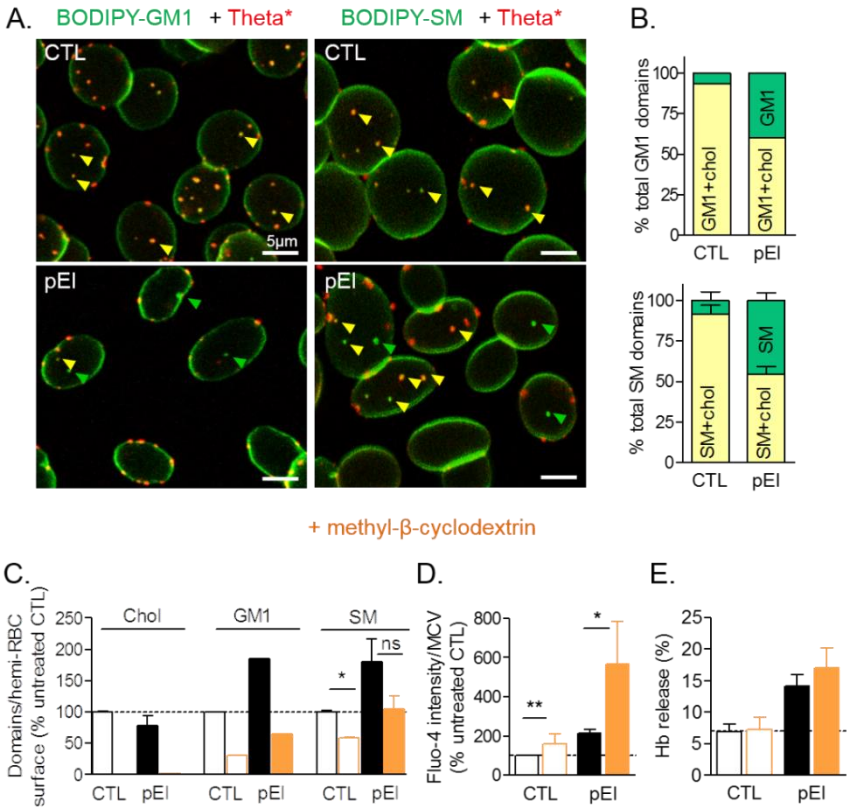

Figure 5. GM1- and SM-enriched domains are dissociated from chol-enriched domains in pEI RBC low-curvature areas, contributing to the calcium accumulation. (A,B) RBCs were labeled in suspension with Theta*, spread onto coverslips and labeled with BODIPY-GM1 or -SM. (A) Representative images. Green arrowheads, BODIPY-GM1 or -SM only; yellow arrowheads, BODIPY-GM1/Theta* or BODIPY-SM/Theta* co-labelled domains. For single channel images, see Figure S9. (B) Quantification of spatial association of GM1- and SM-enriched domains with chol-enriched domains (yellow parts of the columns) (means ± SD/SEM of 2 and 3 independent experiments in which 50-100 RBCs were counted). **(C-E)** Alteration of lipid domains, exacerbation of calcium accumulation and hemolysis upon chol depletion. (C) Abundance of chol-, GM1- and SM-enriched domains in RBCs pretreated with mβCD (means ± SD/SEM of 2-4 independent experiments). (D) Intracellular calcium content measured as in Figure 3F in RBCs incubated with Fluo-4 AM then with mβCD (means ± SEM of 5 independent experiments). (E) Hemoglobin release in the supernatant measured 2min after incubation with mβCD and expressed as percentage of total hemoglobin content in the sample (means ± SEM of 5 independent experiments).

Results

Calcium accumulation and downstream signaling pathways contribute to SM-enriched domain alteration and RBC fragility in pEl. We first tested the possibility that lipid domain impairment resulted from the calcium-dependent upregulation of calmodulin, μ-calpain and protein kinase C (PKC) and/or inhibition of the flippase [2]. We first observed that calmodulin was more associated with the ghost membrane in pEl than in healthy RBCs (Figure 6A). Although calpain membrane association was preserved, its activity was slightly increased, to a similar extent as in RBCs stored for 2 weeks at 4°C (Figure 6A,B). The major targets of PKCs [2] were more phosphorylated in pEl than healthy RBCs, especially PMCA4 (Figure 6C) for which the identified phosphorylation site on serine 328 in the second cytosolic domain was already described. Moreover, upon incubation with phorbol esters in the presence of a phosphatase inhibitor (PMA/CalA), a treatment kown to uncouple membrane:cytoskeleton at 4.1R complexes [6], the abundance of SM-enriched domains increased in healthy RBCs but not in pEl RBCs (Figure 6D), which could suggest PKC upregulation. Accordingly, pEl RBCs exhibited a more than 2-fold increase of intracellular reactive oxygen species (ROS) and this increase was partially restored by intracellular calcium depletion through EGTA treatment (Figure 6E & S5G), suggesting activation of the PKC-activated NADPH oxidase [32].

Surprisingly, phosphatidylserine (PS) exposure at the RBC surface evaluated by flow cytometry using Annexin V was not increased in pEl RBCs and contrasted with the strong increase in RBCs stored for 2 weeks at 4°C (Figure 6F). This could suggest that the flippase inhibition is not amplified in pEl RBCs or that the exposed PS is not recognized by Annexin V (see below).

To therefore evaluate whether the calcium boost in pEl contributes or not to the disease, the intracellular calcium was decreased using the calcium chelator BAPTA-AM and RBCs were evaluated for ROS content and PS exposure as well as lipid domain abundance, circularity and fragility. Although this treatment in pEl RBCs restored the intracellular calcium to normal levels (Figure 6G), it was not able to decrease the PS surface exposure (Figure 6I) and only partially decreased the intracellular ROS content (Figure 6H). Interestingly, a two-fold decreased abundance of SM-enriched domains was observed (Figure 6J), again suggesting that the intracellular calcium increase contributes directly or indirectly to stabilize SM domain in pEl. However, the RBC circularity and fragility were not improved by this treatment (Figure 6K,L).

We concluded that calcium accumulation and downstream signaling contributed to alter SM-enriched domains in pEl, precluding therefore their dynamics needed for RBC shape restoration after deformation [11], but it is not sufficient to explain the disease severity.

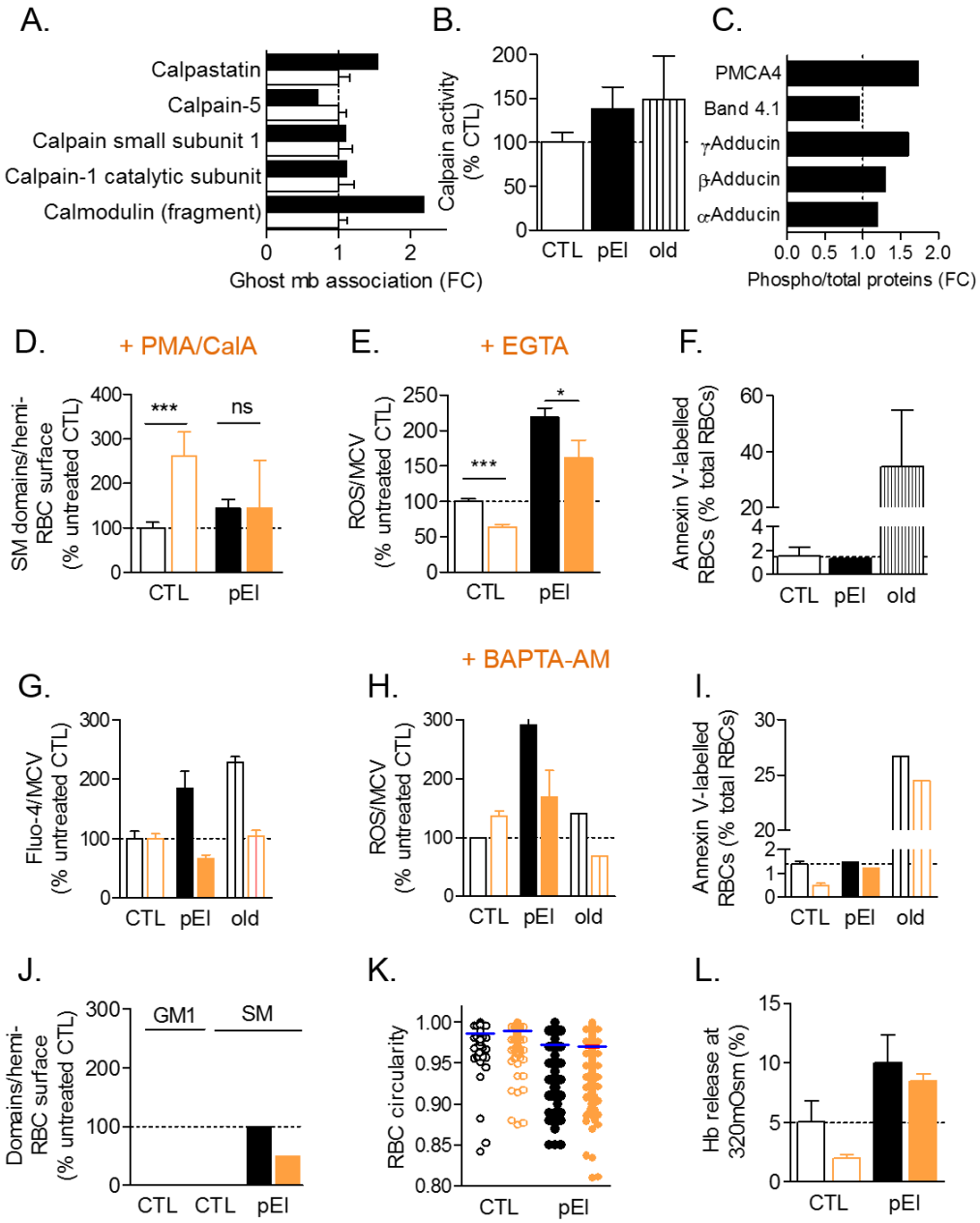
A.
Calpastatin
Calpain-5
Calpain small subunit 1
Calpain-1 catalytic subunit
Calmodulin (fragment)
0
1
2
Ghost mb association (FC)
B.
Calpain activity (% CTL)
200
150
100
50
0
CTL
pEI
old
C.
PMCA4
Band 4.1
γAdducin
βAdducin
αAdducin
0.0 0.5 1.0 1.5 2.0
Phospho/total proteins (FC)
D.
+ PMA/CalA
SM domains/hemi-RBC surface (% untreated CTL)
400
300
200
100
0
***
ns
CTL
pEI
E.
+ EGTA
ROS/MCV (% untreated CTL)
250
200
150
100
50
0
***
*
CTL
pEI
F.
Annexin V-labelled RBCs (% total RBCs)
60
40
20
4
2
0
CTL
pEI
old
+ BAPTA-AM
G.
Fluo-4/MCV (% untreated CTL)
300
200
100
0
CTL
pEI
old
H.
ROS/MCV (% untreated CTL)
300
200
100
0
CTL
pEI
old
I.
Annexin V-labelled RBCs (% total RBCs)
30
25
20
2
1
0
CTL
pEI
old
J.
Domains/hemi-RBC surface (% untreated CTL)
300
200
100
0
GM1
SM
CTL
CTL
pEI
K.
RBC circularity
1.00
0.95
0.90
0.85
0.80
CTL
pEI
L.
Hb release at 320mOsm (%)
15
10
5
0
CTL
pEI

Figure 6. Calcium accumulation and downstream signaling alter SM-enriched domain abundance in pEl RBCs but calcium chelation does improve neither RBC circularity nor fragility. (A) Calcium signaling proteins associated with ghost membranes evaluated by mass spectrometry. Data are expressed as fold changes (FC) in pEl by reference to 6 healthy donors (representative of 2 independent experiments). **(B)** Calpain activity determined by Calpain activity assay kit (mean ± SD of 6 determinations from 2 independent experiments). 15-days old RBCs were used as positive control. **(C)** PKC-dependent phosphorylation of membrane and cytoskeletal proteins determined by mass spectrometry on ghost membranes. The abundance of phosphorylated proteins in pEl is expressed by reference to the corresponding total protein content and then expressed in fold changes *vs* the healthy donor (representative of 2 independent experiments). **(D)** Abundance of SM-enriched domains upon modulation of membrane:cytoskeleton anchorage by PKC activation (incubation with PMA/CalA). Data represent SM-enriched domain abundance per hemi-RBC area (means ± SEM from 3-5 independent experiments/lipid and 300-600 RBCs were counted per condition in each experiment). **(E)** Intracellular ROS level upon calcium depletion. Washed RBCs were incubated with 2',7'-dichlorodihydrofluorescein diacetate (H_2DCFDA) in the presence or not of EGTA to deplete intracellular calcium (means ± SEM of 3 independent experiments). **(F)** Surface exposition of phosphatidylserine (PS) evaluated by flow cytometry on RBCs labeled with Annexin V-FITC. 22-to-25-days old RBCs were used as positive control. Data are means ± SD of 1 to 6 determinations from 1 to 4 experiments. **(G-L)** Effect of calcium chelation by BAPTA-AM on intracellular ROS accumulation, PS surface exposure, lipid domain abundance and RBC circularity and fragility. Diluted blood incubated with BAPTA-AM was washed and assessed**.** (G,H) Intracellular calcium and ROS contents measured as in Figure 4F and 6E (means ± SEM of 1 and 2 independent experiments). (I) PS surface exposure measured as in panel F (means ± SD of 1 independent experiment). (J) Abundance of lipid domains per hemi-RBC area (means ± SEM from 1 independent experiments/lipid and 508-548 RBCs were counted per condition in each experiment). (K) RBC circularity measured as in Figure S2 (representative out of 1 independent experiment). (L) RBC fragility measured in isotonic medium as in Figure 1F (means ± SD of 2 independent experiments).

ROS accumulation and downstream lipid peroxidation contribute to membrane damages and RBC fragility in pEl. As we noticed that the increase of ROS in pEl RBCs was only partially restored by EGTA and BAPTA-AM (see Figure 6E), we tested the hypothesis that the oxidative stress could be also generated in pEl in a calcium-independent manner and could contribute to the disease as well. To this aim, we used ascorbic acid to decrease the intracellular ROS content in both healthy and in

pEl RBCs (Figure S10A). However, this antioxidant did not affect SM-enriched domains and slightly but not significantly modified the abundance of those enriched in GM1 (Figure S10B). Hence, it did restore neither the RBC circularity nor its fragility (Figure S10C,D). This could be due to additional calcium-dependent but ROS-independent enzyme activation, as supported by the inefficiency of ascorbic acid to reduce the calcium level (Figure S10E).

Alternatively, the ROS accumulation could induce membrane changes that could not be reversed by ascorbic acid. For instance, increased ROS levels led to increased membrane lipid peroxidation, as revealed by the increased generation of malondialdehyde (MDA), a product of polyunsaturated fatty acid oxidation [22] (Figure 7A) and ascorbic acid even worsened those membrane damages (data not shown). All those data indicated that the increase of oxidative stress in pEl RBCs resulted from both calcium-dependent and -independent mechanisms and led to membrane damages. Moreover, the specific slight decrease of GM1-enriched domain abundance upon ascorbic acid suggested that oxidative stress could specifically alter the GM1/PC/chol-enriched domains.

Long unsaturated PS and PC species are decreased in abundance while lysoPS accumulates in pEl and the later impairs calcium influx upon RBC deformation. To further test this hypothesis, lipids shown to be associated with those domains (i.e. chol, phosphatidylcholine [33]) or to regulate PIEZO1 activity (i.e. PS [34]) were measured for their abundance, oxidation level and/or hydrolysis products. Total membrane cholesterol content was similar in pEl and healthy RBCs (Figure 7B). Likewise, neither tail-oxidized nor ring-oxidized cholesterol derivatives (respectively mostly formed by enzymatic processses and reactions with free radicals [35]) were modified in pEl, except the 4β-OHC (Figure S11A). Hence, as expected from the above data, the SM membrane content was also similar in pEl and healthy donors (Figure 7C). In contrast, pEl RBCs exhibited a decreased abundance of both PC and PS species, in particular the long and unsaturated ones (Figure 7D,E). Those modifications did not result from an alteration of membrane association of enzymes involved in fatty acid synthesis (Figure S11B). Surpisingly, the oxidized PC species 1-palmitoyl-2-azelaoyl-*sn*-glycero-3-phosphocholine (PAzePC), but not the 1-palmitoyl-2-glutaroyl-*sn*-glycero-3-phosphocholine (PGPC), was strongly decreased in pEl as compared to healthy RBCs (Figure S11C). Moreover, six out of nine lysophosphatidylcholine (lysoPS) species were increased whereas all the lysophosphatidylcholine (lysoPC) species were decreased (Figure 7F,G; S5D,F). To determine whether those alterations could impair PIEZO1 activity, healthy RBCs were incubated with lysoPS and stretched in PDMS chambers. In agreement with impairment of PIEZO1 activity in myoblasts, addition of lysoPS in RBCs led to impaired calcium influx upon RBC deformation (Figure 7H).

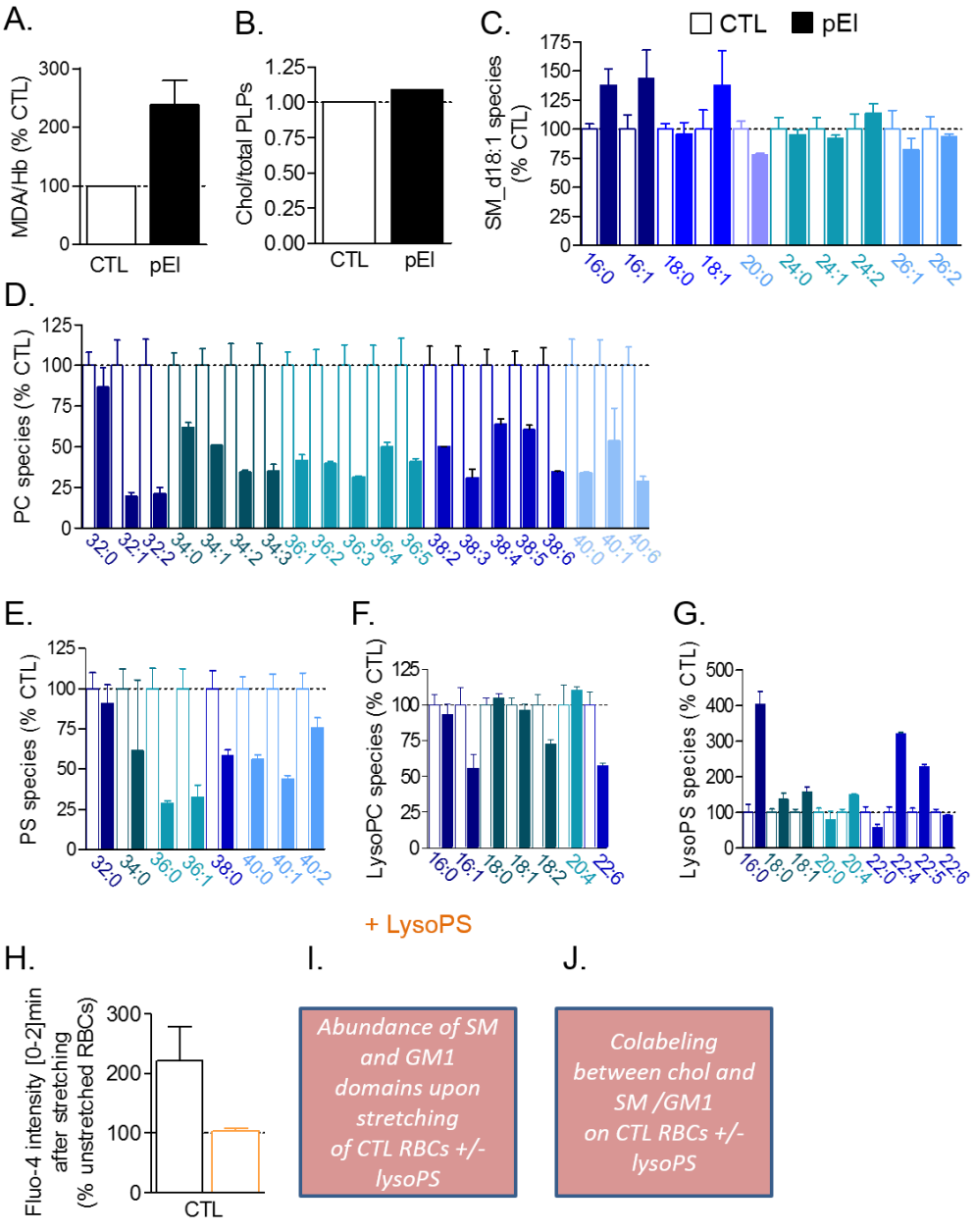
A.
MDA/Hb (% CTL)
300
200
100
0
CTL
pEI
B.
Chol/total PLPs
1.25
1.00
0.75
0.50
0.25
0.00
CTL
pEI
C.
CTL
pEI
SM_d18:1 species (% CTL)
175
150
125
100
75
50
25
0
16:0
16:1
18:0
18:1
20:0
24:0
24:1
24:2
26:1
26:2
D.
PC species (% CTL)
125
100
75
50
25
0
32:0
32:1
32:2
34:0
34:1
34:2
34:3
36:1
36:2
36:3
36:4
36:5
38:2
38:3
38:4
38:5
38:6
40:0
40:1
40:6
E.
PS species (% CTL)
125
100
75
50
25
0
32:0
34:0
36:0
36:1
38:0
40:0
40:1
40:2
F.
LysoPC species (% CTL)
125
100
75
50
25
0
16:0
16:1
18:0
18:1
18:2
20:4
22:6
G.
LysoPS species (% CTL)
500
400
300
200
100
0
16:0
18:0
18:1
20:0
20:4
22:0
22:4
22:5
22:6
+ LysoPS
H.
Fluo-4 intensity [0-2]min after stretching (% unstretched RBCs)
300
200
100
0
CTL
I.
Abundance of SM and GM1 domains upon stretching of CTL RBCs +/- lysoPS
J.
Colabeling between chol and SM /GM1 on CTL RBCs +/- lysoPS

Figure 7. The pEl RBC membrane presents higher lipid peroxidation, lower abundance of long unsaturated PC and PS species and increased content of some lysoPS species, the later abrogating calcium influx. (A) Membrane lipid peroxidation. Washed and lysed RBCs were measured for malondialdehyde (MDA), the natural product of lipid peroxidation which forms an adduct with thiobarbituric acid (TBA). The adduct was then quantified by fluorimetry (means ± SEM of 5 independent experiments). **(B)** Chol content. RBCs were washed, lysed and assessed for chol and total phospholipids. Results are expressed as chol/PLP ratio (mean of 2-3 independent experiments). **(C)** SM content. RBCs were washed, lysed, extracted for lipids and assessed for SM species based on a d18:1 D-erythro-sphingosine backbone by lipidomics (classification based on fatty acid length and insaturation number). Results are expressed as percentage of control RBCs in G (mean of 9 healthy women). **(D-G)** Quantification of PC, PS, lysoPC and lysoPS species. RBCs were washed, lysed, extracted for lipids and measured by lipidomics. Species are classified based on fatty acid length and unsaturation number and results are expressed as percentage of controls (mean of 9 healthy women). **(H)** Calcium entry shortly (0-2 min) after stretching in PDMS chamber upon treatment with lysoPS (mean ± SD of 2 independent experiments). **(I,J)** Abundance of GM1- or SM-enriched domains after stretching in PDMS chamber and spatial relation between GM1- or SM-enriched domains and chol domains upon treatment with lysoPS.

We concluded that several lysoPS species were specifically increased in pEl and could contribute to the disease by impairing calcium influx into RBCs upon deformation. Hence, the decreased total PS content could explain why the extent of PS exposure was not increased in pEl RBCs despite the strong increase in intracellular calcium.

The plasmatic acid SMase modulates the abundance of SM-enriched domains in pEl and contributes to calcium accumulation. We finally asked whether lipid domains could be the target of the plasmatic acid SMase (aSMase), an enzyme known to be activated in Sickle cell disease [36] and which hydrolyses SM into ceramide (Cer), it-self able to compete with chol for the formation of domains with SM [37]. We found that the activity of aSMase was raised in pEl plasma (Figure 8A). Surprisingly, this increase was accompanied by the decrease of nearly all the RBC Cer species measured (Figure 8B). Cer decrease by metabolism into other sphingolipids was precluded, as revealed by the similar decrease of sphingosine content and sphingosine kinase activity in pEl *vs* controls (Figure S11D,E). Cer loss by vesiculation was also excluded as shown by the similar decrease of the different Cer species on vesicles/fragments (Figure S11F). Like other lipids, Cer clustered in domains. Those domains associated with both high and low membrane curvature areas and were increased in pEl (Figure 8C). It remains to be tested whether Cer

could compete with chol in SM-enriched domains, forming domains with altered biophysical properties (Figure 8D).

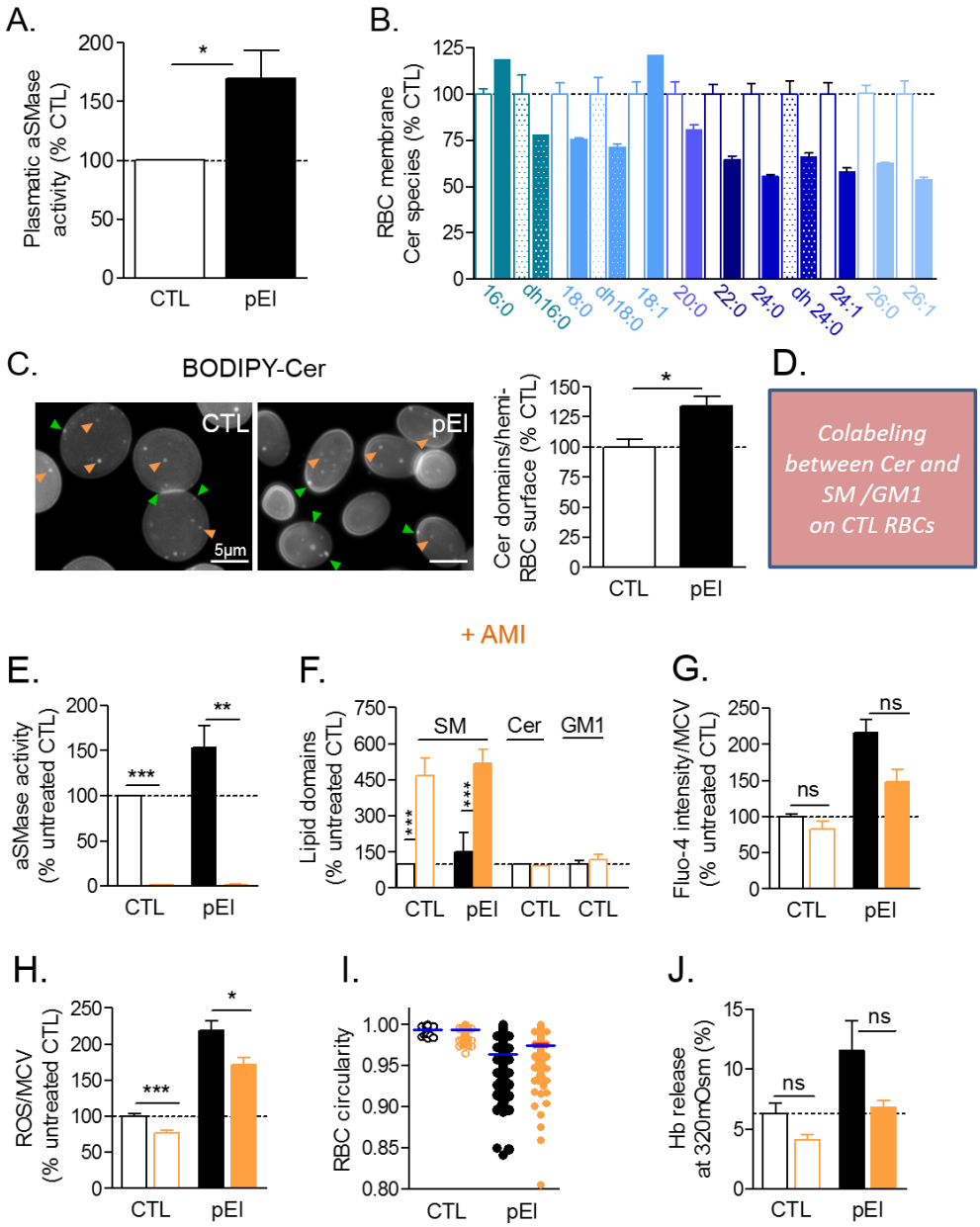

Figure 8. The plasmatic acid SMase activity is increased in pEl and its inhibition by amitryptiline increases SM-enriched domain abundance and improves RBC circularity and fragility. (A) aSMase activity determined in plasma isolated through Ficoll separation (mean ± SEM of 4 independent experiments). **(B)** RBC ceramide (Cer) content assessed by HPLC-MS on washed, lysed and lipid-extracted RBCs. Cer and dihydro (dh)-Cer species are classified based on fatty acid length and insaturation number and results are expressed as percentage of control RBCs (mean of 9 healthy women). **(C)** Abundance of Cer-enriched domains at the RBC surface. RBCs spread on coverslips were labeled with BODIPY-Cer and directly visualized by fluorescence microscopy. Left, representative images. Green arrowheads, domains in high curvature areas (HC); orange arrowheads, domains in low curvature areas (LC). Right, Cer-enriched domain quantification per hemi-RBC surface (means ± SEM of 3 independent experiments in which 200-400 RBCs were counted in each coverslip). **(D)** Spatial relationship between Cer- and SM-enriched domains. RBCs were spread onto coverslips and labeled with BODIPY-Cer and -SM. **(E-J)** Effect of amitriptyline (AMI) on lipid domain abundance, calcium and ROS accumulation and RBC circularity and fragility. Whole blood was incubated with AMI, washed and assessed. (E) aSMase activity determined in plasma (means ± SEM of 3 independent experiments). (F) Abundance of lipid domains determined as in Figure 4 (means ± SEM of 3-4 independent experiments). (G,H) Intracellular calcium and ROS contents measured as in Figure 4F and 6E (means ± SEM of 3-4 independent experiments). (I) RBC circularity measured as in Figure S2 (one representative out of 4 independent experiments; CTL vs CTL+AMI, *; pEl vs pEl+AMI, **). (J) RBC fragility evaluated in isotonic medium as in Figure 1F (means ± SEM of 4 independent experiments).

To further test the implication of the plasmatic aSMase in the alteration of lipid domains and calcium exchanges, we evaluated whether SM domain abundance, calcium content and RBC circularity could be reestablished by reduction of the plasmatic aSMase activity using the tricyclic antidepressor amitriptyline (AMI; ref [36]; Figure 8E). AMI induced a specific ~5-fold increase of SM-enriched domain abundance (Figure 8F). This was accompanied by a lower calcium and ROS accumulation in both healthy and pEl RBCs (Figure 8G,H & S5H) and a partial restoration of RBC circularity and hemoglobin release in pEl RBCs (Figure 5J,K). Those data suggested that the alteration of SM-enriched domains by tha plasmatic acid SMase contributed to calcium and ROS accumulation in pEl RBCs, leading to RBC morphology and deformability impairment.

Results

Discussion

pEl presents a severe form of elliptocytosis, resulting from compound heterozygous mutations on α-spectrin gene SPTA1. The nonsense Arg1811* mutation has not been described before. Expression of the allele carrying this mutation is strongly reduced by nonsense-mediated mRNA decay. The Leu260Pro mutation, already described [23], is located at the end of the second spectrin repeat, next to the linker between α2 and α3 repeats, *i.e.* distal to the tetramerization sites. Although the folding of the domain containing this mutation is normal, the stabilizing interactions between adjacent repeats, and thus the whole proteins, are disrupted [38]. On a mini-spectrin construct incorporating this mutation, reduced tetramer formation is observed without significant changes in the secondary structure [25]. In patients carrying this mutation only, as pElm, these effects are well-compensated by the other allele as α-spectrin is produced in large excess as compared to β-spectrin [39].

The inability of elliptocytotic RBC to recover its original biconcave shape after passage through splenic interendothelial slit was recently linked to impaired elasticity [18]. We here showed that alteration of calcium exchanges through PIEZO1 and PMCA could represent the molecular link between cytoskeleton and deformation impairment in elliptocytosis. Such impairment of calcium exchange resulted from four mechanisms: (i) a reduced calcium transport protein abundance; and (ii-iV) a decreased activation through lipid-independent, lipid-based and lipid domain-dependent mechanisms. We will here below discuss the respective contribution of those four mechanisms to the pathogenesis of this severe form of elliptocytosis.

First, the abundance of PMCA4, and to a lower extent of PIEZO1, was decreased in pEl. Those lower contents could result either from aberrant membrane protein sorting during erythropoiesis [40] or a differential loss by membrane fragmentation.

Second, several features observed in pEl indicated that the calcium-dependent alterations could affect the PMCA pump activity. Indeed, as in other hemolytic anemia, the intracellular calcium content was highly increased in pEl, with downstream increased calmodulin membrane association, calpain activity, PKC-dependent phosphorylation of cytoskeletal/membrane proteins including PMCA and ROS production. Such ROS accumulation in pEl RBCs could originate from abnormal hemoglobin membrane interaction (and its possible auto-oxidation), plasma hemoglobin and free heme increases due to chronic hemolysis as well as calcium signaling via the activation of ROS-generating enzymes [41], as revealed by the ROS reduction upon EGTA (Figure 12). However, decreasing the ROS content by ascorbic acid was inefficient to restore calcium level in pEl and even worsened cell circularity. Such inefficiency, which is in agreement with absence of effect in sickle

cell anemia [42], could result from the inability of ascorbic acid to decrease lipid peroxidation. Thus, in pEl, besides the increased phosphorylation of the PMCA4 by PKC, the pump activity can also be decreased by the increased calpain activity [43] and by the oxidative stress [44-46]. Besides calcium, the cytoskeleton is also predicted to be an important regulator of calcium transport protein activity, and this mechanism is particularly relevant to PIEZO1. Indeed, studies reported that inhibition of actin polymerization with cytochalasin D inhibits whole-cell Piezo1 currents evoked by direct stimulus with a glass pipette, but increases opening in cell-attached pressure-evoked currents [47, 48]. The defect in α-spectrin and related cytoskeletal membrane proteins and the alteration of their lateral distribution at the pEl RBC surface could contribute to impair calcium influx through PIEZO1.

The third mechanism behind calcium exchange alteration in pEl is based on the impairment of PIEZO1 and PMCA by lipids known to affect their activity (for a review, see [49]). Indeed, several lysoPS species were enhanced in pEl RBCs and addition of lysoPS to healthy RBCs abrogated calcium influx upon stretching, suggesting that alteration of PS composition in pEl affects PIEZO1 activity (Figure S12). LysoPS are bioactive signaling phospholipids that have been shown in neutrophils to be generated following activation of the NADPH oxidase, which produces oxidized PS intermediates as potential substrates of phospholipase A_2 [50, 51]. Our observations are in agreement with a recent study showing that lysoPS plasma membrane insertion in myoblasts suppresses PIEZO1 activation, leading to impairment of myotube formation. Those authors found a similar suppression of PIEZO1 activation upon PS surface exposure [34], which was not the case in pEl RBCs. This was quite surprising at first glance based on the level of intracellular calcium which should inhibit the flippase ATP11C. This could be explained by (i) the calcium accumulation which was probably not sufficient to activate the scramblase PLSCR1 [2]; (ii) the increased ATP content which could compensate for flippase inhibition due to higher calcium content; and (iii) the lower content of PS species in pEl as compared to healthy RBCs which could lead to underestimation of the PS surface exposure in pEl RBCs. In any case, the decreased abundance of PS species in pEl RBCs can it-self affect PIEZO1 activity due to their disappearance from the inner leaflet and the same mechanism can take place for PMCA. Indeed, the acidic lipids PS and PI have been shown to increase the activity (V_{max}) of the pump by accelerating dephosphorylation [52] and increasing the Ca^{2+} affinity (*i.e.* decreased Kd) [53]. Hence, Cer species, which are known to increase both the affinity for Ca^{2+} and the V_{max} of the PMCA [54], are decreased in pEl RBCs despite the activation of the aSMase.

The fourth mechanism behind calcium exchange impairment in pEl involves lipid domains and their biophysical properties. Three lines of evidence provided here indicated that lipid domains were impaired in pEl RBCs. First, they presented a

lower chol enrichment and cytoskeleton anchorage and calcium exchanges upon RBC stretching were decreased. Second, GM1-enriched domain increase upon calcium entry stimulation by Yoda1 was abolished and SM-enriched domain increase upon intracellular calcium depletion by EGTA was lowered. Third, alteration of lipid domain chol content by mβCD exacerbated the calcium increase and worsened the RBC fragility. Although the mechanism behind GM1-enriched domain alteration remains to be determined, it can be suggested that the decreased polyunsaturated-to-saturated PC and PS ratio as well as the increased lipid peroxidation at the inner leaflet could affect their membrane packing and thickness, two biophysical properties known to control PIEZO1 activity. Indeed, Vásquez and coll. recently showed that margaric acid (a saturated fatty acid) inhibits Piezo1 activation by increasing membrane bending stiffness while long chain polyunsaturated fatty acids modulate channel inactivation by decreasing membrane bending stiffness [55]. Hence, hydrophobic mismatch was also proposed as a gating mechanism of Piezo channels, as extensively discussed in [49]. Regarding SM-enriched domains, their increased abundance and impaired functionality appeared to result from both permanent uncoupling between the membrane and the cytoskeleton and the upregulation of aSMase. Indeed, upon incubation with phorbol esters in the presence of a phosphatase inhibitor (PMA/CalA), a treatment kown to uncouple membrane:cytoskeleton at 4.1R complexes [6], the abundance of SM-enriched domains increased in healthy RBCs but not in pEl RBCs. The upregulation of the plasmatic aSMase could seriously alter the biophysical properties of SM/chol-enriched domains forming instead SM/Cer-enriched domains, due to competition between Cer and chol [37]. Accordingly, we observed that SM-enriched domains exhibited a lower chol content in pEl. Such modifications would in turn alter the PMCA localization and activity. Indeed, studies have shown that the PMCA pump and calmodulin partition into Liquid-ordered (Lo) domains and that the Lo-associated PMCA activity is much higher than PMCA activity excluded from these domains. Moreover, chol depletion abrogates the Lo-associated PMCA activity without any effects on the non-Lo pool [56], a mechanism that can account here. Accordinly, we have shown that aSMase inhibition by amitriptyline, which has already proven effective in sickle red cells [36], partly restored the calcium content and the morphology of pEl RBCs. However, the aSMase-induced modifications were not accompanied by an increase of the total Cer content. This unexpected observation was explained neither by Cer metabolism into sphingosine nor by Cer loss through vesiculation/fragmentation. It could alternatively result from oxidation in species like 3-ketoceramide [57] following flipping to the inner leaflet. Although this hypothesis remains to be tested, it is supported by the fact that signaling cascades via activation of aSMase can be induced by oxidized phospholipids [58, 59]. Although the mechanistics behind lipid domain alteration was not fully elucidated, our model is in agreement with the

impaired formation of chol-dependent nanodomains in the CHO cell PM treated with oxidized PC species due to upregulated aSMase activity [60].

Thus, the alteration of membrane lipid content and organization in domains with specific biophysical properties seems to be at the center of impairment of calcium influx through PIEZO1 and efflux through PMCA4, precluding RBC deformation and shape reformation after deformation. One could therefore wonder why calcium accumulates in pEl RBCs. Our data suggested that Cav channels could take over, an hypothesis fully supported by the altered lipid composition observed. Indeed, studies indicate that (i) sphingomyelinase activity stimulates Ca_v channels expressed in oocytes [61]; and (ii) lipid membrane disruption and/or fluidization are linked to increased Ca_v channel activation, which could explain the Ca_v channel leakiness and arrhythmias in pathologies [62].

Altogether, calcium accumulation, cytoskeleton alteration as well as membrane lipid composition, biophysical properties and lateral distribution in domains cooperate to impair calcium exchanges upon RBC deformation. Downstream of the alteration of lipid membrane composition and alteration, several perturbations may act in a positive feed-back loop to drive the pathogenesis of elliptocytosis: (i) calcium accumulation and exacerbation of the cytoskeletal instability through PKC activation, (ii) hemolysis and increased ROS production, (iii) increased RBC curvature and aSMase activity [63], and (iv) membrane fragmentation. The latter event is supported by simulation studies [18] and several features provided here, including the RBC perimeter decrease and the rise of oxidative stress, Cer and calcium contents, all known to induce eryptosis and cell fragmentation.

In summary, this study paves the way towards a better understanding of the molecular mechanism behind elliptocytosis. We revealed that plasmatic aSMase and increase of intracellular calcium and oxidative stress cooperate to induce membrane damage and lipid domain impairment, leading to calcium exchange impairment and alteration of RBC curvature and deformation. Moreover, we showed that plasmatic aSMase inhibition by amitriptyline modified lipid domain abundance and partially restored calcium content and RBC circularity, opening new perspectives for treatment.

Results

Acknowledgments

We thank Drs. A. Miyawaki, M. Abe and T. Kobayashi (Riken Brain Science Institute, Saitama, Japan & University of Strasbourg, France) as well as H. Mizuno (KU Leuven, Belgium) for generously supplying the Dronpa-theta-D4 plasmid. We also thank A. Debue and D. Cottem for technical assistance in NGS and Sanger sequencing. This work was supported by grants from the UCLouvain (FSR and Actions de Recherches concertées, ARC), the F.R.S-FNRS and the Salus Sanguinis foundation. The MASSMET platform (UCLouvain, Belgium) is acknowledged for the access to the LC-MS.

Authorship

Contribution: H.P. and D.T. designed the experiments, analyzed and interpreted data and wrote the manuscript. H.P., L.C. and M.C. collected and analyzed the data. A.S.C. was in charge of microvesicle preparation and processing and plasmatic aSMase measurement; A.S. performed lipid peroxidation assays; C.L. evaluated total phospholipids and M.G. performed the PKC activation experiment. A.P. and G.G.M. performed the lipidomics and M.L., S.PDR., D.V. and M.R. the mass spectrometry. M.V. and P.B. were responsible for the genetic analysis. P.V.D.S. did all the electron microscopy experiments and developed imaging analysis methods. C.V. enrolled patients. All authors reviewed the final version of the manuscript.

Conflict-of-interest disclosure: The authors declare no competing financial interests.

Corresponding author: Donatienne Tyteca, CELL Unit, de Duve Institute, Université catholique de Louvain, UCL B1.75.05, avenue Hippocrate, 75, B-1200 Brussels, Belgium. Phone: +32-2-764.75.91; Fax: +32-2-764.75.43; e-mail: donatienne.tyteca@uclouvain.be

References

1. Baines, A.J., *The spectrin-ankyrin-4.1-adducin membrane skeleton: adapting eukaryotic cells to the demands of animal life.* Protoplasma, 2010. **244**(1-4): p. 99-131.
2. Bogdanova, A., et al., *Calcium in red blood cells-a perilous balance.* Int J Mol Sci, 2013. **14**(5): p. 9848-72.
3. Cahalan, S.M., et al., *Piezo1 links mechanical forces to red blood cell volume.* Elife, 2015. **4**.
4. Lutz, H.U. and A. Bogdanova, *Mechanisms tagging senescent red blood cells for clearance in healthy humans.* Front Physiol, 2013. **4**: p. 387.
5. Conrard, L., et al., *Spatial relationship and functional relevance of three lipid domain populations at the erythrocyte surface.* Cell Physiol Biochem, 2018(51): p. 1544-1565.
6. D'Auria, L., et al., *Micrometric segregation of fluorescent membrane lipids: relevance for endogenous lipids and biogenesis in erythrocytes.* J Lipid Res, 2013. **54**(4): p. 1066-76.
7. D'Auria, L., et al., *Segregation of fluorescent membrane lipids into distinct micrometric domains: evidence for phase compartmentation of natural lipids?* PLoS One, 2011. **6**(2): p. e17021.
8. Dumitru, A.P., M.; Conrard, L.; Dufrêne, Y.; Tyteca, D.; Alsteens, D., *Nanoscale membrane architecture of healthy and pathological red blood cells.* Nanoscale Horizons, 2018. **3**: p. 293-304.
9. Tyteca, D., et al., *Three unrelated sphingomyelin analogs spontaneously cluster into plasma membrane micrometric domains.* Biochim Biophys Acta, 2010. **1798**(5): p. 909-27.
10. Carquin, M., et al., *Recent progress on lipid lateral heterogeneity in plasma membranes: From rafts to submicrometric domains.* Prog Lipid Res, 2016. **62**: p. 1-24.
11. Leonard, C., et al., *Contribution of plasma membrane lipid domains to red blood cell (re)shaping.* Sci Rep, 2017. **7**(1): p. 4264.
12. Da Costa, L., et al., *Hereditary spherocytosis, elliptocytosis, and other red cell membrane disorders.* Blood Rev, 2013. **27**(4): p. 167-78.
13. Gallagher, P.G., *Disorders of red cell volume regulation.* Curr Opin Hematol, 2013. **20**(3): p. 201-7.
14. Mohandas, N. and P.G. Gallagher, *Red cell membrane: past, present, and future.* Blood, 2008. **112**(10): p. 3939-48.
15. Gallagher, P.G., *Hereditary elliptocytosis: spectrin and protein 4.1R.* Semin Hematol, 2004. **41**(2): p. 142-64.
16. Barcellini, W., et al., *Hereditary red cell membrane defects: diagnostic and clinical aspects.* Blood Transfus, 2011. **9**(3): p. 274-7.
17. Gallagher, P.G., *Abnormalities of the erythrocyte membrane.* Pediatr Clin North Am, 2013. **60**(6): p. 1349-62.

18. Li, H., et al., *Mechanics of diseased red blood cells in human spleen and consequences for hereditary blood disorders.* Proc Natl Acad Sci U S A, 2018. **115**(38): p. 9574-9579.
19. Bartlett, G.R., *Phosphorus assay in column chromatography.* J Biol Chem, 1959. **234**(3): p. 466-8.
20. Grimm, M.O., et al., *Regulation of cholesterol and sphingomyelin metabolism by amyloid-beta and presenilin.* Nat Cell Biol, 2005. **7**(11): p. 1118-23.
21. Li, Q.F., et al., *Prokineticin-1/endocrine gland-derived vascular endothelial growth factor is a survival factor for human multiple myeloma cells.* Leuk Lymphoma, 2010. **51**(10): p. 1902-12.
22. Tsikas, D., *Assessment of lipid peroxidation by measuring malondialdehyde (MDA) and relatives in biological samples: Analytical and biological challenges.* Anal Biochem, 2017. **524**: p. 13-30.
23. Sahr, K.E., et al., *Sequence and exon-intron organization of the DNA encoding the alpha I domain of human spectrin. Application to the study of mutations causing hereditary elliptocytosis.* J Clin Invest, 1989. **84**(4): p. 1243-52.
24. Glele-Kakai, C., et al., *Epidemiological studies of spectrin mutations related to hereditary elliptocytosis and spectrin polymorphisms in Benin.* Br J Haematol, 1996. **95**(1): p. 57-66.
25. Harper, S.L., et al., *The common hereditary elliptocytosis-associated alpha-spectrin L260P mutation perturbs erythrocyte membranes by stabilizing spectrin in the closed dimer conformation.* Blood, 2013. **122**(17): p. 3045-53.
26. Hertz, L., et al., *Is Increased Intracellular Calcium in Red Blood Cells a Common Component in the Molecular Mechanism Causing Anemia?* Front Physiol, 2017. **8**: p. 673.
27. Leonard, C., et al., *Tuning of differential lipid order between submicrometric domains and surrounding membrane upon erythrocyte reshaping.* Cell Physiol Biochem 2018. **48**(2563-2582).
28. Stauffer, T.P., D. Guerini, and E. Carafoli, *Tissue distribution of the four gene products of the plasma membrane Ca2+ pump. A study using specific antibodies.* J Biol Chem, 1995. **270**(20): p. 12184-90.
29. Hanggi, P., et al., *Red blood cells of sickle cell disease patients exhibit abnormally high abundance of N-methyl D-aspartate receptors mediating excessive calcium uptake.* Br J Haematol, 2014. **167**(2): p. 252-64.
30. Pringos, E., et al., *Peptide neurotoxins that affect voltage-gated calcium channels: a close-up on omega-agatoxins.* Toxins (Basel), 2011. **3**(1): p. 17-42.
31. Carquin, M., et al., *Cholesterol segregates into submicrometric domains at the living erythrocyte membrane: evidence and regulation.* Cell Mol Life Sci, 2015. **72**(23): p. 4633-51.
32. George, A., et al., *Erythrocyte NADPH oxidase activity modulated by Rac GTPases, PKC, and plasma cytokines contributes to oxidative stress in sickle cell disease.* Blood, 2013. **121**(11): p. 2099-107.
33. Conrard, L., et al., *Spatial Relationship and Functional Relevance of Three Lipid Domain Populations at the Erythrocyte Surface.* Cell Physiol Biochem, 2018. **51**(4): p. 1544-1565.

34. Tsuchiya, M., et al., *Cell surface flip-flop of phosphatidylserine is critical for PIEZO1-mediated myotube formation.* Nat Commun, 2018. **9**(1): p. 2049.
35. Mutemberezi, V., O. Guillemot-Legris, and G.G. Muccioli, *Oxysterols: From cholesterol metabolites to key mediators.* Prog Lipid Res, 2016. **64**: p. 152-169.
36. Awojoodu, A.O., et al., *Acid sphingomyelinase is activated in sickle cell erythrocytes and contributes to inflammatory microparticle generation in SCD.* Blood, 2014. **124**(12): p. 1941-50.
37. Goni, F.M. and A. Alonso, *Effects of ceramide and other simple sphingolipids on membrane lateral structure.* Biochim Biophys Acta, 2009. **1788**(1): p. 169-77.
38. Randles, L.G., et al., *Understanding pathogenic single-nucleotide polymorphisms in multidomain proteins--studies of isolated domains are not enough.* FEBS J, 2013. **280**(4): p. 1018-27.
39. Chen, K., et al., *Resolving the distinct stages in erythroid differentiation based on dynamic changes in membrane protein expression during erythropoiesis.* Proc Natl Acad Sci U S A, 2009. **106**(41): p. 17413-8.
40. Salomao, M., et al., *Protein 4.1R-dependent multiprotein complex: new insights into the structural organization of the red blood cell membrane.* Proc Natl Acad Sci U S A, 2008. **105**(23): p. 8026-31.
41. Gorlach, A., et al., *Calcium and ROS: A mutual interplay.* Redox Biol, 2015. **6**: p. 260-71.
42. Arruda, M.M., et al., *Antioxidant vitamins C and E supplementation increases markers of haemolysis in sickle cell anaemia patients: a randomized, double-blind, placebo-controlled trial.* Br J Haematol, 2013. **160**(5): p. 688-700.
43. Guerini, D., B. Pan, and E. Carafoli, *Expression, purification, and characterization of isoform 1 of the plasma membrane Ca2+ pump: focus on calpain sensitivity.* J Biol Chem, 2003. **278**(40): p. 38141-8.
44. Zaidi, A., et al., *Oxidative inactivation of purified plasma membrane Ca2+-ATPase by hydrogen peroxide and protection by calmodulin.* Biochemistry, 2003. **42**(41): p. 12001-10.
45. Sharp, J.S. and K.B. Tomer, *Analysis of the oxidative damage-induced conformational changes of apo- and holocalmodulin by dose-dependent protein oxidative surface mapping.* Biophys J, 2007. **92**(5): p. 1682-92.
46. Zaidi, A., *Plasma membrane Ca-ATPases: Targets of oxidative stress in brain aging and neurodegeneration.* World J Biol Chem, 2010. **1**(9): p. 271-80.
47. Gnanasambandam, R., et al., *Ionic Selectivity and Permeation Properties of Human PIEZO1 Channels.* PLoS One, 2015. **10**(5): p. e0125503.
48. Gottlieb, P.A., C. Bae, and F. Sachs, *Gating the mechanical channel Piezo1: a comparison between whole-cell and patch recording.* Channels (Austin), 2012. **6**(4): p. 282-9.
49. Conrard, L. and D. Tyteca, *Regulation of Membrane Calcium Transport Proteins by the Surrounding Lipid Environment.* Biomolecules, 2019. **9**(10).
50. Frasch, S.C. and D.L. Bratton, *Emerging roles for lysophosphatidylserine in resolution of inflammation.* Prog Lipid Res, 2012. **51**(3): p. 199-207.

51. Frasch, S.C., et al., *NADPH oxidase-dependent generation of lysophosphatidylserine enhances clearance of activated and dying neutrophils via G2A.* J Biol Chem, 2008. **283**(48): p. 33736-49.
52. Filomatori, C.V. and A.F. Rega, *On the mechanism of activation of the plasma membrane Ca2+-ATPase by ATP and acidic phospholipids.* J Biol Chem, 2003. **278**(25): p. 22265-71.
53. Di Leva, F., et al., *The plasma membrane Ca2+ ATPase of animal cells: structure, function and regulation.* Arch Biochem Biophys, 2008. **476**(1): p. 65-74.
54. Colina, C., V. Cervino, and G. Benaim, *Ceramide and sphingosine have an antagonistic effect on the plasma-membrane Ca2+-ATPase from human erythrocytes.* Biochem J, 2002. **362**(Pt 1): p. 247-51.
55. Romero, L.O., et al., *Dietary fatty acids fine-tune Piezo1 mechanical response.* Nat Commun, 2019. **10**(1): p. 1200.
56. Jiang, L., et al., *Partitioning of the plasma membrane Ca2+-ATPase into lipid rafts in primary neurons: effects of cholesterol depletion.* J Neurochem, 2007. **102**(2): p. 378-88.
57. Kishimoto, Y. and N. Kawamura, *Ceramide metabolism in brain.* Mol Cell Biochem, 1979. **23**(1): p. 17-25.
58. Loidl, A., et al., *Oxidized phospholipids in minimally modified low density lipoprotein induce apoptotic signaling via activation of acid sphingomyelinase in arterial smooth muscle cells.* J Biol Chem, 2003. **278**(35): p. 32921-8.
59. Stemmer, U., et al., *Toxicity of oxidized phospholipids in cultured macrophages.* Lipids Health Dis, 2012. **11**: p. 110.
60. Brameshuber, M., et al., *Oxidized Phospholipids Inhibit the Formation of Cholesterol-Dependent Plasma Membrane Nanoplatforms.* Biophys J, 2016. **110**(1): p. 205-13.
61. Combs, D.J., et al., *Tuning voltage-gated channel activity and cellular excitability with a sphingomyelinase.* J Gen Physiol, 2013. **142**(4): p. 367-80.
62. Morris, C.E., P.F. Juranka, and B. Joos, *Perturbed voltage-gated channel activity in perturbed bilayers: implications for ectopic arrhythmias arising from damaged membrane.* Prog Biophys Mol Biol, 2012. **110**(2-3): p. 245-56.
63. Linke, T., et al., *Stimulation of acid sphingomyelinase activity by lysosomal lipids and sphingolipid activator proteins.* Biol Chem, 2001. **382**(2): p. 283-90.

Supplemental methods and figures

Results

Supplemental methods

Blood smears. A blood drop was spread onto a superfrost+ slide. The resulting blood smear was fixed in methanol for 5min, colored with May-Grunwald for 5min and with Giemsa (both from Merk Millipore) for 12min and finally washed with water to favor salt precipitation.

Sequencing. DNAs were extracted from whole blood using Wizard genomic DNA purification kit (Promega). SPTA1 gene was sequenced by Ion Torrent technology using a custom-designed Ampliseq panel (www.ampliseq.com) covering the coding exons and 5bp of flanking introns (= splice sites). DNA libraries for pEl were prepared using Ion AmpliSeq Library Kit according to the manufacturer protocol (Life Technologies) with 10ng of DNA for each of the two Ampliseq primer pools. Sequencing was performed on a *Personal Genome Machine* (PGM, Life Technologies), with chip 316. The sequences were aligned to the human reference genome (hg19) with the Ion Torrent Suite Server v5 (Life Technologies) in the form of *.bam* files. These files were imported in Highlander, a software developed in the DDUV Institute (http://sites.uclouvain.be/highlander/), for variant calling with the embarked Torrent variant Caller v5.2 (Life Technologies), annotation and filtering.
RNAs were extracted from whole blood using TRIzol reagent (Invitrogen) and retrotranscribed with moloney murine leukemia virus reverse transcriptase (M-MLV RT; ThermoFisher). For RT-PCR, primers were chosen in exons distant from those carrying the changes of interest (sequences and conditions available on request). Amplicons were purified using the Wizard® SV gel and PCR clean-up system from Promega, and sequenced on an ABI3130xl sequencer with the Big Dye Terminator v3.1 chemistry (Applied Biosystems). Chromatograms were analysed using CLCbio Main Workbench.

Mass spectrometry. RBC membranes were exploded with hypotonic 5mM PBS and Ghost were generated by recirculariza tion of the membranes in 20mM PBS. Ghost were then lysed in 50mM TEAB, pH 7.6, 150mM NaCl, 1% IGEPAL (CA-630), 0.1% SDS, 0.2% Dodecyl-B-maltoside, 50mM NaF, 5mM Sodium Orthovanadate, 0.5mM PMSF. Detergent was then removed thanks to a spin column (Thermo Fisher Scientific) to obtain proteins in 100mM TEAB. Proteins (300 µg) were then precipitated with 10% TCA and digested sequentially by RapidGest® (Waters) and trypsin. Labelling has been done on 100µg by Tandem Mass Tag (TMT), according to manufacturer's instructions. Alkylation, reduction and acidification were respectively realized with dithiothreitol, chloroacetamide and HCl. Finally phosphopeptides were enriched by $T_{itanium}$ oxide affinity and eluted in 5% ammonia. Samples were vacuum dried in a SpeedVac system before being recovered in solvent A (0.1% TFA in 3.5% ACN), directly loaded onto reversed-phase pre-column

(Acclaim PepMap 100, Thermo Scientific) and eluted in backflush mode. Peptide separation was performed using a reversed-phase analytical column (Acclaim PepMap RSLC, 0.075 x 250 mm,Thermo Scientific) with a linear gradient of 4%-32% solvent B (0.1% FA in 98% ACN) for 110 min, 32%-60% solvent B for 10 min, 60%-95% solvent B for 1 min and holding at 95% for the last 10 min at a constant flow rate of 300 nl/min on an EASY-nLC 1000 UPLC system. The peptides were analyzed by an Orbitrap Fusion Lumos tribrid mass spectrometer (ThermoFisher Scientific). The peptides were subjected to NSI source followed by tandem mass spectrometry (MS/MS) in Fusion Lumos coupled online to the UPLC. Intact peptides were detected and quantified using the synchronous precursor selection (SPS)-based MS3 scan routine implemented in the Orbitrap Fusion Lumos tribrid instrument. The Orbitrap Fusion Lumos was operated at a positive ion spray voltage of 2100 V and a transfer tube temperature of 275°C. Briefly, the full scan was performed in the range 375-1500 m/z at a nominal resolution of 120 000 and AGC set to $4x10^5$, followed by selection of the most intense ions above an intensity threshold of 5000 for collision-induced dissociation (CID)-MS2 fragmentation in the linear ion trap with 35% normalized collision energy. The isolation width was set to 0.7 m/z with no offset. The top 10 fragment ions for each peptide MS2 was notched out with an isolation width of 2 m/z and co-fragmented to produce MS3 scans analysed in the Orbitrap at a nominal resolution of 30 000 after higher-energy collision dissociation (HCD) fragmentation at a normalized collision energy of 65%. Raw data files from Orbitrap Fusion Lumos were processed using Proteome Discoverer (version 2.3). MS/MS spectra were searched against the UniprotKB Human proteome reference database (87 489 total sequences). SEQUEST parameters were specified as: trypsin enzyme, two missed cleavages allowed, minimum peptide length of 6, TMT tags on lysine residues and peptide N-termini (+229.1629 Da) and carbamidomethylation of cysteines residues (+ 57.0214 Da) as fixed modifications and oxidation of methionine residues (+ 15.9949 Da) as a variable modification, precursor mass tolerance of 20 ppm, and a fragment mass tolerance of 0.6 Da. Peptide spectral match (PSM) error rates were determined using the target-decoy strategy coupled to Percolator modeling of true and false matches. Reporter ions were quantified from MS3 scans using an integration tolerance of 20 ppm with the most confident centroid setting. An MS2 spectral assignment false discovery rate (FDR) of less than 1% was achievec. Following spectral assignment, peptides were assembled into proteins and were further filtered based on the combined probabilities of their constituent peptides to a final FDR of 1%. The mass spectrometry proteomics data have been deposited to the ProteomeXchange Consortium (http://proteomecentral.proteomexchange.org) via the PRIDE partner repository with the dataset identifier <PXD000xxx>.

Results

Scanning electron microscopy of RBCs on filters. Washed RBCs were fixed in graded concentrations (0.1% followed by 0.5% then 1.5%) of glutaraldehyde in 0.1M cacodylate buffer for 5min each. Fixed RBCs were then filtered on 0.4µm polycarbonate (it4ip) filters using a syringe and washed by cacodylate buffer pushed gently through the syringe. Post-fixation was performed on the filters in the syringe in 1% OsO_4 in 0.1M cacodylate for 2h. Filters were then washed extensively in 0.1M cacodylate and 6 times for 10min in water. Samples were dissociated from the filter capsule and covered by a second filter in order to protect the sample during further processing, *i.e.* the dehydration and the critical point drying. Dehydration was performed in graded baths of ethanol (50, 60, 70, 80, 90, 95% for 10min each, followed by 100% 3 times for 10min) and critical point dried. Finally, samples were mounted on scanning electron microscopy stubs and sputtered with 10nm gold. All samples were observed in the CM12 electron microscope with the SED detector at 80kV.

Transmission electron microscopy of the RBC cytoskeleton. Formvar/carbon-coated grids were treated with PLL for 15min at RT and washed extensively (3x in water and 2x in medium). Grids were then seeded with washed diluted RBCs for 7min in medium, rinsed 3 times in medium and permeabilized in 0.5% Triton X-100 for 3min at RT. Grids were then washed 3 times in medium, fixed for 15min in 1% glutaraldehyde in 0.1M cacodylate, washed in buffer and post-fixated in 1% OSO_4 in 0.1M cacodylate for 60min at 4°C. Grids were again extensively washed (6x 5min in 0.1M cacodylate and 3x in water) and stained in 1% uranyl acetate for 30min at RT. Finally, samples were washed (6x 10min) in water and overnight air-dried. Samples were then observed in the CM12 electron microscope in transmission mode at 80kV.

Immunofluorescence staining of RBC membrane and cytoskeleton proteins. Diluted washed RBCs were spread onto PLL-precoated coverslips, fixed with 4% paraformaldehyde for 10min and blocked with 1% bovine serum albumin (BSA; Sigma-Aldrich) for 30min. To label membrane proteins, RBCs were then incubated for 1h with rabbit monoclonal antibodies to glycophorin C (Abcam) together with mouse monoclonal antibodies to CD47 (Invitrogen), washed 4 times in 1% BSA, incubated for 1h with the appropriate Alexa-secondary antibodies (5µg/ml) and washed 4 times with 1% BSA. Total spectrin was revealed with antibodies against α/β-spectrins (Abcam) using the same protocol as above except that a permeabilization step with 0.5% Triton X-100 for 3min was done before the fixation. All coverslips were mounted in Mowiol in the dark for 24h and examined with a Zeiss LSM 510 confocal microscope using a plan-Apochromat 63x NA 1.4 oil immersion objective.

Results

Lipid quantification. The quantification was achieved as previously described[1,2]. Briefly, lipids from 250*10^6 RBCs or fragments and microvesicles were measured after liquid/liquid extraction and SPE purification in the presence of respective internal standards. Lipid fractions were then analyzed using a LTQ Orbitrap mass spectrometer coupled to an Accela HPLC system (both from Thermo Fischer Scientific). Analyte separation was achieved using a Kinetex LC-18 column coupled to an appropriate guard column (Phenomenex). For the analyses, we used two mobile phase systems as described in Guillemot-Legris et al. for lysophospholipids, phospholipids, sphingomyelin and sphingosine[1] and in Mutemberezi et al. for oxysterols and ceramides[2]. Lipid relative quantification was based on the ratio of area under the curve (AUC) of the lipid species on the AUC of the respective internal standard. The data are normalized to the CTL red blood cells condition (expressed in %).

Coomassie blue and Western blotting. RBC ghosts were prepared using a hypo-osmotic hemolysis method at 4°C[3]. Ghosts were then analyzed using 4-15% sodium dodecysufalte-polyacrylamide gel electrophoresis (SDS-PAGE; Bio-rad) and PageBlue™ Protein staining solution (ThermoFisher) following Fairbanks et al instruction[4]. Quantification of the relative abundance of proteins in PageBlue stained gels was performed using Fiji software. Western blotting were performed using antibodies against PIEZO1 (ProteIntech), PMCA (ThermoFisher) or GAPDH (Invitrogen), followed by HRP-conjugated secondary antibodies and revelation by chemiluminescence (SuperSignal® west pico/femto chemiluminescent substrate, ThermoFisher) with the Fusion Solo S from Vilber.

RBC hemoglobin release measurements. Four types of measurements were performed. First, to evaluate the effect of a chemical agent, washed RBCs were incubated with the agent as explained above in isosmotic medium (*i.e.* 320mOsm) and pelleted by centrifugation at 200g for 2min. Supernatants and pellets broken with 0.5% Triton X-100 were both assessed for hemoglobin at 450nm in 96-well plates (SpectraCountTM, Packard BioScience Co). Hemoglobin release in the supernatant was expressed as percentage of the total hemoglobin present in the sample. Second, to compare RBC fragility between donors, washed RBCs were incubated in isosmotic medium for 1h at 37°C under constant agitation, centrifuged, collected and measured for hemoglobin release as above. Third, to measure RBC osmotic resistance, washed RBCs were maintained at 37°C under constant agitation for 16h. RBCs were then incubated into gradually hypotonic media at RT for 10min and pelleted by centrifugation at 200g for 2min. Supernatants and pellets were separated and assessed for hemoglobin release as above. Ratio of the supernatant to the sum of the supernatant and the pellet for each medium was expressed as percentage of the hemoglobin released upon RBC

full hemolysis (*i.e.* RBCs in 0mOsm). Half-maximal effective hemolysis (EC50) was finally extrapolated using GraphPad Prism. Fourth, cryohemolysis was measured at Saint-Luc Hospital following Strechman and Gescheidt's instructions[5].

Isolation and analysis of microvesicles. Whole blood maintained for 0, 7 or 14 days at 4°C was centrifuged at 2000g for 10min. The plasma was recovered and centrifuged again at 2000g for 10min. The obtained plasma was diluted in sterile filtered PBS and centrifuged at 20.000g for 20min at 4°C. The resulting pellet was resuspended in sterile PBS before reiteration of the centrifugation step at 20.000g. The final pellet was resuspended in 1ml sterile PBS. Part of the pellet was fixed and allowed to attach for 8min onto coverslips pretreated with PLL. Coverslips were then washed, fixed on 1% glutaraldehyde in 0.1M cacodylate and processed by scanning electron microscopy as for RBCs on filters (see above). The other part of the pellet was kept at -80°C for determination of the MV size and abundance using a Zetaview® from Particle Metrix.

Phosphatidylserine externalization. Washed diluted RBCs were incubated with Annexin-V FITC (Invitrogen) in calcium-containing medium upon constant agitation at RT for 20min. Labelled RBCs were then analyzed by flow cytometry (FACSVerse).

Calpain activity. RBCs were lysed in the buffer provided in the Calpain activity assay kit (Abcam). To determine the calpain activity, 25µg of proteins in the RBC lysates were mixed with the "reaction buffer" and the calpain substrate, incubated for 1h at 37°C and measured for fluorescence.

Image analysis and data quantification. RBC morphology (area, perimeter, circularity), spectrin intensity/occupation and line intensity profiles on confocal images as well as protein abundance on SDS-PAGE and western blots were determined using the Fiji software. Line intensity profiles were further analyzed for the (non)-overlapping between GPC and CD47 as follows. After threshold value determination to define the effective dynamic range, peaks were identified and classified into three categories: (i) only red, indicating non-overlapping of GPC with CD47; (ii) only green, indicating non-overlapping of CD47 with GPC; and (iii) red+green, indicating overlapping between both proteins. The abundance of peaks in each category was then expressed as percentage of total peaks. For simple and double labeling, lipid domain abundance/hemi-RBC surface was assessed by manual counting on confocal or fluorescence images and expressed by reference to the hemi-RBC projected area.

Data presentation and statistical analyses. Data are expressed as means ± SEM when the number of independent experiments was n≥3 or means ± SD if n≤2,

except for RBC morphology. In the latter case, a representative experiment is presented in the figure to highlight the distribution within the sample while the statistical analysis is indicated in the legend. Statistical tests were performed only when $n \geq 3$. Two-sample t-test or one-way ANOVA followed by Bonferroni's post-hoc test were used in lipid domain abundance experiments while non-parametrical tests (Mann-Whitney test or Kruskal Wallis followed by Dunn's comparison test) were preferred in the other cases. ns, not significant; *, $p<0.05$; **, $p<0.01$; ***, $p<0.001$.

Supplemental figures

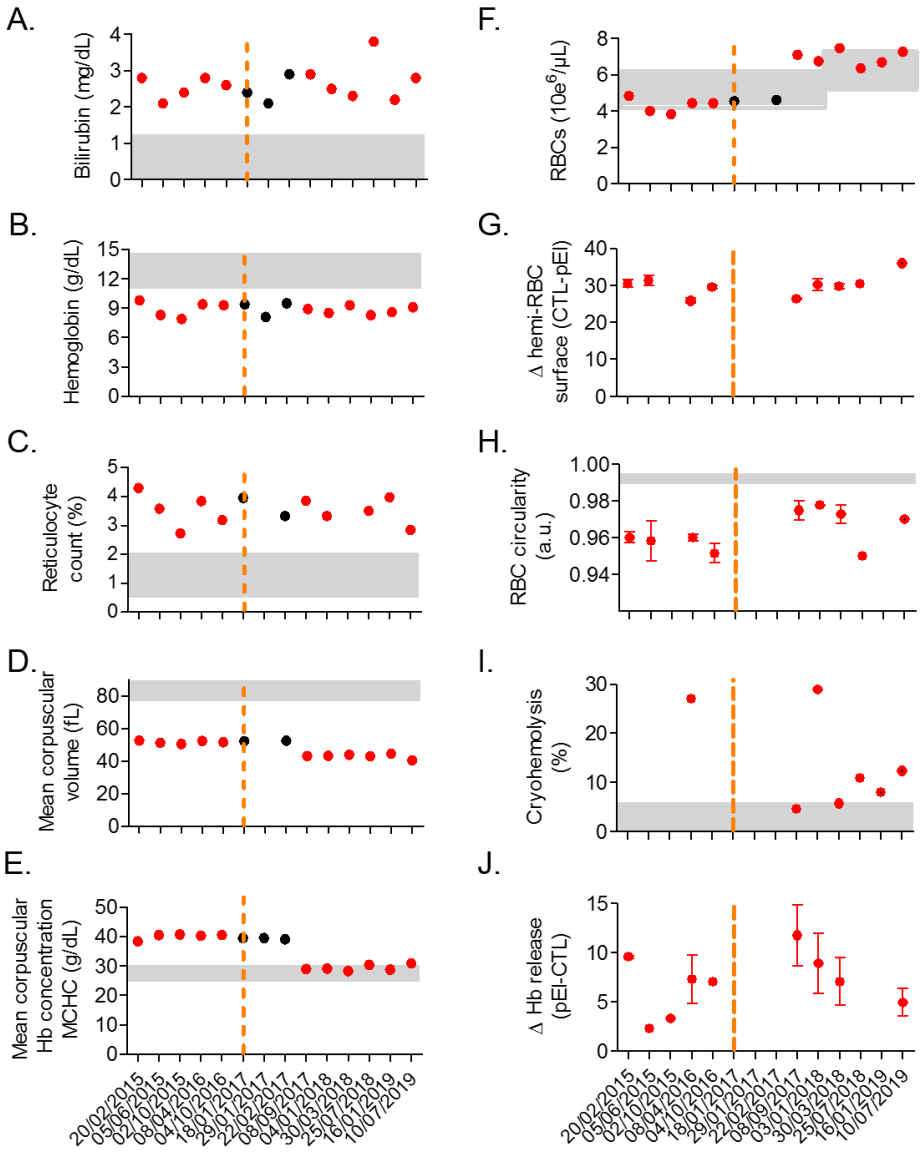

Supplemental Figure 1. Evolution of diagnostic parameters as well as RBC morphology and fragility in pEI throughout the study. (A-F) Parameters used to monitor the disease. Cholecystectomy was performed in January 2017 (orange dotted line) to avoid chronic inflammation due to gallstones. The normal range expected for pEI age is indicated by grey boxes. Red dots indicate venipunctures at which experiments have been performed. **(G-J)** Evolution of RBC surface projection (G), circularity (H) and fragility (I,J).

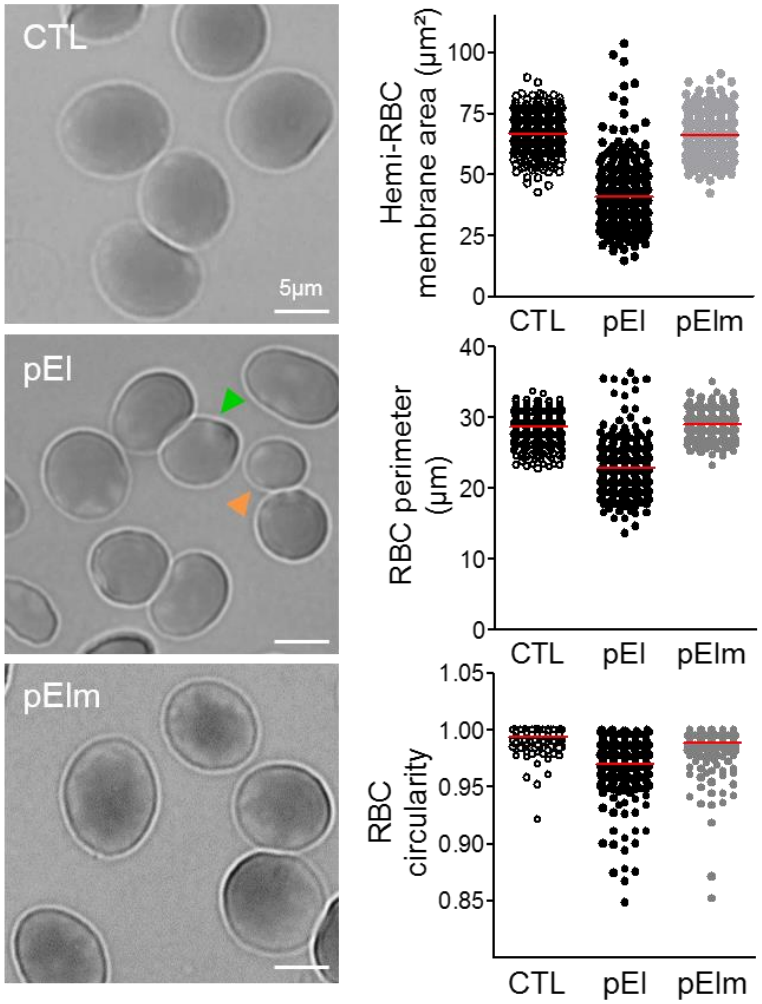

Supplemental Figure 2. Decreased membrane surface, perimeter and circularity of pEl RBCs on PLL-coated coverlips – Extension of Figure 1B. RBC hemi-surface, RBC perimeter and circularity determined on microscopy images of living RBCs laid down on PLL-precoated coverslips. Left, representative images; green arrowhead, poïkilocytotic RBC; orange arrowhead, small spherical RBC. Right, quantification shown for one representative PLL-coated coverslip per condition (n=20; area and perimeter: CTL *vs* pEl: ***, CTL *vs* pElm: ns, pEl *vs* pElm: ***; circularity: CTL *vs* pEl: ***, CTL *vs* pElm: *, pEl *vs* pElm: *).

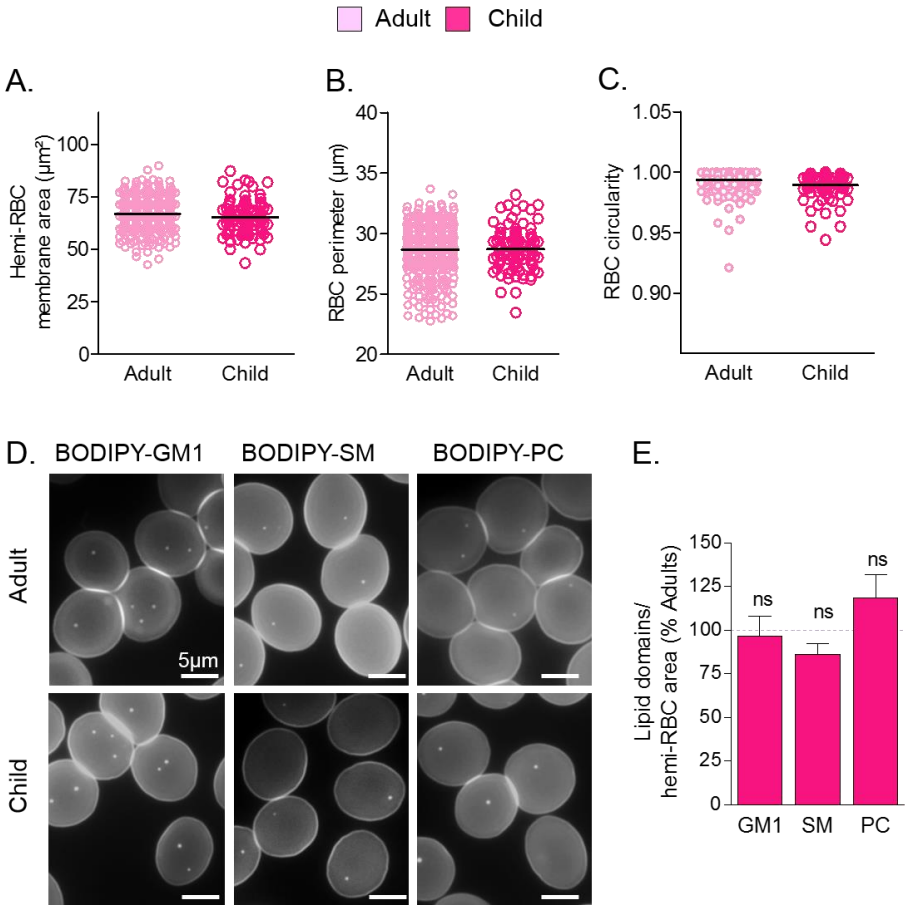

Supplemental Figure 3. Comparison of adult and child healthy donors for RBC morphology and lipid domain abundance. Washed and diluted RBCs from adults or childs were spread onto PLL-coated coverslips, labeled with BODIPY-GM1, -SM or -PC and directly visualized by fluorescence microscopy. **(A-C)** Quantification of the hemi-RBC membrane area, perimeter and circularity for one representative coverslip (out of 4). **(D)** Representative images of lipid domains. **(E)** Quantification of lipid domain abundance per hemi-RBC area (means ± SEM from 3 independent experiments/lipid and 300-600 RBCs were counted per condition in each experiment).

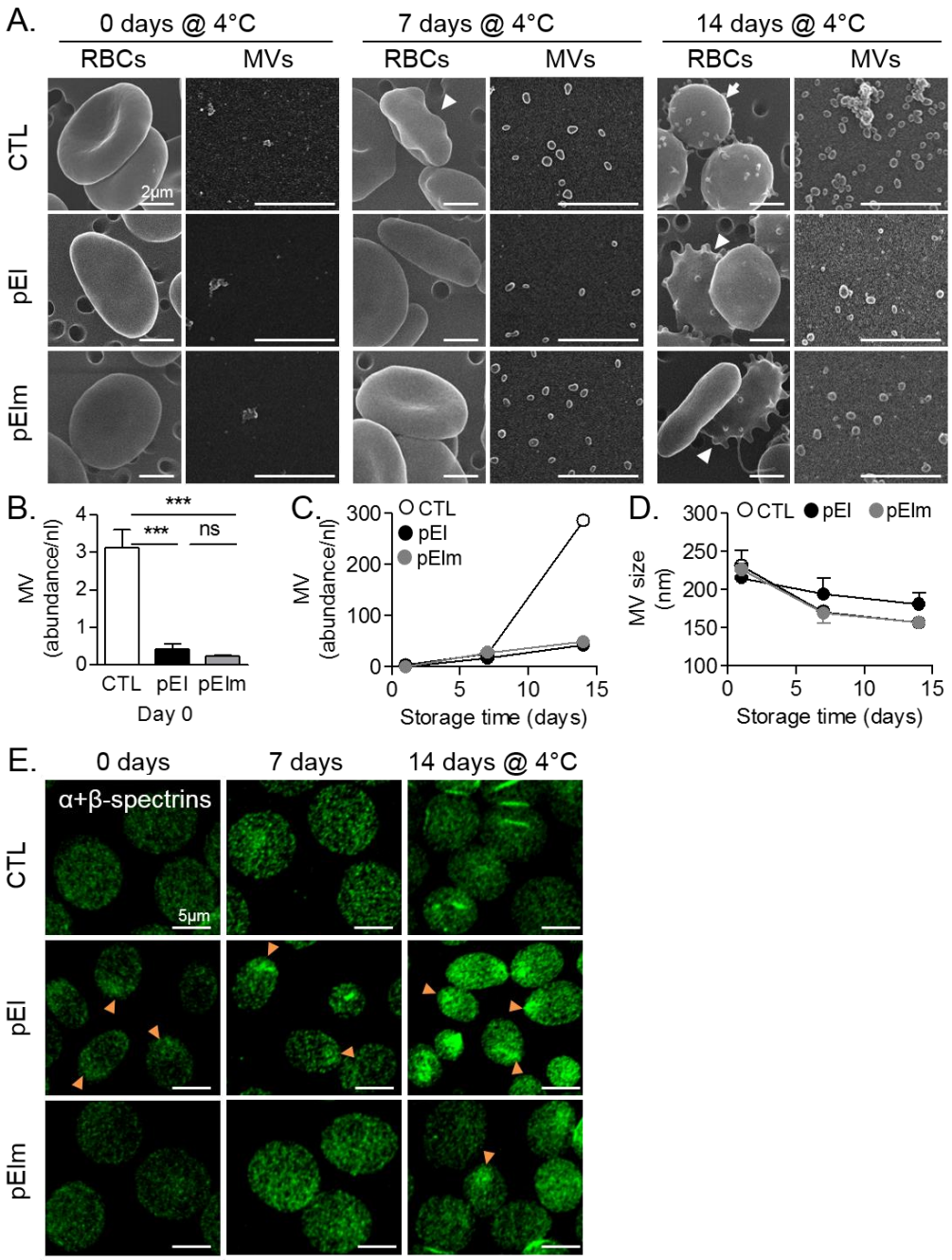
A.
0 days @ 4°C
7 days @ 4°C
14 days @ 4°C
RBCs
MVs
CTL
pEI
pElm
2µm
B.
MV (abundance/nl)
***
***
ns
CTL
pEI
pElm
Day 0
C.
MV (abundance/nl)
CTL
pEI
pElm
Storage time (days)
D.
MV size (nm)
CTL
pEI
pElm
Storage time (days)
E.
0 days
7 days
14 days @ 4°C
α+β-spectrins
5µm
CTL
pEI
pElm

Supplemental figure 4. Evolution of the RBC morphology, microvesicle release and spectrin density during blood storage at 4°C. (A) Representative scanning electron microscopy images. RBCs maintained at 4°C for the indicated times were washed, fixed in suspension and laid down on filters (left images). MVs, isolated from the same blood samples by multiple centrifugation steps, were laid down on PLL-precoated coverslips and fixed (right images). Arrowheads, echinocytes; arrow, spherocyte. Representative images of 2 independent experiments. **(B-D)** Abundance and size of MVs, either from fresh blood (B) or upon storage (C,D) (means ± SD of 3 independent measures of the same MV preparations). **(E)** Spectrin density determined as in Figure 2A (3 experiments). Orange arrowheads point to increased spectrin density.

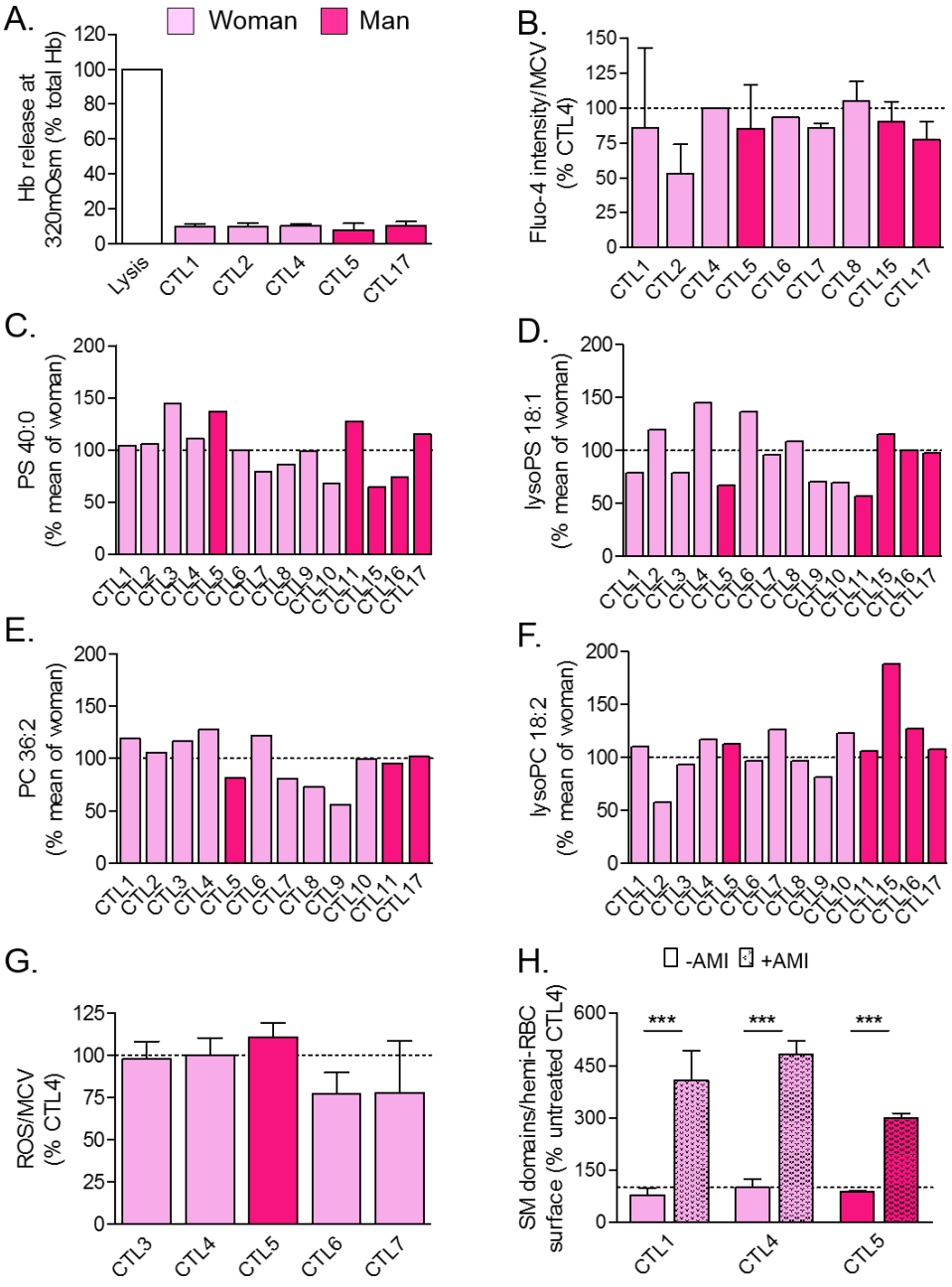
A.
Woman
Man
Hb release at 320mOsm (% total Hb)
120
100
80
60
40
20
0
Lysis
CTL1
CTL2
CTL4
CTL5
CTL17
B.
Fluo-4 intensity/MCV (% CTL4)
150
125
100
75
50
25
0
CTL1
CTL2
CTL4
CTL5
CTL6
CTL7
CTL8
CTL15
CTL17
C.
PS 40:0 (% mean of woman)
200
150
100
50
0
CTL1
CTL2
CTL3
CTL4
CTL5
CTL6
CTL7
CTL8
CTL9
CTL10
CTL11
CTL15
CTL16
CTL17
D.
lysoPS 18:1 (% mean of woman)
200
150
100
50
0
CTL1
CTL2
CTL3
CTL4
CTL5
CTL6
CTL7
CTL8
CTL9
CTL10
CTL11
CTL15
CTL16
CTL17
E.
PC 36:2 (% mean of woman)
200
150
100
50
0
CTL1
CTL2
CTL3
CTL4
CTL5
CTL6
CTL7
CTL8
CTL9
CTL10
CTL11
CTL17
F.
lysoPC 18:2 (% mean of woman)
200
150
100
50
0
CTL1
CTL2
CTL3
CTL4
CTL5
CTL6
CTL7
CTL8
CTL9
CTL10
CTL11
CTL15
CTL16
CTL17
G.
ROS/MCV (% CTL4)
125
100
75
50
25
0
CTL3
CTL4
CTL5
CTL6
CTL7
H.
-AMI
+AMI
SM domains/hemi-RBC surface (% untreated CTL4)
600
450
300
150
0
***
***
***
CTL1
CTL4
CTL5

Supplemental Figure 5. Comparison of different healthy donors for RBC fragility, intracellular calcium and ROS contents, lipid content and abundance of lipid domains. (A) Hemoglobin release determined after blood incubation at 37°C for 1h (means ± SEM of 3 independent experiments). **(B,G)** Intracellular calcium and ROS contents measured as in Figures 3F and 6D and expressed as percentage of healthy donor 4 (CTL4) (means ± SD of 1 to 6 independent experiments). **(C-F)** PS 40:0, lysoPS 18:1, PC 36:2 and lysoPC 18:2 species determined by lipidomics, expressed as percentage of healthy woman and taken as examples of lipids highlighted at Figures 7 and S10. **(H)** SM-enriched domain abundance on RBCs pretreated or not with amitriptyline (AMI) (means ± SEM of 3-4 independent experiments and 200-400 RBCs were counted per condition in each experiment).

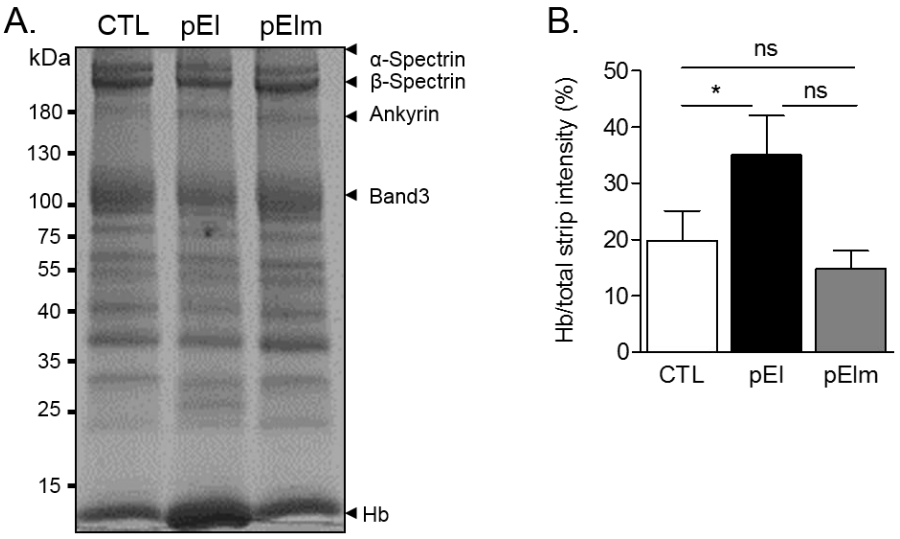

Supplemental Figure 6. Decrease of the major RBC cytoskeletal and membrane proteins contrasting with higher hemoglobin retention in the pEl ghost membrane. (A,B) Abundance of hemoglobin retained in the ghost membrane determined by SDS-PAGE. (A) Representative SDS-PAGE and Coomassie blue staining of ghost membrane proteins. (B) Quantification of hemoglobin (Hb) associated with the membrane, expressed as the percentage of the sum of all strips in the track. All data are means ± SEM of 5-9 independent experiments.

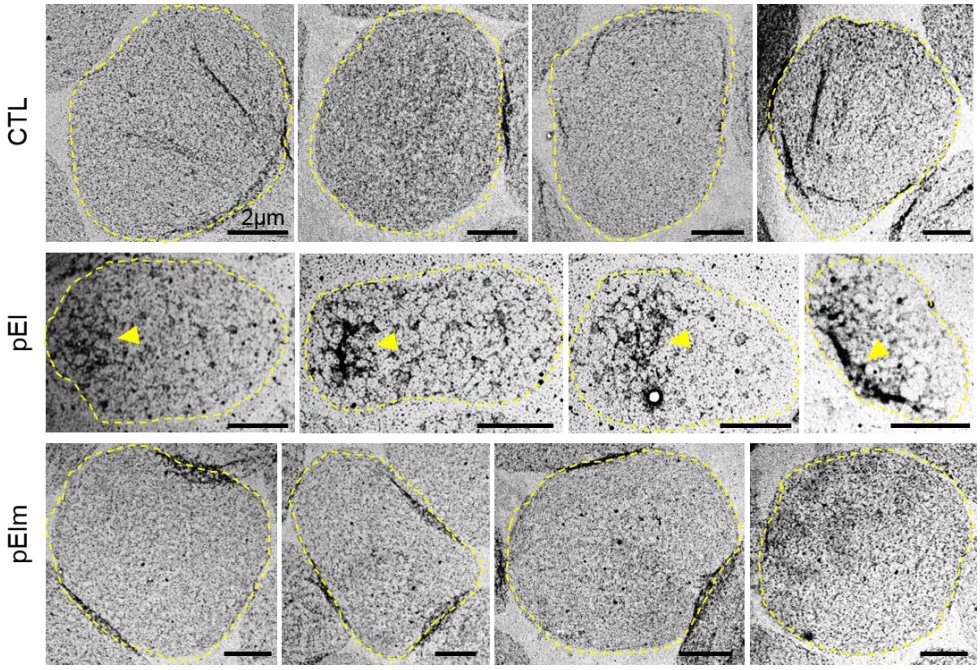

Supplemental Figure 7. Gathering of cytoskeleton proteins at one edge of pEl RBCs – Extension of Figure 2D. RBCs were laid down on PLL-precoated formvar coated grids, permeabilized with 0.5% Triton X-100, fixed and analyzed by transmission electron microscopy. Yellow lines, outlines of the RBCs. Yellow arrows, increased protein density.

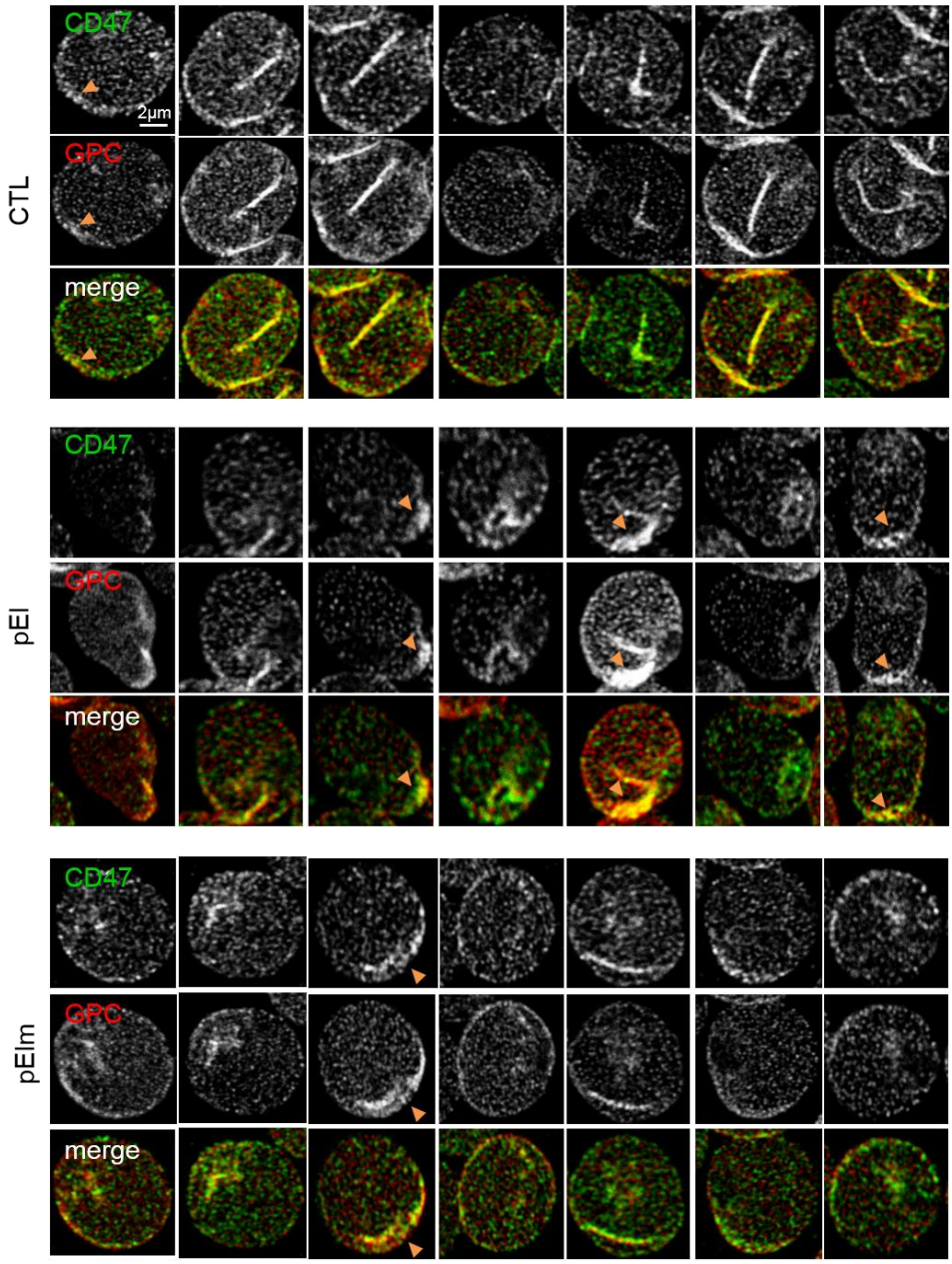

Supplemental Figure 8. Altered distribution of membrane proteins from the two anchorage complexes – Gallery of images presented at Figure 2E. RBCs were laid down on PLL-precoated coverslips, fixed and stained with antibodies against CD47 (ankyrin complexes; green) and glycophorin C (GPC; 4.1R complexes; red). Orange arrowheads point to high local protein density.

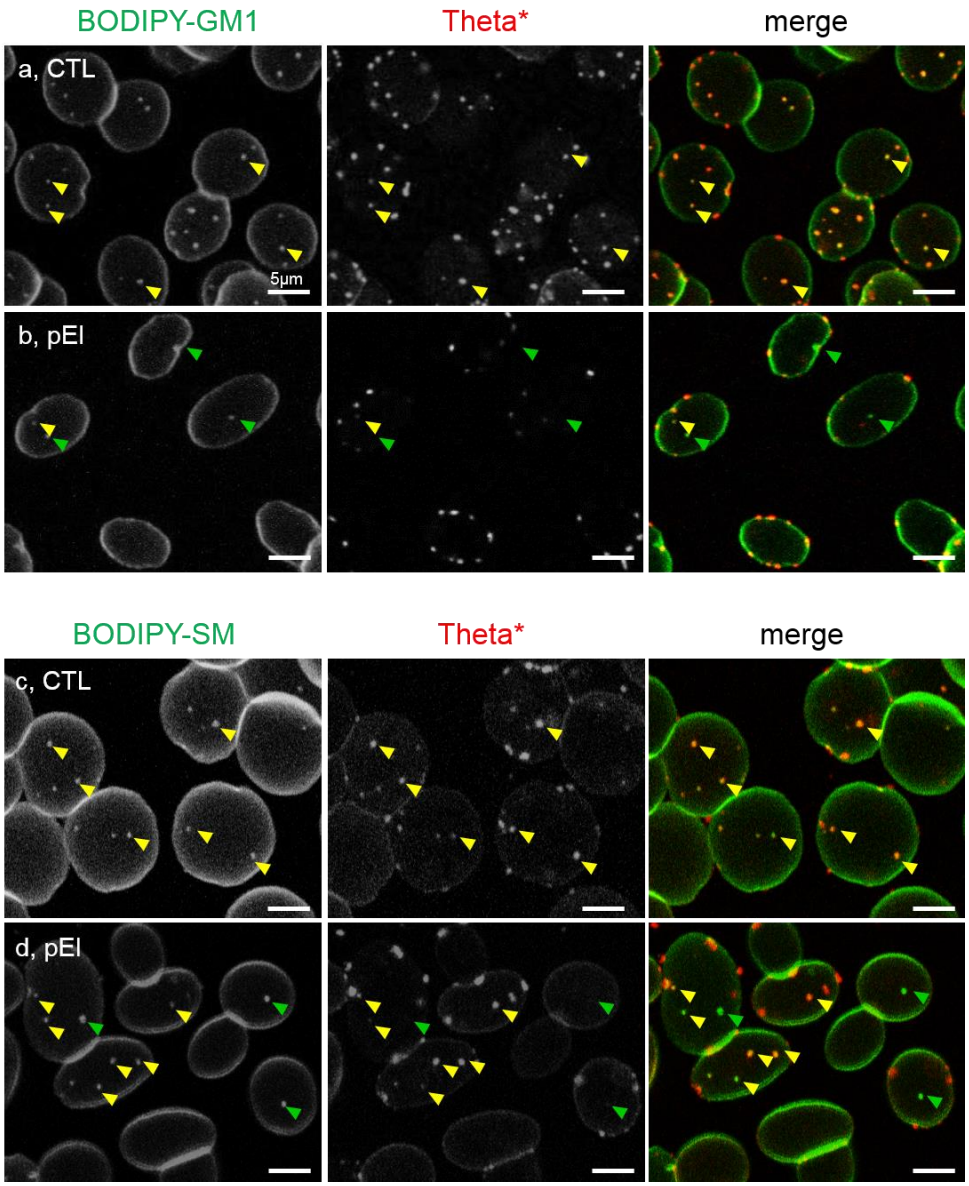

Supplemental Figure 9. Lower spatial association of GM1- and SM-enriched domains with those enriched in chol in pEl RBCs - Illustration of quantification presented at Figure 4B. RBCs were labeled in suspension with Theta*, spread onto coverslips and labeled with either BODIPY-GM1 (a,b) or -SM (c,d). Green arrowheads, BODIPY-GM1 or -SM only; yellow arrowheads, BODIPY-GM1/Theta* or BODIPY-SM/Theta* co-labelled domains. Images presented at (a,b) and (c,d) are representative of 2 and 3 independent experiments, respectively.

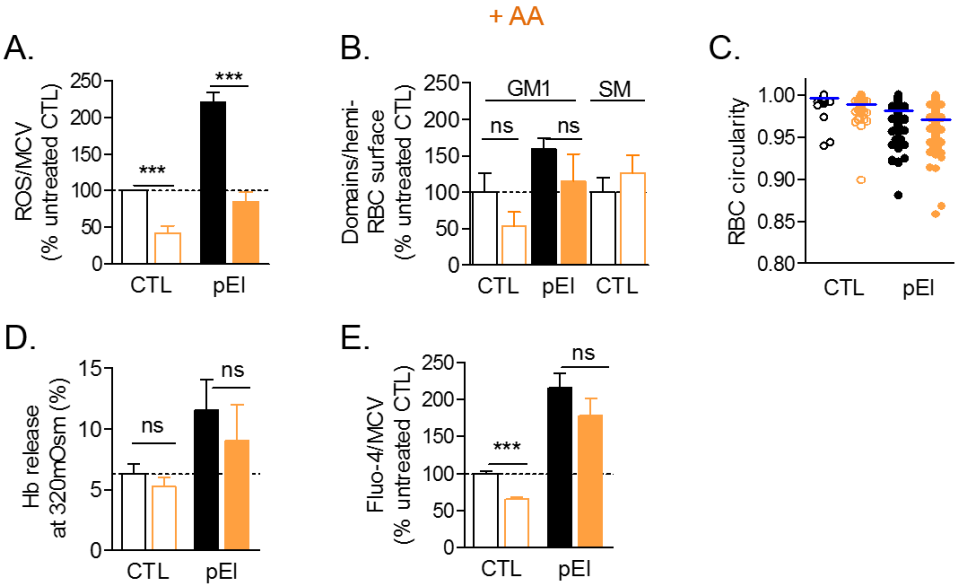

Supplemental Figure 10. The antioxidant ascorbic acid does improve neither lipid domain abundance nor RBC circularity and fragility in pEI. Effect of ascorbic acid (AA) on lipid domain abundance, RBC circularity and fragility and calcium accumulation. Diluted blood incubated with AA was washed and assessed**.** (A) ROS measured as in Figure 6E (means ± SEM of 4 independent experiments). (B) Lipid domain abundance per hemi-RBC surface determined as in Figure 4B (means ± SEM of 2-3 independent experiments). (C) RBC circularity measured as in Figure S2 (one representative out of 4 independent experiments; CTL vs CTL+AA, **; pEI vs pEI+AA, *). (D) RBC fragility evaluated in isotonic medium as in Figure 1F. (E) Intracellular calcium content evaluated as in Figure 4F (means ± SEM of 3-4 independent experiments).

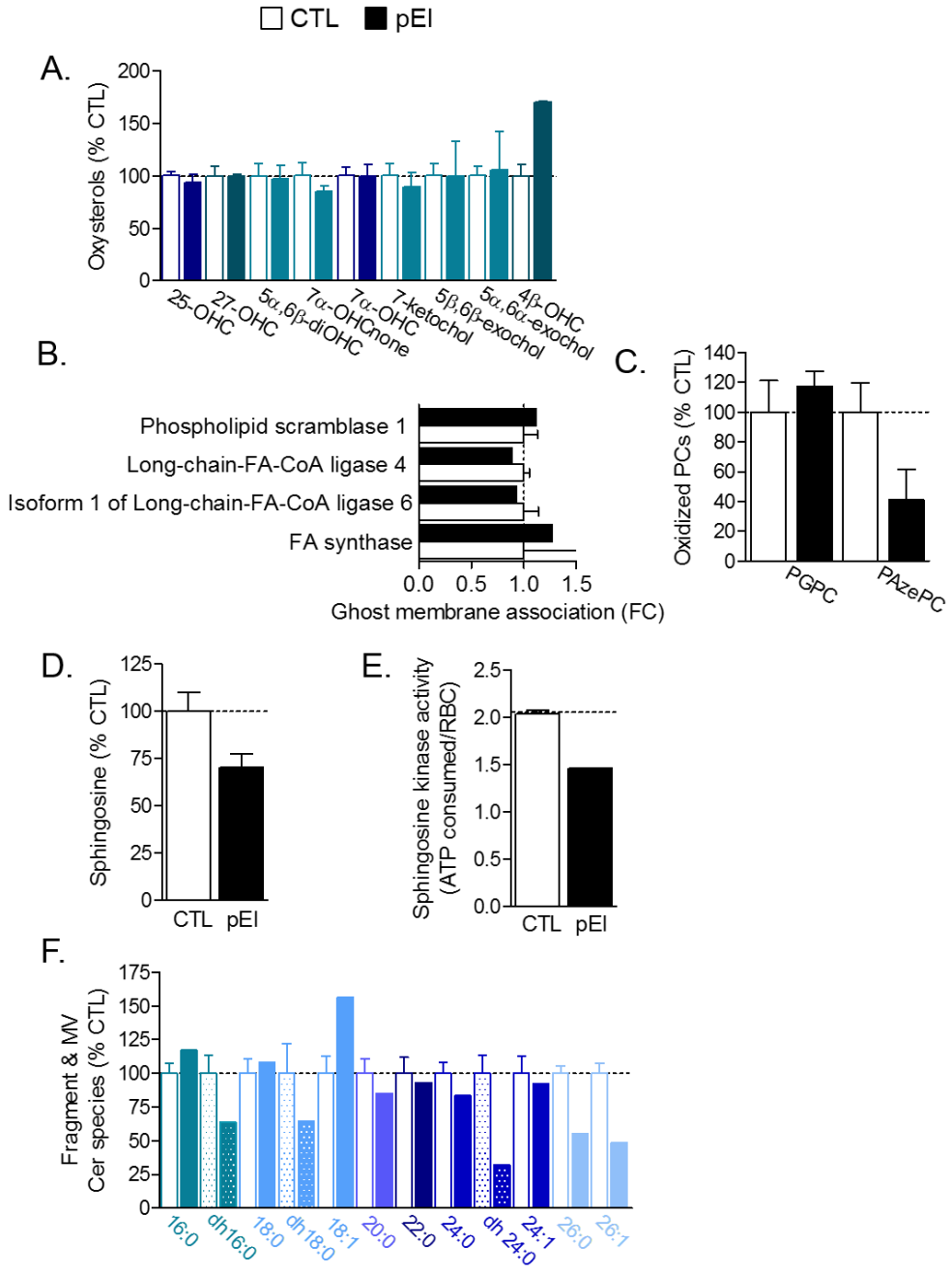
CTL
pEI
A.
Oxysterols (% CTL)
200
150
100
50
0
25-OHC
27-OHC
5α,6β-diOHC
7α-OHCnone
7α-OHC
7-ketochol
5β,6β-exochol
5α,6α-exochol
4β-OHC
B.
Phospholipid scramblase 1
Long-chain-FA-CoA ligase 4
Isoform 1 of Long-chain-FA-CoA ligase 6
FA synthase
0.0
0.5
1.0
1.5
Ghost membrane association (FC)
C.
Oxidized PCs (% CTL)
140
120
100
80
60
40
20
0
PGPC
PAzePC
D.
Sphingosine (% CTL)
125
100
75
50
25
0
CTL
pEI
E.
Sphingosine kinase activity (ATP consumed/RBC)
2.5
2.0
1.5
1.0
0.5
0.0
CTL
pEI
F.
Fragment & MV Cer species (% CTL)
175
150
125
100
75
50
25
0
16:0
dh16:0
18:0
dh18:0
18:1
20:0
22:0
24:0
dh 24:0
24:1
26:0
26:1

Supplemental Figure 11. Altered sphingolipid and oxidized lipid content in pEl RBCs – Extension of Figures 5 and 7. (A) Content in oxysterols. RBCs were washed, lysed, extracted for lipids and determined for (i) tail-oxidized sterols: 25-hydroxycholesterol (25-OHC) and 27-hydroxycholesterol (27-OHC); and (ii) ring-oxidized sterols: 5α,6β-dihydroxycholesterol (5α,6β-diOHC), 7α-hydroxycholestenone (7α-OHCnone), 7α-hydroxycholesterol (7α-OHC), 7-ketocholesterol (7-ketochol), 5β,6β-epoxycholesterol (5β,6β-exochol), 5α,6α-epoxycholesterol (5α,6α-exochol) and 4β-hydroxycholesterol (4β-OHC). Blue bars, enzymatic and non-enzymatic production; dark green bars, enzymatic production; light green bars, non-enzymatic production. Results are expressed as chol/PLP ratio in A (mean of 2-3 independent experiments) and as percentage of control RBCs in B-J (mean of 9 healthy women). **(B)** Abundance of lipid biosynthesis enzymes associated to pEl ghost membrane and determined by mass spectrometry. Results are expressed by reference to the healthy donor. **(C)** Content in oxidized PC species carrying a carboxylic group. RBCs were washed, supernatants were collected, lysed and assessed by HPLC-MS for the 1-palmitoyl-2-glutaroyl-sn-glycero-3-phosphocholine (PGPC) and the 1-palmitoyl-2-azelaoyl-sn-glycero-3-phosphocholine (PAzePC). Open bars, RBCs; spotted bars, supernatants. **(D)** RBC sphingosine assessed by HPLC-MS on washed, lysed and lipid-extracted RBCs. **(E)** RBC membrane sphingosine kinase activity measured by consumption of ATP added to the samples (means ± SD of quadruplicates from 1 experiment). **(F)** Fragment/microvesicle-associated Cer species. RBCs were washed, supernatants were collected, lysed and assessed by lipidomics. Cer and dihydro (dh)-Cer species are classified based on fatty acid length and insaturation number and results are expressed as percentage of results obtained in control RBCs fragments (mean of 7 healthy women).

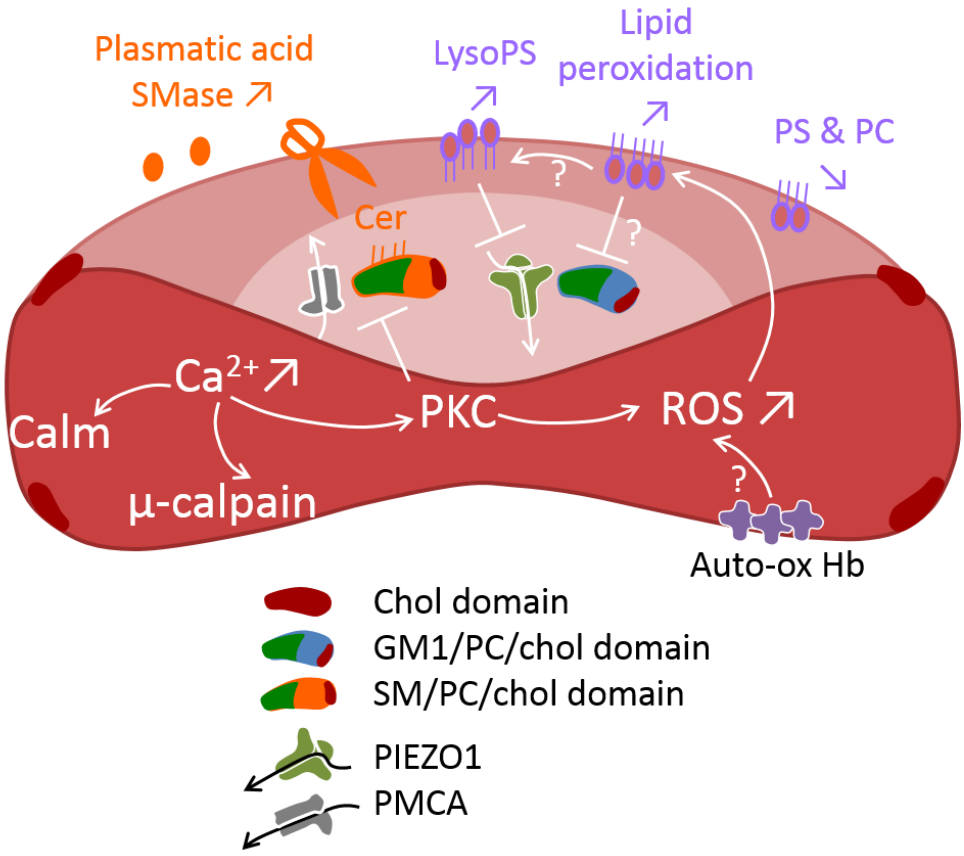

Supplemental Figure 12. Model for the molecular mechanism behind alteration of calcium influx and efflux in a severe case of elliptocytosis. ?, remains to be demonstrated. PLP, phospholipid; ox., oxidized. For additional information, see discussion.

Results

References

1. Guillemot-Legris O, Masquelier J, Everard A, Cani PD, Alhouayek M, Muccioli GG. High-fat diet feeding differentially affects the development of inflammation in the central nervous system. *J Neuroinflammation*. 2016;13(1):206.
2. Mutemberezi V, Masquelier J, Guillemot-Legris O, Muccioli GG. Development and validation of an HPLC-MS method for the simultaneous quantification of key oxysterols, endocannabinoids, and ceramides: variations in metabolic syndrome. *Anal Bioanal Chem*. 2016;408(3):733-745.
3. Prausnitz MR, Lau BS, Milano CD, Conner S, Langer R, Weaver JC. A quantitative study of electroporation showing a plateau in net molecular transport. *Biophys J*. 1993;65(1):414-422.
4. Fairbanks G, Steck TL, Wallach DF. Electrophoretic analysis of the major polypeptides of the human erythrocyte membrane. *Biochemistry*. 1971;10(13):2606-2617.
5. Streichman S, Gescheidt Y. Cryohemolysis for the detection of hereditary spherocytosis: correlation studies with osmotic fragility and autohemolysis. *Am J Hematol*. 1998;58(3):206-212.

Results

CHAPTER IV – GENERAL DISCUSSION AND PERSPECTIVES

This thesis contributes to a better understanding of lipid domains at the surface of RBCs, regarding their real existence, organization, roles, biophysical properties and alteration in diseases. The major findings are recapitulated in section 1 of this chapter. After that, a brief evaluation of the experimental strategies used to label Ca^{2+}, to deform RBCs and to analyse domain biophysical properties is provided (section 2). Then, as our results suggest a close relation between lipid domain abundance and Ca^{2+} exchanges at the RBC surface, we extensively discuss the ways by which membrane lipid composition and organization might regulate Ca^{2+} transport proteins (section 3). Finally, perspectives for this study are proposed in section 4.

1. Summary of key findings, general discussion and proposed models

To deliver O_2 to tissues, RBCs undergo high deformation while passing through narrow capillaries. Such exceptional deformability relies on RBC intrinsic features, including (i) a biconcave shape resulting from an excess of PM surface and the fine regulation of the intracellular volume and viscosity; and (ii) a resistant but dynamic cytoskeleton of spectrin that is strongly anchored to the membrane through two non-redundant protein complexes. However, the importance of membrane lateral heterogeneity for RBC deformability had not been often explored. This could be linked to the lack of a map of coexisting submicrometric lipid domains at the RBC surface as well as the poor understanding of their biophysical properties.

1.1. At least three types of submicrometric lipid domains coexist at the RBC surface

Our group was the first to evidence stable submicrometric lipid domains at the external leaflet of living RBCs, thanks to the use of complementary probes that are compatible with live cell imaging (Carquin et al., 2016). Those domains were defined as follows: (i) they exhibit a size of 200 to 500 nm in diameter (i.e. smaller

than lipid rafts); (ii) their lipid enrichment is not restricted to sphingolipids and chol found in lipid rafts; (iii) they are stable in time (through minutes) and in space (in contrast to the transient lipid rafts); and (iv) they can be controlled by both lipid-lipid and protein-lipid interaction, including the cytoskeleton. The first part of my thesis was to establish a mapping of submicrometric lipid domains at the surface of resting healthy RBCs. We have shown that cholesterol-, SM-, PC- and GM1-enriched domains differ in abundance, curvature association, fluidity and dependence on cholesterol content and on temperature. Based on all those observations and co-labelling experiments, we concluded that three types of submicrometric domains differentially enriched in lipids coexist at the PM of RBCs at resting state and at physiological temperature (figure 4.1. #1). First, there are domains that are mostly enriched in cholesterol, abundant (~8/hemi-RBC), associated to high macroscopic curvature and that exhibit a higher lipid order than the other domains. The second type of domains is co-enriched in GM1, PC and cholesterol. They are less abundant (~1.5/hemi-RBC), preferentially located in macroscopic low curvature areas and they present a lower ordering. Third, domains co-enriched in SM, PC and cholesterol also coexist at the RBC PM, even though they are quite rare at resting state (~0.6/hemi-RBC). They are also located in low-curvature areas and present a low order.

In addition to those three types of lipid domains, other stable submicrometric domains might co-exist at the RBC surface. For example, ceramide-enriched domains have been evidenced in Chapter III, publication 4. The relationship between ceramide-enriched and other lipid-enriched domains remains to be established and could be addressed by multiple labelling between BODIPY-ceramide and Lysenin, Theta or cholera toxin derivatives.

An important question is whether those different types of domains are regulated by similar mechanisms or not. Hence, one can ask why some of those domains present a so low abundance on RBCs at resting state. Considering the wide range of domain features that lipid-lipid interactions can generate in molecular dynamic simulations of simple and complex bilayers (Ackerman and Feigenson, 2015; Gu et al., 2017; Koldso et al., 2014) as well as in experimental data of simple lipid mixtures (Kahya and Schwille, 2006; Sezgin et al., 2015; Veatch and Keller, 2005), it is not so surprising to unveil such a diversity of lipid domains in living cell membranes. Direct lipid-lipid interactions could be able to induce lipid clusters in systems devoid of proteins and certainly help to understand some of the lipid domain behaviors that we evidenced on RBCs. For instance, differential temperature dependence of lipid domains is partly explainable by individual lipid intrinsic properties (e.g. head group, acyl chain length and saturation) (Chapman, 1975). Moreover, lipid domain biogenesis and/or maintenance also depend on the

chol content, as chol is a key regulator of membrane fluidity (and thus space between phospholipids for optimal head group interactions) and is able to directly interact with SM or GM1 (Garcia-Arribas et al., 2016; Gu et al., 2017).

In complex active system including lipids and proteins like living cell membranes, it is however unlikely that such lipid-lipid interactions are the only key regulators of lipid domains. Several regulators for chol-enriched domains located in RBC high curvature areas have been proposed in (Leonard et al., 2017) (see annex 2). Regarding low curvature-associated domains (i.e. GM1/PC/chol-enriched and SM/PC/chol-enriched), their maintenance at low level at resting state could involve membrane:cytoskeleton anchorage and/or charge-mediated interactions. Lipid domain stability in time and space at resting state support the hypothesis of their restriction by anchorage of the membrane to the cytoskeleton, either via direct interactions with anchorage complex proteins or via inner PM leaflet coupling. Considering that an inter-digitation between SM and PIP2 at the inner leaflet has been evidenced during cytokinesis (Abe et al., 2012), we currently favor the hypothesis that SM/PC/chol-enriched domains are restricted via inner PM leaflet coupling, while GM1/PC/chol-enriched domains might interact directly with the anchorage complex proteins. Those hypothesis should be tested as exposed in section 4.

1.2. Lipid domains differ in elasticity and are relevant to unlabeled RBCs

In order to assess the relevance of those domains on labelled RBCs, we turned toward AFM. This technique allows the high resolution scanning of the RBC surface, but also to study the cell nanomechanical properties, *i.e.* the resistance to an applied deformation by the tip (=elasticity). Thanks to AFM experiments, we confirmed the existence at the RBC surface of numerous submicrometric, but also nanometric, domains with differential height and elasticity (either higher or lower than the surrounding membrane). Furthermore, some of those domains were correlated with fluorescently-labelled SM-enriched domains. Those results thus suggest that a wide variety of lipid domains of different size, composition and biophysical properties coexist at the PM of RBCs, and that the submicrometric lipid domains that we show in fluorescence microscopy only represent a portion of the lateral lipid heterogeneity. Evidencing the extent of the lipid lateral heterogeneity in the PM would definitely require the use of complementary approaches to ally specific probes, high spatial resolution and high temporal resolution. Indeed, a

subpopulation of highly dynamic lipid domains might remain invisible by AFM due to the relatively low temporal resolution (see section 2.3).

AFM also allowed us to compare the effect of differential indentation rates on the measured nanomechanical properties and evidenced that the contribution of the PM and of the cytoskeleton to the local elasticity can be separated. This ability was used to compare the properties of healthy RBCs *vs* poorly deformable spherocytotic RBCs. Interestingly, the loss of anchorage between the cytoskeleton and the membrane in the disease not only stiffens the cell through the cytoskeleton (as observed at high indentation rates) but also results in an increased membrane stiffness (as observed in low indentation rates). Therefore, the AFM results suggest that the PM lipid content and it nanoscale organization also influence the nanomechanics of RBCs.

To evaluate the composition of this multitude of lipid domains evidenced by AFM, we then took advantage of the ability to functionalize the sharp AFM tip with the fluorescent toxin fragments that specifically recognize SM (*i.e.* Lysenin toxin) or cholesterol (*i.e.* Theta toxin) at the outer leaflet (Carquin et al., 2015; Carquin et al., 2014). To achieve coupling between the toxin and the AFM gold tip, two separate techniques were used. On one hand, the HIS-tagged fluorescent Lysenin toxin was bound to a gold tip coated with PEG-NTA (*i.e.* a metal chelating ligand that has excellent affinity toward Ni^{+}) linkers. On the other hand, HIS-tagged fluorescent Theta toxin was modified to remove the fluorescent group and add a LPETGG sequence. The sequence can react with a tip coated with PEG-poly-G sequence to form a covalent bond in a sortase A-mediated reaction. Those functionalized tips represent novel and valuable tools to study cholesterol and SM lateral heterogeneity at high resolution. Their use was already validated on artificial membranes of controlled composition as well as on cancerous cells with differential invasive patterns (collaboration with Pr. Alsteens, their unpublished results). In those experiments, spots of tip-membrane adhesion were correlated with variation of membrane height and elasticity. This study suggests that the further use of functionalized tips on RBCs could allow to specifically and precisely study the morphological and nanomechanical properties of cholesterol- and SM-enriched domains. However, their use on RBCs is so far challenged due to high fragility but also important curvature, leading to an increased contact area between the probe and the cell, which results in unspecific adhesion events.

1.3. Lipid domains contribute to RBC deformation

After the morphological and biophysical characterization of lipid domains at the surface of RBCs at resting state, we extended the study to RBC upon deformation. To do so, we simulated deformation by immobilizing and transiently (for one minute) stretching RBCs in a silicon (PDMS) chamber before allowing them to restore their initial shape. Thank to this technique, a gathering of cholesterol-enriched domains in high-curvature membrane areas has previously been revealed (Leonard et al., 2017). In this thesis, I studied the intracellular Ca^{2+} content and the GM1- and SM-enriched domains upon this simulation. As expected from the literature (Danielczok et al., 2017), I observed that the RBC stretching is associated with a rapid and transient increase of the intracellular Ca^{2+} concentration, validating this technique. Interestingly, we showed a concomitance between the Ca^{2+} influx and an increase of the abundance of GM1-enriched domains as well as a concomitance between the Ca^{2+} efflux and an increased abundance of SM-enriched domains. We further examined those relations by directly or indirectly activating and inhibiting the Ca^{2+} influx through mechanosensitive cation channel Piezo1 and Ca^{2+} efflux through the Ca^{2+} pump PMCA. Our results confirmed that the activation of Piezo1 is correlated with an increase of GM1-enriched domains (figure 4.1. #3, left), whose specific biophysical properties could modulate the channel conformation changes. On the other hand, SM-enriched domain abundance was not affected by Piezo1 activation, but well upon PMCA pump activity modulation (figure 4.1. #3, right). We suggest that domains could promote the pump activation either directly or through modulation of the cytoskeleton anchorage or the inner leaflet organization.

The many ways by which lipids could modulate the Ca^{2+} exchanges are extensively discussed below in section 3.1. In section 3.2, we selected some of those mechanisms that could apply to RBCs, based on our results and on the literature.

1.4. Lipid domains and membrane composition are altered in hereditary elliptocytosis

Finally, we explored the lipid domain organization in a membrane fragility disease in which RBC deformability is decreased, namely hereditary elliptocytosis. We extensively analyzed the RBCs from one patient who suffers from mutations in the α-spectrin gene. We observed that the RBC size, circularity and deformation are impaired in this patient. We evidenced that SM- and GM1-enriched domains are modified in abundance, cholesterol content and response to Ca^{2+} exchange stimulation. This results from three features (figure 4.1. #4). First, the plasmatic acid

sphingomyelinase (SMase) is upregulated, leading to increased Cer-enriched domains. Second, the intracellular Ca^{2+} content is strongly increased, inducing downstream (i) PKC-dependent cytoskeletal and membrane protein phosphorylation; (ii) NADPH oxidase-dependent ROS production and lipid peroxidation; and (iii) scramblase-dependent PS exposition at the RBC surface. Third, the membrane content of long unsaturated PS species is decreased whereas the content of several lysoPS species is increased. All these features could lead to membrane fragmentation. Some linking chains however remain to be tested. As a matter of fact, the mechanistic behind Ca^{2+} accumulation in the patient still needs to be determined and could imply NMDA receptors, Ca^{2+} channels that have been described in RBC precursors but that might be still present in mature elliptocytotic RBCs. $Ca_v2.1$ channels, described at the surface of mature healthy RBCs, could also be involved. The study of the Ca^{2+} accumulation consequences is currently completed through the measurement of the activity of the Ca^{2+}-activated protease μ-calpain. Finally, whether accumulation of ROS content and of lysophospholipids at the external leaflet could lead to specific effects on lipid domains, Ca^{2+} transport protein activity and RBC stretching response also remains to be established. Altogether, this study shows that alteration of membrane lipids and lipid domains contribute to the pathophysiology of elliptocytosis, which could help in novel therapies development.

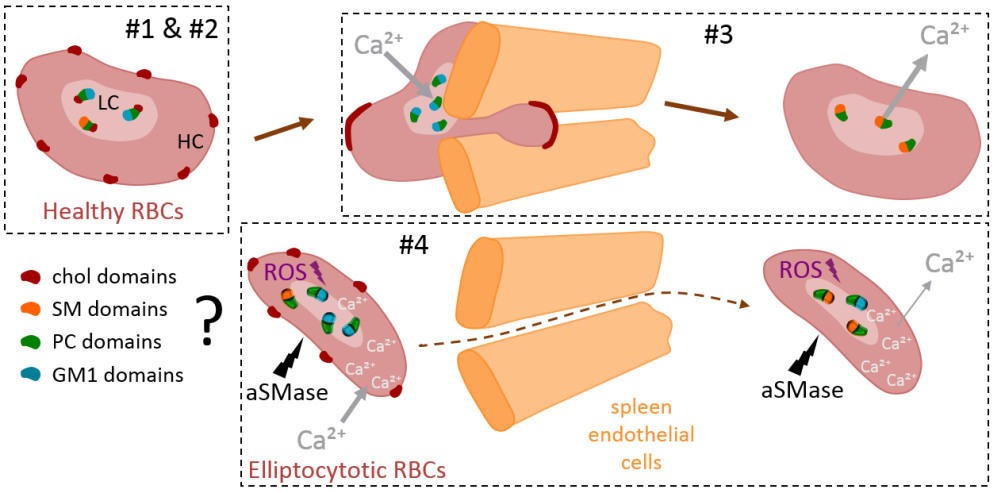

Figure 4.1. Current hypothetical model for the mapping and role of lipid domains at the surface of: (#1-3) healthy RBCs upon resting (#1 & #2) and upon deformation and shape restoration (#3); and **(#4)** diseased RBCs (hereditary elliptocytosis). LC, low curvature; HC, high curvature; ROS, reactive oxygen species; aSMase, acid sphingomyelinase.

Altogether, the results presented in this thesis show that several types of lipid domains coexist at the PM of RBCs. They differ in lipid composition, abundance, size and biophysical properties. We have demonstrated that some lipid domains are modified in abundance during the RBC deformation process, suggesting that they might play a role in cell deformation. The possible regulation of Ca^{2+} exchanges by lipids and lipid domains is discussed in section 3 of this chapter. On the other side, poorly deformable elliptocytotic RBCs expose altered membrane lipid composition and lipid domain properties, suggesting that the membrane composition/organization could play a role in the pathophysiology of this disease.

2. Experimental strategy: strengths and weaknesses

The cell model as well as the lipid probes used in this study present several advantages, but also some limitations. As they have already been extensively discussed in our previous papers, I invite the reader to refer to those reviews (Carquin et al., 2016; Léonard et al., 2017) for more information. One additional weakness of this study is that the microscopy observations using the stretching device could only be made at room temperature, even though the labelling and the pharmacological treatments were achieved at physiological temperature. This could of course have important repercussions on the kinetics of the modulations observed (*e.g.* the PMCA activity has been shown to drastically decrease with the temperature (Lew et al., 2003)) as well as on the real abundance of lipid domains. The immobilization and consecutive partial stretching of RBCs could also lead to an underestimation of the domain abundance, as demonstrated by the important number of chol- and SM-enriched domains at the surface of RBCs in suspension in a 3D-gel (Carquin et al., 2015; Carquin et al., 2014).

In the following section, I will focus on the probe we used to measure Ca^{2+} inside the RBC (section 2.1.) as well as on the strategies we used to simulate RBC deformation (i.e. silicon chambers, section 2.2.) and to characterize the RBC membrane biophysical properties (i.e. AFM, section 2.3.).

2.1. Ca^{2+} labelling and measurement in RBCs

Several probes are available to measure the intracellular Ca^{2+} content, including Indo-1, Fura-2 and Fluo-4. The excitation wavelength for the first two probes ranges in the UV while it is of 480nm for Fluo-4 (figure 4.2.). The UV irradiation of RBC, however, results in generation of a highly fluorescent specimen, probably a bilirubin isomer. As the emission spectra of this bilirubin isomer largely overlaps with the spectra of both Indo-1 and Fura-2, those two indicators are not recommended for RBC measurements (Kaestner et al., 2006). Additionally, the

presence of Hb induces a significant emission and/or excitation quenching of all the three indicators in a concentration-dependent manner. However, while this quenching effect is homogeneous on the spectral shift of Fluo-4, Indo-1 and Fura-2 display dramatic heterogeneous alterations of their Ca^{2+}-dependent spectral properties (Kaestner et al., 2006). As a consequence, although detection of Fluo-4 emission will certainly be more difficult in the presence of Hb, changes in intracellular Ca^{2+} concentrations can be measured readily. Moreover, with the assumption of a resting Ca^{2+} concentration, it might even be possible to obtain good estimations of absolute Ca^{2+} concentrations (Thomas et al., 2000).

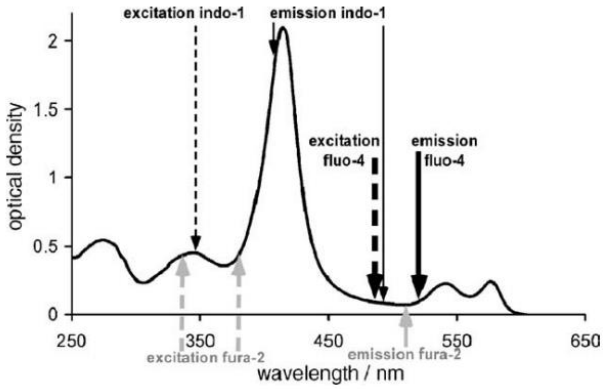

Figure 4.2. Absorption spectrum of Hb. The arrows point to the typical excitation wavelength and emission maxima of the Ca^{2+} fluorophores Fura-2, Indo-1 and Fluo-4. Reproduced from (Kaestner et al., 2006).

Finally, almost all of our Ca^{2+} measurements were achieved or confirmed by fluorescence microscopy imaging followed by individual cell contouring and measurement. This was suggested to be a superior technique over fluorescence spectrometer measurements for inherently heterogeneous RBCs populations (Kaestner et al., 2006), as confirmed in our study. Moreover, it allows to consider the occasional Fluo-4 surprising release from the cells that can lead to important background noise.

2.2. RBC deformation in silicon chambers

As described in the introduction (Chapter I, Section 6.1), there are several techniques that allow the study of cell deformation. We choose stretchable PolyDiMethylSiloxane (PDMS) chambers as this system presents several advantages for our study. First, the chambers are compatible with vital fluorescence imaging of RBCs. Indeed, their thin (100-200µm of thickness), optically transparent, membranes allow immobilization of living RBCs prior coating with

poly-L-lysine. This technique thus allowed us to observe in real time the intracellular Ca^{2+} content and the lipid domains at the surface of unstretched RBCs and then through stretching and shape recovering. Other techniques like ektacytometry or filtration do not allow real-time visualization in microscopy. Microfluidic filtration, on the other side, is microscopy-compatible, but the applied flow renders the deformation process extremely fast (up to ~10 cells/second in sorting experiments) and a specific equipment including high speed camera is thus required.

Second, PDMS chambers allow the analysis of multiple cells. This is quite important for RBC analysis as there might be a variability resulting from the heterogeneity of the cell population. Indeed, in blood at all time, newly formed RBCs will flow aside old, soon-to-be-eliminated, RBCs. This heterogeneity is characterized by a variability in the cell deformability (which decreases as the RBC get older) and the basal Ca^{2+} content (which increases as the RBC get older). Analysis of single cells would thus have to be repeated a high number of times to circumvent the population heterogeneity. Using PDMS chambers, we are able to analyze ~100 cells at each time, making the experiment highly efficient.

Third, the stretching system shows good reproducibility concerning uniformity of direction and force. It is simple of use and allows a strict control of stretching intensity and duration.

Cell stretching in PDMS chambers also present limitations. Among them, one can cite the monoaxial direction of stretching. This is a limitation for most microscopy-compatible techniques including micropipette and optical tweezers. However, this can be circumvented in newly developed stretching systems using an isotropic stretch (Schurmann et al., 2016). Another limitation is that we are unable to follow the same cell through deformation and shape restoration, as the stretching modify the focal plane. Finally, the kinetic of the Ca^{2+} exchanges observed by this technique are slower than expected in the blood flow. This could originate from the axial stretching or from the fact that RBCs are already spread and immobilized on poly-L-lysine prior to stretching.

2.3. RBC biophysical properties analysis by AFM

AFM is a unique technique whose limitations are constantly pushed back by improvement of the technology and development of new tools. It was ideal in complementation of our confocal approach for the following reasons. First of all, the technique does not require any labelling of the cell. This eliminates any possible artefacts linked to the insertion at the membrane of lipid analogs or to the addition of lipid-binding toxin fragments. For instance, it allowed us to confirm the existence

of submicrometric lipid domains of differential height and elasticity at the PM of unlabelled RBCs. Of course, one can hypothesize that all lipid domains would not necessarily present differential biophysical properties and that AFM would therefore not allow to evidence all the extent of lipid domain variety at the cell surface. This is why the use of complementary techniques is important.

Next, AFM does not require cell fixation (as confocal microscopy) and has a nanoscale resolution, i.e. ~10 nm in lateral resolution (*vs* ~300 nm for confocal microcopy) and up to the Angstroms in Z-axis upon ideal conditions (*vs* ~500nm for confocal microscopy). This high resolution allows to evidence nanometric heterogeneities, probably the 'lipid rafts', which are undefinable in classic microscopy. Other high resolution microscopy techniques exist. Among them, electron microscopy is a very useful tool for nanoscopic morphological studies but presents huge limitations for the membrane organization study as it requires cell fixation as well as efficient lipid labelling with gold microbeads. Other high resolution microscopy techniques like PALM (Photo-Activation Localization Microscopy), STORM (Stochastic Optical Reconstruction Microscopy) and SIM (Structured Illumination Microscopy) also have the inherent disadvantage of requiring the use of exogenous probes and are so far difficult to apply to living cells due to phototoxicity and photobleaching.

Another advantage of AFM is that, using the force-distance curve approach, the nanomechanical properties of the cell can be analyzed and correlated to variations of the membrane topology. Moreover, using variable indentation rates, the respective contributions of the membrane and the cytoskeleton components can be separated. This has come in very handful for determining that the rigidity of the spherocytotic cells originates from the decrease of both membrane and cytoskeleton elasticity.

Finally, functionalization of the sharp tip with a specific probe allows to link the high resolution mapping of a specific lipid (cholesterol or SM in our study) or protein to the nanomechanical properties of the membrane. In that way, AFM is the only high resolution technique that can study both lipid organization and membrane biophysical properties at a time.

AFM however also presents limitations, and the bigger one is the time resolution. Indeed, the imaging of a single RBC at high resolution currently still takes over 20 minutes as the tip oscillates close or at its resonance frequency. This thus greatly limits the number of cells that can be analysed during one experiment. Moreover, the dynamic scanning of the cell and the repeated application of indentations on weaken RBCs can lead to their bursting during the analysis. Finally, it is not possible to reveal several molecules and/or structures at the same time.

3. Membrane lipid composition and organization as a major determinant for Ca^{2+} transport protein activity?

The possible regulation of membrane proteins, and especially of Ca^{2+} transporters, by lipids is a field with increasing interest. Here under, we gather evidences for the regulation of Ca^{2+} transport proteins by lipids (section 3.1) and then integrate the hypothetical mechanisms by which lipids could regulate this transport in RBCs (section 3.2). We then provide first evidences linking lipid alterations and disturbed Ca^{2+} transport in physiological aging and diseases (section 3.3) and report the potential use of lipids as therapeutic targets in Ca^{2+} transport-related disease (section 3.4). Finally, we conclude on the current observations and lay down the future challenges (section 3.5).

This section is part of an invited review (Conrard, L.; Tyteca, D. Regulation of Membrane Calcium Transport Proteins by the Surrounding Lipid Environment. Biomolecules ***2019****,* 9*, 513.).*

3.1. Hypothetical mechanisms for the regulation of membrane Ca^{2+} transport proteins by lipids

Ca^{2+} transport proteins have been proposed to interact with, and to be possibly modulated through, the surrounding lipids. In general, those interactions can be classified according to the relative "residence" time of a particular lipid at the protein–lipid interface (Lee, 2003). If a lipid displays a low degree of interaction with the protein transmembrane domain (TMD), it exhibits a fast exchange rate with lipids in close proximity and is considered as a "bulk" lipid (red in Figure 4.3A). Increased retention around the protein can result from specific interactions between the protein and the lipid polar headgroup, hydrophobic matching to the lipid hydrocarbon chains and creation of a membrane curvature, a.o. Such interactions reduce the exchange rates with the lipids and lead to the formation of a shell of "annular" lipids that surrounds the membrane protein (green in Figure 4.3A; section 3.1.2) (Marsh, 2008). For large, multiple transmembrane (TM)-spanning proteins, the composition of this shell can be heterogeneous, because the interactions depend on the local architecture of the membrane protein and its compatibility with the various lipids (Anderson and Jacobson, 2002). This immobilizing effect of the protein might extend beyond the first shell of directly interacting annular lipids (orange in Figure 4.3A; section 3.1.3), leading to further outer shells with a lesser extent of lipid immobilization (Koldso and Sansom, 2012). Lipids with even lower exchange rates are denominated as "non-annular" lipids

(blue in Figure 4.3A; section 3.1.1). These lipids are buried within the protein and generally directly interact with distinct hydrophobic sites of membrane proteins, named lipid pockets. Those lipids may fulfill diverse functions, from structural building blocks to allosteric effectors of enzymatic activity.

Besides those three modes of interactions, a fourth still hypothetical way has emerged. It implies the gathering and downstream signaling of several proteins inside lipid domains (Figure 4.3B; section 3.1.4) which can be quite diverse. Among those are the lipid rafts, in which sphingolipids (SLs) form detergent-resistant membranes (DRMs) enriched in cholesterol and glycosylphosphatidylinositol (GPI)-anchored proteins in cold non-ionic detergents (Simons and Ikonen, 1997). Recent progress in microscopy (such as combined fluorescence correlation spectroscopy (FCS) with stimulated emission depletion microscopy (STED) (Vicidomini et al., 2015) or super-resolution microscopy (Stone et al., 2017)) provides evidence for the existence of such transient, nanoscale, cholesterol-, and SL-enriched membrane clusters. In addition to rafts, other nanoscale domains have been described at the PM of eukaryotes (i.e., caveolae and tetraspanin-rich domains (Parton and del Pozo, 2013; Yanez-Mo et al., 2009)). Those lipid domains are controlled by lipid-based mechanisms through cohesive interactions. Lipid and protein clustering into lipid domains can also be regulated by protein-based mechanisms, involving specific interactions between lipids on one hand and membrane or cytoskeletal proteins on the other hand. Interaction between membrane and the cortical cytoskeleton is supported by experimental data from several groups and is integrated in the picket and fence Kusumi's model (for additional information, see (Baumgart et al., 2007; Carquin et al., 2016)). In agreement with the lipid-based independent mechanisms for lipid domain biogenesis, stable submicrometric lipid domains of different composition and biophysical properties than lipid rafts have been reported in artificial (Baumgart et al., 2007; Bernardino de la Serna et al., 2004; Kahya et al., 2003) and highly specialized biological membranes (Bernardino de la Serna et al., 2004; Plasencia et al., 2007), and a variety of cells from prokaryotes to yeast and mammalian cells (Bach and Bramkamp, 2013; Carquin et al., 2015; Carquin et al., 2014; D'Auria et al., 2013; Grossmann et al., 2007; Sanchez et al., 2012; Tyteca et al., 2010a).

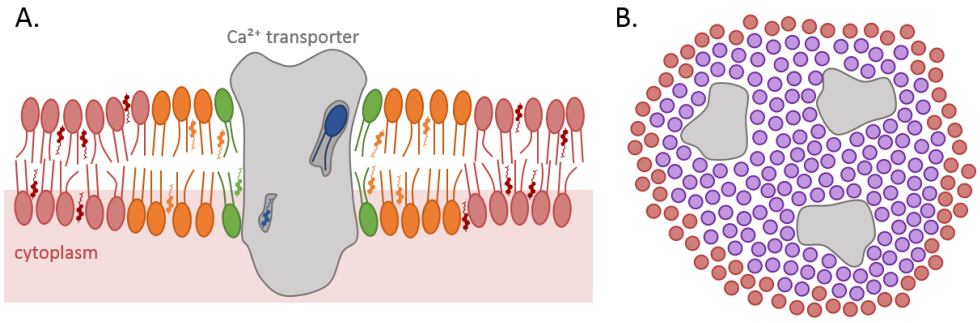

Figure 4.3. Simplified representation of potential modes of interactions between lipids and Ca^{2+} transport proteins. (**A**) Side view of a single protein anchored in the membrane. First, non-annular lipids (blue) interact directly with the protein (grey) inside its structure. Second, annular lipids from the first shell (green) can closely interact with the protein. Third, the annulus of surrounding lipids (orange) can also modulate protein activity through its biophysical properties. (**B**) Top view of several proteins gathered in one lipid domain (purple), as a fourth potential mode of interaction. Bulk lipids are represented in red.

Before describing those four mechanisms, we would like to emphasize that the type of protein–lipid interaction will not only depend on the protein properties but also on lipid abundance, structure, membrane localization, and enzymatic modifications, a.o. We chose three examplative lipids, $PI(4,5)P_2$, DAG, and cholesterol, to illustrate this statement. First, $PI(4,5)P_2$, which is the best-known lipid modulator of Ca^{2+} channels, exchangers, and pumps (as described in Chapter I, Section 3.1 and in Figure 1.9) (Muallem et al., 2017), is a minor PLP of the inner PM leaflet and thus its effect on protein regulation is expected to be achieved through direct interactions, as a non-annular or an annular lipid. It is still unclear how membrane proteins bind to this lipid with such a large headgroup extending away from the hydrophobic bilayer into the cytoplasm (up to 17 Å). It was nevertheless suggested that the membrane proteins might approach $PI(4,5)P_2$ from the cytoplasmic side, which means that the principal determinants of the binding site would lie in the cytoplasmic loops (Suh and Hille, 2008). The regulation achieved by $PI(4,5)P_2$ could also result from the loss of interaction with the protein upon decrease of surrounding $PI(4,5)P_2$ levels following PLC stimulation and/or translocation of $PI(4,5)P_2$ into and out of specific domains. In support of this hypothesis, it has been suggested that cholesterol levels differently regulate $PI(4,5)P_2$ hydrolysis, probably through compartmentation of the latter and related metabolic pathways in rafts (Gamper and Shapiro, 2007). Nevertheless, partitioning of $PI(4,5)P_2$ into lipid rafts has been criticized on the basis of energetic considerations. For instance, $PI(4,5)P_2$ has a polyunsaturated acyl chain that would

not spontaneously partition into ordered rafts (Haag et al., 2012). On the other hand, $PI(4,5)P_2$ is also involved in the regulation of Ca^{2+} transport through indirect mechanisms, implying the recruitment of regulating/interacting proteins from the cytoplasm in the SOCE mechanism.

A second example is provided by DAG. This poorly-abundant lipid can potentially act directly on Ca^{2+} transport proteins. However, additional activation and inhibition of desensitization through the activation of PKC, as well as the synthesis of other important signaling molecules (e.g., PA) from DAG and IP_3, should also be taken into account once integrating the effect of PLC-derived lipid products on Ca^{2+} transport protein activity.

As a third example, one can cite cholesterol, another major Ca^{2+} transport protein regulator. It is expected to easily act as a non-annular lipid in small lipid pockets of proteins, but it is also a key regulator of membrane fluidity and biophysical properties. Besides its modulation as a non-annular or annular lipid, cholesterol could contribute to compartmentalize the different actors of Ca^{2+} signaling in rafts.

3.1.1. Direct Interaction with Non-Annular Lipids

Non-annular lipids are defined based on their interaction with a great specificity with the protein. Most of those interactions, which have been shown by X-ray crystallography, NMR, and MD simulation approaches, have evidenced small cavities that could contain a specific lipid (i.e., lipid pockets), suggesting that once a lipid occupies the pocket, the protein activity is affected. However, resolution of crystal structures of proteins is often not sufficient to perfectly resolve lipid structures, in particular the positions of unsaturated bonds and acyl chain lengths of the hydrophobic moieties (Ernst et al., 2010). These non-annular lipids generally make contact with the annular lipid molecules and adopt an orientation similar to the one exhibited by the lipids in the bilayer, which could suggest that non-annular lipids incorporate into their binding sites by simple diffusion from the bilayer (Lee, 2011). However, it is still extremely difficult to experimentally confirm the biological relevance of those pockets. Hence, most of their functions are deduced based on their location in the structure. As a matter of fact, Lee suggested that those lipids could act as traditional cofactors or as “molecular glue”, strengthening the contact between the subunits of oligomeric membrane protein assemblies, a.o. (Lee, 2004a).

Multiple non-annular lipid sites have been described in the prokaryotic K^+ channel KcsA (Marius et al., 2012) or in G protein-coupled receptors to which cholesterol molecules bind (Paila et al., 2009). However, to the best of our

knowledge, SERCA pumps are the only Ca^{2+} transport proteins to be shown to bind non-annular lipids so far. The binding of those lipids between the α-helices could affect the rotation/movement that is needed for the protein activity, as suggested by studies of the effects of the drug thapsigargin, a cholesterol-like inhibitor of SERCA (Figure 4.4) (Lee, 2002). The drug binds to the inactive E2 intermediate state, in a cleft between TM α-helices M3, M5, and M7, and prevents the conversion to the active E1 state. Indeed, in this state, the space between helices M3 and M7 is much smaller than in the thapsigargin-bound form. Thus, thapsigargin acts as an inhibitor, preventing the relative movement of helices necessary for function (Lee, 2002). However, and interestingly, even though thapsigargin shares chemical features with cholesterol, Thogersen et al have shown, by MD simulations, that cholesterol does not bind to the thapsigargin pocket. On the other side, two major cholesterol-binding pockets have been revealed, one of which co-localizes to a position known to bind sarcolipin, a small protein that regulates SERCA (Autzen et al., 2015). Besides, a pocket for PLPs has been evidenced between the TM helices M2 and M4 on the cytosolic leaflet of the SERCA only in the E2 state (Drachmann et al., 2014). This non-annular site was shown to affect neither the E2 structural integrity nor its stability, and was speculated to become functionally significant during the E2-to-E1 transition of the pump (Espinoza-Fonseca, 2019). Therefore, it remains to deepen to which extent non-annular lipid binding to SERCA affects its activity.

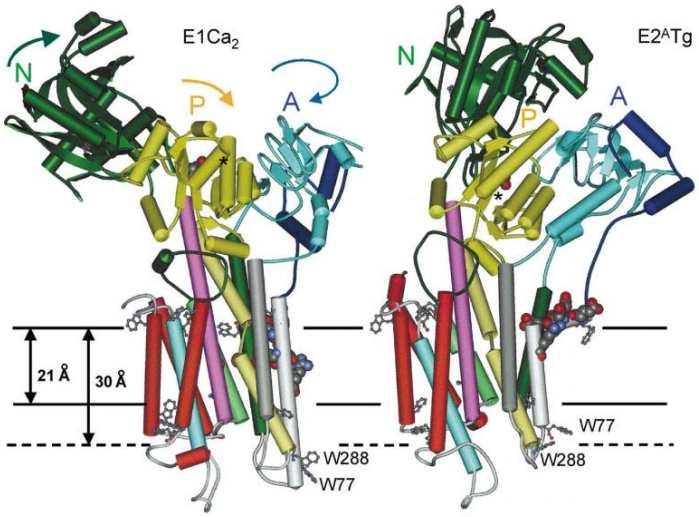

Figure 4.4. Comparison of the structures of the Sarco/Endoplasmic Ca^{2+} ATPase (SERCA) in its Ca^{2+}-bound ($E1Ca_2$) and Ca^{2+}-free, thapsigargin-bound ($E2^ATg$) forms. Thapsigargin binds in a pocket between the helices M3 (dark grey), M5 (lilac), and M7 (red); therefore, preventing the conformational change to the active E1 state, in which the pocket is smaller. Reproduced from (Lee, 2002).

3.1.2. Close Interaction with the First Shell of Annular Lipids

The first shell of annular lipids can interact with membrane proteins, mostly thanks to polar interactions between the lipid headgroup and aromatic amino acids (Contreras et al., 2011), which allow those lipids to be co-crystallized with the protein and analyzed by X-ray. Tyrosine residues present in the interfacial region interact with the lipid phosphodiester group either alone (via ion pair or hydrogen bond) or in combination with positively-charged amino acids. Likewise, tryptophan residues are mainly localized in the interfacial region, with the indole group pointing toward the center of the bilayer (Deisenhofer and Michel, 1989). The indole nitrogen atom can indeed form a hydrogen bond with the lipid phosphodiester group (Ridder et al., 2000), while a perpendicular orientation of the indole ring can help to stabilize the lipid acyl chains. Besides, the binding can be stabilized by non-polar interactions between the hydrophobic lipid acyl chains and the TM domain (Lange et al., 2001; Luecke et al., 1999).

Those interactions might have several roles. First, they might orient the protein into the membrane (van Klompenburg et al., 1997). X-ray data show that the majority of lipids tightly bound to PM proteins are localized on the electronegative side of the membrane. Hence, recognition of protein TM helices by the ER

translocon could critically involve direct protein–lipid interactions that help to guide the membrane protein incorporation (Rapoport, 2007; von Heijne, 2006; White and von Heijne, 2005). For instance, when a hydrophobic segment emerges from the ribosome, it can intercalate reversibly in two different orientations into the lateral gate. If the hydrophobic sequence is long and the N terminus is not retained in the cytosol by positive charges, or by the folding of the preceding polypeptide segment, it can flip across the channel and subsequently exit it laterally into the lipid phase. If the N terminus is retained in the cytosol and the polypeptide chain is further elongated, the C terminus can translocate across the channel (Rapoport, 2007).

Second, composition and organization of the lipid headgroup region could affect the structure of a protein penetrating into this bilayer region, because of the requirements of the polypeptide backbone and of any polar residues for hydrogen bonding tending to drive the formation of secondary structures. As differences in the areas occupied by different lipid molecules (e.g., PE occupies a smaller space than PC) are associated with different patterns of hydrogen bonding and hydration in the bilayer, specific lipid composition around the membrane protein might be required. This protein stabilization role explains why less harsh detergents that avoid delipidation are important means to increase the chances of crystallizing membrane proteins (Sonoda et al., 2011).

Finally, the close annular lipids might affect the change of protein conformation during activation/auto-inhibition, as this change is often associated with a variation of the amount of associated lipids. This has been shown for the PMCA, with differences depending on the pump isoform. As a matter of fact, activation of PMCA2 and 4 involves a reorganization of the TM region with the removal of lipid molecules from the protein annulus. Although activation of PMCA4 involves the loss of approximately 15 PLP molecules per protein, the loss is of only six PLPs for PMCA2. This fact probably reflects that, during transport of Ca^{2+}, PMCA2 changes its conformation to a lesser extent than PMCA4, an isoform that requires a higher calmodulin or PS local concentration for activation (Mangialavori et al., 2012). The number of first-layer PLPs also varies during SERCA conformational changes, from 23 to 26 lipid molecules in the cytoplasmic leaflet, as determined by X-ray crystallography (Norimatsu et al., 2017).

3.1.3. Regulation of Membrane Biophysical Properties Directly Around the Protein Through Annular Lipids

Besides direct lipid–protein interaction, Ca^{2+} transport proteins can also be influenced by membrane trafficking, interaction with the underlying

cytoskeleton/extracellular matrix, and biophysical properties of the lipid environment, such as packing, thickness, or curvature. Although those three membrane biophysical properties are intimately interconnected, they will be described separately for sake of clarity.

Membrane Lipid Packing

Membrane lipid packing depends on the ratio between small and large polar heads and the ratio between unsaturated and saturated acyl chains. This can be illustrated by several examples. First, the cis-unsaturated oleyl chain (C18:1) occupies a larger volume than the palmitoyl chain (C16:0) because the double bond induces a ‘‘kink’’ in the middle of the chain which lowers the acyl chain packing density (Koynova and Caffrey, 1998). Second, owing to its acyl chain composition, SM forms a taller, narrower cylinder than PC, increasing its membrane packing density. Consequently, at physiological temperature, a SM bilayer exists in a solid gel phase with tightly-packed acyl chains (Slotte, 2013; van Meer et al., 2008). Third, as compared to PG, CL (or bis-PG) has a smaller head-to-tail surface area ratio and has been shown to form CL-enriched domains in bacteria (Kawai et al., 2004; Mileykovskaya and Dowhan, 2000). By interfering with acyl chain packing, sterols inhibit the transition of the membrane to the solid gel state, while rigidifying fluid membranes by reducing the flexibility of neighboring unsaturated acyl chains, thereby increasing membrane thickness (Brown and London, 1998). Based on membrane packing criteria, the membrane can be viewed as a patchwork with areas characterized by differences in membrane fluidity. The areas of low fluidity are named solid-ordered (So) phases, in which the lipid acyl chains are tightly packed and in which there is a low rate of lateral diffusion. In contrast, the more fluid areas are named the liquid-disordered (Ld) state, which exhibits both low packing and high lateral diffusion. In addition, at the proper concentration, cholesterol may promote liquid-ordered (Lo) phase, which exposes high packing and high lateral diffusion.

Membrane lipid packing is critical to warrant proper protein sorting. MD simulations of simplified lipid membranes have suggested that prokaryotic membrane proteins form with their adjacent lipids dynamic protein–lipid complexes with up to 50 to 100 lipids that diffuse laterally together (Niemela et al., 2010). Considering that lipid diffusion rates are significantly reduced within these shells and accepting that membranes are “more mosaic than fluid” (Engelman, 2005), it becomes difficult to tell apart an actively recruited annulus from lipids from preexisting Lo domains, in which the lateral mobility of lipids is reduced.

Several Ca^{2+} transport proteins have been shown to be modulated through lipid packing and/or to associate preferentially to Lo or Ld phases. For example, the

PMCA pump and calmodulin partition into Lo domains, as observed by density gradient in primary cultured neurons. The Lo-associated PMCA activity is much higher than PMCA activity excluded from these domains. As a consequence, cholesterol depletion abrogates the Lo-associated PMCA activity without any effects on the non-Lo pool (Jiang et al., 2007). Those results were supported by the observation of Paterson et al that PMCA has a higher activity when reconstituted with ordered lipids (such as lens fiber lipid or the synthetic 1,2-dipalmitoyl-sn-glycero-3-phosphocholine, DPPC) than into fluid lipids (e.g., 1,2-dioleoyl-sn-glycero-3-phosphocholine, DOPC) (Tang et al., 2006).

In contrast to PMCA, the SERCA pump is located in the ER/SR membrane, a naturally more fluid environment than the PM due to its low content in complex SLs and cholesterol (3 %–6 % of total lipids vs 30 %–50 % in PM) vs a high level in unsaturated PCs (Lange, 1991; van Meer and de Kroon, 2011; van Meer et al., 2008). In support of the importance of such a fluid environment for its activity is the observation that reconstitution of purified SERCA in membranes with increased lipid order reduces the rate of Ca^{2+} pumping by decreasing the phosphorylation rate in the catalytic site (Starling et al., 1995). Moreover, the cholesterol enrichment of ER membranes by mβCD–sterol complexes results into inhibition of the SERCA2b in macrophages (Li et al., 2004). However, this fluid environment might favor SERCA susceptibility to oxidative damages. Indeed, by increasing the percentage of saturated fatty acids within SERCA's lipid annulus through diet, LeBlanc et al showed greater protection to thermal stress (i.e., to oxidative damages) (Fajardo et al., 2017).

Besides pumps, several lines of evidence indicate that Ca^{2+} channels are also affected by the surrounding membrane fluidity. As a matter of fact, using mechanical blebbing injury during pipette aspiration-induced membrane stretch (to simulate the damages imposed to the cardiac smooth muscle cells during ischemia, reperfusion, inflammation, a.o.), Joós et al showed that the resulting lipid membrane disruption and/or fluidization are linked to increased Ca_v channel activation, which could explain the Ca_v channel leakiness and arrhythmias in pathologies (Morris et al., 2012). On the other side, cholesterol increases the L-type Ca_v channel currents in arterial smooth muscle cells (Sen et al., 1992) and cholesterol decrease impairs Ca_v channel function in pancreatic β cells (Xia et al., 2008). TRP channels (including TRPC1/3/4/5, TRPV1/4, and TRPM8) preferentially segregate into Lo phases at resting state (Kumari et al., 2015; Morenilla-Palao et al., 2009; Szoke et al., 2010). Interestingly, cholesterol regulates these channel activity in distinct manners. For instance, depletion of cholesterol reduces the activity of TRPV1 (Szoke et al., 2010) and TRPV4 (Lakk et al., 2017), but increases the stimulation of TRPM8 (Morenilla-Palao et al., 2009). For further information on TRP

channel regulation by biophysical properties, please refer to (Startek et al., 2019). Piezo1 channel is also highly dependent on its surrounding lipid packing environment which can be modulated by dietary fatty acids, as recently demonstrated by Vásquez et al. They showed that margaric acid (a saturated fatty acid) inhibits Piezo1 activation by increasing membrane bending stiffness while long chain polyunsaturated fatty acids modulate channel inactivation by decreasing membrane bending stiffness (Romero et al., 2019).

Membrane Thickness

An important factor that influences the structure and dynamics of membrane proteins is the lateral pressure profile of membranes (Contreras et al., 2011). It describes the influence of membrane as a solvent of proteins. The highest pressure is at the interfacial region between hydrophobic and hydrophilic areas, because of the high cost of exposing either fatty acyl chains or hydrophobic amino acids to water (Lee, 2004a). This force; therefore, depends on the degree of hydrophobic mismatch at the protein–lipid interface and across the bilayer (Cantor, 1999). A hydrophobic mismatch is observed when the hydrophobic thickness of the lipid bilayer, defined by the distance between opposing headgroups of the inner and outer leaflets (i.e., typically between 35 and 55 Å for the PM, higher than in the ER), does not perfectly match the hydrophobic length of the embedded protein. For an extensive review, please refer to (Brown, 2017).

The requirement of an ideal bilayer thickness for optimal Ca^{2+} transport protein activity has been extensively studied for the SERCA pump. Early studies found a maximal activity for lipids with 18:0 fatty acids (i.e., a bilayer thickness of ~ 30 Å) (Lewis and Engelman, 1983), with a gradual decrease in activity for either thicker or thinner bilayers (Froud et al., 1986). Moreover, the effect of bilayer thickness is correlated to the degree of SERCA oligomerization (Cornea and Thomas, 1994). Those observations are in agreement with the biphasic dependence of SERCA to bilayer thickness, reaching a maximal activity for lipids with 22:1 fatty acids (or ~ 34 Å bilayer thickness) (Gustavsson et al., 2011). Those biochemical results were supported by MD simulations, revealing that SERCA can adapt to the thickness of the bilayer through small conformational changes, but that this adaptation is not efficient in thin (~ 22 Å thickness) bilayers made of lipids with 14:1 fatty acids, resulting in defective ATPase function (Sonntag et al., 2011). Moreover, those MD simulations also calculated that, even though the TM domain of SERCA seems to be adequately shielded by a detergent-containing bilayer of ~ 25 Å thickness, the enzyme requires a larger hydrophobic span of ~ 30 Å in the absence of detergent. Contrasting with those data and predictions, Lee suggested that a 30 Å-thick bilayer would locate a Lysine residue (Lys-972) totally within the hydrocarbon core, which seems unlikely. The hydrophobic thickness would have to be ~ 21 Å to locate Lysine-

972 at the luminal surface (Lee, 2003). Supporting this suggestion, LeBlanc et al showed that SERCA lipid annulus is enriched in short chain fatty acids (12-14 carbons) (Fajardo et al., 2017). Thus, the bilayer thickness appears important for SERCA activity, but contradictory results are obtained concerning the ideal membrane thickness for its V_{max}.

Most of the time, the protein tends to localize in a part of the bilayer where the hydrophobic thickness is favorable. If the protein does not find a match, two adaptation mechanisms could occur: (i) Neighboring lipids could adjust to the protein requirements; or (ii) proteins can tilt to hide the hydrophobic part of their TM domain in the hydrophobic part of the bilayer. As a matter of fact, MD simulation studies suggest that there is a mutual adaptation of a membrane protein and the lipid bilayer during conformational changes (Sonntag et al., 2011). The first adaptation mechanism implies that the conformational changes of Ca^{2+} transport proteins during Ca^{2+} exchanges could induce a change in their hydrophobic thickness, which should result in an adaptation of the surrounding lipids. This is needed to decrease the energy barriers to allow the smooth transition between the various steps of the catalytic cycle. This requirement cannot be fulfilled for too thin membranes, whereas for too thick membranes, the hydrophobic mismatch becomes too pronounced for proper interaction between the protein and the lipids. For SERCA, the conformational changes between E1 and E2 states is suggested in some studies to not affect the membrane thickness (Lee, 2003). However, in X-ray crystallography analysis, the change of conformation has been shown not only to change the thickness of the bilayer (from 30.9 to 33.4 Å) but also to induce a tilt of the entire protein (by approximately 18 °), resulting in a variation of the cross-section of the TM region (from 959 to 1142 Å²) (Norimatsu et al., 2017).

The second adaptation mechanism is based on the fact that changes in the bilayer thickness, for example, following membrane stretching, could induce modulations of Ca^{2+} transport proteins. Thus, tension is closely linked to bilayer thickness as it can cause changes in it and in lateral pressure profiles, thereby creating hydrophobic mismatch and subsequent adaptive changes in protein conformation that could gate the pore (Janmey and Kinnunen, 2006). MSCs are expected to be highly sensitive to the local lateral pressure fields and their modifications were proposed as one of the molecular mechanisms that provides the mechanical force to shift the channels from an open to a closed state (Contreras et al., 2011). This was shown for the prokaryotic MSCs, where decreased bilayer thickness lowers the channel activation energy (Perozo et al., 2002). Sens et al analyzed the gating free energy of those bacterial MSCs and revealed that the quantitative dependence of the gating tension on the length of the lipid acyl tail matches the prediction from elastic bilayer models. Their conclusion not only

reveals that the lipid surrounding environment is crucial for the MSC channel activity, but also that the mechanism behind can be understood in terms of a CG elastic model of the lipid bilayer (Phillips et al., 2009). Besides prokaryotic MSCs, hydrophobic mismatch was also proposed as a gating mechanism of Piezo channels. For those channels though, the mismatch can either originate from membrane thinning following increased tension or from the reduced local curvature around those channels (see below for this particular point) (Figure 4.5) (Wu et al., 2017). Mechanical force can be directly transmitted to the channel through lateral tension in the membrane bilayer, whereby the conformation with the greater cross-sectional area is favored under higher tension. This value will be proportional to the work required to open the channel. All those observations indicate that MSCs are gated by stretching the membrane bilayer (i.e., force-from-lipids). However, as discussed below, changes in membrane curvature must also be integrated in the stretching-based gating mechanism of MSCs. Hence, stretching is not the only actor and force conveyed to the channels from the cytoskeleton (i.e., force-from-filament) has to be considered as well (Bavi, 2017), but is beyond the scope of this review.

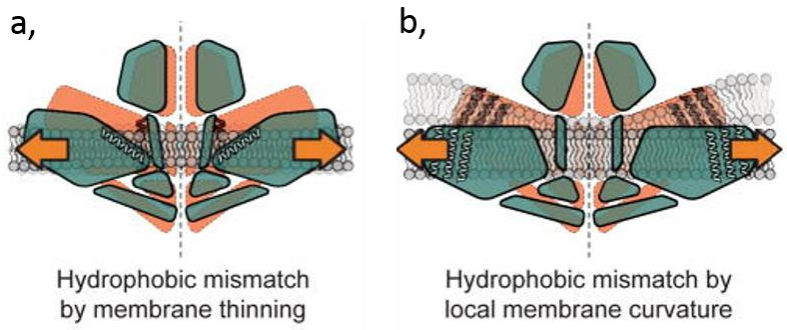

Figure 4.5. Two of the proposed gating mechanisms for Piezo channels. Alterations of the membrane thickness originating from membrane thinning (**a**) or reduced curvature through stretching (**b**) result in hydrophobic mismatch and adaptive changes of Piezo conformation. Reproduced from (Wu et al., 2017).

Membrane Curvature

Remodeling of cell shape is accomplished by recruiting specialized proteins which contain motifs able to generate, sense, or stabilize membrane curvature and which act in synergy with changes in the lipid bilayer (see below) and the cytoskeleton. Regarding proteins, three main mechanisms are currently known: (i) Protein crowding and partitioning of TM domains; (ii) direct insertion of small

hydrophobic protein motifs between the lipid headgroups (e.g., Bin/Amphiphysin/RVS (BAR) domain containing proteins); and (iii) scaffold by peripheral proteins and their oligomeric assemblies (e.g., clathrin, COPI, or COPII) (McMahon and Boucrot, 2015). Besides proteins, generation of membrane shape by lipids is generally attributed to intrinsic lipid molecular shapes (Cullis and de Kruijff, 1979) and lipid membrane transversal asymmetry (bilayer couple hypothesis (Sheetz and Singer, 1974)). We will here below focus on those lipid-based mechanisms.

One possible type of molecular curvature sensors are MSCs, whose gating would respond to bending in their local environment. Numerous reports indicate that alterations in local curvature induced by asymmetric incorporation of lipids or conical/amphipathic compounds can change the response of prokaryotic MSCs to pressure (Perozo et al., 2002). It is important to note that only local curvature seems to have an impact on MSCs. As a matter of fact, using a finite element model, Martinac et al showed that the global curvature (radius > 0.1 µm) of a patch-clamped membrane on a model MSC has little energetic consequences (Bavi et al., 2016). However, curvature at the local level (curvature radius < 100 nm) and the direction of bending (i.e., both concave and convex curvatures of the membrane) are able to cause considerable changes in the stress distribution and the pressure profile through the thickness of the membrane. Clearly, the channel sensitivity to the applied force directly dictates the degree with which local curvature impacts on its gating. However, although it is theoretically possible that MSCs sense convex and concave membrane curvature with equal sensitivity, this mechanism would require curvature sensing structures that are symmetrical. This seems unlikely since those proteins do not contain any amino acid sequences with similarity to any known curvature-sensing proteins and Piezo1 shows no symmetrical features with respect to the bilayer plane, as recently revealed by cryo-electron microscopy (Antonny, 2011; McMahon and Boucrot, 2015). It is rather proposed that membrane curvature might just be a means to increase the tension sensed by the MSCs (Lewis and Grandl, 2015). It must be remembered that the contribution of the cytoskeleton was not integrated in those analyses, a factor that contributes to membrane properties (Gauthier et al., 2012), and that is predicted to be an important regulator of Piezo1 sensitivity. Indeed, studies reported that inhibition of actin polymerization with cytochalasin D inhibits whole-cell Piezo1 currents evoked by direct stimulus with a glass pipette, but increases opening in cell-attached pressure-evoked currents (Gnanasambandam et al., 2015). A particularity of Piezo channels is also that, based on the strongly curved shape of its large blades, it is thought to induce itself a locally-distinct membrane curvature and a, a fortiori, distinct membrane thickness and tension environment (Wu et al., 2017). Consequently, Piezo channels might sense changes in the membrane geometry and

tension particularly sensitively (Moe and Blount, 2005; Nomura et al., 2012; Sukharev, 1999; Sukharev, 2002).

3.1.4. Contribution to Ca^{2+} Exchange/Signaling Inside Lipid Domains

As exposed in the Introduction, lipid domains have been evidenced in a large variety of cells. For a substantial, albeit non-exhaustive, list of examples, see (Carquin et al., 2016) and (Léonard et al., 2017a). Those lipid domains vary in size, abundance, lipid composition, biophysical properties, and regulation by extrinsic factors (including the cytoskeleton) (Léonard et al., 2017a). Due to such diversity, domains could serve as recruitment/exclusion and/or activation/inactivation platforms for specific membrane proteins, thereby participating in the spatiotemporal regulation of dynamic cellular events. We here discuss their potential role in Ca^{2+} signaling by: (i) Gathering several components of the Ca^{2+} signaling machinery; (ii) providing platforms of annular lipids with appropriate biophysical properties around the Ca^{2+} transport protein; and/or (iii) creating a lipid environment that differs in charge through modification of local Ca^{2+} concentration following a primary transient Ca^{2+} influx.

The protein gathering hypothesis is supported by the following lines of evidence. First, analysis of lipid rafts from presynaptic membranes reveals that $Ca_v2.1$, but not $Ca_v1.2$, co-distributes and interacts with the SNARE complexes present in the domains. Thus, lipid domains might contribute to optimize compartmentalization of exocytosis machinery and the Ca^{2+} influx that triggers synaptic vesicle exocytosis (Taverna et al., 2004). Second, Ca^{2+} transport proteins have also been spotted at membrane contact sites (MCSs, defined as domains where the ER/SR membrane is tethered to other organelle membranes such as PM, mitochondria, endosomes, a.o.) by specific tether proteins and where lipid transfer proteins and cell signaling proteins are located (Muallem et al., 2017). For example, in muscles and neurons, the PM Ca_v channels communicate with the SR-associated RyR channels at MCSs (Saheki and De Camilli, 2017). At the apical pole of polarized epithelial cells, all Ca^{2+} signaling proteins are clustered in MCSs where they form complexes (Hong et al., 2011; Shin et al., 2001). Thus, physiological cell stimulation evokes Ca^{2+} signals confined to the apical pole (Petersen, 2015). Although such regulation by lipids suggests the localization of ion channels and transporters at MCSs, this remains to be clearly demonstrated.

The lipid platform hypothesis is based on the specific biophysical properties of lipid domains, which might in turn contribute to regulate Ca^{2+} transport protein activity. One class of Ca^{2+} transport proteins that appears to depend on lipid domain biophysical properties are the TRP channels, as supported by the following lines of evidences. First, upon prevention of the association of TRPM8 with lipid rafts,

menthol and cold-mediated responses are potentiated, suggesting that this association is a key regulator for TRPM8 activity. Similarly, lipid raft disruption shifts the threshold for TRPM8 activation to higher temperatures (Morenilla-Palao et al., 2009). Cholesterol suppresses TRPM3 constitutive and stimulated activity (Naylor et al., 2010), suggesting its role as a negative modulator of this channel, even if a recent study reported opposite results (Saghy et al., 2015). Likewise, the effect of TRPV1 segregation in lipid rafts is still unclear. Indeed, it seems to regulate the protein level at the cell surface without any effect on the channel response(Liu et al., 2003; Liu et al., 2006; Szoke et al., 2010). However, another group has, rather, suggested that direct interaction with cholesterol (i.e., that might not require segregation in rafts) inhibits TRPV1 opening (Picazo-Juarez et al., 2011). Thus, all the above studies seem to indicate the importance of lipid rafts and/or cholesterol in TRP channel activity, but further studies are needed to clarify some discrepancies. The activity of MSCs also appears to be regulated by lipid rafts. In 2015, Hu et al showed that force transfer, and thus sensibility of MSCs, including Piezo channels, is regulated through stomatin-like protein-3 (STOML3) and its binding to cholesterol (Qi et al., 2015). Since STOML3 is detected in lipid rafts, this could suggest that Piezo channels are also associated with rafts. Finally, lipid domains could also modulate the activity of Ca_v channels. For instance, disruption of caveolae by cholesterol depletion perturbs the response of $Ca_v1.2$ activity in heart cells and the response of $Ca_v2.1$ to β2-adrenergic stimulation (Balijepalli et al., 2006; Calaghan and White, 2006). Moreover, $Ca_v1.2$ channels have been associated with caveolin-3 (a major caveolae protein) and signaling molecules from the β2-adrenergic pathway (Balijepalli et al., 2006) (Figure 4.6A).

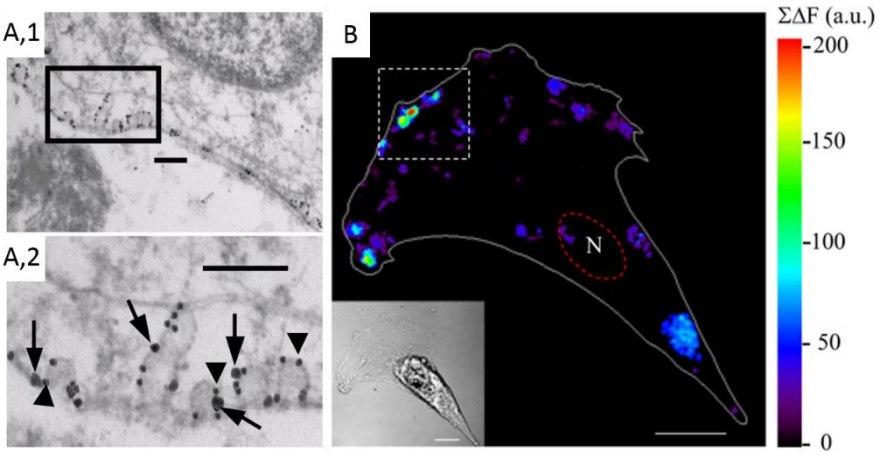

Figure 4.6. Illustration of the interplay between lipid domains and Ca^{2+} signaling. (**A**) Association of a Ca^{2+} channel with caveolae (A,1; zoom in A,2). Immunogold colocalization of the $Ca_v1.2$ subunit of L-type Ca^{2+} channel (large particle, arrows) and caveolin 3 (small particle, arrowheads) in the caveolae in isolated mouse cardiomyocytes. Scale bars, 200 nm. Reproduced from (Balijepalli et al., 2006). Copyright (2006) National Academy of Sciences, USA. (**B**) Ca^{2+} domains in migrating cells. Local Ca^{2+} increases (ΣΔF) were summed over 30 consecutive images acquired at 6 s intervals. N points to the nucleus of the fibroblast. Scale bar, 15 µm. Reproduced from (Wei et al., 2009).

The Ca^{2+}-induced domain formation hypothesis is based on the observation that localized membrane domains that differ in charge can be created in cells through the modification of local Ca^{2+} concentration by transient Ca^{2+} influx from membrane channels like TRPs. Those Ca^{2+} ions in turn interact with negatively-charged membrane lipids, forming Ca^{2+}-induced domains (Shi et al., 2013). For example, TRMP7 drives the formation of Ca^{2+} domains during invadosome formation in neuroblastoma cells (Visser et al., 2013) and upon migration of human embryonic lung fibroblasts (Wei et al., 2009). In the latter study, the Ca^{2+} domains are most active at the leading lamella of migrating cells (Figure 4.6B) (Wei et al., 2009). It remains to determine if such localized membrane charge in the inner PM can in turn affect the organization of the lipids in the outer PM leaflet and recruit and/or activate other membrane Ca^{2+} transport proteins, thereby contributing to Ca^{2+} exchanges.

3.2. Focus on RBCs

Regarding the ways by which submicrometric lipid domains could modulate Ca^{2+} exchanges at the RBC surface, the quite large size of GM1- and SM-enriched domains as well as their low abundance, even upon simulation, suggest that those

domains could represent platforms in which Piezo1 and PMCA are respectively concentrated. This suggestion is supported by the to-be-published results of Martinac et al showing that Piezo1-GFP form chol-dependent clusters at the surface of HEK293T (Ridone et al., to be published). The gathering of Piezo1 or PMCA in submicrometric lipid domains could be dictated by energetic concerns (i.e. fusion of several lipid domains containing Piezo1 with the same biophysical properties) or through the linkage to the cytoskeleton anchorage, as supported by their spatial stability. Those hypotheses could be tested by the approaches proposed in section 4.

3.3. Lipid and Ca^{2+} Transport Alterations in Physiological Aging and Diseases

Like during physiological aging, several diseases have been linked to, or are exacerbated by, altered Ca^{2+} signaling. One can cite neurodegenerative diseases (e.g., Alzheimer and Huntington diseases), cardiac or muscular diseases (e.g., Duchenne muscular dystrophy), and RBC deformation-linked diseases (e.g., hereditary spherocytosis and elliptocytosis), a.o. Those diseases have also been linked to altered membrane lipid composition, organization in lipid domains, and/or biophysical properties, which might be the missing link between the initial perturbation and the Ca^{2+} exchange perturbation.

For example, in Huntington disease, the mutation in the huntingtin protein is believed to alter lipid metabolism, and perturbation of PM fluidity represents an early event of the disease onset (Sameni et al., 2018). On the other side, the disease is also linked to a Ca^{2+} dyshomeostasis, which is believed to be the main cause of the disease phenotype (Kolobkova et al., 2017).

Another example relates to RBC membrane fragility diseases. We have recently described a close link between Ca^{2+} exchanges during erythrocyte deformation and the modulation of the abundance of several lipid domains at their surface (Conrard et al., 2018). Moreover, in RBCs from patients with spherocytosis and elliptocytosis resulting from cytoskeleton defects, we evidenced that Ca^{2+} intracellular content and exchanges as well as PM lipid organization in domains are altered. In elliptocytosis in particular, the lipid domains involved in Ca^{2+} exchange exhibit altered cytoskeleton anchorage and cholesterol enrichment, leading to Ca^{2+} exchange impairment upon deformation and increased RBC fragility. Those effects are closely linked to the alteration of the RBC membrane lipid composition by oxidative stress and upregulated plasmatic acid SMase (our unpublished data).

Discussion and perspectives

Cell membrane fragility, mechanical alteration of cytoskeletal-extracellular connection, modification of Ca^{2+} homeostasis and oxidative stress are similarly observed in Duchenne muscular dystrophy (Allen et al., 2007). This progressive neuromuscular disease is characterized by muscle degeneration and is caused by the deficiency of dystrophin, a huge protein that constitutes the link between the cytoskeleton and the extracellular matrix. As the disease progresses, fibrosis and atrophy become apparent and regenerating fibers are less frequent. Importantly, many proteins involved in the pathophysiological production of Ca^{2+} and reactive oxygen species (ROS) in dystrophic muscle have been shown to localize in caveolae. Those include TRPC1/4, NADPH oxidase 2, and the small GTPase Rac1. Those observations suggest that caveolae could act as signaling platform for Ca^{2+} and ROS production. For an extensive review on early damage pathways in muscular dystrophy, see (Allen et al., 2007).

The PMCA pump appears to be altered in neurons during aging (Michaelis et al., 1996) and in neurodegenerative diseases like Alzheimer's disease (Berrocal et al., 2015). For the latter, the inhibition was shown to be induced by the Tau protein, whose effect surprisingly decreases with aging. Interestingly, age-dependent changes in ganglioside total content and species were observed in rat brain synaptic PMs, with an important increase of the monosialoganglioside GM1, without any modification of the fatty acid composition (Jiang et al., 2014). These findings are consistent with the age-associated, high-density clustering of GM1 at presynaptic terminals reported previously (Yamamoto et al., 2008). As gangliosides are major regulators of PMCA (see Chapter I, Section 3.1.2), the authors suggested that an alteration of its activity might result from ganglioside perturbation during aging. Hence, the inhibition due to ganglioside perturbation might take over the alteration caused by the Tau protein in neurodegenerative diseases. Finally, alterations caused by perturbation of membrane lipid composition could also be linked to increased sensitivity of the PMCA to oxidative stress upon aging (Zaidi, 2010).

3.4. Lipids as Therapeutic Targets in Ca^{2+} Transport-Related Diseases

Induction of PM lipid alterations might help to treat diseases linked to Ca^{2+} transport alterations. As a first example, one can cite the thermosensitive TRP channels expressed in nociceptive sensory neurons (TRPV1–4, TRPM2/3/8, and TRPA1) and which contribute to inflammatory and neuropathic pain conditions. The current first-line therapeutics for pain provide only partial relief and have harmful side effects when used long-term. Consequently, identification of new molecular targets for analgesic drug development is crucial and urgent. In this context, lipid mediators represent attractive targets. Among them, PIP_2 is a choice modulator, although nowadays limited to experimental systems. Considering that major TRP channels specifically partition in rafts (Taberner et al., 2015), disruption of the later

by ω-3 fatty acids could modulate the signaling events and exert anti-inflammatory actions. This supports the use of fatty acids as nutraceuticals for the treatment of inflammatory disorders such as rheumatoid arthritis, inflammatory bowel disease, and asthma (Garattini, 2007; Yaqoob and Shaikh, 2010). In a disease linked to Piezo1 gain-of-function mutations (i.e., hereditary stomatocytosis) dietary fatty-acid supplementation has been shown to abrogate the phenotype in mice and could be proposed as a treatment (Romero et al., 2019).

3.5. Conclusions and Challenges for the Future

In this review, we have highlighted that, through protein interaction with the annular shell of lipids or with immersed lipids in cavities and clefts at their surface, the lipid environment contributes to modulate the activity of Ca^{2+} channels, exchangers, and pumps. Among those lipids, cholesterol, acidic PLPs, SLs, and metabolites appear to play key roles. Elucidation of such lipid–protein interactions was possible thanks to X-ray diffraction, electron crystallography, and/or NMR, which allow to determine the atomic level structure of lipid-binding sites on membrane proteins. Thanks to those techniques, over 100 structures of membrane proteins containing electron density interpreted as bound lipid molecules were already available in 2014 (Yeagle, 2014), and we can expect an exponential increase of this amount from that time. MD simulation is a powerful way to extend those analyses to lipid-binding sites of less affinity and to simulate the repercussion of membrane composition/property modifications on the protein structure and functionality (Hedger and Sansom, 2016). The major challenge of this technique is to transcribe in the model the complexity of the biological membrane, with its extremely diverse composition and asymmetry. However, over time, more and more complex membranes are modeled, nowadays including over 60 different lipids and an asymmetric distribution between leaflets (Corradi et al., 2018), and we can hope that this will soon become the norm. We believe that the combination of imaging studies, protein structural biology, and MD simulations will contribute to help the scientific community to elucidate the mechanistic behind protein–lipid interactions upon Ca^{2+} exchanges and their pathophysiological relevance.

Adding to the above complexity, the link between lipid and proteins can also be seen in terms of (modification of) membrane biophysical properties, lipids creating an appropriate biophysical environment in terms of membrane fluidity, thickness, or curvature. Moreover, lipid domains could provide platforms for communication between membrane proteins and their downstream targets and/or modulators. However, the latter mechanism is nowadays still hypothetical, probably resulting from the difficulty to evidence lipid domains in living cells due to a long-term limitation of probes and imaging techniques (Carquin et al., 2016). Today, thanks to the analysis of a same-target lipid by several complementary probes, for their

respective advantages and drawbacks (when available), and thanks to the development of new technological approaches (e.g., super-resolution techniques), lipid domains have been reported in a variety of cells (reviewed in (Carquin et al., 2016; Léonard et al., 2017a)). One major issue is whether lipid domains can be generalized or if they are restricted to cells exhibiting particular membrane lipid and protein composition, biophysical properties, and/or membrane–cytoskeleton anchorage. In addition, determination of how membrane biophysical properties and extrinsic factors could confine proteins into domains is needed.

4. Perspectives

Study of membrane lipid organization and its potential role in membrane protein activity remains an enormous challenge. As we evidenced a relation between GM1- and SM-enriched domain abundance and, respectively, Ca^{2+} influx and efflux during RBC deformation, the main perspective of this thesis is to examine the possible intermodulation between those lipids and the Piezo1/PMCA proteins.

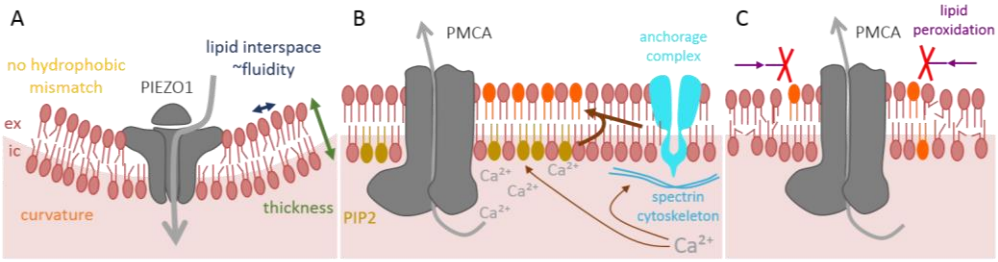

Figure 4.7. Possible means of intermodulation between GM1- and SM-enriched domains and Piezo1 and PMCA protein activity/localization at the RBC surface. (A) Regulation of Piezo1 through the surrounding membrane biophysical properties (e.g. lipid packing, curvature, thickness). **(B)** Regulation of PMCA through interdigitation between the outer leaflet containing SM and the inner leaflet containing $PI(4,5)P_2$. **(C)** Protection of PMCA against oxidative damages through SM-enriched domains. Ex, extracellular medium; ic, intracellular medium.

First, GM1-enriched domains could be linked to Piezo1 channels, either via direct interactions or via regulation of the environment biophysical properties (i.e. membrane fluidity, thickness and curvature, as exposed in section 3.2.3) (figure 4.7A). Whether Piezo-1 localizes upon resting state into GM1-enriched domains that are required for its primary activation or whether the protein is able to recruit GM1 and associated lipids (e.g. cholesterol and PC) in its surrounding environment upon activation is also still to be determined.

To explore the potential relation in space between GM1 and Piezo1, several techniques described in Chapter I would be useful. Notably, molecular dynamic

simulations (Chapter I, section 6.2.4) of Piezo1 embedded in a lipid bilayer with a composition mimicking the RBC PM could be considered. Nanodiscs of controlled composition reconstitution (see Chapter I, section 6.2.2) may also be used in association with super-resolution microscopy techniques or crystallography/NMR/mass spectrometry, as described in Chapter I, section 6.2.3. Finally, we could also consider confocal microscopy analysis of RBCs co-labeled for Piezo1 and GM1 at resting state or upon stimulation of Ca^{2+} exchanges. This is however rendered difficult due to the challenge of immunolabeling Piezo1 together with lipid vizualization. Indeed, immunolabeling with antibodies requires the fixation of the sample to avoid induced co-patching, which is generally not compatible with lipid labeling. Hence, currently tested Piezo1 antibodies all require cell membrane permeabilization, which completely alter the lipid labelling and organization. Those limitations could be overcome thank to the use of erythroid precursors in which a fluorescent-derived Piezo1 would be expressed. Till recently however, the use of those precursors was limited by the fact that *in vitro* generation of RBCs from adult and cord blood progenitors do not provide a sustainable supply and that systems using pluripotent stem cells as progenitors do not generate viable RBCs. Additionally, immortalized cell lines with erythroid characteristics are mostly derived from patients with myelogenous leukemia or erythroleukemia and do not represent 'normal' erythroid cells. However, two years ago, the group of Frayne generated an immortalized cell line of erythroid precursors (BEL-A cell line), using a Tet-inducible HPV16-E6/E7 expression system in healthy adult bone marrow CD34+. Those immortalized precursors provide a continuous supply of RBCs and differentiate efficiently into mature, functional reticulocytes that can be isolated by filtration. Differentiation can be easily induced in a controlled medium containing notably Epo and transferrin and takes place in 15-18 days. The produced RBCs were extensively characterized and no functional or molecular differences between them and adult reticulocytes could be revealed. Moreover, the amenability of this cell line to genetic manipulation was assessed by efficient transducing of GFP-constructs (notably Band3 and glycophorin A) (Trakarnsanga et al., 2017). Frayne recently kindly provided us their BEL-A cell line and their use in our laboratory should start in the next months. After confirming that the lipid organization at the surface of RBCs derived from immortalized precursors is identical to the one of mature blood-originating RBCs, we will be able to notably induce the expression of a fluorescent derivative of Piezo1, whose observation will be compatible with live cell imaging of lipids. If this approach works as expected, it would be appealing to generate mutations in the Piezo1 transmembrane domains and to analyze the consequences for Piezo1 interactions with specific lipids. On the other side, one could consider to alter lipid domains and evaluate the consequences of those alterations for Piezo1 localization at the PM. Finally, if a spatial relation between

specific lipids and Piezo1 protein is demonstrated, the influence of those lipids on Piez1 surrounding membrane biophysical properties will be explored.

The same approaches can be proposed to study the potential spatial interplay between PMCA and SM-enriched domains. Indeed, SM-enriched domains could also be able to modulate PMCA activity through their specific biophysical properties. But additionally, they may induce regulation through the interdigitation with inner leaflet lipid like $PI(4,5)P_2$ as well as cytoskeleton anchorage complex components (figure 4.7B). This hypothesis could also be partially resolved by multiple labelling of the cell for SM, $PI(4,5)P_2$, PMCA and anchorage complex proteins. The use of erythroid precursors would provide an extremely valuable tool to achieve this kind of experiments, which require labelling of membrane proteins, outer leaflet lipids and inner leaflet lipids at the same time.

Another possible mean of PMCA regulation by SM-enriched domains is by preventing its alteration by ROS (figure 4.7C). Indeed, PMCA is a major target of oxidative stress, which lead to its aggregation (Zaidi et al., 2003), and SM has been proposed to be a natural antioxidant as it stops the propagation of lipid peroxidation reactions (Subbaiah et al., 2009). This hypothesis could be tested by comparing the pump localization and activity (either PMCA aggregation measurement or Ca^{2+} basal recovery after a short Ca^{2+} loading) upon ROS damages in RBCs either with intact SM-enriched domains or upon their abrogation through the use of bacterial SMase. Alternatively, erythroid precursors could be a useful tool to reduce or modify SM production.

References

Abe, M., A. Makino, F. Hullin-Matsuda, K. Kamijo, Y. Ohno-Iwashita, K. Hanada, H. Mizuno, A. Miyawaki, and T. Kobayashi. 2012. A role for sphingomyelin-rich lipid domains in the accumulation of phosphatidylinositol-4,5-bisphosphate to the cleavage furrow during cytokinesis. *Molecular and cellular biology*. 32:1396-1407.

Abramowitz, J., and L. Birnbaumer. 2009. Physiology and pathophysiology of canonical transient receptor potential channels. *FASEB journal : official publication of the Federation of American Societies for Experimental Biology*. 23:297-328.

Abugo, O.O., and J.M. Rifkind. 1994. Oxidation of hemoglobin and the enhancement produced by nitroblue tetrazolium. *The Journal of biological chemistry*. 269:24845-24853.

Ackerman, D.G., and G.W. Feigenson. 2015. Multiscale modeling of four-component lipid mixtures: domain composition, size, alignment, and properties of the phase interface. *The journal of physical chemistry. B*. 119:4240-4250.

Ahmmed, G.U., D. Mehta, S. Vogel, M. Holinstat, B.C. Paria, C. Tiruppathi, and A.B. Malik. 2004. Protein kinase Calpha phosphorylates the TRPC1 channel and regulates store-operated Ca2+ entry in endothelial cells. *The Journal of biological chemistry*. 279:20941-20949.

Alaarg, A., R.M. Schiffelers, W.W. van Solinge, and R. van Wijk. 2013. Red blood cell vesiculation in hereditary hemolytic anemia. *Front Physiol*. 4:365.

Albert, A.P., and W.A. Large. 2003. Synergism between inositol phosphates and diacylglycerol on native TRPC6-like channels in rabbit portal vein myocytes. *J Physiol*. 552:789-795.

Albuisson, J., S.E. Murthy, M. Bandell, B. Coste, H. Louis-Dit-Picard, J. Mathur, M. Feneant-Thibault, G. Tertian, J.P. de Jaureguiberry, P.Y. Syfuss, S. Cahalan, L. Garcon, F. Toutain, P. Simon Rohrlich, J. Delaunay, V. Picard, X. Jeunemaitre, and A. Patapoutian. 2013. Dehydrated hereditary stomatocytosis linked to gain-of-function mutations in mechanically activated PIEZO1 ion channels. *Nature communications*. 4:1884.

Alimohamadi, H., and P. Rangamani. 2018. Modeling Membrane Curvature Generation due to Membrane(-)Protein Interactions. *Biomolecules*. 8.

Allen, J.A., R.A. Halverson-Tamboli, and M.M. Rasenick. 2007. Lipid raft microdomains and neurotransmitter signalling. *Nat Rev Neurosci*. 8:128-140.

An, X., and N. Mohandas. 2008. Disorders of red cell membrane. *Br J Haematol*. 141:367-375.

Andersen, O.S., and R.E. Koeppe Ii. 2007. Bilayer thickness and membrane protein function: An energetic perspective. *In* Annual review of biophysics and biomolecular structure. Vol. 36. 107-130.

Andersen, O.S., and R.E. Koeppe, 2nd. 2007. Bilayer thickness and membrane protein function: an energetic perspective. *Annu Rev Biophys Biomol Struct*. 36:107-130.

Anderson, R.G., and K. Jacobson. 2002. A role for lipid shells in targeting proteins to caveolae, rafts, and other lipid domains. *Science*. 296:1821-1825.

Andersson, D.A., M. Nash, and S. Bevan. 2007. Modulation of the cold-activated channel TRPM8 by lysophospholipids and polyunsaturated fatty acids. *J Neurosci*. 27:3347-3355.

Andolfo, I., R. Russo, A. Gambale, and A. Iolascon. 2016. New insights on hereditary erythrocyte membrane defects. *Haematologica*. 101:1284-1294.

Andrews, D.A., L. Yang, and P.S. Low. 2002. Phorbol ester stimulates a protein kinase C-mediated agatoxin-TK-sensitive calcium permeability pathway in human red blood cells. *Blood*. 100:3392-3399.

Antoniou, C., V.Q. Lam, and L.W. Fung. 2008. Conformational changes at the tetramerization site of erythroid alpha-spectrin upon binding beta-spectrin: a spin label EPR study. *Biochemistry*. 47:10765-10772.

Antonny, B. 2011. Mechanisms of membrane curvature sensing. *Annu Rev Biochem*. 80:101-123.

Antos, J.M., J. Ingram, T. Fang, N. Pishesha, M.C. Truttmann, and H.L. Ploegh. 2017. Site-Specific Protein Labeling via Sortase-Mediated Transpeptidation. *Curr Protoc Protein Sci*. 89:15 13 11-15 13 19.

Arashiki, N., N. Kimata, S. Manno, N. Mohandas, and Y. Takakuwa. 2013. Membrane peroxidation and methemoglobin formation are both necessary for band 3 clustering: mechanistic insights into human erythrocyte senescence. *Biochemistry*. 52:5760-5769.

Arnadottir, J., and M. Chalfie. 2010. Eukaryotic mechanosensitive channels. *Annual review of biophysics*. 39:111-137.

Arthurs, G.J., and M. Sudhakar. 2005. Carbon dioxide transport. *Continuing Education in Anaesthesia Critical Care & Pain*. 5:207-210.

Ashkin, A. 1970. Acceleration and Trapping of Particles by Radiation Pressure. *Physical Review Letters*. 24:156-159.

Autzen, H.E., I. Siuda, Y. Sonntag, P. Nissen, J.V. Moller, and L. Thogersen. 2015. Regulation of the Ca(2+)-ATPase by cholesterol: a specific or non-specific effect? *Molecular membrane biology*. 32:75-87.

Awoonor-Williams, E., and C.N. Rowley. 2016. Molecular simulation of nonfacilitated membrane permeation. *Biochimica et biophysica acta*. 1858:1672-1687.

Ayton, G.S., W.G. Noid, and G.A. Voth. 2007. Multiscale modeling of biomolecular systems: in serial and in parallel. *Curr Opin Struct Biol*. 17:192-198.

Bach, J.N., and M. Bramkamp. 2013. Flotillins functionally organize the bacterial membrane. *Mol Microbiol*. 88:1205-1217.

Baines, A.J. 2010. The spectrin-ankyrin-4.1-adducin membrane skeleton: adapting eukaryotic cells to the demands of animal life. *Protoplasma*. 244:99-131.

Baines, A.J., H.C. Lu, and P.M. Bennett. 2014. The Protein 4.1 family: hub proteins in animals for organizing membrane proteins. *Biochimica et biophysica acta*. 1838:605-619.

Bakhtiari, N., S. Hosseinkhani, B. Larijani, M.R. Mohajeri-Tehrani, and A. Fallah. 2012. Red blood cell ATP/ADP & nitric oxide: The best vasodilators in diabetic patients. *J Diabetes Metab Disord*. 11:9.

Balijepalli, R.C., J.D. Foell, D.D. Hall, J.W. Hell, and T.J. Kamp. 2006. Localization of cardiac L-type Ca(2+) channels to a caveolar macromolecular signaling complex is required for beta(2)-adrenergic regulation. *Proceedings of the National Academy of Sciences of the United States of America*. 103:7500-7505.

Bandell, M., G.M. Story, S.W. Hwang, V. Viswanath, S.R. Eid, M.J. Petrus, T.J. Earley, and A. Patapoutian. 2004. Noxious cold ion channel TRPA1 is activated by pungent compounds and bradykinin. *Neuron*. 41:849-857.

Bannerman, R.M., and J.H. Renwick. 1962. The hereditary elliptocytoses: clinical and linkage data. *Ann Hum Genet*. 26:23-38.

Barrett, C.F., L. Liu, and A.R. Rittenhouse. 2001. Arachidonic acid reversibly enhances N-type calcium current at an extracellular site. *Am J Physiol Cell Physiol*. 280:C1306-1318.

Bartesaghi, A., A. Merk, S. Banerjee, D. Matthies, X. Wu, J.L. Milne, and S. Subramaniam. 2015. 2.2 A resolution cryo-EM structure of beta-galactosidase in complex with a cell-permeant inhibitor. *Science*. 348:1147-1151.

Bartkowiak, A., E. Grzelinska, and G. Bartosz. 1983. Aging of the erythrocyte--XVII. Changes in the properties of superoxide dismutase. *Int J Biochem*. 15:763-765.

Bartosz, G. 1980. Aging of the erythrocyte. VII. On the possible causes of inactivation of red cell enzymes. *Mech Ageing Dev*. 13:379-385.

Basora, N., G. Boulay, L. Bilodeau, E. Rousseau, and M.D. Payet. 2003. 20-hydroxyeicosatetraenoic acid (20-HETE) activates mouse TRPC6 channels expressed in HEK293 cells. *The Journal of biological chemistry*. 278:31709-31716.

Baumgart, T., A.T. Hammond, P. Sengupta, S.T. Hess, D.A. Holowka, B.A. Baird, and W.W. Webb. 2007. Large-scale fluid/fluid phase separation of proteins and

lipids in giant plasma membrane vesicles. *Proceedings of the National Academy of Sciences of the United States of America*. 104:3165-3170.

Bavi, N.N., Y. A.; Bavi, O.; Ridone, P.; Martinac, A. D.; Nakayama, Y.; Cox, C. D.; Martinac, B. 2017. Principles of Mechanosensing at the Membrane Interface. *The Biophysics of Cell Membranes. Springer Series in Biophysics*. 19:85-119.

Bavi, O., C.D. Cox, M. Vossoughi, R. Naghdabadi, Y. Jamali, and B. Martinac. 2016. Influence of Global and Local Membrane Curvature on Mechanosensitive Ion Channels: A Finite Element Approach. *Membranes (Basel)*. 6.

Bayburt, T.H., and S.G. Sligar. 2010. Membrane protein assembly into Nanodiscs. *FEBS letters*. 584:1721-1727.

Beech, D.J. 2012. Integration of transient receptor potential canonical channels with lipids. *Acta Physiol (Oxf)*. 204:227-237.

Bell, A.J., T.J. Satchwell, K.J. Heesom, B.R. Hawley, S. Kupzig, M. Hazell, R. Mushens, A. Herman, and A.M. Toye. 2013. Protein distribution during human erythroblast enucleation in vitro. *PLoS One*. 8:e60300.

Benaim, G., A.A. Pimentel, P. Felibertt, A. Mayora, L. Colman, F. Sojo, H. Rojas, and J.B. De Sanctis. 2016. Sphingosine inhibits the sarco(endo)plasmic reticulum Ca(2+)-ATPase (SERCA) activity. *Biochem Biophys Res Commun*. 473:572-577.

Bernardino de la Serna, J., J. Perez-Gil, A.C. Simonsen, and L.A. Bagatolli. 2004. Cholesterol rules: direct observation of the coexistence of two fluid phases in native pulmonary surfactant membranes at physiological temperatures. *The Journal of biological chemistry*. 279:40715-40722.

Berrocal, M., I. Corbacho, M. Vazquez-Hernandez, J. Avila, M.R. Sepulveda, and A.M. Mata. 2015. Inhibition of PMCA activity by tau as a function of aging and Alzheimer's neuropathology. *Biochimica et biophysica acta*. 1852:1465-1476.

Bers, D.M. 2002. Cardiac excitation-contraction coupling. *Nature*. 415:198-205.

Besserer, G.M., M. Ottolia, D.A. Nicoll, V. Chaptal, D. Cascio, K.D. Philipson, and J. Abramson. 2007. The second Ca2+-binding domain of the Na+ Ca2+ exchanger is essential for regulation: crystal structures and mutational analysis. *Proceedings of the National Academy of Sciences of the United States of America*. 104:18467-18472.

Bessis, M., and N. Mohandas. 1975. [Red cell deformability, importance of its measurement in clinical medicine]. *Schweiz Med Wochenschr*. 105:1568-1570.

Bezprozvanny, I. 2007. Inositol 1,4,5-tripshosphate receptor, calcium signalling and Huntington's disease. *Subcell Biochem*. 45:323-335.

Bidaud, I., A. Mezghrani, L.A. Swayne, A. Monteil, and P. Lory. 2006. Voltage-gated calcium channels in genetic diseases. *Biochimica et biophysica acta*. 1763:1169-1174.

Binnig, G., C.F. Quate, and C. Gerber. 1986. Atomic force microscope. *Phys Rev Lett*. 56:930-933.

Bogdanova, A., A. Makhro, J. Wang, P. Lipp, and L. Kaestner. 2013. Calcium in red blood cells-a perilous balance. *Int J Mol Sci*. 14:9848-9872.

Boguslawska, D.M., B. Machnicka, A. Hryniewicz-Jankowska, and A. Czogalla. 2014. Spectrin and phospholipids - the current picture of their fascinating interplay. *Cell Mol Biol Lett*. 19:158-179.

Bolla, J.R., M.T. Agasid, S. Mehmood, and C.V. Robinson. 2019. Membrane Protein-Lipid Interactions Probed Using Mass Spectrometry. *Annu Rev Biochem*. 88:85-111.

Bolotina, V.M. 2008. Orai, STIM1 and iPLA2beta: a view from a different perspective. *J Physiol*. 586:3035-3042.

Bolton-Maggs, P.H., J.C. Langer, A. Iolascon, P. Tittensor, M.J. King, and H. General Haematology Task Force of the British Committee for Standards in. 2012. Guidelines for the diagnosis and management of hereditary spherocytosis--2011 update. *Br J Haematol*. 156:37-49.

Borbiro, I., D. Badheka, and T. Rohacs. 2015. Activation of TRPV1 channels inhibits mechanosensitive Piezo channel activity by depleting membrane phosphoinositides. *Sci Signal*. 8:ra15.

Borch, J., P. Roepstorff, and J. Moller-Jensen. 2011. Nanodisc-based co-immunoprecipitation for mass spectrometric identification of membrane-interacting proteins. *Mol Cell Proteomics*. 10:O110 006775.

Borch, J., F. Torta, S.G. Sligar, and P. Roepstorff. 2008. Nanodiscs for immobilization of lipid bilayers and membrane receptors: kinetic analysis of cholera toxin binding to a glycolipid receptor. *Anal Chem*. 80:6245-6252.

Bosman, G.J., and M.M. Kay. 1990. Alterations of band 3 transport protein by cellular aging and disease: erythrocyte band 3 and glucose transporter share a functional relationship. *Biochem Cell Biol*. 68:1419-1427.

Bosman, G.J., F.L. Willekens, and J.M. Werre. 2005. Erythrocyte aging: a more than superficial resemblance to apoptosis? *Cell Physiol Biochem*. 16:1-8.

Brini, M., T. Cali, D. Ottolini, and E. Carafoli. 2013. Intracellular calcium homeostasis and signaling. *Met Ions Life Sci*. 12:119-168.

Brini, M., and E. Carafoli. 2009. Calcium pumps in health and disease. *Physiol Rev*. 89:1341-1378.

Brini, M., F. Di Leva, C.K. Ortega, T. Domi, D. Ottolini, E. Leonardi, S.C. Tosatto, and E. Carafoli. 2010. Deletions and mutations in the acidic lipid-binding region of the plasma membrane Ca2+ pump: a study on different splicing variants of isoform 2. *The Journal of biological chemistry*. 285:30779-30791.

Broecker, J., B.T. Eger, and O.P. Ernst. 2017. Crystallogenesis of Membrane Proteins Mediated by Polymer-Bounded Lipid Nanodiscs. *Structure*. 25:384-392.

Brown, D.A., and E. London. 1998. Functions of lipid rafts in biological membranes. *Annual review of cell and developmental biology*. 14:111-136.

Brown, D.A., and J.K. Rose. 1992. Sorting of GPI-anchored proteins to glycolipid-enriched membrane subdomains during transport to the apical cell surface. *Cell*. 68:533-544.

Brown, K.A. 1996. Erythrocyte Metabolism and Enzyme Defects. *Laboratory Medicine*. 27:329-333.

Brown, M.F. 2017. Soft Matter in Lipid-Protein Interactions. *Annual review of biophysics*. 46:379-410.

Brown, M.F., U. Chawla, and S.M.D.C. Perera. 2017. Membrane Lipid-Protein Interactions. *The Biophysics of Cell Membranes. Springer Series in Biophysics*. 19:61-84.

Bruce, L.J., S. Ghosh, M.J. King, D.M. Layton, W.J. Mawby, G.W. Stewart, P.A. Oldenborg, J. Delaunay, and M.J. Tanner. 2002. Absence of CD47 in protein 4.2-deficient hereditary spherocytosis in man: an interaction between the Rh complex and the band 3 complex. *Blood*. 100:1878-1885.

Buesing, K.L., E.T. Tracy, C. Kiernan, A.C. Pastor, L.D. Cassidy, J.P. Scott, R.E. Ware, A.M. Davidoff, F.J. Rescorla, J.C. Langer, H.E. Rice, and K.T. Oldham. 2011. Partial splenectomy for hereditary spherocytosis: a multi-institutional review. *J Pediatr Surg*. 46:178-183.

Caffrey, M. 2015. A comprehensive review of the lipid cubic phase or in meso method for crystallizing membrane and soluble proteins and complexes. *Acta Crystallogr F Struct Biol Commun*. 71:3-18.

Cahalan, M.D. 2009. STIMulating store-operated Ca(2+) entry. *Nature cell biology*. 11:669-677.

Cahalan, S.M., V. Lukacs, S.S. Ranade, S. Chien, M. Bandell, and A. Patapoutian. 2015. Piezo1 links mechanical forces to red blood cell volume. *Elife*. 4:e07370.

Cai, X., and J. Lytton. 2004. The cation/Ca(2+) exchanger superfamily: phylogenetic analysis and structural implications. *Mol Biol Evol*. 21:1692-1703.

Calaghan, S., and E. White. 2006. Caveolae modulate excitation-contraction coupling and beta2-adrenergic signalling in adult rat ventricular myocytes. *Cardiovasc Res*. 69:816-824.

Canales, J., D. Morales, C. Blanco, J. Rivas, N. Diaz, I. Angelopoulos, and O. Cerda. 2019. A TR(i)P to Cell Migration: New Roles of TRP Channels in Mechanotransduction and Cancer. *Front Physiol*. 10:757.

Cantor, R.S. 1999. Lipid composition and the lateral pressure profile in bilayers. *Biophysical journal*. 76:2625-2639.

Cao, E., J.F. Cordero-Morales, B. Liu, F. Qin, and D. Julius. 2013. TRPV1 channels are intrinsically heat sensitive and negatively regulated by phosphoinositide lipids. *Neuron*. 77:667-679.

Carafoli, E., L. Santella, D. Branca, and M. Brini. 2001. Generation, control, and processing of cellular calcium signals. *Crit Rev Biochem Mol Biol*. 36:107-260.

Carpi, N., and M. Piel. 2014. Stretching micropatterned cells on a PDMS membrane. *Journal of visualized experiments : JoVE*:e51193.

Carquin, M., L. Conrard, H. Pollet, P. Van Der Smissen, A. Cominelli, M. Veiga-da-Cunha, P.J. Courtoy, and D. Tyteca. 2015. Cholesterol segregates into submicrometric domains at the living erythrocyte membrane: evidence and regulation. *Cellular and molecular life sciences : CMLS*. 72:4633-4651.

Carquin, M., L. D'Auria, H. Pollet, E.R. Bongarzone, and D. Tyteca. 2016. Recent progress on lipid lateral heterogeneity in plasma membranes: From rafts to submicrometric domains. *Progress in lipid research*. 62:1-24.

Carquin, M., H. Pollet, M. Veiga-da-Cunha, A. Cominelli, P. Van Der Smissen, F. N'Kuli, H. Emonard, P. Henriet, H. Mizuno, P.J. Courtoy, and D. Tyteca. 2014. Endogenous sphingomyelin segregates into submicrometric domains in the living erythrocyte membrane. *Journal of lipid research*. 55:1331-1342.

Chan, M.M., J.M. Wooden, M. Tsang, D.M. Gilligan, S.D. Hirenallur, G.L. Finney, E. Rynes, M. Maccoss, J.A. Ramirez, H. Park, and B.M. Iritani. 2013. Hematopoietic protein-1 regulates the actin membrane skeleton and membrane stability in murine erythrocytes. *PloS one*. 8:e54902.

Chapman, D. 1975. Phase transitions and fluidity characteristics of lipids and cell membranes. *Q Rev Biophys*. 8:185-235.

Chasis, J.A., and N. Mohandas. 2008. Erythroblastic islands: niches for erythropoiesis. *Blood*. 112:470-478.

Chaudhuri, P., S.M. Colles, M. Bhat, D.R. Van Wagoner, L. Birnbaumer, and L.M. Graham. 2008. Elucidation of a TRPC6-TRPC5 channel cascade that restricts endothelial cell movement. *Molecular biology of the cell*. 19:3203-3211.

Chemin, J., A.J. Patel, F. Duprat, F. Sachs, M. Lazdunski, and E. Honore. 2007. Up- and down-regulation of the mechano-gated K(2P) channel TREK-1 by PIP (2) and other membrane phospholipids. *Pflugers Arch*. 455:97-103.

Chiabrando, D., S. Mercurio, and E. Tolosano. 2014. Heme and erythropoieis: more than a structural role. *Haematologica*. 99:973-983.

Choe, C.U., and B.E. Ehrlich. 2006. The inositol 1,4,5-trisphosphate receptor (IP3R) and its regulators: sometimes good and sometimes bad teamwork. *Sci STKE*. 2006:re15.

Chu, A., and E. Stefani. 1991. Phosphatidylinositol 4,5-bisphosphate-induced Ca2+ release from skeletal muscle sarcoplasmic reticulum terminal cisternal

membranes. Ca2+ flux and single channel studies. *The Journal of biological chemistry*. 266:7699-7705.

Chu, H., E. Puchulu-Campanella, J.A. Galan, W.A. Tao, P.S. Low, and J.F. Hoffman. 2012. Identification of cytoskeletal elements enclosing the ATP pools that fuel human red blood cell membrane cation pumps. *Proc Natl Acad Sci U S A*. 109:12794-12799.

Chunduri, S., S. Gaitonde, S.O. Ciurea, R. Hoffman, and D. Rondelli. 2008. Pulmonary extramedullary hematopoiesis in patients with myelofibrosis undergoing allogeneic stem cell transplantation. *Haematologica*. 93:1593-1595.

Ciana, A., C. Achilli, C. Balduini, and G. Minetti. 2011. On the association of lipid rafts to the spectrin skeleton in human erythrocytes. *Biochimica et biophysica acta*. 1808:183-190.

Ciardo, M.G., and A. Ferrer-Montiel. 2017. Lipids as central modulators of sensory TRP channels. *Biochim Biophys Acta Biomembr*. 1859:1615-1628.

Cimen, M.Y. 2008. Free radical metabolism in human erythrocytes. *Clin Chim Acta*. 390:1-11.

Cinar, E., S. Zhou, J. DeCourcey, Y. Wang, R.E. Waugh, and J. Wan. 2015. Piezo1 regulates mechanotransductive release of ATP from human RBCs. *Proceedings of the National Academy of Sciences of the United States of America*. 112:11783-11788.

Civjan, N.R., T.H. Bayburt, M.A. Schuler, and S.G. Sligar. 2003. Direct solubilization of heterologously expressed membrane proteins by incorporation into nanoscale lipid bilayers. *BioTechniques*. 35:556-560, 562-553.

Cohen, B.E. 2018. Membrane Thickness as a Key Factor Contributing to the Activation of Osmosensors and Essential Ras Signaling Pathways. *Front Cell Dev Biol*. 6:76.

Colina, C., V. Cervino, and G. Benaim. 2002. Ceramide and sphingosine have an antagonistic effect on the plasma-membrane Ca2+-ATPase from human erythrocytes. *The Biochemical journal*. 362:247-251.

Colina, C., A. Flores, H. Rojas, A. Acosta, C. Castillo, R. Garrido Mdel, A. Israel, R. DiPolo, and G. Benaim. 2005. Ceramide increase cytoplasmic Ca2+ concentration in Jurkat T cells by liberation of calcium from intracellular stores and activation of a store-operated calcium channel. *Arch Biochem Biophys*. 436:333-345.

Combs, D.J., and Z. Lu. 2015. Sphingomyelinase D inhibits store-operated Ca2+ entry in T lymphocytes by suppressing ORAI current. *J Gen Physiol*. 146:161-172.

Combs, D.J., H.G. Shin, Y. Xu, Y. Ramu, and Z. Lu. 2013. Tuning voltage-gated channel activity and cellular excitability with a sphingomyelinase. *J Gen Physiol*. 142:367-380.

Condrescu, M., and J.P. Reeves. 2001. Inhibition of sodium-calcium exchange by ceramide and sphingosine. *The Journal of biological chemistry*. 276:4046-4054.

Conrard, L., A. Stommen, A.S. Cloos, J. Steinkuhler, R. Dimova, H. Pollet, and D. Tyteca. 2018. Spatial Relationship and Functional Relevance of Three Lipid Domain Populations at the Erythrocyte Surface. *Cell Physiol Biochem*. 51:1544-1565.

Contreras, F.X., A.M. Ernst, P. Haberkant, P. Bjorkholm, E. Lindahl, B. Gonen, C. Tischer, A. Elofsson, G. von Heijne, C. Thiele, R. Pepperkok, F. Wieland, and B. Brugger. 2012. Molecular recognition of a single sphingolipid species by a protein's transmembrane domain. *Nature*. 481:525-529.

Contreras, F.X., A.M. Ernst, F. Wieland, and B. Brugger. 2011. Specificity of intramembrane protein-lipid interactions. *Cold Spring Harb Perspect Biol*. 3.

Contreras, F.X., L. Sanchez-Magraner, A. Alonso, and F.M. Goni. 2010. Transbilayer (flip-flop) lipid motion and lipid scrambling in membranes. *FEBS letters*. 584:1779-1786.

Cooper, R.A., E.C. Arner, J.S. Wiley, and S.J. Shattil. 1975. Modification of red cell membrane structure by cholesterol-rich lipid dispersions. A model for the primary spur cell defect. *The Journal of clinical investigation*. 55:115-126.

Cornea, R.L., and D.D. Thomas. 1994. Effects of membrane thickness on the molecular dynamics and enzymatic activity of reconstituted Ca-ATPase. *Biochemistry*. 33:2912-2920.

Corradi, V., E. Mendez-Villuendas, H.I. Ingolfsson, R.X. Gu, I. Siuda, M.N. Melo, A. Moussatova, L.J. DeGagne, B.I. Sejdiu, G. Singh, T.A. Wassenaar, K. Delgado Magnero, S.J. Marrink, and D.P. Tieleman. 2018. Lipid-Protein Interactions Are Unique Fingerprints for Membrane Proteins. *ACS Cent Sci*. 4:709-717.

Coste, B., G. Houge, M.F. Murray, N. Stitziel, M. Bandell, M.A. Giovanni, A. Philippakis, A. Hoischen, G. Riemer, U. Steen, V.M. Steen, J. Mathur, J. Cox, M. Lebo, H. Rehm, S.T. Weiss, J.N. Wood, R.L. Maas, S.R. Sunyaev, and A. Patapoutian. 2013. Gain-of-function mutations in the mechanically activated ion channel PIEZO2 cause a subtype of Distal Arthrogryposis. *Proceedings of the National Academy of Sciences of the United States of America*. 110:4667-4672.

Coste, B., J. Mathur, M. Schmidt, T.J. Earley, S. Ranade, M.J. Petrus, A.E. Dubin, and A. Patapoutian. 2010. Piezo1 and Piezo2 are essential components of distinct mechanically activated cation channels. *Science*. 330:55-60.

Cox, C.D., C. Bae, L. Ziegler, S. Hartley, V. Nikolova-Krstevski, P.R. Rohde, C.A. Ng, F. Sachs, P.A. Gottlieb, and B. Martinac. 2016. Removal of the mechanoprotective influence of the cytoskeleton reveals PIEZO1 is gated by bilayer tension. *Nature communications*. 7:10366.

Crepaldi Domingues, C., A. Ciana, A. Buttafava, C. Balduini, E. de Paula, and G. Minetti. 2009. Resistance of human erythrocyte membranes to Triton X-100 and C12E8. *The Journal of membrane biology*. 227:39-48.

Cui, M., P. Honore, C. Zhong, D. Gauvin, J. Mikusa, G. Hernandez, P. Chandran, A. Gomtsyan, B. Brown, E.K. Bayburt, K. Marsh, B. Bianchi, H. McDonald, W. Niforatos, T.R. Neelands, R.B. Moreland, M.W. Decker, C.H. Lee, J.P. Sullivan, and C.R. Faltynek. 2006. TRPV1 receptors in the CNS play a key role in broad-spectrum analgesia of TRPV1 antagonists. *J Neurosci*. 26:9385-9393.

Cullis, P.R., and B. de Kruijff. 1979. Lipid polymorphism and the functional roles of lipids in biological membranes. *Biochimica et biophysica acta*. 559:399-420.

Curtis, H.B., S. 1989. Biology. W. H. Freeman; Fifth Edition edition. 1192 pp.

D'Auria, L., M. Fenaux, P. Aleksandrowicz, P. Van Der Smissen, C. Chantrain, C. Vermylen, M. Vikkula, P.J. Courtoy, and D. Tyteca. 2013. Micrometric segregation of fluorescent membrane lipids: relevance for endogenous lipids and biogenesis in erythrocytes. *Journal of lipid research*. 54:1066-1076.

D'Auria, L., P. Van Der Smissen, F. Bruyneel, P.J. Courtoy, and D. Tyteca. 2011. Segregation of fluorescent membrane lipids into distinct micrometric domains: evidence for phase compartmentation of natural lipids? *PloS one*. 6:e17021.

Da Costa, L., J. Galimand, O. Fenneteau, and N. Mohandas. 2013. Hereditary spherocytosis, elliptocytosis, and other red cell membrane disorders. *Blood Rev*. 27:167-178.

Da Costa, L., L. Suner, J. Galimand, A. Bonnel, T. Pascreau, N. Couque, O. Fenneteau, N. Mohandas, H. Society of, g. Pediatric Immunology, and H. French Society of. 2016. Diagnostic tool for red blood cell membrane disorders: Assessment of a new generation ektacytometer. *Blood Cells Mol Dis*. 56:9-22.

Dalton, K.A., J.M. East, S. Mall, S. Oliver, A.P. Starling, and A.G. Lee. 1998. Interaction of phosphatidic acid and phosphatidylserine with the Ca2+-ATPase of sarcoplasmic reticulum and the mechanism of inhibition. *The Biochemical journal*. 329 (Pt 3):637-646.

Danielczok, J.G., E. Terriac, L. Hertz, P. Petkova-Kirova, F. Lautenschlager, M.W. Laschke, and L. Kaestner. 2017. Red Blood Cell Passage of Small Capillaries Is Associated with Transient Ca(2+)-mediated Adaptations. *Front Physiol*. 8:979-990.

Dao, M., C.T. Lim, and S. Suresh. 2003. Mechanics of the human red blood cell deformed by optical tweezers. *Journal of the Mechanics and Physics of Solids*. 51:2259-2280.

Das, N., D.T. Murray, and T.A. Cross. 2013. Lipid bilayer preparations of membrane proteins for oriented and magic-angle spinning solid-state NMR samples. *Nat Protoc*. 8:2256-2270.

de Almeida, R.F., L.M. Loura, A. Fedorov, and M. Prieto. 2005. Lipid rafts have different sizes depending on membrane composition: a time-resolved fluorescence resonance energy transfer study. *J Mol Biol*. 346:1109-1120.

de Back, D.Z., E.B. Kostova, M. van Kraaij, T.K. van den Berg, and R. van Bruggen. 2014. Of macrophages and red blood cells; a complex love story. *Front Physiol*. 5:9.

De Colibus, L., A.F. Sonnen, K.J. Morris, C.A. Siebert, P. Abrusci, J. Plitzko, V. Hodnik, M. Leippe, E. Volpi, G. Anderluh, and R.J. Gilbert. 2012. Structures of lysenin reveal a shared evolutionary origin for pore-forming proteins and its mode of sphingomyelin recognition. *Structure*. 20:1498-1507.

de la Cruz, L., E.I. Puente, A. Reyes-Vaca, I. Arenas, J. Garduno, J. Bravo-Martinez, and D.E. Garcia. 2016. PIP2 in pancreatic beta-cells regulates voltage-gated calcium channels by a voltage-independent pathway. *Am J Physiol Cell Physiol*. 311:C630-C640.

De Petrocellis, L., and V. Di Marzo. 2009. Role of endocannabinoids and endovanilloids in Ca2+ signalling. *Cell Calcium*. 45:611-624.

Deisenhofer, J., and H. Michel. 1989. The Photosynthetic Reaction Center from the Purple Bacterium Rhodopseudomonas viridis. *Science*. 245:1463-1473.

Denisov, I.G., and S.G. Sligar. 2016. Nanodiscs for structural and functional studies of membrane proteins. *Nat Struct Mol Biol*. 23:481-486.

Denning, E.J., and O. Beckstein. 2013. Influence of lipids on protein-mediated transmembrane transport. *Chemistry and physics of lipids*. 169:57-71.

Deplaine, G., I. Safeukui, F. Jeddi, F. Lacoste, V. Brousse, S. Perrot, S. Biligui, M. Guillotte, C. Guitton, S. Dokmak, B. Aussilhou, A. Sauvanet, D. Cazals Hatem, F. Paye, M. Thellier, D. Mazier, G. Milon, N. Mohandas, O. Mercereau-Puijalon, P.H. David, and P.A. Buffet. 2011. The sensing of poorly deformable red blood cells by the human spleen can be mimicked in vitro. *Blood*. 117:e88-95.

Derler, I., I. Jardin, P.B. Stathopulos, M. Muik, M. Fahrner, V. Zayats, S.K. Pandey, M. Poteser, B. Lackner, M. Absolonova, R. Schindl, K. Groschner, R. Ettrich, M. Ikura, and C. Romanin. 2016. Cholesterol modulates Orai1 channel function. *Sci Signal*. 9:ra10.

Devaux, P.F., and R. Morris. 2004. Transmembrane asymmetry and lateral domains in biological membranes. *Traffic*. 5:241-246.

Di Leva, F., T. Domi, L. Fedrizzi, D. Lim, and E. Carafoli. 2008. The plasma membrane Ca2+ ATPase of animal cells: structure, function and regulation. *Arch Biochem Biophys*. 476:65-74.

Diez-Silva, M., M. Dao, J. Han, C.T. Lim, and S. Suresh. 2010. Shape and Biomechanical Characteristics of Human Red Blood Cells in Health and Disease. *MRS Bull*. 35:382-388.

Doerner, J.F., H. Hatt, and I.S. Ramsey. 2011. Voltage- and temperature-dependent activation of TRPV3 channels is potentiated by receptor-mediated PI(4,5)P2 hydrolysis. *J Gen Physiol*. 137:271-288.

Domingues, C.C., A. Ciana, A. Buttafava, B.R. Casadei, C. Balduini, E. de Paula, and G. Minetti. 2010. Effect of cholesterol depletion and temperature on the isolation of detergent-resistant membranes from human erythrocytes. *The Journal of membrane biology*. 234:195-205.

Drachmann, N.D., C. Olesen, J.V. Moller, Z. Guo, P. Nissen, and M. Bublitz. 2014. Comparing crystal structures of Ca(2+) -ATPase in the presence of different lipids. *The FEBS journal*. 281:4249-4262.

Dror, R.O., R.M. Dirks, J.P. Grossman, H. Xu, and D.E. Shaw. 2012. Biomolecular simulation: a computational microscope for molecular biology. *Annual review of biophysics*. 41:429-452.

Duan, J., J. Zhang, Y. Zhao, F. Yang, and X. Zhang. 2006. Ganglioside GM2 modulates the erythrocyte Ca2+-ATPase through its binding to the calmodulin-binding domain and its 'receptor'. *Arch Biochem Biophys*. 454:155-159.

Dufrene, Y.F., T. Ando, R. Garcia, D. Alsteens, D. Martinez-Martin, A. Engel, C. Gerber, and D.J. Muller. 2017. Imaging modes of atomic force microscopy for application in molecular and cell biology. *Nat Nanotechnol*. 12:295-307.

Dufrene, Y.F., D. Martinez-Martin, I. Medalsy, D. Alsteens, and D.J. Muller. 2013. Multiparametric imaging of biological systems by force-distance curve-based AFM. *Nat Methods*. 10:847-854.

Dulinska, I., M. Targosz, W. Strojny, M. Lekka, P. Czuba, W. Balwierz, and M. Szymonski. 2006. Stiffness of normal and pathological erythrocytes studied by means of atomic force microscopy. *J Biochem Biophys Methods*. 66:1-11.

Dumitru, A., M. Poncin, L. Conrard, Y. Dufrêne, D. Tyteca, and D. Alsteens. 2018. Nanoscale membrane architecture of healthy and pathological red blood cells. *Nanoscale Horizons*. 3:293-304.

Dunn, J.-O., M. Mythen, and M. Grocott. 2016. Physiology of oxygen transport. *BJA Education*. 16:341-348.

Durham, W.J., X.H. Wehrens, S. Sood, and S.L. Hamilton. 2007. Diseases associated with altered ryanodine receptor activity. *Subcell Biochem*. 45:273-321.

Dyrda, A., U. Cytlak, A. Ciuraszkiewicz, A. Lipinska, A. Cueff, G. Bouyer, S. Egee, P. Bennekou, V.L. Lew, and S.L. Thomas. 2010. Local membrane deformations activate Ca2+-dependent K+ and anionic currents in intact human red blood cells. *PloS one*. 5:e9447.

Dzierzak, E., and S. Philipsen. 2013. Erythropoiesis: development and differentiation. *Cold Spring Harb Perspect Med*. 3:a011601.

East, J.M., and A.G. Lee. 1982. Lipid selectivity of the calcium and magnesium ion dependent adenosinetriphosphatase, studied with fluorescence quenching by a brominated phospholipid. *Biochemistry*. 21:4144-4151.

Emerson, S.G., C.A. Sieff, E.A. Wang, G.G. Wong, S.C. Clark, and D.G. Nathan. 1985. Purification of fetal hematopoietic progenitors and demonstration of recombinant multipotential colony-stimulating activity. *The Journal of clinical investigation*. 76:1286-1290.

Engelman, D.M. 2005. Membranes are more mosaic than fluid. *Nature*. 438:578-580.

Ercan, E., F. Momburg, U. Engel, K. Temmerman, W. Nickel, and M. Seedorf. 2009. A conserved, lipid-mediated sorting mechanism of yeast Ist2 and mammalian STIM proteins to the peripheral ER. *Traffic*. 10:1802-1818.

Ernst, A.M., F.X. Contreras, B. Brugger, and F. Wieland. 2010. Determinants of specificity at the protein-lipid interface in membranes. *FEBS letters*. 584:1713-1720.

Ertel, E.A., K.P. Campbell, M.M. Harpold, F. Hofmann, Y. Mori, E. Perez-Reyes, A. Schwartz, T.P. Snutch, T. Tanabe, L. Birnbaumer, R.W. Tsien, and W.A. Catterall. 2000. Nomenclature of voltage-gated calcium channels. *Neuron*. 25:533-535.

Espinoza-Fonseca, L.M. 2019. Probing the effects of nonannular lipid binding on the stability of the calcium pump SERCA. *Sci Rep*. 9:3349.

Evans, E., N. Mohandas, and A. Leung. 1984. Static and dynamic rigidities of normal and sickle erythrocytes. Major influence of cell hemoglobin concentration. *The Journal of clinical investigation*. 73:477-488.

Fajardo, V.A., N. Trojanowski, L.M. Castelli, P.M. Miotto, F. Amoye, W.E. Ward, A.R. Tupling, and P.J. LeBlanc. 2017. Saturation of SERCA's lipid annulus may protect against its thermal inactivation. *Biochem Biophys Res Commun*. 484:456-460.

Faramarz, N. 2008. Disorder of Red Blood Cells: Anemias. *Hematopathology*. Chapter 23:529-565.

Feigenson, G.W. 2006. Phase behavior of lipid mixtures. *Nat Chem Biol*. 2:560-563.

Feske, S., J. Giltnane, R. Dolmetsch, L.M. Staudt, and A. Rao. 2001. Gene regulation mediated by calcium signals in T lymphocytes. *Nat Immunol*. 2:316-324.

Feske, S., Y. Gwack, M. Prakriya, S. Srikanth, S.H. Puppel, B. Tanasa, P.G. Hogan, R.S. Lewis, M. Daly, and A. Rao. 2006. A mutation in Orai1 causes immune deficiency by abrogating CRAC channel function. *Nature*. 441:179-185.

Filomatori, C.V., and A.F. Rega. 2003. On the mechanism of activation of the plasma membrane Ca2+-ATPase by ATP and acidic phospholipids. *The Journal of biological chemistry*. 278:22265-22271.

Filoteo, A.G., A. Enyedi, and J.T. Penniston. 1992. The lipid-binding peptide from the plasma membrane Ca2+ pump binds calmodulin, and the primary calmodulin-binding domain interacts with lipid. *The Journal of biological chemistry*. 267:11800-11805.

Fisher, K.A. 1982. Monolayer freeze-fracture autoradiography: quantitative analysis of the transmembrane distribution of radioiodinated concanavalin A. *J Cell Biol*. 93:155-163.

Fleischer, S. 2008. Personal recollections on the discovery of the ryanodine receptors of muscle. *Biochem Biophys Res Commun*. 369:195-207.

Flemming, P.K., A.M. Dedman, S.Z. Xu, J. Li, F. Zeng, J. Naylor, C.D. Benham, A.N. Bateson, K. Muraki, and D.J. Beech. 2006. Sensing of lysophospholipids by TRPC5 calcium channel. *The Journal of biological chemistry*. 281:4977-4982.

Foller, M., R.S. Kasinathan, S. Koka, C. Lang, E. Shumilina, L. Birnbaumer, F. Lang, and S.M. Huber. 2008. TRPC6 contributes to the Ca(2+) leak of human erythrocytes. *Cell Physiol Biochem*. 21:183-192.

Fornaini, G., M. Magnani, A. Fazi, A. Accorsi, V. Stocchi, and M. Dacha. 1985. Regulatory properties of human erythrocyte hexokinase during cell ageing. *Arch Biochem Biophys*. 239:352-358.

Forsyth, A.M., J. Wan, P.D. Owrutsky, M. Abkarian, and H.A. Stone. 2011. Multiscale approach to link red blood cell dynamics, shear viscosity, and ATP release. *Proceedings of the National Academy of Sciences of the United States of America*. 108:10986-10991.

Foskett, J.K., C. White, K.H. Cheung, and D.O. Mak. 2007. Inositol trisphosphate receptor Ca2+ release channels. *Physiol Rev*. 87:593-658.

Fosso-Tande, J., C. Black, S. G. Aller, L. Lu, and R. D. Hills Jr. 2017. Simulation of lipid-protein interactions with the CgProt force field. *AIMS Molecular Science*. 4:352-369.

Franco, T., and P.S. Low. 2010. Erythrocyte adducin: a structural regulator of the red blood cell membrane. *Transfus Clin Biol*. 17:87-94.

Froud, R.J., C.R. Earl, J.M. East, and A.G. Lee. 1986. Effects of lipid fatty acyl chain structure on the activity of the (Ca2+ + Mg2+)-ATPase. *Biochimica et biophysica acta*. 860:354-360.

Fujiwara, T., K. Ritchie, H. Murakoshi, K. Jacobson, and A. Kusumi. 2002. Phospholipids undergo hop diffusion in compartmentalized cell membrane. *The Journal of cell biology*. 157:1071-1081.

Gaetani, M., S. Mootien, S. Harper, P.G. Gallagher, and D.W. Speicher. 2008. Structural and functional effects of hereditary hemolytic anemia-associated point mutations in the alpha spectrin tetramer site. *Blood*. 111:5712-5720.

Gallagher, P.G. 2004. Hereditary elliptocytosis: spectrin and protein 4.1R. *Seminars in hematology*. 41:142-164.

Gallagher, P.G. 2005. Red cell membrane disorders. *Hematology / the Education Program of the American Society of Hematology. American Society of Hematology. Education Program*:13-18.

Gallagher, P.G. 2017. Disorders of erythrocyte hydration. *Blood*. 130:2699-2708.

Galvan, D.L., E. Borrego-Diaz, P.J. Perez, and G.A. Mignery. 1999. Subunit oligomerization, and topology of the inositol 1,4, 5-trisphosphate receptor. *The Journal of biological chemistry*. 274:29483-29492.

Gamper, N., and M.S. Shapiro. 2007. Target-specific PIP(2) signalling: how might it work? *J Physiol*. 582:967-975.

Gao, Y., E. Cao, D. Julius, and Y. Cheng. 2016. TRPV1 structures in nanodiscs reveal mechanisms of ligand and lipid action. *Nature*. 534:347-351.

Garattini, S. 2007. Long-chain n-3 fatty acids in lipid rafts: implications for anti-inflammatory effects. *J Cardiovasc Med (Hagerstown)*. 8 Suppl 1:S30-33.

Garbarz, M., I. Devaux, O. Bournier, B. Grandchamp, and D. Dhermy. 1995. Protein 4.1 Lille, a novel mutation in the downstream initiation codon of protein 4.1 gene associated with heterozygous 4,1(-) hereditary elliptocytosis. *Hum Mutat*. 5:339-340.

Garcia-Arribas, A.B., A. Alonso, and F.M. Goni. 2016. Cholesterol interactions with ceramide and sphingomyelin. *Chemistry and physics of lipids*. 199:26-34.

Gault, C.R., L.M. Obeid, and Y.A. Hannun. 2010. An overview of sphingolipid metabolism: from synthesis to breakdown. *Adv Exp Med Biol*. 688:1-23.

Gaus, K., E. Gratton, E.P. Kable, A.S. Jones, I. Gelissen, L. Kritharides, and W. Jessup. 2003. Visualizing lipid structure and raft domains in living cells with two-photon microscopy. *Proceedings of the National Academy of Sciences of the United States of America*. 100:15554-15559.

Gauthier, N.C., T.A. Masters, and M.P. Sheetz. 2012. Mechanical feedback between membrane tension and dynamics. *Trends in cell biology*. 22:527-535.

George, A., S. Pushkaran, D.G. Konstantinidis, S. Koochaki, P. Malik, N. Mohandas, Y. Zheng, C.H. Joiner, and T.A. Kalfa. 2013. Erythrocyte NADPH oxidase activity modulated by Rac GTPases, PKC, and plasma cytokines contributes to oxidative stress in sickle cell disease. *Blood*. 121:2099-2107.

Glader, B. 2013. Other Hereditary Red Blood Cell Disorders. *Emery and Rimoin's Principles and Practice of Medical Genetics (Sixth Edition)*. Chapter 72:1-25.

Gladwyn-Ng, I., L. Cordon-Barris, C. Alfano, C. Creppe, T. Couderc, G. Morelli, N. Thelen, M. America, B. Bessieres, F. Encha-Razavi, M. Bonniere, I.K. Suzuki, M. Flamand, P. Vanderhaeghen, M. Thiry, M. Lecuit, and L. Nguyen. 2018. Stress-induced unfolded protein response contributes to Zika virus-associated microcephaly. *Nature neuroscience*. 21:63-71.

Glogowska, E., E.R. Schneider, Y. Maksimova, V.P. Schulz, K. Lezon-Geyda, J. Wu, K. Radhakrishnan, S.B. Keel, D. Mahoney, A.M. Freidmann, R.A. Altura, E.O. Gracheva, S.N. Bagriantsev, T.A. Kalfa, and P.G. Gallagher. 2017. Novel mechanisms of PIEZO1 dysfunction in hereditary xerocytosis. *Blood*. 130:1845-1856.

Gnanasambandam, R., C. Bae, P.A. Gottlieb, and F. Sachs. 2015. Ionic Selectivity and Permeation Properties of Human PIEZO1 Channels. *PloS one*. 10:e0125503.

Gnanasambandam, R., C. Ghatak, A. Yasmann, K. Nishizawa, F. Sachs, A.S. Ladokhin, S.I. Sukharev, and T.M. Suchyna. 2017. GsMTx4: Mechanism of Inhibiting Mechanosensitive Ion Channels. *Biophysical journal*. 112:31-45.

Gokhin, D.S., and V.M. Fowler. 2016. Feisty filaments: actin dynamics in the red blood cell membrane skeleton. *Curr Opin Hematol*. 23:206-214.

Gonen, T., Y. Cheng, P. Sliz, Y. Hiroaki, Y. Fujiyoshi, S.C. Harrison, and T. Walz. 2005. Lipid-protein interactions in double-layered two-dimensional AQP0 crystals. *Nature*. 438:633-638.

Gonzalez-Manas, J.M., J.H. Lakey, and F. Pattus. 1992. Brominated phospholipids as a tool for monitoring the membrane insertion of colicin A. *Biochemistry*. 31:7294-7300.

Gorlach, A., K. Bertram, S. Hudecova, and O. Krizanova. 2015. Calcium and ROS: A mutual interplay. *Redox Biol*. 6:260-271.

Gousset, K., W.F. Wolkers, N.M. Tsvetkova, A.E. Oliver, C.L. Field, N.J. Walker, J.H. Crowe, and F. Tablin. 2002. Evidence for a physiological role for membrane rafts in human platelets. *Journal of cellular physiology*. 190:117-128.

Gov, N.S., and S.A. Safran. 2005. Red blood cell membrane fluctuations and shape controlled by ATP-induced cytoskeletal defects. *Biophysical journal*. 88:1859-1874.

Grimm, C., R. Kraft, G. Schultz, and C. Harteneck. 2005. Activation of the melastatin-related cation channel TRPM3 by D-erythro-sphingosine [corrected]. *Mol Pharmacol*. 67:798-805.

Grossmann, G., M. Opekarova, J. Malinsky, I. Weig-Meckl, and W. Tanner. 2007. Membrane potential governs lateral segregation of plasma membrane proteins and lipids in yeast. *The EMBO journal*. 26:1-8.

Gu, R.X., H.I. Ingolfsson, A.H. de Vries, S.J. Marrink, and D.P. Tieleman. 2017. Ganglioside-Lipid and Ganglioside-Protein Interactions Revealed by Coarse-Grained and Atomistic Molecular Dynamics Simulations. *The journal of physical chemistry. B*. 121:3262-3275.

Guerini, D., B. Pan, and E. Carafoli. 2003. Expression, purification, and characterization of isoform 1 of the plasma membrane Ca2+ pump: focus on calpain sensitivity. *The Journal of biological chemistry*. 278:38141-38148.

Guerrero-Hernandez, A., A. Dagnino-Acosta, and A. Verkhratsky. 2010. An intelligent sarco-endoplasmic reticulum Ca2+ store: release and leak channels have differential access to a concealed Ca2+ pool. *Cell Calcium*. 48:143-149.

Gupta, K., J. Li, I. Liko, J. Gault, C. Bechara, D. Wu, J.T.S. Hopper, K. Giles, J.L.P. Benesch, and C.V. Robinson. 2018. Identifying key membrane protein lipid interactions using mass spectrometry. *Nat Protoc*. 13:1106-1120.

Gustavsson, M., N.J. Traaseth, and G. Veglia. 2011. Activating and deactivating roles of lipid bilayers on the Ca(2+)-ATPase/phospholamban complex. *Biochemistry*. 50:10367-10374.

Haag, M., A. Schmidt, T. Sachsenheimer, and B. Brugger. 2012. Quantification of Signaling Lipids by Nano-Electrospray Ionization Tandem Mass Spectrometry (Nano-ESI MS/MS). *Metabolites*. 2:57-76.

Haas, E., and D.W. Stanley. 2007. Phospholipases. *xPharm: The Comprehensive Pharmacology Reference*:1-3.

Hadley, T.J., and L.H. Miller. 1988. Invasion of erythrocytes by malaria parasites: erythrocyte ligands and parasite receptors. *Prog Allergy*. 41:49-71.

Hannun, Y.A., and L.M. Obeid. 2002. The Ceramide-centric universe of lipid-mediated cell regulation: stress encounters of the lipid kind. *The Journal of biological chemistry*. 277:25847-25850.

Hara, Y., M. Wakamori, M. Ishii, E. Maeno, M. Nishida, T. Yoshida, H. Yamada, S. Shimizu, E. Mori, J. Kudoh, N. Shimizu, H. Kurose, Y. Okada, K. Imoto, and Y. Mori. 2002. LTRPC2 Ca2+-permeable channel activated by changes in redox status confers susceptibility to cell death. *Mol Cell*. 9:163-173.

Harayama, T., and H. Riezman. 2018. Understanding the diversity of membrane lipid composition. *Nature reviews. Molecular cell biology*. 19:281-296.

Harper, S.L., S. Sriswasdi, H.Y. Tang, M. Gaetani, P.G. Gallagher, and D.W. Speicher. 2013. The common hereditary elliptocytosis-associated alpha-spectrin L260P mutation perturbs erythrocyte membranes by stabilizing spectrin in the closed dimer conformation. *Blood*. 122:3045-3053.

Hassoun, H., and J. Palek. 1996. Hereditary spherocytosis: a review of the clinical and molecular aspects of the disease. *Blood Rev*. 10:129-147.

Hattangadi, S.M., P. Wong, L. Zhang, J. Flygare, and H.F. Lodish. 2011. From stem cell to red cell: regulation of erythropoiesis at multiple levels by multiple proteins, RNAs, and chromatin modifications. *Blood*. 118:6258-6268.

He, B.J., L. Liao, Z.F. Deng, Y.F. Tao, Y.C. Xu, and F.Q. Lin. 2018. Molecular Genetic Mechanisms of Hereditary Spherocytosis: Current Perspectives. *Acta Haematol*. 139:60-66.

He, Z., S. Feng, Q. Tong, D.W. Hilgemann, and K.D. Philipson. 2000. Interaction of PIP(2) with the XIP region of the cardiac Na/Ca exchanger. *Am J Physiol Cell Physiol*. 278:C661-666.

Heberle, F.A., and G.W. Feigenson. 2011. Phase separation in lipid membranes. *Cold Spring Harb Perspect Biol*. 3.

Heberle, F.A., R.S. Petruzielo, J. Pan, P. Drazba, N. Kucerka, R.F. Standaert, G.W. Feigenson, and J. Katsaras. 2013. Bilayer thickness mismatch controls domain size in model membranes. *J Am Chem Soc*. 135:6853-6859.

Hedger, G., and M.S.P. Sansom. 2016. Lipid interaction sites on channels, transporters and receptors: Recent insights from molecular dynamics simulations. *Biochimica et biophysica acta*. 1858:2390-2400.

Heideveld, E., and E. van den Akker. 2017. Digesting the role of bone marrow macrophages on hematopoiesis. *Immunobiology*. 222:814-822.

Hilgemann, D.W., and R. Ball. 1996. Regulation of cardiac Na+,Ca2+ exchange and KATP potassium channels by PIP2. *Science*. 273:956-959.

Hinterdorfer, P., and Y.F. Dufrene. 2006. Detection and localization of single molecular recognition events using atomic force microscopy. *Nat Methods*. 3:347-355.

Hoffmann, A., C. Grimm, R. Kraft, O. Goldbaum, A. Wrede, C. Nolte, U.K. Hanisch, C. Richter-Landsberg, W. Bruck, H. Kettenmann, and C. Harteneck. 2010. TRPM3 is expressed in sphingosine-responsive myelinating oligodendrocytes. *Journal of neurochemistry*. 114:654-665.

Hofmann, T., A.G. Obukhov, M. Schaefer, C. Harteneck, T. Gudermann, and G. Schultz. 1999. Direct activation of human TRPC6 and TRPC3 channels by diacylglycerol. *Nature*. 397:259-263.

Holendova, B., L. Grycova, M. Jirku, and J. Teisinger. 2012. PtdIns(4,5)P2 interacts with CaM binding domains on TRPM3 N-terminus. *Channels (Austin)*. 6:479-482.

Hong, J.H., Q. Li, M.S. Kim, D.M. Shin, S. Feske, L. Birnbaumer, K.T. Cheng, I.S. Ambudkar, and S. Muallem. 2011. Polarized but differential localization and recruitment of STIM1, Orai1 and TRPC channels in secretory cells. *Traffic*. 12:232-245.

Horton, R.E. 2017. Microfluidics for investigating vaso-occlusions in sickle cell disease. *Microcirculation*. 24.

Hou, X., L. Pedi, M.M. Diver, and S.B. Long. 2012. Crystal structure of the calcium release-activated calcium channel Orai. *Science*. 338:1308-1313.

Hu, M., and W. Lin. 2012. Effects of exercise training on red blood cell production: implications for anemia. *Acta Haematol*. 127:156-164.

Huang, G.N., W. Zeng, J.Y. Kim, J.P. Yuan, L. Han, S. Muallem, and P.F. Worley. 2006. STIM1 carboxyl-terminus activates native SOC, I(crac) and TRPC1 channels. *Nature cell biology*. 8:1003-1010.

Huisjes, R., A. Makhro, E. Llaudet-Planas, L. Hertz, P. Petkova-Kirova, L.P. Verhagen, S. Pignatelli, M.A. Rab, R.M. Schiffelers, E. Seiler, W.W. van Solinge, J.L. Vives Corrons, M. Manu-Pereira, L. Kaestner, A. Bogdanova, and R. van

Wijk. 2019. Density, heterogeneity and deformability of red cells as markers of clinical severity in hereditary spherocytosis. *Haematologica*.
Hunte, C., and S. Richers. 2008. Lipids and membrane protein structures. *Curr Opin Struct Biol*. 18:406-411.
Huster, D. 2014. Solid-state NMR spectroscopy to study protein-lipid interactions. *Biochimica et biophysica acta*. 1841:1146-1160.
Iftinca, M.C., and G.W. Zamponi. 2009. Regulation of neuronal T-type calcium channels. *Trends Pharmacol Sci*. 30:32-40.
Ikonen, E. 2008. Cellular cholesterol trafficking and compartmentalization. *Nature reviews. Molecular cell biology*. 9:125-138.
Ingolfsson, H.I., M.N. Melo, F.J. van Eerden, C. Arnarez, C.A. Lopez, T.A. Wassenaar, X. Periole, A.H. de Vries, D.P. Tieleman, and S.J. Marrink. 2014. Lipid organization of the plasma membrane. *J Am Chem Soc*. 136:14554-14559.
Iribe, G., C.W. Ward, P. Camelliti, C. Bollensdorff, F. Mason, R.A. Burton, A. Garny, M.K. Morphew, A. Hoenger, W.J. Lederer, and P. Kohl. 2009. Axial stretch of rat single ventricular cardiomyocytes causes an acute and transient increase in Ca2+ spark rate. *Circ Res*. 104:787-795.
Islam, M.S. 2011. TRP channels of islets. *Adv Exp Med Biol*. 704:811-830.
Jaggar, J.H., A.S. Stevenson, and M.T. Nelson. 1998. Voltage dependence of Ca2+ sparks in intact cerebral arteries. *Am J Physiol*. 274:C1755-1761.
Janmey, P.A., and P.K. Kinnunen. 2006. Biophysical properties of lipids and dynamic membranes. *Trends in cell biology*. 16:538-546.
Jensen, F.B. 2009. The dual roles of red blood cells in tissue oxygen delivery: oxygen carriers and regulators of local blood flow. *J Exp Biol*. 212:3387-3393.
Jiang, L., M.D. Bechtel, J.L. Bean, R. Winefield, T.D. Williams, A. Zaidi, E.K. Michaelis, and M.L. Michaelis. 2014. Effects of gangliosides on the activity of the plasma membrane Ca2+-ATPase. *Biochimica et biophysica acta*. 1838:1255-1265.
Jiang, L., D. Fernandes, N. Mehta, J.L. Bean, M.L. Michaelis, and A. Zaidi. 2007. Partitioning of the plasma membrane Ca2+-ATPase into lipid rafts in primary neurons: effects of cholesterol depletion. *Journal of neurochemistry*. 102:378-388.
Johnson, I.D., H.C. Kang, and R.P. Haugland. 1991. Fluorescent membrane probes incorporating dipyrrometheneboron difluoride fluorophores. *Analytical biochemistry*. 198:228-237.
Kaestner, L., P. Steffen, D.B. Nguyen, J. Wang, L. Wagner-Britz, A. Jung, C. Wagner, and I. Bernhardt. 2012. Lysophosphatidic acid induced red blood cell aggregation in vitro. *Bioelectrochemistry*. 87:89-95.
Kaestner, L., W. Tabellion, P. Lipp, and I. Bernhardt. 2004. Prostaglandin E2 activates channel-mediated calcium entry in human erythrocytes: an

indication for a blood clot formation supporting process. *Thromb Haemost*. 92:1269-1272.

Kaestner, L., W. Tabellion, E. Weiss, I. Bernhardt, and P. Lipp. 2006. Calcium imaging of individual erythrocytes: problems and approaches. *Cell Calcium*. 39:13-19.

Kahya, N., D. Scherfeld, K. Bacia, B. Poolman, and P. Schwille. 2003. Probing lipid mobility of raft-exhibiting model membranes by fluorescence correlation spectroscopy. *The Journal of biological chemistry*. 278:28109-28115.

Kahya, N., and P. Schwille. 2006. Fluorescence correlation studies of lipid domains in model membranes. *Molecular membrane biology*. 23:29-39.

Kanias, T., and J.P. Acker. 2010. Biopreservation of red blood cells--the struggle with hemoglobin oxidation. *FEBS J*. 277:343-356.

Kapavarapu, P.K., A. Paul, A.V. Lalitha, and A.S. Shet. 2012. Transient aplastic crisis in hereditary elliptocytosis. *Indian J Pediatr*. 79:1666-1668.

Kapus, A., and P. Janmey. 2013. Plasma membrane--cortical cytoskeleton interactions: a cell biology approach with biophysical considerations. *Compr Physiol*. 3:1231-1281.

Kawai, F., M. Shoda, R. Harashima, Y. Sadaie, H. Hara, and K. Matsumoto. 2004. Cardiolipin domains in Bacillus subtilis marburg membranes. *J Bacteriol*. 186:1475-1483.

Keerthivasan, G., A. Wickrema, and J.D. Crispino. 2011. Erythroblast enucleation. *Stem Cells Int*. 2011:139851.

Killian, J.A. 1998. Hydrophobic mismatch between proteins and lipids in membranes. *Biochimica et Biophysica Acta - Reviews on Biomembranes*. 1376:401-415.

Kim, J.L., H.; Shin, S. 2015. Advances in the measurement of red blood cell deformability: A brief review. *Journal of Cellular Biotechnology*. 1:63-79.

Kleinbongard, P., R. Schulz, T. Rassaf, T. Lauer, A. Dejam, T. Jax, I. Kumara, P. Gharini, S. Kabanova, B. Ozuyaman, H.G. Schnurch, A. Godecke, A.A. Weber, M. Robenek, H. Robenek, W. Bloch, P. Rosen, and M. Kelm. 2006. Red blood cells express a functional endothelial nitric oxide synthase. *Blood*. 107:2943-2951.

Knapp, E.W., S.F. Fischer, W. Zinth, M. Sander, W. Kaiser, J. Deisenhofer, and H. Michel. 1985. Analysis of optical spectra from single crystals of Rhodopseudomonas viridis reaction centers. *Proceedings of the National Academy of Sciences of the United States of America*. 82:8463-8467.

Koldso, H., and M.S. Sansom. 2012. Local Lipid Reorganization by a Transmembrane Protein Domain. *J Phys Chem Lett*. 3:3498-3502.

Koldso, H., D. Shorthouse, J. Helie, and M.S. Sansom. 2014. Lipid clustering correlates with membrane curvature as revealed by molecular simulations of complex lipid bilayers. *PLoS Comput Biol*. 10:e1003911.

Kolobkova, Y.A., V.A. Vigont, A.V. Shalygin, and E.V. Kaznacheyeva. 2017. Huntington's Disease: Calcium Dyshomeostasis and Pathology Models. *Acta Naturae*. 9:34-46.

Konstantinidis, D.G., S. Pushkaran, J.F. Johnson, J.A. Cancelas, S. Manganaris, C.E. Harris, D.A. Williams, Y. Zheng, and T.A. Kalfa. 2012. Signaling and cytoskeletal requirements in erythroblast enucleation. *Blood*. 119:6118-6127.

Koury, M.J., and P. Ponka. 2004. New insights into erythropoiesis: the roles of folate, vitamin B12, and iron. *Annu Rev Nutr*. 24:105-131.

Koynova, R., and M. Caffrey. 1998. Phases and phase transitions of the phosphatidylcholines. *Biochimica et biophysica acta*. 1376:91-145.

Kuerschner, L., C.S. Ejsing, K. Ekroos, A. Shevchenko, K.I. Anderson, and C. Thiele. 2005. Polyene-lipids: a new tool to image lipids. *Nat Methods*. 2:39-45.

Kuhn, V., L. Diederich, T.C.S.t. Keller, C.M. Kramer, W. Luckstadt, C. Panknin, T. Suvorava, B.E. Isakson, M. Kelm, and M.M. Cortese-Krott. 2017. Red Blood Cell Function and Dysfunction: Redox Regulation, Nitric Oxide Metabolism, Anemia. *Antioxid Redox Signal*. 26:718-742.

Kumari, S., A. Kumar, P. Sardar, M. Yadav, R.K. Majhi, A. Kumar, and C. Goswami. 2015. Influence of membrane cholesterol in the molecular evolution and functional regulation of TRPV4. *Biochem Biophys Res Commun*. 456:312-319.

Kwon, Y., T. Hofmann, and C. Montell. 2007. Integration of phosphoinositide- and calmodulin-mediated regulation of TRPC6. *Mol Cell*. 25:491-503.

La Celle, P.L. 1969. Alteration of deformability of the erythrocyte membrane in stored blood. *Transfusion*. 9:238-245.

Lacroix, J.J., W.M. Botello-Smith, and Y. Luo. 2018. Probing the gating mechanism of the mechanosensitive channel Piezo1 with the small molecule Yoda1. *Nature communications*. 9:2029.

Lakk, M., O. Yarishkin, J.M. Baumann, A. Iuso, and D. Krizaj. 2017. Cholesterol regulates polymodal sensory transduction in Muller glia. *Glia*. 65:2038-2050.

Lam, V.Q., C. Antoniou, R. Rolius, and L.W. Fung. 2009. Association studies of erythroid alpha-spectrin at the tetramerization site. *Br J Haematol*. 147:392-395.

Lang, K.S., C. Duranton, H. Poehlmann, S. Myssina, C. Bauer, F. Lang, T. Wieder, and S.M. Huber. 2003. Cation channels trigger apoptotic death of erythrocytes. *Cell Death Differ*. 10:249-256.

Lange, C., J.H. Nett, B.L. Trumpower, and C. Hunte. 2001. Specific roles of protein-phospholipid interactions in the yeast cytochrome bc1 complex structure. *The EMBO journal*. 20:6591-6600.

Lange, Y. 1991. Disposition of intracellular cholesterol in human fibroblasts. *Journal of lipid research*. 32:329-339.

Langton, P.D. 1993. Calcium channel currents recorded from isolated myocytes of rat basilar artery are stretch sensitive. *J Physiol*. 471:1-11.

Laursen, T., A. Singha, N. Rantzau, M. Tutkus, J. Borch, P. Hedegard, D. Stamou, B.L. Moller, and N.S. Hatzakis. 2014. Single molecule activity measurements of cytochrome P450 oxidoreductase reveal the existence of two discrete functional states. *ACS Chem Biol*. 9:630-634.

Layton, M.R., D. 2017. Investigation of the Hereditary Haemolytic Anaemias. *Dacie and Lewis Practical Haematology (Twelfth Edition)*:228-253.

Leal, J.K.F., M.J.W. Adjobo-Hermans, and G. Bosman. 2018. Red Blood Cell Homeostasis: Mechanisms and Effects of Microvesicle Generation in Health and Disease. *Front Physiol*. 9:703.

Ledeen, R.W., and G. Wu. 2008. Nuclear sphingolipids: metabolism and signaling. *Journal of lipid research*. 49:1176-1186.

Lee, A.G. 2002. Ca2+ -ATPase structure in the E1 and E2 conformations: mechanism, helix-helix and helix-lipid interactions. *Biochimica et biophysica acta*. 1565:246-266.

Lee, A.G. 2003. Lipid-protein interactions in biological membranes: a structural perspective. *Biochimica et biophysica acta*. 1612:1-40.

Lee, A.G. 2004a. How lipids affect the activities of integral membrane proteins. *Biochimica et biophysica acta*. 1666:62-87.

Lee, A.G. 2004c. How lipids affect the activities of integral membrane proteins. *Biochimica et Biophysica Acta - Biomembranes*. 1666:62-87.

Lee, A.G. 2011. Lipid-protein interactions. *Biochemical Society transactions*. 39:761-766.

Lee, S., J.C. Kim, Y. Li, M.J. Son, and S.H. Woo. 2008. Fluid pressure modulates L-type Ca2+ channel via enhancement of Ca2+-induced Ca2+ release in rat ventricular myocytes. *Am J Physiol Cell Physiol*. 294:C966-976.

Leinders, T., R.G. van Kleef, and H.P. Vijverberg. 1992. Single Ca(2+)-activated K+ channels in human erythrocytes: Ca2+ dependence of opening frequency but not of open lifetimes. *Biochimica et biophysica acta*. 1112:67-74.

Léonard, C., D. Alsteens, A.C. Dumitru, M.-P. Mingeot-Leclercq, and D. Tyteca. 2017a. Lipid Domains and Membrane (Re)Shaping: From Biophysics to Biology. 19:121-175.

Léonard, C., D. Alsteens, A.C. Dumitru, M.P. Mingeot-Leclercq, and D. Tyteca. 2017d. Lipid Domains and Membrane (Re)Shaping: From Biophysics to Biology. *The biophysics of cell membranes*. 19:121-175.

Leonard, C., L. Conrard, M. Guthmann, H. Pollet, M. Carquin, C. Vermylen, P. Gailly, P. Van Der Smissen, M.P. Mingeot-Leclercq, and D. Tyteca. 2017.

Contribution of plasma membrane lipid domains to red blood cell (re)shaping. *Sci Rep*. 7:4264-4281.

Leonard, C., H. Pollet, C. Vermylen, N. Gov, D. Tyteca, and M.P. Mingeot-Leclercq. 2018. Tuning of Differential Lipid Order Between Submicrometric Domains and Surrounding Membrane Upon Erythrocyte Reshaping. *Cell Physiol Biochem*. 48:2563-2582.

Levi, V., J.P. Rossi, M.M. Echarte, P.R. Castello, and F.L. Gonzalez Flecha. 2000. Thermal stability of the plasma membrane calcium pump. Quantitative analysis of its dependence on lipid-protein interactions. *The Journal of membrane biology*. 173:215-225.

Levine, J.D., and N. Alessandri-Haber. 2007. TRP channels: targets for the relief of pain. *Biochimica et biophysica acta*. 1772:989-1003.

Lew, V.L., N. Daw, Z. Etzion, T. Tiffert, A. Muoma, L. Vanagas, and R.M. Bookchin. 2007. Effects of age-dependent membrane transport changes on the homeostasis of senescent human red blood cells. *Blood*. 110:1334-1342.

Lew, V.L., N. Daw, D. Perdomo, Z. Etzion, R.M. Bookchin, and T. Tiffert. 2003. Distribution of plasma membrane Ca2+ pump activity in normal human red blood cells. *Blood*. 102:4206-4213.

Lew, V.L., Z. Etzion, and R.M. Bookchin. 2002. Dehydration response of sickle cells to sickling-induced Ca(++) permeabilization. *Blood*. 99:2578-2585.

Lew, V.L., and T. Tiffert. 2017. On the Mechanism of Human Red Blood Cell Longevity: Roles of Calcium, the Sodium Pump, PIEZO1, and Gardos Channels. *Front Physiol*. 8:977.

Lewis, A.H., and J. Grandl. 2015. Mechanical sensitivity of Piezo1 ion channels can be tuned by cellular membrane tension. *Elife*. 4.

Lewis, B.A., and D.M. Engelman. 1983. Lipid bilayer thickness varies linearly with acyl chain length in fluid phosphatidylcholine vesicles. *J Mol Biol*. 166:211-217.

Li, H., L. Lu, X. Li, P.A. Buffet, M. Dao, G.E. Karniadakis, and S. Suresh. 2018. Mechanics of diseased red blood cells in human spleen and consequences for hereditary blood disorders. *Proceedings of the National Academy of Sciences of the United States of America*. 115:9574-9579.

Li, J., G. Lykotrafitis, M. Dao, and S. Suresh. 2007. Cytoskeletal dynamics of human erythrocyte. *Proceedings of the National Academy of Sciences of the United States of America*. 104:4937-4942.

Li, Y., M. Ge, L. Ciani, G. Kuriakose, E.J. Westover, M. Dura, D.F. Covey, J.H. Freed, F.R. Maxfield, J. Lytton, and I. Tabas. 2004. Enrichment of endoplasmic reticulum with cholesterol inhibits sarcoplasmic-endoplasmic reticulum calcium ATPase-2b activity in parallel with increased order of membrane lipids: implications for depletion of endoplasmic reticulum calcium stores

and apoptosis in cholesterol-loaded macrophages. *The Journal of biological chemistry*. 279:37030-37039.

Liang, B., and L.K. Tamm. 2016. NMR as a tool to investigate the structure, dynamics and function of membrane proteins. *Nat Struct Mol Biol*. 23:468-474.

Lim, H.W.G., M. Wortis, and R. Mukhopadhyay. 2002. Stomatocyte-discocyte-echinocyte sequence of the human red blood cell: evidence for the bilayer-couple hypothesis from membrane mechanics. *Proceedings of the National Academy of Sciences of the United States of America*. 99:16766-16769.

Lindahl, E., and M.S. Sansom. 2008. Membrane proteins: molecular dynamics simulations. *Curr Opin Struct Biol*. 18:425-431.

Lingwood, D., and K. Simons. 2010. Lipid rafts as a membrane-organizing principle. *Science*. 327:46-50.

Liou, J., M.L. Kim, W.D. Heo, J.T. Jones, J.W. Myers, J.E. Ferrell, Jr., and T. Meyer. 2005. STIM is a Ca2+ sensor essential for Ca2+-store-depletion-triggered Ca2+ influx. *Current biology : CB*. 15:1235-1241.

Lisanti, M.P., I.W. Caras, M.A. Davitz, and E. Rodriguez-Boulan. 1989. A glycophospholipid membrane anchor acts as an apical targeting signal in polarized epithelial cells. *The Journal of cell biology*. 109:2145-2156.

Liu, B., K. Hui, and F. Qin. 2003. Thermodynamics of heat activation of single capsaicin ion channels VR1. *Biophysical journal*. 85:2988-3006.

Liu, J., X. Guo, N. Mohandas, J.A. Chasis, and X. An. 2010. Membrane remodeling during reticulocyte maturation. *Blood*. 115:2021-2027.

Liu, L., C.F. Barrett, and A.R. Rittenhouse. 2001. Arachidonic acid both inhibits and enhances whole cell calcium currents in rat sympathetic neurons. *Am J Physiol Cell Physiol*. 280:C1293-1305.

Liu, M., W. Huang, D. Wu, and J.V. Priestley. 2006. TRPV1, but not P2X, requires cholesterol for its function and membrane expression in rat nociceptors. *Eur J Neurosci*. 24:1-6.

Liu, S.C., L.H. Derick, and J. Palek. 1987. Visualization of the hexagonal lattice in the erythrocyte membrane skeleton. *The Journal of cell biology*. 104:527-536.

Ljubojevic, S., and D.M. Bers. 2015. Nuclear calcium in cardiac myocytes. *J Cardiovasc Pharmacol*. 65:211-217.

Lopreiato, R., M. Giacomello, and E. Carafoli. 2014. The plasma membrane calcium pump: new ways to look at an old enzyme. *The Journal of biological chemistry*. 289:10261-10268.

Lucas, P., K. Ukhanov, T. Leinders-Zufall, and F. Zufall. 2003. A diacylglycerol-gated cation channel in vomeronasal neuron dendrites is impaired in TRPC2 mutant mice: mechanism of pheromone transduction. *Neuron*. 40:551-561.

Luecke, H., B. Schobert, H.T. Richter, J.P. Cartailler, and J.K. Lanyi. 1999. Structure of bacteriorhodopsin at 1.55 A resolution. *J Mol Biol*. 291:899-911.

Luo, D., D. Yang, X. Lan, K. Li, X. Li, J. Chen, Y. Zhang, R.P. Xiao, Q. Han, and H. Cheng. 2008. Nuclear Ca2+ sparks and waves mediated by inositol 1,4,5-trisphosphate receptors in neonatal rat cardiomyocytes. *Cell Calcium*. 43:165-174.

Lupu, V.D., E. Kaznacheyeva, U.M. Krishna, J.R. Falck, and I. Bezprozvanny. 1998. Functional coupling of phosphatidylinositol 4,5-bisphosphate to inositol 1,4,5-trisphosphate receptor. *The Journal of biological chemistry*. 273:14067-14070.

Lutz, H.U. 2004. Innate immune and non-immune mediators of erythrocyte clearance. *Cellular and molecular biology*. 50:107-116.

Lutz, H.U., and A. Bogdanova. 2013. Mechanisms tagging senescent red blood cells for clearance in healthy humans. *Front Physiol*. 4:387.

Lux, S.E.t. 2016. Anatomy of the red cell membrane skeleton: unanswered questions. *Blood*. 127:187-199.

Lyman, E., C.L. Hsieh, and C. Eggeling. 2018. From Dynamics to Membrane Organization: Experimental Breakthroughs Occasion a "Modeling Manifesto". *Biophysical journal*. 115:595-604.

Ma, G., M. Wei, L. He, C. Liu, B. Wu, S.L. Zhang, J. Jing, X. Liang, A. Senes, P. Tan, S. Li, A. Sun, Y. Bi, L. Zhong, H. Si, Y. Shen, M. Li, M.S. Lee, W. Zhou, J. Wang, Y. Wang, and Y. Zhou. 2015. Inside-out Ca(2+) signalling prompted by STIM1 conformational switch. *Nature communications*. 6:7826.

Maeda, R., T. Sato, K. Okamoto, M. Yanagawa, and Y. Sako. 2018. Lipid-Protein Interplay in Dimerization of Juxtamembrane Domains of Epidermal Growth Factor Receptor. *Biophysical journal*. 114:893-903.

Makhro, A., P. Hanggi, J.S. Goede, J. Wang, A. Bruggemann, M. Gassmann, M. Schmugge, L. Kaestner, O. Speer, and A. Bogdanova. 2013. N-methyl-D-aspartate receptors in human erythroid precursor cells and in circulating red blood cells contribute to the intracellular calcium regulation. *Am J Physiol Cell Physiol*. 305:C1123-1138.

Makhro, A., L. Kaestner, and A. Bogdanova. 2017. NMDA Receptor Activity in Circulating Red Blood Cells: Methods of Detection. *Methods in molecular biology*. 1677:265-282.

Malcuit, C., M. Kurokawa, and R.A. Fissore. 2006. Calcium oscillations and mammalian egg activation. *Journal of cellular physiology*. 206:565-573.

Mangialavori, I.C., G. Corradi, D.E. Rinaldi, M.C. de la Fuente, H.P. Adamo, and J.P. Rossi. 2012. Autoinhibition mechanism of the plasma membrane calcium pump isoforms 2 and 4 studied through lipid-protein interaction. *The Biochemical journal*. 443:125-131.

Manno, S., Y. Takakuwa, and N. Mohandas. 2005. Modulation of erythrocyte membrane mechanical function by protein 4.1 phosphorylation. *The Journal of biological chemistry*. 280:7581-7587.

Marchesi, S.L., J. Conboy, P. Agre, J.T. Letsinger, V.T. Marchesi, D.W. Speicher, and N. Mohandas. 1990. Molecular analysis of insertion/deletion mutations in protein 4.1 in elliptocytosis. I. Biochemical identification of rearrangements in the spectrin/actin binding domain and functional characterizations. *The Journal of clinical investigation*. 86:516-523.

Marius, P., M.R. de Planque, and P.T. Williamson. 2012. Probing the interaction of lipids with the non-annular binding sites of the potassium channel KcsA by magic-angle spinning NMR. *Biochimica et biophysica acta*. 1818:90-96.

Marrink, S.J., and D.P. Tieleman. 2013. Perspective on the Martini model. *Chem Soc Rev*. 42:6801-6822.

Marsh, D. 2008. Protein modulation of lipids, and vice-versa, in membranes. *Biochimica et biophysica acta*. 1778:1545-1575.

Marty, M.T., A. Das, and S.G. Sligar. 2012. Ultra-thin layer MALDI mass spectrometry of membrane proteins in nanodiscs. *Anal Bioanal Chem*. 402:721-729.

Marty, M.T., K.K. Hoi, J. Gault, and C.V. Robinson. 2016. Probing the Lipid Annular Belt by Gas-Phase Dissociation of Membrane Proteins in Nanodiscs. *Angew Chem Weinheim Bergstr Ger*. 128:560-564.

McMahon, H.T., and E. Boucrot. 2015. Membrane curvature at a glance. *Journal of cell science*. 128:1065-1070.

Mebius, R.E., and G. Kraal. 2005. Structure and function of the spleen. *Nat Rev Immunol*. 5:606-616.

Michaelis, M.L., D.J. Bigelow, C. Schoneich, T.D. Williams, L. Ramonda, D. Yin, A.F. Huhmer, Y. Yao, J. Gao, and T.C. Squier. 1996. Decreased plasma membrane calcium transport activity in aging brain. *Life Sci*. 59:405-412.

Mileykovskaya, E., and W. Dowhan. 2000. Visualization of phospholipid domains in Escherichia coli by using the cardiolipin-specific fluorescent dye 10-N-nonyl acridine orange. *J Bacteriol*. 182:1172-1175.

Miller, N.J., J. Sampson, L.P. Candeias, P.M. Bramley, and C.A. Rice-Evans. 1996. Antioxidant activities of carotenes and xanthophylls. *FEBS Lett*. 384:240-242.

Mills, J.P., L. Qie, M. Dao, C.T. Lim, and S. Suresh. 2004. Nonlinear elastic and viscoelastic deformation of the human red blood cell with optical tweezers. *Mech Chem Biosyst*. 1:169-180.

Mio, K., and C. Sato. 2018. Lipid environment of membrane proteins in cryo-EM based structural analysis. *Biophys Rev*. 10:307-316.

Mizuno, H., M. Abe, P. Dedecker, A. Makino, S. Rocha, Y. Ohno-Iwashita, J. Hofkens, T. Kobayashi, and A. Miyawaki. 2011. Fluorescent probes for superresolution imaging of lipid domains on the plasma membrane. *Chem Sci*. 2:1548-1553.

Moe, P., and P. Blount. 2005. Assessment of potential stimuli for mechano-dependent gating of MscL: effects of pressure, tension, and lipid headgroups. *Biochemistry*. 44:12239-12244.

Mohandas, N., M.R. Clark, M.S. Jacobs, W. Groner, and S.B. Shohet. 1980. Ektacytometric analysis of factors regulating red cell deformability. *Blood Cells*. 6:329-334.

Mohandas, N., and P.G. Gallagher. 2008. Red cell membrane: past, present, and future. *Blood*. 112:3939-3948.

Mohanty, J.G., E. Nagababu, and J.M. Rifkind. 2014. Red blood cell oxidative stress impairs oxygen delivery and induces red blood cell aging. *Front Physiol*. 5:84.

Monet, M., D. Gkika, V. Lehen'kyi, A. Pourtier, F. Vanden Abeele, G. Bidaux, V. Juvin, F. Rassendren, S. Humez, and N. Prevarsakaya. 2009. Lysophospholipids stimulate prostate cancer cell migration via TRPV2 channel activation. *Biochimica et biophysica acta*. 1793:528-539.

Monteith, G.R., D. McAndrew, H.M. Faddy, and S.J. Roberts-Thomson. 2007. Calcium and cancer: targeting Ca2+ transport. *Nat Rev Cancer*. 7:519-530.

Montel-Hagen, A., M. Sitbon, and N. Taylor. 2009. Erythroid glucose transporters. *Curr Opin Hematol*. 16:165-172.

Moras, M., S.D. Lefevre, and M.A. Ostuni. 2017. From Erythroblasts to Mature Red Blood Cells: Organelle Clearance in Mammals. *Front Physiol*. 8:1076.

Morenilla-Palao, C., M. Pertusa, V. Meseguer, H. Cabedo, and F. Viana. 2009. Lipid raft segregation modulates TRPM8 channel activity. *The Journal of biological chemistry*. 284:9215-9224.

Moroni, M., M.R. Servin-Vences, R. Fleischer, O. Sanchez-Carranza, and G.R. Lewin. 2018. Voltage gating of mechanosensitive PIEZO channels. *Nature communications*. 9:1096.

Morris, C.E., P.F. Juranka, and B. Joos. 2012. Perturbed voltage-gated channel activity in perturbed bilayers: implications for ectopic arrhythmias arising from damaged membrane. *Prog Biophys Mol Biol*. 110:245-256.

Morrot, G., S. Cribier, P.F. Devaux, D. Geldwerth, J. Davoust, J.F. Bureau, P. Fellmann, P. Herve, and B. Frilley. 1986. Asymmetric lateral mobility of phospholipids in the human erythrocyte membrane. *Proc Natl Acad Sci U S A*. 83:6863-6867.

Mortensen, A.M., and R.F. Novak. 1992. Dynamic changes in the distribution of the calcium-activated neutral protease in human red blood cells following cellular insult and altered Ca2+ homeostasis. *Toxicol Appl Pharmacol*. 117:180-188.

Muallem, S., W.Y. Chung, A. Jha, and M. Ahuja. 2017. Lipids at membrane contact sites: cell signaling and ion transport. *EMBO reports*. 18:1893-1904.

Muik, M., I. Frischauf, I. Derler, M. Fahrner, J. Bergsmann, P. Eder, R. Schindl, C. Hesch, B. Polzinger, R. Fritsch, H. Kahr, J. Madl, H. Gruber, K. Groschner, and C. Romanin. 2008. Dynamic coupling of the putative coiled-coil domain of ORAI1 with STIM1 mediates ORAI1 channel activation. *The Journal of biological chemistry*. 283:8014-8022.

Muller, M.P., T. Jiang, C. Sun, M. Lihan, S. Pant, P. Mahinthichaichan, A. Trifan, and E. Tajkhorshid. 2019. Characterization of Lipid-Protein Interactions and Lipid-Mediated Modulation of Membrane Protein Function through Molecular Simulation. *Chem Rev*. 119:6086-6161.

Munro, S. 2003. Lipid rafts: elusive or illusive? *Cell*. 115:377-388.

Murate, M., and T. Kobayashi. 2016. Revisiting transbilayer distribution of lipids in the plasma membrane. *Chemistry and physics of lipids*. 194:58-71.

Murthy, S.E., A.E. Dubin, and A. Patapoutian. 2017. Piezos thrive under pressure: mechanically activated ion channels in health and disease. *Nature reviews. Molecular cell biology*. 18:771-783.

Nandakumar, S.K., J.C. Ulirsch, and V.G. Sankaran. 2016. Advances in understanding erythropoiesis: evolving perspectives. *Br J Haematol*. 173:206-218.

Naylor, J., J. Li, C.J. Milligan, F. Zeng, P. Sukumar, B. Hou, A. Sedo, N. Yuldasheva, Y. Majeed, D. Beri, S. Jiang, V.A. Seymour, L. McKeown, B. Kumar, C. Harteneck, D. O'Regan, S.B. Wheatcroft, M.T. Kearney, C. Jones, K.E. Porter, and D.J. Beech. 2010. Pregnenolone sulphate- and cholesterol-regulated TRPM3 channels coupled to vascular smooth muscle secretion and contraction. *Circ Res*. 106:1507-1515.

Neu, T.R., and J.R. Lawrence. 2015. Innovative techniques, sensors, and approaches for imaging biofilms at different scales. *Trends Microbiol*. 23:233-242.

Niemela, P.S., M.S. Miettinen, L. Monticelli, H. Hammaren, P. Bjelkmar, T. Murtola, E. Lindahl, and I. Vattulainen. 2010. Membrane proteins diffuse as dynamic complexes with lipids. *J Am Chem Soc*. 132:7574-7575.

Nieto-Posadas, A., G. Picazo-Juarez, I. Llorente, A. Jara-Oseguera, S. Morales-Lazaro, D. Escalante-Alcalde, L.D. Islas, and T. Rosenbaum. 2011. Lysophosphatidic acid directly activates TRPV1 through a C-terminal binding site. *Nature chemical biology*. 8:78-85.

Niggli, V., E.S. Adunyah, J.T. Penniston, and E. Carafoli. 1981. Purified (Ca2+-Mg2+)-ATPase of the erythrocyte membrane. Reconstitution and effect of calmodulin and phospholipids. *The Journal of biological chemistry*. 256:395-401.

Nikolaev, M., E. Round, I. Gushchin, V. Polovinkin, T. Balandin, P. Kuzmichev, V. Shevchenko, V. Borshchevskiy, A. Kuklin, A. Round, F. Bernhard, D. Willbold, G. Büldt, and V. Gordeliy. 2017. Integral Membrane Proteins Can Be Crystallized Directly from Nanodiscs. *Crystal Growth & Design*. 17:945-948.

Nilius, B. 2007. TRP channels in disease. *Biochimica et biophysica acta*. 1772:805-812.

Nomura, T., C.G. Cranfield, E. Deplazes, D.M. Owen, A. Macmillan, A.R. Battle, M. Constantine, M. Sokabe, and B. Martinac. 2012. Differential effects of lipids and lyso-lipids on the mechanosensitivity of the mechanosensitive channels MscL and MscS. *Proceedings of the National Academy of Sciences of the United States of America*. 109:8770-8775.

Norimatsu, Y., K. Hasegawa, N. Shimizu, and C. Toyoshima. 2017. Protein-phospholipid interplay revealed with crystals of a calcium pump. *Nature*. 545:193-198.

Nunomura, W., and Y. Takakuwa. 2006. Regulation of protein 4.1R interactions with membrane proteins by Ca2+ and calmodulin. *Front Biosci*. 11:1522-1539.

Otsuguro, K., J. Tang, Y. Tang, R. Xiao, M. Freichel, V. Tsvilovskyy, S. Ito, V. Flockerzi, M.X. Zhu, and A.V. Zholos. 2008. Isoform-specific inhibition of TRPC4 channel by phosphatidylinositol 4,5-bisphosphate. *The Journal of biological chemistry*. 283:10026-10036.

Ovchynnikova, E., F. Aglialoro, M. von Lindern, and E. van den Akker. 2018. The Shape Shifting Story of Reticulocyte Maturation. *Front Physiol*. 9:829.

Pacheco, J., L. Dominguez, A. Bohorquez-Hernandez, A. Asanov, and L. Vaca. 2016. A cholesterol-binding domain in STIM1 modulates STIM1-Orai1 physical and functional interactions. *Sci Rep*. 6:29634.

Paila, Y.D., S. Tiwari, and A. Chattopadhyay. 2009. Are specific nonannular cholesterol binding sites present in G-protein coupled receptors? *Biochimica et biophysica acta*. 1788:295-302.

Palis, J. 2014. Primitive and definitive erythropoiesis in mammals. *Front Physiol*. 5:3.

Palis, J., and G.B. Segel. 1998. Developmental biology of erythropoiesis. *Blood Rev*. 12:106-114.

Pan, B.T., and R.M. Johnstone. 1983. Fate of the transferrin receptor during maturation of sheep reticulocytes in vitro: selective externalization of the receptor. *Cell*. 33:967-978.

Pantaleo, A., E. Ferru, G. Giribaldi, F. Mannu, F. Carta, A. Matte, L. de Franceschi, and F. Turrini. 2009. Oxidized and poorly glycosylated band 3 is selectively phosphorylated by Syk kinase to form large membrane clusters in normal and G6PD-deficient red blood cells. *Biochem J*. 418:359-367.

Park, C.G., Y. Park, and B.C. Suh. 2017. The HOOK region of voltage-gated Ca2+ channel beta subunits senses and transmits PIP2 signals to the gate. *J Gen Physiol*. 149:261-276.

Parpaite, T., and B. Coste. 2017. Piezo channels. *Current biology : CB*. 27:R250-R252.

Parton, R.G., and M.A. del Pozo. 2013. Caveolae as plasma membrane sensors, protectors and organizers. *Nature reviews. Molecular cell biology*. 14:98-112.

Paszty, K., G. Antalffy, L. Hegedus, R. Padanyi, A.R. Penheiter, A.G. Filoteo, J.T. Penniston, and A. Enyedi. 2007. Cleavage of the plasma membrane Ca+ATPase during apoptosis. *Annals of the New York Academy of Sciences*. 1099:440-450.

Patel, A., R. Sharif-Naeini, J.R. Folgering, D. Bichet, F. Duprat, and E. Honore. 2010. Canonical TRP channels and mechanotransduction: from physiology to disease states. *Pflugers Arch*. 460:571-581.

Pauling, L., and C.D. Coryell. 1936. The Magnetic Properties and Structure of Hemoglobin, Oxyhemoglobin and Carbonmonoxyhemoglobin. *Proc Natl Acad Sci U S A*. 22:210-216.

Pedersen, S.F., G. Owsianik, and B. Nilius. 2005. TRP channels: an overview. *Cell Calcium*. 38:233-252.

Perez-Gordones, M.C., M.R. Lugo, M. Winkler, V. Cervino, and G. Benaim. 2009. Diacylglycerol regulates the plasma membrane calcium pump from human erythrocytes by direct interaction. *Arch Biochem Biophys*. 489:55-61.

Periasamy, M., and A. Kalyanasundaram. 2007. SERCA pump isoforms: their role in calcium transport and disease. *Muscle Nerve*. 35:430-442.

Perozo, E., A. Kloda, D.M. Cortes, and B. Martinac. 2002. Physical principles underlying the transduction of bilayer deformation forces during mechanosensitive channel gating. *Nat Struct Biol*. 9:696-703.

Perrotta, S., P.G. Gallagher, and N. Mohandas. 2008. Hereditary spherocytosis. *Lancet*. 372:1411-1426.

Peters, L.L., R.A. Shivdasani, S.C. Liu, M. Hanspal, K.M. John, J.M. Gonzalez, C. Brugnara, B. Gwynn, N. Mohandas, S.L. Alper, S.H. Orkin, and S.E. Lux. 1996. Anion exchanger 1 (band 3) is required to prevent erythrocyte membrane surface loss but not to form the membrane skeleton. *Cell*. 86:917-927.

Petersen, O.H. 2015. Ca(2)(+) signalling in the endoplasmic reticulum/secretory granule microdomain. *Cell Calcium*. 58:397-404.

Petersen, O.H., and A.V. Tepikin. 2008. Polarized calcium signaling in exocrine gland cells. *Annu Rev Physiol*. 70:273-299.

Petho, Z., K. Najder, E. Bulk, and A. Schwab. 2019. Mechanosensitive ion channels push cancer progression. *Cell Calcium*. 80:79-90.

Phillips, M.J., and G.K. Voeltz. 2016. Structure and function of ER membrane contact sites with other organelles. *Nature reviews. Molecular cell biology*. 17:69-82.

Phillips, R., T. Ursell, P. Wiggins, and P. Sens. 2009. Emerging roles for lipids in shaping membrane-protein function. *Nature*. 459:379-385.

Picazo-Juarez, G., S. Romero-Suarez, A. Nieto-Posadas, I. Llorente, A. Jara-Oseguera, M. Briggs, T.J. McIntosh, S.A. Simon, E. Ladron-de-Guevara, L.D. Islas, and T. Rosenbaum. 2011. Identification of a binding motif in the S5

helix that confers cholesterol sensitivity to the TRPV1 ion channel. *The Journal of biological chemistry*. 286:24966-24976.

Pittman, R.N. 2011. Regulation of Tissue Oxygenation. *Morgan & Claypool Life Sciences*. Chapter 4, Oxygen Transport.

Pivkin, I.V., Z. Peng, G.E. Karniadakis, P.A. Buffet, M. Dao, and S. Suresh. 2016. Biomechanics of red blood cells in human spleen and consequences for physiology and disease. *Proceedings of the National Academy of Sciences of the United States of America*. 113:7804-7809.

Plasencia, I., L. Norlen, and L.A. Bagatolli. 2007. Direct visualization of lipid domains in human skin stratum corneum's lipid membranes: effect of pH and temperature. *Biophysical journal*. 93:3142-3155.

Pliotas, C., A.C. Dahl, T. Rasmussen, K.R. Mahendran, T.K. Smith, P. Marius, J. Gault, T. Banda, A. Rasmussen, S. Miller, C.V. Robinson, H. Bayley, M.S. Sansom, I.R. Booth, and J.H. Naismith. 2015. The role of lipids in mechanosensation. *Nat Struct Mol Biol*. 22:991-998.

Pollard, T.D., J. Lippincott-Schwartz, W.S. Earnshaw, and G.T. Johnson. 2017. Chapter 13-Membrane structure and dynamics. *In* Cell biology. Elsevier.

Powl, A.M., J. Carney, P. Marius, J.M. East, and A.G. Lee. 2005. Lipid interactions with bacterial channels: fluorescence studies. *Biochemical Society transactions*. 33:905-909.

Powl, A.M., J.M. East, and A.G. Lee. 2008. Anionic phospholipids affect the rate and extent of flux through the mechanosensitive channel of large conductance MscL. *Biochemistry*. 47:4317-4328.

Prakriya, M., S. Feske, Y. Gwack, S. Srikanth, A. Rao, and P.G. Hogan. 2006. Orai1 is an essential pore subunit of the CRAC channel. *Nature*. 443:230-233.

Puchulu-Campanella, E., H. Chu, D.J. Anstee, J.A. Galan, W.A. Tao, and P.S. Low. 2013. Identification of the components of a glycolytic enzyme metabolon on the human red blood cell membrane. *The Journal of biological chemistry*. 288:848-858.

Purves, D., G.J. Augustine, D. Fitzpatrick, L.C. Katz, A. LaMantia, J.O. McNamara, and S.M. Williams. 2001. Neuroscience (2nd ed.). Sinauer Associates.

Qi, Y., L. Andolfi, F. Frattini, F. Mayer, M. Lazzarino, and J. Hu. 2015. Membrane stiffening by STOML3 facilitates mechanosensation in sensory neurons. *Nature communications*. 6:8512-8525.

Ramaiah, L., D.I. Bounous, and S.A. Elmore. 2018. Hematopoietic System. *Fundamental of toxicologic pathology (3rd edition)*:315-349.

Ramos-Franco, J., D. Galvan, G.A. Mignery, and M. Fill. 1999. Location of the permeation pathway in the recombinant type 1 inositol 1,4,5-trisphosphate receptor. *J Gen Physiol*. 114:243-250.

Rao, S., S. Balint, B. Cossins, V. Guallar, and D. Petrov. 2009. Raman study of mechanically induced oxygenation state transition of red blood cells using optical tweezers. *Biophysical journal*. 96:209-216.

Rapetti-Mauss, R., C. Lacoste, V. Picard, C. Guitton, E. Lombard, M. Loosveld, V. Nivaggioni, N. Dasilva, D. Salgado, J.P. Desvignes, C. Beroud, P. Viout, M. Bernard, O. Soriani, H. Vinti, V. Lacroze, M. Feneant-Thibault, I. Thuret, H. Guizouarn, and C. Badens. 2015. A mutation in the Gardos channel is associated with hereditary xerocytosis. *Blood*. 126:1273-1280.

Rapoport, T.A. 2007. Protein translocation across the eukaryotic endoplasmic reticulum and bacterial plasma membranes. *Nature*. 450:663-669.

Reece, J.B., L.A. Urry, M.L. Cain, S.A. Wasserman, P.V. Minorsky, and R.B. Jackson. 2011. Campbell Biology. Pearson Education.

Reeves, J.P., and M. Condrescu. 2008. Ionic regulation of the cardiac sodium-calcium exchanger. *Channels (Austin)*. 2:322-328.

Reid, H.L., A.J. Barnes, P.J. Lock, J.A. Dormandy, and T.L. Dormandy. 1976. A simple method for measuring erythrocyte deformability. *J Clin Pathol*. 29:855-858.

Reliene, R., M. Mariani, A. Zanella, W.H. Reinhart, M.L. Ribeiro, E.M. del Giudice, S. Perrotta, A. Iolascon, S. Eber, and H.U. Lutz. 2002. Splenectomy prolongs in vivo survival of erythrocytes differently in spectrin/ankyrin- and band 3-deficient hereditary spherocytosis. *Blood*. 100:2208-2215.

Ridder, A.N., S. Morein, J.G. Stam, A. Kuhn, B. de Kruijff, and J.A. Killian. 2000. Analysis of the role of interfacial tryptophan residues in controlling the topology of membrane proteins. *Biochemistry*. 39:6521-6528.

Rifkind, J.M., and E. Nagababu. 2013. Hemoglobin redox reactions and red blood cell aging. *Antioxid Redox Signal*. 18:2274-2283.

Rimessi, A., L. Coletto, P. Pinton, R. Rizzuto, M. Brini, and E. Carafoli. 2005. Inhibitory interaction of the 14-3-3 protein with isoform 4 of the plasma membrane Ca(2+)-ATPase pump. *The Journal of biological chemistry*. 280:37195-37203.

Rivella, S. 2012. The role of ineffective erythropoiesis in non-transfusion-dependent thalassemia. *Blood Rev*. 26 Suppl 1:S12-15.

Robison, P., M.A. Caporizzo, H. Ahmadzadeh, A.I. Bogush, C.Y. Chen, K.B. Margulies, V.B. Shenoy, and B.L. Prosser. 2016. Detyrosinated microtubules buckle and bear load in contracting cardiomyocytes. *Science*. 352:aaf0659.

Rodriguez-Menchaca, A.A., S.K. Adney, L. Zhou, and D.E. Logothetis. 2012. Dual Regulation of Voltage-Sensitive Ion Channels by PIP(2). *Front Pharmacol*. 3:170.

Rohacs, T. 2013. Regulation of transient receptor potential channels by the phospholipase C pathway. *Adv Biol Regul*. 53:341-355.

Rohacs, T. 2014. Phosphoinositide regulation of TRP channels. *Handb Exp Pharmacol*. 223:1143-1176.

Romero, L.O., A.E. Massey, A.D. Mata-Daboin, F.J. Sierra-Valdez, S.C. Chauhan, J.F. Cordero-Morales, and V. Vasquez. 2019. Dietary fatty acids fine-tune Piezo1 mechanical response. *Nature communications*. 10:1200.

Runnels, L.W., L. Yue, and D.E. Clapham. 2002. The TRPM7 channel is inactivated by PIP(2) hydrolysis. *Nature cell biology*. 4:329-336.

Sadler, E.E., A.N. Kapanidis, and S.J. Tucker. 2016. Solution-Based Single-Molecule FRET Studies of K(+) Channel Gating in a Lipid Bilayer. *Biophysical journal*. 110:2663-2670.

Safeukui, I., P.A. Buffet, G. Deplaine, S. Perrot, V. Brousse, A. Ndour, M. Nguyen, O. Mercereau-Puijalon, P.H. David, G. Milon, and N. Mohandas. 2012. Quantitative assessment of sensing and sequestration of spherocytic erythrocytes by the human spleen. *Blood*. 120:424-430.

Saghy, E., E. Szoke, M. Payrits, Z. Helyes, R. Borzsei, J. Erostyak, T.Z. Janosi, G. Setalo, Jr., and J. Szolcsanyi. 2015. Evidence for the role of lipid rafts and sphingomyelin in Ca2+-gating of Transient Receptor Potential channels in trigeminal sensory neurons and peripheral nerve terminals. *Pharmacol Res*. 100:101-116.

Saheki, Y., and P. De Camilli. 2017. Endoplasmic Reticulum-Plasma Membrane Contact Sites. *Annu Rev Biochem*. 86:659-684.

Salomao, M., K. Chen, J. Villalobos, N. Mohandas, X. An, and J.A. Chasis. 2010. Hereditary spherocytosis and hereditary elliptocytosis: aberrant protein sorting during erythroblast enucleation. *Blood*. 116:267-269.

Salomao, M., X. Zhang, Y. Yang, S. Lee, J.H. Hartwig, J.A. Chasis, N. Mohandas, and X. An. 2008. Protein 4.1R-dependent multiprotein complex: new insights into the structural organization of the red blood cell membrane. *Proceedings of the National Academy of Sciences of the United States of America*. 105:8026-8031.

Salzer, U., and R. Prohaska. 2001. Stomatin, flotillin-1, and flotillin-2 are major integral proteins of erythrocyte lipid rafts. *Blood*. 97:1141-1143.

Sameni, S., L. Malacrida, Z. Tan, and M.A. Digman. 2018. Alteration in Fluidity of Cell Plasma Membrane in Huntington Disease Revealed by Spectral Phasor Analysis. *Sci Rep*. 8:734.

Sanchez, S.A., M.A. Tricerri, and E. Gratton. 2012. Laurdan generalized polarization fluctuations measures membrane packing micro-heterogeneity in vivo. *Proceedings of the National Academy of Sciences of the United States of America*. 109:7314-7319.

Sanderson, M.J., P. Delmotte, Y. Bai, and J.F. Perez-Zogbhi. 2008. Regulation of airway smooth muscle cell contractility by Ca2+ signaling and sensitivity. *Proc Am Thorac Soc*. 5:23-31.

Saotome, K., S.E. Murthy, J.M. Kefauver, T. Whitwam, A. Patapoutian, and A.B. Ward. 2017. Structure of the mechanically activated ion channel Piezo1. *Nature*. 554:481-486.

Saotome, K., S.E. Murthy, J.M. Kefauver, T. Whitwam, A. Patapoutian, and A.B. Ward. 2018. Structure of the mechanically activated ion channel Piezo1. *Nature*. 554:481-486.

Sawada, K., S.B. Krantz, C.H. Dai, S.T. Koury, S.T. Horn, A.D. Glick, and C.I. Civin. 1990. Purification of human blood burst-forming units-erythroid and demonstration of the evolution of erythropoietin receptors. *Journal of cellular physiology*. 142:219-230.

Schmidt, M.R., P.J. Stansfeld, S.J. Tucker, and M.S. Sansom. 2013. Simulation-based prediction of phosphatidylinositol 4,5-bisphosphate binding to an ion channel. *Biochemistry*. 52:279-281.

Schroeder, F., G. Nemecz, W.G. Wood, C. Joiner, G. Morrot, M. Ayraut-Jarrier, and P.F. Devaux. 1991. Transmembrane distribution of sterol in the human erythrocyte. *Biochimica et biophysica acta*. 1066:183-192.

Schuh, K., E.J. Cartwright, E. Jankevics, K. Bundschu, J. Liebermann, J.C. Williams, A.L. Armesilla, M. Emerson, D. Oceandy, K.P. Knobeloch, and L. Neyses. 2004. Plasma membrane Ca2+ ATPase 4 is required for sperm motility and male fertility. *The Journal of biological chemistry*. 279:28220-28226.

Schuh, K., S. Uldrijan, M. Telkamp, N. Rothlein, and L. Neyses. 2001. The plasmamembrane calmodulin-dependent calcium pump: a major regulator of nitric oxide synthase I. *The Journal of cell biology*. 155:201-205.

Schuler, M.A., I.G. Denisov, and S.G. Sligar. 2013. Nanodiscs as a new tool to examine lipid-protein interactions. *Methods in molecular biology*. 974:415-433.

Schurmann, S., S. Wagner, S. Herlitze, C. Fischer, S. Gumbrecht, A. Wirth-Hucking, G. Prolss, L.A. Lautscham, B. Fabry, W.H. Goldmann, V. Nikolova-Krstevski, B. Martinac, and O. Friedrich. 2016. The IsoStretcher: An isotropic cell stretch device to study mechanical biosensor pathways in living cells. *Biosens Bioelectron*. 81:363-372.

Scott, K.A., P.J. Bond, A. Ivetac, A.P. Chetwynd, S. Khalid, and M.S. Sansom. 2008. Coarse-grained MD simulations of membrane protein-bilayer self-assembly. *Structure*. 16:621-630.

Seigneuret, M., A. Zachowski, A. Hermann, and P.F. Devaux. 1984. Asymmetric lipid fluidity in human erythrocyte membrane: new spin-label evidence. *Biochemistry*. 23:4271-4275.

Sen, L., R.A. Bialecki, E. Smith, T.W. Smith, and W.S. Colucci. 1992. Cholesterol increases the L-type voltage-sensitive calcium channel current in arterial smooth muscle cells. *Circ Res*. 71:1008-1014.

Setty, B.N., S. Kulkarni, and M.J. Stuart. 2002. Role of erythrocyte phosphatidylserine in sickle red cell-endothelial adhesion. *Blood*. 99:1564-1571.

Sezgin, E., T. Gutmann, T. Buhl, R. Dirkx, M. Grzybek, U. Coskun, M. Solimena, K. Simons, I. Levental, and P. Schwille. 2015. Adaptive lipid packing and bioactivity in membrane domains. *PloS one*. 10:e0123930.

Sezgin, E., I. Levental, S. Mayor, and C. Eggeling. 2017. The mystery of membrane organization: composition, regulation and roles of lipid rafts. *Nature reviews. Molecular cell biology*. 18:361-374.

Sheetz, M.P., J.E. Sable, and H.G. Dobereiner. 2006. Continuous membrane-cytoskeleton adhesion requires continuous accommodation to lipid and cytoskeleton dynamics. *Annu Rev Biophys Biomol Struct*. 35:417-434.

Sheetz, M.P., and S.J. Singer. 1974. Biological membranes as bilayer couples. A molecular mechanism of drug-erythrocyte interactions. *Proc Natl Acad Sci U S A*. 71:4457-4461.

Shelby, J.P., J. White, K. Ganesan, P.K. Rathod, and D.T. Chiu. 2003. A microfluidic model for single-cell capillary obstruction by Plasmodium falciparum-infected erythrocytes. *Proceedings of the National Academy of Sciences of the United States of America*. 100:14618-14622.

Shemin, D., and D. Rittenberg. 1946. The life span of the human red blood cell. *The Journal of biological chemistry*. 166:627-636.

Shi, X., Y. Bi, W. Yang, X. Guo, Y. Jiang, C. Wan, L. Li, Y. Bai, J. Guo, Y. Wang, X. Chen, B. Wu, H. Sun, W. Liu, J. Wang, and C. Xu. 2013. Ca2+ regulates T-cell receptor activation by modulating the charge property of lipids. *Nature*. 493:111-115.

Shimada, Y., M. Maruya, S. Iwashita, and Y. Ohno-Iwashita. 2002. The C-terminal domain of perfringolysin O is an essential cholesterol-binding unit targeting to cholesterol-rich microdomains. *European journal of biochemistry / FEBS*. 269:6195-6203.

Shin, D.M., X. Luo, T.M. Wilkie, L.J. Miller, A.B. Peck, M.G. Humphreys-Beher, and S. Muallem. 2001. Polarized expression of G protein-coupled receptors and an all-or-none discharge of Ca2+ pools at initiation sites of [Ca2+]i waves in polarized exocrine cells. *The Journal of biological chemistry*. 276:44146-44156.

Shogomori, H., and T. Kobayashi. 2008. Lysenin: a sphingomyelin specific pore-forming toxin. *Biochimica et biophysica acta*. 1780:612-618.

Simons, K., and E. Ikonen. 1997. Functional rafts in cell membranes. *Nature*. 387:569-572.

Simons, K., and W.L. Vaz. 2004. Model systems, lipid rafts, and cell membranes. *Annu Rev Biophys Biomol Struct*. 33:269-295.

Slotte, J.P. 2013. Biological functions of sphingomyelins. *Progress in lipid research*. 52:424-437.

Smani, T., S.I. Zakharov, P. Csutora, E. Leno, E.S. Trepakova, and V.M. Bolotina. 2004. A novel mechanism for the store-operated calcium influx pathway. *Nature cell biology*. 6:113-120.

Smyth, J.T., W.I. Dehaven, G.S. Bird, and J.W. Putney, Jr. 2008. Ca2+-store-dependent and -independent reversal of Stim1 localization and function. *Journal of cell science*. 121:762-772.

Socolovsky, M. 2007. Molecular insights into stress erythropoiesis. *Curr Opin Hematol*. 14:215-224.

Sonntag, Y., M. Musgaard, C. Olesen, B. Schiott, J.V. Moller, P. Nissen, and L. Thogersen. 2011. Mutual adaptation of a membrane protein and its lipid bilayer during conformational changes. *Nature communications*. 2:304.

Sonoda, Y., S. Newstead, N.J. Hu, Y. Alguel, E. Nji, K. Beis, S. Yashiro, C. Lee, J. Leung, A.D. Cameron, B. Byrne, S. Iwata, and D. Drew. 2011. Benchmarking membrane protein detergent stability for improving throughput of high-resolution X-ray structures. *Structure*. 19:17-25.

Sonveaux, P., Lobysheva, II, O. Feron, and T.J. McMahon. 2007. Transport and peripheral bioactivities of nitrogen oxides carried by red blood cell hemoglobin: role in oxygen delivery. *Physiology (Bethesda)*. 22:97-112.

Stansfeld, P.J., and M.S. Sansom. 2011. From Coarse Grained to Atomistic: A Serial Multiscale Approach to Membrane Protein Simulations. *J Chem Theory Comput*. 7:1157-1166.

Starling, A.P., J.M. East, and A.G. Lee. 1995. Effects of phospholipid fatty acyl chain length on phosphorylation and dephosphorylation of the Ca(2+)-ATPase. *The Biochemical journal*. 310 (Pt 3):875-879.

Startek, J.B., B. Boonen, K. Talavera, and V. Meseguer. 2019. TRP Channels as Sensors of Chemically-Induced Changes in Cell Membrane Mechanical Properties. *Int J Mol Sci*. 20.

Steck, T.L., and Y. Lange. 2018. Transverse distribution of plasma membrane bilayer cholesterol: Picking sides. *Traffic*. 19:750-760.

Steck, T.L., J. Ye, and Y. Lange. 2002. Probing red cell membrane cholesterol movement with cyclodextrin. *Biophysical journal*. 83:2118-2125.

Stokes, N.R., H.D. Murray, C. Subramaniam, R.L. Gourse, P. Louis, W. Bartlett, S. Miller, and I.R. Booth. 2003. A role for mechanosensitive channels in survival of stationary phase: regulation of channel expression by RpoS. *Proceedings of the National Academy of Sciences of the United States of America*. 100:15959-15964.

Stone, M.B., S.A. Shelby, and S.L. Veatch. 2017. Super-Resolution Microscopy: Shedding Light on the Cellular Plasma Membrane. *Chem Rev*. 117:7457-7477.

Strehler, E.E., P. James, R. Fischer, R. Heim, T. Vorherr, A.G. Filoteo, J.T. Penniston, and E. Carafoli. 1990. Peptide sequence analysis and molecular cloning reveal two calcium pump isoforms in the human erythrocyte membrane. *The Journal of biological chemistry*. 265:2835-2842.

Suh, B.C., and B. Hille. 2008. PIP2 is a necessary cofactor for ion channel function: how and why? *Annual review of biophysics*. 37:175-195.

Suh, B.C., K. Leal, and B. Hille. 2010. Modulation of high-voltage activated Ca(2+) channels by membrane phosphatidylinositol 4,5-bisphosphate. *Neuron*. 67:224-238.

Sukharev, S. 1999. Mechanosensitive channels in bacteria as membrane tension reporters. *FASEB journal : official publication of the Federation of American Societies for Experimental Biology*. 13 Suppl:S55-61.

Sukharev, S. 2002. Purification of the small mechanosensitive channel of Escherichia coli (MscS): the subunit structure, conduction, and gating characteristics in liposomes. *Biophysical journal*. 83:290-298.

Sutko, J.L., J.A. Airey, W. Welch, and L. Ruest. 1997. The pharmacology of ryanodine and related compounds. *Pharmacol Rev*. 49:53-98.

Syeda, R., M.N. Florendo, C.D. Cox, J.M. Kefauver, J.S. Santos, B. Martinac, and A. Patapoutian. 2016. Piezo1 Channels Are Inherently Mechanosensitive. *Cell Rep*. 17:1739-1746.

Szallasi, A., and M. Sheta. 2012. Targeting TRPV1 for pain relief: limits, losers and laurels. *Expert Opin Investig Drugs*. 21:1351-1369.

Szoke, E., R. Borzsei, D.M. Toth, O. Lengl, Z. Helyes, Z. Sandor, and J. Szolcsanyi. 2010. Effect of lipid raft disruption on TRPV1 receptor activation of trigeminal sensory neurons and transfected cell line. *Eur J Pharmacol*. 628:67-74.

Taberner, F.J., G. Fernandez-Ballester, A. Fernandez-Carvajal, and A. Ferrer-Montiel. 2015. TRP channels interaction with lipids and its implications in disease. *Biochimica et biophysica acta*. 1848:1818-1827.

Takahashi, K., Y. Kakimoto, K. Toda, and K. Naruse. 2013. Mechanobiology in cardiac physiology and diseases. *Journal of cellular and molecular medicine*. 17:225-232.

Tang, D., W.L. Dean, D. Borchman, and C.A. Paterson. 2006. The influence of membrane lipid structure on plasma membrane Ca2+ -ATPase activity. *Cell Calcium*. 39:209-216.

Taverna, E., E. Saba, J. Rowe, M. Francolini, F. Clementi, and P. Rosa. 2004. Role of lipid microdomains in P/Q-type calcium channel (Cav2.1) clustering and function in presynaptic membranes. *The Journal of biological chemistry*. 279:5127-5134.

Tesoriere, L., D. D'Arpa, D. Butera, M. Allegra, D. Renda, A. Maggio, A. Bongiorno, and M.A. Livrea. 2001. Oral supplements of vitamin E improve measures of

oxidative stress in plasma and reduce oxidative damage to LDL and erythrocytes in beta-thalassemia intermedia patients. *Free Radic Res*. 34:529-540.

Thomas, D., S.C. Tovey, T.J. Collins, M.D. Bootman, M.J. Berridge, and P. Lipp. 2000. A comparison of fluorescent Ca2+ indicator properties and their use in measuring elementary and global Ca2+ signals. *Cell Calcium*. 28:213-223.

Timmann, C., T. Thye, M. Vens, J. Evans, J. May, C. Ehmen, J. Sievertsen, B. Muntau, G. Ruge, W. Loag, D. Ansong, S. Antwi, E. Asafo-Adjei, S.B. Nguah, K.O. Kwakye, A.O. Akoto, J. Sylverken, M. Brendel, K. Schuldt, C. Loley, A. Franke, C.G. Meyer, T. Agbenyega, A. Ziegler, and R.D. Horstmann. 2012. Genome-wide association study indicates two novel resistance loci for severe malaria. *Nature*. 489:443-446.

Tornquist, K., T. Blom, R. Shariatmadari, and M. Pasternack. 2004. Ceramide 1-phosphate enhances calcium entry through voltage-operated calcium channels by a protein kinase C-dependent mechanism in GH4C1 rat pituitary cells. *The Biochemical journal*. 380:661-668.

Travlos, G.S. 2006. Normal structure, function, and histology of the bone marrow. *Toxicol Pathol*. 34:548-565.

Trebak, M., L. Lemonnier, W.I. DeHaven, B.J. Wedel, G.S. Bird, and J.W. Putney, Jr. 2009. Complex functions of phosphatidylinositol 4,5-bisphosphate in regulation of TRPC5 cation channels. *Pflugers Arch*. 457:757-769.

Tsuchiya, M., Y. Hara, M. Okuda, K. Itoh, R. Nishioka, A. Shiomi, K. Nagao, M. Mori, Y. Mori, J. Ikenouchi, R. Suzuki, M. Tanaka, T. Ohwada, J. Aoki, M. Kanagawa, T. Toda, Y. Nagata, R. Matsuda, Y. Takayama, M. Tominaga, and M. Umeda. 2018. Cell surface flip-flop of phosphatidylserine is critical for PIEZO1-mediated myotube formation. *Nature communications*. 9:2049.

Tycko, R. 2001. Biomolecular solid state NMR: advances in structural methodology and applications to peptide and protein fibrils. *Annu Rev Phys Chem*. 52:575-606.

Tyteca, D., L. D'Auria, P.V. Der Smissen, T. Medts, S. Carpentier, J.C. Monbaliu, P. de Diesbach, and P.J. Courtoy. 2010a. Three unrelated sphingomyelin analogs spontaneously cluster into plasma membrane micrometric domains. *Biochim Biophys Acta*. 1798:909-927.

Tyteca, D., L. D'Auria, P. Van Der Smissen, T. Medts, S. Carpentier, J.C. Monbaliu, P. de Diesbach, and P.J. Courtoy. 2010d. Three unrelated sphingomyelin analogs spontaneously cluster into plasma membrane micrometric domains. *Biochimica et biophysica acta*. 1798:909-927.

Ufret-Vincenty, C.A., R.M. Klein, M.D. Collins, M.G. Rosasco, G.Q. Martinez, and S.E. Gordon. 2015. Mechanism for phosphoinositide selectivity and activation of TRPV1 ion channels. *J Gen Physiol*. 145:431-442.

Ufret-Vincenty, C.A., R.M. Klein, L. Hua, J. Angueyra, and S.E. Gordon. 2011. Localization of the PIP2 sensor of TRPV1 ion channels. *The Journal of biological chemistry*. 286:9688-9698.

Ulker, P., L. Sati, C. Celik-Ozenci, H.J. Meiselman, and O.K. Baskurt. 2009. Mechanical stimulation of nitric oxide synthesizing mechanisms in erythrocytes. *Biorheology*. 46:121-132.

van Klompenburg, W., I. Nilsson, G. von Heijne, and B. de Kruijff. 1997. Anionic phospholipids are determinants of membrane protein topology. *The EMBO journal*. 16:4261-4266.

van Meer, G., and A.I. de Kroon. 2011. Lipid map of the mammalian cell. *Journal of cell science*. 124:5-8.

van Meer, G., and K. Simons. 1988. Lipid polarity and sorting in epithelial cells. *Journal of cellular biochemistry*. 36:51-58.

van Meer, G., D.R. Voelker, and G.W. Feigenson. 2008. Membrane lipids: where they are and how they behave. *Nature reviews. Molecular cell biology*. 9:112-124.

van Wijk, R., and W.W. van Solinge. 2005. The energy-less red blood cell is lost: erythrocyte enzyme abnormalities of glycolysis. *Blood*. 106:4034-4042.

van Zwieten, R., A.J. Verhoeven, and D. Roos. 2014. Inborn defects in the antioxidant systems of human red blood cells. *Free Radic Biol Med*. 67:377-386.

Vanderheyden, V., B. Devogelaere, L. Missiaen, H. De Smedt, G. Bultynck, and J.B. Parys. 2009. Regulation of inositol 1,4,5-trisphosphate-induced Ca2+ release by reversible phosphorylation and dephosphorylation. *Biochimica et biophysica acta*. 1793:959-970.

Veatch, S.L., and S.L. Keller. 2005. Seeing spots: complex phase behavior in simple membranes. *Biochimica et biophysica acta*. 1746:172-185.

Vemuri, R., and K.D. Philipson. 1988. Phospholipid composition modulates the Na+-Ca2+ exchange activity of cardiac sarcolemma in reconstituted vesicles. *Biochimica et biophysica acta*. 937:258-268.

Venkatachalam, K., F. Zheng, and D.L. Gill. 2003. Regulation of canonical transient receptor potential (TRPC) channel function by diacylglycerol and protein kinase C. *The Journal of biological chemistry*. 278:29031-29040.

Vicidomini, G., H. Ta, A. Honigmann, V. Mueller, M.P. Clausen, D. Waithe, S. Galiani, E. Sezgin, A. Diaspro, S.W. Hell, and C. Eggeling. 2015. STED-FLCS: An Advanced Tool to Reveal Spatiotemporal Heterogeneity of Molecular Membrane Dynamics. *Nano Lett*. 15:5912-5918.

Visser, D., M. Langeslag, K.M. Kedziora, J. Klarenbeek, A. Kamermans, F.D. Horgen, A. Fleig, F.N. van Leeuwen, and K. Jalink. 2013. TRPM7 triggers Ca2+ sparks and invadosome formation in neuroblastoma cells. *Cell Calcium*. 54:404-415.

Vitturi, D.A., C.W. Sun, V.M. Harper, B. Thrash-Williams, N. Cantu-Medellin, B.K. Chacko, N. Peng, Y. Dai, J.M. Wyss, T. Townes, and R.P. Patel. 2013. Antioxidant functions for the hemoglobin beta93 cysteine residue in erythrocytes and in the vascular compartment in vivo. *Free Radic Biol Med*. 55:119-129.

von Heijne, G. 2006. Membrane-protein topology. *Nature reviews. Molecular cell biology*. 7:909-918.

Wagner, C.A. 2009. Hydrogen sulfide: a new gaseous signal molecule and blood pressure regulator. *J Nephrol*. 22:173-176.

Walder, J.A., R. Chatterjee, T.L. Steck, P.S. Low, G.F. Musso, E.T. Kaiser, P.H. Rogers, and A. Arnone. 1984. The interaction of hemoglobin with the cytoplasmic domain of band 3 of the human erythrocyte membrane. *The Journal of biological chemistry*. 259:10238-10246.

Walsh, C.M., M. Chvanov, L.P. Haynes, O.H. Petersen, A.V. Tepikin, and R.D. Burgoyne. 2009. Role of phosphoinositides in STIM1 dynamics and store-operated calcium entry. *The Biochemical journal*. 425:159-168.

Wan, J., A.M. Forsyth, and H.A. Stone. 2011. Red blood cell dynamics: from cell deformation to ATP release. *Integr Biol (Camb)*. 3:972-981.

Wan, J., W.D. Ristenpart, and H.A. Stone. 2008. Dynamics of shear-induced ATP release from red blood cells. *Proceedings of the National Academy of Sciences of the United States of America*. 105:16432-16437.

Wang, H.W., and J.W. Wang. 2017. How cryo-electron microscopy and X-ray crystallography complement each other. *Protein Sci*. 26:32-39.

Wang, Y., X. Deng, S. Mancarella, E. Hendron, S. Eguchi, J. Soboloff, X.D. Tang, and D.L. Gill. 2010. The calcium store sensor, STIM1, reciprocally controls Orai and CaV1.2 channels. *Science*. 330:105-109.

Wassenaar, T.A., H.I. Ingolfsson, R.A. Bockmann, D.P. Tieleman, and S.J. Marrink. 2015. Computational Lipidomics with insane: A Versatile Tool for Generating Custom Membranes for Molecular Simulations. *J Chem Theory Comput*. 11:2144-2155.

Wassenaar, T.A., K. Pluhackova, R.A. Bockmann, S.J. Marrink, and D.P. Tieleman. 2014. Going Backward: A Flexible Geometric Approach to Reverse Transformation from Coarse Grained to Atomistic Models. *J Chem Theory Comput*. 10:676-690.

Waugh, S.M., and P.S. Low. 1985. Hemichrome binding to band 3: nucleation of Heinz bodies on the erythrocyte membrane. *Biochemistry*. 24:34-39.

Wei, C., X. Wang, M. Chen, K. Ouyang, L.S. Song, and H. Cheng. 2009. Calcium flickers steer cell migration. *Nature*. 457:901-905.

Weiss, G., T. Houston, S. Kastner, K. Johrer, K. Grunewald, and J.H. Brock. 1997. Regulation of cellular iron metabolism by erythropoietin: activation of iron-

regulatory protein and upregulation of transferrin receptor expression in erythroid cells. *Blood*. 89:680-687.

Wettschureck, N., and S. Offermanns. 2005. Mammalian G proteins and their cell type specific functions. *Physiol Rev*. 85:1159-1204.

White, S.H., and G. von Heijne. 2005. Do protein-lipid interactions determine the recognition of transmembrane helices at the ER translocon? *Biochemical Society transactions*. 33:1012-1015.

Williams, A.J., D.J. West, and R. Sitsapesan. 2001. Light at the end of the Ca(2+)-release channel tunnel: structures and mechanisms involved in ion translocation in ryanodine receptor channels. *Q Rev Biophys*. 34:61-104.

Wlodawer, A., J.P. Segrest, B.H. Chung, R. Chiovetti, Jr., and J.N. Weinstein. 1979. High-density lipoprotein recombinants: evidence for a bicycle tire micelle structure obtained by neutron scattering and electron microscopy. *FEBS letters*. 104:231-235.

Wolf, M.G., M. Hoefling, C. Aponte-Santamaria, H. Grubmuller, and G. Groenhof. 2010. g_membed: Efficient insertion of a membrane protein into an equilibrated lipid bilayer with minimal perturbation. *J Comput Chem*. 31:2169-2174.

Woo, D.H., S.J. Jung, M.H. Zhu, C.K. Park, Y.H. Kim, S.B. Oh, and C.J. Lee. 2008. Direct activation of transient receptor potential vanilloid 1(TRPV1) by diacylglycerol (DAG). *Mol Pain*. 4:42.

Wu, G., Z.H. Lu, J. Wang, Y. Wang, X. Xie, M.F. Meyenhofer, and R.W. Ledeen. 2005. Enhanced susceptibility to kainate-induced seizures, neuronal apoptosis, and death in mice lacking gangliotetraose gangliosides: protection with LIGA 20, a membrane-permeant analog of GM1. *J Neurosci*. 25:11014-11022.

Wu, G., X. Xie, Z.H. Lu, and R.W. Ledeen. 2009. Sodium-calcium exchanger complexed with GM1 ganglioside in nuclear membrane transfers calcium from nucleoplasm to endoplasmic reticulum. *Proceedings of the National Academy of Sciences of the United States of America*. 106:10829-10834.

Wu, J., A.H. Lewis, and J. Grandl. 2017. Touch, Tension, and Transduction - The Function and Regulation of Piezo Ion Channels. *Trends in biochemical sciences*. 42:57-71.

Wu, L., C.S. Bauer, X.G. Zhen, C. Xie, and J. Yang. 2002. Dual regulation of voltage-gated calcium channels by PtdIns(4,5)P2. *Nature*. 419:947-952.

Wu, M.M., J. Buchanan, R.M. Luik, and R.S. Lewis. 2006. Ca2+ store depletion causes STIM1 to accumulate in ER regions closely associated with the plasma membrane. *The Journal of cell biology*. 174:803-813.

Xia, F., L. Xie, A. Mihic, X. Gao, Y. Chen, H.Y. Gaisano, and R.G. Tsushima. 2008. Inhibition of cholesterol biosynthesis impairs insulin secretion and voltage-

gated calcium channel function in pancreatic beta-cells. *Endocrinology*. 149:5136-5145.

Xie, B., P.M. Nguyen, A. Gucek, A. Thonig, S. Barg, and O. Idevall-Hagren. 2016. Plasma Membrane Phosphatidylinositol 4,5-Bisphosphate Regulates Ca(2+)-Influx and Insulin Secretion from Pancreatic beta Cells. *Cell Chem Biol*. 23:816-826.

Xu, S.Z., K. Muraki, F. Zeng, J. Li, P. Sukumar, S. Shah, A.M. Dedman, P.K. Flemming, D. McHugh, J. Naylor, A. Cheong, A.N. Bateson, C.M. Munsch, K.E. Porter, and D.J. Beech. 2006. A sphingosine-1-phosphate-activated calcium channel controlling vascular smooth muscle cell motility. *Circ Res*. 98:1381-1389.

Yamamoto, N., T. Matsubara, T. Sato, and K. Yanagisawa. 2008. Age-dependent high-density clustering of GM1 ganglioside at presynaptic neuritic terminals promotes amyloid beta-protein fibrillogenesis. *Biochimica et biophysica acta*. 1778:2717-2726.

Yan, R., S. Moon, S.J. Kenny, and K. Xu. 2018. Spectrally Resolved and Functional Super-resolution Microscopy via Ultrahigh-Throughput Single-Molecule Spectroscopy. *Acc Chem Res*. 51:697-705.

Yanez-Mo, M., O. Barreiro, M. Gordon-Alonso, M. Sala-Valdes, and F. Sanchez-Madrid. 2009. Tetraspanin-enriched microdomains: a functional unit in cell plasma membranes. *Trends in cell biology*. 19:434-446.

Yang, L., D.A. Andrews, and P.S. Low. 2000. Lysophosphatidic acid opens a Ca(++) channel in human erythrocytes. *Blood*. 95:2420-2425.

Yao, W., Z. Wen, Z. Yan, D. Sun, W. Ka, L. Xie, and S. Chien. 2001. Low viscosity Ektacytometry and its validation tested by flow chamber. *J Biomech*. 34:1501-1509.

Yaqoob, P., and S.R. Shaikh. 2010. The nutritional and clinical significance of lipid rafts. *Curr Opin Clin Nutr Metab Care*. 13:156-166.

Yaradanakul, A., S. Feng, C. Shen, V. Lariccia, M.J. Lin, J. Yang, T.M. Kang, P. Dong, H.L. Yin, J.P. Albanesi, and D.W. Hilgemann. 2007. Dual control of cardiac Na+ Ca2+ exchange by PIP(2): electrophysiological analysis of direct and indirect mechanisms. *J Physiol*. 582:991-1010.

Yeagle, P.L. 2014. Non-covalent binding of membrane lipids to membrane proteins. *Biochimica et biophysica acta*. 1838:1548-1559.

Yechiel, E., and M. Edidin. 1987. Micrometer-scale domains in fibroblast plasma membranes. *The Journal of cell biology*. 105:755-760.

Yin, J., and W.M. Kuebler. 2010. Mechanotransduction by TRP channels: general concepts and specific role in the vasculature. *Cell Biochem Biophys*. 56:1-18.

Yoshida, T., and S.S. Shevkoplyas. 2010. Anaerobic storage of red blood cells. *Blood Transfus*. 8:220-236.

Yoshida, Y., and S. Imai. 1997. Structure and function of inositol 1,4,5-trisphosphate receptor. *Jpn J Pharmacol*. 74:125-137.

Yu, S.P., and D.W. Choi. 1997. Na(+)-Ca2+ exchange currents in cortical neurons: concomitant forward and reverse operation and effect of glutamate. *Eur J Neurosci*. 9:1273-1281.

Yu, S.P., C.H. Yeh, S.L. Sensi, B.J. Gwag, L.M. Canzoniero, Z.S. Farhangrazi, H.S. Ying, M. Tian, L.L. Dugan, and D.W. Choi. 1997. Mediation of neuronal apoptosis by enhancement of outward potassium current. *Science*. 278:114-117.

Yule, D.I., M.J. Betzenhauser, and S.K. Joseph. 2010. Linking structure to function: Recent lessons from inositol 1,4,5-trisphosphate receptor mutagenesis. *Cell Calcium*. 47:469-479.

Zachowski, A., and P.F. Devaux. 1990. Transmembrane movements of lipids. *Experientia*. 46:644-656.

Zaidi, A. 2010. Plasma membrane Ca-ATPases: Targets of oxidative stress in brain aging and neurodegeneration. *World J Biol Chem*. 1:271-280.

Zaidi, A., M. Adewale, L. McLean, and P. Ramlow. 2018. The plasma membrane calcium pumps-The old and the new. *Neurosci Lett*. 663:12-17.

Zamponi, G.W., J. Striessnig, A. Koschak, and A.C. Dolphin. 2015. The Physiology, Pathology, and Pharmacology of Voltage-Gated Calcium Channels and Their Future Therapeutic Potential. *Pharmacol Rev*. 67:821-870.

Zarychanski, R., V.P. Schulz, B.L. Houston, Y. Maksimova, D.S. Houston, B. Smith, J. Rinehart, and P.G. Gallagher. 2012. Mutations in the mechanotransduction protein PIEZO1 are associated with hereditary xerocytosis. *Blood*. 120:1908-1915.

Zeng, F., S.Z. Xu, P.K. Jackson, D. McHugh, B. Kumar, S.J. Fountain, and D.J. Beech. 2004. Human TRPC5 channel activated by a multiplicity of signals in a single cell. *J Physiol*. 559:739-750.

Zhang, B., J.S. Naik, N.L. Jernigan, B.R. Walker, and T.C. Resta. 2018. Reduced membrane cholesterol after chronic hypoxia limits Orai1-mediated pulmonary endothelial Ca(2+) entry. *Am J Physiol Heart Circ Physiol*. 314:H359-H369.

Zhang, J., Y. Zhao, J. Duan, F. Yang, and X. Zhang. 2005. Gangliosides activate the phosphatase activity of the erythrocyte plasma membrane Ca2+-ATPase. *Arch Biochem Biophys*. 444:1-6.

Zhang, R., C. Zhang, Q. Zhao, and D. Li. 2013. Spectrin: structure, function and disease. *Sci China Life Sci*. 56:1076-1085.

Zhao, Y., X. Fan, F. Yang, and X. Zhang. 2004. Gangliosides modulate the activity of the plasma membrane Ca(2+)-ATPase from porcine brain synaptosomes. *Arch Biochem Biophys*. 427:204-212.

Zheng, L., P.B. Stathopulos, R. Schindl, G.Y. Li, C. Romanin, and M. Ikura. 2011. Auto-inhibitory role of the EF-SAM domain of STIM proteins in store-operated

calcium entry. *Proceedings of the National Academy of Sciences of the United States of America*. 108:1337-1342.

Zheng, Y., J. Nguyen, C. Wang, and Y. Sun. 2013. Electrical measurement of red blood cell deformability on a microfluidic device. *Lab Chip*. 13:3275-3283.

Zhou, Y., P. Meraner, H.T. Kwon, D. Machnes, M. Oh-hora, J. Zimmer, Y. Huang, A. Stura, A. Rao, and P.G. Hogan. 2010. STIM1 gates the store-operated calcium channel ORAI1 in vitro. *Nat Struct Mol Biol*. 17:112-116.

Ziman, A.P., C.W. Ward, G.G. Rodney, W.J. Lederer, and R.J. Bloch. 2010. Quantitative measurement of Ca(2)(+) in the sarcoplasmic reticulum lumen of mammalian skeletal muscle. *Biophysical journal*. 99:2705-2714.

Zoghbi, M.E., and G.A. Altenberg. 2017. Membrane protein reconstitution in nanodiscs for luminescence spectroscopy studies. *Nanotechnology Reviews*. 6.

Annexes

Annex 1: Cholesterol segregates into submicrometric domains at the living erythrocyte membrane: evidence and regulation

M. Carquin[1], **L. Conrard**[1], H. Pollet[1], P. Van Der Smissen[1], A. Cominelli[1], M. Veiga-da-Cunha[2], P.J. Courtoy[1], D. Tyteca[1]

[1]CELL Unit and [2]Laboratory of physiological chemistry, de Duve Institute & Université catholique de Louvain, 1200 Brussels, Belgium

Abstract

Although cholesterol is essential for membrane fluidity and deformability, the level of its lateral heterogeneity at the plasma membrane of living cells is poorly understood due to lack of appropriate probe. We here report on the usefulness of the D4 fragment of Clostridium perfringens toxin fused to mCherry (theta*), as specific, non-toxic, sensitive and quantitative cholesterol-labeling tool, using erythrocyte flat membrane. By confocal microscopy, theta* labels cholesterol-enriched submicrometric domains in coverslip-spread but also gel-suspended (non-stretched) fresh erythrocytes, suggesting in vivo relevance. Cholesterol domains on spread erythrocytes are stable in time and space, restricted by membrane:spectrin anchorage via 4.1R complexes, and depend on temperature and sphingomyelin, indicating combined regulation by extrinsic membrane:cytoskeleton interaction and by intrinsic lipid packing. Cholesterol domains partially co-localize with BODIPY-sphingomyelin-enriched domains. In conclusion, we show that theta* is a useful vital probe to study cholesterol organization and demonstrate that cholesterol forms submicrometric domains in living cells.

Cell Mol Life Sci. 2015 Dec;72(23):4633-51.

DOI 10.1007/s00018-015-1951-x

Annex 2: Contribution of plasma membrane lipid domains to red blood cell (re)shaping

C. Leonard[1,2], **L. Conrard**[2], M. Guthmann[2], H. Pollet[2], M. Carquin[2], C. Vermylen[3], P. Gailly[4], P. Van Der Smissen[2], M-P. Mingeot-Leclercq[1], D. Tyteca[2]

[1] FACM Unit, Louvain Drug Research Institute & Université catholique de Louvain, 1200 Brussels, Belgium [2] CELL Unit, de Duve Institute & Université catholique de Louvain, 1200 Brussels, Belgium [3] PEDI Unit, Institut de Recherche expérimentale et clinique & Université catholique de Louvain, 1200 Brussels, Belgium [4] CEMO Unit, Institute of Neuroscience & Université catholique de Louvain, 1200 Brussels, Belgium

Abstract

Although lipid domains have been evidenced in several living cell plasma membranes, their roles remain largely unclear. We here investigated whether they could contribute to function-associated cell (re)shaping. To address this question, we used erythrocytes as cellular model since they (i) exhibit a specific biconcave shape, allowing for reversible deformation in blood circulation, which is lost by membranevesiculation upon aging; and (ii) display at their outer plasma membrane leaflet two types of submicrometric domains differently enriched in cholesterol and sphingomyelin. We here reveal the specific association of cholesterol- and sphingomyelin-enriched domains with distinct curvature areas of the erythrocyte biconcave membrane. Upon erythrocyte deformation, cholesterol-enriched domains gathered in high curvature areas. In contrast, sphingomyelin-enriched domains increased in abundance upon calcium efflux during shape restoration. Upon erythrocyte storage at 4 °C (to mimick aging), lipid domains appeared as specific vesiculation sites. Altogether, our data indicate that lipiddomains could contribute to erythrocyte function-associated (re)shaping.

Sci Rep. 2017 Jun 27;7(1):4264.

DOI: 10.1038/s41598-017-04388-z.

Annex 3: Plasma Membrane Lipid Domains as Platforms for Vesicle Biogenesis and Shedding?

H. Pollet**, L. Conrard**, A-S. Cloos and D. Tyteca

CELL Unit, de Duve Institute & Université Catholique de Louvain, UCL B1.75.05, Avenue Hippocrate, 75, B-1200 Brussels, Belgium;

Abstract

Extracellular vesicles (EVs) contribute to several pathophysiological processes and appear as emerging targets for disease diagnosis and therapy. However, successful translation from bench to bedside requires deeper understanding of EVs, in particular their diversity, composition, biogenesis and shedding mechanisms. In this review, we focus on plasma membrane-derived microvesicles (MVs), far less appreciated than exosomes. We integrate documented mechanisms involved in MV biogenesis and shedding, focusing on the red blood cell as a model. We then provide a perspective for the relevance of plasma membrane lipid composition and biophysical properties in microvesiculation on red blood cells but also platelets, immune and nervous cells as well as tumor cells. Although only a few data are available in this respect, most of them appear to converge to the idea that modulation of plasma membrane lipid content, transversal asymmetry and lateral heterogeneity in lipid domains may play a significant role in the vesiculation process. We suggest that lipid domains may represent platforms for inclusion/exclusion of membrane lipids and proteins into MVs and that MVs could originate from distinct domains during physiological processes and disease evolution.

Biomolecules 2018 Sep 14;8(3). pii: E94.

DOI: 10.3390/biom8030094.